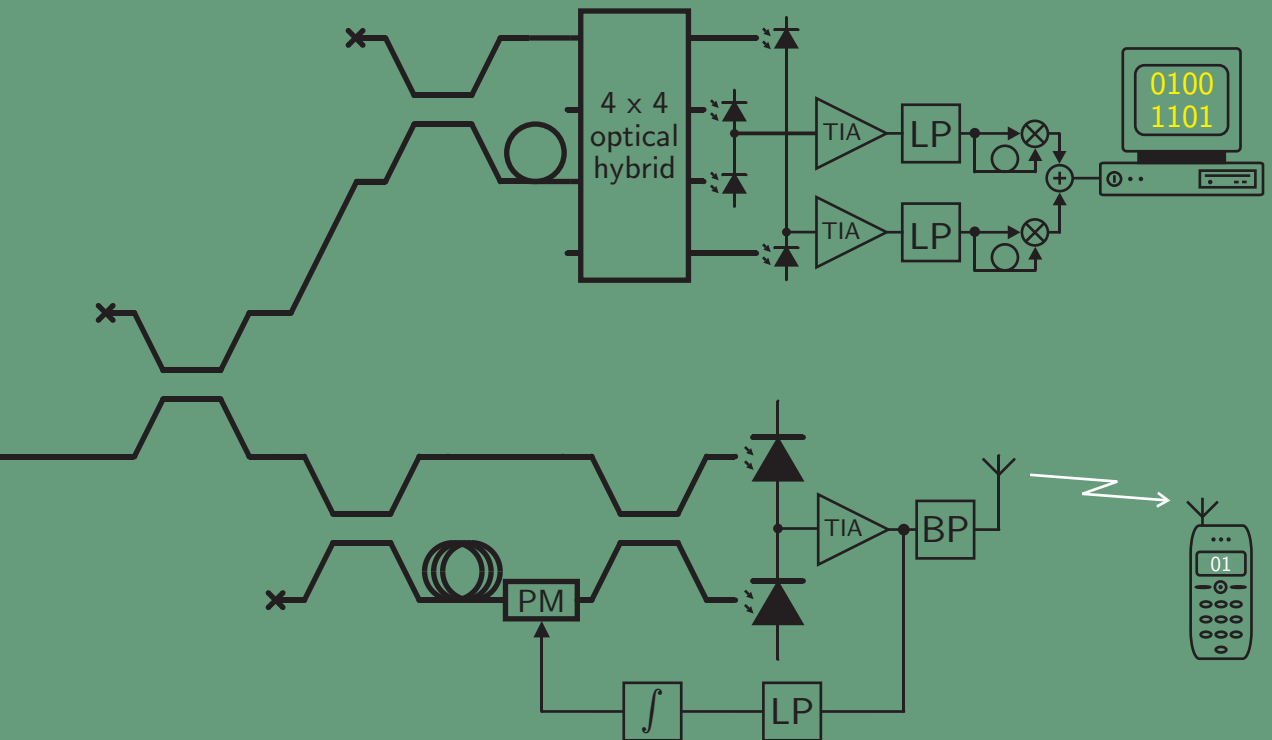
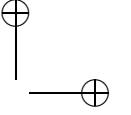
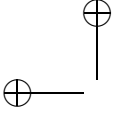


Coherence multiplexing for optical communication systems

Arjan
Meijerink



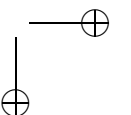
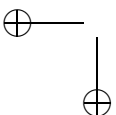


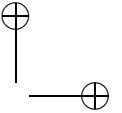
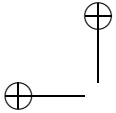


COHERENCE MULTIPLEXING FOR OPTICAL COMMUNICATION SYSTEMS

by

Arjan Meijerink





Samenstelling van de promotiecommissie:

Voorzitter & secretaris:

Prof.dr.ir. A.J. Mouthaan

Promotor:

Prof.dr.ir. W. van Etten

Assistent-promotor:

Ir. G.H.L.M. Heideman

Interne leden:

Prof.dr.ir. J.C. Haartsen (Tevens Ericsson Telecommunicatie B.V.)

Prof.dr. A. Driessen

Prof.ir. A.C. van Bochove (Tevens KPN Telecom)

Externe leden:

Prof.dr.ir. A.-J. van der Veen (Technische Universiteit Delft)

Prof.dr.ir. G. Morthier (Universiteit Gent)



Het onderzoek beschreven in dit proefschrift is uitgevoerd in de leerstoel Telecommunication Engineering, die deel uitmaakt van de Faculteit Elektrotechniek, Wiskunde en Informatica aan de Universiteit Twente, Enschede.



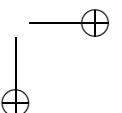
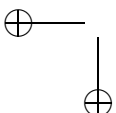
De promotieplaats van de auteur is mede gefinancierd door Philips Research, Eindhoven.

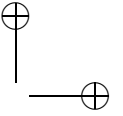
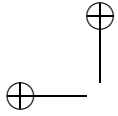
Copyright © 2005 by Arjan Meijerink

All rights reserved. No part of this publication may be reproduced, stored in a retrieval system, or transmitted, in any form or by any means, electronic, mechanical, photocopying, recording, or otherwise, without the prior written consent of the copyright owner.

ISBN: 90-365-2263-3

Printed by Wöhrmann Print Service, Zutphen, The Netherlands
Typeset in L^AT_EX 2_ε





COHERENCE MULTIPLEXING FOR
OPTICAL COMMUNICATION SYSTEMS

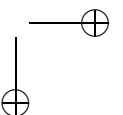
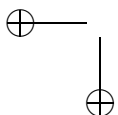
PROEFSCHRIFT

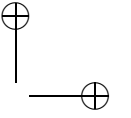
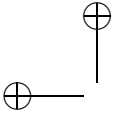
ter verkrijging van
de graad van doctor aan de Universiteit Twente,
op gezag van de rector magnificus,
prof.dr. W.H.M. Zijm,
volgens besluit van het College voor Promoties
in het openbaar te verdedigen
op vrijdag 11 november 2005 om 15.00 uur

door

Arjan Meijerink

geboren op 24 december 1976
te Almelo

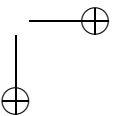
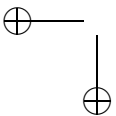


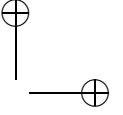
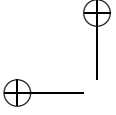


Dit proefschrift is goedgekeurd door:

De promotor: Prof.dr.ir. W. van Etten

De assistent-promotor: Ir. G.H.L.M. Heideman





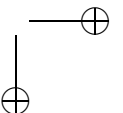
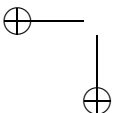
Summary

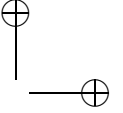
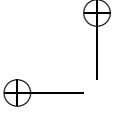
Overcapacity in core networks and increasing demands of end users have led to a shift of focus in optical communication research in the last few years. There is more interest now in relatively short-range networks such as subscriber networks, LANs, and optical interconnects. An essential criterion is low costs per user which can, for example, be achieved by multiplexing information signals of different users in a common fiber.

Coherence multiplexing (CM) is an interesting optical code division multiplexing technique, particularly from a cost point of view. It uses relatively simple optical sources like LEDs or SLEDs, and simple planar optical circuits consisting of Mach-Zehnder interferometers (MZIs).

A CM transmitter launches two mutually delayed versions of a broad band light wave into the fiber. One wave acts as reference whereas the other is modulated by an information signal. The mutual delay is much larger than the optical coherence time, so that the light waves are mutually incoherent and do not interfere. Therefore, the information signal does not become visible as an intensity modulation of the total transmitted signal. The information signal can be detected in the receiver by combining the received signal with its delayed version, by means of another MZI. A modulated wave interferes with a reference wave only if the delay in transmitter and receiver are identical. Hence, the relation between the delays in a transmitter-receiver pair determines whether or not the corresponding information signal is demodulated. The detected signal is disturbed by interferometric noise, shot noise, and thermal receiver noise.

Optical signals generated in this manner can be multiplexed by means of a passive coupler, resulting in the so-called parallel array (PA). An interesting alternative is the single intrinsic reference ladder (SIRL) system, which uses a common source. A relatively high-power version of the source signal is transmitted as a reference whereas multiple modulated versions are sent with different delays with respect to the reference. A third option that has been studied is the so-called discontinuous series (DS) system in which the channels are generated by means of a common optical source and serially cascaded MZIs. The three topologies differ mainly in performance and flexibility with respect to transmitter localization.



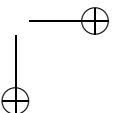
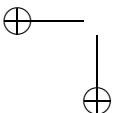


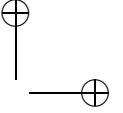
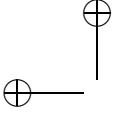
Optical detection at the output(s) of the MZI in a CM receiver can be achieved either by means of a single photodiode or a balanced photodiode pair. The latter results in a significantly better performance. Moreover, it enables the phase modulation (PSK) in the transmitter to be replaced by intensity modulation (OOK). In both cases, significant fluctuation of the demodulated signal amplitude can occur due to differences between the delays in a matched transmitter-receiver pair, even for differences in the order of the optical wavelength. Known techniques for combating this problem are optical phase synchronization by means of a feedback loop and frequency dithering, and self-heterodyne detection by means of an optical frequency shifter. Furthermore it has been shown, both by analysis and simulation, that the output signal can be stabilized by means of phase diversity. This detection principle can be combined with OOK or differential PSK (DPSK) modulation. Binary DPSK turns out to give the best performance.

A particular disadvantage of CM is that the broadband optical signals are sensitive to chromatic dispersion (CD) in the transmission fiber, resulting in a distortion of the received signal. The significance of this effect depends on the optical center wavelength and is minimal at 1310 nm in case of standard single-mode fiber. Calculation has shown that—in cases when CD causes significant distortion—the performance can be improved by using QPSK instead of binary PSK. The performance can be further enhanced by means of electrical and/or optical equalization.

Apart from digital transmission, CM can also be used for (analog) RF signal distribution. Multiple RF channels can be multiplexed through one CM channel by means of subcarrier multiplexing. If this is realized by multiplexing RF signals in the electrical domain prior to transmitting them through the same CM channel by means of a single coherence multiplexer, the number of RF channels per CM channel and the resulting signal-to-noise ratio will be limited by intermodulation distortion. The same stabilization techniques as used for digital transmission can possibly be used for microwave signal distribution. However, this requires some adjustment, particularly in the case of subcarrier multiplexing.

Numerical examples illustrate that CM could be an interesting multiplexing technique for applications like subscriber networks, LANs and optical interconnects. However, more research needs to be done, not only at system level and on corresponding simulation techniques, but also on broadband optical sources, integrated optical circuits, electronics for optical receivers, and how to apply CM according to existing or yet to be developed transmission and/or networking standards. Despite its seeming conceptual complexity and high development costs concerning integrated circuit design, massive deployment of CM-based networks could lead to huge cost savings. Therefore, investment in further research on both technological and economical feasibility is certainly useful.





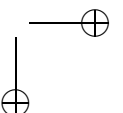
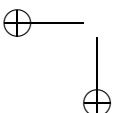
Samenvatting

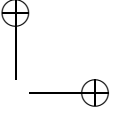
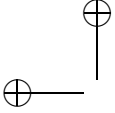
Overcapaciteit in trunks en toenemende eisen van eindgebruikers hebben de laatste jaren een verschuiving in onderzoeksinteresse op het gebied van optische communicatietechniek teweeggebracht, naar netwerken voor relatief korte afstanden, zoals abonneenetwerken, LANs en optische interconnects. Daarbij is het belangrijk de kosten per gebruiker laag te houden, bijvoorbeeld door informatiekanalen van verschillende gebruikers in één glasvezel te multiplexen.

Coherentiemultiplexen (CM) is een optische codemultiplextechniek die vanuit kostenoverwegingen in het oog springt. Hierin wordt namelijk gebruik gemaakt van relatief eenvoudige lichtbronnen als LEDs of SLEDs, en simpele planaire optische circuits bestaande uit Mach-Zehnder-interferometers (MZIs).

Daarmee worden door een CM zender twee onderling vertraagde versies van een breedbandige lichtgolf in de vezel gestuurd. Eén daarvan treedt op als referentiedraaggolf, terwijl de ander is gemoduleerd door een informatiesignaal. De onderlinge vertraging is veel groter dan de optische coherentietijd, zodat de lichtgolven onderling incoherent zijn, er dus geen interferentie optreedt, en het informatiesignaal niet als een intensiteitsmodulatie zichtbaar wordt in het totale verzonden signaal. Het informatiesignaal kan in de ontvanger al dan niet worden gedetecteerd door het ontvangen signaal door middel van een tweede MZI samen te voegen met een vertraagde versie ervan. Slechts indien de vertragingen in zender en ontvanger gelijk zijn, interfereert een gemoduleerde draaggolf met een referentiedraaggolf. Op deze wijze bepaalt de relatie tussen de vertragingen in een zender-ontvangerpaar of het bijbehorende informatiesignaal wordt gemoduleerd. Het gedetecteerde signaal wordt verstoord door interferometrische ruis, hagelruis en thermische ontvangerruis.

De aldus gegenereerde optische signalen kunnen worden samengevoegd door middel van een passieve koppelaar, resulterend in de zogenaamde parallelle array (PA). Een interessant alternatief is het SIRL-systeem, waarbij één gemeenschappelijke lichtbron wordt gebruikt. Een relatief sterke versie van het bron-signaal wordt als referentiedraaggolf verzonden, terwijl meerdere gemoduleerde versies met verschillende vertragingen ten opzichte van de referentiedraaggolf worden verstuurd. Als derde mogelijkheid is het zogenaamde DS-systeem bestudeerd, waarin de kanalen worden opgewekt door een gemeenschappelijke lichtbron en serieel gecascadeerde MZIs. De drie architecturen verschillen met name op het gebied van prestatie en flexibiliteit qua plaatsing van de zenders.



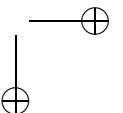
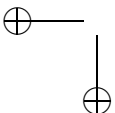


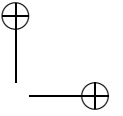
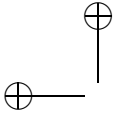
Optische detectie aan de uitgang(en) van de MZI in een CM-ontvanger kan zowel met één fotodiode als met een gebalanceerd fotodiodepaar. Deze laatste geeft een aanzienlijk betere prestatie. Bovendien kan de fasemodulatie (PSK) in de zender dan worden vervangen door intensiteitmodulatie (OOK). In beide gevallen leiden verschillen tussen de vertragingen in een gekoppeld zender-ontvangerpaar in de ordegrrootte van de optische golflengte reeds tot aanzienlijke fluctuaties in de amplitude van het gedemoduleerde signaal. Bekende technieken om dit probleem op te lossen, zijn optische fasesynchronisatie door middel van een terugkoppellus en frequentiedithering, en zelf-heterodyne detectie met behulp van een optische frequentieschuiver. Daarnaast is zowel door middel van analyse als simulatie aangetoond, dat het uitgangssignaal kan worden gestabiliseerd met behulp van faseversiteit. Dit detectieprincipe kan worden gecombineerd met OOK of differentiële PSK (DPSK) modulatie. Binnaire DPSK resulteert in de beste prestatie.

Een specifiek nadeel van CM is dat de breedbandige lichtsignalen gevoelig zijn voor chromatische dispersie (CD) in de transmissievezel, resulterende in vervorming van het ontvangen signaal. De sterkte van dit effect is afhankelijk van de centrale golflengte van de optische bron, en is voor standaard single-mode vezel minimaal bij 1310 nm. Met berekeningen is aangetoond, dat —voor het geval CD aanzienlijke vervorming veroorzaakt— de prestatie kan worden verbeterd door QPSK te gebruiken in plaats van binaire PSK. De prestatie kan verder worden verbeterd door middel van elektronische en/of optische egalitatie.

Behalve voor digitale transmissie kan CM ook worden gebruikt voor het distribueren van (analoge) RF-signalen. Er kunnen zelfs meerdere RF-kanalen in één CM-kanaal worden samengevoegd door middel van subdraaggolfmultiplexen. Indien dit is gerealiseerd door de RF-signalen eerst te multiplexen in het elektrische domein en vervolgens door middel van één coherentmultiplexer op hetzelfde CM-kanaal te versturen, wordt het aantal RF-kanalen per CM-kanaal en de uiteindelijke signaal-ruisverhouding echter beperkt door intermodulatiestorsie. Dezelfde stabilisatietechnieken als bij digitale transmissie kunnen mogelijk ook bij microgolfdistributie worden toegepast, maar vereisen enige aanpassing, met name in het geval van subdraaggolfmultiplexen.

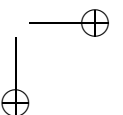
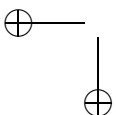
Numerieke voorbeelden laten zien, dat CM een interessante multiplexetechniek voor toepassingen als abonneenetwerken, LANs en optische interconnects zou kunnen zijn. Er dient echter meer onderzoek te worden gedaan, niet alleen op systeemniveau en naar bijbehorende simulatietechnieken, maar ook op het gebied van breedbandige lichtbronnen, geïntegreerde optische circuits, elektronica voor optische ontvangers en toepassing van CM binnen bestaande of nog te ontwerpen transmissie- en/of netwerkstandaarden. Ondanks haar schijnbare conceptuele complexiteit en hoge ontwikkelkosten op het gebied van geïntegreerd circuitontwerp, zou grootschalige toepassing van CM tot enorme kostenbesparingen kunnen leiden. Investing in verder onderzoek naar zowel de technische als economische haalbaarheid is daarom zeker zinvol.

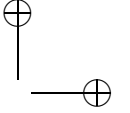
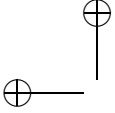




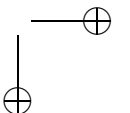
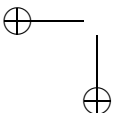
Contents

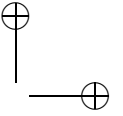
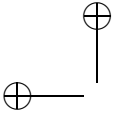
Summary	v
Samenvatting	vii
1 Introduction	1
1.1 Optical fiber communication	1
1.2 The “last mile” problem	2
1.3 Optical interconnects	3
1.4 Optical multiplexing schemes	4
1.4.1 Wavelength Division Multiplexing (WDM)	5
1.4.2 Time Division Multiplexing (TDM)	5
1.4.3 Subcarrier multiplexing (SCM)	6
1.4.4 Optical Code Division Multiplexing (OCDM)	7
1.5 Coherence multiplexing (CM)	9
1.5.1 The original idea	10
1.5.2 Some extensions to the original idea	11
1.5.3 Advantages and disadvantages	12
1.6 Research objective	14
1.7 Outline of the thesis	14
2 Analytical models of components	15
2.1 Introduction	15
2.2 Representation of optical signals	15
2.3 Optical sources	18
2.3.1 Thermal light model	18
2.3.2 Spectral characteristics	19
2.3.3 Gaussian spectral profile	20
2.3.4 Intensity noise	21
2.4 Optical encoders and decoders	22
2.4.1 Couplers	23
2.4.2 Delay lines	24
2.4.3 Modulators	24
2.5 Single-mode optical fiber	25
2.5.1 Attenuation	25



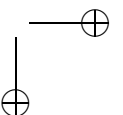
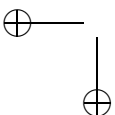


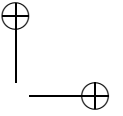
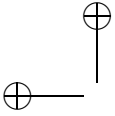
2.5.2	Dispersion	26
2.6	Photodetectors	28
2.7	Transimpedance amplifiers	30
2.8	Conclusion	31
3	Simulation tool	33
3.1	Introduction	33
3.2	Discrete-time representation of optical signals	34
3.3	LED sources	36
3.3.1	Generating white Gaussian noise	36
3.3.2	Filtering the white Gaussian noise	37
3.4	Optical encoders and decoders	41
3.5	Single-mode optical fibers	42
3.5.1	First order dispersion	42
3.5.2	Second order dispersion	46
3.6	Photodiodes	49
3.6.1	Discrete-time Poisson model	49
3.6.2	A simplified model	51
3.7	Transimpedance amplifiers	52
3.8	Conclusion	52
4	Coherence modulation and demodulation	53
4.1	Introduction	53
4.2	Optical beating	54
4.2.1	Coherent beating: interference	55
4.2.2	Incoherent beating: beat noise	57
4.2.3	Partial interference	58
4.3	Coherence modulation	60
4.4	Coherence demodulation	60
4.4.1	Single-ended detection	61
4.4.2	Balanced detection	65
4.5	Choosing the path delays	69
4.6	Noise in the receiver	71
4.7	Digital transmission	74
4.7.1	BPSK modulation	76
4.7.2	OOK modulation	78
4.8	Practical considerations	80
4.8.1	Polarization	80
4.8.2	Optical phase offset	81
4.8.3	Balancing	82
4.9	Conclusion	83



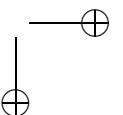
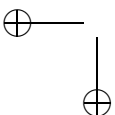


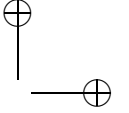
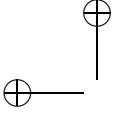
5	Coherence multiplexing topologies	85
5.1	Introduction	85
5.2	The parallel array (PA)	86
5.2.1	Multiplexed signal	86
5.2.2	Output signal of balanced receiver	88
5.2.3	Choosing the path delays	89
5.2.4	Noise performance	90
5.2.5	Digital transmission	92
5.2.6	Practical aspects	100
5.3	The single intrinsic reference ladder (SIRL) system	100
5.3.1	Multiplexed signal	100
5.3.2	Output signal of balanced receiver	102
5.3.3	Choosing the path delays	103
5.3.4	Noise performance	104
5.3.5	Digital transmission using BPSK modulation	105
5.4	The discontinuous series (DS) system	109
5.4.1	Multiplexed signal	109
5.4.2	Output signal of balanced receiver	110
5.4.3	Choosing the path delays	112
5.4.4	Noise performance	114
5.4.5	Digital transmission using BPSK modulation	115
5.5	Comparison	118
5.5.1	Modulation formats	118
5.5.2	Noise performance	119
5.5.3	Flexibility	119
5.5.4	Complexity	120
5.5.5	Balancing	121
5.5.6	Robustness	122
5.6	Conclusion	122
6	Receiver output stabilization by phase diversity	123
6.1	Introduction	123
6.2	Phase sensitivity issue	123
6.3	Existing stabilization solutions	125
6.3.1	Phase-synchronized balanced detection	125
6.3.2	Self-heterodyning	128
6.4	Phase diversity detection principles	129
6.4.1	Four-way phase diversity detection of OOK	130
6.4.2	Three-way phase diversity detection of OOK	136
6.4.3	Phase-synchronized detection of QPSK and M -ary PSK	138
6.4.4	Phase diversity detection of binary DPSK	140
6.4.5	Phase diversity detection of DQPSK and M -ary DPSK	141
6.5	Noise performance	143
6.5.1	Phase diversity detection of OOK	143
6.5.2	Four-way detection of (D)PSK	147



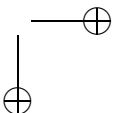
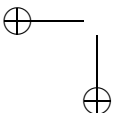


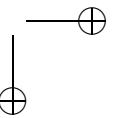
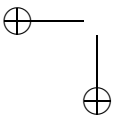
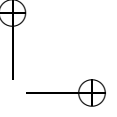
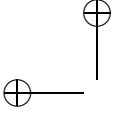
6.6	Practical considerations	152
6.6.1	Phase diversity couplers	152
6.6.2	Balancing	153
6.7	Conclusions	154
7	Chromatic fiber dispersion	155
7.1	Introduction	155
7.2	Impact of chromatic dispersion on receiver output signal	156
7.2.1	Input signal of the receiver	156
7.2.2	Expected value of the output signal of the receiver	158
7.2.3	Noise in the output signal of the receiver	162
7.3	Impact of chromatic dispersion on digital transmission	167
7.3.1	Pulse distortion	167
7.3.2	Noise variance	177
7.3.3	Phase-synchronized BPSK	179
7.3.4	Phase-synchronized OOK	182
7.3.5	Phase-synchronized M -ary PSK	182
7.4	Equalization techniques	185
7.4.1	Electrical equalization techniques	186
7.4.2	Optical equalization techniques	186
7.5	Conclusions	187
8	Radio-frequency signal distribution	189
8.1	Introduction	189
8.2	Coherence (de)multiplexing of radio-frequency signals	191
8.2.1	Phase modulation (PM)	191
8.2.2	Intensity modulation (IM)	194
8.2.3	Chromatic dispersion	195
8.2.4	Noise performance	197
8.3	Output stabilization	202
8.3.1	Phase synchronization	202
8.3.2	Self-heterodyning	202
8.3.3	Phase diversity detection	203
8.4	Subcarrier multiplexing over coherence multiplexing	210
8.4.1	Single-channel subcarrier multiplexing	211
8.4.2	Multi-channel subcarrier multiplexing	220
8.5	Conclusions	231
9	Conclusions and directions for further research	233
9.1	Conclusions	233
9.2	Directions for further research	236
9.2.1	System level research	236
9.2.2	Simulation	237
9.2.3	Broadband optical sources	239
9.2.4	Integrated optics technology	240
9.2.5	Optical receiver design	242

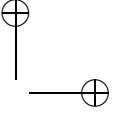
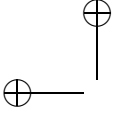




9.2.6	Transmission and networking standards	243
9.2.7	Application as wireless transmission technique	244
References		245
Appendix		
A	Doubly-stochastic Poisson processes	255
A.1	Definition	255
A.2	Expected value	256
A.3	Autocorrelation function	256
A.4	Cross-correlation function	257
B	Bit error rate analysis of phase diversity receivers	259
B.1	Noise in four-way phase diversity receivers	259
B.2	Four-way phase diversity detection of OOK	263
B.3	Four-way phase-synchronized detection of QPSK	266
B.4	Four-way phase-synchronized detection of M -ary PSK	267
B.5	Four-way phase diversity detection of binary DPSK	270
B.6	Four-way phase diversity detection of DQPSK	272
B.7	Three-way phase diversity detection of OOK	276
Acknowledgments		283
Biography		285
List of publications		287







Chapter 1

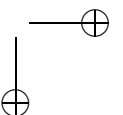
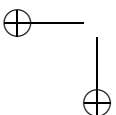
Introduction

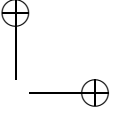
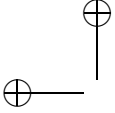
1.1 Optical fiber communication

Transmission through optical fiber cables plays an important role in the communication networks of nowadays. The main motivation for this is the enormous potential bandwidth of optical fibers (>100 THz) which is several orders of magnitude larger than the bandwidth of copper media like coaxial cables or twisted wire pairs. Other advantages of optical fiber as a transmission medium are:

- its relatively small size, weight, and bending diameter.
- low attenuation (<0.2 dB/km for standard single-mode fiber (SMF) [1]) and low dispersion, which enhances the distance between repeaters in a long-haul transmission link and hence increases reliability and decreases maintenance costs, because the resulting network requires less active components than a copper-based network;
- inherent immunity to crosstalk and electromagnetic interference (EMI), and its lack of radiation, which enhances electromagnetic compatibility (EMC), enables tight cable bundling and complicates eavesdropping;
- the absence of electrical signals, which avoids eventual fire hazard due to sparks and hence provides inherent safety;
- transparency and hence flexibility: upgrading an optical network to a higher speed and adding new services only require upgrading the transmission units, and not replacing the transmission media.

Optical fiber has therefore become the main transmission medium for long-haul telecommunication links in core networks, where expensive techniques are used to realize high bit rate transmission over large distances. Fortunately, the huge costs of these networks can be shared by a vast number of end users.





The Internet hype and the resulting telecom industry boom at the end of the nineties has actually led to such an excessive deployment of optical fibers in core networks that a considerable overcapacity has resulted. That is, the capacity that is offered by core networks is by no means fully utilized by the end users, simply because the transmission capacities of their current access connections to the core networks (the so-called “last mile”) add up to an aggregate capacity which is much lower.

1.2 The “last mile” problem

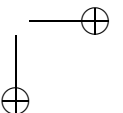
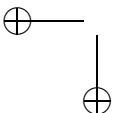
This overcapacity in core networks, combined with increasing bandwidth demands of multimedia applications that subscribers are using, has led to a clear shift of focus in optical communication research from core networks to access networks and local area networks (LANs). Most of these networks are still constituted of copper transmission media like coaxial cables (for example for cable television) or twisted wire pairs (for example for telephony, ISDN or Ethernet LANs). Although some successful effort has been spent to enhance the capacity of the existing links (for example by means of ADSL), the limited bandwidth and the dispersion of these media create a bottleneck that will disable the upgrades that are required to satisfy the increasing capacity demands in the next few decades.

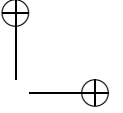
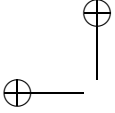
Therefore, it seems obvious to extend the trend from the wide and metropolitan area to the access and local area, and hence replace these media by optical fibers, since these offer enough potential capacity to cover all wired telecommunication services in the near future (telephony, television, Internet access, etcetera) simply through one access wire per subscriber.

Realizing this so-called Fiber-to-the-Home (FttH) is not so straightforward, however, mainly due to economical reasons. The point is that—in contrast to the core networks—each subscriber in the access and local area has to settle for his individual part of the infrastructure.

First of all, this involves installing the fiber itself. Although the price of optical fiber may be comparable to that of conventional copper media, it is the actual digging that causes it to be a drastic and costly operation, especially to subscribers in existing low-rise buildings in suburban and rural areas. On the other hand, installing optical fiber during the actual construction of new buildings is relatively inexpensive, especially in densely built urban areas with many high-rise buildings. (This has actually already been realized in many large towns in the Far East.) Consequently, the questions are not only when and how, but also where, and moreover: how to distribute the total costs. This is not only a technical and economical issue, but also a social and hence political matter.

Secondly, the equipment that is installed in the transmission nodes in optical core networks is typically not the kind of equipment that is suitable for access networks and LANs, simply because end users cannot afford to individually purchase components like the high-power, spectrally pure lasers that





are required for long-haul transmission at high bit rates. The main technical challenge for designing this kind of networks is hence to design the end nodes such that that components can be used that are way less expensive than the ones that are conventional in core networks, and to enable cost sharing as much as possible.

Moreover the maintenance costs should be limited by minimizing the number of active components like amplifiers and active switches (which are likely points of failure) and localizing them in centralized places that can easily be accessed by the operator.

A last technical challenge for such networks is to design them in such a way that they become *transparent*, so that different services can be provided independently and added or upgraded without drastically upgrading the infrastructure.

A network topology that provides transparency and component sharing without requiring active components between the operator and the subscriber area is the *passive optical network (PON)*, which is often proposed for access networks. Moreover, the PON has also proven to be a suitable topology for realizing optical LANs [2]. The PON topology is shown in Figure 1.1.

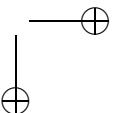
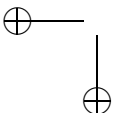
The *optical line termination (OLT)* at the left represents the operator's side, where the interface between the access network and the transport network is established. From the OLT information is transmitted in the *downlink* direction through the common optical fiber cable to a passive optical coupler, where the optical signal is divided and directed to the *optical networking units (ONUs)*, which are located at the subscribers' premises. Similarly, ONUs can send information to the OLT by transmitting signals in the *uplink* direction, which are combined in the passive optical coupler and directed to the OLT. A multiplexing scheme is required for transmission through the common fiber in both directions:

- For the downlink, the OLT needs to be able to address different messages to different ONUs simultaneously, such that each ONU recognizes its individual message;
- For the uplink, the ONUs need to be able to access the common fiber simultaneously, such that the OLT can receive all messages and distinguish between them.

Some multiplexing schemes will be discussed in Section 1.4.

1.3 Optical interconnects

Increasing speeds of digital systems have recently brought optical techniques even into the inside of digital systems, to realize high-speed communication between subsystems. Examples are communication between printed circuit boards (PCBs), between integrated circuits (ICs) on a PCB and even inside ICs. Another reason for using optical techniques in these so-called interconnects



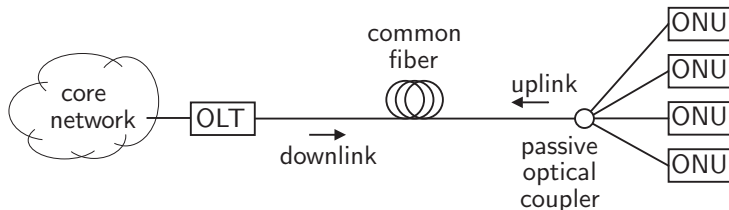


Figure 1.1: Passive optical network (PON) topology (OLT=optical line termination, ONU=optical networking unit)

is their inherent lack of radiation and immunity to electromagnetic interference (EMI), which is a significant issue in high-speed copper interconnects.

Since waveguide or fiber dispersion does not play a role in such short range applications, the electronics form the bottleneck, especially when inexpensive techniques like CMOS are to be used for optical detection [3]. Therefore, high-speed interconnects are often realized as a parallel array of multiple parallel waveguides. An alternative is to multiplex several interconnects through a common optical medium, so that the number of optical connections can be reduced, which simplifies installation.

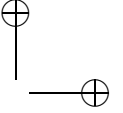
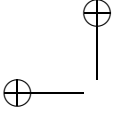
1.4 Optical multiplexing schemes

In the previous two sections the desire for optical multiplexing schemes has been motivated. That is, several communication channels (eventually created by different users) are to be transmitted through a common optical transmission medium, in such a way that different receivers can distinguish between these channels and can detect particular channels with a certain accuracy.

Optical multiplexing can have different purposes:

- to overcome bandwidth limitations of optical modulators and detectors and hence efficiently utilize the available bandwidth of the optical transmission medium, which reduces the number of required fibers in a high-speed link;
- to enable distributed users to share a common transmission medium (perform multiple access) and provide a way to distinguish between these users, but also to distinguish between services and between providers;
- to reduce the number of optical connections and hence simplify installation.

For relatively short-range applications like access networks, LANs and optical interconnects a particular criterion is that the multiplexing scheme is supposed to be realized in a relatively inexpensive way. Moreover, a desirable criterion for access networks and LANs is that the multiplexing scheme is transparent. That



is, it should impose only minimum restrictions on the format of the signals that are to be transmitted, and the channels should operate independently. The data rates are moderate (ranging from tens or hundreds of megabits per second in access networks, up to several gigabits per second in LANs and interconnects) and the link lengths are relatively low (from a few kilometers in access networks, a few hundreds of meters in LANs down to less than a meter in interconnects.)

Some multiplexing schemes will be discussed and compared in the following subsections, mainly based on the above-mentioned criteria.

1.4.1 Wavelength Division Multiplexing (WDM)

The most well-known optical multiplexing technique is Wavelength Division Multiplexing (WDM). The idea of WDM is that all data signals are transmitted simultaneously at different optical wavelengths (or colors), either by combining optical signals from separate lasers, or by spectrally slicing a broadband optical signal from for example a light emitting diode. In the receivers the channels are demultiplexed by means of optical wavelength filters like Mach-Zehnder interferometers, Fabry-Perot resonators or arrayed-waveguide gratings.

WDM is a very mature technique and has the main advantage that the available bandwidth of an optical fiber can be utilized very efficiently: total data rates of more than 1 terabit per second have been demonstrated by multiplexing 128 WDM channels with less than 1 nm channel spacing (so-called dense WDM, or DWDM [4]).

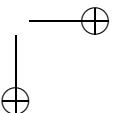
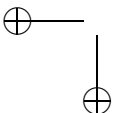
This has made DWDM the most popular technique for core networks. The main disadvantage of DWDM is that the lasers and selection filters have very strict requirements on wavelength accuracy, bandwidth, wavelength stability and wavelength selectivity. Particularly the stability of the lasers and selection filters requires them to be temperature-controlled, which involves (expensive) external electronics.

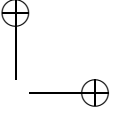
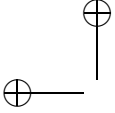
A cheaper alternative is coarse WDM (CWDM) [5] which uses 20 nm channel spacing, so that relatively broadband sources (for example vertical cavity surface-emitting lasers (VCSELs)) and filters can be used and temperature control can be omitted. However, the number of channels is then limited by the predefined wavelength grid (16 according to ITU-T recommendation G.694.2).

A general disadvantage of WDM is that a transmission node which is supposed to be able to access different channels, requires either multiple or tunable light sources and selection filters, which significantly raises the costs.

1.4.2 Time Division Multiplexing (TDM)

In case of Time Division Multiplexing (TDM) the data signals are transmitted at the same wavelength, but in different time slots, according to a certain predefined medium access mechanism. This access mechanism can be either synchronous or asynchronous.





In case of synchronous TDM the time is divided in fixed-size time slots, which are alternately assigned to the different channels in a periodic fashion. In one time slot either a single bit or a fixed-size frame of bits is transmitted. The instantaneous data rate on the common transmission medium should be at least equal to the aggregate data rate of the multiplexed channels, plus some eventual margin in order to create some guard time between the time slots. The latter is required for relaxing the requirements on the mutual timing of distributed transmitters, in cases where synchronous TDM is used for performing multiple access onto a common transmission medium, for example in a PON.

Synchronized TDM can be performed in the electrical domain or—in case the aggregate data rate exceeds the speed of the electronics—bit-based TDM can be performed in the optical domain by using (expensive) narrow laser pulse sources.

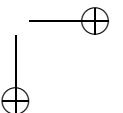
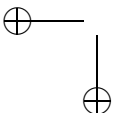
Especially electrical TDM is very simple: multiplexing can be performed in the electrical domain, so that the required optical components are simple and can be shared in case the channels are multiplexed or demultiplexed in a single node. However, strict timing between the channels is required in order to avoid crosstalk and minimize the guard bands between the time slots. This is particularly complicated when the transmitters are not localized to a single node, especially when the transmitters have different distances to the common transmission medium, so that the synchronization should take into account the differences in propagation time. Moreover, the short pulses are very sensitive to distortion due to dispersion of the transmission medium;

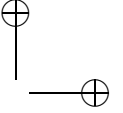
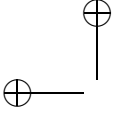
In case of asynchronous (or statistical) TDM, the data in each channel is divided in frames to which a header is added, resulting in a packet. These packets are stored in a buffer, until they are transmitted through the common transmission medium. This can either be one central buffer where the packets of all channels are collected prior to transmission, or local buffers where the packets of the individual channels are stored until the corresponding transmitter gains access to the common medium. The latter can be established either by a centralized access granting mechanism like in ATM-based PON (APON) [6] or through a certain predefined medium access protocol like Carrier Sense Multiple Access with Collision Detection (CSMA/CD) in Ethernet [7].

The main advantage of asynchronous TDM with respect to synchronous TDM is that the transmission medium can be utilized more efficiently when the transmitters are not continuously active. However, some bandwidth is still wasted on overhead (because a header is added to each packet) and eventually on retransmissions due to collisions.

1.4.3 Subcarrier multiplexing (SCM)

Another multiplexing alternative is Subcarrier Multiplexing (SCM), where multiple electrical microwave carriers are frequency-multiplexed in the electrical domain and modulated on the same optical wavelength, hence acting as subcarriers of the optical wave. These microwave carriers can be modulated in-





dependently, so they may transport different signal formats. In the receiver a particular channel is selected either by means of a microwave band-pass filter or a heterodyne receiver, in a similar way as in radio tuners.

SCM can be categorized in two forms: single-channel SCM and multi-channel SCM. In single-channel SCM one unique subcarrier is assigned to each optical transmitter, whereas in multi-channel SCM each optical transmitter may emit multiple SCM channels which are multiplexed in the electrical domain prior to modulating the optical wave.

The main advantage of SCM is that it does not require complicated optical components, because creating different channels simply requires using different frequencies in the electrical domain, and multiplexing these simply involves superposing the resulting optical signals (single-channel SCM) and eventually multiplexing the electrical signals prior to optical modulation (multi-channel SCM). Relatively inexpensive RF components are available from analog cable television (CATV) applications.

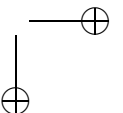
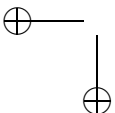
The number of SCM channels is limited, however, because of the limited modulation bandwidth of the optical sources and detectors, the limited power budget due to passive optical signal distribution, clipping, intermodulation distortion and optical beat interference (OBI) noise.

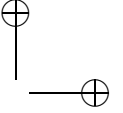
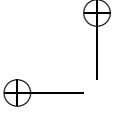
The main applications of SCM are analog CATV distribution, remote antenna feeding in wireless access systems and carrying header information in packet-switched networks.

1.4.4 Optical Code Division Multiplexing (OCDM)

In Code Division Multiplexing (CDM) the data signals are transmitted simultaneously in the same wavelength band. Channels are distinguished by means of unique codes. When coding and decoding are performed in the optical domain, we speak about Optical Code Division Multiplexing (OCDM) [8]. This optical coding can be based on any combination of spatial, temporal, frequency and polarization properties of the optical signal. A general property of OCDM schemes is that the bandwidth of the transmitted optical signals is much larger than the bandwidth of the actual data signal. This broadband encoded signal appears as noise, from which the original data signal can only be recovered if the code is known at the receiver.

Most OCDM schemes that have been proposed so far are based on optical pulse position coding (also called time-spreading). That is, each bit is represented by a short optical pulse, which is spreaded in time (encoded) to a so-called chip sequence, by means of an optical lattice filter in which the values of the tap delays are determined by a unique *signature code*. In the receiver the original data signal can be recovered by means of a decoding filter that is matched to the encoding filter: their impulse responses are time-reversed with respect to each other, such that the encoded signal is de-spread to relatively large intensity pulses that correspond to the original data signal. The signature codes are designed such that optical signals remain spread in time after



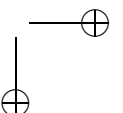
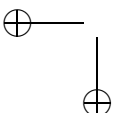


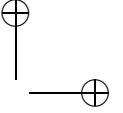
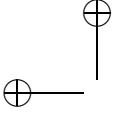
passing the decoding filter in an unmatched receiver. When the tap delays in the decoding filter are precisely matched to the tap delays in the encoding filter (within the coherence time of the sources), the pulses add up in optical field; this is called *coherent matched filtering*. In *incoherent matched filtering* the pulses add up in intensity. The advantage of coherent matched filtering is that phase coding can be performed next to pulse position coding, resulting in less sparse codes, higher performance and more channels, especially when bipolar modulation and balanced detection are performed. The disadvantage is that the tap delays in the code filters have to be matched on a wavelength scale in order to guarantee correct interference. Moreover this requires polarization matching. In both cases time-gating of the decoded pulse may be required in the detector in order to achieve the desired performance.

Some alternative OCDM schemes are based on wavelength-hopping [9–11] or spectral coding of broadband continuous-wave (CW) sources [12–20]. In fact various OCDM techniques have been published, sharing numerous similarities but also having a lot of differences. Many overview papers on OCDM schemes have been published as well (for example [8, 21–25]), mainly showing that the diversity of OCDM techniques published throughout the years hampers strict categorization.

Most OCDM schemes that have been proposed so far share the following advantages:

- Many OCDM schemes can be realized using relatively simple optical components;
- Some OCDM schemes are very robust in the sense that they are not sensitive to environmental changes like temperature drift, so that external temperature control can be omitted;
- In some OCDM schemes the channels operate asynchronously so that distributed transmitters do not need to be mutually synchronized. This facilitates a low access delay to the network (especially when time gating is not required), which is suited to bursty traffic in for example LANs;
- Channels can be added without reconfiguring the system;
- OCDM provides soft capacity: if one channel does not require a high data rate, it can leave part of its allocated bandwidth to a different channel;
- A particular channel can only be demodulated if the corresponding code is known, which provides inherent security;
- OCDM does not require active equipment in the network, which reduces maintenance costs;
- A relatively large number of codes can be supported, provided that the corresponding channels are not all active at the same time.





OCDM also has particular disadvantages:

- Unmatched channels appear to a receiver as crosstalk or optical beat interference (OBI) noise, which limits the number of channels that can be multiplexed simultaneously and the data rates that can be achieved;
- The power budget is limited because the optical power of each transmitter is passively distributed over the receivers, which limits the number of channels;
- Most OCDM schemes are based either on encoding ultra-short pulses or spectrally encoding broadband CW light, both introducing vulnerability to chromatic fiber dispersion.

Therefore, most OCDM schemes are restricted to applications with relatively short fiber lengths, moderate data rates and moderate numbers of simultaneously active channels. Especially the potentially low installation and maintenance costs seem to make OCDM particularly suitable for access networks, LANs and interconnects.

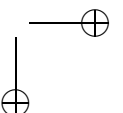
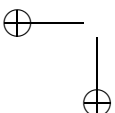
Compared to WDM, TDM and SCM, OCDM is a very immature technique, however: although many schemes have been proposed and analyzed in literature, there have been much fewer experimental verifications, let alone commercial applications. This seems to be caused by the following facts:

- Optical communication research has only recently shifted its interest to applications that OCDM seems to have particular benefits for, namely access networks, LANs and interconnects;
- Most OCDM schemes require specialized components that are currently not mature, hence not massively produced and therefore still very expensive;
- OCDM suffers from a lack of appeal due to seeming conceptual complexity, which makes companies and funding organizations hesitate to spend money on the (relative expensive) research and development of OCDM systems, subsystems and components.

The subject of this thesis is a particularly simple OCDM technique called *coherence multiplexing (CM)*, which is based on spectral coding of CW sources and coherent matched filtering. It is further introduced in the next section.

1.5 Coherence multiplexing (CM)

Coherence Multiplexing (CM) is actually the oldest known OCDM scheme. The original concept was invented in Canada in the mid seventies by Claude Delisle and Paolo Cielo [26, 27] and will be described in the next subsection. Some extensions to that will be discussed in Subsection 1.5.2. Subsection 1.5.3 will describe some advantages and disadvantages of CM with respect to the previously described multiplexing schemes.



1.5.1 The original idea

CM is based on a channel generation technique called *coherence modulation*. It is illustrated in Figure 1.2, which shows one coherence modulator (transmitter) and demodulator (receiver).

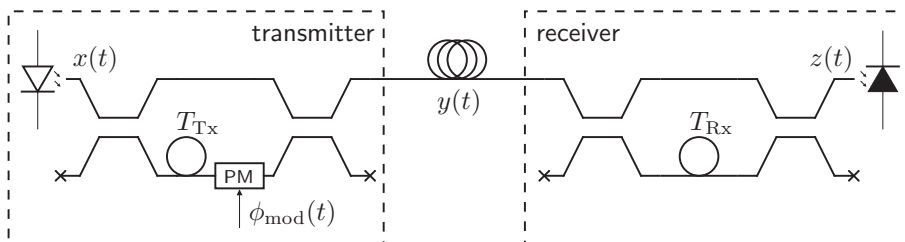
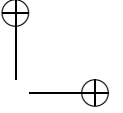
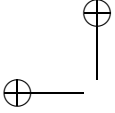


Figure 1.2: Coherence modulation and demodulation

The transmitter consists of a broadband optical source and an interferometer with path length difference T_{Tx} . (Although Delisle and Cielo used Michelson interferometers [26], the coherence modulator and demodulator in Figure 1.2 consist of Mach-Zehnder interferometers (MZIs). This does not make a conceptual difference, however.) The idea of coherence modulation is that a (phase-) modulated and unmodulated version of the broadband source signal $x(t)$ are transmitted, with a mutual delay that is equal to T_{Tx} . This delay is chosen to be much larger than the coherence time of the source signal, so that the two optical signals do not interfere, and the modulating signal $\phi_{mod}(t)$ does not result in an observable intensity modulation in the output signal of the transmitter $y(t)$. The modulating signal can be made observable in the intensity of the output signal of the receiver $z(t)$ by means of an interferometer with path length difference T_{Rx} that equals T_{Tx} ; in that case the modulated optical signal that traveled the lower path in the transmitter and upper path in the receiver will interfere with the unmodulated signal that traveled the upper path in the transmitter and lower path in the receiver, as they have zero path length difference and hence are mutually coherent. On the other hand, $\phi_{mod}(t)$ will not be observable when the difference between T_{Rx} and T_{Tx} is much larger than the coherence time of the source signal, because all optical signals in the receiver are mutually incoherent in that case, hence only resulting in optical beat interference (OBI) noise. As a result, the relation between the path delays in transmitter and receiver determines whether a coherence-modulated channel is demodulated or not.

Actually, Delisle and Cielo denoted this technique as “spectral modulation of white light”, since the interferometers can be considered as filters that encode and decode the optical spectrum of the source signal, where the actual spectral code is altered by means of the modulator.

Coherence-modulated channels can be multiplexed by combining multiple optical signal pairs in a common transmission fiber, each pair having a unique



delay between the constituting signals. Delisle and Cielo achieved this by serially cascading interferometers with different path delays [27], but an even more straightforward way is to combine the output signals of several parallel coherence modulators by means of an optical coupler [28, 29]. Simultaneous demultiplexing and demodulation is performed by passively splitting the common fiber signals over several receivers, each having a unique path delay that corresponds to the delay of one of the channels.

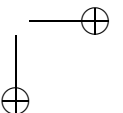
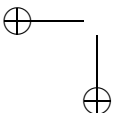
The papers of Deslisle and Cielo describe some experiments in which bulk-optics Michelson interferometers were used to transmit several channels of a few hundred Hertz over a few meters in free space. Unfortunately, both papers were published in French, and therefore not very widely noticed.

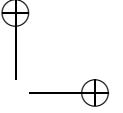
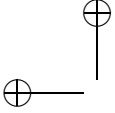
1.5.2 Some extensions to the original idea

In the early eighties, the work of Cielo and Delisle was picked up in France, by Jean-Pierre Goedgebuer, Henri Porte, André Hamel and several other co-workers. They published several tens of papers related to this subject (even until very recently) in which they mainly focused on device technology. Their first experiments were based on bulk-optics polarization interferometers (consisting of birefringent plates and polarizers) and demonstrated how several TV-channels can be multiplexed onto a multimode fiber by coherence modulation of white light produced by a xenon lamp [30, 31] or multimode laser light [28, 32, 33]. Some improvements were made, first by replacing the bulk phase modulator inside the interferometer by a modulator that was integrated in Lithium Niobate (LiNbO_3) [34, 35], and later by completely integrating the coherence modulators in LiNbO_3 [36], thereby more carefully controlling the geometries and reducing the driving voltages, resulting in modulation bandwidths in the GHz range [37, 38]. Polarization independent LiNbO_3 integrated coherence modulators and demodulators were made by realizing them as MZIs rather than polarization interferometers [39–43]. Both implementation forms have also been realized in GaAlAs-GaAs in order to allow monolithic integration with electronics [44, 45].

Seemingly independently, CM was developed within the framework of interferometric fiber-optic sensors. In 1985, Brooks et al. (Stanford, USA) described four architectures that enable multiplexing several sensor signals onto a single SMF using a common short coherence length CW light source [46]. In 1989, the first analysis on noise performance of CM systems was published by Robert H. Wentworth [47]. It describes a general framework for calculating the signal-to-noise ratio (incorporating OBI noise, shot noise and thermal receiver noise) for systems consisting of coherence-multiplexed sensors and a common light source. In 1990, K.W. Chu and Fred M. Dickey [29] extended Wentworth's results to CM for digital communication systems employing distinct sources.

In the remainder of the nineties, a considerable amount of research on optical spectral coding schemes was done by David D. Sampson, Robert A. Griffin, David A. Jackson, Graeme J. Pendock and some other co-workers, most of it





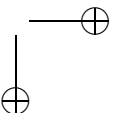
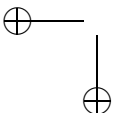
in Melbourne, Australia. Their work has resulted in the (to our knowledge) highest capacity demonstrated in a CM system to date: 4 Gbps in four CM channels, each channel having a bit rate of 1 Gbps. The interferometers were constructed from standard SMFs (requiring polarization controllers for polarization matching), and the source was an Erbium-doped fiber (EDF). The main contribution of Pendock and Sampson was their finding that the OBI noise performance of CM systems can be significantly enhanced by using differential optical detection rather than single-ended detection, which moreover enables intensity modulation instead of phase modulation. The latter has the advantage that modulation can be performed outside the interferometer, so that the encoding filter can be realized in a passive material.

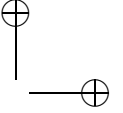
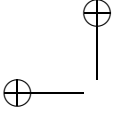
The most mature CM system prototype reported so far is a PON-based optical access network proposed by Kani et al. in 2001 [48]. They report an experiment in which eight-channel 155 Mbps half-duplex bidirectional packet transmission is demonstrated on 7 km of standard SMF, using super luminescence diode (SLD) sources and planar lightwave circuit (PLC) MZIs. A major drawback of their proposed network is that the interferometers were temperature-controlled in order to synchronize the phases of the interfering light waves, and hence guarantee complete interference. Moreover, their predictions on dispersion effects are fully based on simulation (which is not further described) and can therefore not be generalized to other fiber lengths.

1.5.3 Advantages and disadvantages

In general, CM has the following advantages with respect to other multiplexing techniques:

- Relatively simple optical sources like light-emitting diodes (LEDs) or superluminescent LEDs (SLEDs) can be used as broadband optical sources, and channel generation and selection can be performed by simple MZIs, which can be integrated as for example planar optical circuits;
- The channel selection concept is relatively robust in the sense that temperature fluctuations will not result in crosstalk from undesired channels;
- The channel generation and selection concept does not require any active components in the network;
- The concept is transparent and can be used both for digital and analog transmission, eventually simultaneously;
- An interferometer can be used both as an encoding and decoding device, which enables component-sharing in a duplex link;
- Optical modulation and detection is simply performed at the baseband rate rather than at the much higher aggregate data rate like in TDM or chip rate like in some OCDM schemes. This reduces the modulation and





processing speeds that are required, and moreover reduces the vulnerability to fiber dispersion;

- Modulation and demodulation do not require time slot synchronization like in synchronous TDM or code synchronization and/or time gating like in some pulse-position-modulated OCDM schemes.

CM also has particular disadvantages, however:

- The optical beating of mutually incoherent signals in the receiver results in OBI noise. Its power increases with increasing number of channels;
- The large bandwidth of the optical carrier signal makes the modulated transmitted optical signal vulnerable to chromatic dispersion in the transmission fiber;
- The transmitted optical power has to be shared by all receivers;

These disadvantages fundamentally limit the number of CM channels that can be multiplexed, the bit rates that can be supported and distances that can be spanned.

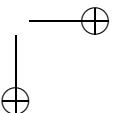
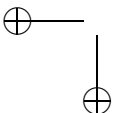
Another particular disadvantage of the CM systems published so far is that they all used relatively complicated active components in order to synchronize the phases and/or polarization states of the coherent light waves and hence guarantee complete interference.

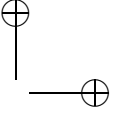
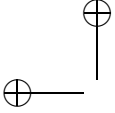
Moreover, CM is quite a conceptually complicated technique, in the sense that rather involved mathematical analysis is required for deriving the design constraints of CM systems. This might be one of the causes for the fact that CM is not a very mature technique yet: even though it has existed for almost thirty years, only few research groups have worked on it so that the technology has not really progressed beyond theoretical proposals and analyses, and the rather preliminary laboratory demonstrations that have been described above. Quite some papers have been published, but most were written very compactly and are therefore not easy to read.

The main challenges that seem to remain in CM technology are:

- to design dedicated optical sources, optical circuits and optical receivers with high bandwidths, low losses (so that EDFAs are not required) and low costs;
- to find a simple way to achieve phase synchronization or avoid the need of phase synchronization, so that external control electronics can be omitted;
- to design network structures and protocols that optimally cope with the limitations of CM as a physical layer technique.

Especially the conceptually challenging appeal of CM makes it a very interesting topic for multidisciplinary academic research.





1.6 Research objective

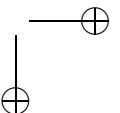
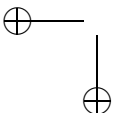
The goal of the research that is presented in this thesis was to investigate the opportunities of CM on a system level basis, or more specifically:

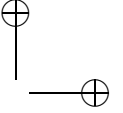
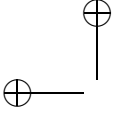
- to compare different implementation alternatives of CM systems, based on both theoretical performance and practical implementation aspects;
- to derive design constraints for CM systems in terms of
 - number of channels that can be multiplexed;
 - bit rates that can be supported;
 - maximum link lengths;
- to propose new system concepts to improve performance, increase robustness and reliability and/or lower the costs;
- to investigate the specific applicability of CM as an RF feeder technology;
- to specify requirements on the several parts that are to be used in CM systems, in order to give directions for further research on circuit and component level.

This implies that the actual technology for the electrical and optical circuits has not been considered in detail; focus was on the actual signal processing that is involved. The research has been confined to theoretical analysis and simulation, because the specialized optical components that would be required for realizing a proper laboratory demonstration have not been available during the project, so that experimental verification was not possible.

1.7 Outline of the thesis

After this introduction in the first chapter, the thesis starts with an analytical description for modeling the behavior of the various optical and electrical components that are used in CM systems. These models form the basis of the theoretical analyses that are presented in the remainder of the thesis. Chapter 3 describes a tool that was developed for verifying these theoretical results by means of simulation. This tool is based on time-discrete equivalents of the continuous-time models that are described in Chapter 2. Chapter 4 continues with an elaborate explanation of the coherence modulation and demodulation concept on which CM is based. Some different topologies for multiplexing several coherence-modulated channels are described, analyzed and compared in Chapter 5. Chapter 6 presents some alternative receiver schemes for demultiplexing CM channels, with particular emphasis on phase diversity reception. The effect of chromatic dispersion in single-mode fiber is neglected in Chapter 4–6; this is studied in detail in Chapter 7. Chapter 8 is devoted to specific aspects of using CM as an RF feeder technology in wireless access systems. The thesis ends with conclusions and recommendations in Chapter 9.





Chapter 2

Analytical models of components

2.1 Introduction

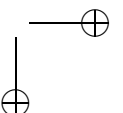
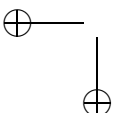
Since the focus of this research is on the system-level analysis of coherence multiplexing (CM), mathematical models are required to describe the behavior of the several components that are present in CM systems. Because some of these models are not quite straightforward, they are discussed in this chapter. Moreover they will serve as a basis for the simulation tool that is described in Chapter 3.

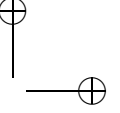
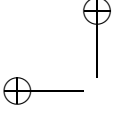
First, an explanation is given on the way in which the optical signal is described by a scalar wave representation. Based on this description method, the model for polarized thermal light is described, followed by a description of the optical encoders and decoders and their constituting components: couplers, delay lines and modulators. Then it will be explained how the attenuation and chromatic dispersion in single-mode optical fibers are modeled, succeeded by a description of the photon-electron conversion process in the photodiodes, in terms of the doubly-stochastic Poisson arrival model. Finally, a model for the behavior of the transimpedance amplifiers in the optical receivers is given.

2.2 Representation of optical signals

As was explained in Section 1.5, the concept of CM is based on optical interference, which is related to the mutual temporal coherence between light waves. This effect can be described by considering the instantaneous powers and phases of the light waves that are involved in the interference process.

It is well-known that the electromagnetic waves in an optical waveguide or fiber travel in different *modes* [49], each mode having its own *mode profile* (for the electric and magnetic field vectors) and *propagation constant*. The mode





profile describes how the electric and magnetic field vector elements depend on the spatial coordinates in the directions perpendicular to the propagation direction. For a homogeneous waveguide (that is, a waveguide in which the dimensions perpendicular to the propagation direction do not depend on the coordinate along the propagation direction), the shapes of these mode profiles do not change as the modes propagate through the waveguide.

Hence, when we consider a *monochromatic wave* propagating in the z -direction through a *single-mode* homogeneous waveguide, then the complex electric and magnetic field vectors in the waveguide as a function of the spatial coordinates and time t can be written as

$$\mathbf{E}(\mathbf{s}, z, t) = \sqrt{2P_0} \mathbf{E}_0(\mathbf{s}) \exp(j2\pi f_c t - \gamma z), \quad (2.1)$$

$$\mathbf{H}(\mathbf{s}, z, t) = \sqrt{2P_0} \mathbf{H}_0(\mathbf{s}) \exp(j2\pi f_c t - \gamma z), \quad (2.2)$$

where \mathbf{s} is a two-dimensional vector denoting the coordinates in the direction perpendicular to the propagation direction z , P_0 is the total power passing through the cross-section of the waveguide in the s -plane at $z = 0$, $\mathbf{E}_0(\mathbf{s})$ and $\mathbf{H}_0(\mathbf{s})$ are the electric and magnetic mode field profiles, respectively, f_c is the optical carrier frequency and

$$\gamma = \alpha + j\beta \quad (2.3)$$

is the propagation constant, where α is the attenuation constant (in Np/m) and β is the phase constant (in rad/m). The mode profiles and the propagation constant depend on the optical frequency and the geometry of the waveguide, and follow from Maxwell's equations.

The complex power flow per unit area and its direction follow from the *complex Poynting vector*, which is given by

$$\mathbf{S}(\mathbf{s}, z, t) = \mathbf{E}(\mathbf{s}, z, t) \times \mathbf{H}^*(\mathbf{s}, z, t), \quad (2.4)$$

where \times denotes vector product and $*$ denotes complex conjugate. The total power passing through a cross-section C_1 in the s -plane at $z = z_1$ follows by integrating the real part of the Poynting vector over C_1 :

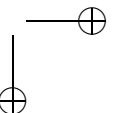
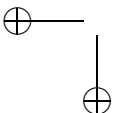
$$P(z_1, t) = \frac{1}{2} \iint_{C_1} \operatorname{Re}\{\mathbf{S}(\mathbf{s}, z_1, t)\} \bullet d\mathbf{A}, \quad (2.5)$$

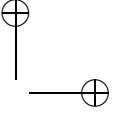
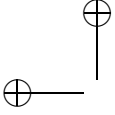
where $\operatorname{Re}\{\cdot\}$ denotes real part and \bullet denotes inner product. Since we know that $P(0, t) = P_0$ (by definition), it follows that the mode profiles should be normalized such that

$$\iint_{C_1} \operatorname{Re}\{\mathbf{E}_0(\mathbf{s}) \times \mathbf{H}_0^*(\mathbf{s})\} \bullet d\mathbf{A} = 1, \quad (2.6)$$

resulting in

$$P(z_1, t) = P_0 \exp(-2\alpha z_1). \quad (2.7)$$





When a non-monochromatic wave is considered, the electric and magnetic fields can be considered as continuous sums of all the spectral components that constitute the optical wave. (This follows from the linearity of Maxwell's equations.) Taking into account that the mode profiles and the propagation constant are functions of frequency, one can write:

$$\mathbf{E}(\mathbf{s}, z, t) = \int_{-\infty}^{\infty} X(f) \mathbf{E}_0(\mathbf{s}, f) \exp(j 2\pi f t - \gamma(f) z) df, \quad (2.8)$$

$$\mathbf{H}(\mathbf{s}, z, t) = \int_{-\infty}^{\infty} X(f) \mathbf{H}_0(\mathbf{s}, f) \exp(j 2\pi f t - \gamma(f) z) df, \quad (2.9)$$

where $X(f)$ can be considered as the complex amplitude density of the spectral components that constitute the optical wave at $z = 0$, and the frequency-dependent mode profiles are defined such that (2.6) holds for every individual frequency.

In this thesis it will be assumed that the considered optical signals are relatively narrowband (that is, their bandwidths are much smaller than the optical center frequency) so that the mode profiles can be considered constant in the frequency range of interest. The total instantaneous power passing through a cross-section of the waveguide at $z = z_1$ can now be derived by following a similar procedure as for the monochromatic case, resulting in

$$P(z_1, t) = \frac{1}{2} \left| \int_{-\infty}^{\infty} X(f) \exp(j 2\pi f t - \gamma(f) z_1) df \right|^2. \quad (2.10)$$

As a result, the vector field of an optical wave propagating through a single-mode homogeneous waveguide can be described by a scalar complex band-pass signal $x(t)$ (also called pre-envelope or analytic signal) which is the inverse Fourier transform of $X(f)$. It is called the *scalar wave representation* of the optical field [50, 51]. This signal simply represents the optical power and phase—and not the actual mode field profile. Propagation through the waveguide over a distance l simply implies that $x(t)$ is filtered by a linear system with transfer function

$$H(f) = \exp(-\gamma(f) l), \quad (2.11)$$

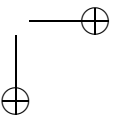
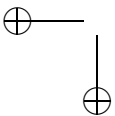
and optical modulation can simply be modeled as scalar modulation of $x(t)$.

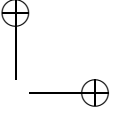
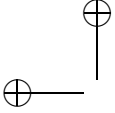
The scalar wave representation can be written in the amplitude and phase form:

$$x(t) \triangleq \sqrt{2P_x(t)} \exp(j 2\pi f_c t + j \phi_x(t)), \quad (2.12)$$

where

- the carrier frequency f_c corresponds to the optical center frequency, so we have $f_c = c_0/\lambda_c$ where c_0 is the speed of light in vacuum and λ_c is the optical center wavelength in vacuum;
- the (time-varying) phase $\phi_x(t)$ corresponds to the optical phase;





- the (time-varying) power $P_x(t)$ corresponds to the total optical power passing through the corresponding cross-section. Note that it can be calculated from $x(t)$ as

$$P_x(t) \triangleq \frac{1}{2}|x(t)|^2. \quad (2.13)$$

Alternatively, we can write $x(t)$ in terms of its quadrature components $u_x(t)$ and $v_x(t)$, respectively:

$$x(t) = [u_x(t) + jv_x(t)] \exp(j2\pi f_c t), \quad (2.14)$$

where

$$u_x(t) \triangleq \sqrt{2P_x(t)} \cos(\phi_x(t)), \quad (2.15)$$

$$v_x(t) \triangleq \sqrt{2P_x(t)} \sin(\phi_x(t)). \quad (2.16)$$

Obviously, the unit of $x(t)$ (and its quadrature components) is $\sqrt{\text{W}}$ (square-root of Watts). In the remainder of this thesis, when we speak about “optical field” or “optical signal”, the pre-envelope of the scalar wave representation will tacitly be addressed.

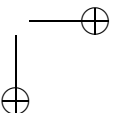
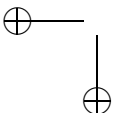
Note that the scalar wave representation can only describe an optical wave in one single (polarization) mode. When unpolarized (or partially polarized) light is to be described, two separate (eventually correlated) scalar wave representations are required for describing the two (orthogonal) polarization modes. For describing the optical signals in a multimode waveguide, the required number of scalar wave representations equals the number of excited modes. The spatial orthogonality of the modes then implies that the total instantaneous power in the optical wave follows from the sum of the powers in the scalar wave representations. In this thesis, however, it will be assumed that the optical waves are completely polarized and travel in one single mode, so that only one scalar wave representation is required.

2.3 Optical sources

The actual behavior of the optical signal $x(t)$ depends on the type of optical source that is used. In this thesis, broadband optical sources are considered. They are represented schematically as shown in Figure 2.1. The model that is used to describe their behavior is explained in the following subsections.

2.3.1 Thermal light model

For the broadband sources that are considered in this thesis, it is assumed that the *thermal light model* applies [47, 51]. This implies that $x(t)$ is a *circular complex Gaussian band-pass process*, meaning that the quadrature processes $u_x(t)$ and $v_x(t)$ are jointly Gaussian distributed. This is a reasonably accurate



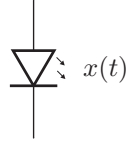
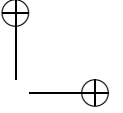
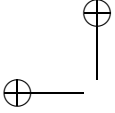


Figure 2.1: Schematic representation of a broadband optical source

approximation for sources where the light is generated by means of spontaneous emission, such that the actual optical field corresponds to the superposition of many (independent) hole-electron recombinations, such that the Central Limit Theorem can be applied.

2.3.2 Spectral characteristics

The spectral properties of $x(t)$ can be described in terms of its autocorrelation function or *coherence function*

$$R_{x^*x}(t_1, t_2) \triangleq E[x^*(t_1)x(t_2)]. \quad (2.17)$$

Since $x(t)$ is assumed to be a wide-sense stationary (or circular) process, this can be written as [51]

$$R_{x^*x}(\tau) \triangleq R_{x^*x}(t, t + \tau) = 2 \left[R_{u_x u_x}(\tau) + j R_{u_x v_x}(\tau) \right] \exp(j 2\pi f_c \tau), \quad (2.18)$$

where $R_{u_x u_x}(\tau)$ is the autocorrelation function of $u_x(t)$ and $R_{u_x v_x}(\tau)$ is the cross-correlation function of the $u_x(t)$ and $v_x(t)$, according to the notation in (2.14). $u_x(t)$ and $v_x(t)$ are also wide-sense stationary, and both $R_{u_x u_x}(\tau)$ and $R_{u_x v_x}(\tau)$ are real-valued functions, with

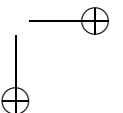
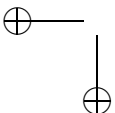
$$R_{u_x u_x}(\tau) = R_{u_x u_x}(-\tau), \quad (2.19)$$

$$R_{u_x v_x}(\tau) = -R_{u_x v_x}(-\tau). \quad (2.20)$$

Alternatively, the spectral properties of $x(t)$ can be described in terms of its power spectral density function $S_{x^*x}(f)$, which follows from the Wiener-Khinchin Theorem:

$$\begin{aligned} S_{x^*x}(f) &\triangleq \int_{-\infty}^{\infty} R_{x^*x}(\tau) \exp(-j 2\pi f \tau) d\tau \\ &= 2S_{u_x u_x}(f - f_c) + 2j S_{u_x v_x}(f - f_c), \end{aligned} \quad (2.21)$$

where $S_{u_x u_x}(f)$ is the (real-valued) power spectral density function of $u_x(t)$ and $S_{u_x v_x}(f)$ is the (imaginary-valued) cross-power spectral density function of $u_x(t)$ and $v_x(t)$. Both $S_{u_x u_x}(f)$ and $S_{u_x v_x}(f)$ are located at the baseband, so that $S_{x^*x}(f)$ is a real-valued, single-sided positive function of frequency.



The mean power P_x of $x(t)$ can be derived either from the autocorrelation function or the power spectral density function, using (2.13):

$$P_x \triangleq \mathbb{E}[P_x(t)] = \frac{1}{2}R_{x^*x}(0) = \frac{1}{2} \int_{-\infty}^{\infty} S_{x^*x}(f) \, df. \quad (2.22)$$

The spectral behavior of $x(t)$ can also be described by the so-called *coherence time* τ_c , which is a measure for the length of a time interval over which one can reasonably predict the power and phase of $x(t)$, and is formally defined as [51]

$$\tau_c \triangleq \frac{\int_{-\infty}^{\infty} |R_{x^*x}(\tau)|^2 \, d\tau}{R_{x^*x}^2(0)}, \quad (2.23)$$

so actually the coherence time corresponds to the effective width of $|R_{x^*x}(\tau)|^2$. By applying Parseval's Theorem one can rewrite this definition as

$$\tau_c = \frac{1}{4P_x^2} \int_{-\infty}^{\infty} S_{x^*x}^2(f) \, df. \quad (2.24)$$

2.3.3 Gaussian spectral profile

In case of a light-emitting diode (LED) or superluminescent LED (SLED), the coherence function of $x(t)$ can be approximated by a Gaussian shape [47]:

$$R_{x^*x}(\tau) \approx 2P_x \exp\left(-\frac{\pi}{2} \left(\frac{\tau}{\tau_c}\right)^2 + j2\pi f_c \tau\right). \quad (2.25)$$

From (2.18) (and from the fact that $R_{u_x u_x}(\tau)$ and $R_{u_x v_x}(\tau)$ should be real-valued) it then follows that

$$R_{u_x u_x}(\tau) = P_x \exp\left(-\frac{\pi}{2} \left(\frac{\tau}{\tau_c}\right)^2\right), \quad (2.26)$$

$$R_{u_x v_x}(\tau) = 0. \quad (2.27)$$

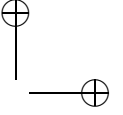
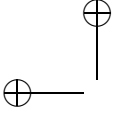
Hence, the quadrature components $u_x(t)$ and $v_x(t)$ are uncorrelated and —since they are Gaussian— independent.

The power spectral density functions of $u_x(t)$ and $x(t)$ follow by Fourier transformation:

$$S_{u_x u_x}(f) = \sqrt{2}P_x \tau_c \exp\left(-2\pi(f \tau_c)^2\right) \quad (2.28)$$

$$S_{x^*x}(f) = 2\sqrt{2}P_x \tau_c \exp\left(-2\pi(f - f_c)^2 \tau_c^2\right). \quad (2.29)$$

Using this formula it can be proven that the full-width-at-half-maximum bandwidth Δf of $x(t)$ —that is, the difference between the frequencies at which



$S_{x^*x}(f)$ takes half of its maximum value— is related to τ_c as

$$\tau_c = \sqrt{\frac{2 \ln 2}{\pi}} \cdot \frac{1}{\Delta f}. \quad (2.30)$$

This can be related to a corresponding linewidth $\Delta\lambda$ in the wavelength domain by

$$\Delta f \approx \left| \frac{\partial f}{\partial \lambda}(\lambda = \lambda_c) \right| \cdot \Delta\lambda = \frac{c_0}{\lambda_c^2} \cdot \Delta\lambda, \quad (2.31)$$

resulting in

$$\tau_c \approx \sqrt{\frac{2 \ln 2}{\pi}} \cdot \frac{\lambda_c^2}{c_0} \cdot \frac{1}{\Delta\lambda}. \quad (2.32)$$

Example 2.1

Using (2.31) and (2.32) it can be calculated that an LED with a linewidth of 40 nm operating at 1310 nm has a bandwidth of approximately 7 THz and a coherence time of approximately 0.1 ps. The same coherence time and bandwidth are obtained for an LED with a linewidth of approximately 56 nm operating at 1550 nm. All of these are realistic values for practical LEDs. (Note that LEDs with equal coherence times and different center wavelengths have the same bandwidth but different linewidths.) □

2.3.4 Intensity noise

The instantaneous power of thermal light is also a random process and hence not constant. This can be seen by writing the instantaneous power as

$$P_x(t) = \frac{1}{2} [u_x^2(t) + v_x^2(t)] \quad (2.33)$$

Since $u_x(t)$ and $v_x(t)$ are Gaussian distributed and $R_{u_x v_x}(0) = 0$, $P_x(t)$ can actually be proven to be χ^2 -distributed. The autocorrelation function of $P_x(t)$ follows from

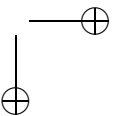
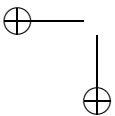
$$R_{P_x P_x}(t_1, t_2) \triangleq \mathbb{E}[P_x(t_1)P_x(t_2)] = \frac{1}{4} \mathbb{E} [|x(t_1)|^2 |x(t_2)|^2]. \quad (2.34)$$

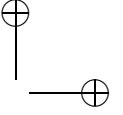
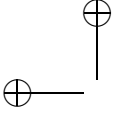
Using the complex Gaussian moment theorem [51], which states the fourth order moment of four zero-mean circular complex Gaussian variables X_1 , X_2 , X_3 and X_4 is given by

$$\mathbb{E}[X_1 X_2^* X_3 X_4^*] = \mathbb{E}[X_1 X_2^*] \mathbb{E}[X_3 X_4^*] + \mathbb{E}[X_1 X_4^*] \mathbb{E}[X_2^* X_3], \quad (2.35)$$

(2.34) can be written as

$$\begin{aligned} R_{P_x P_x}(t_1, t_2) &= \frac{1}{4} \mathbb{E} [|x(t_1)|^2] \mathbb{E} [|x(t_2)|^2] + \frac{1}{4} \mathbb{E} [x(t_1)x^*(t_2)] \mathbb{E} [x^*(t_1)x(t_2)] \\ &= \mathbb{E}[P_x(t_1)] \mathbb{E}[P_x(t_2)] + \frac{1}{4} |R_{x^*x}(t_1, t_2)|^2. \end{aligned} \quad (2.36)$$





When $x(t)$ corresponds to an unmodulated source signal, it is wide-sense stationary and we have

$$R_{P_x P_x}(\tau) = P_x^2 + \frac{1}{4} |R_{x^* x}(\tau)|^2. \quad (2.37)$$

The power spectral density function of $P_x(t)$ follows by Fourier transformation, resulting in

$$S_{P_x P_x}(f) = P_x^2 \delta(f) + \frac{1}{4} \int_{-\infty}^{\infty} S_{x^* x}(\nu) S_{x^* x}(\nu - f) d\nu, \quad (2.38)$$

where $\delta(\cdot)$ is the Dirac delta function. Obviously, the instantaneous power $P_x(t)$ consists of a constant term P_x plus noise with a bandwidth that is in the order of the bandwidth of $x(t)$.

For sources with a Gaussian spectral profile one can find

$$R_{P_x P_x}(\tau) = P_x^2 \left[1 + \exp\left(-\pi \left(\frac{\tau}{\tau_c}\right)^2\right) \right], \quad (2.39)$$

$$S_{P_x P_x}(f) = P_x^2 \left[\delta(f) + \tau_c \exp\left(-\pi(f \tau_c)^2\right) \right]. \quad (2.40)$$

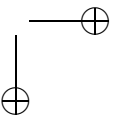
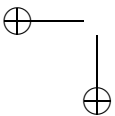
The intensity noise of two correlated optical signals $x_1(t)$ and $x_2(t)$ is also correlated, as follows from the cross-correlation functions of $P_{x_1}(t)$ and $P_{x_2}(t)$. Using (2.35) one can find that it can be written as

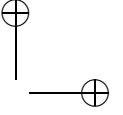
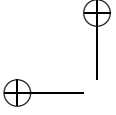
$$\begin{aligned} R_{P_{x_1} P_{x_2}}(t_1, t_2) &\triangleq \text{E}[P_{x_1}(t_1)P_{x_2}(t_2)] = \frac{1}{4} \text{E}[|x_1(t_1)|^2 |x_2(t_2)|^2] \\ &= \frac{1}{4} \text{E}[|x_1(t_1)|^2] \text{E}[|x_2(t_2)|^2] \\ &\quad + \frac{1}{4} \text{E}[x_1(t_1)x_2^*(t_2)] \text{E}[x_1^*(t_1)x_2(t_2)] \\ &= \text{E}[P_{x_1}(t_1)] \text{E}[P_{x_2}(t_2)] + \frac{1}{4} |R_{x_1^* x_2}(t_1, t_2)|^2. \end{aligned} \quad (2.41)$$

2.4 Optical encoders and decoders

In order to realize the coding and decoding operation in CM transmitters and receivers, interferometers with large path imbalances are required. In this thesis, it is assumed that these devices are realized as Mach-Zehnder interferometers (MZIs) using planar integrated optical circuits, since this implies that certain assumptions can be made about the state of polarization (SOP) of the optical signals at the outputs of the circuits. The assumptions that will be made here are that:

1. the optical signals at the input of a specific optical device all have the same SOP;
2. birefringence and polarization mode coupling in the optical device are assumed to result in eventual SOP shifts such that all the signals at the output of the device still have the same SOP.





All devices in the system are assumed to satisfy these conditions. Hence, the optical signals at all inputs and outputs can each be described by just one scalar wave representation. Moreover, the optical circuits are required to satisfy these criteria in order to guarantee that maximal interference will occur in a matched receiver.

The interferometers consist of couplers and delay lines, and—in case of an encoder—a modulator might be added to one of the interferometer arms. These components are described in the following subsections.

2.4.1 Couplers

Two-arm interferometers can be fabricated by means of simple 2×2 directional couplers. A schematic representation of such a coupler is shown in Figure 2.2.

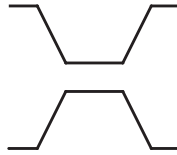


Figure 2.2: Schematic representation of an optical 2×2 directional coupler

Ideally, these couplers are lossless. In that case the transfer of the optical signals from each input to each output can be described by the following matrix [52]:

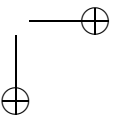
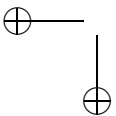
$$[H_{2 \times 2}] = \begin{bmatrix} \sqrt{1 - \kappa} & j\sqrt{\kappa} \\ j\sqrt{\kappa} & \sqrt{1 - \kappa} \end{bmatrix}, \quad (2.42)$$

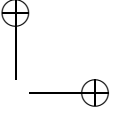
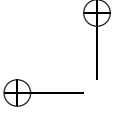
κ is called the *coupling constant*. Although κ will generally be wavelength dependent, it will be assumed in this thesis that it is constant in the entire frequency range of the considered optical signals. Hence, the complex optical signal at a particular output simply follows by multiplying the complex optical signals at the inputs by the corresponding matrix elements and summing them.

When $\kappa = 1/2$, the power of each input port is equally split over the two output ports, and the coupler is said to be *uniform*. The 2×2 couplers in this thesis are all assumed to be uniform, unless otherwise stated.

Obviously, cross-port transmissions have a phase shift of $\frac{\pi}{2}$ radians with respect to the through-port transmissions. We will see later that this last phenomenon is relevant in a balanced detector configuration.

For other splitters and combiners in CM systems, this phase shift is not really relevant. Therefore, it will simply be assumed that each transmission in an N -port splitter or combiner can be characterized by a real constant that simply denotes an intrinsic splitting/combining loss N and eventually some excess loss.





2.4.2 Delay lines

In order to create mutually incoherent light waves, the interferometers need to have a difference in group delay between the upper and lower arm (or path-imbalance) that exceeds the coherence time of the light. Since actually only the *difference* in delay between the arms matters for studying interference effects, the delay of the upper arm (which will always be considered as the so-called reference arm) will be written as zero, whereas the other arms are attributed delay values T that actually correspond to the difference in delay with respect to the reference arm. This is illustrated in Figure 2.3.

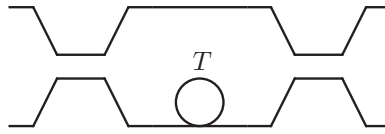


Figure 2.3: Schematic representation of a Mach-Zehnder interferometer with path-imbalance T

The delay lines are assumed to have negligible loss and dispersion. Moreover, it is assumed—for convenience—that the delay values denote both the phase delay and the group delay, so that the transfer function in the frequency range of interest corresponds to (2.11) with

$$\gamma(f)l = j2\pi fT. \quad (2.43)$$

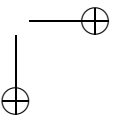
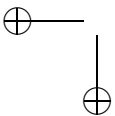
Although the phase delay and group delay are not equal in practice, one can verify that this assumption does not fundamentally affect the results of the analyses.

2.4.3 Modulators

The encoder circuit in the transmitter also comprises a modulator. Basically, there are two possibilities:

1. Phase modulation (PM): in that case, the lower arm of the interferometer contains a modulator that modulates the phase of the light wave through the lower arm by a value $\phi_{\text{mod}}(t)$, with $-\pi < \phi_{\text{mod}}(t) \leq \pi$. This is illustrated in Figure 2.4(a);
2. Intensity modulation (IM): in that case, a modulator is put in front of the interferometer, which modulates the intensity (or power) of the light wave that enters the interferometer by a (dimensionless) value $m_{\text{mod}}(t)$, so the amplitude of the optical field is modulated by a value $\sqrt{m_{\text{mod}}(t)}$, with $0 \leq m_{\text{mod}}(t) \leq 1$. This is illustrated in Figure 2.4(b).

In general analyses of CM systems, it will be assumed that both modulators are there, and when PM is considered, it is assumed that $m_{\text{mod}}(t) = 1$, whereas when IM is considered, it is assumed that $\phi_{\text{mod}}(t) = 0$.



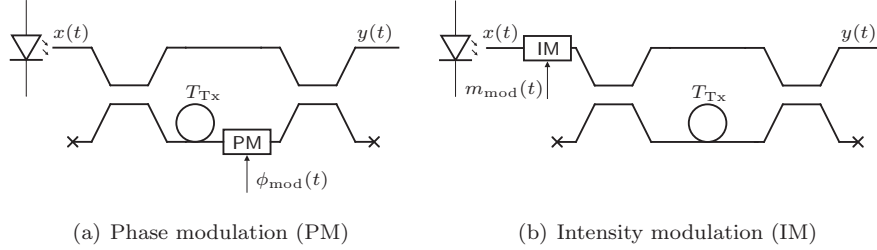


Figure 2.4: Schematic representation of a CM transmitter for phase modulation (PM) and intensity modulation (IM)

2.5 Single-mode optical fiber

In CM systems, several communication channels are multiplexed through a common optical fiber cable. In case of large fiber lengths, the transmission will be hampered by attenuation and chromatic dispersion. In case of a single-mode fiber (SMF) cable, these effects are reflected by the transfer function of the fiber, which relates the optical fields at the input and output of the fiber. It can be written as:

$$H_f(f) = 10^{-\alpha(f)l_f/20} \exp(-j\beta(f)l_f), \quad (2.44)$$

where $\alpha(f)$ and $\beta(f)$ are the (frequency-dependent) optical power loss per unit length (in dB/m) and phase change per unit length (in rad/m), respectively, and l_f is the length of the fiber (in m).

2.5.1 Attenuation

Although the attenuation of the fiber depends on the optical frequency (and hence on the wavelength), it can be considered constant in the frequency range where the power spectral density of the source is located. This is illustrated in Figure 2.5(a), where the optical attenuation per unit length $\alpha(f)$ is drawn as a function of frequency. The dotted lines are (normalized) graphs of the power spectral densities of typical optical signals that could be used in CM, with center wavelengths and bandwidths as described in Example 2.1.

As a result, the attenuation in the frequency range that corresponds to the source's frequency range only depends on the central frequency f_c of the source such that one can write

$$\alpha(f) \approx \alpha(f_c). \quad (2.45)$$

This is illustrated by the bold horizontal lines in Figure 2.5(a).

Example 2.2

For standard SMF [1], typical losses are 0.3–0.4 dB/km in the 1310 nm wavelength region and 0.15–0.25 dB/km in the 1550 nm region. ▣

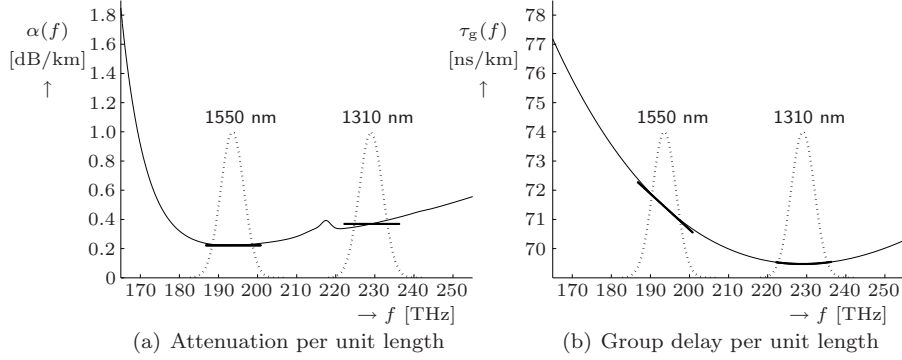


Figure 2.5: Attenuation and group delay per unit length of a typical standard SMF as a function of optical frequency

2.5.2 Dispersion

Since broadband sources are used in CM systems, it is important to consider the fact that the group delay per unit length

$$\tau_g(f) \triangleq \frac{\beta'(f)}{2\pi} = \frac{1}{2\pi} \frac{\partial \beta}{\partial f} \quad (2.46)$$

varies with frequency. This is illustrated in Figure 2.5(b), where the group delay per unit length of a typical SMF has been plotted as a function of the optical frequency.

Obviously, the effect of dispersion is that the different spectral components of the optical signal propagate at different speeds. When the center frequency f_c is for example 194 THz, $\tau_g(f)$ can be approximated by its first order Taylor series :

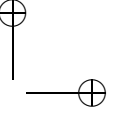
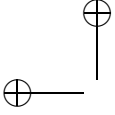
$$\tau_g(f) \approx \tau_g(f_c) + \tau_g'(f_c) \cdot (f - f_c). \quad (2.47)$$

This is illustrated by the bold straight line around 194 THz in Figure 2.5(b). $\beta(f)$ can now be written as

$$\beta(f) \approx \beta(f_c) + 2\pi \left[\tau_g(f_c) \cdot (f - f_c) + \frac{1}{2} \tau_g'(f_c) \cdot (f - f_c)^2 \right]. \quad (2.48)$$

The first term corresponds to a constant phase shift, whereas the second (linear) term corresponds to a constant delay (per unit length). The third term corresponds to what is called *first order dispersion*. $\tau_g'(f_c)$ is called the *first order dispersion coefficient*.

From Figure 2.5(b), it can be seen that as f_c gets closer to 230 THz, the first order dispersion becomes smaller. Note however, that although the first order dispersion coefficient becomes zero at 230 THz (therefore 1310 nm is called the *zero-dispersion wavelength*), there is still variation in group delay around



230 THz. This is called *second order dispersion*, and it can be incorporated by extending the approximation of $\tau_g(f)$ to the second order Taylor series:

$$\tau_g(f) \approx \tau_g(f_c) + \tau_g'(f_c) \cdot (f - f_c) + \frac{1}{2}\tau_g''(f_c) \cdot (f - f_c)^2. \quad (2.49)$$

This is illustrated by the bold parabolic line around 230 THz in Figure 2.5(b). $\beta(f)$ can now be written as

$$\beta(f) \approx \beta(f_c) + 2\pi \left[\tau_g(f_c) \cdot (f - f_c) + \frac{1}{2}\tau_g'(f_c) \cdot (f - f_c)^2 + \frac{1}{6}\tau_g''(f_c) \cdot (f - f_c)^3 \right], \quad (2.50)$$

where $\tau_g''(f_c)$ is the *second order dispersion coefficient*. Note that the first order dispersion term can be omitted when the corresponding coefficient is zero.

For most fibers, the first and second order dispersion coefficients are specified in terms of the derivatives of the group delay per unit length with respect to wavelength instead of frequency. In those cases, the following conversion formulas can be used:

$$\frac{d\tau_g}{df} = \frac{d\lambda}{df} \frac{d\tau_g}{d\lambda} = -\frac{c_0}{f^2} \frac{d\tau_g}{d\lambda} = -\frac{\lambda^2}{c_0} \frac{d\tau_g}{d\lambda}, \quad (2.51)$$

$$\frac{d^2\tau_g}{df^2} = \frac{d\lambda}{df} \frac{d}{d\lambda} \left[-\frac{\lambda^2}{c_0} \frac{d\tau_g}{d\lambda} \right] = \frac{\lambda^3}{c_0^2} \left[2 \frac{d\tau_g}{d\lambda} + \lambda \frac{d^2\tau_g}{d\lambda^2} \right], \quad (2.52)$$

or

$$\tau_g'(f_c) = -\frac{\lambda_c^2}{c_0} \tau_g'(\lambda_c), \quad (2.53)$$

$$\tau_g''(f_c) = \frac{\lambda_c^3}{c_0^2} \left[2 \tau_g'(\lambda_c) + \lambda_c \tau_g''(\lambda_c) \right]. \quad (2.54)$$

Example 2.3

For standard SMF [1], chromatic dispersion around 1550 nm is dominated by first order dispersion, with a typical dispersion coefficient

$$\tau_g'(1550 \text{ nm}) \approx 20 \text{ ps}/(\text{nm} \cdot \text{km}), \quad (2.55)$$

so we have

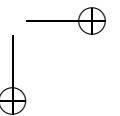
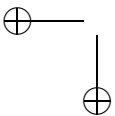
$$\tau_g'(194 \text{ THz}) \approx -160 \text{ ps}/(\text{THz} \cdot \text{km}). \quad (2.56)$$

The zero-dispersion wavelength of a standard SMF is approximately 1310 nm. The second order dispersion coefficient is typically

$$\tau_g''(1310 \text{ nm}) \approx 0.1 \text{ ps}/((\text{nm})^2 \cdot \text{km}), \quad (2.57)$$

or

$$\tau_g''(230 \text{ THz}) \approx 3.3 \text{ ps}/((\text{THz})^2 \cdot \text{km}). \quad (2.58)$$



2.6 Photodetectors

Photodetectors convert the detected optical power $P(t)$ into a current $I_{\text{pd}}(t)$. This is schematically represented in Figure 2.6.

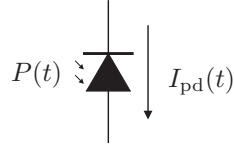


Figure 2.6: Schematic representation of a photodiode

There are two reasons why the calculation of the output current of the photodiode in a CM system is not straightforward:

1. The power of the light that is to be detected by the photodiode will generally be random, because of the broadband sources that are used (see Subsection 2.3.4);
2. The power-current conversion process is also random, since the generation of hole/electron pairs can be considered as a random point process, even when the instantaneous input power is deterministic.

In this thesis it will be assumed that PIN photodiodes rather than avalanche photodiodes (APDs) are used for photodetection, because:

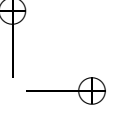
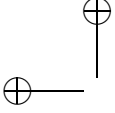
- APDs are more expensive than PIN photodiodes;
- APDs require a much higher biasing voltage and require external cooling, hence requiring a more expensive driving circuit than PIN photodiodes;
- APDs have a much slower response than PIN photodiodes;
- APDs grew outdated since the introduction of the erbium-doped fiber amplifier (EDFA).

For a PIN photodiode, the actual photocurrent can be written as

$$I_{\text{pd}}(t) = \sum_i e h_{\text{pd}}(t - t_i), \quad (2.59)$$

where $e \approx 1.60 \cdot 10^{-19}$ C is the electron charge, $\{t_i\}$ are the random electron-hole pair generation event times, and $h_{\text{pd}}(t)$ is the impulse response of the photodiode which is normalized such that

$$\int_{-\infty}^{\infty} h_{\text{pd}}(\rho) d\rho = 1. \quad (2.60)$$



The random event times $\{t_i\}$ are assumed to be governed by a doubly-stochastic inhomogeneous Poisson process [49, 51, 53]. This kind of process is extensively analyzed in Appendix A.

In this case, the rate $\Lambda(t)$ of the process corresponds to the average generation rate of electron-hole pairs, which is given by

$$\Lambda(t) = \frac{P(t)\lambda_c\eta}{h c_0}, \quad (2.61)$$

where $P(t)$ and λ_c are the (random) power and center wavelength of the incident optical signal, respectively, η is the quantum efficiency of the photodiode, $h \approx 6.63 \cdot 10^{-34}$ J s is Planck's constant and $c_0 \approx 3.00 \cdot 10^8$ m/s is the speed of light in vacuum.

In Appendix A it is proven that the photocurrent (2.59) has expected value

$$\mathbb{E}[I_{\text{pd}}(t)] = e \int_{-\infty}^{\infty} h_{\text{pd}}(t - \rho) \mathbb{E}[\Lambda(\rho)] d\rho,$$

and autocorrelation function

$$\begin{aligned} R_{I_{\text{pd}}I_{\text{pd}}}(t_1, t_2) &= e^2 \int_{-\infty}^{\infty} h_{\text{pd}}(t_1 - \rho) h_{\text{pd}}(t_2 - \rho) \mathbb{E}[\Lambda(\rho)] d\rho \\ &+ e^2 \int_{-\infty}^{\infty} \int_{-\infty}^{\infty} h_{\text{pd}}(t_1 - \rho_1) h_{\text{pd}}(t_2 - \rho_2) R_{\Lambda\Lambda}(\rho_1, \rho_2) d\rho_1 d\rho_2. \end{aligned} \quad (2.62)$$

Moreover, the cross-correlation function of the currents $I_{\text{pd},1}(t)$ and $I_{\text{pd},2}(t)$ of two photodiodes with correlated input rates $\Lambda_1(t)$ and $\Lambda_2(t)$ is proven to be

$$\begin{aligned} R_{I_{\text{pd},1}I_{\text{pd},2}}(t_1, t_2) &= \\ &e^2 \int_{-\infty}^{\infty} \int_{-\infty}^{\infty} h_{\text{pd},1}(t_1 - \rho_1) h_{\text{pd},2}(t_2 - \rho_2) R_{\Lambda_1\Lambda_2}(\rho_1, \rho_2) d\rho_1 d\rho_2. \end{aligned} \quad (2.63)$$

Using (2.61) and defining the *responsivity* of the photodiode as

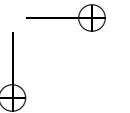
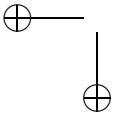
$$R_{\text{pd}} \triangleq \frac{e \lambda_c \eta}{h c_0}, \quad (2.64)$$

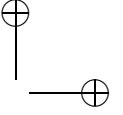
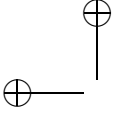
we can write these equations as

$$\mathbb{E}[I_{\text{pd}}(t)] = R_{\text{pd}} \int_{-\infty}^{\infty} h_{\text{pd}}(t - \rho) \mathbb{E}[P(\rho)] d\rho, \quad (2.65)$$

$$\begin{aligned} R_{I_{\text{pd}}I_{\text{pd}}}(t_1, t_2) &= R_{\text{pd}} e \int_{-\infty}^{\infty} h_{\text{pd}}(t_1 - \rho) h_{\text{pd}}(t_2 - \rho) \mathbb{E}[P(\rho)] d\rho \\ &+ R_{\text{pd}}^2 \int_{-\infty}^{\infty} \int_{-\infty}^{\infty} h_{\text{pd}}(t_1 - \rho_1) h_{\text{pd}}(t_2 - \rho_2) \\ &\quad \cdot R_{PP}(\rho_1, \rho_2) d\rho_1 d\rho_2, \end{aligned} \quad (2.66)$$

$$\begin{aligned} R_{I_{\text{pd},1}I_{\text{pd},2}}(t_1, t_2) &= R_{\text{pd}}^2 \int_{-\infty}^{\infty} \int_{-\infty}^{\infty} h_{\text{pd},1}(t_1 - \rho_1) h_{\text{pd},2}(t_2 - \rho_2) \\ &\quad \cdot R_{P_1P_2}(\rho_1, \rho_2) d\rho_1 d\rho_2. \end{aligned} \quad (2.67)$$





From (2.66) it follows that two types of fluctuations occur in the photocurrent:

1. Fluctuations induced by a fluctuating power at the input of the photodiode, for example due to source intensity noise or beat noise. (We will get back to this in Section 4.2.) This is reflected by the second term of (2.66);
2. Fluctuations induced by the random generation times of hole/electron pairs. This is called *shot noise*. It is present even when the detected optical power is constant, as reflected by the first term of (2.66).

From (2.67) it can be concluded that correlation between optical power fluctuations at the inputs of two photodiodes induces correlation between the photodiode currents. (The shot noise currents are not correlated, however.)

Example 2.4

As can be seen from (2.64), the responsivity R_{pd} of a PIN photodiode depends on the wavelength range in which it is applied, but also on the quantum efficiency η , which is determined amongst others by the geometry and constituting material of the junction. In practice photodiodes have been realized for application in the higher wavelength range (1.3–1.6 μm) in Ge and InGaAs, with responsivities in the order of 0.8 A/W, and bandwidths up to several GHz.



2.7 Transimpedance amplifiers

Since photocurrents are very small (in the order of 10–100 μA) amplification is required to process this signal. The optical receivers in CM systems are based on configurations where the photodiodes are operated in reverse bias mode, and their current is amplified by means of a transimpedance amplifier (TIA). The main motivation for this is to achieve a linear relation between optical power and output signal of the receiver, which is critical in coherence demodulation, as we will see later. A TIA converts the input current $I_{in}(t)$ in a voltage $V_{out}(t)$, as shown in Figure 2.7.

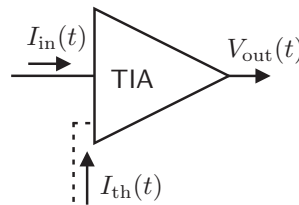
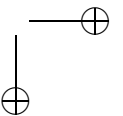
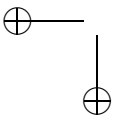
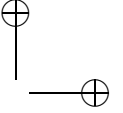
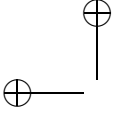


Figure 2.7: Schematic representation of a transimpedance amplifier (TIA)





Due to the random motion of charge carriers in the resistive parts and semiconductor components inside the TIA, thermal noise and shot noise are added to the output signal. This can be modeled as a Gaussian distributed equivalent input noise current $I_{\text{th}}(t)$, so that we can write

$$V_{\text{out}}(t) = Z_{\text{TIA}} \left[I_{\text{in}}(t) + I_{\text{th}}(t) \right], \quad (2.68)$$

where Z_{TIA} is the transimpedance of the TIA. Note that it is assumed that the TIA has infinite bandwidth, since in practice the bandwidth of the TIA will be larger than the bandwidth of the detection filter that follows the TIA. The thermal noise $I_{\text{th}}(t)$ is assumed to be white in the frequency range of interest, so that its power spectral density function can be written as:

$$S_{I_{\text{th}}I_{\text{th}}}(f) = S_{\text{th}}.^1 \quad (2.69)$$

$I_{\text{in}}(t)$ and $I_{\text{th}}(t)$ can be considered as independent signals, and $I_{\text{th}}(t)$ can be assumed to be zero-mean, so that the expected value and autocorrelation function of $V_{\text{out}}(t)$ can be written as


$$\text{E}[V_{\text{out}}(t)] = Z_{\text{TIA}} \text{E}[I_{\text{in}}(t)], \quad (2.70)$$

$$R_{V_{\text{out}}V_{\text{out}}}(t_1, t_2) = Z_{\text{TIA}}^2 \left[R_{I_{\text{in}}I_{\text{in}}}(t_1, t_2) + S_{\text{th}}\delta(t_1 - t_2) \right]. \quad (2.71)$$

Example 2.5

Various types of TIAs are available as commercial products, often integrated together with the photodiode(s) as complete optical receiver modules, with specifications that strongly depend on the type of application.

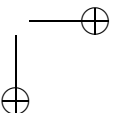
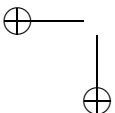
The transimpedance of these TIAs ranges from hundreds of ohms to several tens of kilo-ohms, and the power spectral density of the equivalent input noise current ranges from several up to several hundreds of $(\text{pA})^2/\text{Hz}$, both depending on amongst others bandwidth and power supply.

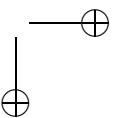
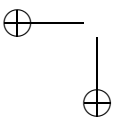
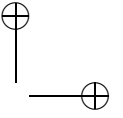
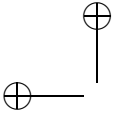
Other important specifications of TIAs are bandwidth and dynamic range, which determine the amplitude and frequency range for which input signals are amplified without (non-)linear distortion. This is not further considered in this thesis, however, as implicitly stated by (2.68). 

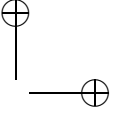
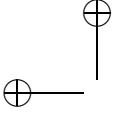
2.8 Conclusion

This concludes the description of the analytical models for the various components that constitute CM systems. In the next chapter it will be shown how these (continuous-time) models can be represented in discrete-time form and hence be applied in computer simulations. In the remaining chapters, the continuous-time models will serve as a basis for the theoretical analyses of various CM systems.

¹For many optical receivers the noise power is specified by the root mean square equivalent input noise current per $\sqrt{\text{Hz}}$, which is the square root of S_{th} .







Chapter 3

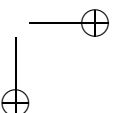
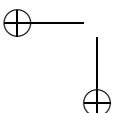
Simulation tool

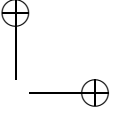
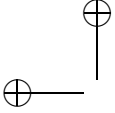
3.1 Introduction

The results that will be presented in this thesis are mainly based on theoretical analyses. There are four reasons, however, why it is useful also to refer to simulations next to theoretical analyses:

- The simulation results can be used to verify the results of the analyses. In this way it can be checked whether mistakes have been made in the derivations and whether all the mathematical approximations are accurate;
- Especially in the case of complicated systems, models are often greatly simplified in order to facilitate theoretical analysis, resulting into inaccuracies of analytical results. These inaccuracies can be identified by running simulations based on more advanced models;
- Particularly in cases where random processes play an important role, simulations can provide a good way of visualizing the actual signals that are involved, which enhances the understanding of the system concepts;
- Theoretical analysis may in some cases be a more time-consuming procedure than simply running a short simulation. Therefore, simulation can in some cases be a good way of quickly obtaining a first impression about a certain new system concept.

Most commercially available simulators for optical communication systems are not suitable for studying the kind of systems that are considered in this thesis, however. The reason for this is that most simulators base their calculations purely on the *power* of the optical signals that are involved, and not on the optical phase. Consequently, it is not possible to study systems that are based on interference of broadband light waves, as is the case in CM. Therefore, it was decided to create a tool dedicated to the simulation of broadband light wave communication systems.





Simulink[™] [54] was chosen as a simulation environment, since it enables the user to describe and simulate dynamical systems using a graphical user interface (GUI). These systems consist of building blocks that are taken either from standard or customized block libraries. Matlab[™] [55] is used as the underlying math package.

This chapter describes the Simulink[™] block library that was created for simulating CM systems. The blocks in this library are based on the analytical models that are described in Chapter 2.

3.2 Discrete-time representation of optical signals

Since the calculations of the simulator are to be carried out on a digital computer, the actual signals that are involved in the simulated systems need to be represented in discrete-time form. This means that the signals that are processed in the simulator are actually sampled versions of the simulated continuous-time signals.

According to Nyquist's criterion, a signal that has an absolute bandwidth of B Hz is completely described by specifying its values at time instants separated by T_{samp} seconds, provided that $T_{\text{samp}} \leq \frac{1}{2B}$ [56].

In Section 2.2 it was explained how one polarization mode of an optical signal can be analytically described by means of a scalar wave representation. It was defined as a complex band-pass signal $x(t)$. Representing the optical signal in the simulator by means of samples of $x(t)$ would require very high sample rates, however, because of the large center frequency of optical signals.

Example 3.1

For a center wavelength of 1310 nm, the center frequency is

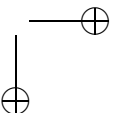
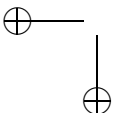
$$f_c = \frac{c_0}{\lambda_c} = \frac{3.00 \cdot 10^8}{1.31 \cdot 10^{-6}} \text{ Hz} \approx 230 \text{ THz}, \quad (3.1)$$

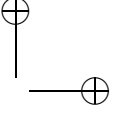
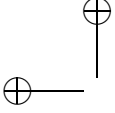
so if $x(t)$ were directly sampled, the sampling frequency should be at least

$$f_{\text{samp}} \triangleq \frac{1}{T_{\text{samp}}} \geq 2f_c \approx 4.6 \cdot 10^{14} \text{ samples/s}. \quad (3.2)$$

This means that simulation of 1 Gbps transmission would require

$$\frac{f_{\text{samp}}}{R_b} \approx \frac{4.6 \cdot 10^{14}}{10^9} \text{ samples/bit} = 4.6 \cdot 10^5 \text{ samples/bit}. \quad (3.3)$$





A better approach is to take samples of the *complex envelope* rather than the *pre-envelope*, because $x(t)$ is a band-pass signal with a bandwidth which is generally much lower than the center frequency. Therefore, the signals in the simulator consist of sequences of complex numbers

$$\{\tilde{x}(n)\} \triangleq \{\tilde{u}_x(n) + j\tilde{v}_x(n)\}, \quad (3.4)$$

which represents the set of sample values of the complex envelope of the optical signal. (So the tilde denotes discrete-time representation of the corresponding continuous-time signal.) Hence, the real and imaginary parts of these numbers correspond to the in-phase and quadrature component of the optical field, $\{\tilde{u}_x(n)\}$ and $\{\tilde{v}_x(n)\}$, respectively. The phase corresponds to the optical phase, and the optical power can be calculated as

$$P_{\tilde{x}}(n) = \frac{1}{2}|\tilde{x}(n)|^2 = \frac{1}{2}[\tilde{u}_x^2(n) + \tilde{v}_x^2(n)]. \quad (3.5)$$

Recall that the spectrum of $u_x(t)$ is Gaussian and hence not limited to a strictly bounded frequency interval. Therefore, it is not possible to choose a sampling frequency that does not introduce aliasing. Hence, choosing the sampling frequency is a trade-off between minimizing the amount of simulation time and minimizing the effect of aliasing. As a criterion one could state that the Nyquist interval should encompass at least 99% of the power of the source, so:

$$\int_{-\frac{1}{2T_{\text{samp}}}}^{\frac{1}{2T_{\text{samp}}}} S_{u_x u_x}(f) df \geq 0.99P_x. \quad (3.6)$$

From (2.28) it then follows that

$$Q\left(\frac{\sqrt{\pi}\tau_c}{T_{\text{samp}}}\right) \leq 0.005 \Rightarrow T_{\text{samp}} \lesssim 0.69\tau_c, \quad (3.7)$$

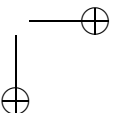
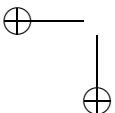
where the Gaussian tail probability $Q(\cdot)$ is defined as

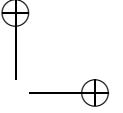
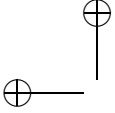
$$Q(z) \triangleq \frac{1}{\sqrt{2\pi}} \int_z^{\infty} \exp\left(-\frac{1}{2}x^2\right) dx. \quad (3.8)$$

For convenience, one could choose $T_{\text{samp}} = \tau_c/2$; one can verify that this results in a Nyquist interval that encompasses approximately 99.96% of the source power.

Example 3.2

For a center wavelength of 1310 nm and an absolute linewidth of 40 nm, the coherence time is approximately 0.1 ps (see Example 2.1). If half this value were taken for the sample time, the sampling rate would be $2 \cdot 10^{13}$ samples/s, which is roughly 23 times smaller than in Example 3.1. □





All the components in the simulator should be modeled as baseband equivalents. Note that for some components, the baseband equivalent characteristics depend on the center frequency of the optical signal. Therefore, all the sources in one simulation should have the same center frequency and it should be known prior to the simulation run because all the components have to be initialized based on this knowledge.

Another desirable design criterion for the simulator is that the procedure for converting the values of the system parameters into the values of the simulator parameters must be programmable, so that the simulation can be automatically initialized based on the system parameters that are supplied by the user, without having to consult external tools.

3.3 LED sources

The LED block should generate a sequence of complex numbers $\{\tilde{x}(n)\}$ with characteristics that correspond to the LED model that was described in Section 2.3. This implies that the samples should have a Gaussian probability distribution and a Gaussian baseband power spectral density function, with a prescribed average power and bandwidth (or linewidth, or coherence time). The in-phase and quadrature signals (the real and imaginary part of the complex envelope) are mutually independent, so they can simply be generated by:

1. generating two independent white Gaussian noise (WGN) sequences;
2. filtering these two WGN sequences in such a way that their power spectral density functions become approximately Gaussian.

3.3.1 Generating white Gaussian noise

Discrete-time WGN can be generated in Matlab[™] using the `RANDN` command. Although the generated numbers $\{\tilde{w}(n)\}$ are actually pseudo-random, it will be assumed that they can be considered as mutually independent random variables which are Gaussian distributed with mean zero and variance 1. As a result, autocorrelation sequence of this sequence can be written as

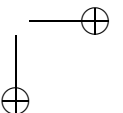
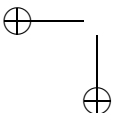
$$R_{\tilde{w}\tilde{w}}(m) \triangleq \text{E}[\tilde{w}(n)\tilde{w}(n+m)] = \begin{cases} 1 & , m = 0, \\ 0 & , m \neq 0. \end{cases} \quad (3.9)$$

The power spectral density follows by taking the discrete-time Fourier transform (DTFT):

$$S_{\tilde{w}\tilde{w}}(\nu) \triangleq \sum_m R_{\tilde{w}\tilde{w}}(m) \exp(-j2\pi\nu m) = 1, \quad (3.10)$$

where ν is the normalized frequency. It is related to the corresponding frequency f in the power spectral density function of the sampled continuous-time signal by

$$\nu = f T_{\text{samp}}. \quad (3.11)$$



3.3.2 Filtering the white Gaussian noise

After filtering $\tilde{w}(n)$ by means of a discrete-time filter with impulse response sequence $\tilde{h}_s(n)$, an output signal $\tilde{u}_x(n)$ results with power spectral density

$$S_{\tilde{u}_x \tilde{u}_x}(\nu) = S_{\tilde{w} \tilde{w}}(\nu) |\tilde{H}_s(\nu)|^2 = |\tilde{H}_s(\nu)|^2, \quad (3.12)$$

where the frequency response $\tilde{H}_s(\nu)$ of the filter is the DTFT of $\tilde{h}_s(n)$:

$$\tilde{H}_s(\nu) \triangleq \sum_n \tilde{h}_s(n) \exp(-j 2\pi \nu n). \quad (3.13)$$

Note that the result of this DTFT is periodic in ν with period 1, so (3.12) will also be periodic with period 1. Now the aim is to design a filter with a frequency response such that (3.12) corresponds to the power spectral density function (2.28) that was found in Section 2.3, for $|\nu| < 1/2$. Hence, the samples $\tilde{u}_x(n) \triangleq u_x(n \cdot T_{\text{samp}})$ of $u_x(t)$ should have power spectral density

$$\begin{aligned} S_{\tilde{u}_x \tilde{u}_x}(\nu) &\approx \frac{1}{T_{\text{samp}}} S_{u_x u_x} \left(\frac{\nu}{T_{\text{samp}}} \right) \\ &= \frac{\sqrt{2} P_x \tau_c}{T_{\text{samp}}} \exp \left(-2\pi \left(\frac{\nu \tau_c}{T_{\text{samp}}} \right)^2 \right), \quad |\nu| < 1/2. \end{aligned} \quad (3.14)$$

It follows that the magnitude of the transfer function of the filter should satisfy

$$|\tilde{H}_s(\nu)| \approx \sqrt{\frac{\sqrt{2} P_x \tau_c}{T_{\text{samp}}}} \exp \left(-\pi \left(\frac{\nu \tau_c}{T_{\text{samp}}} \right)^2 \right), \quad |\nu| < 1/2. \quad (3.15)$$

For a linear phase filter we can take $\tilde{H}_s(\nu) = |\tilde{H}_s(\nu)|$, so that the desired impulse response $\tilde{h}_s(n)$ follows by taking the inverse DTFT of (3.15):

$$\begin{aligned} \tilde{h}_s(n) &= \int_{-1/2}^{1/2} |\tilde{H}_s(\nu)| \exp(j 2\pi \nu n) d\nu \\ &\approx \sqrt{\frac{\sqrt{2} P_x \tau_c}{T_{\text{samp}}}} \int_{-1/2}^{1/2} \exp \left(-\pi \left(\frac{\nu \tau_c}{T_{\text{samp}}} \right)^2 + j 2\pi \nu n \right) d\nu. \end{aligned} \quad (3.16)$$

When the sample time T_{samp} is smaller than $\tau_c/2$ (as derived in the previous section), we can approximate this as

$$\begin{aligned} \tilde{h}_s(n) &\approx \sqrt{\frac{\sqrt{2} P_x \tau_c}{T_{\text{samp}}}} \int_{-\infty}^{\infty} \exp \left(-\pi \left(\frac{\nu \tau_c}{T_{\text{samp}}} \right)^2 + j 2\pi \nu n \right) d\nu \\ &= \sqrt{\frac{\sqrt{2} P_x T_{\text{samp}}}{\tau_c}} \exp \left(-\pi \left(\frac{n T_{\text{samp}}}{\tau_c} \right)^2 \right). \end{aligned} \quad (3.17)$$

In Figure 3.1 part of this impulse response is shown for $T_{\text{samp}} = \tau_c/2$.

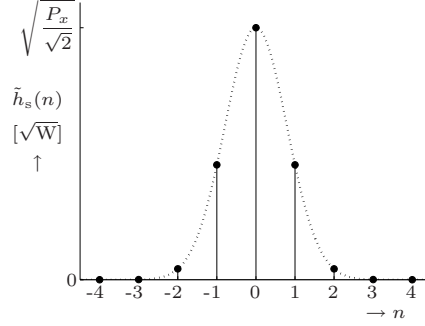


Figure 3.1: Desired impulse response of the LED filter for $T_{\text{samp}} = \tau_c/2$

When the filter is realized as a finite impulse response (FIR) filter, this desired response can be approximated by choosing the filter coefficients $\tilde{f}_s(n)$ as a windowed and shifted version of $\tilde{h}_s(n)$ [57]. Since $\tilde{H}_s(\nu)$ does not contain sharp transitions, this can simply be performed by means of a rectangular window:

$$\tilde{f}_s(n) = \begin{cases} \tilde{h}_s(n - N) & , 0 \leq n \leq 2N, \\ 0 & , \text{elsewhere,} \end{cases} \quad (3.18)$$

so the length of the window (and hence the number of coefficients) is $2N + 1$. The resulting power spectral density at the output of the filter now follows from (3.12), (3.13), (3.17) and (3.18) as

$$\begin{aligned} S_{\tilde{u}_x \tilde{u}_x}(\nu) &= \left| \sum_n \tilde{f}_s(n) \exp(-j 2\pi \nu n) \right|^2 = \left| \sum_{n=-N}^N \tilde{h}_s(n) \exp(-j 2\pi \nu n) \right|^2 \\ &= \frac{\sqrt{2} P_x T_{\text{samp}}}{\tau_c} \left[1 + 2 \sum_{n=1}^N \exp\left(-\pi \left(\frac{n T_{\text{samp}}}{\tau_c}\right)^2\right) \cos(2\pi \nu n) \right]^2. \end{aligned} \quad (3.19)$$

In Figure 3.2(a), this has been plotted for $T_{\text{samp}} = \tau_c/2$ and different values of N , and compared to the desired power spectral density (3.14) (dotted curve).

The autocorrelation function of \tilde{u}_x follows from

$$\begin{aligned}
 R_{\tilde{u}_x \tilde{u}_x}(m) &\triangleq \mathbb{E}[\tilde{u}_x(n)\tilde{u}_x(n+m)] = \sum_n \tilde{f}_s(n)\tilde{f}_s(n+m) \\
 &= \begin{cases} \sum_{n=-N}^{N-|m|} \tilde{h}_s(n)\tilde{h}_s(n+|m|) & , |m| \leq 2N, \\ 0 & , |m| > 2N, \end{cases} \\
 &= \begin{cases} \frac{\sqrt{2}P_x T_{\text{samp}}}{\tau_c} \sum_{n=-N}^{N-|m|} \exp\left(-\pi(2n^2 + 2|m|n + m^2) \left(\frac{T_{\text{samp}}}{\tau_c}\right)^2\right) & , |m| \leq 2N, \\ 0 & , |m| > 2N. \end{cases} \quad (3.20)
 \end{aligned}$$

It has been plotted in Figure 3.2(b) for $T_{\text{samp}} = \tau_c/2$ and different values of N . The dotted curve represents the autocorrelation function of $u_x(t)$, as given by (2.26).

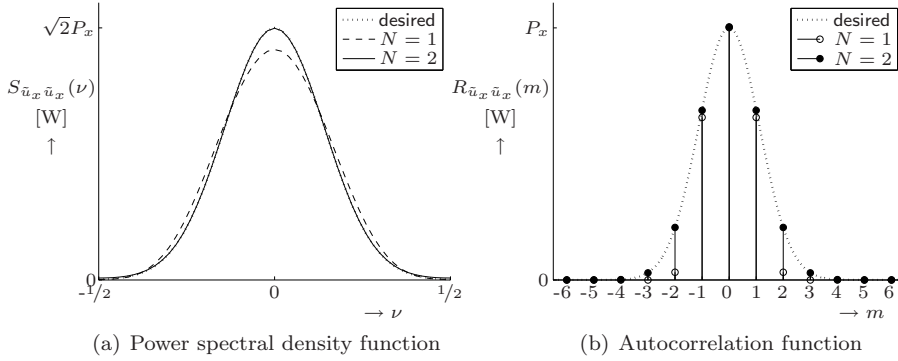


Figure 3.2: Theoretical power spectral density function and autocorrelation function at the output of the designed LED filter for $T_{\text{samp}} = \tau_c/2$ and different values of N

Figure 3.2 shows that an accurate approximation is obtained when $N = 2$ is chosen. (This should not be surprising since from Figure 3.1 one can find that the value of $\tilde{h}_s(n)$ can be neglected for $|n| > 2$.)

Example 3.3

The described discrete-time LED model was realized as a Simulink[™] library block, based on the parameter values that were given in Example 2.1. (Note that both the LEDs that were described in Example 2.1 result in the same parameter values for the Simulink[™] library block, because they have the same coherence time.) An average optical output power of $P_x = 10$ mW was specified. The sample time was set to $T_{\text{samp}} = \tau_c/2 = 50$ fs, and the virtual total

simulation time was chosen to be 100 ns. Hence, 2 million samples of a realization of $\{\tilde{x}(n)\}$ were generated. Some simulation results are shown in Figure 3.3.

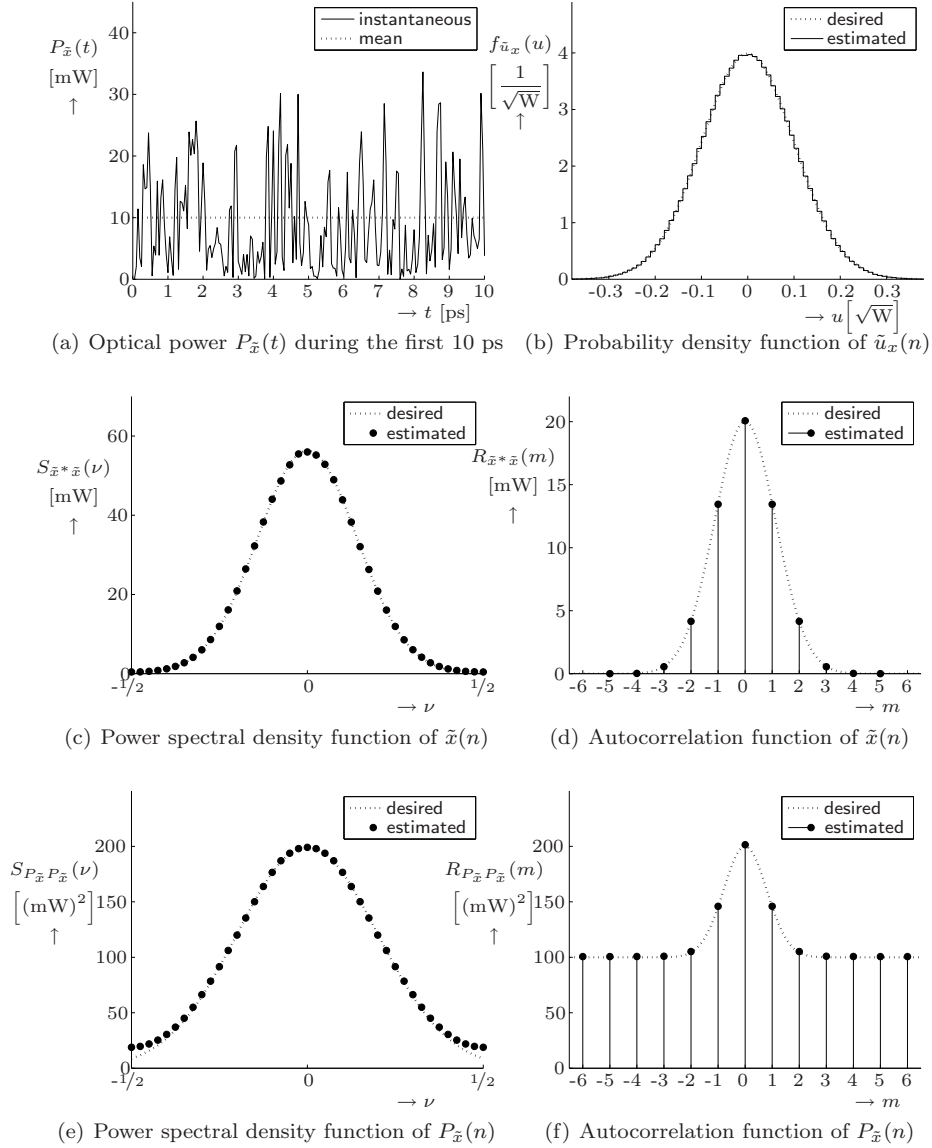
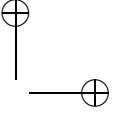
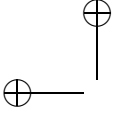



Figure 3.3: Some simulation results for the LED block with $P_x = 10$ mW, $\tau_c = 100$ fs, $T_{\text{samp}} = 50$ fs. The virtual simulation time is 100 ns (2 million samples).



In Figure 3.3(a) the power of $\tilde{x}(n)$ during the first 10 ps has been plotted as a function of time. The dotted curve corresponds to the average optical power that was measured, which indeed corresponds to the 10 mW that was specified.

It can also be verified whether the generated realization satisfied the prescribed probability distribution. That is, the real and imaginary parts of the samples should be mutually independent and follow a Gaussian distribution with mean zero and a variance P_x (see Section 2.2). This checked by classifying the outcomes of the samples of $\tilde{u}_x(n)$ in intervals of length $0.01 \sqrt{W}$, and counting the number of samples in each interval using Matlab[™]'s HIST function. The resulting estimation of the probability density function has been plotted in Figure 3.3(b). It corresponds well to the theoretical Gaussian curve (dotted).

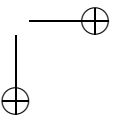
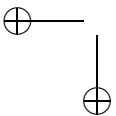
The power spectral density function and autocorrelation function of $\tilde{x}(n)$ are estimated using Matlab[™]'s PSD and XCORR function, respectively. The results are plotted in Figure 3.3(c) and 3.3(d), respectively, and turn out to correspond well to the theoretical results (dotted curves).

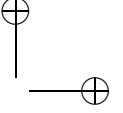
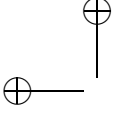
In a similar way, estimations of the power spectral density function and autocorrelation function of the power $P_{\tilde{x}}(n)$ are found. These are plotted in Figure 3.3(e) and 3.3(f), respectively, together with the theoretical results for the corresponding continuous-time power $P_x(t)$ that were derived in Section 2.3.4 (dotted curves). Prior to calculating the power spectral density function, the mean value had been subtracted from $P_{\tilde{x}}(n)$ in order to remove the δ -function from the spectrum. Note that there is some mismatch at frequencies close to $\nu = 1/2$, due to the fact that the frequency range of the theoretical power spectral density function slightly exceeds the Nyquist interval, so that aliasing occurs. Later on we will see that this will hardly affect the result of CM system simulations, because the noise performance of such systems is mainly determined by the power spectral density of intensity noise at relatively low frequencies. 

3.4 Optical encoders and decoders

The optical encoders and decoders can be constructed in the simulator by combining building blocks that represent couplers, delay lines and—in case of transmitters—modulators. Since the couplers and modulators are memoryless devices, their corresponding building blocks are a straightforward sample-by-sample implementation of the behavior that is described in Section 2.4. Phase modulation, for example, simply involves a multiplication by $\exp(j\tilde{\phi}_{\text{mod}}(n))$, where $\tilde{\phi}_{\text{mod}}(n)$ is the discrete-time modulating signal.

When implementing the time-discrete baseband equivalent of a delay line one should note that delaying a complex band-pass signal involves delaying both the carrier and the complex envelope. For example, when an analytical signal $x(t)$ as defined in (2.14) is delayed by T seconds, then the resulting signal





can be written as

$$\begin{aligned} x(t-T) &= \left[u_x(t-T) + j v_x(t-T) \right] \exp(j 2\pi f_c(t-T)) \\ &= \left\{ \left[u_x(t-T) + j v_x(t-T) \right] \exp(-j 2\pi f_c T) \right\} \exp(j 2\pi f_c t), \end{aligned} \quad (3.21)$$

so the corresponding complex envelope (the expression between braces) is in fact delayed by T seconds and multiplied by a fixed constant $\exp(-j 2\pi f_c T)$. Hence, the delay lines can be modeled in the simulator as a combination of a shift by T/T_{samp} samples (to model the group delay) and a multiplication by $\exp(-j 2\pi f_c T)$ (to model the phase delay).

3.5 Single-mode optical fibers

A single-mode fiber (SMF) can be modeled in Simulink[™] by means of a discrete-time filter with a transfer function $\tilde{H}_f(\nu)$ that corresponds to the base-band equivalent of (2.44). Using the approximations in (2.45) and (2.50) and omitting the irrelevant constant phase shift and constant time delay this results in

$$\tilde{H}_f(\nu) = H_f \left(\frac{\nu}{T_{\text{samp}}} + f_c \right) \approx H_0 \exp \left(-j 2\pi \left[b_1 \nu^2 + b_2 \nu^3 \right] \right), \quad |\nu| < 1/2, \quad (3.22)$$

where

$$H_0 \triangleq 10^{-\alpha(f_c)l_f/20}, \quad (3.23)$$

$$b_1 \triangleq \frac{l_f \tau_g'(f_c)}{2T_{\text{samp}}^2}, \quad (3.24)$$

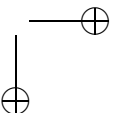
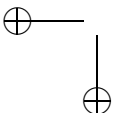
$$b_2 \triangleq \frac{l_f \tau_g''(f_c)}{6T_{\text{samp}}^3}. \quad (3.25)$$

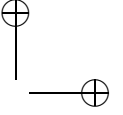
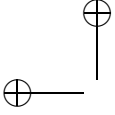
The two terms in the argument of the exponent of (3.22) denote first and second order dispersion, respectively. In general we have $\tilde{H}_f(\theta) \neq \tilde{H}_f^*(-\theta)$ and $\tilde{H}_f(\theta) \neq \tilde{H}_f(-\theta)$, so the desired impulse response $\tilde{h}_f(n)$ may be complex and asymmetric, that is, $\tilde{h}_f(n) \neq \tilde{h}_f(-n)$. In practice, however, one of the two terms can be neglected so that $\tilde{h}_f(n)$ is either real or symmetric. These two simplified cases will be discussed in the following two subsections.

3.5.1 First order dispersion

In case of first order dispersion (3.22) reduces to

$$\tilde{H}_f(\nu) = H_0 \exp \left(-j 2\pi b_1 \nu^2 \right), \quad |\nu| < 1/2. \quad (3.26)$$





We now have $\tilde{H}_f(\nu) = \tilde{H}_f(-\nu) \neq \tilde{H}_f^*(-\nu)$ so the desired impulse response $\tilde{h}_f(n)$ is complex and symmetric. It is related to $\tilde{H}_f(\nu)$ by the inverse DTFT:

$$\begin{aligned} \tilde{h}_f(n) &= \int_{-1/2}^{1/2} \tilde{H}_f(\nu) \exp(j 2\pi \nu n) d\nu \\ &= H_0 \int_{-1/2}^{1/2} \exp\left(-j 2\pi \left[b_1 \nu^2 - \nu n\right]\right) d\nu. \end{aligned} \quad (3.27)$$

Unfortunately this integral is not analytically tractable, and its outcome depends on the value of b_1 . Hence, it is not possible to find an analytical result that can be used for every coherence time and fiber length. This means that—if the filter coefficients were to be determined by means of window design—numerical integration techniques would have to be implemented in Matlab[™] in order to have a fully programmed initialization of the fiber model.

A less complicated programmable alternative for finding the filter coefficients of a FIR filter is the frequency sampling (FS) method [57]. The idea of FS design is that a certain desired frequency response $\tilde{H}(\nu)$ is sampled at N equidistant points in the frequency interval $0 \leq \nu < 1$. From these samples the filter coefficients $\tilde{f}(n)$ are calculated by means of an inverse discrete Fourier transform (DFT):

$$\tilde{f}(n) = \begin{cases} \frac{1}{N} \sum_{k=0}^{N-1} \tilde{H}\left(\frac{k}{N}\right) \exp\left(\frac{j 2\pi k n}{N}\right) & , 0 \leq n \leq N-1, \\ 0 & , \text{elsewhere.} \end{cases} \quad (3.28)$$

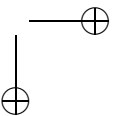
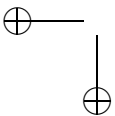
This can be performed in Matlab[™] using the IFFT command. The relation between the filter coefficients $\tilde{f}(n)$ and the desired impulse response $\tilde{h}(n)$ can be found by writing the desired response $\tilde{H}(\nu)$ as the DTFT of $\tilde{h}(n)$ and substituting this in (3.28), resulting in:

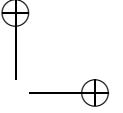
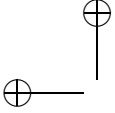
$$\tilde{f}(n) = \begin{cases} \sum_k \tilde{h}(n + k N) & , 0 \leq n \leq N-1, \\ 0 & , \text{elsewhere.} \end{cases} \quad (3.29)$$

Apparently, the filter coefficients that result from FS effectively correspond to a windowed version of a periodic sequence that results from infinitely summing time-shifted versions of $\tilde{h}(n)$. Hence, the values of $\tilde{h}(n)$ should be negligible for values of n outside the interval $0 \leq n \leq N-1$; otherwise aliasing will occur.

The actual frequency response $\tilde{F}(\nu)$ of the filter follows by taking the DTFT of $\tilde{f}(n)$. One can verify that $\tilde{F}(\nu)$ exactly corresponds to the desired frequency response $\tilde{H}(\nu)$ at the sampled frequency points, whereas $\tilde{F}(\nu)$ is a polynomial interpolation of $\tilde{H}(\nu)$ in $z = \exp(j 2\pi \nu)$ for intermediate frequency values. The smoother the desired frequency response and the larger the number of frequency samples N , the smaller the error between $\tilde{F}(\nu)$ and $\tilde{H}(\nu)$.

Note that the procedure described above assumes that the desired frequency response $\tilde{H}(\nu)$ is specified for the frequency values $0 \leq \nu < 1$, and moreover,





that the corresponding desired impulse response $\tilde{h}(n)$ has significant values only for $0 \leq n \leq N - 1$. In our case, however, the desired frequency response $\tilde{H}_f(\nu)$ is specified for $|\nu| < 1/2$, and the desired impulse response $\tilde{h}_f(n)$ is symmetric so it has significant values for $n = -N/2 \leq n \leq N/2$ (assuming that N is even).

Hence, if the Matlab[™] function `IFFT` is to be used for computing the inverse DFT of the frequency samples, it has to be done in four steps:

1. Samples of (3.26) are taken at frequencies

$$\nu = -1/2, -1/2 + \frac{1}{N}, \dots, -\frac{1}{N}, 0, \frac{1}{N}, \dots, 1/2 - \frac{1}{N}; \quad (3.30)$$

2. Since the desired response $\tilde{H}_f(\nu)$ is periodic in ν with period 1, a corresponding sequence of samples for $0 \leq \nu < 1$ can be obtained by means of a cyclic shift by $N/2$ samples (that is, by interchanging the first $N/2$ samples with the last $N/2$ samples);
3. The inverse DFT of the new frequency sample sequence is computed using the `IFFT` command;
4. The proper filter coefficients $\tilde{f}_f(n)$ can be obtained by means of a cyclic shift by $N/2$ samples.

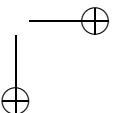
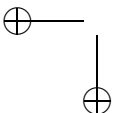
(The last step can be removed when the frequency sample sequence is multiplied by a factor $\exp(-j\pi\nu N)$ prior to performing the inverse DFT.)

The disadvantage of the FS method is that the frequency response of the resulting filter shows ripple or overshoot around points of discontinuity in the desired frequency response. In our case this happens around $\nu = 1/2$, where the group delay response shows a discontinuity. This is illustrated in Figure 3.4, where the solid curve represents the (periodic) desired group delay response of the filter. The dotted line represents the shape of the (also periodic) power spectral density function of the source signal when $T_{\text{samp}} = \tau_c/2$.

This problem can be solved by replacing the discontinuity by a smoother transition. In our case we do this by choosing a certain value ν_1 close to $1/2$, and replacing the desired response for $\nu_1 < \nu < 1 - \nu_1$ by a response in which the group delay response is linearly interpolated between the values of the desired group delay at $\nu = \nu_1$ and $\nu = 1 - \nu_1$. This is illustrated by the dashed curve in Figure 3.4. Adding a constant phase to this part of the response so that the overall phase response is continuous as well, results in an overall desired frequency response that replaces (3.26) by

$$\tilde{H}_f(\nu) = \begin{cases} H_0 \exp(-j2\pi b_1 \nu^2) & , |\nu| < \nu_1, \\ H_0 \exp\left(-j\pi b_1 \nu_1 \left[1 - \frac{2(1/2 - |\nu|)^2}{1/2 - \nu_1}\right]\right) & , \nu_1 < |\nu| < 1/2. \end{cases} \quad (3.31)$$

(Note that both the phase response and the group delay response are now continuous.) Now assume that we choose the value of ν_1 such that it corresponds



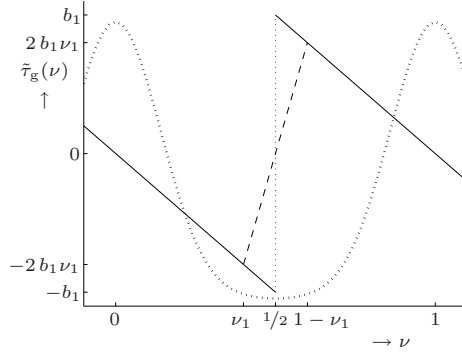


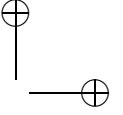
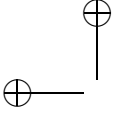
Figure 3.4: Desired group delay response of the fiber model in case of first order dispersion (solid line). The dashed line represents the proposed continuity correction and the dotted line represent the shape of the power spectral density function of the source signal.

to the position of a frequency sample (so it is a multiple of $1/N$). Furthermore assume (for convenience) that the number of samples N is always chosen as a multiple of 10. Then it is rather obvious to set $\nu_1 = 0.4$, since this will coincide with a frequency sample for any value of N that is a multiple of 10, and it is the value closest to $\nu = 1/2$ for the case that $N = 10$. Note in Figure 3.4 that, on one hand, this value of ν_1 results in a relatively wide transition interval, which should significantly reduce ripples and overshoot in the frequency response. On the other hand, it results in a transition interval where the optical signal has only little spectral content (as can be seen from the dotted curve, which represents the shape of the power spectral density function of the source signal), so that smoothening the transition in this way is not expected to result in a significant degradation of the accuracy of the simulation results.

Now we have a procedure to calculate the filter coefficients $\tilde{f}_f(n)$ for a given value of b_1 and a given number of frequency samples N . The value of b_1 follows directly from the fiber parameters and the sampling time T_{samp} . The relation between b_1 and the required value of N is derived heuristically by visually inspecting the resulting magnitude and group delay responses of the resulting filters for various values of b_1 and N .

Example 3.4

For a standard SMF and a center wavelength of 1550 nm (194 THz) we have an attenuation coefficient $\alpha(f_c) \approx 0.2$ dB/km (see Example 2.2). The chromatic dispersion is dominated by first order dispersion, with dispersion coefficient (see Example 2.3) $\tau'_g(194 \text{ THz}) \approx -160$ ps/(THz · km). When we choose $T_{\text{samp}} = \tau_c/2$ and consider a system with 1550 nm sources as described in Example 3.3, we have a coherence time $\tau_c = 0.1$ ps and sampling time $T_{\text{samp}} = 50$ fs.



Now consider a fiber of 1 m length, so we have

$$H_0 = 10^{-0.00001} \approx 1, \quad (3.32)$$

$$b_1 = -\frac{0.001 \cdot 160}{2(0.05)^2} = -32. \quad (3.33)$$

Now the (complex) filter coefficients $\tilde{f}_f(n)$ can be found for several values of the number of frequency samples N , by means of the procedure described above. Matlab[™]'s Filter Visualization Tool (FVTool) is used to find the corresponding magnitude response and group delay response. Varying N it is observed that the passband ripple is well below 0.1 dB when we choose $N = 160$. This also results in an accurate group delay response. This is illustrated in Figure 3.5, where the resulting filter coefficients, magnitude response and group delay response are plotted for $N = 80$ and $N = 160$, respectively. When Figure 3.5(a) and 3.5(b) are compared, it can be noticed that some aliasing occurs in $\tilde{f}_f(n)$ near $n = 0$ and $n = 80$ when $N = 80$ is chosen, whereas aliasing can be neglected when $N = 160$ is chosen. This explains the differences between the plotted magnitude and group delay responses. □

In Example 3.4 it is found that approximately 160 filter coefficients are required when $b_1 = -32$. If b_1 were $+32$ (for standard SMF this could occur for center wavelengths below 1310 nm), the desired impulse response would simply be the complex conjugate of the one that is found for $b_1 = -32$. Hence, the required number of filter coefficients N only depends on the absolute value of b_1 , and not on its sign.

The procedure was repeated for several other values of $|b_1|$, up to 100,000. (Beyond this value, the required number of filter coefficients becomes so large that Matlab[™]'s FVTool is getting extremely slow and moreover, it results in a library model that is so computationally intensive that it will result in an unacceptable simulation running time.) From the results it followed that the following rule of thumb can be used as a rough upper bound for the required number of filter coefficients N as a function of b_1 :

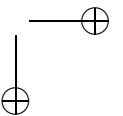
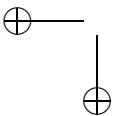
$$N = 20 \left\lceil \frac{|b_1|}{10} \right\rceil + 200, \quad (3.34)$$

where $\lceil \cdot \rceil$ is the ceiling operator (which is used in order to make sure that N is a multiple of 10). This completes the description of the procedure for finding the filter coefficients for given fiber parameters in case of first order dispersion.

3.5.2 Second order dispersion

In case of second order dispersion (3.22) reduces to

$$\tilde{H}_f(\nu) = H_0 \exp(-j 2\pi b_2 \nu^3), \quad |\nu| < 1/2. \quad (3.35)$$



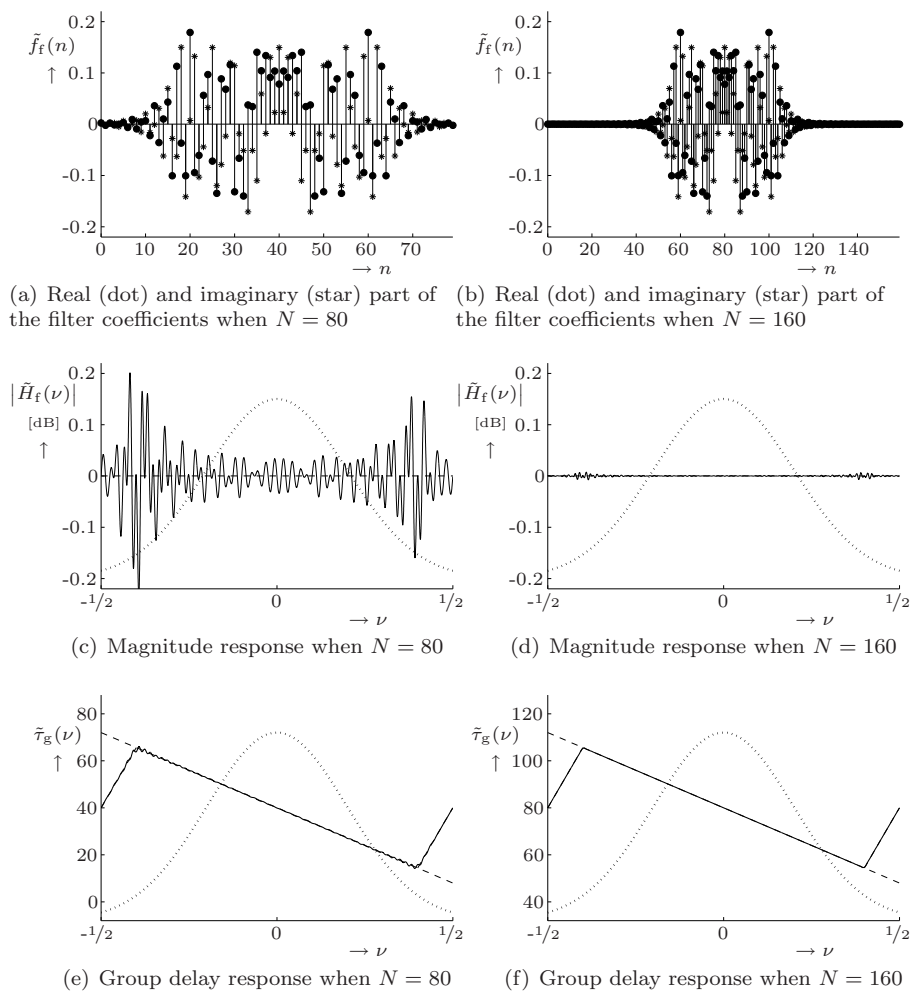


Figure 3.5: Filter coefficients, magnitude response and group delay response of the first order dispersion fiber model by frequency sampling (FS) for $N = 80$ and $N = 160$. The dashed lines represent the desired responses and the dotted lines represent the shape of the power spectral density function of the source signal.

We now have $\tilde{H}_f(\nu) = \tilde{H}_f^*(-\nu) \neq \tilde{H}_f(-\nu)$ so the desired impulse response $\tilde{h}_f(n)$ is real and asymmetric. It follows from the inverse DTFT:

$$\begin{aligned} \tilde{h}_f(n) &= \int_{-1/2}^{1/2} \tilde{H}_f(\nu) \exp(j 2\pi \nu n) d\nu \\ &= H_0 \int_{-1/2}^{1/2} \exp\left(-j 2\pi \left[b_2 \nu^3 - \nu n\right]\right) d\nu. \end{aligned} \quad (3.36)$$

This inverse DTFT is not analytically tractable so we again refer to the FS method for finding the filter coefficients $\tilde{f}_f(n)$. This can be done in a similar way as in the previous subsection. There are two differences, however.

First, the desired response $\tilde{H}_f(\nu)$ has a different kind of discontinuity at $\nu = 1/2$. In the case of first order dispersion, the phase response was continuous and the group delay was discontinuous. In the case of second order dispersion it is the other way around: the group delay dispersion is continuous whereas the phase response is discontinuous. Note, however, that the difference between the left limit and the right limit of the phase response at $\nu = 1/2$ is a multiple of 2π in case the value of b_2 is a multiple of 4. This implies that $\tilde{H}_f(\nu)$ can be made continuous by rounding the value of b_2 to a multiple of 4.

The second difference is that the desired impulse response $\tilde{h}_f(n)$ is no longer symmetric in case of second order dispersion. This implies that the cyclic shift that has to be performed after the inverse DFT should be a number of samples N_s to the right that is not necessarily equal to $N/2$. This will be illustrated in the following example.

Example 3.5

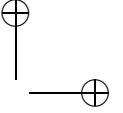
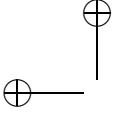
For a standard SMF and a center wavelength of 1310 nm (230 THz) we have an attenuation $\alpha(f_c) \approx 0.35$ dB/km (see Example 2.2). The chromatic dispersion is now dominated by second order dispersion, with dispersion coefficient (see Example 2.3) $\tau_g''(230 \text{ THz}) \approx 3.3$ ps/((THz)² · km). When we choose $T_{\text{samp}} = \tau_c/2$ and consider a system with 1310 nm sources as described in Example 3.3, we have a coherence time $\tau_c = 0.1$ ps and sampling time $T_{\text{samp}} = 50$ fs.


Now consider a fiber of 50 m length, so we have

$$H_0 = 10^{-0.000875} \approx 1, \quad (3.37)$$

$$b_2 = 4 \left\lceil \frac{0.05 \cdot 3.3}{4 \cdot 6(0.05)^3} \right\rceil = 4[55] = 220. \quad (3.38)$$

Now the (real-valued) filter coefficients $\tilde{f}_f(n)$ can be found for several combinations of values of the number of frequency samples N and cyclic shift N_s , by means of the procedure described above. Matlab[™]'s `FVTool` is again used to plot the corresponding magnitude response and group delay response. Varying N and N_s it is observed that the passband ripple is well below 0.1 dB when we choose $N = 216$ and $N_s = 13$. This also results in an accurate group delay response. This is illustrated in Figure 3.6, where the resulting filter coefficients, magnitude response and group delay response are plotted for $N_s = 0$



and $N_s = 13$, respectively. $N = 216$ in both cases. Note that the filter coefficients $\tilde{f}_f(n)$ in Figure 3.6(b) are indeed cyclically shifted to the right with respect to the ones in Figure 3.6(a). 

In Example 3.5 it is found that one should approximately choose $N = 216$ and $N_s = 13$ when $b_2 = 220$. If b_2 were -220 (note that this will not happen for a standard SMF), the desired impulse response would simply be the mirrored version of the one that is found for $b_2 = 220$. Hence, the required number of filter coefficients N only depends on the absolute value of b_1 , and not on its sign. The size of the cyclic shift would also be the same, but its direction would reverse, so N_s would be -13 instead of $+13$.

This procedure was repeated for several other values of b_2 , up to 100,000. From the results it follows that the following rules of thumb can be used as rough upper bounds for the required number of filter coefficients N and the required cyclic shift size N_s as a function of b_2 :

$$N = 2 \left\lceil \frac{7|b_2|}{16} \right\rceil + 24, \quad (3.39)$$

$$N_s = \left\lceil 2 \sqrt[3]{|b_2|} \right\rceil \text{sign}(b_2), \quad (3.40)$$

where the signum function is defined by

$$\text{sign}(x) \triangleq \begin{cases} 1 & , x > 0, \\ 0 & , x = 0, \\ -1 & , x < 0. \end{cases} \quad (3.41)$$

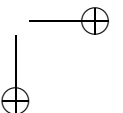
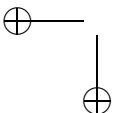
(N is chosen to be even, just for programming convenience.) This completes the description of the procedure for finding the filter coefficients for given fiber parameters in case of second order dispersion.

3.6 Photodiodes

3.6.1 Discrete-time Poisson model

The most straightforward way of representing the photocurrent is by means of a discrete-time doubly stochastic Poisson process, similar to the approximation $\hat{Y}(t)$ that is made in the analysis of the continuous-time Poisson process $Y(t)$ in Appendix A. This implies that at every sampling instant, the (random) power $\tilde{P}(n)$ of the input signal is calculated by means of (3.5). Then the number of electron-hole pairs $K(n)$ that is generated in an interval of length T_{samp} is determined according to a Poisson distribution with rate

$$\tilde{\Lambda}(n) = \frac{\tilde{P}(n)\lambda_c\eta T_{\text{samp}}}{h c_0}. \quad (3.42)$$



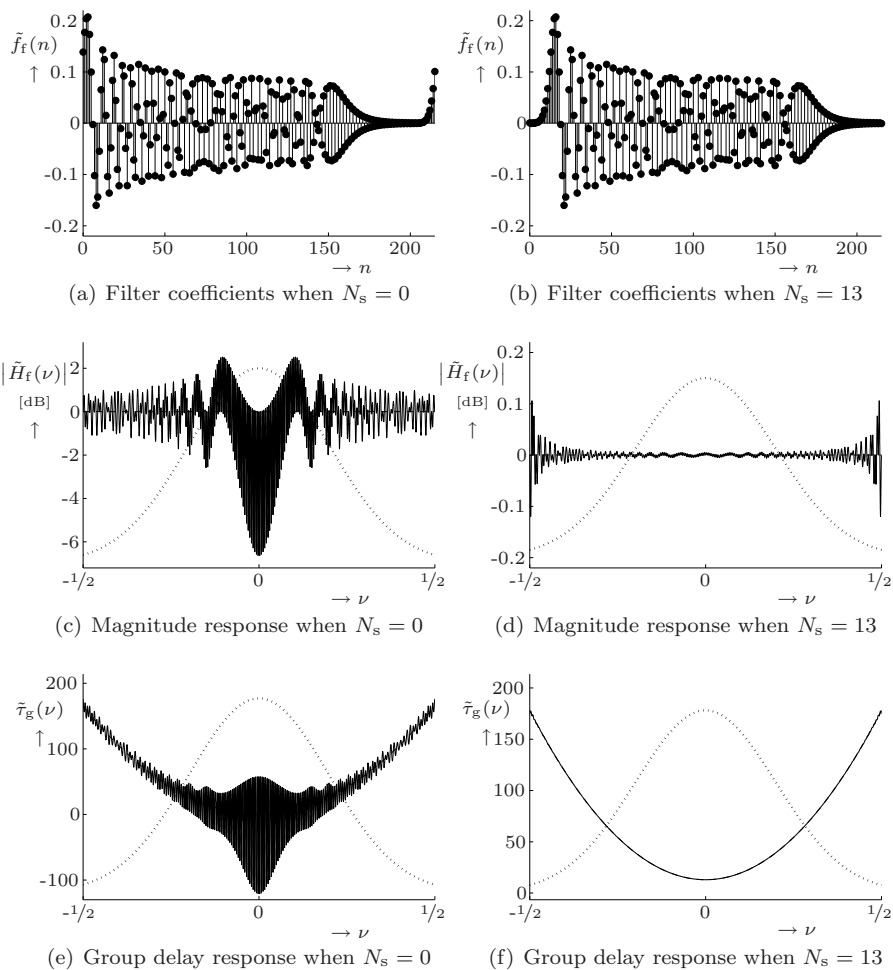
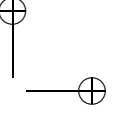
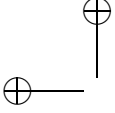


Figure 3.6: Filter coefficients, magnitude response and group delay response of the second order dispersion fiber model by frequency sampling (FS) for $N_s = 0$ and $N_s = 13$. ($N = 216$ in both cases.) The dashed lines represent the desired responses and the dotted lines represent the shape of the power spectral density function of the source signal.



This can be done by means of Matlab[™]'s POISSRND function. Each generation should result in a current pulse $e\tilde{h}_{\text{pd}}(n)/T_{\text{samp}}$, where $\tilde{h}_{\text{pd}}(n)$ is the impulse response of the photodiode, which is normalized such that

$$\sum_n \tilde{h}_{\text{pd}}(n) = 1. \quad (3.43)$$

Hence, the discrete-time representation of the photocurrent can be written as

$$\tilde{I}_{\text{pd}}(n) = \sum_k \frac{K(k)e\tilde{h}_{\text{pd}}(n-k)}{T_{\text{samp}}}. \quad (3.44)$$

It can be easily shown (the proof is very similar to the derivation in Appendix A) that the expected value and autocorrelation function of $\tilde{I}_{\text{pd}}(n)$ can be calculated as

$$\text{E}[\tilde{I}_{\text{pd}}(n)] = R_{\text{pd}} \sum_k \tilde{h}_{\text{pd}}(n-k) \text{E}[\tilde{P}(n)], \quad (3.45)$$

$$\begin{aligned} R_{\tilde{I}_{\text{pd}}\tilde{I}_{\text{pd}}}(n_1, n_2) &= R_{\text{pd}}e \sum_k \tilde{h}_{\text{pd}}(n_1-k)\tilde{h}_{\text{pd}}(n_2-k) \text{E}[\tilde{P}(n)] \\ &\quad + R_{\text{pd}}^2 \sum_{k_1} \sum_{k_2} \tilde{h}_{\text{pd}}(n_1-k_1)\tilde{h}_{\text{pd}}(n_2-k_2) R_{\tilde{P}\tilde{P}}(k_1, k_2), \end{aligned} \quad (3.46)$$

while the cross-correlation function between the discrete-time output signals of two photodiode blocks with input powers $\tilde{P}_1(n)$ and $\tilde{P}_2(n)$ is given by

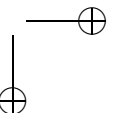
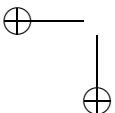
$$\begin{aligned} R_{\tilde{I}_{\text{pd},1}\tilde{I}_{\text{pd},2}}(n_1, n_2) &= \\ &R_{\text{pd}}^2 \sum_{k_1} \sum_{k_2} \tilde{h}_{\text{pd},1}(n_1-k_1)\tilde{h}_{\text{pd},2}(n_2-k_2) R_{\tilde{P}_1\tilde{P}_2}(k_1, k_2), \end{aligned} \quad (3.47)$$

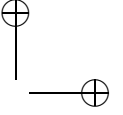
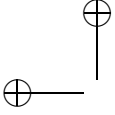
where R_{pd} is given by (2.64). These relations are the discrete-time equivalents of the corresponding continuous-time relations (2.65) through (2.67), showing that the described approach is a proper way of modeling the photodiodes' behavior.

The problem with this approach, however, is that it creates a bottleneck in the simulations as far as simulation speed is concerned. This is due to the fact that at every sampling instant n , the random Poisson variable $K(n)$ has to be realized, using the (laborious) POISSRND function.

3.6.2 A simplified model

A straightforward way of speeding up the simulations is to use a simpler alternative for the POISSRND function, in which the rate $\tilde{\Lambda}(n)$ is converted into the number of electron-hole pairs $K(n)$ in a less computationally intensive way. This could for example be done by means of a Gaussian approximation of the Poisson distribution, using Matlab[™]'s RANDN function.





An even much simpler alternative is to completely remove the random photon generation mechanism from the simulation model and directly calculate the photocurrent $\tilde{I}_{\text{pd}}(n)$ from the input power $\tilde{P}(n)$ as

$$\tilde{I}_{\text{pd}}(n) = R_{\text{pd}} \sum_k \tilde{h}_{\text{pd}}(n-k) \tilde{P}(k). \quad (3.48)$$

One can easily verify that this results in almost the same expected value, auto-correlation function and cross-correlation function as in the previous subsection. The only difference is that the first line in (3.46) is missing, which corresponds to the shot noise current. Hence, this simplified approach should only be used in cases where the shot noise can be neglected with respect to other kinds of noise. Later on we will see that this will be the case in practical CM systems.

Moreover it will be assumed that the impulse response can be approximated by a unit impulse, so that (3.48) simply becomes

$$\tilde{I}_{\text{pd}}(n) = R_{\text{pd}} \tilde{P}(n). \quad (3.49)$$

3.7 Transimpedance amplifiers

Like the modulators, the TIA is also assumed to be a memoryless device, so its library block is a straightforward implementation of the behavior that is described in Section 2.7. Hence, the output voltage $\tilde{V}_{\text{out}}(n)$ for a given input current $\tilde{I}_{\text{in}}(n)$ is calculated as

$$\tilde{V}_{\text{out}}(n) = Z_{\text{TIA}} \left[\tilde{I}_{\text{in}}(n) + \tilde{I}_{\text{th}}(n) \right], \quad (3.50)$$

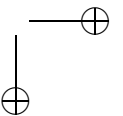
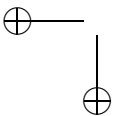
where the equivalent input noise current $\tilde{I}_{\text{th}}(n)$ should be a zero mean WGN sequence with power spectral density

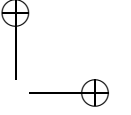
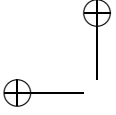
$$S_{\tilde{I}_{\text{th}}\tilde{I}_{\text{th}}}(\nu) = \frac{S_{\text{th}}}{T_{\text{samp}}}. \quad (3.51)$$

Therefore, $\tilde{I}_{\text{th}}(n)$ can be generated by creating a zero mean WGN sequence with variance $S_{\text{th}}/T_{\text{samp}}$ by means of Matlab[™]'s `RANDN` command.

3.8 Conclusion

This concludes the description of the software tool for simulating broadband light wave communication systems. In the remaining chapters it will be used to visualize the signals that are involved in the various CM systems under study, and —wherever possible— it will be used to verify the results of the theoretical analyses.





Chapter 4

Coherence modulation and demodulation

4.1 Introduction

Coherence multiplexing (CM) is based on a channel generation and selection concept that was proposed by Claude Delisle and Paolo Cielo in Canada in 1975 [26]. They called the technique 'spectral modulation of light'. Later on it became known as 'coherence modulation' [34].

In this chapter, coherence modulation will be explained by considering a simple CM system consisting of one transmitter (or coherence modulator) and one receiver (or coherence demodulator), as shown in Figure 4.1. Although the first coherence modulation systems were based on Michelson interferometers [26, 27] and polarization interferometers [28, 33], respectively, we will consider transmitters and receivers that consist of Mach-Zehnder interferometers (MZIs) [29, 46, 58, 59].

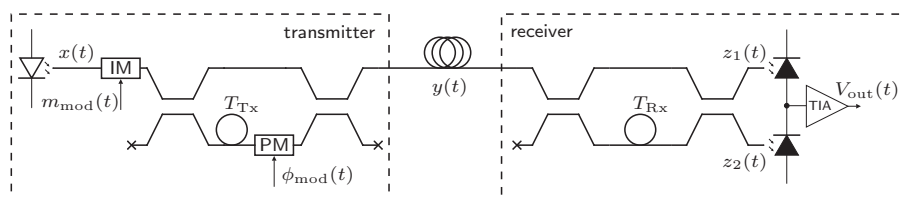
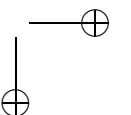
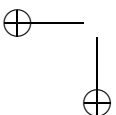


Figure 4.1: Simple CM system with one transmitter and one (balanced) receiver

Note that there is no multiplexing yet. Different methods to multiplex several coherence-modulated channels over one fiber will be considered in Chapter 5. The receiver is a simple balanced receiver. Alternative receiver schemes will be discussed in Chapter 6. And finally, it will for the time being be assumed that



the transmission fiber is so short that chromatic fiber dispersion and propagation losses can be neglected; this will be considered in Chapter 7. Even the propagation delay itself is neglected, for convenience, since it will merely introduce a delay in the output signal of the receiver.

Coherence modulation is based on optical beating and its dependency on the mutual temporal coherence between optical signals. This phenomenon will be explained in Section 4.2, by considering the optical signal $y(t)$ that is launched into the transmission fiber. Then, the output signal of the receiver will be derived, and how it depends on the relation between the delays in the transmitter and receiver, T_{Tx} and T_{Rx} , respectively. Subsequently, the quality of this output signal in terms of the signal-to-noise ratio (SNR) will be studied, followed by a calculation of the bit error rate (BER) in case of digital transmission.

4.2 Optical beating

For convenience, first consider the situation in which only phase modulation (PM) is applied, as illustrated in Figure 4.2.

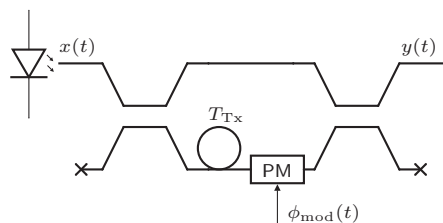


Figure 4.2: Coherence modulator with phase modulation

Following the models in Section 2.4, the output signal of the transmitter in Figure 4.2 can be written as

$$y(t) = \frac{1}{2\sqrt{L_{Tx}}} \left[x(t) - x(t - T_{Tx}) \exp(j\phi_{\text{mod}}(t)) \right], \quad (4.1)$$

where L_{Tx} denote the total excess losses in the transmitter, which include:

- the coupling losses between the source and the interferometer;
- the excess losses in the interferometer (it is assumed that these are the same for both interferometer arms);
- the coupling losses between the interferometer and the transmission fiber.

(Differences in losses of the upper and lower arm are supposed to be incorporated in the coupling coefficients of the 2×2 directional couplers.)

$y(t)$ has zero mean and autocorrelation function

$$\begin{aligned} R_{y^*y}(t_1, t_2) &\triangleq \text{E}[y^*(t_1)y(t_2)] \\ &= \frac{1}{4L_{\text{Tx}}} \left[R_{x^*x}(t_2 - t_1) - R_{x^*x}(t_2 - t_1 - T_{\text{Tx}}) \exp(j\phi_{\text{mod}}(t_2)) \right. \\ &\quad \left. - R_{x^*x}(t_2 - t_1 + T_{\text{Tx}}) \exp(-j\phi_{\text{mod}}(t_1)) \right. \\ &\quad \left. + R_{x^*x}(t_2 - t_1) \exp(j\phi_{\text{mod}}(t_2) - j\phi_{\text{mod}}(t_1)) \right]. \end{aligned} \quad (4.2)$$

The instantaneous power of $y(t)$ follows from

$$\begin{aligned} P_y(t) &= \frac{1}{2} |y(t)|^2 \\ &= \frac{1}{8L_{\text{Tx}}} \left[|x(t)|^2 + |x(t - T_{\text{Tx}})|^2 - x(t)x^*(t - T_{\text{Tx}}) \exp(-j\phi_{\text{mod}}(t)) \right. \\ &\quad \left. - x^*(t)x(t - T_{\text{Tx}}) \exp(j\phi_{\text{mod}}(t)) \right] \\ &= \frac{1}{4L_{\text{Tx}}} \left[P_x(t) + P_x(t - T_{\text{Tx}}) \right] + P_{\text{beat}}(t). \end{aligned} \quad (4.3)$$

Apparently, the power of the output signal of the transmitter consists of the (attenuated) individual powers of $x(t)$ and its delayed version $x(t - T_{\text{Tx}})$, and a beating term (or mutual power term) $P_{\text{beat}}(t)$ that is given by

$$P_{\text{beat}} \triangleq -\frac{1}{4L_{\text{Tx}}} \text{Re} \left\{ x^*(t)x(t - T_{\text{Tx}}) \exp(j\phi_{\text{mod}}(t)) \right\}. \quad (4.4)$$

The actual behavior of this beating term $P_{\text{beat}}(t)$ depends on the mutual coherence of $x(t)$ and $x(t - T_{\text{Tx}})$, which is determined by the relation between the value of T_{Tx} and the coherence time τ_c of the source signal $x(t)$. In the following subsections, three situations will be considered.

4.2.1 Coherent beating: interference

When $T_{\text{Tx}} \ll \tau_c$, $x(t)$ and $x(t - T_{\text{Tx}})$ are mutually coherent, resulting in

$$\begin{aligned} x(t - T_{\text{Tx}}) &= \sqrt{2P_x(t - T_{\text{Tx}})} \exp(j2\pi f_c(t - T_{\text{Tx}}) + j\phi_x(t - T_{\text{Tx}})) \\ &\approx \sqrt{2P_x(t)} \exp(j2\pi f_c(t - T_{\text{Tx}}) + j\phi_x(t)) \\ &= x(t) \exp(-j2\pi f_c T_{\text{Tx}}). \end{aligned} \quad (4.5)$$

so that we can write (4.4) as

$$P_{\text{beat}}(t) \approx -\frac{P_x(t)}{2L_{\text{Tx}}} \cos(\phi_{\text{mod}}(t) - 2\pi f_c T_{\text{Tx}}), \quad (4.6)$$

and hence (4.3) becomes

$$\begin{aligned} P_y(t) &\approx \frac{P_x(t)}{2L_{Tx}} \left[1 - \cos\left(\phi_{\text{mod}}(t) - 2\pi f_c T_{Tx}\right) \right] \\ &= \frac{P_x(t)}{L_{Tx}} \sin^2\left(\frac{1}{2}\phi_{\text{mod}}(t) - \pi f_c T_{Tx}\right). \end{aligned} \quad (4.7)$$

Obviously, when $T_{Tx} \ll \tau_c$, the phase modulation $\phi_{\text{mod}}(t)$ results in an intensity modulation in the output signal $y(t)$: *interference* occurs. Note that $P_x(t)$ suffers from source intensity noise (see Section 2.3.4), so $P_y(t)$ consists of a signal part and a noise part.

Example 4.1

Consider the case that $\phi_{\text{mod}}(t)$ is a rectangular periodic signal that takes values 0 and π , with a period of 20 ps and a duty cycle of 50 %, as illustrated in Figure 4.3(a).

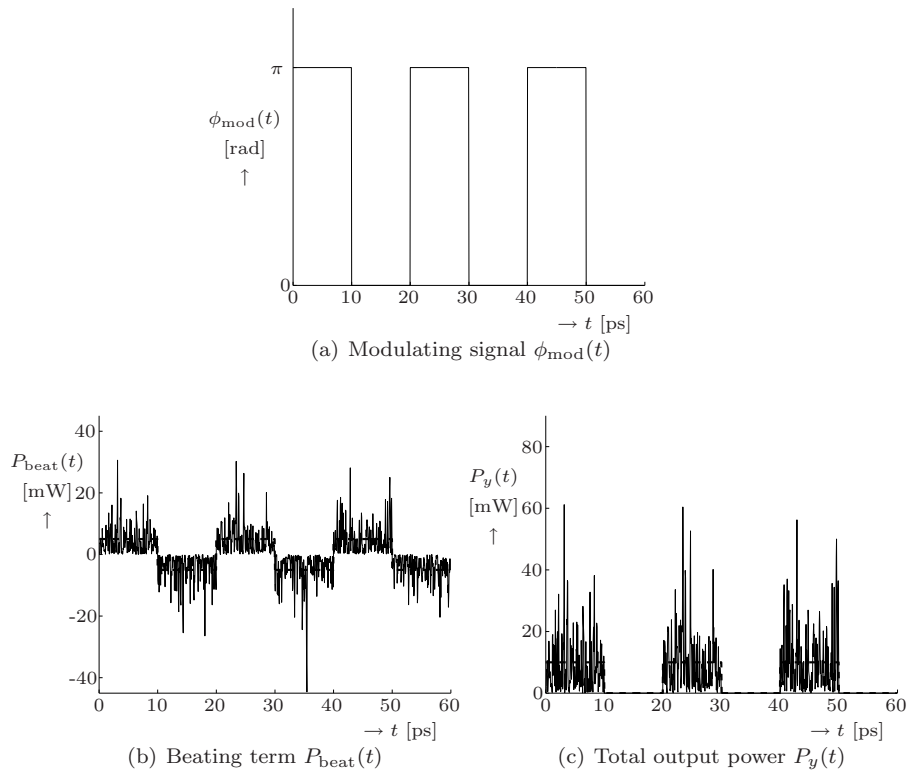
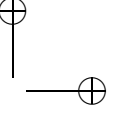
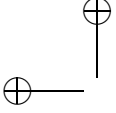


Figure 4.3: Simulation results for coherent beating



A simulation has been run with the LED source that is described in Example 3.3, so $P_x = 10$ mW, $\tau_c = 100$ fs and $T_{\text{samp}} = \tau_c/2 = 50$ fs. The path-imbalance of the MZI is set to $T_{\text{Tx}} = 0$, and losses are neglected, so $L_{\text{Tx}} = 1$. The resulting realizations for the beating term $P_{\text{beat}}(t)$ and output power of the MZI $P_y(t)$ are shown in Figure 4.3(b) and 4.3(c), respectively. (The actual beating term was calculated from the simulation results by subtracting the output powers of the upper and lower output ports of the MZI.) The dashed lines reflect the theoretical expected values that were derived above.

Obviously, the phase modulation results in a full intensity modulation of the output signal of the MZI. (The full input signal is passed through by the MZI when $\phi_{\text{mod}} = \pi$, and the input signal is entirely blocked when $\phi_{\text{mod}} = 0$.)



4.2.2 Incoherent beating: beat noise

When $T_{\text{Tx}} \gg \tau_c$, on the contrary, $x(t)$ and $x(t - T_{\text{Tx}})$ are mutually incoherent. In that case, the beating term $P_{\text{beat}}(t)$ in (4.4) corresponds to the multiplication of two mutually uncorrelated signals, resulting into zero-mean broadband noise. The latter is called *interferometric noise* or *optical beat interference (OBI) noise*. In the remainder of this thesis we will speak of *beat noise*, for short. Note that beat noise also occurs when two signals from different sources beat, provided that these sources operate in the same wavelength band.

Since $x(t)$ and $x(t - T_{\text{Tx}})$ are uncorrelated and Gaussian distributed, they are independent. Hence, the autocorrelation function of $P_{\text{beat}}(t)$ follows as

$$\begin{aligned} R_{P_{\text{beat}}P_{\text{beat}}}(t_1, t_2) &= \frac{1}{16L_{\text{Tx}}^2} \text{E} \left[\text{Re} \left\{ x^*(t_1)x(t_1 - T_{\text{Tx}}) \exp(j\phi_{\text{mod}}(t_1)) \right\} \right. \\ &\quad \left. \cdot \text{Re} \left\{ x^*(t_2)x(t_2 - T_{\text{Tx}}) \exp(j\phi_{\text{mod}}(t_2)) \right\} \right] \\ &= \frac{1}{32L_{\text{Tx}}^2} |R_{x^*x}(t_2 - t_1)|^2 \cos(\phi_{\text{mod}}(t_1) - \phi_{\text{mod}}(t_2)). \end{aligned} \quad (4.8)$$

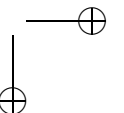
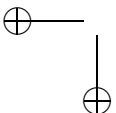
When the modulating signal has a bandwidth which is much lower than the bandwidth of the source signal $x(t)$ (this will in general be the case in CM systems), this becomes

$$R_{P_{\text{beat}}P_{\text{beat}}}(t_1, t_2) \approx \frac{1}{32L_{\text{Tx}}^2} |R_{x^*x}(t_2 - t_1)|^2, \quad (4.9)$$

so in that case the modulating signal is not observable in the power of $y(t)$.

Example 4.2

Another simulation has been run that is similar to the one in Example 4.1, but this time the path-imbalance is set to $T_{\text{Tx}} = 5\tau_c = 500$ fs. The results are shown in Figure 4.4.



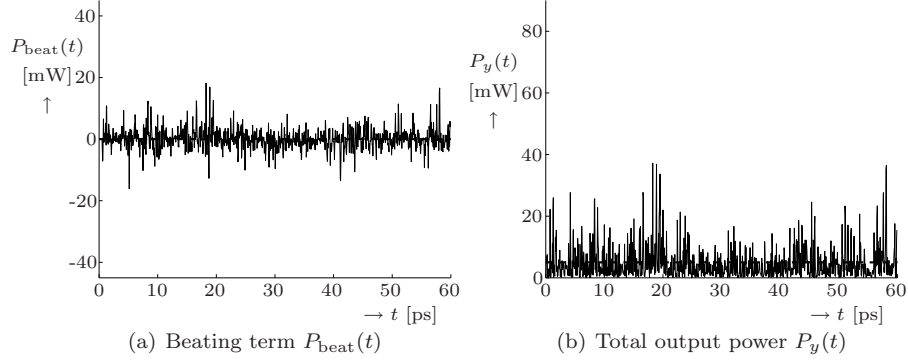


Figure 4.4: Simulation results for incoherent beating

Obviously, the beating term now only consists of beat noise, so that the modulating signal is not observable in the output power of the MZI. The total output power now consists of a constant term (dashed line), beat noise and intensity noise of the individual power terms. □

4.2.3 Partial interference

In general, when neither $T_{\text{Tx}} \ll \tau_c$ nor $T_{\text{Tx}} \gg \tau_c$ holds, $P_{\text{beat}}(t)$ contains an interference term, a source intensity noise term and a beat noise term. This can be seen by considering the expected value and autocorrelation function of $P_{\text{beat}}(t)$. Using (4.4) and (2.25), we find

$$\begin{aligned} \mathbb{E}[P_{\text{beat}}(t)] &= -\frac{1}{4L_{\text{Tx}}} \text{Re} \left\{ R_{x^*x}(-T_{\text{Tx}}) \exp(j\phi_{\text{mod}}(t)) \right\} \\ &= -\frac{P_x}{2L_{\text{Tx}}} \exp \left(-\frac{\pi}{2} \left(\frac{T_{\text{Tx}}}{\tau_c} \right)^2 \right) \cos(\phi_{\text{mod}}(t) - 2\pi f_c T_{\text{Tx}}). \end{aligned} \quad (4.10)$$

This corresponds to the interference term. Its amplitude depends on the value of T_{Tx} , since it determines the degree of *mutual coherence* of the two optical signals; this is reflected by the exponential, which is the envelope of the coherence function. Moreover, small changes in T_{Tx} result in rapid oscillations of the interference term (this is reflected by the cosine), which are called *fringes*. The envelope of the coherence function is therefore known as the *fringe visibility*.

The fringe visibility is maximal when $T_{\text{Tx}} \ll \tau_c$; this corresponds to the situation in Subsection 4.2.1. It is minimal when $T_{\text{Tx}} \gg \tau_c$; this corresponds to the situation in Subsection 4.2.2. In the latter case there is no observable interference.

The autocorrelation of $P_{\text{beat}}(t)$ can be found using (4.4), (2.35) and (2.25):

$$\begin{aligned}
 R_{P_{\text{beat}}P_{\text{beat}}}(t_1, t_2) &= \frac{1}{16L_{\text{Tx}}^2} \mathbb{E} \left[\text{Re} \left\{ x^*(t_1)x(t_1 - T_{\text{Tx}}) \exp(j\phi_{\text{mod}}(t_2)) \right\} \right. \\
 &\quad \left. \cdot \text{Re} \left\{ x^*(t_2)x(t_2 - T_{\text{Tx}}) \exp(j\phi_{\text{mod}}(t_2)) \right\} \right] \\
 &= \mathbb{E}[P_{\text{beat}}(t_1)]\mathbb{E}[P_{\text{beat}}(t_2)] + \frac{P_x^2}{8L_{\text{Tx}}^2} \exp \left(-\pi \left(\frac{t_2 - t_1}{\tau_c} \right)^2 \right) \\
 &\quad \cdot \left\{ 2 \exp \left(-\pi \left(\frac{T_{\text{Tx}}}{\tau_c} \right)^2 \right) \cos(\phi_{\text{mod}}(t_1) - 2\pi f_c T_{\text{Tx}}) \right. \\
 &\quad \quad \cdot \cos(\phi_{\text{mod}}(t_2) - 2\pi f_c T_{\text{Tx}}) \\
 &\quad \left. + \left[1 - \exp \left(-\pi \left(\frac{T_{\text{Tx}}}{\tau_c} \right)^2 \right) \right] \cos(\phi_{\text{mod}}(t_1) - \phi_{\text{mod}}(t_2)) \right\}. \quad (4.11)
 \end{aligned}$$

The two terms inside the braces correspond to source intensity noise and beat noise, respectively. Note that the source intensity term scales in the same way as the interference term and disappears for $T_{\text{Tx}} \gg \tau_c$, whereas the beat noise term disappears for $T_{\text{Tx}} \ll \tau_c$.

Example 4.3

Another simulation has been run that is similar to the ones in Example 4.1 and 4.2, but this time the path-imbalance is set to $T_{\text{Tx}} = \tau_c = 100$ fs. The results are shown in Figure 4.5.

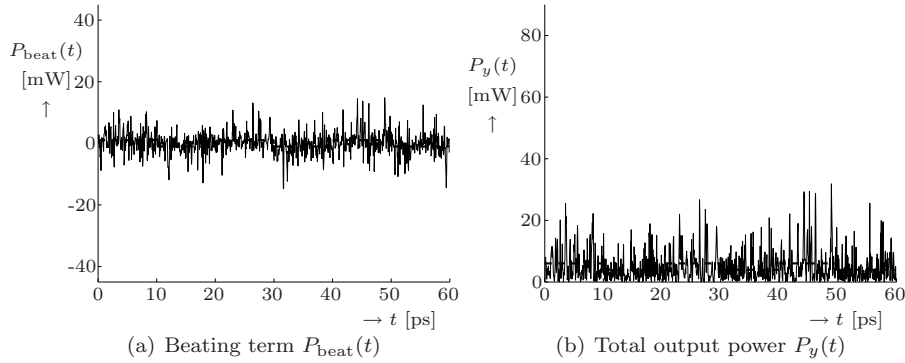
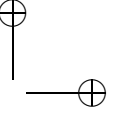
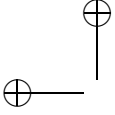


Figure 4.5: Simulation results for partially coherent beating

Obviously, the modulating signal is now observable in both the beating term and the total output power, but much less significantly than in Figure 4.3. ▣



4.3 Coherence modulation

In CM, the idea is that T_{Tx} is much larger than τ_c , such that the two transmitted optical signals are mutually incoherent and do not interfere. When both IM and PM are applied, the transmitted signal can be written as

$$y(t) = \frac{1}{2\sqrt{L_{Tx}}} \left[x(t)\sqrt{m_{\text{mod}}(t)} - x(t - T_{Tx})\sqrt{m_{\text{mod}}(t - T_{Tx})} \exp(j\phi_{\text{mod}}(t)) \right]. \quad (4.12)$$

For deterministic modulating signals $m_{\text{mod}}(t)$ and $\phi_{\text{mod}}(t)$ with bandwidths that are much smaller than $1/T_{Tx}$ and hence smaller than $1/\tau_c$ (later it will become clear why this assumption is made), $y(t)$ has zero mean and autocorrelation function

$$\begin{aligned} R_{y^*y}(t_1, t_2) &\triangleq \text{E}[y^*(t_1)y(t_2)] \\ &= \frac{1}{4L_{Tx}} m_{\text{mod}}(t_1) \left[2R_{x^*x}(t_2 - t_1) - R_{x^*x}(t_2 - t_1 - T_{Tx}) \exp(j\phi_{\text{mod}}(t_1)) - R_{x^*x}(t_2 - t_1 + T_{Tx}) \exp(-j\phi_{\text{mod}}(t_1)) \right]. \end{aligned} \quad (4.13)$$

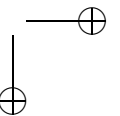
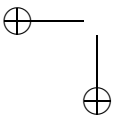
Hence, the mean optical power at the output of the CM transmitter can be written as

$$\text{E}[P_y(t)] = \frac{1}{2} R_{y^*y}(t, t) \approx \frac{P_x m_{\text{mod}}(t)}{2L_{Tx}}. \quad (4.14)$$

Obviously, only the IM results in a significant variation of the transmitted optical power, because the two transmitted optical signals do not interfere. (Note that the term "coherence modulation" is actually a bit misleading, because it might suggest that the degree of mutual coherence between the two transmitted optical signals is modulated, whereas the two signals are always fully incoherent.)

4.4 Coherence demodulation

At the receiver end, the PM can be revealed by introducing another time delay, in such a way that the modulated signal and the reference signal are mutually coherent, resulting in interference. This can be achieved by means of another MZI, with path-imbalance T_{Rx} . In this section it will be shown that the actual output signal of the receiver depends on the relation between the delays in transmitter and receiver, T_{Tx} and T_{Rx} , respectively. Single-ended and balanced detection will be considered.



4.4.1 Single-ended detection

The simplest way to perform optical detection in a CM receiver is by means of a single-ended structure with just one photodiode; this is illustrated in Figure 4.6.

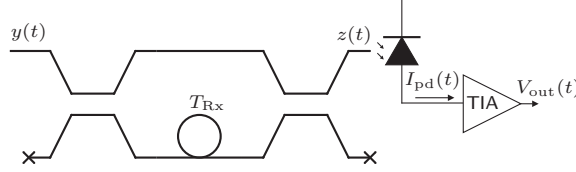


Figure 4.6: A single-ended CM receiver

The relation between the signal in the transmission fiber $y(t)$ and the optical signal $z(t)$ that is detected by the photodiode, is given by

$$z(t) = \frac{1}{2\sqrt{L_{\text{Rx}}}} \left[y(t) - y(t - T_{\text{Rx}}) \right], \quad (4.15)$$

where L_{Rx} denotes the total excess losses in the transmitter, which include:

- the coupling losses between the transmission fiber and the interferometer;
- the excess losses in the interferometer;
- the coupling losses between the interferometer and the photodiode.

The autocorrelation function of this signal can be written as

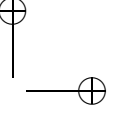
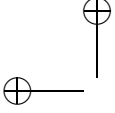
$$\begin{aligned} R_{z^*z}(t_1, t_2) &\triangleq \mathbb{E}[z^*(t_1)z(t_2)] \\ &= \frac{1}{4L_{\text{Rx}}} \left[R_{y^*y}(t_1, t_2) - R_{y^*y}(t_1, t_2 - T_{\text{Rx}}) \right. \\ &\quad \left. - R_{y^*y}(t_1 - T_{\text{Rx}}, t_2) + R_{y^*y}(t_1 - T_{\text{Rx}}, t_2 - T_{\text{Rx}}) \right], \quad (4.16) \end{aligned}$$

so for the mean power of $z(t)$ one can find

$$\begin{aligned} \mathbb{E}[P_z(t)] &= \frac{1}{2} R_{z^*z}(t, t) \\ &= \frac{1}{4L_{\text{Rx}}} \left(\mathbb{E}[P_y(t) + P_y(t - T_{\text{Rx}})] - \text{Re}\{R_{y^*y}(t - T_{\text{Rx}}, t)\} \right). \quad (4.17) \end{aligned}$$

The mean photodiode current can now be found using (2.65), resulting in

$$\begin{aligned} \mathbb{E}[I_{\text{pd}}(t)] &= \frac{R_{\text{pd}}}{4L_{\text{Rx}}} \int_{-\infty}^{\infty} h_{\text{pd}}(t - \rho) \left(\mathbb{E}[P_y(\rho) + P_y(\rho - T_{\text{Rx}})] \right. \\ &\quad \left. - \text{Re}\{R_{y^*y}(\rho - T_{\text{Rx}}, \rho)\} \right) d\rho. \quad (4.18) \end{aligned}$$



After amplification by the TIA this results in an expected output voltage

$$\begin{aligned} \mathbb{E}[V_{\text{out}}(t)] = \frac{Z_{\text{TIA}}R_{\text{pd}}}{4L_{\text{Rx}}} \int_{-\infty}^{\infty} h_{\text{pd}}(t - \rho) & \left(\mathbb{E}[P_y(\rho) + P_y(\rho - T_{\text{Rx}})] \right. \\ & \left. - \text{Re}\{R_{y^*y}(\rho - T_{\text{Rx}}, \rho)\} \right) d\rho. \quad (4.19) \end{aligned}$$

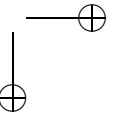
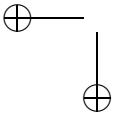
Apparently, the expected output voltage is related to the instantaneous expected powers of $y(t)$ and its delayed version $y(t - T_{\text{Rx}})$, and the degree of correlation between these two signals. As shown in (4.13), the latter depends on the relation between T_{Rx} and T_{Tx} . Using (4.13) and (2.25), and assuming that the bandwidths of $m_{\text{mod}}(t)$ and $\phi_{\text{mod}}(t)$ are much smaller than $1/T_{\text{Tx}}$ and $1/T_{\text{Rx}}$, one can find

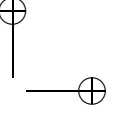
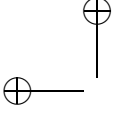
$$\begin{aligned} \mathbb{E}[V_{\text{out}}(t)] \approx \frac{Z_{\text{TIA}}R_{\text{pd}}P_x}{8L_{\text{Tx}}L_{\text{Rx}}} \int_{-\infty}^{\infty} h_{\text{pd}}(t - \rho) m_{\text{mod}}(\rho) & \cdot \left[2 - 2 \exp\left(-\frac{\pi}{2} \left(\frac{T_{\text{Tx}}}{\tau_c}\right)^2\right) \cos(-2\pi f_c T_{\text{Tx}} + \phi_{\text{mod}}(\rho)) \right. \\ & - 2 \exp\left(-\frac{\pi}{2} \left(\frac{T_{\text{Rx}}}{\tau_c}\right)^2\right) \cos(2\pi f_c T_{\text{Rx}}) \\ & + \exp\left(-\frac{\pi}{2} \left(\frac{T_{\text{Rx}} - T_{\text{Tx}}}{\tau_c}\right)^2\right) \cos(2\pi f_c (T_{\text{Rx}} - T_{\text{Tx}}) + \phi_{\text{mod}}(\rho)) \\ & \left. + \exp\left(-\frac{\pi}{2} \left(\frac{T_{\text{Rx}} + T_{\text{Tx}}}{\tau_c}\right)^2\right) \cos(2\pi f_c (T_{\text{Rx}} + T_{\text{Tx}}) - \phi_{\text{mod}}(\rho)) \right] d\rho. \quad (4.20) \end{aligned}$$

Assuming that $T_{\text{Rx}}, T_{\text{Tx}} \gg \tau_c$ it follows that

$$\begin{aligned} \mathbb{E}[V_{\text{out}}(t)] = \frac{Z_{\text{TIA}}R_{\text{pd}}P_x}{8L_{\text{Tx}}L_{\text{Rx}}} \int_{-\infty}^{\infty} h_{\text{pd}}(t - \rho) m_{\text{mod}}(\rho) & \cdot \left[2 + \exp\left(-\frac{\pi}{2} \left(\frac{T_{\text{Rx}} - T_{\text{Tx}}}{\tau_c}\right)^2\right) \right. \\ & \left. \cdot \cos(2\pi f_c (T_{\text{Rx}} - T_{\text{Tx}}) + \phi_{\text{mod}}(\rho)) \right] d\rho. \quad (4.21) \end{aligned}$$

Now the two modulation methods, PM and IM, will be separately considered.





Phase modulation (PM)

In case of PM (so when $m_{\text{mod}}(t) = 1$), we have

$$\begin{aligned} E[V_{\text{out}}(t)] = & \frac{Z_{\text{TIA}} R_{\text{pd}} P_x}{8L_{\text{Tx}} L_{\text{Rx}}} \left[2 + \exp\left(-\frac{\pi}{2} \left(\frac{T_{\text{Rx}} - T_{\text{Tx}}}{\tau_c}\right)^2\right) \right. \\ & \left. \cdot \int_{-\infty}^{\infty} h_{\text{pd}}(t - \rho) \cos\left(2\pi f_c (T_{\text{Rx}} - T_{\text{Tx}}) + \phi_{\text{mod}}(\rho)\right) d\rho \right]. \end{aligned} \quad (4.22)$$

Apparently, the output voltage consists of a constant (DC) part and a part that is modulated by $\phi_{\text{mod}}(t)$. The significance of the latter part depends on the relation between T_{Rx} and T_{Tx} :

- The observability of the PM is maximal when $T_{\text{Rx}} = T_{\text{Tx}}$, resulting in

$$E[V_{\text{out}}(t)] = \frac{Z_{\text{TIA}} R_{\text{pd}} P_x}{8L_{\text{Tx}} L_{\text{Rx}}} \left[2 + \int_{-\infty}^{\infty} h_{\text{pd}}(t - \rho) \cos\left(\phi_{\text{mod}}(\rho)\right) d\rho \right]. \quad (4.23)$$

In that case, the corresponding CM channel is *selected*, and the transmitter and receiver form a *matched pair*;

- The PM is not observable when $|T_{\text{Rx}} - T_{\text{Tx}}| \gg \tau_c$. In that case, the corresponding CM channel is *suppressed*; the transmitter and receiver do not form a matched pair;

(For intermediate values of $|T_{\text{Rx}} - T_{\text{Tx}}|$ partial interference occurs, such that the PM is observable but not with maximum amplitude. This is not a desirable situation, so it will not be further considered.)

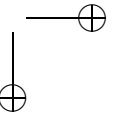
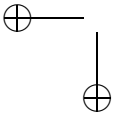
Apparently, T_{Rx} can be used as a parameter to select or suppress CM channels.

Intensity modulation (IM)

Now consider the case in which IM is used instead of PM, so $\phi_{\text{mod}}(t) = 0$ and the mean output voltage becomes

$$\begin{aligned} E[V_{\text{out}}(t)] = & \frac{Z_{\text{TIA}} R_{\text{pd}} P_x}{8L_{\text{Tx}} L_{\text{Rx}}} \left[2 + \exp\left(-\frac{\pi}{2} \left(\frac{T_{\text{Rx}} - T_{\text{Tx}}}{\tau_c}\right)^2\right) \right. \\ & \left. \cdot \cos\left(2\pi f_c (T_{\text{Rx}} - T_{\text{Tx}})\right) \right] \int_{-\infty}^{\infty} h_{\text{pd}}(t - \rho) m_{\text{mod}}(\rho) d\rho, \end{aligned} \quad (4.24)$$

Apparently, the IM is always observable; although the amplitude does depend on the relation between T_{Rx} and T_{Tx} , the corresponding channel cannot be completely suppressed. Consequently, the single-ended receiver is not a suitable configuration for demodulating coherence-modulated channels when IM is used.



Example 4.4

As an example, consider a simulation of system with a coherence modulator as simulated in Example 4.2, so with $P_x = 10$ mW, $\tau_c = 100$ fs, $T_{\text{samp}} = \tau_c/2 = 50$ fs, $T_{\text{Tx}} = 5\tau_c = 500$ fs, negligible MZI losses (so $L_{\text{Tx}} = 1$) and a modulating signal $\phi_{\text{mod}}(t)$ as shown in Figure 4.3(a).

For the single-ended coherence demodulator, it is assumed that the MZI losses can be neglected (so $L_{\text{Rx}} = 1$), that the photodiode has a negligible response time (so $h_{\text{pd}}(t) = \delta(t)$) and a responsivity of 0.8 A/W, and that the TIA has a transimpedance of 1 k Ω and equivalent input noise current of 7 pA/ $\sqrt{\text{Hz}}$, so $S_{\text{th}} = 49$ (pA) 2 /Hz.

First consider the situation that $T_{\text{Rx}} = T_{\text{Tx}} = 500$ fs. The resulting output signal of the coherence demodulator is shown in Figure 4.7(a), where the dashed line corresponds to the theoretical expected value. As expected, it consists of a DC part, a signal part that is proportional to $\cos(\phi_{\text{mod}}(t))$, and a noise part. The variance of the noise seems to depend on the value of $\phi_{\text{mod}}(t)$. We will come back to this in the next section.

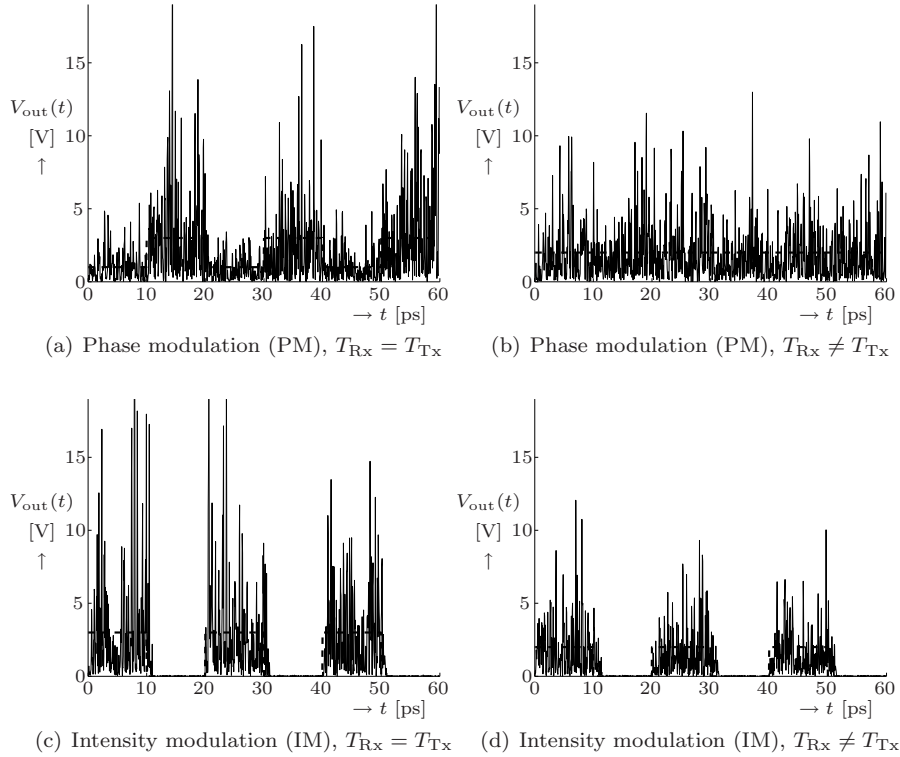


Figure 4.7: Simulated receiver output signal $V_{\text{out}}(t)$ for single-ended coherence demodulation

When the simulation is repeated with $T_{\text{Rx}} = 2T_{\text{Tx}} = 1$ ps, the output signal in Figure 4.7(b) results. Obviously, the modulating signal is no longer observable, neither in the mean value nor in the noise variance.

Both these simulation experiments were repeated with a coherence modulator in which IM is performed instead of PM. The modulating signal $m_{\text{mod}}(t)$ had the same shape as $\phi_{\text{mod}}(t)$ in the previous experiments, but now took values 0 and 1 instead of 0 and π ; the remaining parameter values were left unchanged. The results are shown in Figure 4.7(c) and 4.7(d), respectively. Obviously, the modulating signal $m_{\text{mod}}(t)$ is observable in both cases, although there is some difference in amplitude (as expected). The noise variance appears to be very low when $m_{\text{mod}}(t) = 0$, which is not surprising since there is no beat noise or intensity noise in that case, so only the (apparently much smaller) thermal receiver noise remains. □

4.4.2 Balanced detection

An alternative is to add another photodiode that detects the optical signal $z_2(t)$ at the lower output of the receiver interferometer; this results in the balanced detector configuration in Figure 4.8.

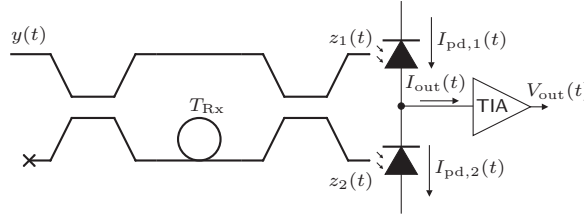


Figure 4.8: A balanced CM receiver

Similarly to the procedure in the previous subsection, one can subsequently find for the optical signals $z_1(t)$ and $z_2(t)$

$$z_1(t) = \frac{1}{2\sqrt{L_{\text{Rx}}}} [y(t) - y(t - T_{\text{Rx}})], \quad (4.25)$$

$$z_2(t) = \frac{j}{2\sqrt{L_{\text{Rx}}}} [y(t) + y(t - T_{\text{Rx}})], \quad (4.26)$$

$$R_{z_1^* z_1}(t_1, t_2) = \frac{1}{4L_{\text{Rx}}} \left[R_{y^* y}(t_1, t_2) - R_{y^* y}(t_1, t_2 - T_{\text{Rx}}) - R_{y^* y}(t_1 - T_{\text{Rx}}, t_2) + R_{y^* y}(t_1 - T_{\text{Rx}}, t_2 - T_{\text{Rx}}) \right], \quad (4.27)$$

$$R_{z_2^* z_2}(t_1, t_2) = \frac{1}{4L_{\text{Rx}}} \left[R_{y^* y}(t_1, t_2) + R_{y^* y}(t_1, t_2 - T_{\text{Rx}}) + R_{y^* y}(t_1 - T_{\text{Rx}}, t_2) + R_{y^* y}(t_1 - T_{\text{Rx}}, t_2 - T_{\text{Rx}}) \right], \quad (4.28)$$

$$R_{z_1^* z_2}(t_1, t_2) = \frac{j}{4L_{\text{Rx}}} \left[R_{y^* y}(t_1, t_2) + R_{y^* y}(t_1, t_2 - T_{\text{Rx}}) \right. \\ \left. - R_{y^* y}(t_1 - T_{\text{Rx}}, t_2) - R_{y^* y}(t_1 - T_{\text{Rx}}, t_2 - T_{\text{Rx}}) \right], \quad (4.29)$$

$$E[P_{z_1}(t)] = \frac{1}{4L_{\text{Rx}}} \left(E[P_y(t) + P_y(t - T_{\text{Rx}})] - \text{Re}\{R_{y^* y}(t - T_{\text{Rx}}, t)\} \right), \quad (4.30)$$

$$E[P_{z_2}(t)] = \frac{1}{4L_{\text{Rx}}} \left(E[P_y(t) + P_y(t - T_{\text{Rx}})] + \text{Re}\{R_{y^* y}(t - T_{\text{Rx}}, t)\} \right). \quad (4.31)$$

The output current $I_{\text{out}}(t)$ of the balanced detector corresponds to the difference between the photodiode currents:

$$I_{\text{out}}(t) \triangleq I_{\text{pd},1}(t) - I_{\text{pd},2}(t). \quad (4.32)$$

Hence, its mean value can be written as

$$E[I_{\text{out}}(t)] = R_{\text{pd}} \int_{-\infty}^{\infty} h_{\text{pd}}(t - \rho) \left\{ E[P_{z_1}(\rho)] - E[P_{z_2}(\rho)] \right\} d\rho \\ = -\frac{R_{\text{pd}}}{2L_{\text{Rx}}} \int_{-\infty}^{\infty} h_{\text{pd}}(t - \rho) \text{Re}\{R_{y^* y}(t - T_{\text{Rx}}, t)\} d\rho. \quad (4.33)$$

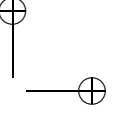
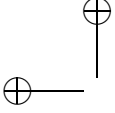
After amplification by the TIA this results in an expected output voltage

$$E[V_{\text{out}}(t)] = -\frac{Z_{\text{TIA}} R_{\text{pd}}}{2L_{\text{Rx}}} \int_{-\infty}^{\infty} h_{\text{pd}}(t - \rho) \text{Re}\{R_{y^* y}(t - T_{\text{Rx}}, t)\} d\rho. \quad (4.34)$$

Note that this implies that the expected output current of the balanced receiver is only related to the degree of correlation between $y(t)$ and its delayed version $y(t - T_{\text{Rx}})$, and not to the individual powers of these signals like was the case in the single-ended receiver. (The corresponding terms are canceled by subtracting the photodiode currents.)

Using (2.25) and (4.2), and again assuming that the bandwidths of $m_{\text{mod}}(t)$ and $\phi_{\text{mod}}(t)$ are much smaller than $1/T_{\text{Rx}}$, one can write

$$E[V_{\text{out}}(t)] \approx \frac{Z_{\text{TIA}} R_{\text{pd}} P_x}{4L_{\text{Tx}} L_{\text{Rx}}} \int_{-\infty}^{\infty} h_{\text{pd}}(t - \rho) m_{\text{mod}}(\rho) \\ \cdot \left[-2 \exp\left(-\frac{\pi}{2} \left(\frac{T_{\text{Rx}}}{\tau_c}\right)^2\right) \cos(2\pi f_c T_{\text{Rx}}) \right. \\ + \exp\left(-\frac{\pi}{2} \left(\frac{T_{\text{Rx}} - T_{\text{Tx}}}{\tau_c}\right)^2\right) \cos\left(2\pi f_c (T_{\text{Rx}} - T_{\text{Tx}}) + \phi_{\text{mod}}(\rho)\right) \\ \left. + \exp\left(-\frac{\pi}{2} \left(\frac{T_{\text{Rx}} + T_{\text{Tx}}}{\tau_c}\right)^2\right) \cos\left(2\pi f_c (T_{\text{Rx}} + T_{\text{Tx}}) - \phi_{\text{mod}}(\rho)\right) \right] d\rho. \quad (4.35)$$



Assuming that $T_{\text{Rx}} \gg \tau_c$, this becomes

$$\begin{aligned} \mathbb{E}[V_{\text{out}}(t)] &= \frac{Z_{\text{TIA}} R_{\text{pd}} P_x}{4L_{\text{Tx}} L_{\text{Rx}}} \exp\left(-\frac{\pi}{2} \left(\frac{T_{\text{Rx}} - T_{\text{Tx}}}{\tau_c}\right)^2\right) \\ &\cdot \int_{-\infty}^{\infty} h_{\text{pd}}(t - \rho) m_{\text{mod}}(\rho) \cos\left(2\pi f_c(T_{\text{Rx}} - T_{\text{Tx}}) + \phi_{\text{mod}}(\rho)\right) d\rho. \end{aligned} \quad (4.36)$$

Phase modulation (PM)

In case of PM, we get

$$\begin{aligned} \mathbb{E}[V_{\text{out}}(t)] &= \frac{Z_{\text{TIA}} R_{\text{pd}} P_x}{4L_{\text{Tx}} L_{\text{Rx}}} \exp\left(-\frac{\pi}{2} \left(\frac{T_{\text{Rx}} - T_{\text{Tx}}}{\tau_c}\right)^2\right) \\ &\cdot \int_{-\infty}^{\infty} h_{\text{pd}}(t - \rho) \cos\left(2\pi f_c(T_{\text{Rx}} - T_{\text{Tx}}) + \phi_{\text{mod}}(\rho)\right) d\rho. \end{aligned} \quad (4.37)$$

Obviously, balancing has resulted in a removal of the DC term in the output current, so that it only consists of an interference term. When $T_{\text{Rx}} = T_{\text{Tx}}$, it becomes

$$\mathbb{E}[V_{\text{out}}(t)] = \frac{Z_{\text{TIA}} R_{\text{pd}} P_x}{4L_{\text{Tx}} L_{\text{Rx}}} \int_{-\infty}^{\infty} h_{\text{pd}}(t - \rho) \cos\left(\phi_{\text{mod}}(\rho)\right) d\rho, \quad (4.38)$$

whereas the mean output voltage becomes zero when $|T_{\text{Rx}} - T_{\text{Tx}}| \gg \tau_c$.

Moreover, it can be proven that the noise performance of a balanced receiver is significantly better than the noise performance of a single-ended receiver [59–62].

Intensity modulation (IM)

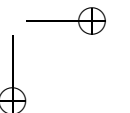
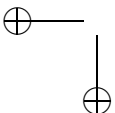
In case of IM, we have

$$\begin{aligned} \mathbb{E}[V_{\text{out}}(t)] &= \frac{Z_{\text{TIA}} R_{\text{pd}} P_x}{4L_{\text{Tx}} L_{\text{Rx}}} \exp\left(-\frac{\pi}{2} \left(\frac{T_{\text{Rx}} - T_{\text{Tx}}}{\tau_c}\right)^2\right) \\ &\cdot \int_{-\infty}^{\infty} h_{\text{pd}}(t - \rho) m_{\text{mod}}(\rho) \cos\left(2\pi f_c(T_{\text{Rx}} - T_{\text{Tx}})\right) d\rho. \end{aligned} \quad (4.39)$$

Hence, it can be seen that balancing has enabled the receiver to distinguish between intensity modulated CM channels: when $T_{\text{Rx}} = T_{\text{Tx}}$, we have

$$\mathbb{E}[V_{\text{out}}(t)] = \frac{Z_{\text{TIA}} R_{\text{pd}} P_x}{4L_{\text{Tx}} L_{\text{Rx}}} \int_{-\infty}^{\infty} h_{\text{pd}}(t - \rho) m_{\text{mod}}(\rho) d\rho, \quad (4.40)$$

whereas the mean output voltage becomes zero when $|T_{\text{Rx}} - T_{\text{Tx}}| \gg \tau_c$.



Example 4.5

The simulation experiments in Example 4.4 have been repeated with a balanced receiver instead of a single-ended receiver. The results are shown in Figure 4.9.

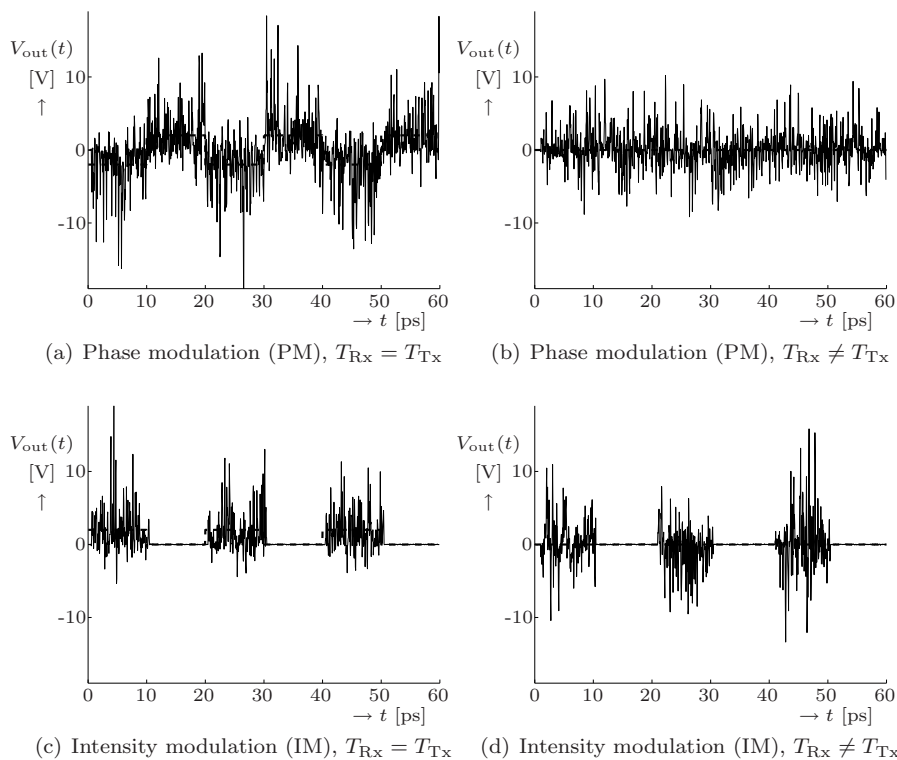
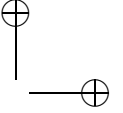
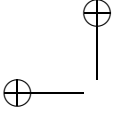


Figure 4.9: Simulated receiver output signal $V_{out}(t)$ for balanced coherence demodulation

Note that it is demonstrated that T_{R_x} now indeed serves as a channel selection parameter for both modulation methods: the modulating signal is observable when $T_{R_x} = T_{T_x}$ and not observable when $T_{R_x} \neq T_{T_x}$, both in case of PM and IM. (That is: in case of IM, the modulating signal only affects the noise variance and not the mean output signal.)

Also note that in case of PM, the output signal of a matched balanced receiver (Figure 4.9(a)) is indeed less noisy than the output signal of a matched single-ended receiver (Figure 4.7(a)).






4.5 Choosing the path delays

As described in the previous section, the output signal of the receiver depends on the values of the path delays T_{Tx} and T_{Rx} . It was assumed that both of them are much larger than the coherence time τ_c , and then it was shown that the modulating signal is recovered by setting $T_{Rx} = T_{Tx}$ and that it is suppressed by setting $|T_{Rx} - T_{Tx}| \gg \tau_c$.

In practice, however, T_{Rx} and T_{Tx} should be chosen as small as possible in order to simplify implementation. A criterion for choosing the values follows from (4.20) and (4.34), where it can be seen that the residual coherence terms (those are the terms that have been neglected in (4.21) and (4.35)) are more than 40 dB below the desired interference term when the delays are chosen in the order of twice the coherence time. The same goes for the difference between T_{Rx} and T_{Tx} when the modulating signal should be suppressed.

Example 4.6

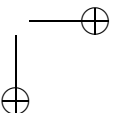
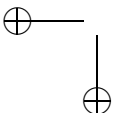
For a light source with a coherence time of 0.1 ps (see Example 2.1), the path delays should be in the order of 0.2 ps and multiples thereof. For waveguides with an effective index N_{eff} in the order of 1.5, this corresponds to a path length difference of $l_{Tx} = c_0 T_{Tx} / N_{\text{eff}} \approx 40 \mu\text{m}$. 

In some applications it might be desirable to have adjustable delay values in the transmitter and/or receiver, so that a transmitter can address a particular receiver and/or a receiver can tune to a particular transmitter. This can be done by means of multiple delays and switches. Two examples are shown in Figure 4.10.

In the MZI in Figure 4.10(a), one of the interferometer arms is replaced by a binary tree configuration of parallel delay lines, from which one delay line can be selected by properly setting the Y-switches. The disadvantage of such configuration is that the number of required switches rapidly increases with the number of delay values: when N is the number of switching stages of the binary tree, then 2^N different delay values can be selected by means of $2(2^N - 1)$ switches. $2N$ switches have to be configured properly for selecting a particular delay.

The MZI in Figure 4.10(b) consists of multiple stages that are connected by cross-bar switches. The path-length difference in each stage is twice the path-length difference of the preceding stage. When a switch is in the bar state, the path-length differences of the two adjacent stages are effectively summed, whereas they are effectively subtracted when the switch is in the cross-state. Hence, when there are N stages, $N - 1$ cross-bar switches are required and 2^{N-1} different effective path-length differences can be selected.

An MZI can actually be alternately used for encoding and decoding in the same channel, so that a half-duplex link can be established [48]. In case of single-ended detection this can simply be done by connecting a broadband source to the free output port of a coherence demodulator. In case of balanced



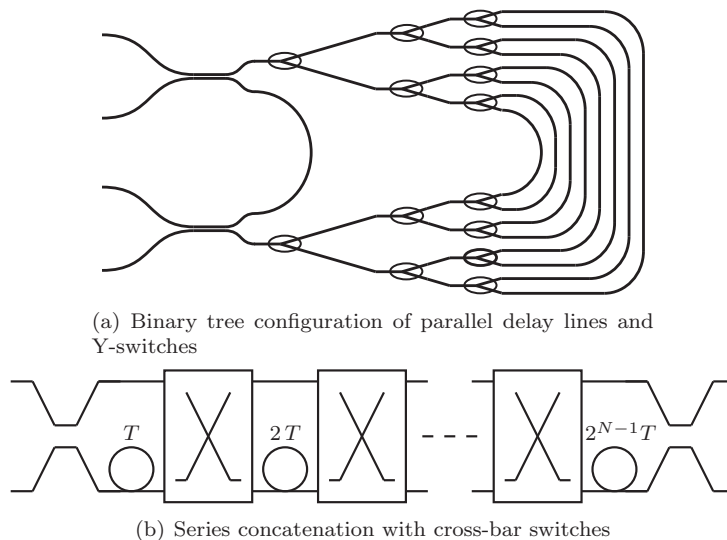


Figure 4.10: Two examples of Mach-Zehnder Interferometers with adjustable path-length differences

detection it can be done by inserting a Y-switch in one of the output ports of the coherence demodulator, which enables this port to connect to either a photodiode or a broadband source. This is illustrated in Figure 4.11. Modulation can be performed in the same way as described before; PM is illustrated in Figure 4.11.

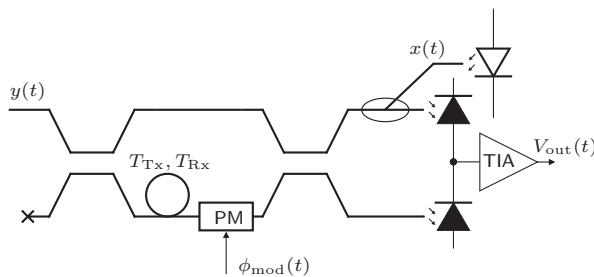


Figure 4.11: A CM transceiver with PM and balanced detection

Alternatively, full-duplexing can be performed by means of separate transmitters and receivers with different path delay differences, eventually combined with coarse WDM in order to distinguish between upstream and downstream traffic [63].

4.6 Noise in the receiver

Apart from the information-carrying term and residual coherence terms, the output signal of the TIA also contains noise. This was illustrated by the simulation examples in Section 4.4, and it will be quantified by calculating the autocorrelation function of $V_{\text{out}}(t)$ in this section. Since the balanced receiver has obvious advantages over the single-ended receiver, we will do this for the balanced receiver. (Moreover, the calculation for the single-ended receiver is far more laborious since $V_{\text{out}}(t)$ contains more terms in that case.)

First the autocorrelation function of the output current $I_{\text{out}}(t)$ of the photodiode pair is found using (4.32), (2.66) and (2.67):

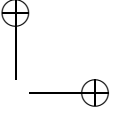
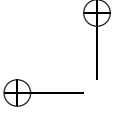
$$\begin{aligned}
 R_{I_{\text{out}}I_{\text{out}}}(t_1, t_2) &= R_{I_{\text{pd},1}I_{\text{pd},1}}(t_1, t_2) - R_{I_{\text{pd},1}I_{\text{pd},2}}(t_1, t_2) \\
 &\quad - R_{I_{\text{pd},2}I_{\text{pd},1}}(t_1, t_2) + R_{I_{\text{pd},2}I_{\text{pd},2}}(t_1, t_2) \\
 &= R_{\text{pd}}e \int_{-\infty}^{\infty} h_{\text{pd}}(t_1 - \rho)h_{\text{pd}}(t_2 - \rho)E[P_{z_1}(\rho) + P_{z_2}(\rho)] d\rho \\
 &\quad + R_{\text{pd}}^2 \int_{-\infty}^{\infty} \int_{-\infty}^{\infty} h_{\text{pd}}(t_1 - \rho_1)h_{\text{pd}}(t_2 - \rho_2) \left[R_{P_{z_1}P_{z_1}}(\rho_1, \rho_2) \right. \\
 &\quad \left. - R_{P_{z_1}P_{z_2}}(\rho_1, \rho_2) - R_{P_{z_2}P_{z_1}}(\rho_1, \rho_2) + R_{P_{z_2}P_{z_2}}(\rho_1, \rho_2) \right] d\rho_1 d\rho_2. \quad (4.41)
 \end{aligned}$$

This can be expressed in the autocorrelation and cross-correlation functions of $z_1(t)$ and $z_2(t)$ by means of (2.36) and (2.41):

$$\begin{aligned}
 R_{I_{\text{out}}I_{\text{out}}}(t_1, t_2) &= R_{\text{pd}}e \int_{-\infty}^{\infty} h_{\text{pd}}(t_1 - \rho)h_{\text{pd}}(t_2 - \rho)E[P_{z_1}(\rho) + P_{z_2}(\rho)] d\rho \\
 &\quad + R_{\text{pd}}^2 \int_{-\infty}^{\infty} \int_{-\infty}^{\infty} h_{\text{pd}}(t_1 - \rho_1)h_{\text{pd}}(t_2 - \rho_2) \\
 &\quad \cdot \left[\left(P_{z_1}(\rho_1) - P_{z_2}(\rho_1) \right) \left(P_{z_1}(\rho_2) - P_{z_2}(\rho_2) \right) \right. \\
 &\quad \left. + \frac{1}{4} |R_{z_1^*z_1}(\rho_1, \rho_2)|^2 - \frac{1}{4} |R_{z_1^*z_2}(\rho_1, \rho_2)|^2 \right. \\
 &\quad \left. - \frac{1}{4} |R_{z_2^*z_1}(\rho_1, \rho_2)|^2 + \frac{1}{4} |R_{z_2^*z_2}(\rho_1, \rho_2)|^2 \right] d\rho_1 d\rho_2. \quad (4.42)
 \end{aligned}$$

Using (4.27) through (4.31) and (4.33) this becomes

$$\begin{aligned}
 R_{I_{\text{out}}I_{\text{out}}}(t_1, t_2) &= E[I_{\text{out}}(t_1)]E[I_{\text{out}}(t_2)] \\
 &\quad + \frac{R_{\text{pd}}e}{2L_{\text{Rx}}} \int_{-\infty}^{\infty} h_{\text{pd}}(t_1 - \rho)h_{\text{pd}}(t_2 - \rho)E\left[P_y(\rho) + P_y(\rho - T_{\text{Rx}})\right] d\rho \\
 &\quad + \frac{R_{\text{pd}}^2}{8L_{\text{Rx}}^2} \int_{-\infty}^{\infty} \int_{-\infty}^{\infty} h_{\text{pd}}(t_1 - \rho_1)h_{\text{pd}}(t_2 - \rho_2) \\
 &\quad \cdot \text{Re} \left\{ R_{y^*y}(\rho_1, \rho_2)R_{y^*y}(\rho_2 - T_{\text{Rx}}, \rho_1 - T_{\text{Rx}}) \right. \\
 &\quad \left. + R_{y^*y}(\rho_1 - T_{\text{Rx}}, \rho_2)R_{y^*y}(\rho_2 - T_{\text{Rx}}, \rho_1) \right\} d\rho_1 d\rho_2. \quad (4.43)
 \end{aligned}$$



One can actually verify that the first integral corresponds to shot noise, and that the two terms in the second integral correspond to intensity noise and beat noise, respectively.

After amplification, thermal noise is added to the signal, as described in Section 2.7. The autocorrelation function of the output voltage can be written as

$$\begin{aligned}
 R_{V_{\text{out}}V_{\text{out}}}(t_1, t_2) &= Z_{\text{TIA}}^2 \left[R_{I_{\text{out}}I_{\text{out}}}(t_1, t_2) + S_{\text{th}}\delta(t_1 - t_2) \right] \\
 &= E[V_{\text{out}}(t_1)]E[V_{\text{out}}(t_2)] \\
 &\quad + \frac{Z_{\text{TIA}}^2 R_{\text{pd}} e}{2L_{\text{Rx}}} \int_{-\infty}^{\infty} h_{\text{pd}}(t_1 - \rho) h_{\text{pd}}(t_2 - \rho) E \left[P_y(\rho) + P_y(\rho - T_{\text{Rx}}) \right] d\rho \\
 &\quad + \frac{Z_{\text{TIA}}^2 R_{\text{pd}}^2}{8L_{\text{Rx}}^2} \int_{-\infty}^{\infty} \int_{-\infty}^{\infty} h_{\text{pd}}(t_1 - \rho_1) h_{\text{pd}}(t_2 - \rho_2) \\
 &\quad \quad \cdot \text{Re} \left\{ R_{y^*y}(\rho_1, \rho_2) R_{y^*y}(\rho_2 - T_{\text{Rx}}, \rho_1 - T_{\text{Rx}}) \right. \\
 &\quad \quad \quad \left. + R_{y^*y}(\rho_1 - T_{\text{Rx}}, \rho_2) R_{y^*y}(\rho_2 - T_{\text{Rx}}, \rho_1) \right\} d\rho_1 d\rho_2 \\
 &\quad + Z_{\text{TIA}}^2 S_{\text{th}}\delta(t_1 - t_2) \tag{4.44}
 \end{aligned}$$

The impact of the noise can be minimized by low-pass filtering the output voltage of the TIA. This is illustrated in Figure 4.12.

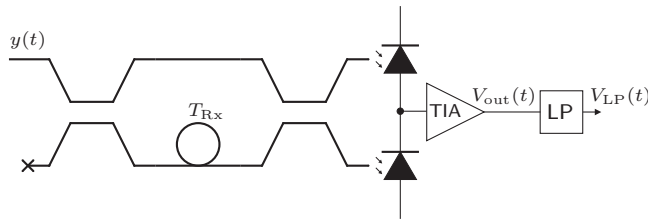
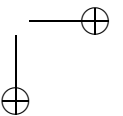
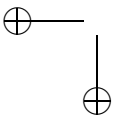


Figure 4.12: A balanced CM receiver with low-pass filter

When the low-pass filter can be considered linear and time-invariant, with an impulse response $h_{\text{LP}}(t)$ that is much longer than the impulse response of the photodiode $h_{\text{pd}}(t)$, then the signal $V_{\text{LP}}(t)$ at the output of this filter has



expected value

$$\begin{aligned}
\mathbb{E}[V_{\text{LP}}(t)] &= \int_{-\infty}^{\infty} h_{\text{LP}}(t - \rho) V_{\text{out}}(\rho) \, d\rho \\
&\approx -\frac{Z_{\text{TIA}} R_{\text{pd}}}{2L_{\text{Rx}}} \int_{-\infty}^{\infty} h_{\text{LP}}(t - \rho) \text{Re}\{R_{y^*y}(\rho - T_{\text{Rx}}, \rho)\} \, d\rho \\
&= \frac{Z_{\text{TIA}} R_{\text{pd}} P_x}{4L_{\text{Tx}} L_{\text{Rx}}} \exp\left(-\frac{\pi}{2} \left(\frac{T_{\text{Rx}} - T_{\text{Tx}}}{\tau_c}\right)^2\right) \\
&\quad \cdot \int_{-\infty}^{\infty} h_{\text{LP}}(t - \rho) m_{\text{mod}}(\rho) \cos\left(2\pi f_c (T_{\text{Rx}} - T_{\text{Tx}}) + \phi_{\text{mod}}(\rho)\right) \, d\rho, \quad (4.45)
\end{aligned}$$

and autocorrelation function

$$\begin{aligned}
R_{V_{\text{LP}} V_{\text{LP}}}(t_1, t_2) &= \int_{-\infty}^{\infty} \int_{-\infty}^{\infty} h_{\text{LP}}(t_1 - \rho_1) h_{\text{LP}}(t_2 - \rho_2) R_{V_{\text{out}} V_{\text{out}}}(\rho_1, \rho_2) \, d\rho_1 \, d\rho_2 \\
&\approx \mathbb{E}[V_{\text{LP}}(t_1)] \mathbb{E}[V_{\text{LP}}(t_2)] \\
&\quad + \frac{Z_{\text{TIA}}^2 R_{\text{pd}} e}{2L_{\text{Rx}}} \int_{-\infty}^{\infty} h_{\text{LP}}(t_1 - \rho) h_{\text{LP}}(t_2 - \rho) \mathbb{E}[P_y(\rho) + P_y(\rho - T_{\text{Rx}})] \, d\rho \\
&\quad + \frac{Z_{\text{TIA}}^2 R_{\text{pd}}^2}{8L_{\text{Rx}}^2} \int_{-\infty}^{\infty} \int_{-\infty}^{\infty} h_{\text{LP}}(t_1 - \rho_1) h_{\text{LP}}(t_2 - \rho_2) \\
&\quad \quad \cdot \text{Re}\{R_{y^*y}(\rho_1, \rho_2) R_{y^*y}(\rho_2 - T_{\text{Rx}}, \rho_1 - T_{\text{Rx}}) \\
&\quad \quad \quad + R_{y^*y}(\rho_1 - T_{\text{Rx}}, \rho_2) R_{y^*y}(\rho_2 - T_{\text{Rx}}, \rho_1)\} \, d\rho_1 \, d\rho_2 \\
&\quad + Z_{\text{TIA}}^2 S_{\text{th}} \int_{-\infty}^{\infty} h_{\text{LP}}(t_1 - \rho) h_{\text{LP}}(t_2 - \rho) \, d\rho. \quad (4.46)
\end{aligned}$$

Using (4.13) and again assuming that the bandwidth of the modulating signals is much smaller than $1/T_{\text{Tx}}$ and $1/T_{\text{Rx}}$, that T_{Tx} and T_{Rx} are much larger than τ_c and that their difference is much smaller than τ_c , one can find

$$\mathbb{E}[P_y(\rho)] \approx \mathbb{E}[P_y(\rho - T_{\text{Rx}})] \approx \frac{m_{\text{mod}}(\rho) P_x}{2L_{\text{Tx}}}, \quad (4.47)$$

$$\begin{aligned}
R_{y^*y}(\rho_1, \rho_2) R_{y^*y}(\rho_2 - T_{\text{Rx}}, \rho_1 - T_{\text{Rx}}) &\approx \frac{m_{\text{mod}}^2(\rho_1)}{16L_{\text{Tx}}^2} \left[4|R_{x^*x}(\rho_2 - \rho_1)|^2 \right. \\
&\quad \left. + |R_{x^*x}(\rho_2 - \rho_1 - T_{\text{Tx}})|^2 + |R_{x^*x}(\rho_2 - \rho_1 + T_{\text{Tx}})|^2\right], \quad (4.48)
\end{aligned}$$

$$\begin{aligned}
R_{y^*y}(\rho_1 - T_{\text{Rx}}, \rho_2) R_{y^*y}(\rho_2 - T_{\text{Rx}}, \rho_1) &\approx \\
\frac{m_{\text{mod}}^2(\rho_1)}{16L_{\text{Tx}}^2} |R_{x^*x}(\rho_2 - \rho_1)|^2 \exp\left(j4\pi f_c (T_{\text{Rx}} - T_{\text{Tx}}) + j2\phi_{\text{mod}}(\rho_1)\right), \quad (4.49)
\end{aligned}$$

so that (4.46) can be written as

$$\begin{aligned}
R_{V_{LP}V_{LP}}(t_1, t_2) &\approx E[V_{LP}(t_1)]E[V_{LP}(t_2)] \\
&+ \frac{Z_{TIA}^2 R_{pd} P_x e}{2L_{Tx} L_{Rx}} \int_{-\infty}^{\infty} h_{LP}(t_1 - \rho) h_{LP}(t_2 - \rho) m_{\text{mod}}(\rho) d\rho \\
&+ \frac{Z_{TIA}^2 R_{pd}^2}{128L_{Rx}^2 L_{Tx}^2} \int_{-\infty}^{\infty} \int_{-\infty}^{\infty} h_{LP}(t_1 - \rho_1) h_{LP}(t_2 - \rho_2) m_{\text{mod}}^2(\rho_1) \\
&\quad \cdot \left[4|R_{x^*x}(\rho_2 - \rho_1)|^2 + |R_{x^*x}(\rho_2 - \rho_1 - T_{Tx})|^2 + |R_{x^*x}(\rho_2 - \rho_1 + T_{Tx})|^2 \right. \\
&\quad \left. + |R_{x^*x}(\rho_2 - \rho_1)|^2 \cos\left(4\pi f_c(T_{Rx} - T_{Tx}) + 2\phi_{\text{mod}}(\rho_1)\right) \right] d\rho_1 d\rho_2 \\
&+ Z_{TIA}^2 S_{\text{th}} \int_{-\infty}^{\infty} h_{LP}(t_1 - \rho) h_{LP}(t_2 - \rho) d\rho. \tag{4.50}
\end{aligned}$$

When it is assumed that the bandwidth of the low-pass filter is much smaller than the bandwidth of $x(t)$, so that the duration of $h_{LP}(t)$ is much larger than the width of $R_{x^*x}(\tau)$, then (2.23) can be used to approximate

$$|R_{x^*x}(\tau)|^2 \approx 4P_x^2 \tau_c \delta(\tau), \tag{4.51}$$

so that (4.50) can be written as

$$\begin{aligned}
R_{V_{LP}V_{LP}}(t_1, t_2) &\approx E[V_{LP}(t_1)]E[V_{LP}(t_2)] \\
&+ \frac{Z_{TIA}^2 R_{pd} P_x e}{2L_{Tx} L_{Rx}} \int_{-\infty}^{\infty} h_{LP}(t_1 - \rho) h_{LP}(t_2 - \rho) m_{\text{mod}}(\rho) d\rho \\
&+ \frac{Z_{TIA}^2 R_{pd}^2 P_x^2 \tau_c}{32L_{Rx}^2 L_{Tx}^2} \int_{-\infty}^{\infty} h_{LP}(t_1 - \rho) h_{LP}(t_2 - \rho) m_{\text{mod}}^2(\rho) \\
&\quad \cdot \left[6 + \cos\left(4\pi f_c(T_{Rx} - T_{Tx}) + 2\phi_{\text{mod}}(\rho)\right) \right] d\rho \\
&+ Z_{TIA}^2 S_{\text{th}} \int_{-\infty}^{\infty} h_{LP}(t_1 - \rho) h_{LP}(t_2 - \rho) d\rho. \tag{4.52}
\end{aligned}$$

4.7 Digital transmission

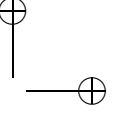
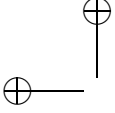
When digital transmission is performed with a rectangular symbol shape of length T_s , we can write

$$\phi_{\text{mod}}(t) = \sum_k \phi_k \Pi\left(\frac{t - kT_s}{T_s}\right), \tag{4.53}$$

$$m_{\text{mod}}(t) = \sum_k m_k \Pi\left(\frac{t - kT_s}{T_s}\right), \tag{4.54}$$

where $\Pi(\cdot)$ is the rectangular unit pulse, which is defined by

$$\Pi(x) \triangleq \begin{cases} 1 & , \text{ when } |x| < 1/2, \\ 0 & , \text{ when } |x| \geq 1/2, \end{cases} \tag{4.55}$$



and the coefficients $\{\phi_k\}$ and $\{m_k\}$ are related to the transmitted information symbols, according to the modulation format that is chosen. We will come back to this in the following subsections.

In order to optimize the SNR prior to detection, $h_{LP}(t)$ is assumed to be matched to these pulses. Hence, the low-pass filter is an integrate-and-dump filter that averages over one symbol time period, so we have

$$h_{LP}(t) = \frac{1}{T_s} \Pi \left(\frac{t}{T_s} \right). \quad (4.56)$$

Now we can use (4.45) to find the expected output signal of a matched receiver ($T_{Rx} = T_{Tx}$):

$$\mathbb{E}[V_{LP}(t)] \approx \frac{Z_{TIA} R_{pd} P_x}{4L_{Tx} L_{Rx}} \sum_k m_k \cos(\phi_k) \Lambda \left(\frac{t - k T_s}{T_s} \right), \quad (4.57)$$

where $\Lambda(\cdot)$ is the triangular unit pulse, which is defined by

$$\Lambda(x) \triangleq \begin{cases} 1 - |x| & , \text{ when } |x| < 1, \\ 0 & , \text{ when } |x| \geq 1. \end{cases} \quad (4.58)$$

Obviously, this output signal should be sampled by the detector at time instants $t = k T_s$, resulting in decision samples with expected value

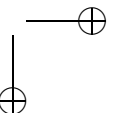
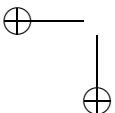
$$\mathbb{E}[V_{LP}(k T_s)] \approx \frac{Z_{TIA} R_{pd} P_x}{4L_{Tx} L_{Rx}} m_k \cos(\phi_k), \quad (4.59)$$

The variance of the output signal can be found from (4.52) as

$$\begin{aligned} \sigma_{V_{LP}(t)}^2 &= R_{V_{LP} V_{LP}}(t, t) - \mathbb{E}^2[V_{LP}(t)] \\ &\approx \frac{Z_{TIA}^2 R_{pd} P_x e}{2L_{Tx} L_{Rx} T_s} \sum_k m_k \Lambda \left(\frac{t - k T_s}{T_s} \right) \\ &\quad + \frac{Z_{TIA}^2 R_{pd}^2 P_x^2 \tau_c}{32L_{Rx}^2 L_{Tx}^2 T_s} \sum_k m_k^2 [6 + \cos(2\phi_k)] \Lambda \left(\frac{t - k T_s}{T_s} \right) \\ &\quad + \frac{Z_{TIA}^2 S_{th}}{T_s}. \end{aligned} \quad (4.60)$$

so the variance of the decision samples follows as

$$\sigma_{V_{LP}(k T_s)}^2 \approx \frac{Z_{TIA}^2}{T_s} \left\{ \frac{R_{pd} P_x e}{2L_{Tx} L_{Rx}} m_k + \frac{R_{pd}^2 P_x^2 \tau_c}{32L_{Rx}^2 L_{Tx}^2} m_k^2 [6 + \cos(2\phi_k)] + S_{th} \right\}. \quad (4.61)$$



4.7.1 BPSK modulation

When binary phase shift keying (BPSK) modulation is applied, the pulse amplitudes are given by $m_k = 1$ and $\phi_k = A_k\pi$, where $A_k \in \{0, 1\}$ are the binary information digits. Since these are actually random variables, the statistics of the decision sample that have been derived so far should be considered as *conditional statistics*, conditioned on a certain realization of $\{\phi_k\}$. Hence, the expected value and variance of the decision samples become conditional. For the conditional expected value we get:

$$\mathbb{E}[V_{\text{LP}}(kT_s) \mid A_k = 0] = -\mathbb{E}[V_{\text{LP}}(kT_s) \mid A_k = 1] \approx \frac{Z_{\text{TIA}} R_{\text{pd}} P_x}{4L_{\text{Tx}} L_{\text{Rx}}}, \quad (4.62)$$

and when the conditional variances of the output samples for a binary zero and one are abbreviated as σ_0^2 and σ_1^2 , respectively, these become

$$\sigma_0^2 = \sigma_1^2 \approx \frac{Z_{\text{TIA}}^2}{T_s} \left[\frac{R_{\text{pd}} P_x e}{2L_{\text{Tx}} L_{\text{Rx}}} + \frac{7R_{\text{pd}}^2 P_x^2 \tau_c}{32L_{\text{Rx}}^2 L_{\text{Tx}}^2} + S_{\text{th}} \right]. \quad (4.63)$$

As a result, the SNR per symbol can be written as

$$\gamma_{\text{BPSK}} \triangleq \frac{\mathbb{E}^2[V_{\text{LP}}(kT_s) \mid A_k = 0]}{2\sigma_0^2} = \left(\gamma_{\text{sn}}^{-1} + \gamma_{\text{bn}}^{-1} + \gamma_{\text{tn}}^{-1} \right)^{-1}, \quad (4.64)$$

where

$$\gamma_{\text{sn}} = \frac{R_{\text{pd}} P_x T_s}{16L_{\text{Tx}} L_{\text{Rx}} e}, \quad (4.65)$$

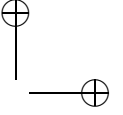
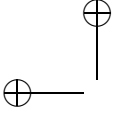
$$\gamma_{\text{bn}} = \frac{T_s}{7\tau_c}, \quad (4.66)$$

$$\gamma_{\text{tn}} = \frac{R_{\text{pd}}^2 P_x^2 T_s}{32L_{\text{Rx}}^2 L_{\text{Tx}}^2 S_{\text{th}}}, \quad (4.67)$$

are the signal-to-shot noise ratio, signal-to-beat noise ratio, and signal-to-thermal noise ratio, respectively. Obviously, all of these have to have a high value in order to have a high value for γ_{BPSK} . This is the case when:

- The integration time T_s of the matched filter is much larger than the coherence time τ_c ;
- The received power is high, such that the average number of received photons in one integration time T_s is high, and the photocurrent is much larger than the equivalent input noise current of the amplifier.

From the latter condition, it follows that the probability density function of each integrated photodiode current is similar to the probability density function of its corresponding integrated input power [51]. Since the integration time T_s is much larger than the correlation time of the optical power (which is in the order



of τ_c), the Central Limit Theorem applies, such that the decision samples can be assumed to be Gaussian distributed. Hence, when the conditional probability functions of the output samples for a binary zero or one are denoted by $f_0(v)$ and $f_1(v)$, respectively, they can be written as

$$f_0(v) = \frac{1}{\sigma_0 \sqrt{2\pi}} \exp\left(-\frac{(v - E[V_{\text{LP}}(k T_s) | A_k = 0])^2}{2\sigma_0^2}\right), \quad (4.68)$$

$$f_1(v) = \frac{1}{\sigma_1 \sqrt{2\pi}} \exp\left(-\frac{(v - E[V_{\text{LP}}(k T_s) | A_k = 1])^2}{2\sigma_1^2}\right). \quad (4.69)$$

Obviously, $f_{V_{\text{LP}}(k T_s) | A_k=0}(v) = f_{V_{\text{LP}}(k T_s) | A_k=1}(-v)$, so that the decision threshold of the detector should be at 0 volts (assuming that binary ones and zeros occur with equal probability), resulting in a probability of bit error

$$P_e = \frac{1}{2} \int_{-\infty}^0 f_1(v) dv + \frac{1}{2} \int_0^{\infty} f_0(v) dv \approx Q\left(\sqrt{2\gamma_{\text{BPSK}}}\right). \quad (4.70)$$

From this it can be calculated that an SNR of $\gamma_{\text{BPSK}} = 18$ (12.6 dB) is required for having a bit error rate of $P_e = 10^{-9}$. From (4.65) through (4.67) it follows that the bit rate that can be achieved is then given by

$$R_b = \frac{1}{T_s} = \frac{\frac{1}{18} R_{\text{pd}}^2 P_x^2}{7R_{\text{pd}}^2 P_x^2 \tau_c + 16R_{\text{pd}} P_x L_{\text{Tx}} L_{\text{Rx}} \epsilon + 32L_{\text{Rx}}^2 L_{\text{Tx}}^2 S_{\text{th}}}. \quad (4.71)$$

Example 4.7

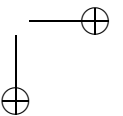
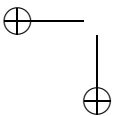
Now consider the following numerical example:

$$\begin{aligned} P_x &= 10 \text{ mW}, \\ R_{\text{pd}} &= 0.8 \text{ A/W}, \\ L_{\text{Rx}} &= L_{\text{Tx}} = 1.12 \text{ (0.5 dB)}, \\ S_{\text{th}} &= 49 \text{ (pA)}^2/\text{Hz}, \\ \tau_c &= 0.1 \text{ ps}, \end{aligned}$$

Substituting these parameter values into (4.71) results in a maximum bit rate $R_b = 80 \text{ Gbps}$. In that case, the individual SNR contributions are given by

$$\begin{aligned} \gamma_{\text{sn}} &\approx 3.1 \cdot 10^4 \text{ (45 dB)}, \\ \gamma_{\text{bn}} &\approx 18 \text{ (12.6 dB)}, \\ \gamma_{\text{tn}} &\approx 3.3 \cdot 10^5 \text{ (55 dB)}. \end{aligned}$$

Obviously, the performance in this numerical example is almost fully determined by beat noise. Hence, the only way to increase the maximum bit rate of this system is to reduce the coherence time τ_c ; increasing the transmitted



power, reducing the losses or improving the TIA will hardly affect the performance. Note, however, that 40 nm is already quite a large linewidth for communication light sources. Moreover, choosing a large source linewidth limits the length of the fiber that can be used, due to chromatic dispersion. This will be further studied in Chapter 7. And finally, it is questionable whether it is possible to achieve a bit rate of 80 Gbps with current state-of-the-art modulators, photodetectors and TIAs in the first place. Note, however, that the calculations in this chapter are merely meant as a preparation for analyzing systems in which several coherence-modulated channels are multiplexed. In these systems, the noise-limited bit rate will certainly be lower.

For graphical illustration, a simulation has been run of a corresponding system in which a bit pattern '01001101' is transmitted at 80 Gbps. The corresponding modulating signal $\phi_{\text{mod}}(t)$ is shown in Figure 4.13(a). The sample time is $T_{\text{samp}} = \tau_c/2 = 50$ fs and the transimpedance of the TIA is set to $Z_{\text{TIA}} = 1$ k Ω . The resulting matched filter output signal is shown in Figure 4.13, where the circles mark the actual decision samples. The dashed line represents the theoretical expected value of the output signal as expressed by (4.57).

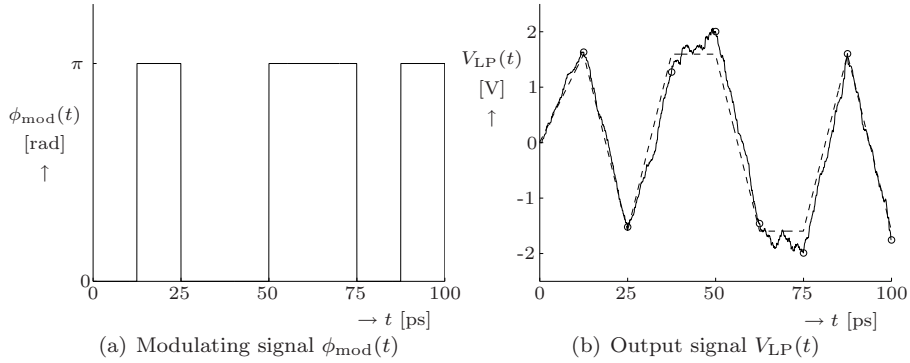


Figure 4.13: Simulation results for BPSK modulation when a bit pattern '01001101' is transmitted at 80 Gbps

4.7.2 OOK modulation

When on-off keying (OOK) modulation is applied, the pulse amplitudes are given by $\phi_k = 0$ and $m_k = A_k \in \{0, 1\}$. The conditional expected value and variance of the decision samples then become

$$\mathbb{E}[V_{\text{LP}}(k T_s) \mid A_k = 0] = 0, \quad (4.72)$$

$$\mathbb{E}[V_{\text{LP}}(k T_s) \mid A_k = 1] \approx \frac{Z_{\text{TIA}} R_{\text{pd}} P_x}{4L_{\text{Tx}} L_{\text{Rx}}}, \quad (4.73)$$

$$\sigma_0^2 \approx \frac{Z_{\text{TIA}}^2 S_{\text{th}}}{T_s}, \quad (4.74)$$

$$\sigma_1^2 \approx \frac{Z_{\text{TIA}}^2}{T_s} \left[\frac{R_{\text{pd}} P_x e}{2L_{\text{Tx}} L_{\text{Rx}}} + \frac{7R_{\text{pd}}^2 P_x^2 \tau_c}{32L_{\text{Rx}}^2 L_{\text{Tx}}^2} + S_{\text{th}} \right]. \quad (4.75)$$

The decision samples can be assumed to be Gaussian like in the case of BPSK modulation, so (4.68) and (4.69) still apply.

Obviously, the optimum decision threshold should be somewhere in between the two possible conditional expected values of $V_{\text{LP}}(k T_s)$ and hence depends on the actual received optical power. Note however, that the decision problem is not symmetric like in the case of BPSK modulation due to the different conditional variances of $V_{\text{LP}}(k T_s)$. Even when binary ones and zeros occur with equal probability, the optimum decision threshold is not exactly halfway the two expected values. When thermal noise dominates, the variances are approximately the same, so that the optimum threshold is approximately halfway the two expected values. In general, however, the optimum detection threshold is lower, due to the larger variance in case a binary one is transmitted.

When the detection threshold is chosen halfway the two expected values, for convenience (this is also easy to realize in practice), the bit error probability can be proven to be given by

$$\begin{aligned} P_e &= \frac{1}{2} \int_{\frac{1}{2} \mathbb{E}[V_{\text{LP}}(k T_s) | A_k=1]}^{\infty} f_0(v) dv + \frac{1}{2} \int_{-\infty}^{\frac{1}{2} \mathbb{E}[V_{\text{LP}}(k T_s) | A_k=1]} f_1(v) dv \\ &\approx \frac{1}{2} \text{Q} \left(\sqrt{\frac{\gamma_{\text{OOK},0}}{2}} \right) + \frac{1}{2} \text{Q} \left(\sqrt{\frac{\gamma_{\text{OOK},1}}{2}} \right), \end{aligned} \quad (4.76)$$

where

$$\gamma_{\text{OOK},0} \triangleq \frac{\mathbb{E}^2[V_{\text{LP}}(k T_s) | A_k = 1]}{2\sigma_0^2} \approx \frac{R_{\text{pd}}^2 P_x^2 T_s}{32L_{\text{Rx}}^2 L_{\text{Tx}}^2 S_{\text{th}}}, \quad (4.77)$$

$$\begin{aligned} \gamma_{\text{OOK},1} &\triangleq \frac{\mathbb{E}^2[V_{\text{LP}}(k T_s) | A_k = 1]}{2\sigma_1^2} \\ &\approx \frac{R_{\text{pd}}^2 P_x^2 T_s}{7R_{\text{pd}}^2 P_x^2 \tau_c + 16R_{\text{pd}} P_x L_{\text{Tx}} L_{\text{Rx}} e + 32L_{\text{Rx}}^2 L_{\text{Tx}}^2 S_{\text{th}}}. \end{aligned} \quad (4.78)$$

Example 4.8

When the same parameter values are chosen as in Example 4.7, the performance will still be fully determined by beat noise. Hence, when the detection threshold is indeed set as described above, bit errors will practically only occur for $A_k = 1$, and the achievable bit rate is approximately 20 Gbps, a quarter of what can be achieved with BPSK. The simulation results for a corresponding system are shown in Figure 4.14.

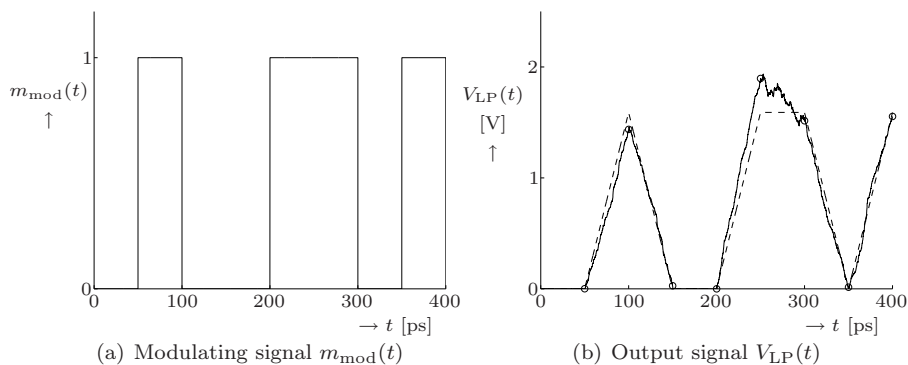


Figure 4.14: Simulation results for OOK modulation when a bit pattern '01001101' is transmitted at 20 Gbps

From Figure 4.14(b) it is obvious that the conditional variance σ_0^2 is much smaller than σ_1^2 in this case, so the performance could be significantly enhanced by lowering the decision threshold. In the next chapter we will see, however, that this will not be the case when several coherence-modulated channels are multiplexed, so we will not elaborate on this further. (Note that this one-channel example is merely meant for illustrating the modulation concept.) \square

4.8 Practical considerations

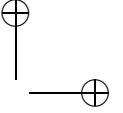
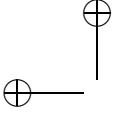
In this last section we will comment on some assumptions that have been made in the theoretical explanation in the preceding sections.

4.8.1 Polarization

In the preceding sections it was assumed that the optical waves were polarized light, and that the polarization state of the light was maintained throughout the system.

In practice, however, light from a spontaneously emitting source will generally be *unpolarized*, meaning that it consists of two polarization modes that have orthogonal mode profiles and uncorrelated electrical fields [51]. Hence, the analysis that is presented only holds when the source light is first passed through a polarizer.

Moreover, the polarization of light at the output of a standard single-mode fiber is not predictable due to birefringence and random mode coupling. In coherent optical communications [64]—where a received signal is interfering with a locally generated optical signal—this turned out to be a significant problem since light waves in different polarization modes do not beat, so that



polarization control or polarization diversity is required. In CM, however, the modulated light wave and reference light wave are generated in the same optical chip, transmitted through the same fiber and demodulated in the same optical chip. Hence, if the optical chips are designed such that polarization is maintained (or at least all light waves get the same shift in polarization state), then the detected light waves will all have the same polarization state so that polarization control and polarization diversity are not required. (Note that this is not the case when the MZIs are constructed by fibers, so that a polarization controller is required in an all-fiber experimental prototype.)

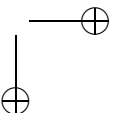
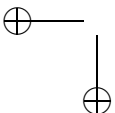
When the optical chips are even designed to be polarization independent (which might be especially challenging in the transmitter, which contains a modulator) it is not required to polarize the source light. This has the advantage that the received power per channel will double, so that the signal-to-shot noise ratio will double and the signal-to-thermal noise ratio will become four times larger. Moreover, the signal-to-beat noise ratio will double because the contributions in the detected power that correspond to the interference in the two polarization modes will add up coherently, whereas the contributions that correspond to beat noise in the two polarization modes will add up incoherently, since the two polarization modes of the source light are uncorrelated. In practice the latter effect might be partly canceled by the fact that random mode coupling introduces partial correlation between the polarization modes. This has not been studied in detail, however.

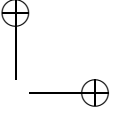
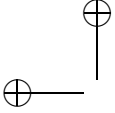
4.8.2 Optical phase offset

A particular advantage of CM is its immunity to crosstalk: small fluctuations in the MZIs' path delays T_{Tx} and T_{Rx} do not result in crosstalk between the channels, as long as the delays and the differences between the delays remain much larger than the coherence time. Hence, it is not difficult to suppress unwanted channels.

It was shown that a desired channels can be detected by setting $T_{Rx} = T_{Tx}$. Note that this assumes that the delays are matched very precisely; their difference is not only assumed to be much smaller than the coherence time, but also smaller than $1/f_c$, where f_c is the optical carrier frequency. Otherwise, there will be an offset $2\pi f_c(T_{Rx} - T_{Tx})$ in the phase difference between the interfering light waves, which affects the observability of the modulating signal.

In practice it might not be too straightforward to achieve matching this accurately, due to fabrication tolerances, temperature fluctuations or aging of components. This problem will be discussed in more detail in Chapter 6, where some receivers are discussed in which this problem is either solved or avoided.





4.8.3 Balancing


In the description of the balanced detection concept it has been assumed that the MZI is perfectly balanced and that the photodiodes have equal responsivities R_{pd} . In practice this might not be the case, for example due to fabrication tolerances. The implication of this is that the subtraction of (4.30) and (4.31) in the first line of (4.33) is not carried out properly, so that $E[P_y(t)]$ becomes observable in the output signal.

In case of PM it follows from (4.13) that $E[P_y(t)]$ is constant so that it will result in a DC bias voltage in the output signal. This unwanted signal can be suppressed by using an AC-coupled TIA. Note that this can only be done when $\cos(\phi_{mod}(t))$ does not contain a DC component; otherwise the TIA will distort the desired signal. In case of digital transmission this requires line coding like bipolar or Manchester coding [56].

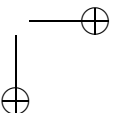
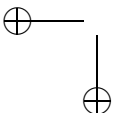
This is not possible in case of IM, however, since the desired signal is then unipolar and hence contains a DC term. Moreover, it follows from (4.13) that $E[P_y(t)]$ is then also proportional to $m_{mod}(t)$ so that the undesired terms have both DC and AC content. As a result, when designing an OOK CM receiver special attention should be paid to well-balancing the balanced detector configuration in order to avoid crosstalk between channels. This especially concerns the rightmost 2×2 coupler and the photodiodes.

Example 4.9

This is illustrated by running similar simulations like in Examples 4.7 and 4.8, but this time we set $T_{Rx} = 2T_{Tx} = 1$ ps (so the receiver is not matched to the transmitter). Simulations are run for BPSK and OOK modulation, like in Examples 4.7 and 4.8; the results are shown in Figure 4.15(a) and 4.15(b). The dashed lines correspond to the theoretical expected value. As expected, the modulating signals (Figure 4.13(a) and 4.14(a), respectively) are not observable in the corresponding output signals.

Both simulations are repeated, but this time an imbalance is introduced in the receiver by setting the responsivity of the upper photodiode to 0.9 A/W and the lower photodiode to 0.7 A/W. (A relatively large imbalance is chosen, for visualization purposes.) As expected, the imbalance introduces a DC bias (after some initial transient) in case of BPSK modulation and crosstalk in case of OOK modulation. The DC bias could be removed by means of AC-coupled amplification, so an eventual imbalance is mainly a problem in CM systems with OOK modulation. 

In the next chapter it will be shown that the requirement for properly balancing the detector configuration becomes stricter as the number of channels increases, and depends on the particular multiplexing topology that is used.



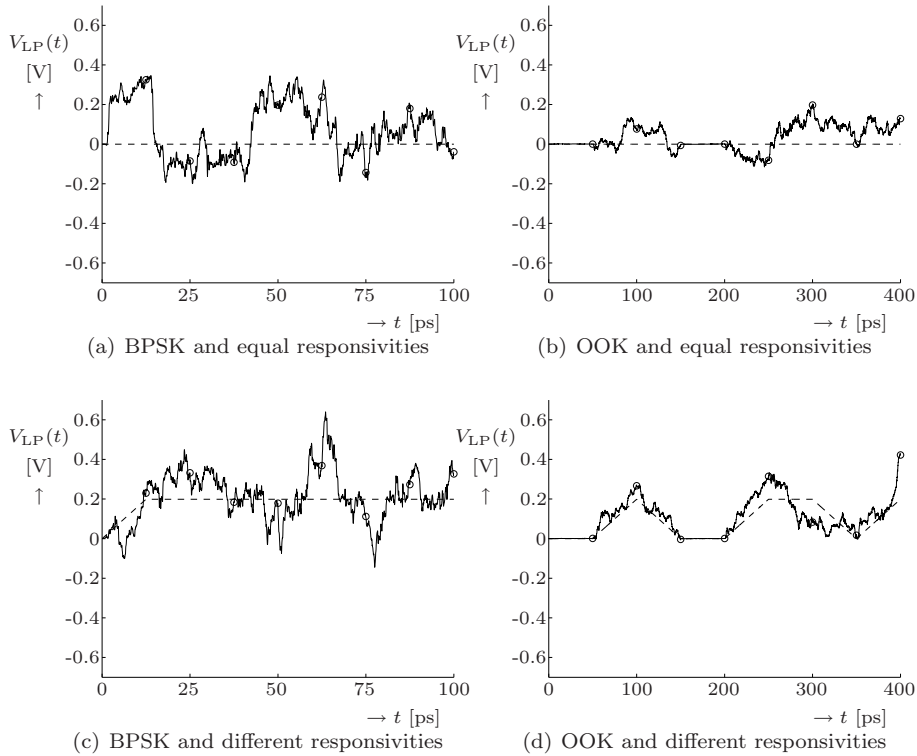
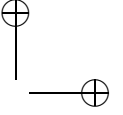
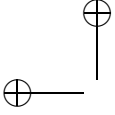


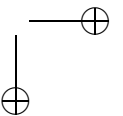
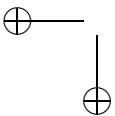
Figure 4.15: Output signal $V_{LP}(t)$ in an unmatched receiver

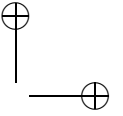
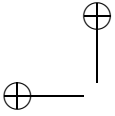
4.9 Conclusion

In this chapter the basic channel generation and selection concept for coherence multiplexing has been explained both physically and mathematically. Moreover, it has been visually illustrated by showing some simulated realizations of the signals that are involved in this concept.

It has been explained that a coherence-modulated channel can be generated by creating two mutually delayed versions of a broadband light wave by means of an interferometer. The path delay imbalance T_{TX} of the interferometer is supposed to be much larger than the coherence time of the light, so that the resulting light waves are mutually incoherent. Information transmission is accomplished by either performing phase modulation (PM) on one of these two versions, or performing intensity modulation (IM) on both versions.

The modulating signal can be recovered in the receiver by means of coherence demodulation, which requires another interferometer with path delay imbalance T_{RX} and either a single-ended or balanced detector configuration. A particular coherence-modulated channel is selected by choosing the path delay



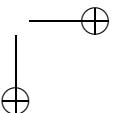
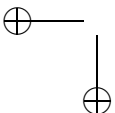


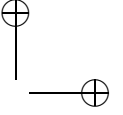
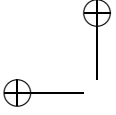
imbalances in transmitter and receiver to be the same (resulting in a matched transmitter-receiver pair), so that optical interference (coherent beating) occurs. A channel can be suppressed by making the path delay imbalances have a difference that is much larger than the coherence time of the light, so that there is no interference. Coherence demodulation does not work properly when IM and single-ended detection are combined: IM requires balanced detection.

The noise in the receiver has been analyzed in terms of beat noise (caused by beating of mutually incoherent light waves), shot noise (caused by the random arrival character of photons) and thermal noise in the transimpedance amplifier (TIA) in the receiver. The results were used to derive the signal-to-noise ratio (SNR) and bit error rate (BER) for BPSK and OOK modulation. The performance can be improved by either increasing the transmitted power (when shot noise and/or thermal noise are dominant) or reducing the coherence time of the optical sources (when beat noise is dominant).

Some practical aspects were considered regarding the polarization of the light waves, the precise matching of the delays in the transmitter and receiver and the proper balancing of the balanced detector configuration.

In the next chapter three topologies will be discussed for multiplexing several coherence-modulated channels into a common optical fiber cable. Some performance results for balanced detection will be derived which are partly based on the analysis that has been presented in this chapter.





Chapter 5

Coherence multiplexing topologies

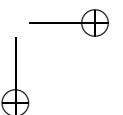
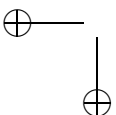
5.1 Introduction

In the previous chapter the basic concepts of coherence modulation and demodulation have been explained. Coherence modulation implies that a pair of two optical signals is transmitted, which are delayed with respect to each other by a time shift that exceeds the coherence time, such that they do not interfere. In the receiver, coherence demodulation is performed, which involves that the data signal is recovered by correlating the received optical signal with its delayed version.

In this chapter it will be explained how coherence modulation can be used to multiplex several channels onto one common optical fiber cable. The idea is that several pairs of optical signals are transmitted, each pair having a different relative delay between the constituting optical signals. A particular receiver can then select a particular pair by correlating the received optical signal with a delayed version, where the delay is equal to the relative delay in the corresponding signal pair.

Several system topologies are known for multiplexing coherence-modulated optical signals. The first CM system was introduced by Paolo Cielo and Claude Delisle and constituted of a series concatenation of coherence modulators [27]. In 1985 Janet Brooks and Robert Wentworth et al. proposed [46] and analyzed [47] four topologies for using coherence multiplexing in a distributed interferometric sensor system, namely:

- the discontinuous series (DS) system;
- the continuous series (CS) system;
- the extrinsic reference ladder (ERL) system;
- the intrinsic reference ladder (IRL) system.



The DS system actually corresponds to the CM system that was proposed by Cielo and Delisle. It will be further considered in Section 5.4.

The CS and ERL system require two separate transmission paths between the transmission and reception unit. Although this might be practical in a distributed sensor application, it is not desirable in an optical fiber communication application, because the polarization states of the optical signals at the outputs of the two optical fibers need to be matched in order to achieve optimal interference. Moreover, the differential length mismatch between the two fibers has significant impact on the performance of the system [65]. Therefore, the CS and ERL system will not be further considered in this thesis.

The IRL system is basically a parallel array (PA) of coherence modulators that are illuminated by a common optical source. A more flexible and power effective approach however was the PA that was proposed by Goedgebuer and Hamel in 1987 [28], where each coherence modulator is illuminated by its own source. The latter form is further considered in Section 5.2.

A considerable performance improvement can be achieved when the MZIs in the IRL system are integrated to one MZI with a common reference branch and several modulated paths with different delays. This is termed the single intrinsic reference ladder (SIRL) system and is further considered in Section 5.3.

5.2 The parallel array (PA)

5.2.1 Multiplexed signal

The most straightforward way of multiplexing several coherence-modulated optical channels is the parallel array (PA), which is illustrated in Figure 5.1.

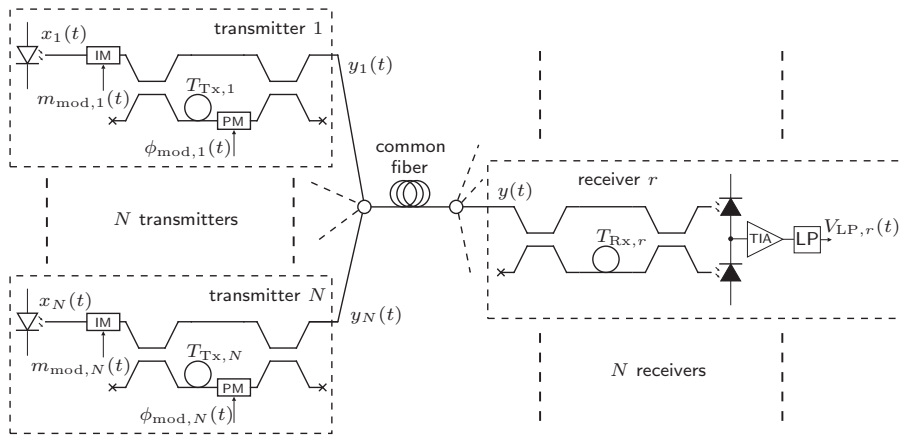
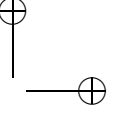
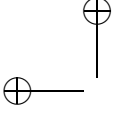


Figure 5.1: Parallel array (PA) of N coherence modulators and demodulators



It consists of N coherence modulators and demodulators. Each coherence modulator i is illuminated by a different source signal $x_i(t)$. The output signals $y_i(t)$ of the coherence modulators are combined into the common transmission fiber using an optical combiner. The aggregate signal is then distributed over the N receivers by means of an optical splitter. When the difference in propagation delay is ignored and splitters and combiners are assumed to be uniform, this implies that each coherence demodulator receives an identical signal $y(t)$. When both IM and PM are applied (like in Chapter 4), and it is assumed that all coherence modulators have the same excess loss L_{Tx} and that the combined signals have matched polarization states, $y(t)$ can be written as

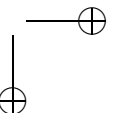
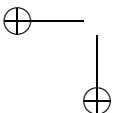
$$y(t) = \frac{1}{\sqrt{L_{\text{nw}}}} \sum_{i=1}^N y_i(t) = \frac{1}{2\sqrt{L_{\text{Tx}}L_{\text{nw}}}} \sum_{i=1}^N \left[x_i(t)m_{\text{mod},i}(t) - x_i(t - T_{\text{Tx},i})m_{\text{mod},i}(t - T_{\text{Tx},i}) \exp(j\phi_{\text{mod},i}(t)) \right], \quad (5.1)$$

where L_{nw} denotes the optical losses in the network (between a transmitter and receiver), due to intrinsic combining and splitting losses, excess losses and coupling losses. (Propagation losses and dispersion in the transmission fibers are still ignored; these will not be considered until Chapter 7.)

For deterministic modulating signals $m_{\text{mod},i}(t)$ and $\phi_{\text{mod},i}(t)$ with bandwidths that are much smaller than $1/T_{\text{Tx},i}$ and $1/\tau_c$, $y(t)$ has zero mean and autocorrelation function

$$\begin{aligned} R_{y^*y}(t_1, t_2) &\triangleq \text{E}[y^*(t_1)y(t_2)] \\ &\approx \frac{1}{4L_{\text{Tx}}L_{\text{nw}}} \sum_{i=1}^N m_{\text{mod},i}(t_1) \left[2R_{x^*x}(t_2 - t_1) \right. \\ &\quad \left. - R_{x^*x}(t_2 - t_1 - T_{\text{Tx},i}) \exp(j\phi_{\text{mod},i}(t_1)) \right. \\ &\quad \left. - R_{x^*x}(t_2 - t_1 + T_{\text{Tx},i}) \exp(-j\phi_{\text{mod},i}(t_1)) \right], \quad (5.2) \end{aligned}$$

where it is assumed that all source signals $x_i(t)$ are independent and have the same autocorrelation function $R_{x^*x}(\tau)$.



5.2.2 Output signal of balanced receiver

When the coherence demodulators consist of balanced receivers, the theory of the previous chapter can be used for analyzing the output signal. Using (4.45) and (5.2), the expected output signal of a particular receiver r with path delay $T_{\text{Rx},r}$ can be written as

$$\begin{aligned}
\mathbb{E}[V_{\text{LP},r}(t)] &\approx -\frac{Z_{\text{TIA}}R_{\text{pd}}}{2L_{\text{Rx}}} \int_{-\infty}^{\infty} h_{\text{LP}}(t-\rho) \text{Re}\{R_{y^*y}(\rho - T_{\text{Rx},r}, \rho)\} d\rho \\
&\approx \frac{Z_{\text{TIA}}R_{\text{pd}}P_x}{4L_{\text{Tx}}L_{\text{Rx}}L_{\text{nw}}} \sum_{i=1}^N \int_{-\infty}^{\infty} h_{\text{LP}}(t-\rho) m_{\text{mod},i}(\rho) \\
&\quad \cdot \left[-2 \exp\left(-\frac{\pi}{2} \left(\frac{T_{\text{Rx},r}}{\tau_c}\right)^2\right) \cos(2\pi f_c T_{\text{Rx},r}) \right. \\
&\quad + \exp\left(-\frac{\pi}{2} \left(\frac{T_{\text{Rx},r} - T_{\text{Tx},i}}{\tau_c}\right)^2\right) \\
&\quad \cdot \cos\left(2\pi f_c (T_{\text{Rx},r} - T_{\text{Tx},i}) + \phi_{\text{mod},i}(\rho)\right) \\
&\quad + \exp\left(-\frac{\pi}{2} \left(\frac{T_{\text{Rx},r} + T_{\text{Tx},i}}{\tau_c}\right)^2\right) \\
&\quad \left. \cdot \cos\left(2\pi f_c (T_{\text{Rx},r} + T_{\text{Tx},i}) - \phi_{\text{mod},i}(\rho)\right) \right] d\rho. \quad (5.3)
\end{aligned}$$

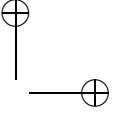
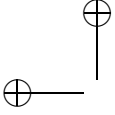
Since $T_{\text{Rx},r} \gg \tau_c$, this can be reduced to

$$\begin{aligned}
\mathbb{E}[V_{\text{LP},r}(t)] &\approx \frac{Z_{\text{TIA}}R_{\text{pd}}P_x}{4L_{\text{Tx}}L_{\text{Rx}}L_{\text{nw}}} \sum_{i=1}^N \exp\left(-\frac{\pi}{2} \left(\frac{T_{\text{Rx},r} - T_{\text{Tx},i}}{\tau_c}\right)^2\right) \\
&\quad \cdot \int_{-\infty}^{\infty} h_{\text{LP}}(t-\rho) m_{\text{mod},i}(\rho) \cos\left(2\pi f_c (T_{\text{Rx},r} - T_{\text{Tx},i}) + \phi_{\text{mod},i}(\rho)\right) d\rho. \quad (5.4)
\end{aligned}$$

Obviously, the expected output signal of receiver r contains contributions from all transmitters i . The significance of each contribution depends on the relation between $T_{\text{Rx},r}$ and $T_{\text{Tx},i}$. When only the contribution of transmitter r is supposed to be observable, one should obviously choose $T_{\text{Rx},r} = T_{\text{Tx},r}$ and $|T_{\text{Rx},r} - T_{\text{Tx},i}| \gg \tau_c$ for $i \neq r$, resulting in

$$\begin{aligned}
\mathbb{E}[V_{\text{LP},r}(t)] &\approx \\
&\quad \frac{Z_{\text{TIA}}R_{\text{pd}}P_x}{4L_{\text{Tx}}L_{\text{Rx}}L_{\text{nw}}} \int_{-\infty}^{\infty} h_{\text{LP}}(t-\rho) m_{\text{mod},i}(\rho) \cos\left(\phi_{\text{mod},i}(\rho)\right) d\rho. \quad (5.5)
\end{aligned}$$

Note that this expression is very similar to the result in the preceding chapter. The only difference is the extra power loss due to the combining and splitting.



5.2.3 Choosing the path delays

From the condition in the previous subsection it follows that the path delays $T_{\text{Tx},i}$ in the transmitters should be chosen such that:

- each individual delay $T_{\text{Tx},i}$ should be much larger than τ_c ;
- the mutual difference between any two delays T_{Tx,i_1} and T_{Tx,i_2} with $i_1 \neq i_2$ should be much larger than τ_c .

A straightforward choice is to set $T_{\text{Tx},1}$ such that $T_{\text{Tx},1} \gg \tau_c$, and then choose the other delays as integer multiples of $T_{\text{Tx},1}$, so that

$$T_{\text{Tx},i} = i \cdot T_{\text{Tx},1}. \quad (5.6)$$

From (5.3) it follows that the crosstalk due to residual coherence is worst for receiver 1; in that case, there are $2N + 1$ crosstalk terms with an amplitude that is $\exp\left(-\frac{\pi}{2} \left(\frac{T_{\text{Tx},1}}{\tau_c}\right)^2\right)$ times smaller than the desired term. (All other crosstalk terms are much smaller, and the other receivers have less than $2N + 1$ of such crosstalk terms.) Hence, the total crosstalk in each receiver is at least

$$\begin{aligned} -20 \log\left((2N + 1) \exp\left(-\frac{\pi}{2} \left(\frac{T_{\text{Tx},1}}{\tau_c}\right)^2\right)\right) \text{ dB} \approx \\ 13.6 \left(\frac{T_{\text{Tx},1}}{\tau_c}\right)^2 - 20 \log(2N + 1) \text{ dB} \end{aligned} \quad (5.7)$$

below the desired signal.

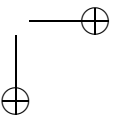
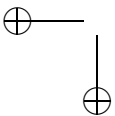
Example 5.1

So when $T_{\text{Tx},1}$ is chosen as $T_{\text{Tx},1} = 2\tau_c$ (like in the previous chapter) and up to 16 channels are to be transmitted, one can show that the crosstalk is at least 24 dB below the desired signal. When $T_{\text{Tx},1} = 3\tau_c$, the crosstalk is at least 92 dB below the desired signal.

When we choose $T_{\text{Tx},1} = 3\tau_c$ to be on the safe side, and we consider light sources with a coherence time of 0.1 ps (like in Example 4.6) in a CM system with 16 transmitters and waveguides with an effective index N_{eff} in the order of 1.5, then the path delays are multiples of 0.3 ps. The minimum and maximum path length difference are given by

$$\begin{aligned} l_{\text{Tx},1} &= \frac{c_0 T_{\text{Tx},1}}{N_{\text{eff}}} \approx 60 \text{ } \mu\text{m}, \\ l_{\text{Tx},16} &= 16 l_{\text{Tx},1} \approx 1 \text{ mm}. \end{aligned}$$

This can easily be fabricated in planar waveguide technology. □



5.2.4 Noise performance

The noise performance of the PA can be analyzed in a similar way as in Chapter 4. The autocorrelation function of the output signal follows from (4.46):

$$\begin{aligned}
R_{V_{LP,r}V_{LP,r}}(t_1, t_2) &\approx \mathbb{E}[V_{LP,r}(t_1)]\mathbb{E}[V_{LP,r}(t_2)] \\
&+ \frac{Z_{TIA}^2 R_{pd} e}{2L_{Rx}} \int_{-\infty}^{\infty} h_{LP}(t_1 - \rho) h_{LP}(t_2 - \rho) \\
&\quad \cdot \mathbb{E}[P_y(\rho) + P_y(\rho - T_{Rx})] d\rho \\
&+ \frac{Z_{TIA}^2 R_{pd}^2}{8L_{Rx}^2} \int_{-\infty}^{\infty} \int_{-\infty}^{\infty} h_{LP}(t_1 - \rho_1) h_{LP}(t_2 - \rho_2) \\
&\quad \cdot \operatorname{Re} \left\{ R_{y^*y}(\rho_1, \rho_2) R_{y^*y}(\rho_2 - T_{Rx,r}, \rho_1 - T_{Rx,r}) \right. \\
&\quad \left. + R_{y^*y}(\rho_1 - T_{Rx,r}, \rho_2) R_{y^*y}(\rho_2 - T_{Rx,r}, \rho_1) \right\} d\rho_1 d\rho_2 \\
&+ Z_{TIA}^2 S_{th} \int_{-\infty}^{\infty} h_{LP}(t_1 - \rho) h_{LP}(t_2 - \rho) d\rho. \tag{5.8}
\end{aligned}$$

Using (5.2) one can find

$$\begin{aligned}
\mathbb{E}[P_y(\rho)] &\approx \mathbb{E}[P_y(\rho - T_{Rx,r})] \approx \frac{P_x}{2L_{Tx}L_{nw}} \sum_{i=1}^N m_{\text{mod},i}(\rho), \tag{5.9} \\
R_{y^*y}(\rho_1, \rho_2) R_{y^*y}(\rho_2 - T_{Rx,r}, \rho_1 - T_{Rx,r}) &\approx \\
\frac{1}{16L_{Tx}^2 L_{nw}^2} &\left\{ 4 \sum_{i_1=1}^N \sum_{i_2=1}^N m_{\text{mod},i_1}(\rho_1) m_{\text{mod},i_2}(\rho_1) |R_{x^*x}(\rho_2 - \rho_1)|^2 \right. \\
&+ \sum_{i=1}^N m_{\text{mod},i}^2(\rho_1) \left[|R_{x^*x}(\rho_2 - \rho_1 - T_{Tx,i})|^2 \right. \\
&\quad \left. \left. + |R_{x^*x}(\rho_2 - \rho_1 + T_{Tx,i})|^2 \right] \right\}. \tag{5.10}
\end{aligned}$$

$R_{y^*y}(\rho_1 - T_{Rx,r}, \rho_2) R_{y^*y}(\rho_2 - T_{Rx,r}, \rho_1)$ can also be found using (5.2), and depends on the actual choice of the path delays. When the delays are chosen as multiples of $T_{Tx,1}$ (as described in the previous section), then in practice they will not be exact multiples but rather approximate multiples, in the sense that

$$|T_{Tx,i} - i \cdot T_{Tx,1}| \ll \tau_c, \tag{5.11}$$

so that one can find

$$\begin{aligned}
R_{y^*y}(\rho_1 - T_{\text{Rx},r}, \rho_2) R_{y^*y}(\rho_2 - T_{\text{Rx},r}, \rho_1) &\approx \\
\frac{1}{16L_{\text{Tx}}^2 L_{\text{nw}}^2} \sum_{i=1}^N &\left\{ -2m_{\text{mod},i}(\rho_1) P_{\text{mod},2r}(\rho_1) \right. \\
&\cdot \left[|R_{x^*x}(\rho_2 - \rho_1 + T_{\text{Rx},r})|^2 + |R_{x^*x}(\rho_2 - \rho_1 - T_{\text{Rx},r})|^2 \right] \\
&\cdot \exp\left(\text{j} 2\pi f_c (2T_{\text{Rx},r} - T_{\text{Tx},2r}) + \text{j} \phi_{\text{mod},2r}(\rho_1)\right) \\
&+ m_{\text{mod},i}(\rho_1) P_{\text{mod},2r-i}(\rho_1) |R_{x^*x}(\rho_2 - \rho_1 + T_{\text{Rx},r} - T_{\text{Tx},i})|^2 \\
&\cdot \exp\left(\text{j} 2\pi f_c (2T_{\text{Rx},r} - T_{\text{Tx},i} - T_{\text{Tx},2r-i}) \right. \\
&\quad \left. + \text{j} \phi_{\text{mod},i}(\rho_1) + \text{j} \phi_{\text{mod},2r-i}(\rho_1)\right) \\
&+ m_{\text{mod},i}(\rho_1) P_{\text{mod},i-2r}(\rho_1) |R_{x^*x}(\rho_2 - \rho_1 + T_{\text{Rx},r} - T_{\text{Tx},i})|^2 \\
&\cdot \exp\left(\text{j} 2\pi f_c (2T_{\text{Rx},r} - T_{\text{Tx},i} + T_{\text{Tx},i-2r}) \right. \\
&\quad \left. + \text{j} \phi_{\text{mod},i}(\rho_1) - \text{j} \phi_{\text{mod},i-2r}(\rho_1)\right) \\
&+ m_{\text{mod},i}(\rho_1) P_{\text{mod},i+2r}(\rho_1) |R_{x^*x}(\rho_2 - \rho_1 + T_{\text{Rx},r} + T_{\text{Tx},i})|^2 \\
&\cdot \exp\left(\text{j} 2\pi f_c (2T_{\text{Rx},r} + T_{\text{Tx},i} - T_{\text{Tx},i+2r}) \right. \\
&\quad \left. - \text{j} \phi_{\text{mod},r}(\rho) + \text{j} \phi_{\text{mod},i+2r}(\rho_1)\right) \left. \right\}. \quad (5.12)
\end{aligned}$$

Due to production inaccuracies, the arguments of most of the complex exponentials can be considered as random, since they constitute differences of delays that are not related, hence resulting in a phase that can be considered as uniformly distributed. As a result, the summation of these complex exponentials in practice results in a value that is on the average negligible to (5.10). This is called phase-averaging [47].

The only term that does not disappear by phase-averaging is the one in which only $T_{\text{Rx},r}$ and $T_{\text{Tx},r}$ occur as delays, since they have a known relation. Hence, we find

$$\begin{aligned}
R_{y^*y}(\rho_1 - T_{\text{Rx},r}, \rho_2) R_{y^*y}(\rho_2 - T_{\text{Rx},r}, \rho_1) &\approx \frac{m_{\text{mod},r}^2(\rho_1)}{16L_{\text{Tx}}^2 L_{\text{nw}}^2} |R_{x^*x}(\rho_2 - \rho_1)|^2 \\
&\cdot \exp\left(\text{j} 4\pi f_c (T_{\text{Rx},r} - T_{\text{Tx},r}) + \text{j} 2\phi_{\text{mod},r}(\rho_1)\right). \quad (5.13)
\end{aligned}$$

It can actually be shown that phase averaging will result in (5.13) for any choice of the path delays, as long as they fulfill the two conditions that were mentioned in the beginning of subsection 5.2.3.

Substituting (5.9), (5.10) and (5.13) in (5.8) and using approximation (4.51) again, we find

$$\begin{aligned}
R_{V_{\text{LP},r}, V_{\text{LP},r}}(t_1, t_2) &\approx \mathbb{E}[V_{\text{LP},r}(t_1)]\mathbb{E}[V_{\text{LP},r}(t_2)] \\
&+ \frac{Z_{\text{TIA}}^2 R_{\text{pd}} P_x e}{2L_{\text{Tx}} L_{\text{Rx}} L_{\text{nw}}} \int_{-\infty}^{\infty} h_{\text{LP}}(t_1 - \rho) h_{\text{LP}}(t_2 - \rho) \sum_{i=1}^N m_{\text{mod},i}(\rho) \, \text{d}\rho \\
&+ \frac{Z_{\text{TIA}}^2 R_{\text{pd}}^2 P_x^2 \tau_c}{32L_{\text{Tx}}^2 L_{\text{Rx}}^2 L_{\text{nw}}^2} \int_{-\infty}^{\infty} h_{\text{LP}}(t_1 - \rho) h_{\text{LP}}(t_2 - \rho) \\
&\quad \cdot \left[4 \sum_{i_1=1}^N \sum_{i_2=1}^N m_{\text{mod},i_1}(\rho) m_{\text{mod},i_2}(\rho) + 2 \sum_{i=1}^N m_{\text{mod},i}^2(\rho) \right. \\
&\quad \left. + m_{\text{mod},r}^2(\rho) \cos\left(4\pi f_c (T_{\text{Rx},r} - T_{\text{Tx},r}) + 2\phi_{\text{mod},r}(\rho)\right) \right] \, \text{d}\rho \\
&+ Z_{\text{TIA}}^2 S_{\text{th}} \int_{-\infty}^{\infty} h_{\text{LP}}(t_1 - \rho) h_{\text{LP}}(t_2 - \rho) \, \text{d}\rho. \tag{5.14}
\end{aligned}$$

5.2.5 Digital transmission

When the PA is used for digital transmission in a similar way as described in Section 4.7 (so with a rectangular symbol shape and matched filtering), the expected value and variance of the detected samples in receiver r are given by

$$\mathbb{E}[V_{\text{LP},r}(k T_s)] \approx \frac{Z_{\text{TIA}} R_{\text{pd}} P_x}{4L_{\text{Tx}} L_{\text{Rx}} L_{\text{nw}}} m_{r,k} \cos(\phi_{r,k}), \tag{5.15}$$

$$\begin{aligned}
\sigma_{V_{\text{LP},r}(k T_s)}^2 &= R_{V_{\text{LP},r}, V_{\text{LP},r}}(k T_s, k T_s) - \mathbb{E}^2[V_{\text{LP},r}(k T_s)] \\
&\approx \frac{Z_{\text{TIA}}^2 R_{\text{pd}} P_x e}{2L_{\text{Tx}} L_{\text{Rx}} L_{\text{nw}} T_s} \sum_{i=1}^N m_{i,k} \\
&\quad + \frac{Z_{\text{TIA}}^2 R_{\text{pd}}^2 P_x^2 \tau_c}{32L_{\text{Tx}}^2 L_{\text{Rx}}^2 L_{\text{nw}}^2 T_s} \left[\sum_{i_1=1}^N \sum_{i_2=1}^N m_{i_1,k} m_{i_2,k} + 2 \sum_{i=1}^N m_{i,k}^2 + m_{r,k}^2 \cos(2\phi_{r,k}) \right] \\
&\quad + \frac{Z_{\text{TIA}}^2 S_{\text{th}}}{T_s}, \tag{5.16}
\end{aligned}$$

where all the transmitters have assumed to be bit-synchronized, for convenience. (It is assumed that this does not significantly affect the results of the performance analysis.)

BPSK modulation

When BPSK modulation is applied (see Subsection 4.7.1) the conditional expected values and variances are given by

$$\begin{aligned} \mathbb{E}[V_{LP,r}(kT_s) \mid A_{r,k} = 0] &= -\mathbb{E}[V_{LP,r}(kT_s) \mid A_{r,k} = 1] \\ &\approx \frac{Z_{TIA} R_{pd} P_x}{4L_{Tx} L_{Rx} L_{nw}}, \end{aligned} \quad (5.17)$$

$$\sigma_0^2 = \sigma_1^2 \approx \frac{Z_{TIA}^2}{T_s} \left[\frac{N R_{pd} P_x e}{2L_{Tx} L_{Rx} L_{nw}} + \frac{(4N^2 + 2N + 1) R_{pd}^2 P_x^2 \tau_c}{32L_{Tx}^2 L_{Rx}^2 L_{nw}^2} + S_{th} \right], \quad (5.18)$$

where $A_{r,k}$ is the k -th bit that is transmitted by transmitter r . As a result, the SNR per symbol can be written as

$$\gamma_{BPSK} \triangleq \frac{\mathbb{E}^2[V_{LP,r}(kT_s) \mid A_{r,k} = 0]}{2\sigma_0^2} = \left(\gamma_{sn}^{-1} + \gamma_{bn}^{-1} + \gamma_{tn}^{-1} \right)^{-1}, \quad (5.19)$$

where

$$\gamma_{sn} = \frac{R_{pd} P_x T_s}{16N L_{Tx} L_{Rx} L_{nw} e}, \quad (5.20)$$

$$\gamma_{bn} = \frac{T_s}{(4N^2 + 2N + 1) \tau_c}, \quad (5.21)$$

$$\gamma_{tn} = \frac{R_{pd}^2 P_x^2 T_s}{32L_{Tx}^2 L_{Rx}^2 L_{nw}^2 S_{th}}. \quad (5.22)$$

Following the theory in Subsection 4.7.1, the bit error probability is given by

$$P_e \approx Q\left(\sqrt{2\gamma_{BPSK}}\right). \quad (5.23)$$

Obviously, the performance degrades when the number of channels N increases, because:

- the number of light waves that is detected in each photodiode increases when N increases, such that the number of shot noise terms increases;
- the number of mutually incoherent light waves that are beating in the receiver increases when N increases, such that the number of beat noise terms increases;
- moreover, the larger the number of coherence modulators and demodulators, the larger the intrinsic combining and splitting loss, such that the received power per demodulator decreases.

Consequently, the bit rate R_b that can be achieved per channel at $P_e = 10^{-9}$ (or $\gamma_{BPSK} \approx 18$; see Example 4.7) also depends on N , and follows from the above equations as

$$\begin{aligned} R_b = \frac{1}{T_s} &= \frac{1}{18} R_{pd}^2 P_x^2 \left[(4N^2 + 2N + 1) R_{pd}^2 P_x^2 \tau_c + 16N R_{pd} P_x L_{Tx} L_{Rx} L_{nw} e \right. \\ &\quad \left. + 32L_{Tx}^2 L_{Rx}^2 L_{nw}^2 S_{th} \right]^{-1}. \end{aligned} \quad (5.24)$$

Example 5.2

Now consider a numerical example of a CM system consisting of N coherence modulators and demodulators. Hence, the splitter and combiner both have an intrinsic splitting and combining loss that equals the number of CM channels N . When an excess loss of 0.1 dB per splitter/combiner is assumed, we have $L_{\text{nw}} \approx 1.047N^2$. The remaining parameters are assumed to have the same values as in Example 4.7. The corresponding bit rate R_b that can be achieved per channel at $P_e = 10^{-9}$ has been plotted as a function of the number of channels N in Figure 5.2(a). In Figure 5.2(b), the corresponding SNRs are plotted as a function of N . Obviously, shot noise and thermal noise hardly play a role in this numerical example; the performance is mainly limited by beat noise. Note that for $N = 1$, the values are the same as in in Example 4.7.

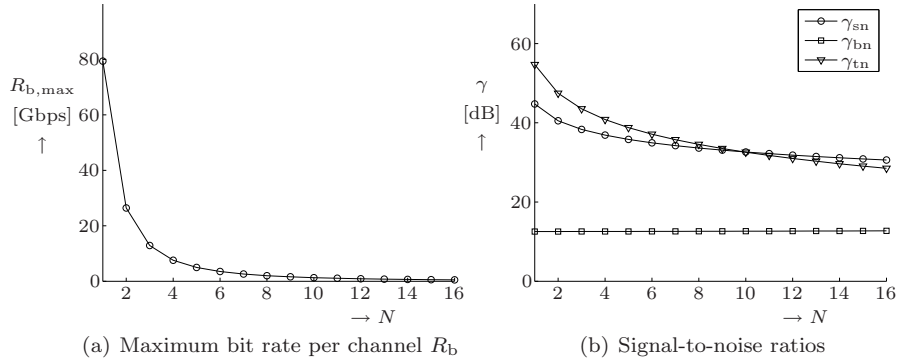


Figure 5.2: Maximum bit rate per channel R_b and corresponding signal-to-noise ratios as a function of number of channels N in a PA with BPSK modulation

A simulation has been run of a corresponding 2-channel PA in which bit patterns '01001101' and '00110100' are transmitted at 25 Gbps. The corresponding modulating signals are shown in Figure 5.3(a) and 5.3(c). The path delay differences in the transmitters and receivers are chosen as $T_{\text{Rx},1} = T_{\text{Tx},1} = 0.5$ ps and $T_{\text{Rx},2} = T_{\text{Tx},2} = 1$ ps. The resulting output signals are shown in Figure 5.3(b) and 5.3(d), where the circles denote the decision samples and the dashed lines represent the theoretical expected values.

Obviously, the output signal of receiver 1 corresponds to the modulating signal in transmitter 1 and the output signal of receiver 2 corresponds to the modulating signal in transmitter 2: there is no visible crosstalk. □

Actually, when a particular coherence modulator has no data to transmit, its optical source should be switched off, so that it does not introduce beat noise and shot noise in demodulators that receive other channels. Then the formulas above can still be used, and N then represents the number of actually active

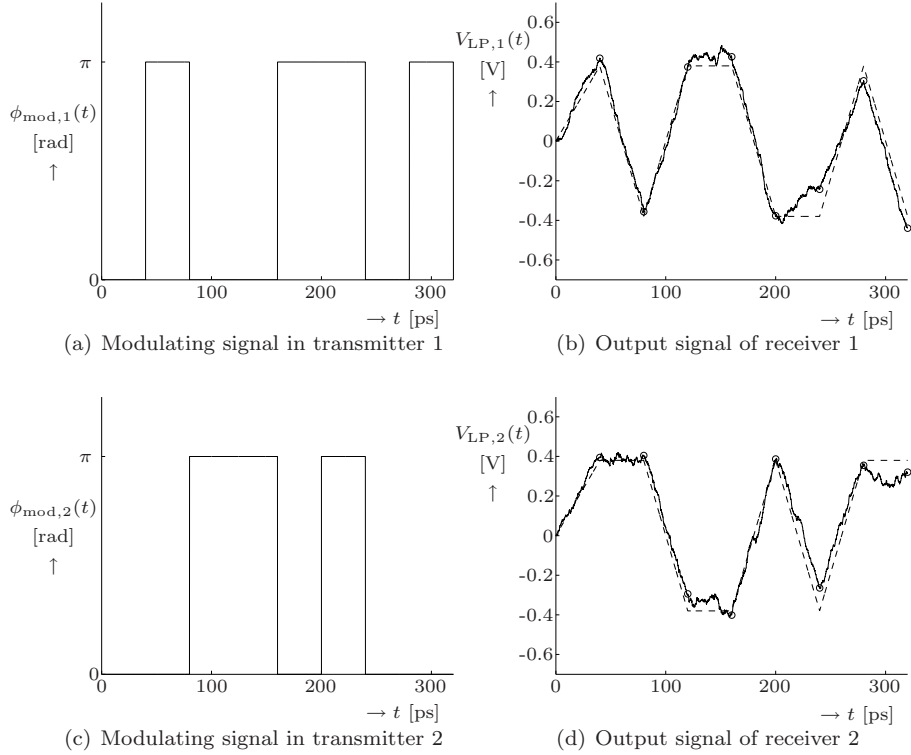


Figure 5.3: Simulation results for a 2-channel PA using BPSK modulation when bit patterns '01001101' and '00110100' are transmitted at 25 Gbps

channels, whereas the losses in the network L_{nw} depend on the intrinsic losses in splitters and combiners, which are determined by the number of coherence modulators and demodulators, no matter whether they are active or not.

Example 5.3

Now consider a numerical example of a CM system consisting of 16 coherence modulators and demodulators. Hence, the splitter and combiner both have an intrinsic splitting and combining loss of 12 dB. When an excess loss of 0.1 dB per splitter/combiner is assumed, and the propagation and coupling losses are neglected, we have $L_{\text{nw}} \approx 268$. The remaining parameters are assumed to have the same values as in Example 5.2.

As explained above, the performance of a particular receiver depends on the number of active channels N . Consequently, the bit rate R_b that can be achieved per channel at $P_e = 10^{-9}$ also depends on N , and follows from (5.24). This has been plotted as a function of N in Figure 5.4(a). In Figure 5.4(b), the corresponding SNRs are plotted as a function of N .

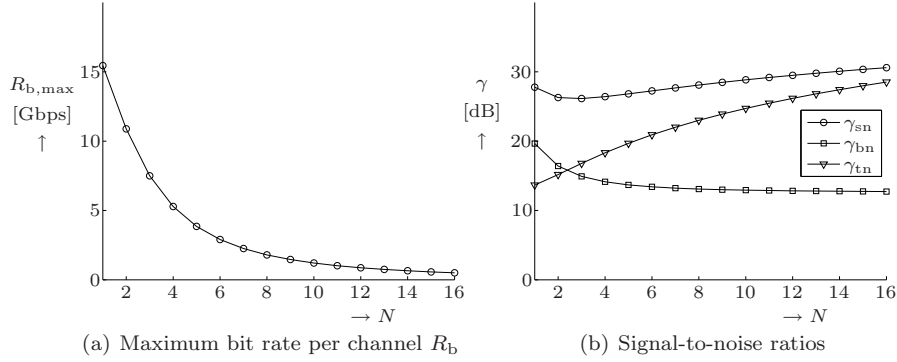
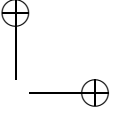
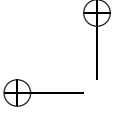


Figure 5.4: Maximum bit rate per channel R_b and corresponding signal-to-noise ratios as a function of number of active channels N in a PA with 16 transmitters and receivers and BPSK modulation

Obviously, shot noise hardly plays a role in this numerical example. For large values of N , the performance is mainly limited by beat noise, whereas for low values of N , the performance is mainly limited by thermal noise. Note that for $N = 16$, the values are the same as in Figure 5.2(a). ▣

OOK modulation

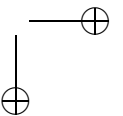
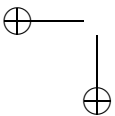
In case of OOK modulation (see Subsection 4.7.2) the conditional expected value of the detected samples are given by

$$E[V_{LP,r}(kT_s) | A_{r,k} = 0] = 0, \quad (5.25)$$

$$E[V_{LP,r}(kT_s) | A_{r,k} = 1] \approx \frac{Z_{TIA} R_{pd} P_x}{4L_{Tx} L_{Rx} L_{nw}}. \quad (5.26)$$

A careful look at (5.16) reveals that the conditional variance of the detected sample not only depends on the detected bit $A_{r,k}$, but also on the other bits $A_{i,k}$ with $i \neq r$. Actually, one can verify that the conditional variance at the sampling instant kT_s depends on the value of $A_{r,k}$ and the total number of transmitters that are transmitting a binary one at time instant kT_s . When we define N_1 as the number of interfering transmitters that are transmitting a binary one at time instant kT_s , or in mathematical form

$$N_1 \triangleq \sum_{\substack{i=1 \\ i \neq r}}^N m_{\text{mod},i}(kT_s) = \sum_{\substack{i=1 \\ i \neq r}}^N A_{i,k}, \quad (5.27)$$



then one can find

$$\sum_{i=1}^N m_{\text{mod},i}^2(k T_s) = \sum_{i=1}^N m_{\text{mod},i}(k T_s) = N_1 + A_{r,k}, \quad (5.28)$$

$$\begin{aligned} \sum_{i_1=1}^N \sum_{i_2=1}^N m_{\text{mod},i_1}(k T_s) m_{\text{mod},i_2}(k T_s) &= (N_1 + A_{r,k})^2 \\ &= N_1^2 + 2N_1 A_{r,k} + A_{r,k}, \end{aligned} \quad (5.29)$$

and the conditional variances of the detected samples can be written as

$$\sigma_{0,N_1=n}^2 \approx \frac{Z_{\text{TIA}}^2}{T_s} \left[\frac{n R_{\text{pd}} P_x e}{2L_{\text{Tx}} L_{\text{Rx}} L_{\text{nw}}} + \frac{(4n^2 + 2n) R_{\text{pd}}^2 P_x^2 \tau_c}{32L_{\text{Tx}}^2 L_{\text{Rx}}^2 L_{\text{nw}}^2} + S_{\text{th}} \right], \quad (5.30)$$

$$\sigma_{1,N_1=n}^2 \approx \frac{Z_{\text{TIA}}^2}{T_s} \left[\frac{(n+1) R_{\text{pd}} P_x e}{2L_{\text{Tx}} L_{\text{Rx}} L_{\text{nw}}} + \frac{(4n^2 + 10n + 7) R_{\text{pd}}^2 P_x^2 \tau_c}{32L_{\text{Tx}}^2 L_{\text{Rx}}^2 L_{\text{nw}}^2} + S_{\text{th}} \right]. \quad (5.31)$$

For given values of $A_{r,k}$ and N_1 , the decision samples $V_{\text{LP},r}(k T_s)$ can be assumed to be Gaussian distributed as in (4.68) and (4.69). Hence, when binary ones and zeros occur with equal probability (so that N_1 is binomially distributed) and the decision threshold is chosen as

$$V_{\text{Th}} = \frac{1}{2} \text{E}[V_{\text{LP},r}(k T_s) \mid A_{r,k} = 1], \quad (5.32)$$

the total probability of bit error can be calculated as

$$\begin{aligned} P_e &= \sum_{n=0}^{N-1} P_e[N_1 = n] \\ &\quad \cdot \left[P_e[V_{\text{LP},r}(k T_s) > V_{\text{Th}} \mid A_{r,k} = 0, N_1 = n] P_e[A_{r,k} = 0] \right. \\ &\quad \left. + P_e[V_{\text{LP},r}(k T_s) < V_{\text{Th}} \mid A_{r,k} = 1, N_1 = n] P_e[A_{r,k} = 1] \right] \\ &\approx \left(\frac{1}{2}\right)^N \sum_{n=0}^{N-1} \binom{N-1}{n} \left[Q\left(\sqrt{\frac{\gamma_{\text{OOK},0}(n)}{2}}\right) \right. \\ &\quad \left. + Q\left(\sqrt{\frac{\gamma_{\text{OOK},1}(n)}{2}}\right) \right], \end{aligned} \quad (5.33)$$

where

$$\begin{aligned} \gamma_{\text{OOK},0}(n) &\triangleq \frac{\text{E}^2[V_{\text{LP},r}(k T_s) \mid A_{r,k} = 1]}{2\sigma_{0,N_1=n}^2} \\ &\approx R_{\text{pd}}^2 P_x^2 T_s \left[(4n^2 + 2n) R_{\text{pd}}^2 P_x^2 \tau_c \right. \\ &\quad \left. + 16n R_{\text{pd}} P_x L_{\text{Tx}} L_{\text{Rx}} L_{\text{nw}} e + 32L_{\text{Tx}}^2 L_{\text{Rx}}^2 L_{\text{nw}}^2 S_{\text{th}} \right]^{-1}, \end{aligned} \quad (5.34)$$

$$\begin{aligned}
\gamma_{\text{OOK},1}(n) &\triangleq \frac{\text{E}^2[V_{\text{LP},r}(kT_s) \mid A_{r,k} = 1]}{2\sigma_{1,N_1=n}^2} \\
&\approx R_{\text{pd}}^2 P_x^2 T_s \left[(4n^2 + 10n + 7) R_{\text{pd}}^2 P_x^2 \tau_c \right. \\
&\quad \left. + 16(n+1) R_{\text{pd}} P_x L_{\text{Tx}} L_{\text{Rx}} L_{\text{nw}} c + 32L_{\text{Tx}}^2 L_{\text{Rx}}^2 L_{\text{nw}}^2 S_{\text{th}} \right]^{-1}. \quad (5.35)
\end{aligned}$$

Example 5.4

Again consider a PA with 16 transmitters and receivers, like in Example 5.3, but now with OOK modulation instead of BPSK modulation. When the same parameter values are assumed, the maximum bit rate for $P_e = 10^{-9}$ can again be found as a function of the number of active channels N , using (5.33). Note that this has to be done numerically. The results are shown in Figure 5.5, together with the maximum bit rates for BPSK modulation.

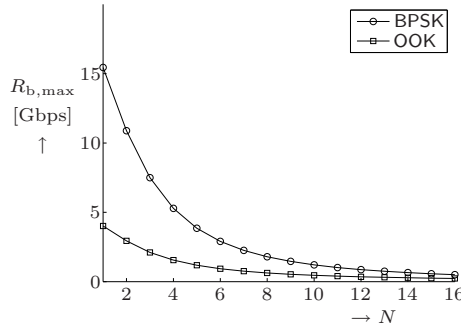


Figure 5.5: Maximum bit rate per channel R_b as a function of number of active channels N in a PA with 16 transmitters and receivers for BPSK and OOK modulation

As expected, the bit rate that can be achieved with OOK modulation is lower than the bit rate that can be achieved with BPSK modulation.

A simulation has been run of a corresponding 16-channel PA with two active transmitters, transmitting bit patterns '01001101' and '00110100' at 5 Gbps. The corresponding modulating signals are shown in Figure 5.6(a) and 5.6(c). The path delay differences in the transmitters and receivers are chosen as $T_{\text{Rx},1} = T_{\text{Tx},1} = 0.5$ ps and $T_{\text{Rx},2} = T_{\text{Tx},2} = 1$ ps. The resulting output signals are shown in Figure 5.6(b) and 5.6(d), where the circles denote the decision samples and the dashed lines represent the theoretical expected values.

Obviously, the output signal of receiver 1 corresponds to the modulating signal in transmitter 1 and the output signal of receiver 2 corresponds to the modulating signal in transmitter 2: there is no visible crosstalk. □

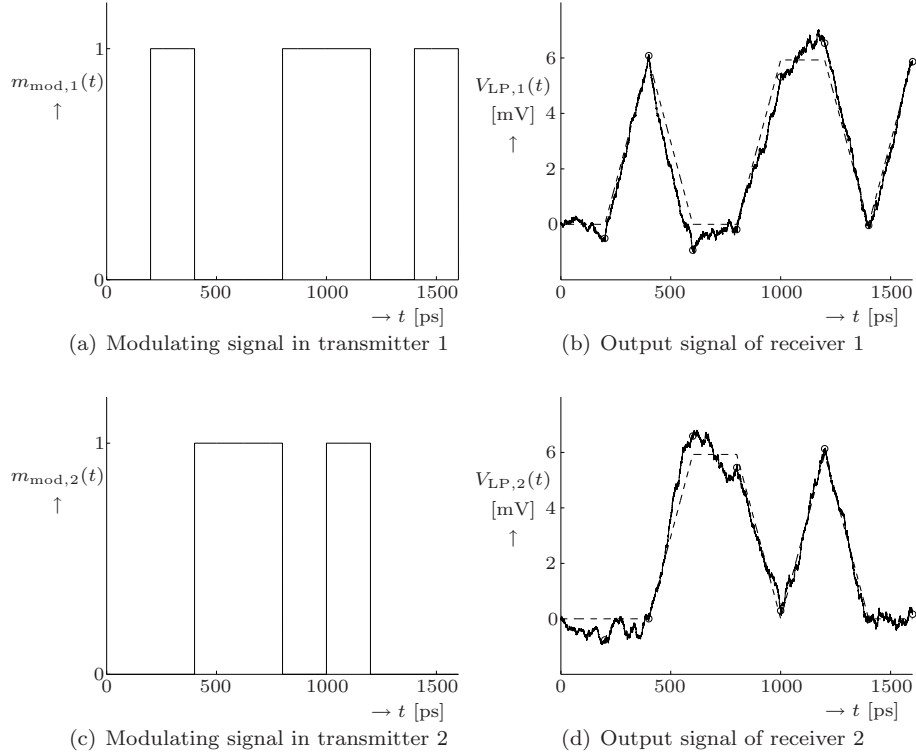
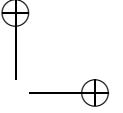
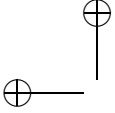


Figure 5.6: Simulation results for a 16-channel PA with two active transmitters using OOK modulation when bit patterns '01001101' and '00110100' are transmitted at 5 Gbps

Traffic control

It has been found that the maximum bit rate that can be achieved in a PA with N users, while keeping the bit error below 10^{-9} , depends on the number of users that are actually active. Hence, when a PA is designed to always operate at the same bit rate, which is higher than the maximum bit rate for N active users, then the bit error rate will obviously be higher than 10^{-9} in cases when all N users are active at the same time. When the data is transmitted in packets and the transmitters operate in burst mode, the CM system will operate properly as long as only a few users transmit simultaneously. Packet errors tend to occur when many users are active. If erroneous packets are simply retransmitted, this might result in a network jam: users keep retransmitting their packet but do not manage to transmit it correctly because too many users are active. In such a case special measures are required in order to avoid or recover from such a jam. In [66] some protocols are proposed and evaluated for controlling the traffic in a PA. These will not be further considered here.



5.2.6 Practical aspects

In Subsection 5.2.1 it was mentioned that the signals from the different transmitters that are combined into the common fiber were assumed to have equal power and equal polarization states. This is not very realistic, however.

Power differences

In practice there will at least be small differences in power between the signals that are received from the different transmitters, due to differences in fiber lengths and coupling differences. This is not really a problem however, as long as the differences are small; it will merely result in some difference in SNR between the different receivers. In case the difference is quite large, however, the receiver demodulating a low-power channel will be more or less jammed by the beat noise resulting from the interfering channels (similar to the near-far effect in wireless communication). This is not a likely situation in short-range applications, however, unless one of the fibers is damaged or not properly coupled to an optical chip.

Polarization

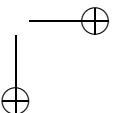
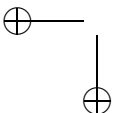
The light waves at the input of the combiner in Figure 5.1 will in practice have random polarization states, so that the signals of different transmitters are more or less randomly distributed over the two polarization modes of the common fiber. Since the two modes are orthogonal, light waves in different modes do not beat, so that the beat noise power will in practice be lower than what has been calculated in this section.

5.3 The single intrinsic reference ladder (SIRL) system

5.3.1 Multiplexed signal

The intrinsic reference ladder (IRL) system that was proposed by Brooks et al. [46] is actually similar to the PA. The only difference is that the IRL has a common source, the power of which is distributed over the coherence modulators using splitters. The input signals of the different coherence modulators can be made mutually incoherent by inserting suitable delays. This will always result in a lower transmitted power than in case of the PA, however, whereas the beat noise performance will be approximately the same.

The beat noise performance can be improved, however, by letting all the channels share the same reference light wave. This can be achieved by means of the optical circuit in Figure 5.7, which is termed the *single intrinsic reference ladder (SIRL) system*.



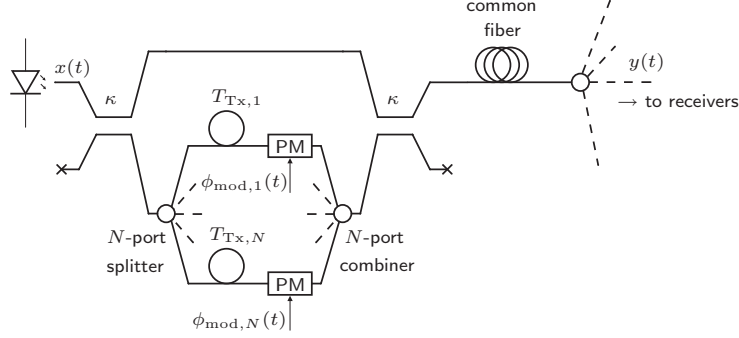


Figure 5.7: Single intrinsic reference ladder (SIRL) system

Only PM is applied. The ratio between the power in the reference light wave and the modulated light waves is controlled by the coupling constant κ , so that each receiver receives a signal that can be written as:

$$y(t) = \frac{1}{\sqrt{L_{Tx}L_{nw}}} \left[(1 - \kappa)x(t) - \frac{\kappa}{N} \sum_{i=1}^N x(t - T_{Tx,i}) \exp(j \phi_{mod,i}(t)) \right]. \quad (5.36)$$

Note that the excess losses of the splitter and combiner are not explicitly incorporated. They are assumed to have been incorporated in the excess loss L_{Tx} of the total circuit and the coupling constant κ .

When the modulating signals $\phi_{mod,i}(t)$ have bandwidths that are much smaller than $1/\tau_c$ and the inverse of the delays, the autocorrelation function of $y(t)$ is given by

$$\begin{aligned} R_{y^*y}(t_1, t_2) &\triangleq E[y^*(t_1)y(t_2)] \\ &\approx \frac{1}{L_{Tx}L_{nw}} \left\{ (1 - \kappa)^2 R_{x^*x}(t_2 - t_1) \right. \\ &\quad - \frac{\kappa(1 - \kappa)}{N} \sum_{i=1}^N \left[R_{x^*x}(t_2 - t_1 - T_{Tx,i}) \exp(j \phi_{mod,i}(t_1)) \right. \\ &\quad \quad \left. + R_{x^*x}(t_2 - t_1 + T_{Tx,i}) \exp(-j \phi_{mod,i}(t_1)) \right] \\ &\quad + \frac{\kappa^2}{N^2} \sum_{i_1=1}^N \sum_{i_2=1}^N R_{x^*x}(t_2 - t_1 + T_{Tx,i_1} - T_{Tx,i_2}) \\ &\quad \quad \left. \cdot \exp(j \phi_{mod,i_2}(t_1) - j \phi_{mod,i_1}(t_1)) \right\}. \quad (5.37) \end{aligned}$$

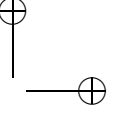
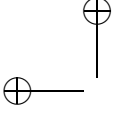
5.3.2 Output signal of balanced receiver

Using (4.45) and (5.37), the expected output signal of a balanced receiver r with path delay $T_{\text{Rx},r}$ can be written as

$$\begin{aligned}
\mathbb{E}[V_{\text{LP},r}(t)] &\approx -\frac{Z_{\text{TIA}}R_{\text{pd}}}{2L_{\text{Rx}}} \int_{-\infty}^{\infty} h_{\text{LP}}(t-\rho) \text{Re}\left\{R_{y^*y}(\rho - T_{\text{Rx},r}, \rho)\right\} d\rho \\
&\approx \frac{Z_{\text{TIA}}R_{\text{pd}}P_x}{L_{\text{Tx}}L_{\text{Rx}}L_{\text{nw}}} \int_{-\infty}^{\infty} h_{\text{LP}}(t-\rho) \\
&\quad \cdot \left\{ -(1-\kappa)^2 \exp\left(-\frac{\pi}{2} \left(\frac{T_{\text{Rx},r}}{\tau_c}\right)^2\right) \cos(2\pi f_c T_{\text{Rx},r}) \right. \\
&\quad + \frac{\kappa(1-\kappa)}{N} \sum_{i=1}^N \left[\exp\left(-\frac{\pi}{2} \left(\frac{T_{\text{Rx},r} - T_{\text{Tx},i}}{\tau_c}\right)^2\right) \right. \\
&\quad \quad \cdot \cos\left(2\pi f_c (T_{\text{Rx},r} - T_{\text{Tx},i}) + \phi_{\text{mod},i}(\rho)\right) \\
&\quad \quad + \exp\left(-\frac{\pi}{2} \left(\frac{T_{\text{Rx},r} + T_{\text{Tx},i}}{\tau_c}\right)^2\right) \\
&\quad \quad \left. \cdot \cos\left(2\pi f_c (T_{\text{Rx},r} + T_{\text{Tx},i}) - \phi_{\text{mod},i}(\rho)\right) \right] \\
&\quad + \frac{\kappa^2}{N^2} \sum_{i_1=1}^N \sum_{i_2=1}^N \exp\left(-\frac{\pi}{2} \left(\frac{T_{\text{Rx},r} + T_{\text{Tx},i_1} - T_{\text{Tx},i_2}}{\tau_c}\right)^2\right) \\
&\quad \quad \cdot \cos\left(2\pi f_c (T_{\text{Rx},r} + T_{\text{Tx},i_1} - T_{\text{Tx},i_2}) \right. \\
&\quad \quad \left. + \phi_{\text{mod},i_2}(\rho) - \phi_{\text{mod},i_1}(\rho)\right) \left. \right\} d\rho. \quad (5.38)
\end{aligned}$$

Since $T_{\text{Rx},r} \gg \tau_c$, this can be reduced to

$$\begin{aligned}
\mathbb{E}[V_{\text{LP},r}(t)] &\approx \frac{Z_{\text{TIA}}R_{\text{pd}}P_x}{L_{\text{Tx}}L_{\text{Rx}}L_{\text{nw}}} \int_{-\infty}^{\infty} h_{\text{LP}}(t-\rho) \\
&\quad \cdot \left[\frac{\kappa(1-\kappa)}{N} \sum_{i=1}^N \exp\left(-\frac{\pi}{2} \left(\frac{T_{\text{Rx},r} - T_{\text{Tx},i}}{\tau_c}\right)^2\right) \right. \\
&\quad \quad \cdot \cos\left(2\pi f_c (T_{\text{Rx},r} - T_{\text{Tx},i}) + \phi_{\text{mod},i}(\rho)\right) \\
&\quad + \frac{\kappa^2}{N^2} \sum_{i_1=1}^N \sum_{i_2=1}^N \exp\left(-\frac{\pi}{2} \left(\frac{T_{\text{Rx},r} + T_{\text{Tx},i_1} - T_{\text{Tx},i_2}}{\tau_c}\right)^2\right) \\
&\quad \left. \cdot \cos\left(2\pi f_c (T_{\text{Rx},r} + T_{\text{Tx},i_1} - T_{\text{Tx},i_2}) + \phi_{\text{mod},i_2}(\rho) - \phi_{\text{mod},i_1}(\rho)\right) \right] d\rho. \quad (5.39)
\end{aligned}$$



Obviously, out of these $N^2 + N$ terms, the only interesting term is the r -th term in the first sum. It can be selected by setting $T_{R_x,r} = T_{T_x,r}$. The other ones are suppressed when $|T_{R_x,r} - T_{T_x,i}| \gg \tau_c$ for $i \neq r$ and $|T_{R_x,r} + T_{T_x,i_1} - T_{T_x,i_2}| \gg \tau_c$ for any i, i_2 . The resulting expected output signal is then

$$E[V_{LP,r}(t)] \approx \frac{\kappa(1-\kappa)Z_{TIA}R_{pd}P_x}{N L_{T_x}L_{R_x}L_{nw}} \int_{-\infty}^{\infty} h_{LP}(t-\rho) \cos(\phi_{\text{mod},r}(\rho)) d\rho. \quad (5.40)$$

5.3.3 Choosing the path delays

From the conditions in the previous subsection it follows that

- each individual delay $T_{T_x,i}$ should be much larger than τ_c ;
- the difference between any two delays T_{T_x,i_1} and T_{T_x,i_2} with $i_1 \neq i_2$ should be much larger than τ_c ;
- the mutual difference between any delay T_{T_x,i_1} on one hand and the difference between any two delays T_{T_x,i_2} and T_{T_x,i_3} with $i_2 \neq i_3$ on the other hand should be much larger than τ_c .

A straightforward choice is to set $T_{T_x,1}$ such that $T_{T_x,1} \gg \tau_c$, and then choose the other delays as odd multiples of $T_{T_x,1}$, so that

$$T_{T_x,i} = (2i-1)T_{T_x,1}. \quad (5.41)$$

(Note that in that case, the difference between any two different path delays is an even multiple of $T_{T_x,1}$, so it is different from all the delays since all delays are odd multiples of $T_{T_x,1}$.)

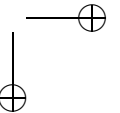
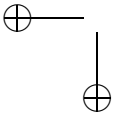
From (5.38) it follows that the crosstalk due to residual coherence is worst for receiver 1. Assuming that κ is chosen in the order of $\kappa \approx 1/2$ (we will see later that this is indeed the case), there is one crosstalk term with an

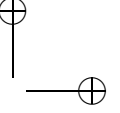
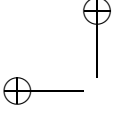
amplitude that is $N \exp\left(-\frac{\pi}{2} \left(\frac{T_{T_x,1}}{\tau_c}\right)^2\right)$ times smaller than the desired term,

and $3N - 3$ crosstalk terms that are $\frac{1}{N} \exp\left(-\frac{\pi}{2} \left(\frac{T_{T_x,1}}{\tau_c}\right)^2\right)$ times smaller than the desired term. Hence, the total crosstalk in each receiver is at least

$$-20 \log \left(\left(N + 3 - \frac{3}{N} \right) \exp \left(-\frac{\pi}{2} \left(\frac{T_{T_x,1}}{\tau_c} \right)^2 \right) \right) \text{ dB} \approx \\ 13.6 \left(\frac{T_{T_x,1}}{\tau_c} \right)^2 - 20 \log \left(N + 3 - \frac{3}{N} \right) \text{ dB} \quad (5.42)$$

below the desired signal.



**Example 5.5**

So when $T_{\text{Tx},1}$ is chosen as $T_{\text{Tx},1} = 2\tau_c$ (like in the previous chapter) and up to 16 channels are to be transmitted, one can show that the crosstalk is at least 29 dB below the desired signal. When $T_{\text{Tx},1} = 3\tau_c$, the crosstalk is at least 97 dB below the desired signal.

When we choose $T_{\text{Tx},1} = 3\tau_c$ to be on the safe side, and we consider light sources with a coherence time of 0.1 ps (like in Example 4.6) in a SIRL system with 16 channels and waveguides with an effective index N_{eff} in the order of 1.5, then the path delays are odd multiples of 0.3 ps. The minimum and maximum path length difference are given by

$$l_{\text{Tx},1} = \frac{c_0 T_{\text{Tx},1}}{N_{\text{eff}}} \approx 60 \text{ } \mu\text{m},$$

$$l_{\text{Tx},16} = (2 \cdot 16 - 1) l_{\text{Tx},1} \approx 1.9 \text{ mm}.$$

This can still easily be fabricated in planar waveguide technology. □

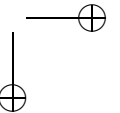
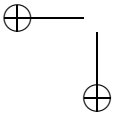
5.3.4 Noise performance

The autocorrelation function of the output signal follows from (5.8). Using (5.37) and applying phase-averaging, one can find

$$\text{E}[P_y(\rho)] \approx \text{E}[P_y(\rho - T_{\text{Rx},r})] \approx \frac{P_x}{L_{\text{Tx}} L_{\text{nw}}} \left[(1 - \kappa)^2 + \frac{\kappa^2}{N} \right], \quad (5.43)$$

$$\begin{aligned} R_{y^*y}(\rho_1, \rho_2) R_{y^*y}(\rho_2 - T_{\text{Rx},r}, \rho_1 - T_{\text{Rx},r}) \approx \\ \frac{1}{L_{\text{Tx}}^2 L_{\text{nw}}^2} \left\{ \left[(1 - \kappa)^4 + \frac{2(1 - \kappa)^2 \kappa^2}{N} \right] |R_{x^*x}(\rho_2 - \rho_1)|^2 \right. \\ \left. + \frac{\kappa^2 (1 - \kappa)^2}{N^2} \sum_{i=1}^N \left[|R_{x^*x}(\rho_2 - \rho_1 - T_{\text{Tx},i})|^2 \right. \right. \\ \left. \left. + |R_{x^*x}(\rho_2 - \rho_1 + T_{\text{Tx},i})|^2 \right] \right. \\ \left. + \frac{\kappa^4}{N^4} \sum_{i_1=1}^N \sum_{i_2=1}^N |R_{x^*x}(t_2 - t_1)|^2 \right. \\ \left. + \frac{\kappa^4}{N^4} \sum_{i_1=1}^N \sum_{\substack{i_2=1 \\ i_2 \neq i_1}}^N |R_{x^*x}(t_2 - t_1 + T_{\text{Tx},i_1} - T_{\text{Tx},i_2})|^2 \right\}, \quad (5.44) \end{aligned}$$

$$\begin{aligned} R_{y^*y}(\rho_1 - T_{\text{Rx},r}, \rho_2) R_{y^*y}(\rho_2 - T_{\text{Rx},r}, \rho_1) \approx \frac{\kappa^2 (1 - \kappa)^2}{N^2 L_{\text{Tx}}^2 L_{\text{nw}}^2} |R_{x^*x}(\rho_2 - \rho_1)|^2 \\ \cdot \exp\left(j 4\pi f_c (T_{\text{Rx},r} - T_{\text{Tx},r}) + j 2\phi_{\text{mod},r}(\rho_1) \right). \quad (5.45) \end{aligned}$$



Substituting these in (5.8) and using the approximation (4.51) again, we find

$$\begin{aligned}
R_{V_{LP,r}V_{LP,r}}(t_1, t_2) &\approx \mathbb{E}[V_{LP,r}(t_1)]\mathbb{E}[V_{LP,r}(t_2)] \\
&+ \frac{Z_{TIA}^2 R_{pd} P_x e}{L_{Tx} L_{Rx} L_{nw}} \left[(1 - \kappa)^2 + \frac{\kappa^2}{N} \right] \int_{-\infty}^{\infty} h_{LP}(t_1 - \rho) h_{LP}(t_2 - \rho) d\rho \\
&+ \frac{Z_{TIA}^2 R_{pd}^2 P_x^2 \tau_c}{2L_{Tx}^2 L_{Rx}^2 L_{nw}^2} \int_{-\infty}^{\infty} h_{LP}(t_1 - \rho) h_{LP}(t_2 - \rho) \\
&\quad \cdot \left[(1 - \kappa)^4 + \frac{4(1 - \kappa)^2 \kappa^2}{N} + \frac{\kappa^4 (2N - 1)}{N^3} \right. \\
&\quad \left. + \frac{(1 - \kappa)^2 \kappa^2}{N^2} \cos\left(4\pi f_c (T_{Rx,r} - T_{Tx,r}) + 2\phi_{\text{mod},r}(\rho)\right) \right] d\rho \\
&+ Z_{TIA}^2 S_{th} \int_{-\infty}^{\infty} h_{LP}(t_1 - \rho) h_{LP}(t_2 - \rho) d\rho. \tag{5.46}
\end{aligned}$$

5.3.5 Digital transmission using BPSK modulation

When BPSK modulation is applied as described in Subsection 4.7.1 (so with a rectangular symbol shape and matched filtering), the conditional expected values and variances of the detected samples in receiver r are given by

$$\begin{aligned}
\mathbb{E}[V_{LP,r}(kT_s) \mid A_{r,k} = 0] &= -\mathbb{E}[V_{LP,r}(kT_s) \mid A_{r,k} = 1] \\
&\approx \frac{\kappa(1 - \kappa)Z_{TIA}R_{pd}P_x}{NL_{Tx}L_{Rx}L_{nw}}, \tag{5.47} \\
\sigma_0^2 = \sigma_1^2 &\approx \frac{Z_{TIA}^2}{T_s} \left\{ \frac{R_{pd}P_x e}{L_{Tx}L_{Rx}L_{nw}} \left[(1 - \kappa)^2 + \frac{\kappa^2}{N} \right] \right. \\
&\quad \left. + \frac{R_{pd}^2 P_x^2 \tau_c}{2L_{Tx}^2 L_{Rx}^2 L_{nw}^2} \left[(1 - \kappa)^4 + \frac{(4N + 1)(1 - \kappa)^2 \kappa^2}{N^2} \right. \right. \\
&\quad \left. \left. + \frac{(2N - 1)\kappa^4}{N^3} \right] + S_{th} \right\}, \tag{5.48}
\end{aligned}$$

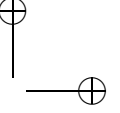
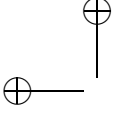
where $A_{r,k}$ is the k -th bit that is transmitted by transmitter r . As a result, the SNR per symbol can be written as

$$\gamma_{\text{BPSK}} \triangleq \frac{\mathbb{E}^2[V_{LP,r}(kT_s) \mid A_{r,k} = 0]}{2\sigma_0^2} = \left(\gamma_{\text{sn}}^{-1} + \gamma_{\text{bn}}^{-1} + \gamma_{\text{tn}}^{-1} \right)^{-1}, \tag{5.49}$$

where

$$\gamma_{\text{sn}} = \frac{\kappa^2(1 - \kappa)^2 R_{pd} P_x T_s}{2N[N(1 - \kappa)^2 + \kappa^2] L_{Tx} L_{Rx} L_{nw} e}, \tag{5.50}$$

$$\gamma_{\text{bn}} = \frac{N \kappa^2 (1 - \kappa)^2 T_s}{[N^3(1 - \kappa)^4 + (4N^2 + N)(1 - \kappa)^2 \kappa^2 + (2N - 1)\kappa^4] \tau_c}, \tag{5.51}$$



$$\gamma_{\text{tn}} = \frac{\kappa^2(1-\kappa)^2 R_{\text{pd}}^2 P_x^2 T_s}{2N^2 L_{\text{Tx}}^2 L_{\text{Rx}}^2 L_{\text{nw}}^2 S_{\text{th}}} . \quad (5.52)$$

Following the theory in Subsection 4.7.1, the bit error probability is given by

$$P_e \approx Q\left(\sqrt{2\gamma_{\text{BPSK}}}\right) . \quad (5.53)$$

The bit rate R_b that can be achieved per channel at $P_e = 10^{-9}$ (or $\gamma_{\text{BPSK}} \approx 18$, see Example 4.7) follows from the above equations as

$$\begin{aligned} R_b = \frac{1}{T_s} = & \frac{1}{18} N \kappa^2 (1-\kappa)^2 R_{\text{pd}}^2 P_x^2 \\ & \cdot \left\{ \left[N^3 (1-\kappa)^4 + (4N^2 + N)(1-\kappa)^2 \kappa^2 + (2N-1)\kappa^4 \right] R_{\text{pd}}^2 P_x^2 \tau_c \right. \\ & + 2N^2 \left[N(1-\kappa)^2 + \kappa^2 \right] R_{\text{pd}} P_x L_{\text{Tx}} L_{\text{Rx}} L_{\text{nw}} e \\ & \left. + 2N^3 L_{\text{Tx}}^2 L_{\text{Rx}}^2 L_{\text{nw}}^2 S_{\text{th}} \right\}^{-1} . \end{aligned} \quad (5.54)$$

Obviously, the performance of the SIRL system depends on the coupling coefficient κ , which determines the ratio between the reference carrier and the modulated carriers. The performance is optimized by optimizing (5.49) with respect to κ . In general this cannot be performed analytically.

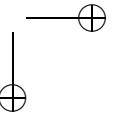
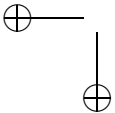
Example 5.6

Now consider a numerical example of a SIRL system for N CM channels. (Since the SIRL system has a common optical source for all the channels, the performance of the system does not depend on the number of active channels.) Hence, the splitter in the network has an intrinsic splitting loss that equals the number of receivers N . When an excess loss of 0.1 dB is assumed, we have $L_{\text{nw}} \approx 1.023N$. The remaining parameters are assumed to have the same values as in Example 5.2.

The bit rate R_b that can be achieved per channel at $P_e = 10^{-9}$ has been plotted as a function of the number of channels N in Figure 5.8(a), where for each value of N , the maximum bit rate is numerically optimized with respect to the coupling coefficient κ . In the same figure, the maximum bit rates are plotted for the case that $\kappa = 1/2$. In Figure 5.8(b), the optimum value of κ has been plotted as a function of the number of channels.

Obviously, the maximum bit rates that can be achieved with this SIRL system are significantly enhanced by setting κ to its optimum value rather than simply choosing $\kappa = 1/2$, especially for large values of N . The optimum value of the coupling coefficient κ increases when the number of channels N increases.

In Figure 5.8(c), the corresponding SNRs are plotted as a function of N for $\kappa = \kappa_{\text{opt}}$. Obviously, the performance is still mainly limited by beat noise,



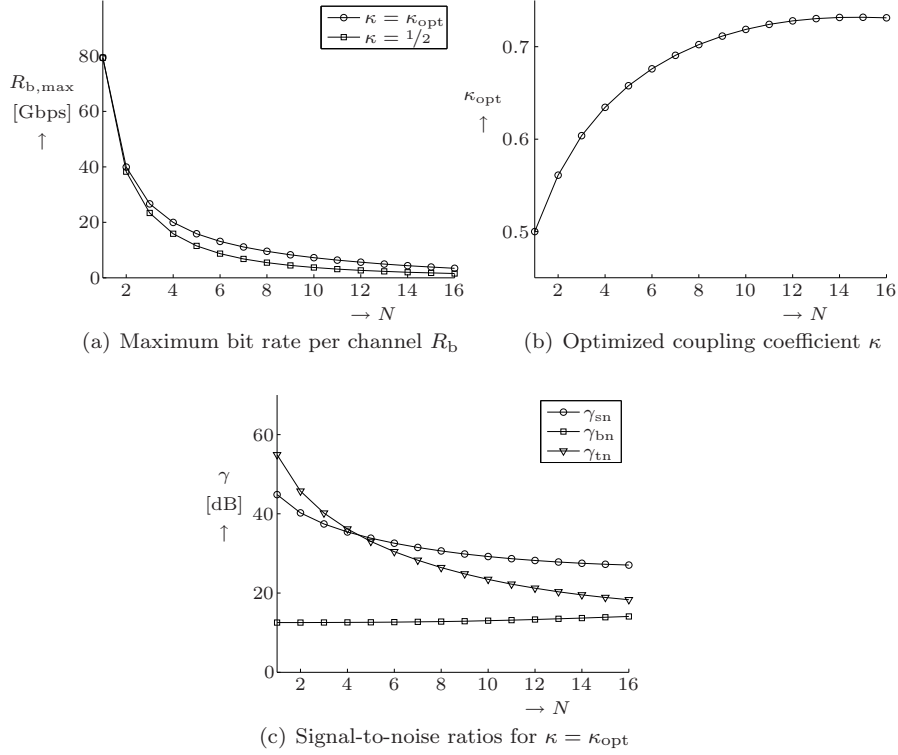


Figure 5.8: Maximum bit rate per channel R_b , optimized coupling coefficient κ and corresponding signal-to-noise ratios as a function of number of channels N in a SIRL system with BPSK modulation

like in Example 5.2. Note that for $N = 1$, the values are the same as in in Example 4.7 and 5.2.

A simulation has been run of a corresponding 2-channel SIRL system in which bit patterns '01001101' and '00110100' are transmitted at 40 Gbps. The corresponding modulating signals are shown in Figure 5.9(a) and 5.9(c). The path delay differences in the transmitters and receivers are chosen as $T_{\text{Rx},1} = T_{\text{Tx},1} = 0.5$ ps and $T_{\text{Rx},2} = T_{\text{Tx},2} = 1.5$ ps, and the coupling coefficients are set to $\kappa = 1/2$. The resulting output signals are shown in Figure 5.9(b) and 5.9(d), where the circles denote the decision samples and the dashed lines represent the theoretical expected values.

Obviously, the output signal of receiver 1 corresponds to the modulating signal in transmitter 1 and the output signal of receiver 2 corresponds to the modulating signal in transmitter 2: there is no visible crosstalk. □

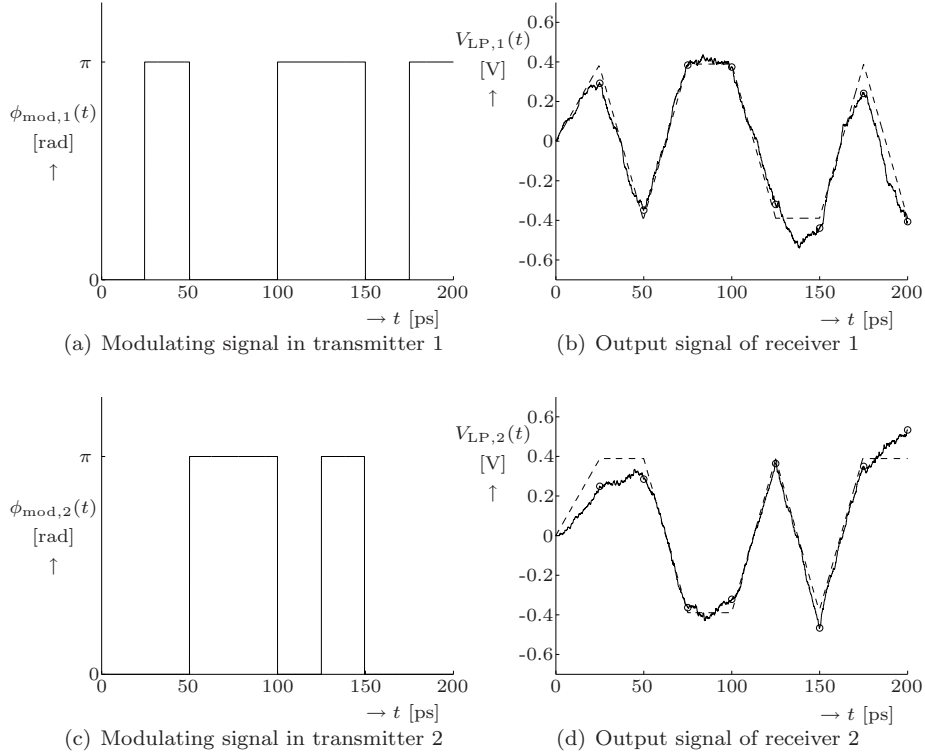
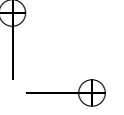
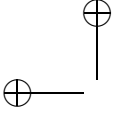


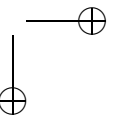
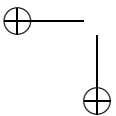
Figure 5.9: Simulation results for a 2-channel SIRL system using BPSK modulation when bit patterns '01001101' and '00110100' are transmitted at 40 Gbps

The great advantage of the SIRL system with respect to the PA is that it can result in a significantly higher signal-to-beat noise ratio. In cases where beat noise determines the performance of the system, we have $\gamma_{\text{BPSK}} \approx \gamma_{\text{bn}}$ so that the performance can be analytically optimized by optimizing (5.51) with respect to κ , resulting in

$$\kappa_{\text{opt}} = \frac{N}{N + \sqrt{4N^2 - N}} \quad (5.55)$$

$$\gamma_{\text{bn,max}} = \frac{T_s}{(4N + 1 + 2\sqrt{4N^2 - N}) \tau_c} \quad (5.56)$$

Comparing this to (5.21), it is obvious that the signal-to-beat noise ratio of the optimized SIRL system is superior to the signal-to-beat noise ratio of the PA, especially for large numbers of channels N . This explains why the maximum bit rates in Example 5.6 were so much higher than the ones in Example 5.2.



5.4 The discontinuous series (DS) system

5.4.1 Multiplexed signal

The discontinuous series (DS) system also has a common source, and is constructed by serially cascading two-arm coherence modulators, as illustrated in Figure 5.10.

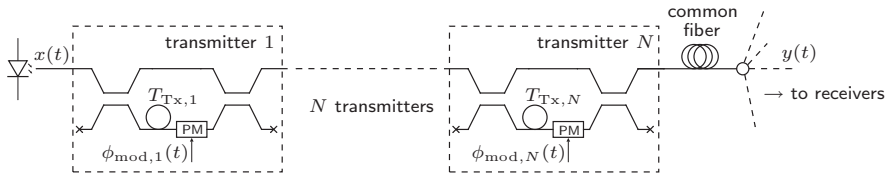


Figure 5.10: Discontinuous series (DS) system

Only PM is applied. Each receiver receives a signal that can be written as:

$$\begin{aligned}
 y(t) = & \frac{1}{2^N \sqrt{L_{Tx}^N L_{nw}}} \sum_{i_1=0}^1 \cdots \sum_{i_N=0}^1 x \left(t - \sum_{k=1}^N i_k T_{Tx,k} \right) \\
 & \cdot \exp \left\{ j i_1 \left[\pi + \phi_{\text{mod},1} \left(t - \sum_{k=2}^N i_k T_{Tx,k} \right) \right] \right. \\
 & \quad + j i_2 \left[\pi + \phi_{\text{mod},2} \left(t - \sum_{k=3}^N i_k T_{Tx,k} \right) \right] \\
 & \quad \left. + \dots + j i_N \left[\pi + \phi_{\text{mod},N}(t) \right] \right\}. \quad (5.57)
 \end{aligned}$$

Note that—in case the coherence modulators are connected by fibers—the optical circuits need to be polarization independent, unless polarization maintaining fiber (PMF) is used. Otherwise, the coherence modulators need to be integrated on a single optical chip.

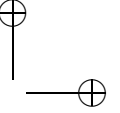
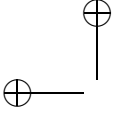
The autocorrelation function of $y(t)$ is given by

$$\begin{aligned}
R_{y^*y}(t_1, t_2) &\triangleq \mathbb{E}[y^*(t_1)y(t_2)] \\
&\approx \frac{1}{4^N L_{\text{Tx}}^N L_{\text{nw}}} \sum_{i_1=0}^1 \cdots \sum_{i_N=0}^1 \sum_{j_1=0}^1 \cdots \sum_{j_N=0}^1 R_{x^*x} \left(t_2 - t_1 + \sum_{k=1}^N (i_k - j_k) T_{\text{Tx},k} \right) \\
&\quad \cdot \exp \left\{ -j i_1 \left[\pi + \phi_{\text{mod},1} \left(t_1 - \sum_{k=2}^N i_k T_{\text{Tx},k} \right) \right] \right. \\
&\quad \quad + j j_1 \left[\pi + \phi_{\text{mod},1} \left(t_2 - \sum_{k=2}^N j_k T_{\text{Tx},k} \right) \right] \\
&\quad \quad - j i_2 \left[\pi + \phi_{\text{mod},2} \left(t_1 - \sum_{k=3}^N i_k T_{\text{Tx},k} \right) \right] \\
&\quad \quad + j j_2 \left[\pi + \phi_{\text{mod},2} \left(t_2 - \sum_{k=3}^N j_k T_{\text{Tx},k} \right) \right] \\
&\quad \quad \left. + \dots - j i_N \left[\pi + \phi_{\text{mod},N}(t_1) \right] - j j_N \left[\pi + \phi_{\text{mod},N}(t_2) \right] \right\}. \quad (5.58)
\end{aligned}$$

5.4.2 Output signal of balanced receiver

Using (4.45) and (5.58), the expected output signal of a balanced receiver r with path delay $T_{\text{Rx},r}$ can be written as

$$\begin{aligned}
\mathbb{E}[V_{\text{LP},r}(t)] &\approx -\frac{Z_{\text{TIA}} R_{\text{pd}}}{2L_{\text{Rx}}} \int_{-\infty}^{\infty} h_{\text{LP}}(t - \rho) \text{Re} \left\{ R_{y^*y}(\rho - T_{\text{Rx},r}, \rho) \right\} d\rho \\
&\approx -\frac{Z_{\text{TIA}} R_{\text{pd}} P_x}{4^N L_{\text{Tx}}^N L_{\text{Rx}} L_{\text{nw}}} \\
&\quad \cdot \sum_{i_1=0}^1 \cdots \sum_{i_N=0}^1 \sum_{j_1=0}^1 \cdots \sum_{j_N=0}^1 \exp \left(-\frac{\pi}{2\tau_c^2} \left(T_{\text{Rx},r} + \sum_{k=1}^N (i_k - j_k) T_{\text{Tx},k} \right)^2 \right) \\
&\quad \cdot \int_{-\infty}^{\infty} h_{\text{LP}}(t - \rho) \cos \left[(i_1 - j_1 + i_2 - j_2 + \dots + i_N - j_N) \pi \right. \\
&\quad \quad + i_1 \phi_{\text{mod},1} \left(\rho - T_{\text{Rx},r} - \sum_{k=2}^N i_k T_{\text{Tx},k} \right) - j_1 \phi_{\text{mod},1} \left(\rho - \sum_{k=2}^N j_k T_{\text{Tx},k} \right) \\
&\quad \quad + i_2 \phi_{\text{mod},2} \left(\rho - T_{\text{Rx},r} - \sum_{k=3}^N i_k T_{\text{Tx},k} \right) - j_2 \phi_{\text{mod},2} \left(\rho - \sum_{k=3}^N j_k T_{\text{Tx},k} \right) \\
&\quad \quad \left. + \dots + i_N \phi_{\text{mod},N}(\rho - T_{\text{Rx},r}) - j_N \phi_{\text{mod},N}(\rho) \right] d\rho. \quad (5.59)
\end{aligned}$$



Now the delays need to be chosen such that —for each value of r — $\phi_{\text{mod},r}(t)$ is the only modulating signal that becomes observable in this expected output signal. For the DS system this is actually a far more complicated problem than for the PA and SIRL system. By carefully inspecting (5.59), one can derive that the following two conditions have to be satisfied:

- The relations between the delays should be chosen such that the value of $\left| T_{\text{Rx},r} + \sum_{k=1}^N (i_k - j_k) T_{\text{Tx},k} \right|$
 - is much smaller than τ_c if and only if $i_k = j_k$ for all $k \neq r$, $i_r = 0$ and $j_r = 1$. (This can simply be done by setting $T_{\text{Rx},r} = T_{\text{Tx},r}$);
 - is much larger than τ_c in all other cases.
- The actual sizes of the delays should be much smaller than the inverse bandwidth of the modulating signal, such that for example the last two terms in the cosine in (5.59) indeed cancel each other when $i_N = j_N$.

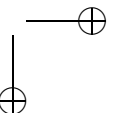
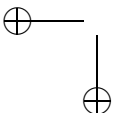
If the first condition is not satisfied, crosstalk will occur in a similar way as described for the PA and SIRL system. If the second condition is not satisfied, crosstalk will occur due to the fact that terms that are supposed to cancel each other, are slightly shifted in time with respect to each other.

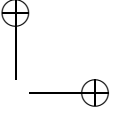
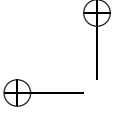
When the conditions are satisfied (we will come back to this in the next subsection), however, we can write (5.59) as

$$\begin{aligned} \mathbb{E}[V_{\text{LP},r}(t)] \approx & \frac{Z_{\text{TIA}} R_{\text{pd}} P_x}{4^N L_{\text{Tx}}^N L_{\text{Rx}} L_{\text{nw}}} \sum_{i_1=0}^1 \cdots \sum_{i_{r-1}=0}^1 \sum_{i_{r+1}=0}^1 \cdots \sum_{i_N=0}^1 \int_{-\infty}^{\infty} h_{\text{LP}}(t - \rho) \\ & \cdot \cos \left[\phi_{\text{mod},r} \left(\rho - \sum_{k=r+1}^N i_k T_{\text{Tx},k} \right) \right] d\rho. \quad (5.60) \end{aligned}$$

This actually reveals a disadvantage of the DS system: the output signal does not simply contain just one term —like is the case for the PA and SIRL system— but rather 2^{N-1} terms, which can be reduced to 2^{N-r} terms that are time-shifted with respect to each other. This generally results in a distortion of the output signal.

This phenomena can also be explained by means of Figure 5.10. Consider the light wave that travels the upper path in all the coherence modulators, and the light wave that travels the upper path in all coherence modulators except the r -th one, where it travels the lower path. Together they form a pair with a mutual path delay of $T_{\text{Tx},r}$; hence receiver r converts this pair in a contribution to the output signal in which $\phi_{\text{mod},r}(t)$ appears. (This corresponds to the first term in (5.60).) Then consider the light wave that travels the lower path in all coherence modulators, and the light wave that travels the lower path in all coherence modulators except the r -th one, where it travels the upper path.





Together they form a pair that also has an internal delay of $T_{\text{Tx},r}$, but it is delayed with respect to the other pair. Hence, this pair is also converted in a contribution to the output signal (it actually corresponds to the last term in (5.60)), but it is delayed with respect to the first contribution. Note that the amount of time shift only depends on the difference in delay that is encountered *after* modulation. The maximum time shift between these contribution occurs in receiver 1 and is given by

$$\Delta T_{\max} = \sum_{k=2}^N T_{\text{Tx},k}. \quad (5.61)$$

Hence, the distortion can only be neglected when this value is much smaller than the inverse of the bandwidth of the modulating signals. (Note that this implies that the largest delay value should actually be assigned to $T_{\text{Tx},1}$.) In that case, the expected output signal can be simplified to

$$E[V_{\text{LP},r}(t)] \approx \frac{Z_{\text{TIA}} R_{\text{pd}} P_x}{2^{N+1} L_{\text{Tx}}^N L_{\text{Rx}} L_{\text{nw}}} \int_{-\infty}^{\infty} h_{\text{LP}}(t - \rho) \cos(\phi_{\text{mod},r}(\rho)) d\rho. \quad (5.62)$$

5.4.3 Choosing the path delays

As already mentioned in the previous section, the problem of choosing the suitable delay values for the DS system is far from straightforward. First a suitable value for $T_{\text{Tx},1}$ should be chosen based on crosstalk considerations. Without going into detail about this, we will for convenience assume that it suffices to set $T_{\text{Tx},1} = 3\tau_c$, like we found for the PA and SIRL system.

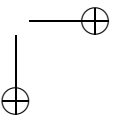
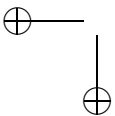
Then the other delays can be chosen as suitable integer multiples of $T_{\text{Tx},1}$, in such a way that the conditions mentioned in the previous subsection are met. This is actually a purely mathematical problem, which has been studied by Bløtekjær et al. [67]. They designed procedures for choosing the path delays based on different criteria like minimizing the value of the largest delay, minimizing the sum of all the delays and minimizing the ratio between minimum and maximum delay. Here we will consider the solution for the minimum sum of the delays, since this will actually result in the minimum distortion. This prescribes the delays to be chosen according to the following recursive equation [67]

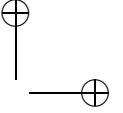
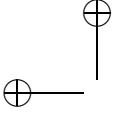
$$T_{\text{Tx},i} = T_{\text{Tx},i-1} + T_{\text{Tx},1} + \sum_{k=1}^{i-1} T_{\text{Tx},k}, \quad (5.63)$$

or in closed form

$$T_{\text{Tx},i} = \frac{T_{\text{Tx},1}}{\sqrt{5}} \left[\left(\frac{3 + \sqrt{5}}{2} \right)^i - \left(\frac{3 - \sqrt{5}}{2} \right)^i \right] \approx 0.447 \cdot 2.62^i T_{\text{Tx},1}, \quad (5.64)$$

where $i > 1$.





Another advantage of this solution with respect to the other solutions that were proposed in [67] is that the individual delays do not depend on the total number of channels N , so that an existing DS system with minimal sum of the delays can be extended by one coherence modulator without changing the values of the present coherence modulators, whilst still keeping the sum of the delays minimal.

The values for the first 16 delays are given in Table 5.1 where they are compared to the values that can be used for the PA and SIRL system.

Table 5.1: Required delay values for the parallel array (PA) single intrinsic reference ladder (SIRL) system and discontinuous series (DS) system

i	$T_{Tx,i}/T_{Tx,1}$			i	$T_{Tx,i}/T_{Tx,1}$		
	PA	SIRL	DS		PA	SIRL	DS
1	1	1	1	9	9	17	2584
2	2	3	3	10	10	19	6765
3	3	5	8	11	11	21	17711
4	4	7	21	12	12	23	46368
5	5	9	55	13	13	25	121393
6	6	11	144	14	14	27	317811
7	7	13	377	15	15	29	832040
8	8	15	987	16	16	31	2178309

Obviously, the required delay values increase very rapidly (exponentially) with increasing number of channels N .

Example 5.7

When we choose $T_{Tx,1} = 3\tau_c$, and we consider light sources with a coherence time of 0.1 ps (like in Example 4.6) in a DS system with 16 transmitters and waveguides with an effective index N_{eff} in the order of 1.5, then the path delays are multiples of 0.3 ps, chosen according to Table 5.1. The minimum and maximum path length difference are given by

$$l_{Tx,1} = \frac{c_0 T_{Tx,1}}{N_{\text{eff}}} \approx 60 \mu\text{m},$$

$$l_{Tx,16} = 2178309 l_{Tx,1} \approx 131 \text{ m}.$$

Obviously, the last one is not a practical value for being realized on an optical integrated circuit. If the path length differences are to be kept below a bound of say 1 cm, then it follows from Table 5.1 that at most 6 channels can be supported by the DS system.

Now consider the distortion in the output signal. As mentioned in the previous subsection, it can be minimized by assigning the largest delay value to $T_{Tx,1}$. In that case, the maximum delay spread in the output signal follows from (5.61) and is given in Table 5.2 as a function of the number of channels N .

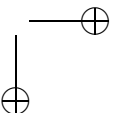
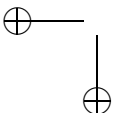


Table 5.2: Maximum delay spread in the output signal of the DS system

i	ΔT_{\max}
1	0 ps
2	0.3 ps
3	1.2 ps
4	3.6 ps
5	9.9 ps
6	26.4 ps



5.4.4 Noise performance

For convenience, it will be assumed that only a few users are supported, so that the maximum delay spread can be kept much smaller than the inverse bandwidth of the modulating signals. Hence, we can simplify $R_{y^*y}(t_1, t_2)$ in (5.58) to

$$R_{y^*y}(t_1, t_2) \approx \frac{1}{4^N L_{\text{Tx}}^N L_{\text{nw}}} \sum_{i_1=0}^1 \cdots \sum_{i_N=0}^1 \sum_{j_1=0}^1 \cdots \sum_{j_N=0}^1 R_{x^*x} \left(t_2 - t_1 + \sum_{k=1}^N (i_k - j_k) T_{\text{Tx},k} \right) \cdot \exp \left[-j \sum_{k=1}^N (i_k - j_k) (\pi + \phi_{\text{mod},k}(t_1)) \right]. \quad (5.65)$$

Now the autocorrelation function of the output signal follows from (5.8). Using (5.65) and applying phase-averaging, one can find

$$\begin{aligned} E[P_y(\rho)] &\approx E[P_y(\rho - T_{\text{Rx},r})] \approx \frac{P_x}{2^N L_{\text{Tx}}^N L_{\text{nw}}}, \quad (5.66) \\ R_{y^*y}(\rho_1, \rho_2) R_{y^*y}(\rho_2 - T_{\text{Rx},r}, \rho_1 - T_{\text{Rx},r}) &\approx \frac{1}{8^N L_{\text{Tx}}^{2N} L_{\text{nw}}^2} \\ &\cdot \sum_{i_1=0}^1 \cdots \sum_{i_N=0}^1 \sum_{j_1=0}^1 \cdots \sum_{j_N=0}^1 \frac{\left| R_{x^*x} \left(\rho_2 - \rho_1 + \sum_{k=1}^N (i_k - j_k) T_{\text{Tx},k} \right) \right|^2}{2^{\left[\sum_{k=1}^N |i_k - j_k| \right]}}, \quad (5.67) \end{aligned}$$

$$\begin{aligned} R_{y^*y}(\rho_1 - T_{\text{Rx},r}, \rho_2) R_{y^*y}(\rho_2 - T_{\text{Rx},r}, \rho_1) &\approx \frac{1}{4^{N+1} L_{\text{Tx}}^{2N} L_{\text{nw}}^2} |R_{x^*x}(\rho_2 - \rho_1)|^2 \\ &\cdot \exp \left(j 4\pi f_c (T_{\text{Rx},r} - T_{\text{Tx},r}) + j 2\phi_{\text{mod},r}(\rho_1) \right). \quad (5.68) \end{aligned}$$

Substituting these in (5.8) and using the approximation (4.51) again, we find

$$\begin{aligned}
R_{V_{LP,r}V_{LP,r}}(t_1, t_2) &\approx \mathbb{E}[V_{LP,r}(t_1)]\mathbb{E}[V_{LP,r}(t_2)] \\
&+ \frac{Z_{TIA}^2 R_{pd} P_x e}{2^N L_{Tx}^N L_{Rx} L_{nw}} \int_{-\infty}^{\infty} h_{LP}(t_1 - \rho) h_{LP}(t_2 - \rho) d\rho \\
&+ \frac{Z_{TIA}^2 R_{pd}^2 P_x^2 \tau_c}{2^{2N+3} L_{Tx}^{2N} L_{Rx}^2 L_{nw}^2} \int_{-\infty}^{\infty} h_{LP}(t_1 - \rho) h_{LP}(t_2 - \rho) \\
&\quad \cdot \left[4 \left(\frac{3}{2}\right)^N + \cos\left(4\pi f_c (T_{Rx,r} - T_{Tx,r}) + 2\phi_{mod,r}(\rho)\right) \right] d\rho \\
&+ Z_{TIA}^2 S_{th} \int_{-\infty}^{\infty} h_{LP}(t_1 - \rho) h_{LP}(t_2 - \rho) d\rho. \tag{5.69}
\end{aligned}$$

5.4.5 Digital transmission using BPSK modulation

When BPSK modulation is applied as described in Subsection 4.7.1 (so with a rectangular symbol shape and matched filtering), the conditional expected values and variances of the detected samples in receiver r are given by

$$\begin{aligned}
\mathbb{E}[V_{LP,r}(kT_s) \mid A_{r,k} = 0] &= -\mathbb{E}[V_{LP,r}(kT_s) \mid A_{r,k} = 1] \\
&\approx \frac{Z_{TIA} R_{pd} P_x}{2^{N+1} L_{Tx}^N L_{Rx} L_{nw}}, \tag{5.70}
\end{aligned}$$

$$\begin{aligned}
\sigma_0^2 = \sigma_1^2 &\approx \frac{Z_{TIA}^2}{T_s} \left\{ \frac{R_{pd} P_x e}{2^N L_{Tx}^N L_{Rx} L_{nw}} \right. \\
&\quad \left. + \frac{R_{pd}^2 P_x^2 \tau_c}{2^{2N+3} L_{Tx}^{2N} L_{Rx}^2 L_{nw}^2} \left[4 \left(\frac{3}{2}\right)^N + 1 \right] + S_{th} \right\}, \tag{5.71}
\end{aligned}$$

where $A_{r,k}$ is the k -th bit that is transmitted by transmitter r . As a result, the SNR per symbol can be written as

$$\gamma_{BPSK} \triangleq \frac{\mathbb{E}^2[V_{LP,r}(kT_s) \mid A_{r,k} = 0]}{2\sigma_0^2} = \left(\gamma_{sn}^{-1} + \gamma_{bn}^{-1} + \gamma_{tn}^{-1} \right)^{-1}, \tag{5.72}$$

where

$$\gamma_{sn} = \frac{R_{pd} P_x T_s}{2^{N+3} L_{Tx}^N L_{Rx} L_{nw} e}, \tag{5.73}$$

$$\gamma_{bn} = \frac{T_s}{\left[4 \left(\frac{3}{2}\right)^N + 1 \right] \tau_c}, \tag{5.74}$$

$$\gamma_{tn} = \frac{R_{pd}^2 P_x^2 T_s}{2^{2N+3} L_{Tx}^{2N} L_{Rx}^2 L_{nw}^2 S_{th}}. \tag{5.75}$$

Following the theory in Subsection 4.7.1, the bit error probability is given by

$$P_e \approx Q\left(\sqrt{2\gamma_{BPSK}}\right). \tag{5.76}$$

The bit rate R_b that can be achieved per channel at $P_e = 10^{-9}$ (or $\gamma_{\text{BPSK}} \approx 18$, see Example 4.7) follows from the above equations as

$$R_b = \frac{1}{T_s} = \frac{1}{18} R_{\text{pd}}^2 P_x^2 \left\{ \left[4 \left(\frac{3}{2} \right)^N + 1 \right] R_{\text{pd}}^2 P_x^2 \tau_c + 2^{N+3} R_{\text{pd}} P_x L_{\text{Tx}}^N L_{\text{Rx}} L_{\text{nw}} e + 2^{2N+3} L_{\text{Tx}}^{2N} L_{\text{Rx}}^2 L_{\text{nw}}^2 S_{\text{th}} \right\}^{-1}. \quad (5.77)$$

Obviously, the performance of the DS system degrades rapidly with increasing number of channels N .

Example 5.8

Now consider a numerical example of a DS system for N channels. (Since the DS system has a common optical source for all the channels, the performance of the system does not depend on the number of active channels.) All parameters are assumed to have the same values as in Example 5.6. Hence, it follows from Example 5.7 that the number of channels is limited to 6, due to the restricted delay values that can be fabricated.

The bit rate R_b that can be achieved per channel at $P_e = 10^{-9}$ has been plotted as a function of the number of channels N in Figure 5.11(a).

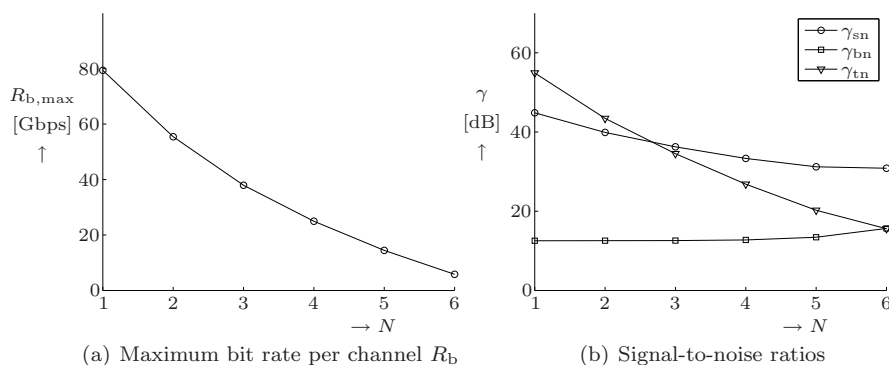


Figure 5.11: Maximum bit rate per channel R_b and corresponding signal-to-noise ratios as a function of number of channels N in a DS system with BPSK modulation

Note that these maximum bit rates have been derived assuming that the distortion due to delay spread in the output signal could be neglected. From Table 5.2 it follows, however, that although the bit times corresponding to the bit rates in Figure 5.11(a) are larger than the delay spreads in Table 5.2, the delay spread is not negligible. Hence, some intersymbol interference (ISI) will occur, so that the bit rates that can be achieved in practice are a bit smaller than the ones that are given in Figure 5.11(a). This will not be considered in further detail.

In Figure 5.11(b), the corresponding SNRs are plotted as a function of N . Obviously, the performance is mainly limited by beat noise for $N < 6$; thermal noise becomes significant only when $N = 6$. Note that for $N = 1$, the values are the same as in in Example 4.7.

A simulation has been run of a corresponding 2-channel DS system in which bit patterns '01001101' and '00110100' are transmitted at 50 Gbps. The corresponding modulating signals are shown in Figure 5.12(a) and 5.12(c). The path delay differences in the transmitters and receivers are chosen as $T_{R_{x,1}} = T_{T_{x,1}} = 0.5$ ps and $T_{R_{x,2}} = T_{T_{x,2}} = 10$ ps. $T_{T_{x,2}}$ has deliberately been chosen in the same order of magnitude as the symbol time T_s (20 ps) in order to illustrate the distortion effect. The resulting output signals are shown in Figure 5.12(b) and 5.12(d), where the circles denote the decision samples, the dashed lines represent the theoretical expected values and the dotted line are the theoretical expected values that would have applied in case $T_{T_{x,2}}$ had been much smaller than T_s .

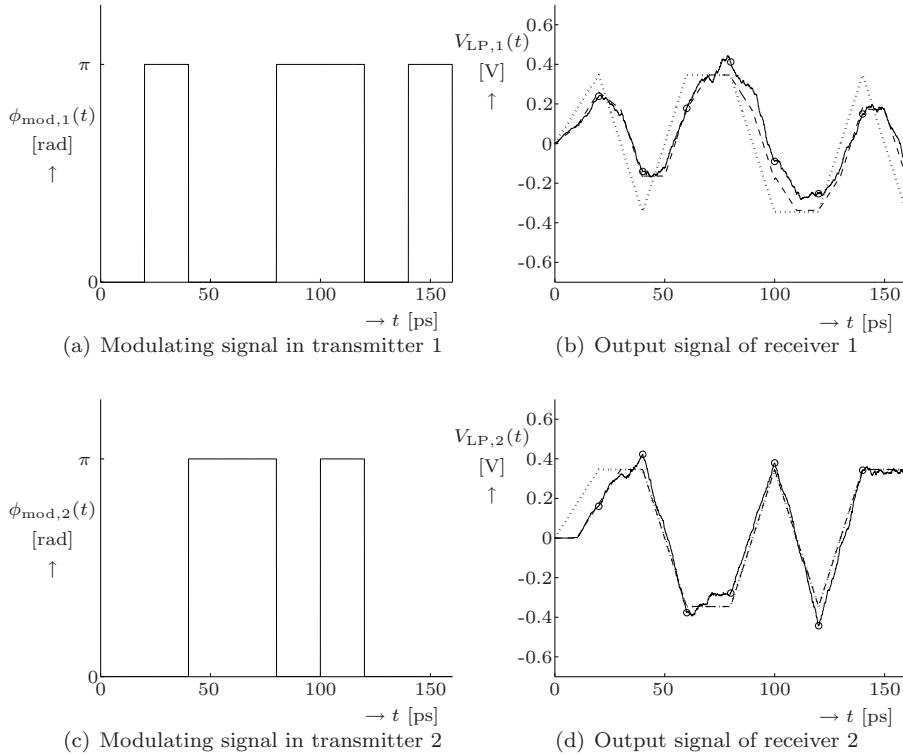
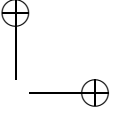
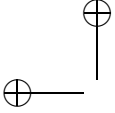


Figure 5.12: Simulation results for a 2-channel DS system using BPSK modulation when bit patterns '01001101' and '00110100' are transmitted at 50 Gbps



Obviously, the output signal of receiver 1 corresponds to the modulating signal in transmitter 1 and the output signal of receiver 2 corresponds to the modulating signal in transmitter 2. In both cases, an initial transient occurs due to the fact that the source is only turned on at $t = 0$, which is observable in this case due to the relatively large value of $T_{T_x,2}$. The output signal of receiver 2 remains undistorted after the initial transient, but the output signal of receiver 1 is significantly distorted due to the relatively large value of $T_{T_x,2}$.



5.5 Comparison

In the previous three sections three different system topologies for performing CM have been explained. Moreover their noise performances have been analyzed. In this section these three alternatives will be compared with respect to both the theoretical noise performance as well as some practical aspects.

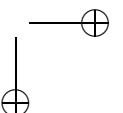
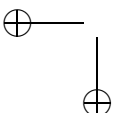
5.5.1 Modulation formats

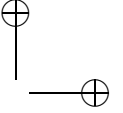
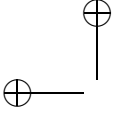
The PA has the most possibilities as far as modulation formats are concerned. Either phase modulation (PM) or intensity modulation (IM) can be performed, the latter either by direct or external modulation. Direct modulation implies that the emitted intensity of the source is modulated by directly modulating the source current. This has the advantage of not requiring any additional optical components for performing the modulation, and it has the disadvantage that—especially in case of broadband sources—the modulation bandwidths are limited to values in the order of a few hundred MHz [49]. The alternative is to apply external modulation. This can be performed by inserting an intensity modulator in either of the following three positions:

- between the source and the MZI;
- in one of the MZI arms;
- between the MZI and the transmission fiber.

There are two reasons why the second option might not be very desirable:

- When only the light through one of the MZI arms is modulated, the coherence modulator will always contribute to beat noise in the receiver, no matter whether a binary one or binary zero is transmitted. Hence, the resulting average bit error rate will be higher than in the case where the light through both MZI arms is modulated;
- When the modulator and the MZI are realized in different technologies, integrating the two functions into one device might be more complicated than realizing them separately and cascading them. (A successful integration in one technology would be the least expensive solution, however.)





The other two options result in approximately the same output signal, provided that the path delay of the MZI is much smaller than the inverse bandwidth of the modulating signal $m_{\text{mod}}(t)$. (Otherwise, the output signal in case of the third option would be proportional to $\sqrt{m_{\text{mod}}(t)m_{\text{mod}}(t - T_{\text{Tx}})}$ rather than $m_{\text{mod}}(t)$, resulting in some distortion.)

Although the SIRL system has only been considered for PM, it is actually possible to use IM. This can however only be performed by external modulation, by putting intensity modulators in the lower N waveguides of the MZI. The reason for this is the fact that the reference light wave is shared by all the channels, so modulating it would modulate all the channels simultaneously.


The DS system can only be used when PM is applied, since all the light wave paths go through all the coherence modulators, so modulating the intensity in one coherence modulator would modulate all the channels simultaneously.

5.5.2 Noise performance

The three multiplexing topologies can be compared with respect to noise performance by considering the equations for the SNRs (for BPSK modulation) in the preceding three sections. It should be noted that the losses in the network L_{nw} are larger for the PA than for the SIRL system and DS system. Obviously, the relation between the performances of the different systems depends on the parameter values, especially on the number of the channels N . The performance of the DS system, for example, degrades very rapidly with increasing number of channels N , whereas the performance of the SIRL system degrades much slower with increasing N . Moreover, the DS system suffers from an inherent distortion, as described in Subsection 5.4.2.

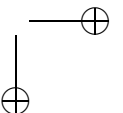
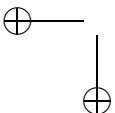
Example 5.9

An easy comparison is made by considering the examples that were discussed in the previous three sections. In Figure 5.13 the results for BPSK modulation are combined in one graph. It shows the maximum bit rate that can be achieved at a bit error rate of 10^{-9} for the PA, SIRL system and DS system. In case of the SIRL system, the coupling coefficient κ has been optimized for each value of N .

Obviously, the DS system performs best for low number of channels N ($N < 5$ in this case), whereas the SIRL system performs best for large number of channels N ($N \geq 5$ in this case). The SIRL system always performs better than the PA. In this particular example, all presented systems are mainly limited by beat noise. 

5.5.3 Flexibility

A drawback of the SIRL system is that the transmitters need to be localized on a single optical chip, so that it can only be applied in network structures where the channels that are to be multiplexed are available in a single node.



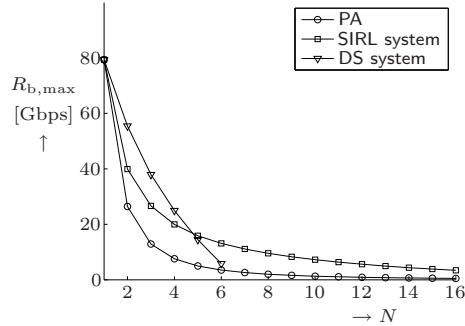
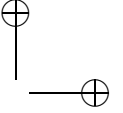
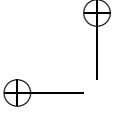


Figure 5.13: Maximum bit rate per channel R_b as a function of number of channels N in a PA, SIRL system and DS system with BPSK modulation

In a passive optical network (PON), for example, the SIRL system can only be used for the downstream channels and not for the upstream.

The PA and DS system provide more flexibility in locating the transmitters, since they are realized in distinct coherence modulators. The PA can be used in a star topology and the DS system is restricted to a bus topology.

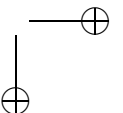
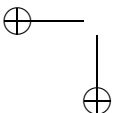
Adding channels is not equally difficult for each alternative. For the DS system for example, adding a channel simply requires breaking the connection somewhere in the series connection of the coherence modulators, and then inserting another coherence modulator. In case of the PA, coherence modulators and demodulators can be added as long as the splitters and combiners in the network provide enough ports. For the SIRL system, adding channels involves replacing the entire chip.

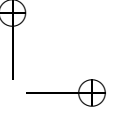
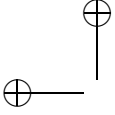
The PA is also most flexible in the sense that channels can be easily switched off, hence reducing the amount of beat noise in the receivers and creating an opportunity to increase the bit rates of the remaining channels.

Capacity could be allocated non-uniformly by increasing the transmitted powers of a node that is supposed to transmit at a higher rate than the others. This is not further analyzed in detail.

5.5.4 Complexity

As far as circuit complexity is involved, the PA and DS system are obviously simpler than the SIRL system, although the realizability of the coherence modulators for the DS system can become an issue when a large number of channels is to be multiplexed, due to the large delay values that are required (see Example 5.7). Moreover the coherence modulators in a DS system need to be either polarization independent or connected by PMF, unless all coherence modulators are integrated together on one single optical chip.





5.5.5 Balancing

In the analysis it had been assumed that the balanced receiver produces a current that is perfectly proportional to the beating product of the light waves in the upper and lower branch of the receiver's MZI. This requires the optical coupler to be perfectly balanced and the photodiodes to be perfectly identical, as discussed in Section 4.8.3. When this is not the case, however, the output current of the balanced receiver will contain undesired terms that correspond to the individual powers of the light waves in the upper and lower arm of the MZI. The significance of these terms is different for each multiplexing topology, as it depends on the ratio between the common terms and the difference terms of the photodiode currents. For a system that is perfectly balanced this ratio can be expressed as:

$$\eta = \frac{E[P_{z_1} + P_{z_2}]_{\max}}{E[P_{z_1} - P_{z_2}]_{\max}} = \frac{2E[P_y]_{\max}}{\text{Re}\{R_{y^*y}(t - T_{\text{Rx},r}, t)\}_{\max}}. \quad (5.78)$$

where (4.30) and (4.31) were used in the last step. From (5.2), (5.37) and (5.58) it follows that

$$\eta = \begin{cases} 2N & , \text{ for the PA,} \\ \frac{1-\kappa}{\kappa}N + \frac{\kappa}{1-\kappa} & , \text{ for the SIRL system,} \\ 2 & , \text{ for the DS system.} \end{cases} \quad (5.79)$$

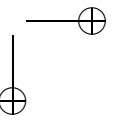
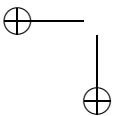
Obviously, the significance of the common terms does not depend on the number of channels N in case of the DS system, whereas it linearly increases with N for both the PA and the SIRL system. Hence, the PA and SIRL system become increasingly vulnerable to receiver imbalances when N increases.

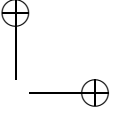
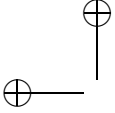
This can also be translated into a requirement on the common-mode rejection ratio (CMRR) of the photodiode pair, which is defined as the ratio between the differential gain and the common-mode gain. For a photodiode pair with responsivities $R_{\text{pd},1}$ and $R_{\text{pd},2}$ this becomes


$$\text{CMRR} = \left(\frac{R_{\text{pd},1} + R_{\text{pd},2}}{2(R_{\text{pd},1} - R_{\text{pd},2})} \right)^2. \quad (5.80)$$

It can be proven that the signal-to-crosstalk ratio (SXR, the power ratio of the desired terms and the common terms) can be written as

$$\text{SXR} \triangleq \left(\frac{(R_{\text{pd},1} + R_{\text{pd},2})\text{Re}\{R_{y^*y}(t - T_{\text{Rx},r}, t)\}_{\max}}{2(R_{\text{pd},1} - R_{\text{pd},2})E[P_y]_{\max}} \right)^2 = \frac{4\text{CMRR}}{\eta^2}. \quad (5.81)$$



**Example 5.10**

Suppose the SXR is required to be at least 20 dB, so that it does not significantly affect the bit rate that can be achieved at $P_e = 10^{-9}$. Then it follows from (5.79) and (5.81) that the CMRR should be at least 20 dB in case of a DS system (irrespective of the number of channels N), and for a PA the CMRR should be at least $20 + 20\log(N)$ dB, so 20 dB for $N = 1$ and an additional 6 dB every time the number of channels doubles. 

5.5.6 Robustness

From a cost point of view it might be seen as an advantage that the SIRL system and DS system require only one common light source for all the transmitted channels, whereas the PA requires one light source for each channel.

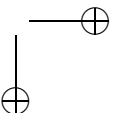
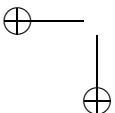
Note, however, that a light source —being an active device— is a typical component that might break down during operation. Hence, the single light source in the SIRL system and DS system can be considered as what is called a *single point of failure*. That is, a breakdown of the light source causes the entire network to be shut down, whereas in the PA, a failing light source only causes one channel to be extinguished. The robustness of the SIRL and DS system can be improved by inserting a backup light source at the (so far) unused lower input port of the left MZI in Figure 5.7 and 5.10.

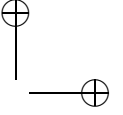
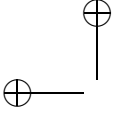
The DS system is most vulnerable because any broken connection in the series connection of the coherence modulators will shut down the network.

5.6 Conclusion

Three coherence multiplexing topologies were explained, analyzed and compared in this chapter. Each topology turned out to have its advantages and disadvantages. Choice for a particular topology depends on several criteria like number of channels, location of the transmission units, frequency and bandwidth of the signals to be transported and allowed system complexity. For a large number of channels the SIRL system shows a superior noise performance with respect to the PA and DS system. The PA is a more universally applicable topology, however, since it provides more flexibility in locating the transmission units. Therefore, the analyzes that are presented in the remainder of this thesis will generally be based on a PA topology, although the derivations will be presented in such a way that results can easily be converted in order to apply to other topologies.

Part of the results that have been presented in this chapter were published in [68].





Chapter 6

Receiver output stabilization by phase diversity

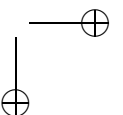
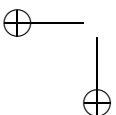
6.1 Introduction

In the previous two chapters the basic coherence modulation and demodulation concept and the three multiplexing topologies have been discussed, where the receiver was assumed to be a simple balanced receiver. Basically, the main idea is that channels are suppressed when the corresponding transmitter and receiver have delays with a mutual difference that is much larger than the coherence time, whereas a channel is selected when the delays of the corresponding transmitter and receiver are the same.

In Section 4.8.2 it has already been noted that precisely matching the delays of a transmitter and (balanced) receiver (so that the optical phases of the interfering light waves are synchronized, resulting in stable output signal) might not be so straightforward. This will be explained in further detail in the next section. In Section 6.3 two existing solutions for stabilizing the receiver's output signal are described, which are based on optical phase synchronization and self-heterodyning, respectively. The disadvantages of these solutions are that they require an external feedback loop and an optical frequency shifter, respectively. In Section 6.4 a new CM detection principle is introduced based on optical phase diversity, which requires neither a feedback loop nor an optical frequency shifter. Several alternatives will be discussed, based on different optical hybrids and different modulation formats. In Section 6.5 the performances of these alternatives will be analyzed and compared.

6.2 Phase sensitivity issue

For a PA consisting of N transmitters and N balanced receivers, the output signal of the low-pass filter in receiver r is given by (5.4), which is repeated



here for convenience:

$$\begin{aligned} \mathbb{E}[V_{\text{LP},r}(t)] &\approx \frac{Z_{\text{TIA}}R_{\text{pd}}P_x}{4L_{\text{Tx}}L_{\text{Rx}}L_{\text{nw}}} \sum_{i=1}^N \exp\left(-\frac{\pi}{2} \left(\frac{T_{\text{Rx},r} - T_{\text{Tx},i}}{\tau_c}\right)^2\right) \\ &\cdot \int_{-\infty}^{\infty} h_{\text{LP}}(t - \rho) m_{\text{mod},i}(\rho) \cos\left(2\pi f_c(T_{\text{Rx},r} - T_{\text{Tx},i}) + \phi_{\text{mod},i}(\rho)\right) d\rho. \end{aligned} \quad (6.1)$$

When all delays are spaced apart much more than a coherence time τ_c (so $|T_{\text{Tx},i} - T_{\text{Tx},j}| \gg \tau_c$ for $i \neq j$), and when receiver r is *approximately* matched to transmitter r (so $|T_{\text{Rx},r} - T_{\text{Tx},r}| < \tau_c$), all exponentials go to zero, except the one with $i = r$. This results in

$$\begin{aligned} \mathbb{E}[V_{\text{LP},r}(t)] &\approx \frac{Z_{\text{TIA}}R_{\text{pd}}P_x}{4L_{\text{Tx}}L_{\text{Rx}}L_{\text{nw}}} \exp\left(-\frac{\pi}{2} \left(\frac{T_{\text{Rx},r} - T_{\text{Tx},r}}{\tau_c}\right)^2\right) \\ &\cdot \int_{-\infty}^{\infty} h_{\text{LP}}(t - \rho) m_{\text{mod},r}(\rho) \cos\left(2\pi f_c(T_{\text{Rx},r} - T_{\text{Tx},r}) + \phi_{\text{mod},r}(\rho)\right) d\rho. \end{aligned} \quad (6.2)$$

Obviously, the values of $T_{\text{Rx},r}$ and $T_{\text{Tx},r}$ should at least match on a coherence time scale ($|T_{\text{Rx},r} - T_{\text{Tx},r}| \ll \tau_c$) such that interference occurs. We can then write

$$\begin{aligned} \mathbb{E}[V_{\text{LP},r}(t)] &\approx \frac{Z_{\text{TIA}}R_{\text{pd}}P_x}{4L_{\text{Tx}}L_{\text{Rx}}L_{\text{nw}}} \int_{-\infty}^{\infty} h_{\text{LP}}(t - \rho) m_{\text{mod},r}(\rho) \\ &\cdot \cos\left(2\pi f_c(T_{\text{Rx},r} - T_{\text{Tx},r}) + \phi_{\text{mod},r}(\rho)\right) d\rho. \end{aligned} \quad (6.3)$$

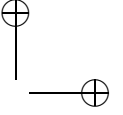
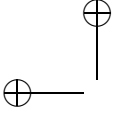
From this expression it follows that, even when $|T_{\text{Rx},r} - T_{\text{Tx},r}| \ll \tau_c$, the observability of the modulating signal is still sensitive to small mismatches in $T_{\text{Tx},r}$ or $T_{\text{Rx},r}$, since small differences between $T_{\text{Rx},r}$ and $T_{\text{Tx},r}$ lead to an offset

$$\Delta\phi_r \triangleq 2\pi f_c(T_{\text{Rx},r} - T_{\text{Tx},r}) \quad (6.4)$$

in the optical phase difference between the interfering optical waves. To achieve complete interference, T_{Rx} and T_{Tx} should match on an optical phase scale (so $|T_{\text{Rx},r} - T_{\text{Tx},r}| \ll 1/f_c$) so that $\Delta\phi_r \approx 0$ rad, resulting in (5.5). This is not so straightforward, however, since the values of $T_{\text{Tx},r}$ and $T_{\text{Rx},r}$ are subject to fabrication inaccuracies, environmental effects (like temperature drift) and component aging.

Example 6.1

Consider a PA for transmitting 16 CM channels, where the sources have a central wavelength of 1310 nm and coherence time of 0.1 ps. The delay values are chosen as multiples of 0.3 ps (see Example 5.1). As an example we assume that the MZIs are fabricated as planar optical waveguide devices in silicon oxynitride (SiON) technology. Fabrication inaccuracies in SiON waveguides lead to typical worst case errors in the effective index in the order



of $\Delta N_{\text{eff}}/N_{\text{eff}} \approx 5 \cdot 10^{-4}$ [69]. This results in small delay mismatches in a matched transmitter-receiver pair. The largest mismatch occurs for the pair with the largest path imbalance and is given by

$$|T_{\text{Rx},r} - T_{\text{Tx},r}|_{\text{max}} \approx 2 \frac{\Delta N_{\text{eff}}}{N_{\text{eff}}} T_{\text{Tx},16} \approx 2 \cdot 5 \cdot 10^{-4} \cdot 16 \cdot 3 \cdot 10^{-13} \text{ s} \approx 4.8 \text{ fs}. \quad (6.5)$$

This is indeed much smaller than the coherence time; using (6.2) one can find that such a mismatch results in a degradation of only 0.03 dB with respect to a perfectly matched situation, as far as coherence matching is concerned.

Now consider the phase offset. Using (6.4) it follows that the maximum phase offset is given by

$$\begin{aligned} |\Delta\phi_r|_{\text{max}} &= 2\pi \frac{c_0}{\lambda_c} |T_{\text{Rx},r} - T_{\text{Tx},r}|_{\text{max}} \\ &\approx 2\pi \frac{3 \cdot 10^8}{1.31 \cdot 10^{-6}} \cdot 4.8 \cdot 10^{-15} \text{ rad} \approx 6.9 \text{ rad} > 2\pi. \end{aligned} \quad (6.6)$$

Phase offsets of this order can lead to a significantly reduced observability and/or a sign ambiguity in the demodulated signal.

This is illustrated by repeating the simulation in Example 5.2 four times, where the delay in receiver 1 is chosen such that the phase mismatch $\Delta\phi_1$ is 0, $\frac{\pi}{4}$, $\frac{\pi}{2}$ and π , respectively. The successive output signals of receiver 1 are shown in Figure 6.1, where the circles denote the decision samples and the dashed lines represent the theoretical expected values.

Obviously, the amplitude of the output signal is maximum when $\Delta\phi_1 = 0$, decreases as $\Delta\phi_1$ increases and becomes zero when $\Delta\phi = \frac{\pi}{2}$. Beyond that value, the output signal inverts, as shown in Figure 6.1(d). □

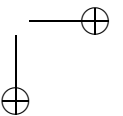
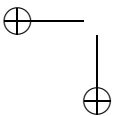
Obviously, special measures are required in order to either synchronize the phases of the interfering light waves, or to avoid the necessity of optical phase synchronization. Two existing solutions —based on optical phase synchronization and self-heterodyning, respectively— will be considered in the next section. In Section 6.4 a new CM receiver concept will be discussed, which is based on optical phase diversity detection.

6.3 Existing stabilization solutions

All CM systems that have been published so far had receivers that were either based on optical phase synchronization or self-heterodyning. Both solutions will be discussed in the following two subsections.

6.3.1 Phase-synchronized balanced detection

Phase-synchronized balanced detection can be performed by means of the previously discussed balanced receiver, extended by a feedback loop which measures the output signal (6.3) and adapts the value of $T_{\text{Rx},r}$ accordingly.



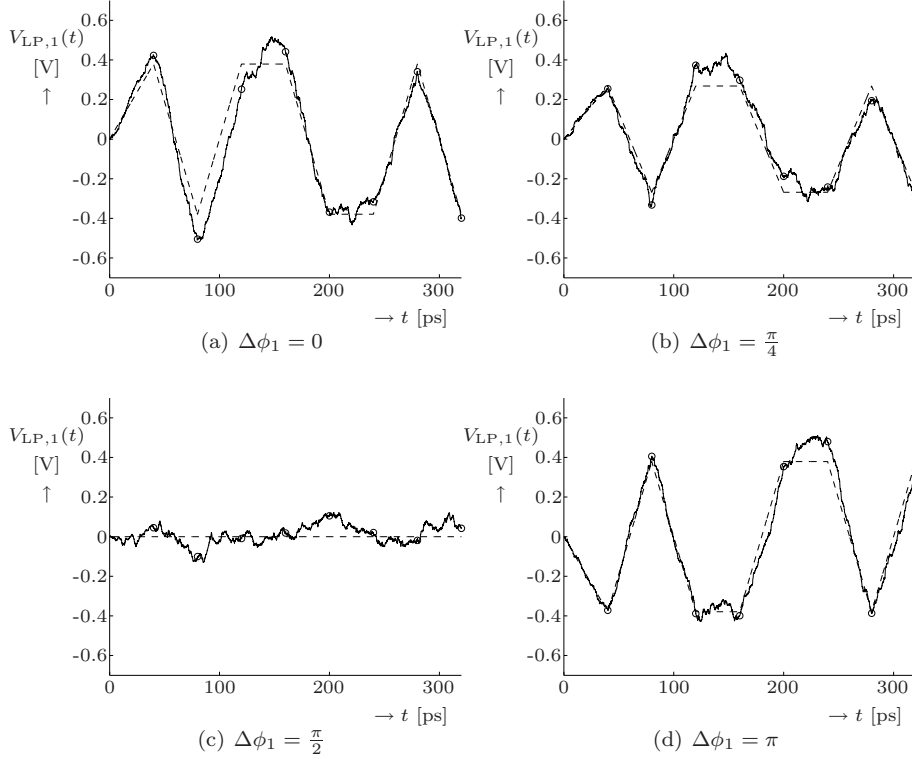


Figure 6.1: Simulated output signal of receiver 1 in a 2-channel PA using BPSK modulation when a bit pattern '01001101' is transmitted at 25 Gbps, for different values of the phase offset $\Delta\phi_1$

There are three problems with this approach:

- When IM is used, synchronization cannot be performed during time periods where $m_{\text{mod},r}(t) \approx 0$;
- When PM is used, synchronization can only be performed during special training periods when $\phi_{\text{mod},r}(t)$ is constant. Otherwise, ambiguities in the measurement arise;
- Even when $m_{\text{mod},r}(t) = 1$ and $\phi_{\text{mod},r}(t) = 0$, the measured value is proportional to $\cos(2\pi f_c(T_{\text{Rx},r} - T_{\text{Tx},r}))$. Since this is an even function of $(T_{\text{Rx},r} - T_{\text{Tx},r})$, it is ambiguous whether the value of $T_{\text{Rx},r}$ should be increased or decreased.

The latter is not really a problem when the tuning of $T_{\text{Rx},r}$ is done manually, as has been done in some prototypes [29].

In a final product, however, automatic tuning is required. This can be done by means of a frequency dithering technique [70], which is illustrated in Figure 6.2.

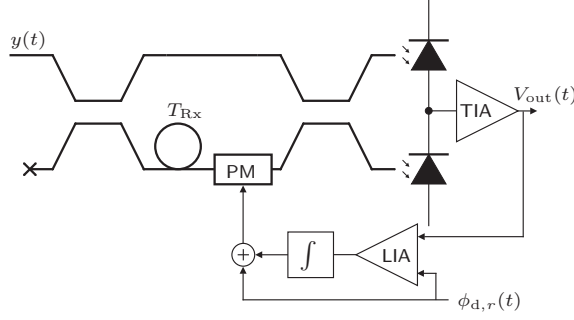


Figure 6.2: Phase-synchronized balanced CM receiver based on frequency dithering

This implies that a small phase modulation

$$\phi_{d,r}(t) = \phi_d \cos(2\pi f_d t) \quad (6.7)$$

is applied in the lower branch of the receiver's MZI. When $m_{\text{mod},r}(t) = 1$ and $\phi_{\text{mod},r}(t) = 0$, the output signal of the TIA becomes

$$\begin{aligned} \mathbb{E}[V_{\text{out},r}(t)] &\approx \frac{Z_{\text{TIA}} R_{\text{pd}} P_x}{4L_{\text{Tx}} L_{\text{Rx}} L_{\text{nw}}} \int_{-\infty}^{\infty} h_{\text{pd}}(t - \rho) \cos(\Delta\phi_r - \phi_{d,r}(\rho)) d\rho \\ &= \frac{Z_{\text{TIA}} R_{\text{pd}} P_x}{4L_{\text{Tx}} L_{\text{Rx}} L_{\text{nw}}} \int_{-\infty}^{\infty} h_{\text{pd}}(t - \rho) \\ &\quad \cdot [\cos(\Delta\phi_r) \cos(\phi_{d,r}(\rho)) + \sin(\Delta\phi_r) \sin(\phi_{d,r}(\rho))] d\rho. \end{aligned} \quad (6.8)$$

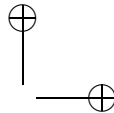
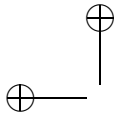
When $|\phi_d|$ is small, first-order Taylor approximations can be used leading to

$$\begin{aligned} \mathbb{E}[V_{\text{out},r}(t)] &\approx \frac{Z_{\text{TIA}} R_{\text{pd}} P_x}{4L_{\text{Tx}} L_{\text{Rx}} L_{\text{nw}}} \int_{-\infty}^{\infty} h_{\text{pd}}(t - \rho) \\ &\quad \cdot [\cos(\Delta\phi_r) + \sin(\Delta\phi_r) \phi_{d,r}(\rho)] d\rho, \end{aligned} \quad (6.9)$$

and when the bandwidth of the photodiode is much larger than the dithering frequency f_d , this becomes

$$\mathbb{E}[V_{\text{out},r}(t)] \approx \frac{Z_{\text{TIA}} R_{\text{pd}} P_x}{4L_{\text{Tx}} L_{\text{Rx}} L_{\text{nw}}} [\cos(\Delta\phi_r) + \sin(\Delta\phi_r) \phi_d \cos(2\pi f_d t)]. \quad (6.10)$$

When this signal is demodulated using a lock-in amplifier (LIA) a signal can be obtained that is proportional to $\sin(\Delta\phi_r) = \sin(2\pi f_c (T_{\text{Rx},r} - T_{\text{Tx},r}))$, which



unambiguously indicates whether the value $T_{R_x,r}$ should be increased or decreased. As a result, a proportional-control feedback loop can be realized that locks the value of $\Delta\phi_r$ at zero or an integer multiple of 2π , resulting in a maximum observability of the modulating signals.

Note that the principle has been explained for constant modulating signals $m_{\text{mod},r}(t)$ and $\phi_{\text{mod},r}(t)$. It can easily be proven that modulation of $\phi_{\text{mod},r}(t)$ results in an alternating value of the control signal. Hence, in case of PM the phase synchronization scheme should only operate during idle periods when $\phi_{\text{mod},r}(t)$ is constant. In case of IM, it can be proven that the control signal is proportional to $m_{\text{mod},r}(t)$, so that it simply vanishes during time periods where $m_{\text{mod},r}(t)$ is zero. Hence, it is not necessary to turn off the feedback loop during transmission.

6.3.2 Self-heterodyning

An alternative for optical phase synchronization is self-heterodyning, as proposed in [65, 71]. This involves inserting a frequency shifter—for example an acousto-optic modulator (AOM)—with frequency shift f_s in one of the interferometer arms in either the transmitters or receivers. In Figure 6.3(a) it is put in the lower arm of the receiver, as an example.

The interfering light waves in the receiver then mix to a band-pass signal instead of a baseband signal. The expected signal at the output of the TIA can then be written as

$$\begin{aligned} E[V_{\text{out},r}(t)] &\approx \frac{Z_{\text{TIA}}R_{\text{pd}}P_x}{4L_{\text{Tx}}L_{\text{Rx}}L_{\text{nw}}} \int_{-\infty}^{\infty} h_{\text{pd}}(t-\rho)m_{\text{mod},r}(\rho) \\ &\quad \cdot \cos\left(2\pi f_s\rho + \Delta\phi_r + \phi_{\text{mod},r}(\rho)\right) d\rho \\ &\approx \frac{Z_{\text{TIA}}R_{\text{pd}}P_x}{4L_{\text{Tx}}L_{\text{Rx}}L_{\text{nw}}} m_{\text{mod},r}(t) \cos\left(2\pi f_s t + \Delta\phi_r + \phi_{\text{mod},r}(t)\right), \quad (6.11) \end{aligned}$$

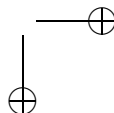
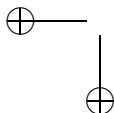
where it is assumed that the bandwidth of the photodiode is larger than f_s .

Hence, both $m_{\text{mod},r}(t)$ and $\phi_{\text{mod},r}(t)$ are observable in the output signal, irrespective of the value of $\Delta\phi_r$. They can be detected by means of electronic demodulation, either coherently or non-coherently. Optical phase synchronization is not required.

Moreover, the balancing problem that is described in Section 4.8.3 is less critical, because the desired signal now appears around f_s Hz, whereas the common terms in the photodiode currents appear at baseband. Hence, they can be easily distinguished by band-pass filtering, even when IM is used.

Note that self-heterodyning results in a degradation of the average power of the expected output signal by 3 dB with respect to the case of optical phase synchronization. The amount of noise will not significantly change as long as the frequency shift is much smaller than the bandwidth of the optical signals, so the SNR will also be lowered by 3 dB.

Moreover, inserting the AOM introduces insertion loss, resulting in an additional SNR degradation, and it is difficult to integrate it in an optical chip.



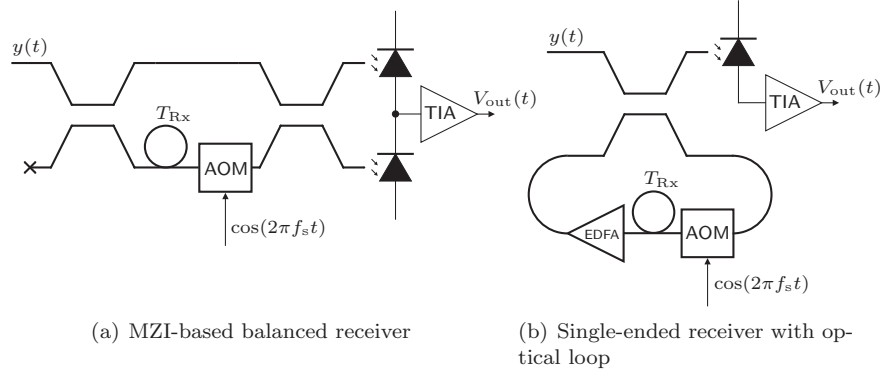


Figure 6.3: Self-heterodyne CM receivers

An alternative form of self-heterodyning in a CM receiver was proposed by Iiyama et al. [72–75]. As shown in Figure 6.3(b), their (unbalanced) receiver consists of a coupler and a loop containing a delay, an optical amplifier—for example an Erbium-doped fiber amplifier (EDFA)—and a frequency shifter. Two light waves that travel through the loop k times and $k + i$ times, respectively, have a mutual time delay $i \cdot T_{Rx}$ and a mutual frequency difference $i \cdot f_s$. Hence, the delays in the coherence modulators should be chosen as multiples of T_{Rx} , so that the CM channel that is transmitted by a coherence modulator with delay $T_{Tx,i} \approx i \cdot T_{Rx}$ will appear as a band-pass signal around frequency $i \cdot f_s$ at the output of the receiver. As a result, all CM channels can be detected simultaneously by means of a single optical receiver, which reduces the number of optical components in case the receiving units are localized to a single node (like in the OLT of a PON), and moreover reduces optical splitting losses. The performance of such a receiver is studied in [74].

Disadvantages of this solution are that it requires two active devices (a frequency shifter and an optical amplifier) in the receiver, which degrades the robustness, and that a very high receiver bandwidth is required in order to accommodate all the channels.

6.4 Phase diversity detection principles

Phase diversity is a detection technique that has extensively been applied in coherent optical communication systems [49, 64]. Although the possibility of stabilizing a CM receiver’s output signal by means of phase diversity had already been suggested in 1987 by Healey [76], no closer studies about the feasibility of such a receiver were published (to our knowledge) until Van Etten’s proposal in 2001 [77].

The idea of phase diversity is that the 2×2 coupler and the two photodiodes in the rightmost part of the balanced receiver are replaced by a multiport

coupler and a corresponding number of photodiodes. As a result of the diversity in the phase transfer of the multiport coupler, multiple interference products are obtained that are similar to (6.3), but each with a different phase offset in the cosine. Proper combining of these interference products then provides an output signal that does not depend on the absolute phase difference between the interfering light waves. Hence, neither an optical phase synchronization mechanism nor an optical frequency shifter is required in order to stabilize the output signal of such a receiver, and the modulating signal can be recovered in baseband.

In the following subsections, two particular phase diversity networks will be described, one being based on a 4×4 optical hybrid and the other being based on a 3×3 optical hybrid. As possible modulation schemes, on-off keying (OOK), binary differential phase shift keying (binary DPSK) and M -ary differential phase shift keying (M -ary DPSK) will be considered.

6.4.1 Four-way phase diversity detection of OOK

The most straightforward solution for performing phase diversity detection is by using a 4×4 phase diversity coupler [78], for example a multimode interference (MMI) coupler. The corresponding detection scheme is shown in Figure 6.4.

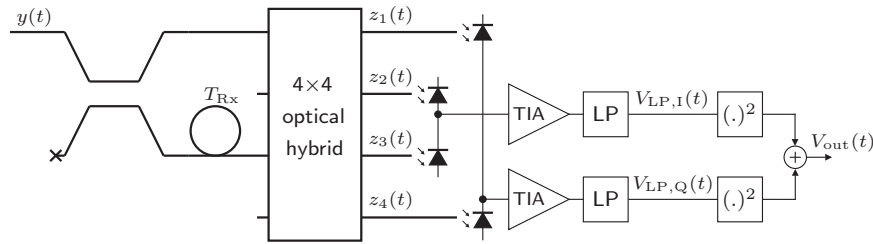
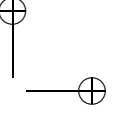
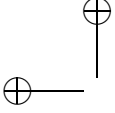


Figure 6.4: A four-way OOK phase diversity receiver

In the frequency range of the considered optical signals, the 4×4 -coupler is assumed to have an ideal transfer matrix

$$[H_{4 \times 4}] = \frac{1}{2} \begin{bmatrix} \exp(j\frac{\pi}{4}) & -1 & 1 & \exp(j\frac{\pi}{4}) \\ -1 & \exp(j\frac{\pi}{4}) & \exp(j\frac{\pi}{4}) & 1 \\ 1 & \exp(j\frac{\pi}{4}) & \exp(j\frac{\pi}{4}) & -1 \\ \exp(j\frac{\pi}{4}) & 1 & -1 & \exp(j\frac{\pi}{4}) \end{bmatrix} \quad (6.12)$$

By Heaton and Jenkins' definition [79], this corresponds to a 7×7 -MMI of which the odd-numbered inputs and outputs are used.



In a CM system with N receivers, all receiving an optical signal $y(t)$, the MMI output signals of a particular receiver r can be written as

$$z_{r,1}(t) = \frac{1}{2\sqrt{2L_{\text{Rx}}}} \left[\exp\left(j\frac{\pi}{4}\right) y(t) + j y(t - T_{\text{Rx},r}) \right], \quad (6.13)$$

$$z_{r,2}(t) = \frac{1}{2\sqrt{2L_{\text{Rx}}}} \left[-y(t) - \exp\left(-j\frac{\pi}{4}\right) y(t - T_{\text{Rx},r}) \right], \quad (6.14)$$

$$z_{r,3}(t) = \frac{1}{2\sqrt{2L_{\text{Rx}}}} \left[y(t) - \exp\left(-j\frac{\pi}{4}\right) y(t - T_{\text{Rx},r}) \right], \quad (6.15)$$

$$z_{r,4}(t) = \frac{1}{2\sqrt{2L_{\text{Rx}}}} \left[\exp\left(j\frac{\pi}{4}\right) y(t) - j y(t - T_{\text{Rx},r}) \right], \quad (6.16)$$

with autocorrelation functions

$$R_{z_{r,1}^* z_{r,1}}(t_1, t_2) = \frac{1}{8L_{\text{Rx}}} \left[R_{y^*y}(t_1, t_2) + \exp\left(j\frac{\pi}{4}\right) R_{y^*y}(t_1, t_2 - T_{\text{Rx},r}) \right. \\ \left. + \exp\left(-j\frac{\pi}{4}\right) R_{y^*y}(t_1 - T_{\text{Rx},r}, t_2) + R_{y^*y}(t_1 - T_{\text{Rx},r}, t_2 - T_{\text{Rx},r}) \right], \quad (6.17)$$

$$R_{z_{r,2}^* z_{r,2}}(t_1, t_2) = \frac{1}{8L_{\text{Rx}}} \left[R_{y^*y}(t_1, t_2) + \exp\left(-j\frac{\pi}{4}\right) R_{y^*y}(t_1, t_2 - T_{\text{Rx},r}) \right. \\ \left. + \exp\left(j\frac{\pi}{4}\right) R_{y^*y}(t_1 - T_{\text{Rx},r}, t_2) + R_{y^*y}(t_1 - T_{\text{Rx},r}, t_2 - T_{\text{Rx},r}) \right], \quad (6.18)$$

$$R_{z_{r,3}^* z_{r,3}}(t_1, t_2) = \frac{1}{8L_{\text{Rx}}} \left[R_{y^*y}(t_1, t_2) - \exp\left(-j\frac{\pi}{4}\right) R_{y^*y}(t_1, t_2 - T_{\text{Rx},r}) \right. \\ \left. - \exp\left(j\frac{\pi}{4}\right) R_{y^*y}(t_1 - T_{\text{Rx},r}, t_2) + R_{y^*y}(t_1 - T_{\text{Rx},r}, t_2 - T_{\text{Rx},r}) \right], \quad (6.19)$$

$$R_{z_{r,4}^* z_{r,4}}(t_1, t_2) = \frac{1}{8L_{\text{Rx}}} \left[R_{y^*y}(t_1, t_2) - \exp\left(j\frac{\pi}{4}\right) R_{y^*y}(t_1, t_2 - T_{\text{Rx},r}) \right. \\ \left. - \exp\left(-j\frac{\pi}{4}\right) R_{y^*y}(t_1 - T_{\text{Rx},r}, t_2) + R_{y^*y}(t_1 - T_{\text{Rx},r}, t_2 - T_{\text{Rx},r}) \right], \quad (6.20)$$

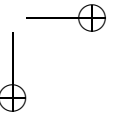
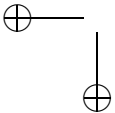
cross-correlation functions

$$R_{z_{r,1}^* z_{r,2}}(t_1, t_2) = \frac{1}{8L_{\text{Rx}}} \left[-\exp\left(-j\frac{\pi}{4}\right) R_{y^*y}(t_1, t_2) + j R_{y^*y}(t_1, t_2 - T_{\text{Rx},r}) \right. \\ \left. + j R_{y^*y}(t_1 - T_{\text{Rx},r}, t_2) + \exp\left(j\frac{\pi}{4}\right) R_{y^*y}(t_1 - T_{\text{Rx},r}, t_2 - T_{\text{Rx},r}) \right], \quad (6.21)$$

$$R_{z_{r,1}^* z_{r,3}}(t_1, t_2) = \frac{1}{8L_{\text{Rx}}} \left[\exp\left(-j\frac{\pi}{4}\right) R_{y^*y}(t_1, t_2) + j R_{y^*y}(t_1, t_2 - T_{\text{Rx},r}) \right. \\ \left. - j R_{y^*y}(t_1 - T_{\text{Rx},r}, t_2) + \exp\left(j\frac{\pi}{4}\right) R_{y^*y}(t_1 - T_{\text{Rx},r}, t_2 - T_{\text{Rx},r}) \right], \quad (6.22)$$

$$R_{z_{r,1}^* z_{r,4}}(t_1, t_2) = \frac{1}{8L_{\text{Rx}}} \left[R_{y^*y}(t_1, t_2) - \exp\left(j\frac{\pi}{4}\right) R_{y^*y}(t_1, t_2 - T_{\text{Rx},r}) \right. \\ \left. + \exp\left(-j\frac{\pi}{4}\right) R_{y^*y}(t_1 - T_{\text{Rx},r}, t_2) - R_{y^*y}(t_1 - T_{\text{Rx},r}, t_2 - T_{\text{Rx},r}) \right], \quad (6.23)$$

$$R_{z_{r,2}^* z_{r,3}}(t_1, t_2) = \frac{1}{8L_{\text{Rx}}} \left[-R_{y^*y}(t_1, t_2) + \exp\left(-j\frac{\pi}{4}\right) R_{y^*y}(t_1, t_2 - T_{\text{Rx},r}) \right. \\ \left. - \exp\left(j\frac{\pi}{4}\right) R_{y^*y}(t_1 - T_{\text{Rx},r}, t_2) + R_{y^*y}(t_1 - T_{\text{Rx},r}, t_2 - T_{\text{Rx},r}) \right], \quad (6.24)$$



$$R_{z_{r,2}^* z_{r,4}}(t_1, t_2) = \frac{1}{8L_{\text{Rx}}} \left[-\exp\left(j\frac{\pi}{4}\right) R_{y^*y}(t_1, t_2) + j R_{y^*y}(t_1, t_2 - T_{\text{Rx},r}) \right. \\ \left. - j R_{y^*y}(t_1 - T_{\text{Rx},r}, t_2) - \exp\left(-j\frac{\pi}{4}\right) R_{y^*y}(t_1 - T_{\text{Rx},r}, t_2 - T_{\text{Rx},r}) \right], \quad (6.25)$$

$$R_{z_{r,3}^* z_{r,4}}(t_1, t_2) = \frac{1}{8L_{\text{Rx}}} \left[\exp\left(j\frac{\pi}{4}\right) R_{y^*y}(t_1, t_2) - j R_{y^*y}(t_1, t_2 - T_{\text{Rx},r}) \right. \\ \left. - j R_{y^*y}(t_1 - T_{\text{Rx},r}, t_2) - \exp\left(-j\frac{\pi}{4}\right) R_{y^*y}(t_1 - T_{\text{Rx},r}, t_2 - T_{\text{Rx},r}) \right], \quad (6.26)$$

and expected powers

$$\mathbb{E}[P_{z_{r,1}}(t)] = \frac{1}{8L_{\text{Rx}}} \left(\mathbb{E}[P_y(t) + P_y(t - T_{\text{Rx},r})] \right. \\ \left. + \text{Re} \left\{ \exp\left(-j\frac{\pi}{4}\right) R_{y^*y}(t - T_{\text{Rx},r}, t) \right\} \right), \quad (6.27)$$

$$\mathbb{E}[P_{z_{r,2}}(t)] = \frac{1}{8L_{\text{Rx}}} \left(\mathbb{E}[P_y(t) + P_y(t - T_{\text{Rx},r})] \right. \\ \left. + \text{Re} \left\{ \exp\left(j\frac{\pi}{4}\right) R_{y^*y}(t - T_{\text{Rx},r}, t) \right\} \right), \quad (6.28)$$

$$\mathbb{E}[P_{z_{r,3}}(t)] = \frac{1}{8L_{\text{Rx}}} \left(\mathbb{E}[P_y(t) + P_y(t - T_{\text{Rx},r})] \right. \\ \left. - \text{Re} \left\{ \exp\left(j\frac{\pi}{4}\right) R_{y^*y}(t - T_{\text{Rx},r}, t) \right\} \right), \quad (6.29)$$

$$\mathbb{E}[P_{z_{r,4}}(t)] = \frac{1}{8L_{\text{Rx}}} \left(\mathbb{E}[P_y(t) + P_y(t - T_{\text{Rx},r})] \right. \\ \left. - \text{Re} \left\{ \exp\left(-j\frac{\pi}{4}\right) R_{y^*y}(t - T_{\text{Rx},r}, t) \right\} \right). \quad (6.30)$$

The output voltages of the low-pass filters in the two branches have expected values

$$\mathbb{E}[V_{\text{LP},\text{I},r}(t)] = Z_{\text{TIA}} R_{\text{pd}} \int_{-\infty}^{\infty} h_{\text{LP}}(t - \rho) \mathbb{E}[P_{z_{r,2}}(\rho) - P_{z_{r,3}}(\rho)] d\rho \\ = \frac{Z_{\text{TIA}} R_{\text{pd}}}{4L_{\text{Rx}}} \int_{-\infty}^{\infty} h_{\text{LP}}(t - \rho) \text{Re} \left\{ \exp\left(j\frac{\pi}{4}\right) R_{y^*y}(\rho - T_{\text{Rx},r}, \rho) \right\} d\rho, \quad (6.31)$$

$$\mathbb{E}[V_{\text{LP},\text{Q},r}(t)] = Z_{\text{TIA}} R_{\text{pd}} \int_{-\infty}^{\infty} h_{\text{LP}}(t - \rho) \mathbb{E}[P_{z_{r,1}}(\rho) - P_{z_{r,4}}(\rho)] d\rho \\ = \frac{Z_{\text{TIA}} R_{\text{pd}}}{4L_{\text{Rx}}} \int_{-\infty}^{\infty} h_{\text{LP}}(t - \rho) \text{Re} \left\{ \exp\left(-j\frac{\pi}{4}\right) R_{y^*y}(\rho - T_{\text{Rx},r}, \rho) \right\} d\rho. \quad (6.32)$$

The output signal $V_{\text{out},r}(t)$ of the receiver results by squaring and adding the output signals of the low-pass filters. When the SNR after filtering is very high (we will come back to this in Section 6.5), the expected value of $V_{\text{out},r}(t)$ can be approximated as

$$\mathbb{E}[V_{\text{out},r}(t)] = \mathbb{E}[V_{\text{LP},\text{I},r}^2(t) + V_{\text{LP},\text{Q},r}^2(t)] \approx \mathbb{E}^2[V_{\text{LP},\text{I},r}(t)] + \mathbb{E}^2[V_{\text{LP},\text{Q},r}(t)] \\ = \frac{Z_{\text{TIA}}^2 R_{\text{pd}}^2}{16L_{\text{Rx}}^2} \left| \int_{-\infty}^{\infty} h_{\text{LP}}(t - \rho) R_{y^*y}(\rho - T_{\text{Rx},r}, \rho) d\rho \right|^2. \quad (6.33)$$

In case of a PA, R_{y^*y} follows from (5.2), resulting in

$$\begin{aligned} \mathbb{E}[V_{\text{out},r}(t)] = & \\ & \frac{Z_{\text{TIA}}^2 R_{\text{pd}}^2 P_x^2}{64L_{\text{Tx}}^2 L_{\text{Rx}}^2 L_{\text{nw}}^2} \left\{ \left[\int_{-\infty}^{\infty} h_{\text{LP}}(t-\rho) m_{\text{mod},r}(\rho) \cos(\phi_{\text{mod},r}(\rho)) \, d\rho \right]^2 \right. \\ & \left. + \left[\int_{-\infty}^{\infty} h_{\text{LP}}(t-\rho) m_{\text{mod},r}(\rho) \sin(\phi_{\text{mod},r}(\rho)) \, d\rho \right]^2 \right\}. \end{aligned} \quad (6.34)$$

Obviously, since $\Delta\phi_r$ does not appear in this expression, the output signal no longer depends on the difference between $T_{\text{Rx},r}$ and $T_{\text{Tx},r}$, as long as it is much smaller than the coherence time.

For digital transmission and matched filtering, (4.53), (4.54) and (4.56) apply. The expected output signal is then given by

$$\begin{aligned} \mathbb{E}[V_{\text{out},r}(t)] = & \frac{Z_{\text{TIA}}^2 R_{\text{pd}}^2 P_x^2}{64L_{\text{Tx}}^2 L_{\text{Rx}}^2 L_{\text{nw}}^2} \sum_k \sum_l m_{r,k} m_{r,l} \cos(\phi_{r,k} - \phi_{r,l}) \\ & \cdot \Lambda\left(\frac{t-kT_s}{T_s}\right) \Lambda\left(\frac{t-lT_s}{T_s}\right). \end{aligned} \quad (6.35)$$

At the sampling instants this results in

$$\mathbb{E}[V_{\text{out},r}(kT_s)] = \frac{Z_{\text{TIA}}^2 R_{\text{pd}}^2 P_x^2}{64L_{\text{Tx}}^2 L_{\text{Rx}}^2 L_{\text{nw}}^2} m_{r,k}^2. \quad (6.36)$$

Note that the output signal at the sampling instants is independent of $\{\phi_{r,k}\}$. Hence, this specific type of receiver is solely suitable for intensity modulation, such as On-Off Keying (OOK).

Example 6.2

The four simulations in Example 6.1 are repeated with four-way phase diversity receivers instead of balanced receivers. The successive output signals $V_{\text{out},1}(t)$ in case of BPSK modulation are shown in Figure 6.5(a)–6.5(d). The branch signals $V_{\text{LP},1,1}(t)$ and $V_{\text{LP},1,2}(t)$ for $\Delta\phi_1 = 0$ are shown in Figure 6.5(e) and 6.5(f). In all figures, the circles denote the decision samples and the dashed lines represent the theoretical expected values.

Obviously, the amplitude of the output signal does not depend on the phase offset $\Delta\phi_1$. However, the decision samples of the output signal also do not depend on the modulating signal, as predicted.

All simulations are repeated for OOK instead of BPSK. The corresponding results are shown in Figure 6.6.

Obviously, the decision samples of the output signal now do depend on the modulating signal. Hence, it has been illustrated that this phase diversity receiver can be used for OOK modulation and not for BPSK modulation. \square

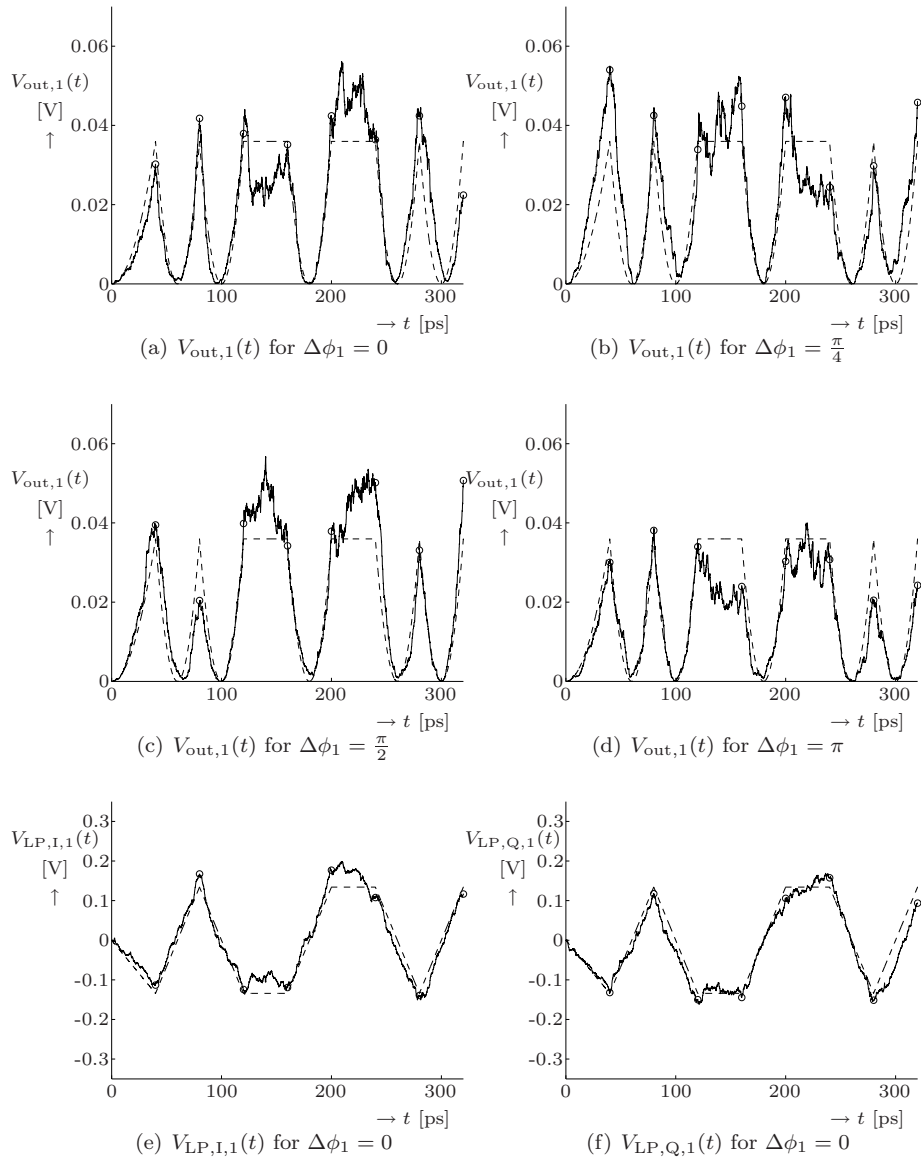


Figure 6.5: Simulated output signal $V_{\text{out},1}(t)$ and branch signals $V_{\text{LP},I,1}(t)$ and $V_{\text{LP},Q,1}(t)$ of phase diversity receiver 1 in a 2-channel PA using BPSK modulation when a bit pattern '01001101' is transmitted at 25 Gbps, for different values of the phase offset $\Delta\phi_1$

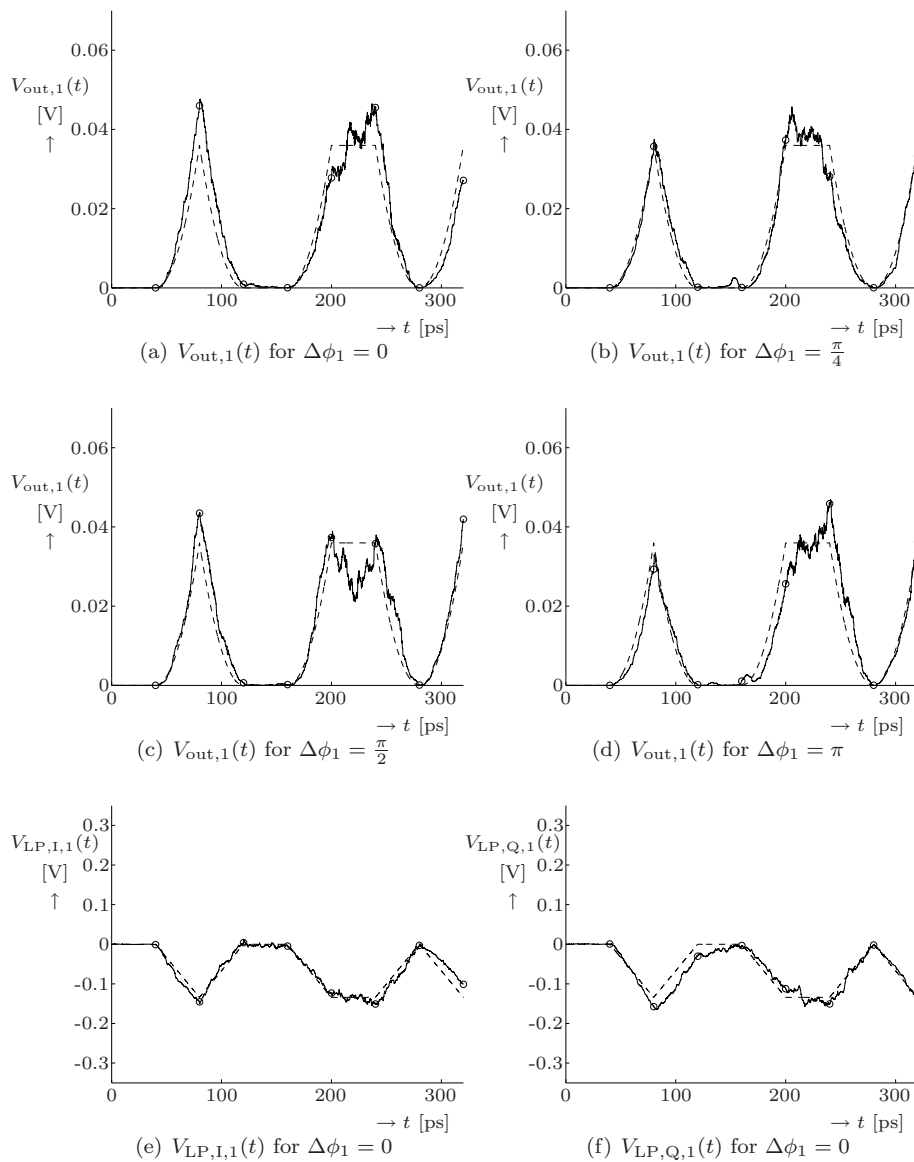


Figure 6.6: Simulated output signal $V_{\text{out},1}(t)$ and branch signals $V_{\text{LP},I,1}(t)$ and $V_{\text{LP},Q,1}(t)$ of phase diversity receiver 1 in a 2-channel PA using OOK modulation when a bit pattern '01001101' is transmitted at 25 Gbps, for different values of the phase offset $\Delta\phi_1$

In a later subsection, a specific receiver for demodulating phase-modulated CM signals will be discussed, but first it will be shown how the same detection operation can be performed using a 3×3 -coupler.

6.4.2 Three-way phase diversity detection of OOK

In Figure 6.7 a CM receiver based on three-way balanced optical phase diversity is shown.

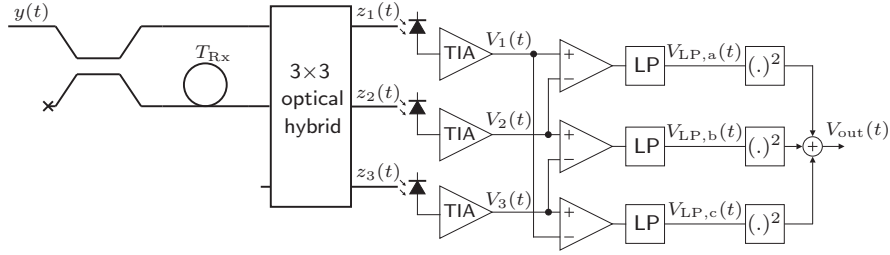


Figure 6.7: A three-way OOK phase diversity receiver

In the frequency range of the considered optical signals, the 3×3 -coupler is assumed to have an ideal transfer matrix [52]

$$[H_{3 \times 3}] = \frac{1}{\sqrt{3}} \begin{bmatrix} 1 & 1 & 1 \\ 1 & \exp(j\frac{2\pi}{3}) & \exp(-j\frac{2\pi}{3}) \\ 1 & \exp(-j\frac{2\pi}{3}) & \exp(j\frac{2\pi}{3}) \end{bmatrix}. \quad (6.37)$$

The electrical fields at the output of such coupler in receiver r are given by

$$z_{r,1}(t) = \frac{1}{\sqrt{6L_{Rx}}} \left[y(t) + j y(t - T_{Rx,r}) \right], \quad (6.38)$$

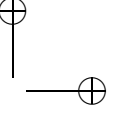
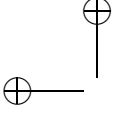
$$z_{r,2}(t) = \frac{1}{\sqrt{6L_{Rx}}} \left[y(t) - \exp(j\frac{\pi}{6}) y(t - T_{Rx,r}) \right], \quad (6.39)$$

$$z_{r,3}(t) = \frac{1}{\sqrt{6L_{Rx}}} \left[y(t) + \exp(-j\frac{\pi}{6}) y(t - T_{Rx,r}) \right], \quad (6.40)$$

with autocorrelation functions

$$R_{z_{r,1}^* z_{r,1}}(t_1, t_2) = \frac{1}{6L_{Rx}} \left[R_{y^* y}(t_1, t_2) + j R_{y^* y}(t_1, t_2 - T_{Rx,r}) - j R_{y^* y}(t_1 - T_{Rx,r}, t_2) + R_{y^* y}(t_1 - T_{Rx,r}, t_2 - T_{Rx,r}) \right], \quad (6.41)$$

$$R_{z_{r,2}^* z_{r,2}}(t_1, t_2) = \frac{1}{8L_{Rx}} \left[R_{y^* y}(t_1, t_2) - \exp(j\frac{\pi}{6}) R_{y^* y}(t_1, t_2 - T_{Rx,r}) - \exp(-j\frac{\pi}{6}) R_{y^* y}(t_1 - T_{Rx,r}, t_2) + R_{y^* y}(t_1 - T_{Rx,r}, t_2 - T_{Rx,r}) \right], \quad (6.42)$$



$$R_{z_{r,3}^* z_{r,3}}(t_1, t_2) = \frac{1}{8L_{\text{Rx}}} \left[R_{y^*y}(t_1, t_2) + \exp(-j\frac{\pi}{6}) R_{y^*y}(t_1, t_2 - T_{\text{Rx},r}) \right. \\ \left. + \exp(j\frac{\pi}{6}) R_{y^*y}(t_1 - T_{\text{Rx},r}, t_2) + R_{y^*y}(t_1 - T_{\text{Rx},r}, t_2 - T_{\text{Rx},r}) \right], \quad (6.43)$$

cross-correlation functions

$$R_{z_{r,1}^* z_{r,2}}(t_1, t_2) = \frac{1}{8L_{\text{Rx}}} \left[R_{y^*y}(t_1, t_2) - \exp(j\frac{\pi}{6}) R_{y^*y}(t_1, t_2 - T_{\text{Rx},r}) \right. \\ \left. - j R_{y^*y}(t_1 - T_{\text{Rx},r}, t_2) - \exp(-j\frac{\pi}{3}) R_{y^*y}(t_1 - T_{\text{Rx},r}, t_2 - T_{\text{Rx},r}) \right], \quad (6.44)$$

$$R_{z_{r,1}^* z_{r,3}}(t_1, t_2) = \frac{1}{8L_{\text{Rx}}} \left[R_{y^*y}(t_1, t_2) + \exp(-j\frac{\pi}{6}) R_{y^*y}(t_1, t_2 - T_{\text{Rx},r}) \right. \\ \left. - j R_{y^*y}(t_1 - T_{\text{Rx},r}, t_2) - \exp(j\frac{\pi}{3}) R_{y^*y}(t_1 - T_{\text{Rx},r}, t_2 - T_{\text{Rx},r}) \right], \quad (6.45)$$

$$R_{z_{r,2}^* z_{r,3}}(t_1, t_2) = \frac{1}{8L_{\text{Rx}}} \left[R_{y^*y}(t_1, t_2) + \exp(-j\frac{\pi}{6}) R_{y^*y}(t_1, t_2 - T_{\text{Rx},r}) \right. \\ \left. - \exp(-j\frac{\pi}{6}) R_{y^*y}(t_1 - T_{\text{Rx},r}, t_2) \right. \\ \left. - \exp(-j\frac{\pi}{3}) R_{y^*y}(t_1 - T_{\text{Rx},r}, t_2 - T_{\text{Rx},r}) \right], \quad (6.46)$$

and expected powers

$$\mathbb{E}[P_{z_{r,1}}(t)] = \frac{1}{6L_{\text{Rx}}} \left(\mathbb{E}[P_y(t) + P_y(t - T_{\text{Rx},r})] \right. \\ \left. - \text{Re} \left\{ j R_{y^*y}(t - T_{\text{Rx},r}, t) \right\} \right), \quad (6.47)$$

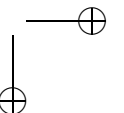
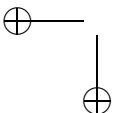
$$\mathbb{E}[P_{z_{r,2}}(t)] = \frac{1}{6L_{\text{Rx}}} \left(\mathbb{E}[P_y(t) + P_y(t - T_{\text{Rx},r})] \right. \\ \left. - \text{Re} \left\{ \exp(-j\frac{\pi}{6}) R_{y^*y}(t - T_{\text{Rx},r}, t) \right\} \right), \quad (6.48)$$

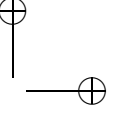
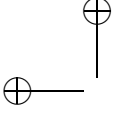
$$\mathbb{E}[P_{z_{r,3}}(t)] = \frac{1}{6L_{\text{Rx}}} \left(\mathbb{E}[P_y(t) + P_y(t - T_{\text{Rx},r})] \right. \\ \left. + \text{Re} \left\{ \exp(j\frac{\pi}{6}) R_{y^*y}(t - T_{\text{Rx},r}, t) \right\} \right). \quad (6.49)$$

The expected output voltages of the low-pass filters in the three branches can now be written as

$$\mathbb{E}[V_{\text{LP},a,r}(t)] = Z_{\text{TIA}} R_{\text{pd}} \int_{-\infty}^{\infty} h_{\text{LP}}(t - \rho) \mathbb{E}[P_{z_{r,1}}(\rho) - P_{z_{r,2}}(\rho)] d\rho \\ = \frac{Z_{\text{TIA}} R_{\text{pd}}}{2\sqrt{3}L_{\text{Rx}}} \int_{-\infty}^{\infty} h_{\text{LP}}(t - \rho) \text{Re} \left\{ \exp(-j\frac{\pi}{3}) R_{y^*y}(\rho - T_{\text{Rx},r}, \rho) \right\} d\rho, \quad (6.50)$$

$$\mathbb{E}[V_{\text{LP},b,r}(t)] = Z_{\text{TIA}} R_{\text{pd}} \int_{-\infty}^{\infty} h_{\text{LP}}(t - \rho) \mathbb{E}[P_{z_{r,2}}(\rho) - P_{z_{r,3}}(\rho)] d\rho \\ = -\frac{Z_{\text{TIA}} R_{\text{pd}}}{2\sqrt{3}L_{\text{Rx}}} \int_{-\infty}^{\infty} h_{\text{LP}}(t - \rho) \text{Re} \left\{ R_{y^*y}(\rho - T_{\text{Rx},r}, \rho) \right\} d\rho, \quad (6.51)$$





$$\begin{aligned} \mathbb{E}[V_{\text{LP},c,r}(t)] &= Z_{\text{TIA}} R_{\text{pd}} \int_{-\infty}^{\infty} h_{\text{LP}}(t - \rho) \mathbb{E}[P_{z_{r,3}}(\rho) - P_{z_{r,1}}(\rho)] d\rho \\ &= \frac{Z_{\text{TIA}} R_{\text{pd}}}{2\sqrt{3}L_{\text{Rx}}} \int_{-\infty}^{\infty} h_{\text{LP}}(t - \rho) \text{Re}\left\{ \exp\left(j\frac{\pi}{3}\right) R_{y^*y}(\rho - T_{\text{Rx},r}, \rho) \right\} d\rho. \end{aligned} \quad (6.52)$$

The expected output signal of the three-way receiver can now be approximated in the same way as for the four-way receiver:

$$\begin{aligned} \mathbb{E}[V_{\text{out},r}(t)] &= \mathbb{E}[V_{\text{LP},a,r}^2(t) + V_{\text{LP},b,r}^2(t) + V_{\text{LP},c,r}^2(t)] \\ &\approx \mathbb{E}^2[V_{\text{LP},a,r}(t)] + \mathbb{E}^2[V_{\text{LP},b,r}(t)] + \mathbb{E}^2[V_{\text{LP},c,r}(t)] \\ &= \frac{Z_{\text{TIA}}^2 R_{\text{pd}}^2}{8L_{\text{Rx}}^2} \left| \int_{-\infty}^{\infty} h_{\text{LP}}(t - \rho) R_{y^*y}(\rho - T_{\text{Rx},r}, \rho) d\rho \right|^2. \end{aligned} \quad (6.53)$$

Note that this expression is similar to (6.33), so the output signal of the three-way receiver is similar to the output signal of the four-way receiver.

The performances of the three-way and four-way receiver will be compared in Section 6.5.

6.4.3 Phase-synchronized detection of QPSK and M -ary PSK

Since the use of a multiport coupler enables the generation of quadrature components, a similar scheme can be used to detect QPSK or M -ary PSK modulated signals [80]. Since this requires phase synchronization, it is not really a phase diversity technique. It will be discussed here as an introduction into the phase diversity receivers that are discussed in the next two sections.

In case of QPSK, we have $m_{r,k} = 1$ and

$$\phi_{r,k} = (2A_{r,k} + 1)\frac{\pi}{4}, \quad (6.54)$$

where the information symbols $A_{r,k}$ are integer values chosen from the set $\{0, 1, 2, 3\}$, representing 2 bits per symbol. In the general case where m bits are transmitted per symbol, M -ary PSK with $M = 2^m$ is used. In that case we have

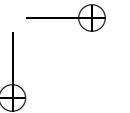
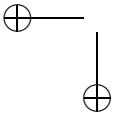
$$\phi_{r,k} = A_{r,k} \frac{2\pi}{M}, \quad (6.55)$$

where the information symbols $A_{r,k}$ are integer values chosen from the set $\{0, 1, \dots, M-1\}$ [81]. The symbols can be detected using the receiver structure in Figure 6.8.

In case of a PA the output samples of the low-pass filters can be found from (5.2), (6.31) and (6.32). Assuming that $\Delta\phi_r = \frac{3\pi}{4}$ (note that this requires phase synchronization) this results in

$$\mathbb{E}[V_{\text{LP},I,r}(k T_s)] = \frac{Z_{\text{TIA}} R_{\text{pd}} P_x}{8L_{\text{Tx}} L_{\text{Rx}} L_{\text{nw}}} \cos(\phi_{r,k}), \quad (6.56)$$

$$\mathbb{E}[V_{\text{LP},Q,r}(k T_s)] = \frac{Z_{\text{TIA}} R_{\text{pd}} P_x}{8L_{\text{Tx}} L_{\text{Rx}} L_{\text{nw}}} \sin(\phi_{r,k}). \quad (6.57)$$



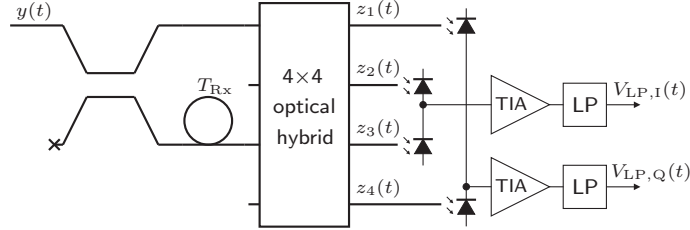


Figure 6.8: A four-way phase-synchronized M -ary PSK receiver

As a result, the transmitted symbols can be extracted by conventional PSK decoding [81]. For QPSK for example, the bits can be extracted by directly thresholding $V_{LP,I,r}$ and $V_{LP,Q,r}$, provided that the symbols $A_{r,k}$ are encoded by Gray coding. This is illustrated in Figure 6.9 for QPSK (6.9(a)) and 8-PSK (6.9(b)). The numbers between the parentheses represent the bits that correspond to that particular combination of values of the output samples.

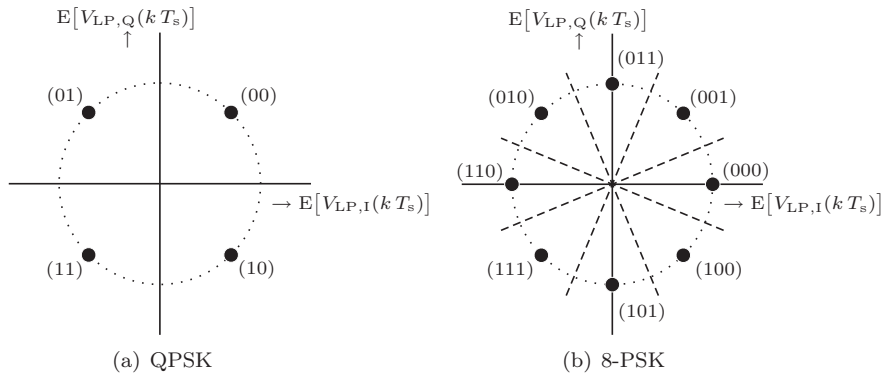


Figure 6.9: Output samples of the low-pass filters for QPSK and 8-PSK

The advantage of using QPSK or M -ary PSK rather than binary PSK is that the symbol time increases with the number of bits per symbol, m . Hence, both the modulation speed and the signal processing speed in the receiver can be reduced, and moreover, the received signal will be less susceptible for inter-symbol interference (ISI) caused by fiber dispersion. Also note from Figure 6.9, however, that increasing m reduces the distance between the symbols in the signal space, which makes the received signal more and more vulnerable to noise. As a result, there is a trade-off between corruption by ISI and corruption by noise. We will come back to this in Chapter 7; ISI will be neglected until then.

QPSK and M -ary PSK can also be demodulated using a three-way receiver. It can be shown that this can for example be done by constructing signals $V_{I,r}(t)$ and $V_{Q,r}(t)$ from the TIA output signal $V_{r,1}(t)$, $V_{r,2}(t)$ and $V_{r,3}(t)$ as

$$V_{I,r}(t) = V_{r,1}(t) - V_{r,2}(t) \quad (6.58)$$

$$V_{Q,r}(t) = \frac{1}{\sqrt{3}} \left(V_{r,1}(t) + V_{r,2}(t) - 2V_{r,3}(t) \right) \quad (6.59)$$

The remaining operations are the same as in the four-way M -ary PSK receiver.

6.4.4 Phase diversity detection of binary DPSK

Although phase diversity is not suitable for detecting the absolute phase difference between the interfering light waves, it can be used to detect changes in this phase difference; digital transmission can be accomplished by performing differential phase shift keying (DPSK) modulation, and by replacing the squarers in the phase diversity receiver in Figure 6.4 by delay-and-multiply circuits: see Figure 6.10 [82].

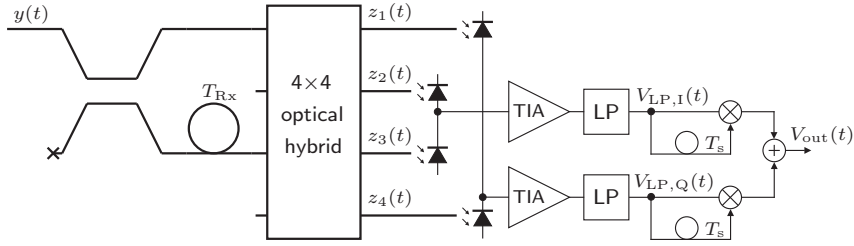


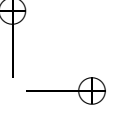
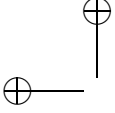
Figure 6.10: A four-way binary DPSK phase diversity receiver

The delay T_s in the delay-and-multiply circuit corresponds to one symbol period. The resulting output signal can then be shown to have expected value

$$\begin{aligned} E[V_{\text{out},r}(t)] &= E[V_{\text{LP},I,r}(t)V_{\text{LP},I,r}(t - T_s) + V_{\text{LP},Q,r}(t)V_{\text{LP},Q,r}(t - T_s)] \\ &\approx E[V_{\text{LP},I,r}(t)]E[V_{\text{LP},I,r}(t - T_s)] \\ &\quad + E[V_{\text{LP},Q,r}(t)]E[V_{\text{LP},Q,r}(t - T_s)] \\ &= \frac{Z_{\text{TIA}}^2 R_{\text{pd}}^2}{16L_{\text{Rx}}^2} \text{Re} \left\{ \int_{-\infty}^{\infty} h_{\text{LP}}(t - \rho) R_{y^*y}(\rho - T_{\text{Rx},r}, \rho) d\rho \right. \\ &\quad \left. \cdot \int_{-\infty}^{\infty} h_{\text{LP}}(t - T_s - \rho) R_{y^*y}(\rho, \rho - T_{\text{Rx},r}) d\rho \right\}. \quad (6.60) \end{aligned}$$

For binary DPSK modulation we have $m_{r,k} = 1$ and

$$\phi_{r,k} = \phi_{r,k-1} + A_{r,k}\pi \text{ mod } 2\pi. \quad (6.61)$$



Hence, successive values of $\phi_{r,k}$ are the same for a binary 1 and have a difference of π for a binary zero. When this is applied in a PA, (6.60) becomes

$$\begin{aligned} \mathbb{E}[V_{\text{out},r}(kT_s)] &= \frac{Z_{\text{TIA}}^2 R_{\text{pd}}^2 P_x^2}{64L_{\text{Tx}}^2 L_{\text{Rx}}^2 L_{\text{nw}}^2} \cos(\phi_{r,k} - \phi_{r,k-1}) \\ &= \frac{Z_{\text{TIA}}^2 R_{\text{pd}}^2 P_x^2}{64L_{\text{Tx}}^2 L_{\text{Rx}}^2 L_{\text{nw}}^2} \cos(A_{r,k}\pi), \end{aligned} \quad (6.62)$$

which is positive for a binary one, and negative for a binary zero, irrespective of small fluctuations in the optical path imbalances in transmitter or receiver. Moreover, note that the delays T_s do not require strict matching either, since the electrical signals $V_{\text{LP},\text{I},r}(t)$ and $V_{\text{LP},\text{Q},r}(t)$ are baseband signals.

Example 6.3

The simulations in Example 6.2 are repeated for $\Delta\phi_1 = 0$, $\Delta\phi_1 = \frac{\pi}{4}$ and $\Delta\phi_1 = \frac{\pi}{2}$, with four-way DPSK phase diversity receivers instead of OOK phase diversity receivers. Binary DPSK modulation is performed, so the bit pattern '01001101' corresponds to the modulating signal in Figure 6.11(a). The successive output signals $V_{\text{out},1}(t)$ are shown in Figure 6.11(b)–6.11(d). The branch signals $V_{\text{LP},\text{I},1}(t)$ and $V_{\text{LP},\text{Q},1}(t)$ for $\Delta\phi_1 = 0$ are shown in Figure 6.11(e) and 6.11(f). In all figures, the circles denote the decision samples and the dashed lines represent the theoretical expected values.

Obviously, the amplitude of the output signal does not depend on the phase offset $\Delta\phi_1$. The decision samples correspond to the transmitted bit sequence, except for the first sample, because it does not have a preceding sample. \square

One can verify that a similar operation can be performed by means of a three-way phase diversity receiver, when the three squarers in Figure 6.7 are replaced by delay-and-multiply circuits, or by constructing signals $V_{\text{I},r}(t)$ and $V_{\text{Q},r}(t)$ from the TIA output signal $V_{r,1}(t)$, $V_{r,2}(t)$ and $V_{r,3}(t)$ as in (6.58) and (6.59) and then carrying out similar operations as described above.

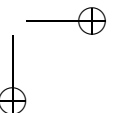
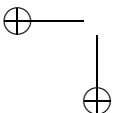
6.4.5 Phase diversity detection of DQPSK and M -ary DPSK

The binary DPSK scheme can be extended to a DQPSK or M -ary DPSK receiver [80] as shown in Figure 6.12, so that it can be used for DQPSK modulation:

$$\phi_{r,k} = \phi_{r,k-1} + (2A_{r,k} + 1)\frac{\pi}{4} \bmod 2\pi, \quad (6.63)$$

or M -ary DPSK modulation:

$$\phi_{r,k} = \phi_{r,k-1} + A_{r,k}\frac{2\pi}{M} \bmod 2\pi. \quad (6.64)$$



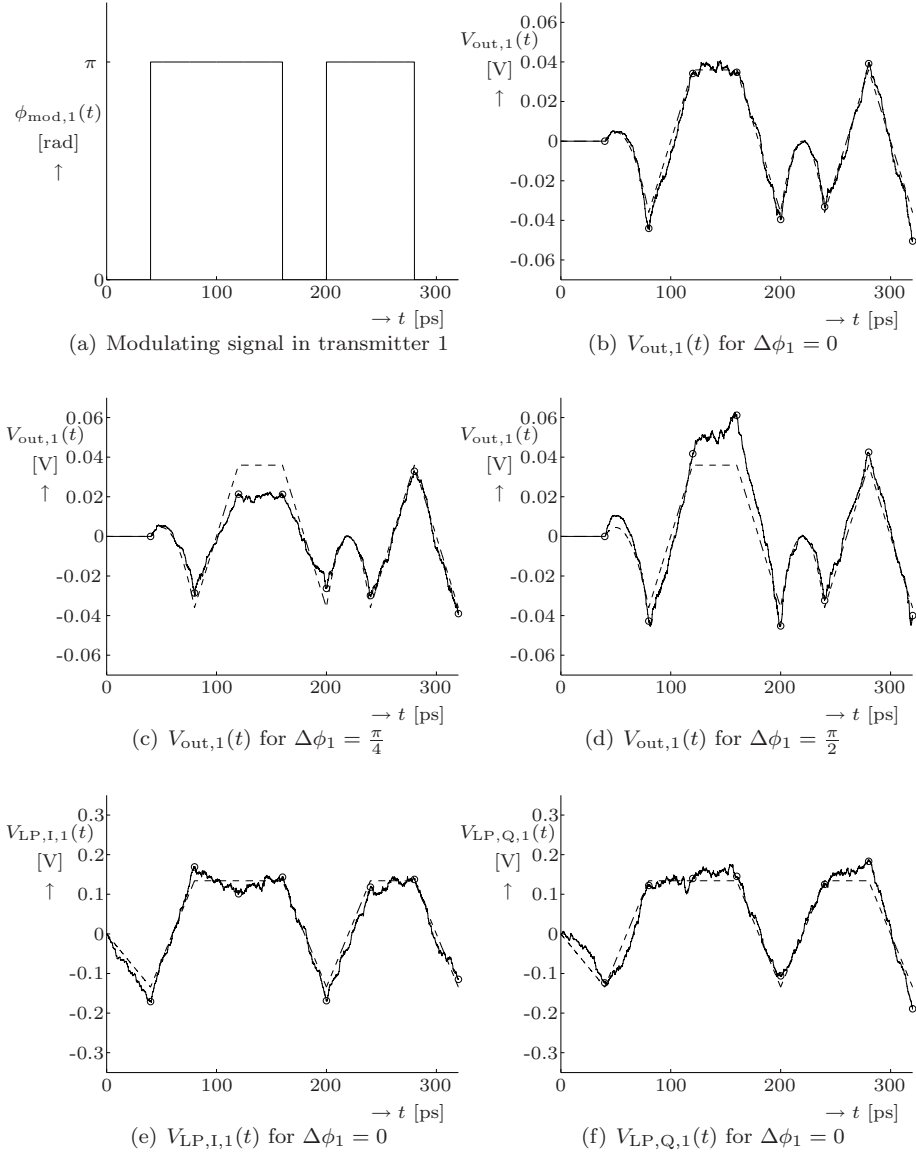


Figure 6.11: Modulating signal in transmitter 1 and simulated output signal $V_{\text{out},1}(t)$ and branch signals $V_{\text{LP},I,1}(t)$ and $V_{\text{LP},Q,1}(t)$ of phase diversity receiver 1 in a 2-channel PA using binary DPSK modulation when a bit pattern '01001101' is transmitted at 25 Gbps, for different values of the phase offset $\Delta\phi_1$

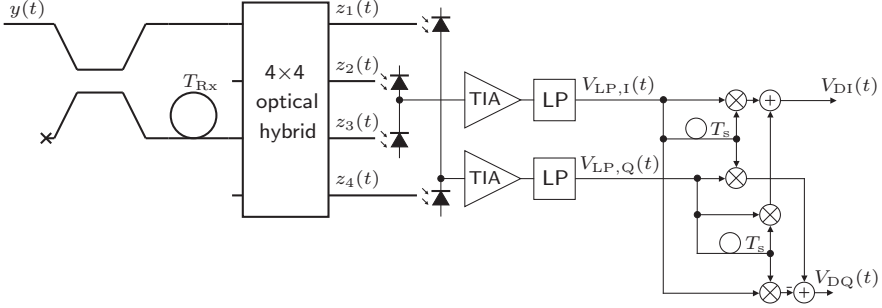


Figure 6.12: A four-way M -ary DPSK phase diversity receiver

Obviously, $V_{DI,r}(t)$ in Figure 6.12 is the same as the output signal $V_{out}(t)$ of the binary DPSK receiver in Figure 6.10, and for $V_{DQ,r}(t)$, one can find

$$\begin{aligned}
 E[V_{DQ,r}(t)] &= E[V_{LP,Q,r}(t)V_{LP,I,r}(t - T_s) - V_{LP,I,r}(t)V_{LP,Q,r}(t - T_s)] \\
 &\approx E[V_{LP,Q,r}(t)]E[V_{LP,I,r}(t - T_s)] - E[V_{LP,I,r}(t)]E[V_{LP,Q,r}(t - T_s)] \\
 &= \frac{Z_{TIA}^2 R_{pd}^2}{16L_{Rx}^2} \text{Im} \left\{ \int_{-\infty}^{\infty} h_{LP}(t - \rho) R_{y^*y}(\rho - T_{Rx,r}, \rho) d\rho \right. \\
 &\quad \left. \cdot \int_{-\infty}^{\infty} h_{LP}(t - T_s - \rho) R_{y^*y}(\rho, \rho - T_{Rx,r}) d\rho \right\}, \quad (6.65)
 \end{aligned}$$

so in case of a PA one can find for the decision samples

$$E[V_{DQ,r}(k T_s)] = \frac{Z_{TIA}^2 R_{pd}^2 P_x^2}{64L_{Tx}^2 L_{Rx}^2 L_{nw}^2} \sin(\phi_{r,k} - \phi_{r,k-1}). \quad (6.66)$$

The transmitted symbols can be extracted in the same way as for the phase-synchronized M -ary PSK receiver.

6.5 Noise performance

In this section the noise performance of the receivers that were described in the previous section will be discussed. Based on analytical expressions for the probability of bit error—which are derived in Appendix B—the maximum bit rate that can be achieved at a bit error rate of 10^{-9} when applied in a PA will be derived. The results for the different receivers will be compared, both to each other and to the results that were obtained for the phase-synchronized balanced receiver in Section 5.2.

6.5.1 Phase diversity detection of OOK

The performance of all the four-way receivers can be derived by first finding the joint probability density function of the output samples of the low-pass filters.

These output samples can then be decorrelated by diagonalizing the covariance matrix of the output samples. This is done in Appendix B.1.

In case of OOK modulation, the conditional probability density functions of the output sample of the receiver can then be found, conditioned on the symbol that is transmitted by the matched transmitter, and the number of interfering transmitters N_1 that is transmitting a binary one. The bit error rate follows by integration and summation over the possible values of N_1 , like in Section 5.2.5. This is done in Appendix B.2; the result is given by

$$P_e \approx \left(\frac{1}{2}\right)^N \sum_{n=0}^{N-1} \binom{N-1}{n} \left[\exp\left(-\frac{\gamma_{\text{OOK},0}(n)}{4}\right) + Q\left(\sqrt{\frac{\gamma_{\text{OOK},1}(n)}{2}}\right) \right], \quad (6.67)$$

where

$$\begin{aligned} \gamma_{\text{OOK},0}(n) = R_{\text{pd}}^2 P_x^2 T_s \left[(4n^2 + 2n) R_{\text{pd}}^2 P_x^2 \tau_c \right. \\ \left. + 32n R_{\text{pd}} P_x L_{\text{Tx}} L_{\text{Rx}} L_{\text{nw}} e + 128 L_{\text{Tx}}^2 L_{\text{Rx}}^2 L_{\text{nw}}^2 S_{\text{th}} \right]^{-1}, \end{aligned} \quad (6.68)$$

$$\begin{aligned} \gamma_{\text{OOK},1}(n) = R_{\text{pd}}^2 P_x^2 T_s \left[(4n^2 + 10n + 7) R_{\text{pd}}^2 P_x^2 \tau_c \right. \\ \left. + 32(n+1) R_{\text{pd}} P_x L_{\text{Tx}} L_{\text{Rx}} L_{\text{nw}} e + 128 L_{\text{Tx}}^2 L_{\text{Rx}}^2 L_{\text{nw}}^2 S_{\text{th}} \right]^{-1}. \end{aligned} \quad (6.69)$$

Now we compare this result to the bit error rate of a phase-synchronized two-way balanced receiver, as given by (5.33). From the expressions for the conditional SNRs $\gamma_{\text{OOK},0}(n)$ and $\gamma_{\text{OOK},1}(n)$ it follows that the four-way OOK phase diversity receiver requires 3 dB more optical power in order to achieve the same conditional SNRs as the two-way balanced OOK receiver, because the optical power is divided over twice as many photodiodes. Even when the received power is very large, however (such that beat noise becomes dominant and the conditional SNRs are nearly the same for the two receivers), the two-way balanced receiver will perform slightly better than the four-way phase diversity receiver, because of the different relations between bit error rate and conditional SNRs. The difference in performance can be quantified by defining the bandwidth efficiency η as the ratio of the total network capacity $N R_b = N/T_s$ and the source bandwidths Δf at which the probability of bit error goes to 10^{-9} for high received powers:

$$\eta \triangleq \frac{N R_b}{\Delta f} \Bigg|_{P_e=10^{-9}, P_x \rightarrow \infty}, \quad (6.70)$$

where the relation between the source bandwidth Δf and the coherence time τ_c is given by (2.30). In Figure 6.13, this has been plotted as a function of the number of channels. Apparently, four-way phase diversity detection introduces only a small degradation in bandwidth efficiency when OOK is used.

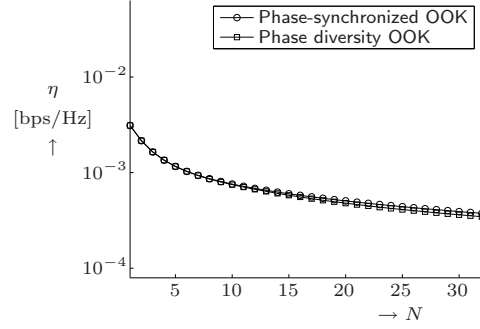


Figure 6.13: Maximum bandwidth efficiency η as a function of the number of channels N for OOK modulation

A similar analysis can be performed for the three-way OOK phase diversity receiver; this is done in Section B.7. The performance of this receiver depends on the way in which it is implemented. In case the photocurrents are amplified before they are subtracted, the bit error rate is given by

$$P_e \approx \left(\frac{1}{2}\right)^N \sum_{n=0}^{N-1} \binom{N-1}{n} \left[\exp\left(-\frac{\gamma_{\text{OOK},0}(n)}{4}\right) + Q\left(\sqrt{\frac{\gamma_{\text{OOK},1}(n)}{2}}\right) \right], \quad (6.71)$$

where

$$\gamma_{\text{OOK},0}(n) = R_{\text{pd}}^2 P_x^2 T_s \left[(4n^2 + 2n) R_{\text{pd}}^2 P_x^2 \tau_c + 32n R_{\text{pd}} P_x L_{\text{Tx}} L_{\text{Rx}} L_{\text{nw}} e + 192 L_{\text{Tx}}^2 L_{\text{Rx}}^2 L_{\text{nw}}^2 S_{\text{th}} \right]^{-1}, \quad (6.72)$$

$$\gamma_{\text{OOK},1}(n) = R_{\text{pd}}^2 P_x^2 T_s \left[(4n^2 + 10n + 7) R_{\text{pd}}^2 P_x^2 \tau_c + 32(n+1) R_{\text{pd}} P_x L_{\text{Tx}} L_{\text{Rx}} L_{\text{nw}} e + 192 L_{\text{Tx}}^2 L_{\text{Rx}}^2 L_{\text{nw}}^2 S_{\text{th}} \right]^{-1}. \quad (6.73)$$

When the photocurrents are first subtracted before amplification, however, the bit error rate is given by

$$P_e \approx Q\left(\sqrt{\frac{\gamma_{\text{OOK},X}}{2}}\right) + \left(\frac{1}{2}\right)^N \sum_{n=0}^N \binom{N-1}{n} \left\{ \sqrt{\frac{\gamma_X}{\gamma_{\text{OOK},X} - \gamma_{\text{OOK},0}(n)}} \exp\left(-\frac{\gamma_{\text{OOK},0}(n)}{4}\right) \cdot \left[1 - 2Q\left(\sqrt{\frac{\gamma_{\text{OOK},X} - \gamma_{\text{OOK},0}(n)}{2}}\right) \right] + Q\left(\sqrt{\frac{\gamma_{\text{OOK},1}(n)}{2}}\right) \right\}, \quad (6.74)$$

where

$$\begin{aligned} \gamma_{\text{OOK},0}(n) = R_{\text{pd}}^2 P_x^2 T_s \left[(4n^2 + 2n) R_{\text{pd}}^2 P_x^2 \tau_c \right. \\ \left. + 32n R_{\text{pd}} P_x L_{\text{Tx}} L_{\text{Rx}} L_{\text{nw}} e + 64L_{\text{Tx}}^2 L_{\text{Rx}}^2 L_{\text{nw}}^2 S_{\text{th}} \right]^{-1}, \end{aligned} \quad (6.75)$$

$$\begin{aligned} \gamma_{\text{OOK},1}(n) = R_{\text{pd}}^2 P_x^2 T_s \left[(4n^2 + 10n + 7) R_{\text{pd}}^2 P_x^2 \tau_c \right. \\ \left. + 32(n+1) R_{\text{pd}} P_x L_{\text{Tx}} L_{\text{Rx}} L_{\text{nw}} e + 64L_{\text{Tx}}^2 L_{\text{Rx}}^2 L_{\text{nw}}^2 S_{\text{th}} \right]^{-1}, \end{aligned} \quad (6.76)$$

$$\gamma_{\text{OOK},\text{X}}(n) = \frac{R_{\text{pd}}^2 P_x^2 T_s}{64L_{\text{Tx}}^2 L_{\text{Rx}}^2 L_{\text{nw}}^2 S_{\text{th}}}. \quad (6.77)$$

(Note that this is the same as (6.71) when thermal noise is neglected, so when $S_{\text{th}} = 0$.) By comparing the two expressions for the bit error probability (for the cases of amplification prior to balancing and amplification after balancing) to the corresponding expression (6.67) that was found for the four-way phase diversity receiver, one can conclude the following:

- When the thermal receiver noise can be neglected with respect to source-induced noise and shot noise, the performance of the three-way and four-way OOK phase diversity receivers are the same. (Hence, they have the same bandwidth efficiency; see Figure 6.13.)
- When the thermal receiver noise is dominating, the three-way OOK phase diversity receiver with amplification prior to balancing requires approximately 0.9 dB more optical power than the four-way OOK phase diversity receiver in order to achieve the same performance (provided that the same amplifiers are used in both cases). The three-way OOK receiver with amplification after balancing requires 1.5 dB less than the four-way OOK receiver, however.

Example 6.4

Now consider a numerical example of a CM system based on a PA with 16 OOK-modulated transmitters and 16 phase diversity receivers, with the same parameter values as in Example 5.4. Using the formulas that were derived in this section, the maximum bit rates for a bit error rate of 10^{-9} as a function of the number of active channels N can be found for the different receivers that were considered. The results are shown in Figure 6.14.

As expected, phase-synchronized OOK results in the highest achievable bit rate, partly because phase-synchronized detection results in a slightly higher bandwidth efficiency (see Figure 6.13), but mainly because the two-way balanced receiver has a lower insertion loss than the phase diversity receivers. The comparison of the remaining results corresponds to the reasoning above. \square

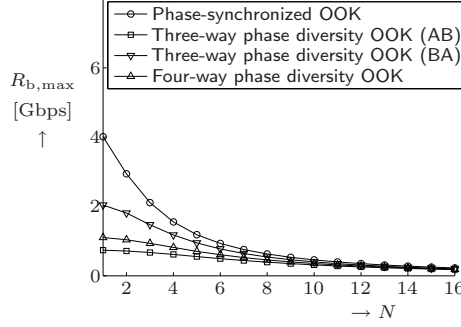


Figure 6.14: Maximum bit rate per channel R_b as a function of the number of active channels N in a PA with 16 transmitters and receivers and OOK modulation (AB=amplification prior to balancing, BA=amplification after balancing)

6.5.2 Four-way detection of (D)PSK

Several four-way receivers for detecting PSK and DPSK modulated signals were described in the previous section. In this subsection their performances will be compared.

The performance of the four-way phase-synchronized QPSK receiver is derived in Section B.3 and is given by

$$P_e = Q(\sqrt{\gamma_{\text{QPSK}}}), \quad (6.78)$$

where

$$\gamma_{\text{QPSK}} = \left(\gamma_{\text{sn}}^{-1} + \gamma_{\text{bn}}^{-1} + \gamma_{\text{tn}}^{-1} \right)^{-1},$$

and

$$\gamma_{\text{sn}} = \frac{R_{\text{pd}} P_x T_s}{32N L_{\text{Tx}} L_{\text{Rx}} L_{\text{nw}} e}, \quad (6.79)$$

$$\gamma_{\text{bn}} = \frac{T_s}{(4N^2 + 2N)\tau_c}, \quad (6.80)$$

$$\gamma_{\text{tn}} = \frac{R_{\text{pd}}^2 P_x^2 T_s}{128L_{\text{Tx}}^2 L_{\text{Rx}}^2 L_{\text{nw}}^2 S_{\text{th}}}. \quad (6.81)$$

Note that for the same bit rate R_b , the symbol time T_s in case of QPSK modulation is twice as large as the symbol time in case of BPSK modulation. Hence, when we compare (6.78) to the bit error rate of a phase-synchronized two-way balanced receiver, as given by (5.23), it can be concluded that the four-way QPSK receiver theoretically requires almost 3 dB more optical power in order to achieve the same performance at the same bit rate, because the

optical power is divided over twice as many photo detectors. In practice this will be more than 3 dB, however, because the four-way QPSK receiver is likely to have a larger excess loss L_{R_x} than the two-way receiver, since an MMI is used instead of a directional coupler.

The bit error rate is equal to 10^{-9} when $\gamma_{\text{QPSK}} \approx 36$. Hence, the bit rate that can be achieved at a bit error rate of 10^{-9} is given by

$$R_b = \frac{2}{T_s} \approx \frac{1}{18} R_{\text{pd}}^2 P_x^2 \left[(4N^2 + 2N) R_{\text{pd}}^2 P_x^2 \tau_c + 32N R_{\text{pd}} P_x L_{T_x} L_{R_x} L_{\text{nw}} e + 128 L_{T_x}^2 L_{R_x}^2 L_{\text{nw}}^2 S_{\text{th}} \right]^{-1}. \quad (6.82)$$

The bandwidth efficiencies of the two receivers are shown in Figure 6.15, and turn out to be nearly the same, since they have nearly the same signal-to-beat noise ratio γ_{bn} . In Chapter 7 it will be shown that QPSK is less susceptible to chromatic dispersion, due to the larger symbol time T_s .

For the four-way phase-synchronized M -ary PSK receiver with $M \geq 8$, an approximation for the symbol error rate for large SNRs is derived in Section B.4. In case of Gray coding this results in a bit error probability that is given by

$$P_e \approx \frac{2}{m} Q \left(\sqrt{2\gamma_{\text{MPSK}}} \sin \left(\frac{\pi}{M} \right) \right), \quad (6.83)$$

where

$$\gamma_{\text{MPSK}} = \left(\gamma_{\text{sn}}^{-1} + \gamma_{\text{bn}}^{-1} + \gamma_{\text{tn}}^{-1} \right)^{-1}, \quad (6.84)$$

and

$$\gamma_{\text{sn}} = \frac{R_{\text{pd}} P_x T_s}{32N L_{T_x} L_{R_x} L_{\text{nw}} e}, \quad (6.85)$$

$$\gamma_{\text{bn}} = \frac{T_s}{(4N^2 + 2N - 1) \tau_c}, \quad (6.86)$$

$$\gamma_{\text{tn}} = \frac{R_{\text{pd}}^2 P_x^2 T_s}{128 L_{T_x}^2 L_{R_x}^2 L_{\text{nw}}^2 S_{\text{th}}}. \quad (6.87)$$

The bit error rate for 8-PSK is equal to 10^{-9} when $\gamma_{\text{MPSK}} \approx 120$. Hence, the bit rate that can be achieved at a bit error rate of 10^{-9} is given by

$$R_b = \frac{3}{T_s} \approx \frac{1}{40} R_{\text{pd}}^2 P_x^2 \left[(4N^2 + 2N - 1) R_{\text{pd}}^2 P_x^2 \tau_c + 32N R_{\text{pd}} P_x L_{T_x} L_{R_x} L_{\text{nw}} e + 128 L_{T_x}^2 L_{R_x}^2 L_{\text{nw}}^2 S_{\text{th}} \right]^{-1}, \quad (6.88)$$

which is obviously lower than the bit rate that can be achieved with QPSK, so it also has a lower bandwidth efficiency: see Figure 6.15. 8-PSK has a longer symbol time T_s than QPSK, however, so 8-PSK could be better than QPSK in systems where dispersion plays a significant role.

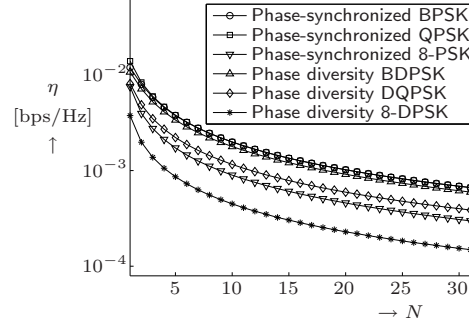


Figure 6.15: Maximum bandwidth efficiency η as a function of the number channels N for (D)PSK modulation

The bit error rate for binary DPSK transmission is derived in Section B.5 and can be approximated as

$$P_e \approx \frac{1}{2} \exp(-\gamma_{\text{BDPSK}}), \quad (6.89)$$

where

$$\gamma_{\text{BDPSK}} = \left(\gamma_{\text{sn}}^{-1} + \gamma_{\text{bn}}^{-1} + \gamma_{\text{tn}}^{-1} \right)^{-1}, \quad (6.90)$$

and

$$\gamma_{\text{sn}} = \frac{R_{\text{pd}} P_x T_s}{32N L_{\text{Tx}} L_{\text{Rx}} L_{\text{nw}} e}, \quad (6.91)$$

$$\gamma_{\text{bn}} = \frac{T_s}{(4N^2 + 2N + 1)\tau_c}, \quad (6.92)$$

$$\gamma_{\text{tn}} = \frac{R_{\text{pd}}^2 P_x^2 T_s}{128L_{\text{Tx}}^2 L_{\text{Rx}}^2 L_{\text{nw}}^2 S_{\text{th}}}. \quad (6.93)$$

This bit error rate is equal to 10^{-9} when $\gamma_{\text{BDPSK}} = -\ln(2 \cdot 10^{-9}) \approx 20$. The corresponding bit rate is given by

$$R_b = \frac{1}{T_s} \approx \frac{1}{20} R_{\text{pd}}^2 P_x^2 \left[(4N^2 + 2N + 1) R_{\text{pd}}^2 P_x^2 \tau_c + 32N R_{\text{pd}} P_x L_{\text{Tx}} L_{\text{Rx}} L_{\text{nw}} e + 128L_{\text{Tx}}^2 L_{\text{Rx}}^2 L_{\text{nw}}^2 S_{\text{th}} \right]^{-1}. \quad (6.94)$$

When this is compared to (5.24) one can conclude that the achievable bit rate for binary DPSK transmission is approximately 10% lower than for binary PSK transmission when beat noise dominates (this also follows from Figure 6.15), and approximately 78% lower when thermal noise dominates.

The bit error rate for DQPSK transmission is derived in Section B.6 and can be approximated as

$$P_e \approx \frac{1}{2} \exp(-\gamma_{\text{DQPSK}}) \left[I_0 \left(\frac{\gamma_{\text{DQPSK}}}{\sqrt{2}} \right) + 2 \sum_{n=1}^{\infty} (\sqrt{2} - 1)^n I_n \left(\frac{\gamma_{\text{DQPSK}}}{\sqrt{2}} \right) \right], \quad (6.95)$$

where $I_n(\cdot)$ is the modified Bessel function of the first kind and order n :

$$I_n(x) \triangleq \frac{1}{2\pi} \int_0^{2\pi} \exp(x \cos \theta) \cos(n\theta) d\theta, \quad n \in \mathbb{Z}, \quad (6.96)$$

and

$$\gamma_{\text{DQPSK}} = \left(\gamma_{\text{sn}}^{-1} + \gamma_{\text{bn}}^{-1} + \gamma_{\text{tn}}^{-1} \right)^{-1}, \quad (6.97)$$

where

$$\gamma_{\text{sn}} = \frac{R_{\text{pd}} P_x T_s}{32N L_{\text{Tx}} L_{\text{Rx}} L_{\text{nw}} e}, \quad (6.98)$$

$$\gamma_{\text{bn}} = \frac{T_s}{(4N^2 + 2N)\tau_c}, \quad (6.99)$$

$$\gamma_{\text{tn}} = \frac{R_{\text{pd}}^2 P_x^2 T_s}{128L_{\text{Tx}}^2 L_{\text{Rx}}^2 L_{\text{nw}}^2 S_{\text{th}}}. \quad (6.100)$$

This bit error rate is equal to 10^{-9} when $\gamma_{\text{DQPSK}} \approx 62$. The corresponding bit rate is given by

$$R_b = \frac{2}{T_s} \approx \frac{1}{31} R_{\text{pd}}^2 P_x^2 \left[(4N^2 + 2N) R_{\text{pd}}^2 P_x^2 \tau_c + 32N R_{\text{pd}} P_x L_{\text{Tx}} L_{\text{Rx}} L_{\text{nw}} e + 128L_{\text{Tx}}^2 L_{\text{Rx}}^2 L_{\text{nw}}^2 S_{\text{th}} \right]^{-1}. \quad (6.101)$$

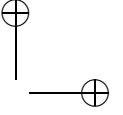
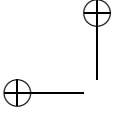
This is approximately 42% lower than the result for phase-synchronized QPSK. The corresponding bandwidth efficiency is shown in Figure 6.15.

M -ary DPSK detection requires approximately 3 dB more SNR in order to achieve the same bit error probability as M -ary PSK [81]. Hence, the bit error rate for M -ary DPSK with Gray coding is given by

$$P_e \approx \frac{2}{m} Q \left(\sqrt{\gamma_{\text{MDPSK}}} \sin \left(\frac{\pi}{M} \right) \right). \quad (6.102)$$

where

$$\gamma_{\text{MDPSK}} = \left(\gamma_{\text{sn}}^{-1} + \gamma_{\text{bn}}^{-1} + \gamma_{\text{tn}}^{-1} \right)^{-1}, \quad (6.103)$$



and

$$\gamma_{\text{sn}} = \frac{R_{\text{pd}} P_x T_s}{32N L_{\text{Tx}} L_{\text{Rx}} L_{\text{nw}} e}, \quad (6.104)$$

$$\gamma_{\text{bn}} = \frac{T_s}{(4N^2 + 2N - 1)\tau_c}, \quad (6.105)$$

$$\gamma_{\text{tn}} = \frac{R_{\text{pd}}^2 P_x^2 T_s}{128L_{\text{Tx}}^2 L_{\text{Rx}}^2 L_{\text{nw}}^2 S_{\text{th}}}. \quad (6.106)$$

The bit error rate for 8-DPSK is equal to 10^{-9} when $\gamma_{\text{MDPSK}} \approx 240$. Hence, the bit rate that can be achieved at a bit error rate of 10^{-9} is given by

$$R_b = \frac{3}{T_s} \approx \frac{1}{80} R_{\text{pd}}^2 P_x^2 \left[(4N^2 + 2N - 1) R_{\text{pd}}^2 P_x^2 \tau_c + 32N R_{\text{pd}} P_x L_{\text{Tx}} L_{\text{Rx}} L_{\text{nw}} e + 128L_{\text{Tx}}^2 L_{\text{Rx}}^2 L_{\text{nw}}^2 S_{\text{th}} \right]^{-1}, \quad (6.107)$$

which is 50% lower than the result for phase-synchronized detection of 8-PSK, and 61% lower than the result for phase diversity detection of DQPSK. Also see Figure 6.15 for the bandwidth efficiency.

Example 6.5

Again consider an example of a CM system like in Example 6.4, but now with (D)PSK modulation instead of OOK modulation. Using the formulas that were derived in this section, the maximum bit rates for a bit error rate of 10^{-9} as a function of the number of active channels N can be calculated for the different receivers that have been considered. The corresponding results are shown in Figure 6.16(a).

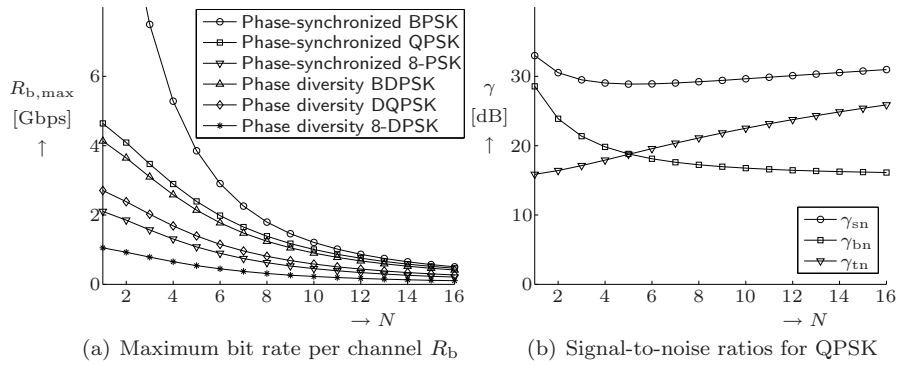
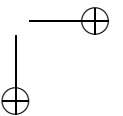
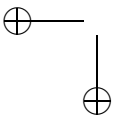
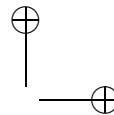
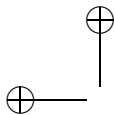



Figure 6.16: Maximum bit rate per channel R_b and corresponding signal-to-noise ratios as a function of number of active channels N in a PA with 16 transmitters and receivers and (D)PSK modulation





Comparing this figure to Figure 6.15, the relatively large difference between phase-synchronized BPSK and QPSK in Figure 6.16(a) seems surprising. It can be explained by the larger loss that is introduced by the four-way MMI in the QPSK receiver, hence causing a relatively lower signal-to-thermal noise ratio. This is illustrated in Figure 6.16(b), where the SNRs are plotted as a function of N for QPSK modulation.

When we compare this to Figure 5.4(b), it is obvious that the thermal noise plays a relatively large role in the phase-synchronized QPSK receiver, especially for a low number of active channels N . 

6.6 Practical considerations

In this section we will comment on some assumptions that have been made with respect to the optical phase diversity couplers and the balanced receivers. Some practical aspects are considered that actually differ for the three-way and four-way receiver.

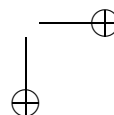
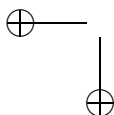
6.6.1 Phase diversity couplers

In the analysis in the previous sections the 3×3 and 4×4 optical phase diversity couplers were simply assumed to be both wavelength and polarization independent, and to have input signals that all have the same polarization state. This is expressed by their transfer matrices in (6.12) and (6.37). In practice this is not so straightforward, however.

The advantage of the three-way phase diversity receiver over the four-way phase diversity receiver is that a 3×3 directional coupler can be fabricated very easily, simply by fusing three fibers. The 4×4 coupler has to be fabricated either as an integrated optical device or as an all-fiber hybrid that requires very strict tuning [83]. Therefore, the three-way receiver is more suitable for experimental prototyping purposes. The disadvantage of a fiber setup, however, is that a polarization controller is required for matching the polarization states of the interfering light waves, which is not desirable in a final product.

The advantage of using either a 3×3 or 4×4 MMI as a phase diversity coupler is that the entire optical interferometer can be realized as a planar optical integrated circuit, hence maintaining polarization states without the need of a polarization controller.

Yet this MMI still needs to be both wavelength and polarization independent in order to provide phase diversity with uniform power splitting. This is a typical device design issue, however, and has not been studied in further detail. In case one would only manage to design phase diversity couplers that are wavelength independent but not polarization independent, a possible solution would be to construct a so-called polarization diversity receiver like in Figure 6.17 [49].



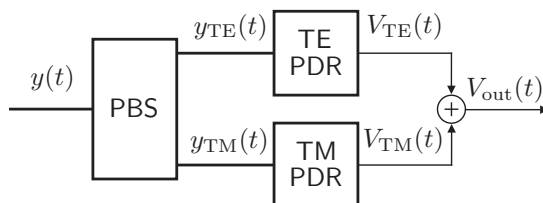


Figure 6.17: A polarization diversity receiver (PBS=polarization beam splitter, PDR=phase diversity receiver)

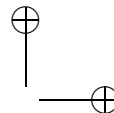
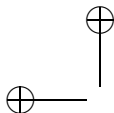
The idea of such a receiver is that the received optical signal is split in a transverse electric (TE) mode and a transverse magnetic (TM) mode, which are demodulated by a TE- and a TM-optimized phase diversity receiver, respectively. (Or alternatively, the TM-optimized phase diversity receiver can be replaced by a polarization converter and another TE-optimized phase diversity receiver.) When the difference in polarization angle between the received optical signal and the TE mode is denoted by Ψ , then one can verify that the output signal of the TE-receiver is approximately proportional to $\cos^2 \Psi$ and the output of the TM-receiver is approximately proportional to $\sin^2 \Psi$. Hence, summing the two output signals will result in a signal that does not depend on Ψ . The performance of such a receiver will be worse than that of a single polarization independent phase diversity receiver, however, because it introduces more thermal noise.

Note that the phase diversity couplers that are considered in this chapter have a higher splitting loss than a 2×2 directional coupler. Hence, when a phase diversity receiver is used in a duplex link where the interferometers are used both as encoding and decoding devices, the performance will be worse than predicted in this chapter.

6.6.2 Balancing

A particular advantage of the four-way phase diversity receiver is that the balanced currents can simply be obtained by two distinct balanced receivers, whereas in the three-way receiver, these have to be obtained either by a circular balancing circuit or by three differential amplifiers. The circular balancing circuit has the problem that the circular configuration conflicts with the requirement of operating the photodiodes in reverse-bias mode, whereas the other solution has the problem that differential amplifiers with very high common-mode rejection ratios (CMRRs) are required, which is particularly difficult at high frequencies.

As explained in Subsection 4.8.3, balancing can be simplified when DPSK modulation is used instead of OOK modulation, so that AC-coupled amplification can be performed instead of DC-coupled amplification.



6.7 Conclusions

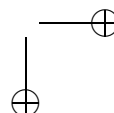
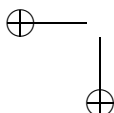
It has been shown both analytically and by simulation that the output signal of a coherence multiplex receiver can be stabilized by means of a phase diversity network. The advantage of this configuration is that neither an external feedback loop nor a frequency shifter is required, resulting in less complicated -and hence potentially less expensive- receiver units.

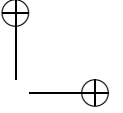
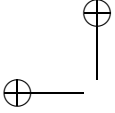
Performance figures for several receiver types (two-way phase-synchronized balanced detection and three-way and four-way balanced phase diversity detection) and several modulation formats (OOK, PSK and DPSK) were derived analytically, showing that phase diversity detection introduces only a minor performance degradation with respect to two-way balanced detection, as long as the received optical power is large such that thermal receiver noise is negligible.

However, numerical examples with networks consisting of 16 transmission units have shown that the inherent increase in splitting loss in a phase diversity coupler significantly decreases the detector performance due to thermal receiver noise. Binary (D)PSK modulation results in the best performance, provided that the effect of chromatic fiber dispersion is negligible. The performances of the three-way and four-way phase diversity receivers are similar, as long as the noise in the receivers is dominated either by beat noise or shot noise. When thermal receiver noise dominates, however, the performance of the three-way receiver differs from the performance of the four-way receiver, depending on the order of the balancing operation and amplification. If balancing were performed prior to amplification, the three-way receiver would require approximately 1.5 dB less optical power than the four-way receiver in order to obtain the same performance. Proper balancing of the photodiodes in the three-way receiver would be achieved in a much easier way, however, if the order of balancing and amplification were reversed. Unfortunately, this would boost the required optical power by up to 2.4 dB.

A remaining issue in designing optically integrated phase diversity receivers for CM is yet to design wavelength and polarization independent MMIs. The need for polarization independence can be avoided by constructing a polarization diversity receiver, but this will degrade the performance.

The results that have been described in this chapter were published in *Journal of Lightwave Technology* [84], and were presented in parts at several symposia [77, 78, 80, 82].





Chapter 7

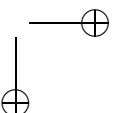
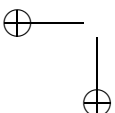
Chromatic fiber dispersion

7.1 Introduction

In the analyses in the previous three chapters the influence of the transmission fiber had been completely ignored. The results had in common that they suggested that the performance would improve when the coherence time τ_c of the optical sources were decreased, or in other words, when the bandwidth of the optical source signals were increased. The reason for this is that the bandwidth of the beat noise after photodetection scales with the bandwidth of the optical signals, so that its total power is distributed over a larger frequency range when τ_c is decreased, hence resulting in a lower noise power spectral density in the baseband, where the information signal is located.

In practice there is a limit to this, however, since the performance of CM systems is degraded by the chromatic dispersion (CD) of the transmission fiber. CD means that the different spectral components of the transmitted optical signal travel at different propagation speeds and hence arrive at the receiver at different time instants, resulting in a distorted receiver output signal. The spread in propagation speed increases with increasing optical bandwidth, so that the distortion increases with decreasing coherence time. Therefore, choosing the coherence time of the optical sources becomes a trade-off between achieving a low beat noise power spectral density and achieving little distortion due to CD.

In this chapter the effect of CD on transmission in CM systems will be studied in further detail. First, expressions will be derived that relate the expected value and autocorrelation function of the output signal of a CM receiver to the modulating signals and the fiber parameters. Then the specific impact of CD on the performance of non-equalized digital transmission through CM will be studied for several modulation formats. The chapter will end with conclusions.



7.2 Impact of chromatic dispersion on receiver output signal

For simplicity, consider a CM system with only one transmitter and receiver, connected by a single-mode fiber (SMF) of length l_f , as shown in Figure 7.1.

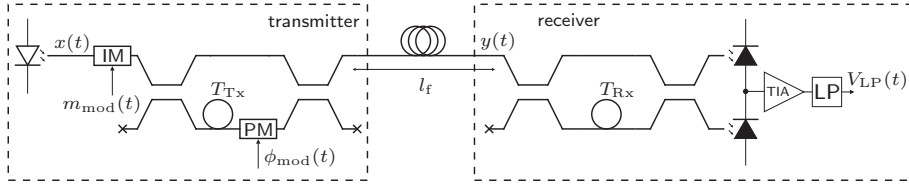


Figure 7.1: CM system with one transmitter and one (balanced) receiver and fiber length l_f

The output signal of the receiver can be found by following a similar approach as done in Chapter 4, and adding a few steps to incorporate the effect of CD. The approach is in a sense analogous to the one that Gimlett and Cheung introduced in order to find the output signal of an IM/DD link with an LED and SMF [85].

7.2.1 Input signal of the receiver

The input signal of the receiver $y(t)$ is obtained by convolving the output signal of the transmitter (4.12) with the impulse response of the fiber $h_f(t)$, resulting in

$$y(t) = \frac{1}{2\sqrt{L_{Tx}}} \int_{-\infty}^{\infty} h_f(\rho) \left[x(t - \rho) \sqrt{m_{\text{mod}}(t - \rho)} - x(t - \rho - T_{Tx}) \sqrt{m_{\text{mod}}(t - \rho - T_{Tx})} \exp(j\phi_{\text{mod}}(t - \rho)) \right] d\rho. \quad (7.1)$$

The impulse response $h_f(t)$ can be found by calculating the inverse Fourier transform of the transfer function $H_f(f)$ of the fiber. Using (2.44) this results in

$$h_f(t) = \int_{-\infty}^{\infty} |H_f(f)| \exp(j2\pi f t - j\beta(f)l_f) df. \quad (7.2)$$

where $\beta(f)$ denotes the phase change per unit length (in rad/m).

The autocorrelation function of $y(t)$ now follows as

$$\begin{aligned}
R_{y^*y}(t_1, t_2) &\triangleq \text{E}[y^*(t_1)y(t_2)] \\
&\approx \frac{1}{4L_{\text{Tx}}} \int_{-\infty}^{\infty} \int_{-\infty}^{\infty} h_f(\rho_1)h_f(\rho_2)m_{\text{mod}}(t_1 - \rho_1) \left[2R_{x^*x}(t_2 - t_1 + \rho_1 - \rho_2) \right. \\
&\quad - R_{x^*x}(t_2 - t_1 + \rho_1 - \rho_2 - T_{\text{Tx}}) \exp(j\phi_{\text{mod}}(t_1 - \rho_1)) \\
&\quad \left. - R_{x^*x}(t_2 - t_1 + \rho_1 - \rho_2 + T_{\text{Tx}}) \exp(-j\phi_{\text{mod}}(t_1 - \rho_1)) \right] d\rho_1 d\rho_2, \quad (7.3)
\end{aligned}$$

where it has been assumed that the bandwidths of $m_{\text{mod}}(t)$ and $\phi_{\text{mod}}(t)$ are much smaller than $1/T_{\text{Tx}}$ and $1/\tau_c$. Using (7.2), denoting the modulating signals as

$$m_{\text{mod}}(t) = \int_{-\infty}^{\infty} M_{\text{mod}}(f) \exp(j2\pi f t) df, \quad (7.4)$$

$$\exp(j\phi_{\text{mod}}(t)) \triangleq s_{\text{mod}}(t) = \int_{-\infty}^{\infty} S_{\text{mod}}(f) \exp(j2\pi f t) df, \quad (7.5)$$

writing the autocorrelation function $R_{x^*x}(\tau)$ as the inverse Fourier transform of the power spectral density function $S_{x^*x}(f)$, and applying some Fourier transform properties, (7.3) becomes

$$\begin{aligned}
R_{y^*y}(t_1, t_2) &= \frac{1}{4L_{\text{Tx}}} \int_{-\infty}^{\infty} \int_{-\infty}^{\infty} |H_f(f_2 - f_1)| \cdot |H_f(f_2)| S_{x^*x}(f_2) \\
&\quad \cdot \exp(j\beta(f_2 - f_1) - j\beta(f_2) + j2\pi[(f_1 - f_2)t_1 + f_2 t_2]) \\
&\quad \cdot \left[2M_{\text{mod}}(f_1) - \exp(-j2\pi f_2 T_{\text{Tx}}) \int_{-\infty}^{\infty} M_{\text{mod}}(f_3) S_{\text{mod}}(f_1 - f_3) df_3 \right. \\
&\quad \left. - \exp(j2\pi f_2 T_{\text{Tx}}) \int_{-\infty}^{\infty} M_{\text{mod}}(f_3) S_{\text{mod}}^*(f_3 - f_1) df_3 \right] df_1 df_2. \quad (7.6)
\end{aligned}$$

The widths of $M_{\text{mod}}(f)$ and $S_{\text{mod}}(f)$ are much smaller than the width of $S_{x^*x}(f)$, so the integral over f_1 is mainly determined by the contribution in the range where f_1 is much less than the width of $S_{x^*x}(f)$. Hence, when $H_f(f)$ is a smooth function inside the frequency range of the source, we can approximate

$$|H_f(f_2 - f_1)| \approx |H_f(f_2)|, \quad (7.7)$$

$$\beta(f_2 - f_1) \approx \beta(f_2) - f_1\beta'(f_2) = \beta(f_2) - 2\pi f_1\tau_g(f_2), \quad (7.8)$$

where $\tau_g(f)$ is the group delay per unit length, which is defined by (2.47).

As a result, (7.6) becomes

$$\begin{aligned}
R_{y^*y}(t_1, t_2) &\approx \frac{1}{4L_{\text{Tx}}} \int_{-\infty}^{\infty} |H_f(f_2)|^2 S_{x^*x}(f_2) \exp(j 2\pi f_2(t_2 - t_1)) \\
&\cdot \int_{-\infty}^{\infty} \exp(j 2\pi f_1[t_1 - \tau_g(f_2)]) \\
&\cdot \left[2M_{\text{mod}}(f_1) - \exp(-j 2\pi f_2 T_{\text{Tx}}) \int_{-\infty}^{\infty} M_{\text{mod}}(f_3) S_{\text{mod}}(f_1 - f_3) df_3 \right. \\
&\quad \left. - \exp(j 2\pi f_2 T_{\text{Tx}}) \int_{-\infty}^{\infty} M_{\text{mod}}(f_3) S_{\text{mod}}^*(f_3 - f_1) df_3 \right] df_1 df_2 \\
&= \frac{1}{4L_{\text{Tx}}} \int_{-\infty}^{\infty} |H_f(f)|^2 S_{x^*x}(f) m_{\text{mod}}(t_1 - l_f \tau_g(f)) \left[2 \exp(j 2\pi f(t_2 - t_1)) \right. \\
&\quad \left. - \exp(j 2\pi f(t_2 - t_1 - T_{\text{Tx}}) + j \phi_{\text{mod}}(t_1 - l_f \tau_g(f))) \right. \\
&\quad \left. - \exp(j 2\pi f(t_2 - t_1 + T_{\text{Tx}}) - j \phi_{\text{mod}}(t_1 - l_f \tau_g(f))) \right] df. \quad (7.9)
\end{aligned}$$

(Note that this expression reduces to (4.13) when $l_f = 0$.)

7.2.2 Expected value of the output signal of the receiver

The expected output signal of a two-way balanced receiver can be found by substituting (7.9) into the first line of (4.45). Assuming that both T_{Tx} and T_{Rx} are much larger than τ_c this results in

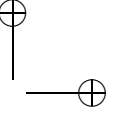
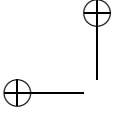
$$\begin{aligned}
E[V_{\text{LP}}(t)] &\approx \\
&\frac{Z_{\text{TIA}} R_{\text{pd}} P_x}{8L_{\text{Tx}} L_{\text{Rx}}} \int_{-\infty}^{\infty} h_{\text{LP}}(t - \rho) \int_{-\infty}^{\infty} |H_f(f)|^2 S_{x^*x}(f) m_{\text{mod}}(\rho - l_f \tau_g(f)) \\
&\quad \cdot \cos(2\pi f(T_{\text{Rx}} - T_{\text{Tx}}) + \phi_{\text{mod}}(\rho - l_f \tau_g(f))) df d\rho. \quad (7.10)
\end{aligned}$$

Obviously, CD does not influence the observability of the CM channels: a channel is still suppressed when $|T_{\text{Rx}} - T_{\text{Tx}}| \gg \tau_c$, and selected when $T_{\text{Rx}} = T_{\text{Tx}}$. In the latter case (so when the balanced receiver is matched and phase-synchronized to the transmitter) we find

$$\begin{aligned}
E[V_{\text{LP}}(t)] &\approx \frac{Z_{\text{TIA}} R_{\text{pd}}}{4L_{\text{Tx}} L_{\text{Rx}}} \int_{-\infty}^{\infty} h_{\text{LP}}(t - \rho) \int_{-\infty}^{\infty} |H_f(f)|^2 S_{x^*x}(f) \\
&\quad \cdot m_{\text{mod}}(\rho - l_f \tau_g(f)) \cos(\phi_{\text{mod}}(\rho - l_f \tau_g(f))) df d\rho. \quad (7.11)
\end{aligned}$$

This can be expressed into the result that would be obtained for $l_f = 0$ as

$$E[V_{\text{LP}}(t)] \approx \frac{1}{2P_x} \int_{-\infty}^{\infty} |H_f(f)|^2 S_{x^*x}(f) E[V_{\text{LP}, l_f=0}(t - l_f \tau_g(f))] df. \quad (7.12)$$



Note that this is an intuitively appealing result: the output signal is a (continuous) sum of time-shifted versions of the output signal that would be obtained for $l_f = 0$, where the time shifts are determined by the group delay as a function of frequency and the power spectral density of the optical carrier signal acts as a weighting function. (Refer to Figure 2.5(b) for typical graphs of the group delay and optical power spectral density as functions of frequency.)

Although this result has been derived for a single-channel CM system with a two-way balanced receiver, it can be verified that it also applies to any of the multiplexing topologies that have been considered in Chapter 5 (this follows from linearity considerations), and also to the output signals of the low-pass filters of the three-way and four-way balanced receivers that have been considered in Chapter 6 (this follows by substituting (7.9) in (6.31), (6.32) and (6.50) through (6.52)).

In case of LED sources, $S_{x^*x}(f)$ is given by (2.29). Moreover, in the frequency range of the optical signal we can use (2.45), so that we can approximate

$$|H_f(f)| \approx |H_f(f_c)| . \tag{7.13}$$

The group delay can be approximated by either a first or second order Taylor series, depending on the center wavelength of the optical signal, as described in Section 2.5.2. Obviously, the most general result is obtained when the second order Taylor series is used, which is given by (2.49). Substituting (2.29), (7.13) and (2.49) in (7.12) and then substituting $\nu = f - f_c$ results in

$$\begin{aligned} E[V_{LP}(t)] \approx & \sqrt{2}\tau_c |H_f(f_c)|^2 \int_{-\infty}^{\infty} \exp(-2\pi \nu^2 \tau_c^2) \\ & \cdot E \left[V_{LP, l_f=0} \left(t - l_f [\tau_g(f_c) + \tau'_g(f_c)\nu + \frac{1}{2}\tau''_g(f_c)\nu^2] \right) \right] d\nu . \end{aligned} \tag{7.14}$$

This expression can be written in the form of a convolution by making a substitution

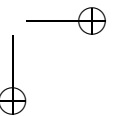
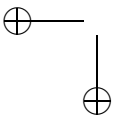
$$\rho = l_f [\tau_g(f_c) + \tau'_g(f_c)\nu + \frac{1}{2}\tau''_g(f_c)\nu^2] . \tag{7.15}$$

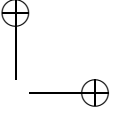
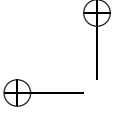
The inverse of this transformation has two solutions $\nu_1(\rho)$ and $\nu_2(\rho)$ that are given by

$$\nu_{1,2}(\rho) = -\frac{\tau'_g(f_c)}{\tau''_g(f_c)} \pm \sqrt{\left(\frac{\tau'_g(f_c)}{\tau''_g(f_c)}\right)^2 + \frac{2(\rho - l_f\tau_g(f_c))}{l_f\tau''_g(f_c)}} . \tag{7.16}$$

If we first assume that $\tau''_g(f_c) \geq 0$ (we will come back to the other case later), (7.14) can now be written as

$$\begin{aligned} E[V_{LP}(t)] \approx & \sqrt{2}\tau_c |H_f(f_c)|^2 \int_{\rho_0}^{\infty} \left[\nu'_1(\rho) \exp(-2\pi \nu_1^2(\rho)\tau_c^2) \right. \\ & \left. - \nu'_2(\rho) \exp(-2\pi \nu_2^2(\rho)\tau_c^2) \right] E[V_{LP, l_f=0}(t - \rho)] d\rho \\ = & |H_f(f_c)|^2 \int_{-\infty}^{\infty} h_{CD}(\rho) E[V_{LP, l_f=0}(t - \rho)] d\rho , \end{aligned} \tag{7.17}$$





where $\nu'_1(\rho)$ and $\nu'_2(\rho)$ are the derivatives of $\nu_1(\rho)$ and $\nu_2(\rho)$ with respect to ρ ,

$$\rho_0 \triangleq l_f \left[\tau_g(f_c) - \frac{(\tau'_g(f_c))^2}{2\tau''_g(f_c)} \right], \quad (7.18)$$

and

$$h_{\text{CD}}(t) \triangleq \sqrt{2}\tau_c u(t - \rho_0) \left[\nu'_1(t) \exp(-2\pi \nu_1^2(t)\tau_c^2) - \nu'_2(t) \exp(-2\pi \nu_2^2(t)\tau_c^2) \right], \quad (7.19)$$

where $u(\cdot)$ is the unit step function:

$$u(x) \triangleq \begin{cases} 1 & , x \geq 0, \\ 0 & , x < 0. \end{cases} \quad (7.20)$$

Similarly, one can find

$$h_{\text{CD}}(t) \triangleq \sqrt{2}\tau_c u(\rho_0 - t) \left[\nu'_1(t) \exp(-2\pi \nu_1^2(t)\tau_c^2) - \nu'_2(t) \exp(-2\pi \nu_2^2(t)\tau_c^2) \right], \quad (7.21)$$

for $\tau''_g(f_c) < 0$.

Apparently, the impact of the CD of the optical fiber on the expected value of the receiver output signal can be modeled as the insertion of a linear time-invariant filter with impulse response $h_{\text{CD}}(t)$. (The attenuation simply results in a constant factor $|H_f(f_c)|^2$.) By defining

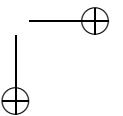
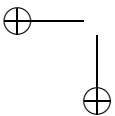
$$T_0 \triangleq l_f \tau_g(f_c), \quad (7.22)$$

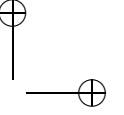
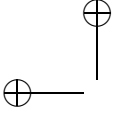
$$T_1 \triangleq \frac{l_f \tau'_g(f_c)}{\sqrt{2}\tau_c}, \quad (7.23)$$

$$T_2 \triangleq \frac{l_f \tau''_g(f_c)}{\tau_c^2}, \quad (7.24)$$

(7.19) and (7.21) can be rewritten as

$$h_{\text{CD}}(t) = \frac{u\left((t - T_0)T_2 + T_1^2\right)}{\sqrt{(t - T_0)T_2 + T_1^2}} \left[\exp\left(-\frac{4\pi}{T_2^2} \left(\sqrt{(t - T_0)T_2 + T_1^2} + T_1\right)^2\right) + \exp\left(-\frac{4\pi}{T_2^2} \left(\sqrt{(t - T_0)T_2 + T_1^2} - T_1\right)^2\right) \right]. \quad (7.25)$$





Obviously, T_0 is a (non-relevant) time delay and does not introduce distortion. The actual amount of time-spreading is determined by the time duration of $h_{CD}(t)$, which depends on T_1 and T_2 . This can be quantified by the root-mean-square delay

$$\sigma_T \triangleq \sqrt{\frac{\int_{-\infty}^{\infty} (t - \langle T \rangle)^2 h_{CD}(t) dt}{\int_{-\infty}^{\infty} h_{CD}(t) dt}}, \tag{7.26}$$

where the mean delay $\langle T \rangle$ is defined as

$$\langle T \rangle \triangleq \frac{\int_{-\infty}^{\infty} t h_{CD}(t) dt}{\int_{-\infty}^{\infty} h_{CD}(t) dt}. \tag{7.27}$$

Substituting (7.25) and performing the integrations one can find

$$\langle T \rangle = T_0 + \frac{T_2}{8\pi}, \tag{7.28}$$

$$\sigma_T = \sqrt{\frac{T_1^2}{2\pi} + \frac{T_2^2}{32\pi^2}}. \tag{7.29}$$

The effect of CD can also be considered in the frequency domain by calculating the corresponding transfer function $H_{CD}(f)$, which follows by Fourier transforming (7.25):

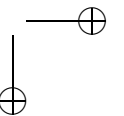
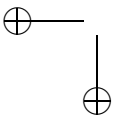
$$\begin{aligned} H_{CD}(f) &= \int_{-\infty}^{\infty} h_{CD}(t) \exp(-j 2\pi f t) dt \\ &= \frac{1}{\sqrt{1 + \frac{1}{2}j f T_2}} \exp\left(-\frac{\pi f^2 T_1^2}{1 + \frac{1}{2}j f T_2} - j 2\pi f T_0\right). \end{aligned} \tag{7.30}$$

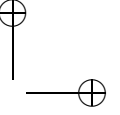
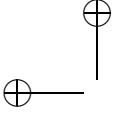
The amplitude response follows by taking the absolute value:

$$|H_{CD}(f)| = \frac{1}{\sqrt{4\sqrt{1 + \frac{1}{4}f^2 T_2^2}}} \exp\left(-\frac{\pi f^2 T_1^2}{1 + \frac{1}{4}f^2 T_2^2}\right). \tag{7.31}$$

Apparently, the impact of CD can be modeled as the insertion of a low-pass filter with a bandwidth that decreases with increasing values of T_1 and T_2 .

When $l_f = 0$, we have $T_0 = T_1 = T_2 = 0$, so that (7.25) and (7.30) reduce to $h_{CD}(t) = \delta(t)$ and $H_{CD}(f) = 1$, as expected.





When $l_f > 0$, T_1 and T_2 depend on the coherence time τ_c and the dispersion coefficients $\tau_g'(f_c)$ and $\tau_g''(f_c)$. The latter two depend on the optical center wavelength λ_c , as described in Subsection 2.5.2. Now consider the following two cases:

1. For wavelengths far from the zero-dispersion wavelength, first order CD is dominant. We then have $|T_2| \ll |T_1|$ so that (7.25) and (7.31) reduce to

$$h_{\text{CD}}(t) \approx \frac{1}{|T_1|} \exp\left(-\pi \left(\frac{t - T_0}{T_1}\right)^2\right), \quad (7.32)$$

$$|H_{\text{CD}}(f)| \approx \exp(-\pi f^2 T_1^2). \quad (7.33)$$

These are shown in Figure 7.2(a) and 7.2(b), for $T_1 > 0$. (Note that the same shapes would result for $T_1 < 0$.)

2. For wavelengths close to the zero-dispersion wavelength, second order CD is dominant. We then have $|T_2| \gg |T_1|$ so that (7.25) and (7.31) reduce to

$$h_{\text{CD}}(t) \approx \frac{2u((t - T_0)T_2)}{\sqrt{(t - T_0)T_2}} \exp\left(-\frac{4\pi(t - T_0)}{T_2}\right), \quad (7.34)$$

$$|H_{\text{CD}}(f)| \approx \frac{1}{\sqrt[4]{1 + \frac{1}{4}f^2 T_2^2}}. \quad (7.35)$$

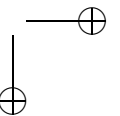
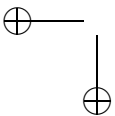
These are shown in Figure 7.2(c) and 7.2(d), for $T_2 > 0$. (When $T_2 < 0$, the curve in Figure 7.2(c) will be mirrored in $t = T_0$.)

Apparently, the two types of CD lead to significantly different distortion effects.

7.2.3 Noise in the output signal of the receiver

The impact of the fiber on the noise in the output signal of the low-pass filter $V_{\text{LP}}(t)$ of a two-way balanced receiver can be studied by means of (4.46). Using (7.9) and assuming that $T_{\text{Rx}}, T_{\text{Tx}} \gg \tau_c$ and $|T_{\text{Rx}} - T_{\text{Tx}}| \ll \tau_c$, one can find

$$\begin{aligned} \mathbb{E}[P_y(\rho)] &\approx \mathbb{E}[P_y(\rho - T_{\text{Rx},r})] \\ &\approx \frac{1}{4L_{\text{Tx}}} \int_{-\infty}^{\infty} |H_f(f)|^2 S_{x^*x}(f) m_{\text{mod}}(\rho - l_f \tau_g(f)) df, \end{aligned} \quad (7.36)$$



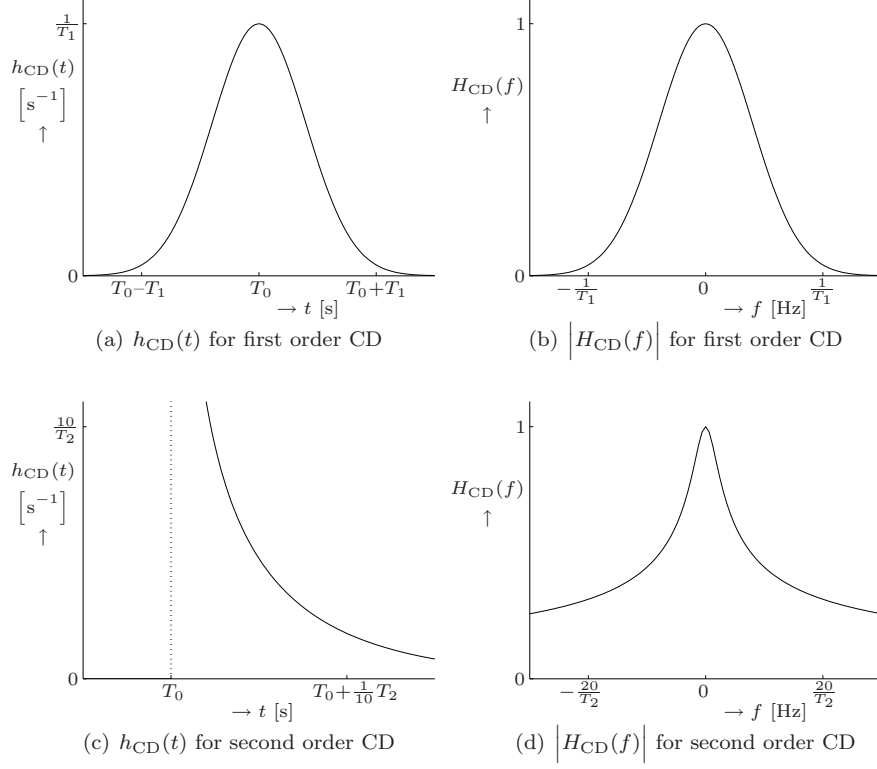


Figure 7.2: CD-induced impulse response $h_{\text{CD}}(t)$ and magnitude response $|H_{\text{CD}}(f)|$ in case of first and second order CD

$$\begin{aligned}
 R_{y^*y}(\rho_1, \rho_2) R_{y^*y}(\rho_2 - T_{\text{Rx}}, \rho_1 - T_{\text{Rx}}) \approx & \\
 \frac{1}{16L_{\text{Tx}}^2} \left[4 \left| \int_{-\infty}^{\infty} |H_f(f)|^2 S_{x^*x}(f) m_{\text{mod}}(\rho_1 - l_f \tau_g(f)) \right. \right. & \\
 \cdot \exp(j 2\pi f(\rho_2 - \rho_1)) df \Big|^2 & \\
 + \left| \int_{-\infty}^{\infty} |H_f(f)|^2 S_{x^*x}(f) m_{\text{mod}}(\rho_1 - l_f \tau_g(f)) \right. & \\
 \cdot \exp(j 2\pi f(\rho_2 - \rho_1 - T_{\text{Tx}}) + j \phi_{\text{mod}}(\rho_1 - l_f \tau_g(f))) df \Big|^2 & \\
 + \left| \int_{-\infty}^{\infty} |H_f(f)|^2 S_{x^*x}(f) m_{\text{mod}}(\rho_1 - l_f \tau_g(f)) \right. & \\
 \cdot \exp(j 2\pi f(\rho_2 - \rho_1 + T_{\text{Tx}}) - j \phi_{\text{mod}}(\rho_1 - l_f \tau_g(f))) df \Big|^2 \Big], & \quad (7.37)
 \end{aligned}$$

$$\begin{aligned}
R_{y^*y}(\rho_1 - T_{\text{Rx}}, \rho_2) R_{y^*y}(\rho_2 - T_{\text{Rx}}, \rho_1) &\approx \\
\frac{1}{16L_{\text{Tx}}^2} \int_{-\infty}^{\infty} &|H_{\text{f}}(f_1)|^2 S_{x^*x}(f_1) m_{\text{mod}}(\rho_1 - l_{\text{f}}\tau_{\text{g}}(f_1)) \\
&\cdot \exp\left(\text{j}2\pi f_1(\rho_2 - \rho_1 + T_{\text{Rx}} - T_{\text{Tx}}) + \text{j}\phi_{\text{mod}}(\rho_1 - l_{\text{f}}\tau_{\text{g}}(f_1))\right) \text{d}f_1 \\
&\cdot \int_{-\infty}^{\infty} |H_{\text{f}}(f_2)|^2 S_{x^*x}(f_2) m_{\text{mod}}(\rho_1 - l_{\text{f}}\tau_{\text{g}}(f_2)) \\
&\cdot \exp\left(\text{j}2\pi f_2(\rho_2 - \rho_1 + T_{\text{Rx}} - T_{\text{Tx}}) + \text{j}\phi_{\text{mod}}(\rho_1 - l_{\text{f}}\tau_{\text{g}}(f_2))\right) \text{d}f_2. \quad (7.38)
\end{aligned}$$

Following the analysis in the previous subsection, (7.36) can be written as

$$\begin{aligned}
\text{E}[P_y(\rho)] &\approx \text{E}[P_y(\rho - T_{\text{Rx},r})] \\
&\approx \frac{P_x}{2L_{\text{Tx}}} |H_{\text{f}}(f_c)|^2 \int_{-\infty}^{\infty} h_{\text{CD}}(\xi) m_{\text{mod}}(\rho - \xi) \text{d}\xi, \quad (7.39)
\end{aligned}$$

where $h_{\text{CD}}(t)$ is given by (7.25).

Note that (7.37) and (7.38) have a significant value for $\rho_2 \approx \rho_1$, where $|\rho_2 - \rho_1|$ is in the order of τ_c or smaller, whereas they become negligible for $|\rho_2 - \rho_1| \gg \tau_c$. On the other hand, when they are substituted into (4.46), one should note that the width of $h_{\text{LP}}(t)$ is much larger than τ_c and T_{Tx} . Therefore, when (7.37) and (7.38) are substituted into (4.46), they can be approximated as delta functions in $\rho_2 - \rho_1$. Since these delta functions are supposed to have the same area as the original functions, the approximations can be written as

$$\begin{aligned}
R_{y^*y}(\rho_1, \rho_2) R_{y^*y}(\rho_2 - T_{\text{Rx}}, \rho_1 - T_{\text{Rx}}) &\approx \\
\frac{\delta(\rho_2 - \rho_1)}{16L_{\text{Tx}}^2} \int_{-\infty}^{\infty} &\left[4 \left| \int_{-\infty}^{\infty} |H_{\text{f}}(f)|^2 S_{x^*x}(f) m_{\text{mod}}(\rho_1 - l_{\text{f}}\tau_{\text{g}}(f)) \right. \right. \\
&\quad \left. \left. \cdot \exp\left(\text{j}2\pi f(\rho_2 - \rho_1)\right) \text{d}f \right|^2 \right. \\
&+ \left| \int_{-\infty}^{\infty} |H_{\text{f}}(f)|^2 S_{x^*x}(f) m_{\text{mod}}(\rho_1 - l_{\text{f}}\tau_{\text{g}}(f)) \right. \\
&\quad \left. \cdot \exp\left(\text{j}2\pi f(\rho_2 - \rho_1 - T_{\text{Tx}}) + \text{j}\phi_{\text{mod}}(\rho_1 - l_{\text{f}}\tau_{\text{g}}(f))\right) \text{d}f \right|^2 \\
&+ \left| \int_{-\infty}^{\infty} |H_{\text{f}}(f)|^2 S_{x^*x}(f) m_{\text{mod}}(\rho_1 - l_{\text{f}}\tau_{\text{g}}(f)) \right. \\
&\quad \left. \cdot \exp\left(\text{j}2\pi f(\rho_2 - \rho_1 + T_{\text{Tx}}) - \text{j}\phi_{\text{mod}}(\rho_1 - l_{\text{f}}\tau_{\text{g}}(f))\right) \text{d}f \right|^2 \Big] \text{d}\rho_2 \\
&\approx \frac{6\delta(\rho_2 - \rho_1)}{16L_{\text{Tx}}^2} \int_{-\infty}^{\infty} |H_{\text{f}}(f)|^4 S_{x^*x}^2(f) m_{\text{mod}}^2(\rho_1 - l_{\text{f}}\tau_{\text{g}}(f)) \text{d}f, \quad (7.40)
\end{aligned}$$

$$\begin{aligned}
R_{y^*y}(\rho_1 - T_{\text{Rx}}, \rho_2) R_{y^*y}(\rho_2 - T_{\text{Rx}}, \rho_1) &\approx \\
\frac{\delta(\rho_2 - \rho_1)}{16L_{\text{Tx}}^2} \int_{-\infty}^{\infty} \int_{-\infty}^{\infty} &|H_f(f_1)|^2 S_{x^*x}(f_1) m_{\text{mod}}(\rho_1 - l_f \tau_g(f_1)) \\
&\cdot \exp\left(j 2\pi f_1(\rho_2 - \rho_1 + T_{\text{Rx}} - T_{\text{Tx}}) + j \phi_{\text{mod}}(\rho_1 - l_f \tau_g(f_1))\right) df_1 \\
&\cdot \int_{-\infty}^{\infty} |H_f(f_2)|^2 S_{x^*x}(f_2) m_{\text{mod}}(\rho_1 - l_f \tau_g(f_2)) \\
&\cdot \exp\left(j 2\pi f_2(\rho_2 - \rho_1 + T_{\text{Rx}} - T_{\text{Tx}}) + j \phi_{\text{mod}}(\rho_1 - l_f \tau_g(f_2))\right) df_2 d\rho_2 \\
&\approx \frac{\delta(\rho_2 - \rho_1)}{16L_{\text{Tx}}^2} \int_{-\infty}^{\infty} |H_f(f)|^4 S_{x^*x}^2(f) m_{\text{mod}}^2(\rho_1 - l_f \tau_g(f)) \\
&\cdot \exp\left(j 4\pi f_c(T_{\text{Rx}} - T_{\text{Tx}}) + j 2\phi_{\text{mod}}(\rho_1 - l_f \tau_g(f))\right) df. \quad (7.41)
\end{aligned}$$

Following the analysis in the previous subsection these can be written as

$$\begin{aligned}
R_{y^*y}(\rho_1, \rho_2) R_{y^*y}(\rho_2 - T_{\text{Rx}}, \rho_1 - T_{\text{Rx}}) &\approx \\
\frac{6P_x^2 \tau_c}{4L_{\text{Tx}}^2} \delta(\rho_2 - \rho_1) |H_f(f_c)|^4 &\int_{-\infty}^{\infty} h_{\text{CDN}}(\xi) m_{\text{mod}}^2(\rho_1 - \xi) d\xi, \quad (7.42) \\
R_{y^*y}(\rho_1 - T_{\text{Rx}}, \rho_2) R_{y^*y}(\rho_2 - T_{\text{Rx}}, \rho_1) &\approx \\
\frac{P_x^2 \tau_c}{4L_{\text{Tx}}^2} \delta(\rho_2 - \rho_1) |H_f(f_c)|^4 &\int_{-\infty}^{\infty} h_{\text{CDN}}(\xi) m_{\text{mod}}^2(\rho_1 - \xi) \\
&\cdot \exp\left(j 2\Delta\phi + j 2\phi_{\text{mod}}(\rho_1 - \xi)\right) d\xi, \quad (7.43)
\end{aligned}$$

where $\Delta\phi \triangleq 2\pi f_c(T_{\text{Rx}} - T_{\text{Tx}})$ and

$$\begin{aligned}
h_{\text{CDN}}(t) &\triangleq \\
\frac{\sqrt{2} u\left((t - T_0)T_2 + T_1^2\right)}{\sqrt{(t - T_0)T_2 + T_1^2}} &\left[\exp\left(-\frac{8\pi}{T_2^2} \left(\sqrt{(t - T_0)T_2 + T_1^2} + T_1\right)^2\right) \right. \\
&\left. + \exp\left(-\frac{8\pi}{T_2^2} \left(\sqrt{(t - T_0)T_2 + T_1^2} - T_1\right)^2\right) \right]. \quad (7.44)
\end{aligned}$$

In case of first order CD ($|T_2| \ll |T_1|$) this reduces to

$$h_{\text{CDN}}(t) = \frac{\sqrt{2}}{|T_1|} \exp\left(-2\pi \left(\frac{t - T_0}{T_1}\right)^2\right) = \sqrt{2} h_{\text{CD}}(\sqrt{2}(t + T_0) - T_0), \quad (7.45)$$

and in case of second order CD ($|T_2| \gg |T_1|$) this reduces to

$$h_{\text{CDN}}(t) = \frac{2\sqrt{2} u\left((t - T_0)T_2\right)}{\sqrt{(t - T_0)T_2}} \exp\left(-\frac{8\pi(t - T_0)}{T_2}\right) = 2h_{\text{CD}}(2t + T_0). \quad (7.46)$$

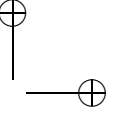
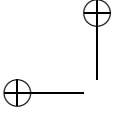
Substituting (7.39), (7.42), (7.43) and $\Delta\phi = 0$ into (4.46) results in

$$\begin{aligned}
R_{V_{LP}V_{LP}}(t_1, t_2) &\approx \mathbb{E}[V_{LP}(t_1)]\mathbb{E}[V_{LP}(t_2)] \\
&+ \frac{Z_{TIA}^2 R_{pd} P_x e}{2L_{Tx} L_{Rx}} |H_f(f_c)|^2 \int_{-\infty}^{\infty} \int_{-\infty}^{\infty} h_{LP}(t_1 - \rho) h_{LP}(t_2 - \rho) h_{CD}(\xi) \\
&\quad \cdot m_{\text{mod}}(\rho - \xi) \, d\xi \, d\rho \\
&+ \frac{Z_{TIA}^2 R_{pd}^2 P_x^2 \tau_c}{32L_{Rx}^2 L_{Tx}^2} |H_f(f_c)|^4 \int_{-\infty}^{\infty} \int_{-\infty}^{\infty} h_{LP}(t_1 - \rho) h_{LP}(t_2 - \rho) h_{CDN}(\xi) \\
&\quad \cdot m_{\text{mod}}^2(\rho - \xi) \left[6 + \cos(2\phi_{\text{mod}}(\rho - \xi)) \right] \, d\xi \, d\rho \\
&+ Z_{TIA}^2 S_{\text{th}} \int_{-\infty}^{\infty} h_{LP}(t_1 - \rho) h_{LP}(t_2 - \rho) \, d\rho. \tag{7.47}
\end{aligned}$$

Similarly, the autocorrelation functions and cross-correlation function of the output signals of the low-pass filters $V_{LP,I}(t)$ and $V_{LP,Q}(t)$ in a four-way balanced receiver can be found by substituting (7.39), (7.42) and (7.43) into (B.7), (B.8) and (B.9), resulting in

$$\begin{aligned}
R_{V_{LP,I}V_{LP,I}}(t_1, t_2) &\approx \mathbb{E}[V_{LP,I}(t_1)]\mathbb{E}[V_{LP,I}(t_2)] \\
&+ \frac{Z_{TIA}^2 R_{pd} P_x e}{4L_{Tx} L_{Rx}} |H_f(f_c)|^2 \int_{-\infty}^{\infty} \int_{-\infty}^{\infty} h_{LP}(t_1 - \rho) h_{LP}(t_2 - \rho) h_{CD}(\xi) \\
&\quad \cdot m_{\text{mod}}(\rho - \xi) \, d\xi \, d\rho \\
&+ \frac{Z_{TIA}^2 R_{pd}^2 P_x^2 \tau_c}{128L_{Rx}^2 L_{Tx}^2} |H_f(f_c)|^4 \int_{-\infty}^{\infty} \int_{-\infty}^{\infty} h_{LP}(t_1 - \rho) h_{LP}(t_2 - \rho) h_{CDN}(\xi) \\
&\quad \cdot m_{\text{mod}}^2(\rho - \xi) \left[6 + \cos(2\Delta\phi + 2\phi_{\text{mod}}(\rho - \xi) + \frac{\pi}{2}) \right] \, d\xi \, d\rho \\
&+ Z_{TIA}^2 S_{\text{th}} \int_{-\infty}^{\infty} h_{LP}(t_1 - \rho) h_{LP}(t_2 - \rho) \, d\rho, \tag{7.48}
\end{aligned}$$

$$\begin{aligned}
R_{V_{LP,Q}V_{LP,Q}}(t_1, t_2) &\approx \mathbb{E}[V_{LP,Q}(t_1)]\mathbb{E}[V_{LP,Q}(t_2)] \\
&+ \frac{Z_{TIA}^2 R_{pd} P_x e}{4L_{Tx} L_{Rx}} |H_f(f_c)|^2 \int_{-\infty}^{\infty} \int_{-\infty}^{\infty} h_{LP}(t_1 - \rho) h_{LP}(t_2 - \rho) h_{CD}(\xi) \\
&\quad \cdot m_{\text{mod}}(\rho - \xi) \, d\xi \, d\rho \\
&+ \frac{Z_{TIA}^2 R_{pd}^2 P_x^2 \tau_c}{128L_{Rx}^2 L_{Tx}^2} |H_f(f_c)|^4 \int_{-\infty}^{\infty} \int_{-\infty}^{\infty} h_{LP}(t_1 - \rho) h_{LP}(t_2 - \rho) h_{CDN}(\xi) \\
&\quad \cdot m_{\text{mod}}^2(\rho - \xi) \left[6 + \cos(2\Delta\phi + 2\phi_{\text{mod}}(\rho - \xi) - \frac{\pi}{2}) \right] \, d\xi \, d\rho \\
&+ Z_{TIA}^2 S_{\text{th}} \int_{-\infty}^{\infty} h_{LP}(t_1 - \rho) h_{LP}(t_2 - \rho) \, d\rho, \tag{7.49}
\end{aligned}$$



$$\begin{aligned}
R_{V_{LP,I}V_{LP,Q}}(t_1, t_2) &\approx E[V_{LP,I}(t_1)]E[V_{LP,Q}(t_2)] \\
&+ \frac{Z_{TIA}^2 R_{pd}^2 P_x^2 \tau_c}{128 L_{Rx}^2 L_{Tx}^2} |H_f(f_c)|^4 \int_{-\infty}^{\infty} \int_{-\infty}^{\infty} h_{LP}(t_1 - \rho) h_{LP}(t_2 - \rho) h_{CDN}(\xi) \\
&\quad \cdot m_{\text{mod}}^2(\rho - \xi) \cos(2\Delta\phi + 2\phi_{\text{mod}}(\rho - \xi)) d\xi d\rho. \quad (7.50)
\end{aligned}$$

7.3 Impact of chromatic dispersion on digital transmission

In case of digital transmission, CD will lead to broadening of the pulses at the output of the receiver. This will deteriorate the detection performance in two ways:

- The expected peak value of the detected pulse will decrease;
- Neighboring pulses will overlap: inter-symbol interference (ISI) occurs.

Moreover, the variance of a particular decision sample depends on the corresponding transmitted bit, but also on the preceding and succeeding bits.

In this section, these effects will be studied in further detail. Non-equalized transmission will be considered, so it will simply be assumed that rectangular pulses are transmitted—as described by (4.53)—and that the pre-detection filter is matched to an undistorted rectangular pulse—as described by (4.56).

First, expressions will be derived for the shape of the resulting distorted pulse after integrate-and-dump filtering, both for first and second order CD. Similarly, expressions will be derived for the noise variance after integrate-and-dump filtering. Then, the resulting performance degradation will be derived for phase-synchronized detection of several modulation formats.

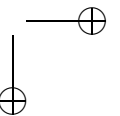
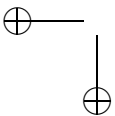
7.3.1 Pulse distortion

In case of digital transmission, the expected value of the output signal of the integrate-and-dump filter $V_{LP}(t)$ of a phase-synchronized two-way balanced receiver can be found by combining (4.57) and (7.17), resulting in

$$E[V_{LP}(t)] \approx \frac{Z_{TIA} R_{pd} P_x}{4 L_{Tx} L_{Rx}} |H_f(f_c)|^2 \sum_k m_k \cos(\phi_k) p(t - k T_s), \quad (7.51)$$

where $p(\cdot)$ is a distorted triangular pulse, which is defined as

$$p(t) \triangleq \int_{-\infty}^{\infty} h_{CD}(t - \rho) \Lambda\left(\frac{\rho}{T_s}\right) d\rho. \quad (7.52)$$



Similarly, the expected values of the output signals of the integrate-and-dump filters $V_{LP,I}(t)$ and $V_{LP,Q}(t)$ of a four-way balanced receiver can be written as

$$\begin{aligned} E[V_{LP,I}(t)] &\approx \\ &\frac{Z_{TIA} R_{pd} P_x}{8L_{Tx} L_{Rx}} |H_f(f_c)|^2 \sum_k m_k \cos\left(\Delta\phi + \phi_k - \frac{3\pi}{4}\right) p(t - kT_s), \end{aligned} \quad (7.53)$$

$$\begin{aligned} E[V_{LP,Q}(t)] &\approx \\ &\frac{Z_{TIA} R_{pd} P_x}{8L_{Tx} L_{Rx}} |H_f(f_c)|^2 \sum_k m_k \cos\left(\Delta\phi + \phi_k + \frac{3\pi}{4}\right) p(t - kT_s). \end{aligned} \quad (7.54)$$

In order to study pulse height reduction and ISI, the expected output signals have to be evaluated at the sampling instants $t_0 + kT_s$, where $k \in \mathbb{Z}$ and t_0 is the time instant where $p(t)$ achieves its maximum. Hence, the values of $p(t_0 + kT_s)$ have to be derived. Before this is done, an important property of $p(t)$ is derived, namely that the sum of its sample values does not depend on t_0 , T_s , T_1 and T_2 . This follows from

$$\begin{aligned} \sum_k p(t_0 + kT_s) &= \sum_k \int_{-\infty}^{\infty} h_{CD}(t_0 + kT_s - \rho) \Lambda\left(\frac{\rho}{T_s}\right) d\rho \\ &= \int_{-\infty}^{\infty} h_{CD}(\rho) \sum_k \Lambda\left(\frac{t_0 + kT_s - \rho}{T_s}\right) d\rho = \int_{-\infty}^{\infty} h_{CD}(\rho) d\rho = 1. \end{aligned} \quad (7.55)$$

where the last step follows directly from (7.25). Note that this is an intuitively appealing result, since it implies that the sampled value of a pulse in case of rectangular modulation and integrate-and-dump filtering, is not affected by CD when this pulse and all its surrounding pulses have the same amplitude.

By rewriting the triangular unit pulse $\Lambda(\cdot)$ as

$$\Lambda(x) = (x+1)u(x+1) - 2xu(x) + (x-1)u(x-1), \quad (7.56)$$

$p(\cdot)$ can be written as

$$p(t) = \frac{1}{T_s} \left[q(t+T_s) - 2q(t) + q(t-T_s) \right], \quad (7.57)$$

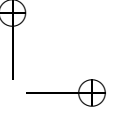
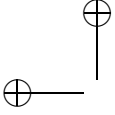
where

$$q(t) = \int_0^{\infty} \rho h_{CD}(t-\rho) d\rho. \quad (7.58)$$

Using (7.25) and substituting $x = \sqrt{(t-T_0)T_2 + T_1^2}$ this can be written as

$$\begin{aligned} q(t) &= \frac{2}{T_2} u\left((t-T_0)T_2 + T_1^2\right) \int_0^{\sqrt{(t-T_0)T_2 + T_1^2}} \left(t - T_0 - \frac{x^2 - T_1^2}{T_2} \right) \\ &\quad \cdot \left[\exp\left(-4\pi \left(\frac{x+T_1}{T_2}\right)^2\right) + \exp\left(-4\pi \left(\frac{x-T_1}{T_2}\right)^2\right) \right] dx, \end{aligned} \quad (7.59)$$

where it has been assumed that $T_2 > 0$, for convenience.



(From (7.25) and the symmetry of $\Lambda(\cdot)$ it follows that the shape of $p(t)$ for $T_2 < 0$ results by mirroring in $t = T_0$.)

Performing the integration and using (3.8), we get

$$\begin{aligned}
 q(t) = u\left((t - T_0)T_2 + T_1^2\right) & \left\{ \frac{1}{4\pi} \left[\left(\sqrt{(t - T_0)T_2 + T_1^2} - T_1 \right) \right. \right. \\
 & \cdot \exp\left(-\frac{4\pi}{T_2^2} \left(\sqrt{(t - T_0)T_2 + T_1^2} + T_1 \right)^2\right) \\
 & \left. \left. + \left(\sqrt{(t - T_0)T_2 + T_1^2} + T_1 \right) \exp\left(-\frac{4\pi}{T_2^2} \left(\sqrt{(t - T_0)T_2 + T_1^2} - T_1 \right)^2\right) \right] \right. \\
 & \left. + \left(t - T_0 - \frac{T_2}{8\pi} \right) \left[1 - Q\left(\frac{2\sqrt{2\pi}}{T_2} \left(\sqrt{(t - T_0)T_2 + T_1^2} + T_1 \right)\right) \right. \right. \\
 & \left. \left. - Q\left(\frac{2\sqrt{2\pi}}{T_2} \left(\sqrt{(t - T_0)T_2 + T_1^2} - T_1 \right)\right) \right] \right\}. \quad (7.60)
 \end{aligned}$$

When $l_f = 0$, we have $T_0 = T_1 = T_2 = 0$, so that (7.60) reduces to $q(t) = t$ and hence (7.57) reduces to $p(t) = \Lambda(t/T_s)$, as expected.

Now the cases of first and second order CD will be considered separately.

First order dispersion

In case of first order CD we have $|T_2| \ll |T_1|$, so that (7.60) reduces to

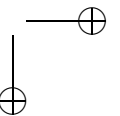
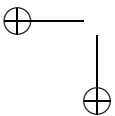
$$q(t) \approx \frac{|T_1|}{2\pi} \exp\left(-\pi \left(\frac{t - T_0}{T_1}\right)^2\right) + (t - T_0) \left[1 - Q\left(\frac{\sqrt{2\pi}(t - T_0)}{|T_1|}\right) \right]. \quad (7.61)$$

The resulting pulse shape $p(t)$ which then follows from (7.57) is shown in Figure 7.3(a), for $T_1 > 0$.

Example 7.1

This is illustrated by repeating the simulation in Example 5.2, where the simulation model has been extended by the SMF block based on the first order CD model, representing a standard SMF of 30 m for the case that the sources have a center wavelength of 1550 nm. The resulting output signal of receiver 1 is shown in Figure 7.4(a), where the circles denote the decision samples, the dashed lines represent the theoretical expected value, and the dotted line shows the theoretical expected value for the case that there is no CD.

Obviously, ISI occurs: the decision samples depend both on the corresponding bit and the adjacent bits. Especially the bits surrounded by bits with different values result in relatively inaccurate decision samples, in this case for example at $t = 80$ ps and $t = 280$ ps. □



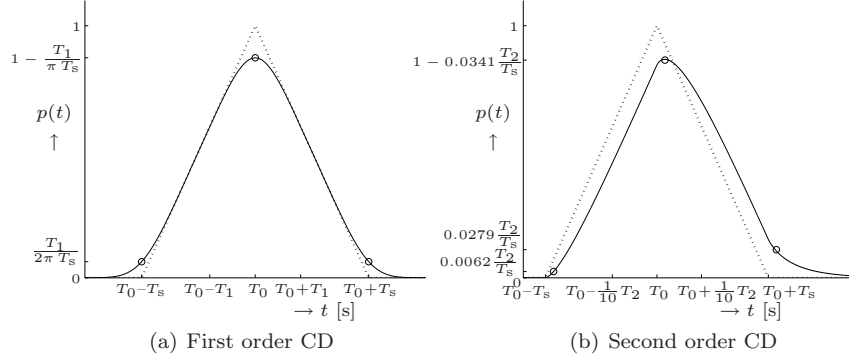


Figure 7.3: Shape of the distorted pulse $p(t)$ after integrate-and-dump filtering in case of first and second order CD. The dotted line represents the undistorted pulse $\Lambda\left(\frac{t-T_0}{T_s}\right)$ and the circles denote approximations of the samples of $p(t)$.

From symmetry considerations, one can easily see that the maximum value of the distorted pulse is achieved at $t = T_0$ (so one should choose $t_0 = T_0$) and is given by

$$\begin{aligned}
 p(T_0) &= \frac{1}{T_s} \left[q(T_0 + T_s) - 2q(T_0) + q(T_0 - T_s) \right] \\
 &\approx \frac{|T_1|}{\pi T_s} \left[\exp\left(-\pi \left(\frac{T_s}{T_1}\right)^2\right) - 1 \right] + 1 - 2Q\left(\frac{\sqrt{2\pi}T_s}{|T_1|}\right). \quad (7.62)
 \end{aligned}$$

Obviously, the peak amplitude of the pulse decreases with increasing $|T_1|/T_s$.

Moreover, ISI occurs as the absolute pulse width is larger than T_s . When the pulse is sampled at $t = t_0 (= T_0$ in this case), the amount of ISI can be quantified by calculating the pulse amplitudes at time instants $t_0 + kT_s$:

$$\begin{aligned}
 p(t_0 + kT_s) &= \frac{1}{T_s} \left[q(t_0 + (k-1)T_s) - 2q(t_0 + kT_s) + q(t_0 + (k+1)T_s) \right] \\
 &\approx \frac{|T_1|}{2\pi T_s} \left[\exp\left(-\pi \left(\frac{(k-1)T_s}{T_1}\right)^2\right) - 2 \exp\left(-\pi \left(\frac{kT_s}{T_1}\right)^2\right) \right. \\
 &\quad \left. + \exp\left(-\pi \left(\frac{(k+1)T_s}{T_1}\right)^2\right) \right] - (k-1)Q\left(\frac{\sqrt{2\pi}(k-1)T_s}{|T_1|}\right) \\
 &\quad + 2kQ\left(\frac{\sqrt{2\pi}kT_s}{|T_1|}\right) - (k+1)Q\left(\frac{\sqrt{2\pi}(k+1)T_s}{|T_1|}\right). \quad (7.63)
 \end{aligned}$$

These values are plotted as a function of T_1 for $k = 0, \pm 1, \pm 2, \pm 3$ in Figure 7.5(a).

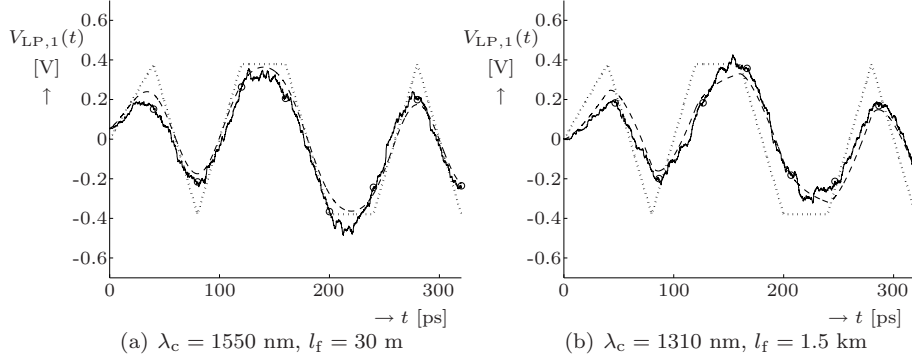


Figure 7.4: Simulated output signal of receiver 1 in a 2-channel PA using BPSK modulation when a bit pattern '01001101' is transmitted at 25 Gbps, for different source center wavelengths λ_c and fiber lengths l_f

For large arguments, the Q-function can be approximated as [81]

$$Q(x) \approx \frac{\exp\left(-\frac{1}{2}x^2\right)}{x\sqrt{2\pi}}, \quad (7.64)$$

so for relatively small values of $|T_1|$, (7.63) can be approximated as

$$p(t_0 + kT_s) \approx \begin{cases} 1 - \frac{|T_1|}{\pi T_s} & , k = 0, \\ \frac{|T_1|}{2\pi T_s} & , k = \pm 1, \\ 0 & , |k| \geq 2. \end{cases} \quad (7.65)$$

These values are indicated by the circles in Figure 7.3(a) and the dashed lines in Figure 7.5(a). From the latter figure it follows that the approximation in (7.65) holds when $|T_1| < T_s$. Note that the sum of the sample values in (7.65) is indeed equal to one, as prescribed by (7.55).

Apparently, in case of first order CD with $|T_1| < T_s$, ISI is dominated by the two directly neighboring pulses, which equally contribute to the ISI. As a result, the expected value of the output samples $V_{LP}(t_0 + kT_s)$ of the low-pass filter of a two-way phase-synchronized balanced receiver follow from (7.51) as

$$\begin{aligned} E[V_{LP}(t_0 + kT_s)] \approx & \frac{Z_{TIA}R_{pd}P_x}{4L_{Tx}L_{Rx}} |H_f(f_c)|^2 \left[m_{k-1} \cos(\phi_{k-1})p(t_0 + T_s) \right. \\ & \left. + m_k \cos(\phi_k)p(t_0) + m_{k+1} \cos(\phi_{k+1})p(t_0 - T_s) \right], \quad (7.66) \end{aligned}$$

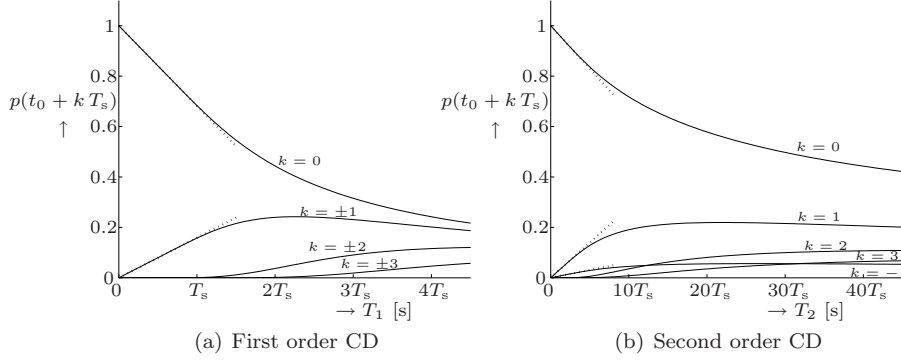


Figure 7.5: Sample values $p(t_0 + k T_s)$ of the distorted pulse after integrate-and-dump filtering as a function of T_1 (for first order CD) and T_2 (for second order CD). The dotted lines represent the corresponding approximations for small values of T_1 and T_2 .

and for a four-way balanced receiver from (7.53) and (7.54) as

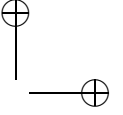
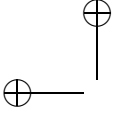
$$\begin{aligned} \mathbb{E}[V_{LP,I}(t_0 + k T_s)] &\approx \\ \frac{Z_{TIA} R_{pd} P_x}{8L_{Tx} L_{Rx}} |H_f(f_c)|^2 &\left[m_{k-1} \cos\left(\Delta\phi + \phi_{k-1} - \frac{3\pi}{4}\right) p(t_0 + T_s) \right. \\ &+ m_k \cos\left(\Delta\phi + \phi_k - \frac{3\pi}{4}\right) p(t_0) \\ &\left. + m_{k+1} \cos\left(\Delta\phi + \phi_{k+1} - \frac{3\pi}{4}\right) p(t_0 - T_s) \right], \quad (7.67) \end{aligned}$$

$$\begin{aligned} \mathbb{E}[V_{LP,Q}(t_0 + k T_s)] &\approx \\ \frac{Z_{TIA} R_{pd} P_x}{8L_{Tx} L_{Rx}} |H_f(f_c)|^2 &\left[m_{k-1} \cos\left(\Delta\phi + \phi_{k-1} + \frac{3\pi}{4}\right) p(t_0 + T_s) \right. \\ &+ m_k \cos\left(\Delta\phi + \phi_k + \frac{3\pi}{4}\right) p(t_0) \\ &\left. + m_{k+1} \cos\left(\Delta\phi + \phi_{k+1} + \frac{3\pi}{4}\right) p(t_0 - T_s) \right]. \quad (7.68) \end{aligned}$$

Second order dispersion

In case of second order CD we have $|T_2| \gg |T_1|$, so that (7.60) reduces to


$$\begin{aligned} q(t) \approx u(t - T_0) &\left\{ \frac{\sqrt{(t - T_0)T_2}}{2\pi} \exp\left(-\frac{4\pi(t - T_0)}{T_2}\right) \right. \\ &\left. + \left(t - T_0 - \frac{T_2}{8\pi}\right) \left[1 - 2Q\left(2\sqrt{\frac{2\pi(t - T_0)}{T_2}}\right) \right] \right\}, \quad T_2 > 0. \quad (7.69) \end{aligned}$$



The resulting pulse shape $p(t)$ which then follows from (7.57) is shown in Figure 7.3(b). (For $T_2 < 0$, the shape would follow by mirroring in $t = T_0$.)

Example 7.2

For illustration, the simulation in Example 7.1 has been repeated, where the SMF block has been replaced by one that is based on the second order CD model, representing a standard SMF of 1.5 km for the case that the sources have a center wavelength of 1310 nm. The resulting output signal of receiver 1 is shown in Figure 7.4(b), where the circles denote the decision samples, the dashed lines represent the theoretical expected value, and the dotted line shows the theoretical expected value for the case that there is no CD.

Again, ISI occurs, and the decision samples corresponding to bits surrounded by bits with different values are the least accurate. 

The pulse $p(t)$ is no longer symmetric. The position of its maximum value can be found by calculating the derivative with respect to time

$$p'(t) = \frac{1}{T_s} \left[q'(t + T_s) - 2q'(t) + q'(t - T_s) \right], \quad (7.70)$$

where

$$q'(t) = u(t - T_0) \left[1 - 2Q \left(2\sqrt{\frac{2\pi(t - T_0)}{T_2}} \right) \right]. \quad (7.71)$$

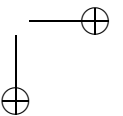
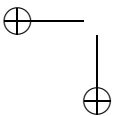
$p(t)$ achieves its maximum value at $t = t_0$ with $p'(t_0) = 0$ or

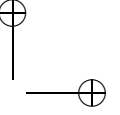
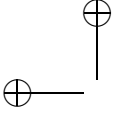
$$\begin{aligned} & u(t_0 - T_0 + T_s) \left[1 - 2Q \left(2\sqrt{\frac{2\pi(t_0 - T_0 + T_s)}{T_2}} \right) \right] \\ & - 2u(t_0 - T_0) \left[1 - 2Q \left(2\sqrt{\frac{2\pi(t_0 - T_0)}{T_2}} \right) \right] \\ & + u(t_0 - T_0 - T_s) \left[1 - 2Q \left(2\sqrt{\frac{2\pi(t_0 - T_0 - T_s)}{T_2}} \right) \right] = 0. \end{aligned} \quad (7.72)$$

From Figure 7.3(b) it follows that $T_0 < t_0 < T_0 + T_s$, so that

$$2Q \left(2\sqrt{\frac{2\pi(t_0 - T_0 + T_s)}{T_2}} \right) - 4Q \left(2\sqrt{\frac{2\pi(t_0 - T_0)}{T_2}} \right) + 1 = 0. \quad (7.73)$$

This cannot be solved analytically, so t_0 has to be determined numerically. Then the sample values $p(t_0 + kT_s)$ follow by substituting the numerical result for t_0 in (7.57) and (7.69). In Figure 7.5(b) these values are plotted as a function of T_2 for $k = -1, 0, 1, 2, 3$.





For relatively small values of T_2 , however, the first Q-function in (7.73) can be neglected, resulting in

$$Q\left(2\sqrt{\frac{2\pi(t_0 - T_0)}{T_2}}\right) \approx 1/4, \quad (7.74)$$

or

$$t_0 \approx T_0 + \frac{[Q^{-1}(1/4)]^2}{8\pi} \approx T_0 + 0.0181T_2, \quad (7.75)$$

where the last step was performed numerically. From mirroring it follows that this also holds for $T_2 < 0$.

The maximum pulse amplitude can now be approximated by

$$\begin{aligned} p(t_0) &= \frac{1}{T_s} [q(t_0 + T_s) - 2q(t_0) + q(t_0 - T_s)] \\ &\approx \frac{1}{T_s} [q(T_0 + 0.0181T_2 + T_s) - 2q(T_0 + 0.0181T_2)] \\ &\approx \frac{\sqrt{(0.0181T_2 + T_s)T_2}}{2\pi T_s} \exp\left(-\frac{4\pi(0.0181T_2 + T_s)}{T_2}\right) \\ &\quad - \frac{\sqrt{0.0181} T_2}{\pi T_s} \exp(-4\pi \cdot 0.0181) \\ &\quad + \left[1 + \left(0.0181 - \frac{1}{8\pi}\right) \frac{T_2}{T_s}\right] \left[1 - 2Q\left(2\sqrt{\frac{2\pi(0.0181T_2 + T_s)}{T_2}}\right)\right] \\ &\quad - 2\left(0.0181 - \frac{1}{8\pi}\right) \frac{T_2}{T_s} \left[1 - 2Q\left(2\sqrt{2\pi \cdot 0.0181}\right)\right]. \end{aligned} \quad (7.76)$$

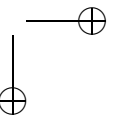
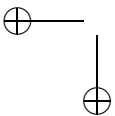
For relatively small values of T_2 , we can approximate

$$\frac{\sqrt{(0.0181T_2 + T_s)T_2}}{2\pi T_s} \exp\left(-\frac{4\pi(0.0181T_2 + T_s)}{T_2}\right) \approx 0, \quad (7.77)$$

$$Q\left(2\sqrt{\frac{2\pi(0.0181T_2 + T_s)}{T_2}}\right) \approx 0, \quad (7.78)$$

so that we get

$$p(t_0) \approx 1 - \frac{\sqrt{0.0181}}{\pi} \exp(-4\pi \cdot 0.0181) \frac{T_2}{T_s} \approx 1 - 0.0341 \frac{T_2}{T_s}. \quad (7.79)$$

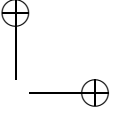
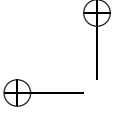


For calculating the amount of ISI, the pulse amplitudes at time instants $t_0 + kT_s$ are calculated. For $k < -2$ this results in $p(t_0 + kT_s) = 0$ and for $k = -1$ this results in

$$p(t_0 - T_s) \approx \frac{q(T_0 + 0.0181T_2)}{T_s} \approx \left\{ \frac{\sqrt{0.0181}}{2\pi} \exp(-4\pi \cdot 0.0181) + \left(0.0181 - \frac{1}{8\pi}\right) \left[1 - 2Q\left(2\sqrt{2\pi \cdot 0.0181}\right)\right] \right\} \frac{T_2}{T_s}. \quad (7.80)$$

For $k \geq 1$ one can find

$$\begin{aligned} p(t_0 + kT_s) &\approx \frac{1}{T_s} \left[q(T_0 + 0.0181T_2 + (k-1)T_s) - 2q(T_0 + 0.0181T_2 + kT_s) \right. \\ &\quad \left. + q(T_0 + 0.0181T_2 + (k+1)T_s) \right] \\ &\approx \frac{\sqrt{(0.0181T_2 + (k-1)T_s)T_2}}{2\pi T_s} \exp\left(-\frac{4\pi(0.0181T_2 + (k-1)T_s)}{T_2}\right) \\ &\quad - \frac{\sqrt{(0.0181T_2 + kT_s)T_2}}{\pi T_s} \exp\left(-\frac{4\pi(0.0181T_2 + kT_s)}{T_2}\right) \\ &\quad + \frac{\sqrt{(0.0181T_2 + (k+1)T_s)T_2}}{2\pi T_s} \exp\left(-\frac{4\pi(0.0181T_2 + (k+1)T_s)}{T_2}\right) \\ &\quad + \left[k-1 + \left(0.0181 - \frac{1}{8\pi}\right) \frac{T_2}{T_s} \right] \\ &\quad \cdot \left[1 - 2Q\left(2\sqrt{\frac{2\pi(0.0181T_2 + (k-1)T_s)}{T_2}}\right) \right] \\ &\quad - 2 \left[k + \left(0.0181 - \frac{1}{8\pi}\right) \frac{T_2}{T_s} \right] \left[1 - 2Q\left(2\sqrt{\frac{2\pi(0.0181T_2 + kT_s)}{T_2}}\right) \right] \\ &\quad + \left[k+1 + \left(0.0181 - \frac{1}{8\pi}\right) \frac{T_2}{T_s} \right] \\ &\quad \cdot \left[1 - 2Q\left(2\sqrt{\frac{2\pi(0.0181T_2 + (k+1)T_s)}{T_2}}\right) \right], \quad k \geq 1. \quad (7.81) \end{aligned}$$



For relatively small values of T_2 , we can approximate

$$\frac{\sqrt{(0.0181T_2 + kT_s)T_2}}{2\pi T_s} \exp\left(-\frac{4\pi(0.0181T_2 + kT_s)}{T_2}\right) \approx 0, \quad k \geq 1, \quad (7.82)$$

$$Q\left(2\sqrt{\frac{2\pi(0.0181T_2 + kT_s)}{T_2}}\right) \approx 0, \quad k \geq 1. \quad (7.83)$$

Hence, we can find

$$\begin{aligned} p(t_0 + T_s) &\approx \left\{ \frac{\sqrt{0.0181}}{2\pi} \exp(-4\pi \cdot 0.0181) \right. \\ &\quad + \left(0.0181 - \frac{1}{8\pi}\right) \left[1 - 2Q\left(2\sqrt{2\pi \cdot 0.0181}\right)\right] \\ &\quad \left. - \left(0.0181 - \frac{1}{8\pi}\right) \right\} \frac{T_2}{T_s} \\ &\approx 0.0279 \frac{T_2}{T_s}, \end{aligned} \quad (7.84)$$

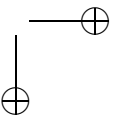
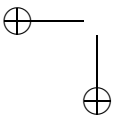
and $p(t_0 + kT_s) \approx 0$ for $k \geq 2$.

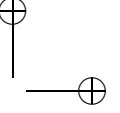
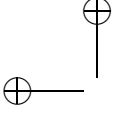
In the preceding it has been assumed that $T_2 > 0$. For $T_2 < 0$, the same results follow by mirroring, resulting in

$$p(t_0 + kT_s) \approx \begin{cases} 0.0062 \frac{|T_2|}{T_s} & , k = -1, \\ 1 - 0.0341 \frac{|T_2|}{T_s} & , k = 0, \\ 0.0279 \frac{|T_2|}{T_s} & , k = 1, \\ 0 & , |k| \geq 2. \end{cases} \quad (7.85)$$

These values are indicated by the circles in Figure 7.3(b) and the dashed lines in Figure 7.5(b). From the latter figure it follows that the approximation in (7.85) holds when $|T_2| < 3T_s$. Note that the sum of the sample values in (7.85) is again one.

Apparently, in case of second order CD with $|T_2| < 3T_s$, ISI is again dominated by the two directly neighboring pulses. The preceding pulse contributes more than the succeeding pulse, however. The expected value of the output samples of the integrate-and-dump filters can again be written as in (7.66) through (7.68).





7.3.2 Noise variance

The noise variance at the output of the integrate-and-dump filter in a two-way phase-synchronized balanced receiver follows directly from (7.47), (4.53), (4.54) and (4.56) as

$$\begin{aligned}
 \sigma_{V_{LP}(t)}^2 &= R_{V_{LP}V_{LP}}(t, t) - E^2[V_{LP}(t)] \\
 &\approx \frac{Z_{TIA}^2 R_{pd} P_x e}{2L_{Tx} L_{Rx} T_s} |H_f(f_c)|^2 \sum_k m_k p(t - k T_s) \\
 &\quad + \frac{Z_{TIA}^2 R_{pd}^2 P_x^2 \tau_c}{32L_{Rx}^2 L_{Tx}^2 T_s} |H_f(f_c)|^4 \sum_k m_k^2 [6 + \cos(2\phi_k)] p_N(t - k T_s) \\
 &\quad + \frac{Z_{TIA}^2 S_{th}}{T_s}, \tag{7.86}
 \end{aligned}$$

where $p(t)$ is defined by (7.52) and $p_N(t)$ is defined as

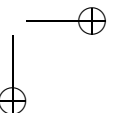
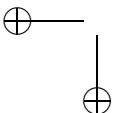
$$p_N(t) \triangleq \int_{-\infty}^{\infty} h_{CDN}(t - \rho) \Lambda\left(\frac{\rho}{T_s}\right) d\rho. \tag{7.87}$$

In order to evaluate the variances of the decision samples, (7.86) has to be evaluated at the sample instants $t_0 + k T_s$. Therefore, we need to evaluate both $p(t)$ and $p_N(t)$ at $t = t_0 + k T_s$. For $p(t)$ this has already been done in the previous subsection; the results are given by (7.65) and (7.85), for first and second order CD with $|T_1| < T_s$ and $|T_2| < 3T_s$, respectively. For $p_N(t)$ it can be done in the same way. For first order CD with $|T_1| < T_s$ this results in

$$p_N(t_0 + k T_s) = p_N(T_0 + k T_s) \approx \begin{cases} 1 - \frac{|T_1|}{\pi\sqrt{2}T_s}, & k = 0, \\ \frac{|T_1|}{2\pi\sqrt{2}T_s}, & k = \pm 1, \\ 0 & |k| \geq 2, \end{cases} \tag{7.88}$$

and for second order CD with $|T_2| < 3T_s$ this results in

$$p_N(t_0 + k T_s) \approx p_N(T_0 + 0.0181T_2 + k T_s) \approx \begin{cases} 0.0084 \frac{|T_2|}{T_s}, & k = -1, \\ 1 - 0.0186 \frac{|T_2|}{T_s}, & k = 0, \\ 0.0102 \frac{|T_2|}{T_s}, & k = 1, \\ 0 & |k| \geq 2. \end{cases} \tag{7.89}$$



In both cases $p(t_0 + k T_s) = p_N(t_0 + k T_s) = 0$ for $|k| > 2$ so that the variance of the decision samples $V_{LP}(t_0 + k T_s)$ follows from (7.86) as

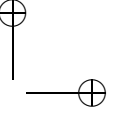
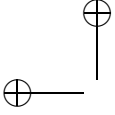
$$\begin{aligned} \sigma_{V_{LP}(t_0+k T_s)}^2 &\approx \\ &\frac{Z_{TIA}^2 R_{pd} P_x e}{2L_{Tx} L_{Rx} T_s} |H_f(f_c)|^2 \left[m_{k-1} p(t_0 + T_s) + m_k p(t_0) + m_{k+1} p(t_0 - T_s) \right] \\ &+ \frac{Z_{TIA}^2 R_{pd}^2 P_x^2 \tau_c}{32L_{Rx}^2 L_{Tx}^2 T_s} |H_f(f_c)|^4 \left\{ m_{k-1}^2 \left[6 + \cos(2\phi_{k-1}) \right] p_N(t_0 + T_s) \right. \\ &\quad \left. + m_k^2 \left[6 + \cos(2\phi_k) \right] p_N(t_0) + m_{k+1}^2 \left[6 + \cos(2\phi_{k+1}) \right] p_N(t_0 - T_s) \right\} \\ &+ \frac{Z_{TIA}^2 S_{th}}{T_s}. \end{aligned} \quad (7.90)$$

Similarly the variances and covariance of the output samples $V_{LP,I}(t_0 + k T_s)$ and $V_{LP,Q}(t_0 + k T_s)$ follow from (7.48) through (7.50) as

$$\begin{aligned} \sigma_{V_{LP,I}(t_0+k T_s)}^2 &\approx \\ &\frac{Z_{TIA}^2 R_{pd} P_x e}{4L_{Tx} L_{Rx} T_s} |H_f(f_c)|^2 \left[m_{k-1} p(t_0 + T_s) + m_k p(t_0) + m_{k+1} p(t_0 - T_s) \right] \\ &+ \frac{Z_{TIA}^2 R_{pd}^2 P_x^2 \tau_c}{128L_{Rx}^2 L_{Tx}^2 T_s} |H_f(f_c)|^4 \left\{ m_{k-1}^2 \left[6 - \cos(2\Delta\phi + 2\phi_{k-1}) \right] p_N(t_0 + T_s) \right. \\ &\quad \left. + m_k^2 \left[6 - \cos(2\Delta\phi + 2\phi_k) \right] p_N(t_0) \right. \\ &\quad \left. + m_{k+1}^2 \left[6 - \cos(2\Delta\phi + 2\phi_{k+1}) \right] p_N(t_0 - T_s) \right\} + \frac{Z_{TIA}^2 S_{th}}{T_s}. \end{aligned} \quad (7.91)$$

$$\begin{aligned} \sigma_{V_{LP,Q}(t_0+k T_s)}^2 &\approx \\ &\frac{Z_{TIA}^2 R_{pd} P_x e}{4L_{Tx} L_{Rx} T_s} |H_f(f_c)|^2 \left[m_{k-1} p(t_0 + T_s) + m_k p(t_0) + m_{k+1} p(t_0 - T_s) \right] \\ &+ \frac{Z_{TIA}^2 R_{pd}^2 P_x^2 \tau_c}{128L_{Rx}^2 L_{Tx}^2 T_s} |H_f(f_c)|^4 \left\{ m_{k-1}^2 \left[6 - \cos(2\Delta\phi + 2\phi_{k-1}) \right] p_N(t_0 + T_s) \right. \\ &\quad \left. + m_k^2 \left[6 - \cos(2\Delta\phi + 2\phi_k) \right] p_N(t_0) \right. \\ &\quad \left. + m_{k+1}^2 \left[6 - \cos(2\Delta\phi + 2\phi_{k+1}) \right] p_N(t_0 - T_s) \right\} + \frac{Z_{TIA}^2 S_{th}}{T_s}. \end{aligned} \quad (7.92)$$

$$\begin{aligned} C_{V_{LP,I}(t_0+k T_s)} &\approx \\ &\frac{Z_{TIA}^2 R_{pd}^2 P_x^2 \tau_c}{128L_{Rx}^2 L_{Tx}^2 T_s} |H_f(f_c)|^4 \left\{ m_{k-1}^2 \sin(2\Delta\phi + 2\phi_{k-1}) p_N(t_0 + T_s) \right. \\ &\quad \left. + m_k^2 \sin(2\Delta\phi + 2\phi_k) p_N(t_0) \right. \\ &\quad \left. + m_{k+1}^2 \sin(2\Delta\phi + 2\phi_{k+1}) p_N(t_0 - T_s) \right\}. \end{aligned} \quad (7.93)$$



7.3.3 Phase-synchronized BPSK

In case of phase-synchronized BPSK, the expected value and variance of the decision samples $V_{LP}(t_0 + kT_s)$ at the output of the two-way balanced receiver follow from (7.66) and (7.90) with $m_k = 1$ and $\phi_k = A_k\pi$, where $A_k \in \{0, 1\}$. The expected value can be written as

$$E[V_{LP}(t_0 + kT_s)] \approx \frac{Z_{TIA}R_{pd}P_x}{4L_{Tx}L_{Rx}} |H_f(f_c)|^2 B_k, \quad (7.94)$$

where the “distorted” symbol B_k depends on the corresponding bit A_k and its predecessor A_{k-1} and successor A_{k+1} :

$$B_k \triangleq \cos(A_{k-1}\pi)p(t_0 + T_s) + \cos(A_k\pi)p(t_0) + \cos(A_{k+1}\pi)p(t_0 - T_s), \quad (7.95)$$

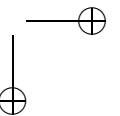
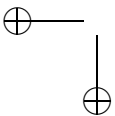
in which the sample values of $p(t)$ are given by (7.65) and (7.85) for first and second order CD with $|T_1| < T_s$ and $|T_2| < 3T_s$, respectively. The resulting values for B_k for all combinations of A_{k-1} , A_k and A_{k+1} are shown in Table 7.1.

Table 7.1: Distorted symbol values B_k for different bit combinations $A_{k-1}A_kA_{k+1}$ for first and second order CD, where it is assumed that $|T_1| < T_s$ and $|T_2| < 3T_s$, respectively

A_{k-1}	A_k	A_{k+1}	B_k	
			first order CD	second order CD
0	0	0	1	1
0	0	1	$1 - \frac{ T_1 }{\pi T_s}$	$1 - 0.0124 \frac{ T_2 }{T_s}$
0	1	0	$-1 + \frac{2 T_1 }{\pi T_s}$	$-1 + 0.0682 \frac{ T_2 }{T_s}$
0	1	1	$-1 + \frac{ T_1 }{\pi T_s}$	$-1 + 0.0558 \frac{ T_2 }{T_s}$
1	0	0	$1 - \frac{ T_1 }{\pi T_s}$	$1 - 0.0558 \frac{ T_2 }{T_s}$
1	0	1	$1 - \frac{2 T_1 }{\pi T_s}$	$1 - 0.0682 \frac{ T_2 }{T_s}$
1	1	0	$-1 + \frac{ T_1 }{\pi T_s}$	$-1 + 0.0124 \frac{ T_2 }{T_s}$
1	1	1	-1	-1

The variance follows from (7.90) and (7.55) as

$$\sigma_{V_{LP}(t_0+kT_s)}^2 \approx \frac{Z_{TIA}^2}{T_s} \left[\frac{R_{pd}P_x e}{2L_{Tx}L_{Rx}} |H_f(f_c)|^2 + \frac{7R_{pd}^2 P_x^2 \tau_c}{32L_{Rx}^2 L_{Tx}^2} |H_f(f_c)|^4 + S_{th} \right]. \quad (7.96)$$



Apparently, the variance of the decision samples is not affected by CD in case of BPSK modulation.

When the bits are assumed to be independent and to take values 0 and 1 with equal probability, then the computed values of B_k are all equally likely. Hence, the conditional probability density functions of $V_{\text{LP}}(t_0 + kT_s)$ for $A_k = 0$, $f_0(v)$, and for $A_k = 1$, $f_1(v)$, can be derived. $f_0(v)$ and $f_1(v)$ each consist of four Gaussian terms, representing the four possible combinations of A_{k-1} and A_{k+1} . The resulting bit error probability then follows from (4.70) as

$$\begin{aligned} P_e \approx \frac{1}{4}Q\left(\sqrt{2\gamma_{\text{BPSK}}}\right) + \frac{1}{2}Q\left(\left(1 - \frac{|T_1|}{\pi T_s}\right)\sqrt{2\gamma_{\text{BPSK}}}\right) \\ + \frac{1}{4}Q\left(\left(1 - \frac{2|T_1|}{\pi T_s}\right)\sqrt{2\gamma_{\text{BPSK}}}\right), \end{aligned} \quad (7.97)$$

in case of first order CD with $|T_1| < T_s$, and

$$\begin{aligned} P_e \approx \frac{1}{4}Q\left(\sqrt{2\gamma_{\text{BPSK}}}\right) + \frac{1}{4}Q\left(\left(1 - 0.0124\frac{|T_2|}{T_s}\right)\sqrt{2\gamma_{\text{BPSK}}}\right) \\ + \frac{1}{4}Q\left(\left(1 - 0.0682\frac{|T_2|}{T_s}\right)\sqrt{2\gamma_{\text{BPSK}}}\right) \\ + \frac{1}{4}Q\left(\left(1 - 0.0558\frac{|T_2|}{T_s}\right)\sqrt{2\gamma_{\text{BPSK}}}\right), \end{aligned} \quad (7.98)$$

in case of second order CD with $|T_2| < 3T_s$, where

$$\gamma_{\text{BPSK}} \triangleq \left(\gamma_{\text{sn}}^{-1} + \gamma_{\text{bn}}^{-1} + \gamma_{\text{tn}}^{-1}\right)^{-1}, \quad (7.99)$$

with

$$\gamma_{\text{sn}} = \frac{R_{\text{pd}}P_x T_s}{16L_{\text{Tx}}L_{\text{Rx}}e} |H_f(f_c)|^2, \quad (7.100)$$

$$\gamma_{\text{bn}} = \frac{T_s}{7\tau_c} |H_f(f_c)|^4, \quad (7.101)$$

$$\gamma_{\text{tn}} = \frac{R_{\text{pd}}^2 P_x^2 T_s}{32L_{\text{Rx}}^2 L_{\text{Tx}}^2 S_{\text{th}}}. \quad (7.102)$$

This result has been derived for a system with just one transmitter and receiver. It can be shown that the same result also applies to the multiplexing topologies that have been studied in Chapter 5, when the expressions (7.100) through (7.102) are replaced by the corresponding expressions in Chapter 5, provided that the factor $|H_f(f_c)|^2$ (the propagation loss in the fiber) is accounted for in the losses in the network L_{nw} . For a PA, for example, they should be replaced by (5.20) through (5.22).

Example 7.3

Consider an example of a PA like in Example 5.2, with $N = 16$ channels and optical sources with center wavelength $\lambda_c = 1550$ nm.

In that case, the attenuation is typically $\alpha \approx 0.2$ dB/km. When l_f is expressed in kilometers, the total propagation loss is $0.2 l_f$ dB so that the total losses in the network L_{nw} can be written as

$$L_{nw} \approx 1.047 N^2 |H_f(f_c)|^2 = 1.047 \cdot 16^2 \cdot 10^{0.02 l_f} \approx 268.032 \cdot 10^{0.02 l_f}. \quad (7.103)$$

First order CD is dominant with $\tau'_g(f_c) \approx -160$ ps/(THz·km), so that the maximum achievable bit rate at $P_e = 10^{-9}$ can be found numerically using the approximation in (7.97), provided that the fiber lengths are chosen such that $|T_1| < T_s$. The remaining parameters are simply chosen the same as in Example 5.2.

The results are shown in Figure 7.6(a) for coherence times of 80, 100 and 120 fs. (It can be verified that these results indeed satisfy $|T_1| < T_s$ in the considered fiber length range.)

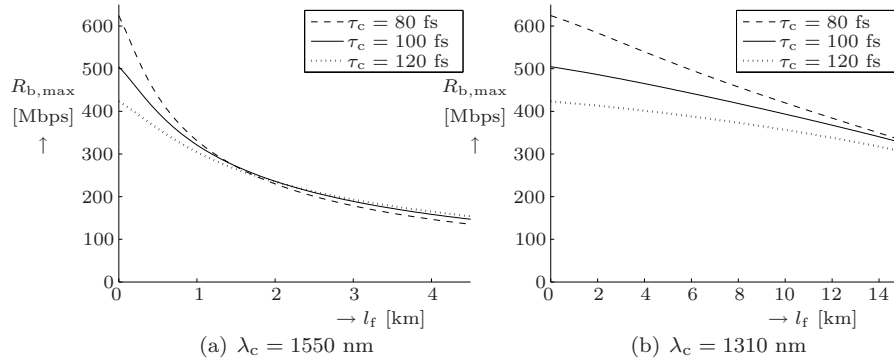
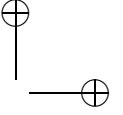
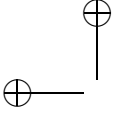


Figure 7.6: Maximum bit rate per channel R_b as a function of fiber length l_f in a 16-channel PA with BPSK modulation, for center wavelengths $\lambda_c = 1550$ nm and $\lambda_c = 1310$ nm

Obviously, the maximum bit rate decreases with increasing fiber length, because of the increasing CD effect. Note that the optimum coherence time τ_c depends on the fiber length l_f : for short fibers the maximum bit rate is mainly determined by the beat noise, so that a small τ_c should be chosen, whereas for long fibers, the maximum bit rate is also determined by the CD, so that a larger τ_c should be chosen. □

**Example 7.4**


Now consider the same PA as in Example 7.3, but now with a center wavelength $\lambda_c = 1310$ nm, which corresponds to the zero-dispersion wavelength of standard SMF.

In that case, the attenuation is typically $\alpha \approx 0.35$ dB/km. When l_f is expressed in kilometers, the total propagation loss is $0.35 l_f$ dB so that the total losses in the network L_{nw} can be written as

$$L_{nw} \approx 1.047 N^2 |H_f(f_c)|^2 = 1.047 \cdot 16^2 \cdot 10^{0.035 l_f} \approx 268.032 \cdot 10^{0.035 l_f}. \quad (7.104)$$

Second order CD is now dominant with $\tau_g''(f_c) \approx 3.3$ ps/(THz²·km), so that the maximum achievable bit rate at $P_e = 10^{-9}$ can be found numerically using the approximation in (7.98), provided that the fiber lengths are chosen such that $|T_2| < 3T_s$. The remaining parameters are simply chosen the same as in Example 7.3.

The results are shown in Figure 7.6(b) for coherence times of 80, 100 and 120 fs. (It can be verified that these results indeed satisfy $|T_2| < 3T_s$ in the considered fiber length range.)

The results show the same trend as in the previous example: the maximum bit rate decreases with increasing fiber length, and the lower the coherence time, the faster the maximum bit rate decreases. The intersection points are not visible in this graph, because they occur at fiber lengths were $|T_2| > 3T_s$, so that the approximation in (7.98) is not accurate anymore. 

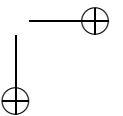
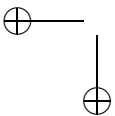
7.3.4 Phase-synchronized OOK

In case of phase-synchronized OOK, the expected value and variance of the decision samples at the output of the two-way balanced receiver follow from (7.66) and (7.90) with $\phi_k = 0$ and $m_k = A_k$ with $A_k \in \{0, 1\}$. The rest of the procedure for finding the bit error rate is similar as done for BPSK. The main difference is that the variance of the decision samples $V_{LP}(t_0 + k T_s)$ now also depends on the bit combinations $A_{k-1} A_k A_{k+1}$. For multiple channels, this variance even depends on the bit combinations of both the matched transmitter and the interfering transmitters, resulting in a very complicated expression for the total bit error probability.

It is expected, however, that the effective degradation due to pulse distortion is in the same order of magnitude as in the case of BPSK modulation, because OOK has the same symbol length T_s as BPSK when the bit rates are the same. Therefore, phase-synchronized OOK is not considered in further detail here.

7.3.5 Phase-synchronized M -ary PSK

In case of phase-synchronized M -ary PSK, the expected value and variance of the decision samples $V_{LP,I}(t_0 + k T_s)$ and $V_{LP,Q}(t_0 + k T_s)$ at the output of the four-way balanced receiver follows from (7.67), (7.68), (7.91) and (7.92) with $m_k = 1$.



For QPSK, we have $\phi_k = (2A_k + 1)\frac{\pi}{4}$, where $A_k \in \{0, 1, 2, 3\}$. The expected values can then be written as

$$E[V_{LP,I}(t_0 + kT_s)] \approx \frac{Z_{TIA}R_{pd}P_x}{8L_{Tx}L_{Rx}} |H_f(f_c)|^2 B_k, \quad (7.105)$$

$$E[V_{LP,Q}(t_0 + kT_s)] \approx \frac{Z_{TIA}R_{pd}P_x}{8L_{Tx}L_{Rx}} |H_f(f_c)|^2 C_k. \quad (7.106)$$

where

$$B_k \triangleq \cos\left((2A_{k-1} + 1)\frac{\pi}{4}\right)p(t_0 + T_s) + \cos\left((2A_k + 1)\frac{\pi}{4}\right)p(t_0) \\ + \cos\left((2A_{k+1} + 1)\frac{\pi}{4}\right)p(t_0 - T_s), \quad (7.107)$$

$$C_k \triangleq \sin\left((2A_{k-1} + 1)\frac{\pi}{4}\right)p(t_0 + T_s) + \sin\left((2A_k + 1)\frac{\pi}{4}\right)p(t_0) \\ + \sin\left((2A_{k+1} + 1)\frac{\pi}{4}\right)p(t_0 - T_s), \quad (7.108)$$

and using (7.55) the variances can be written as

$$\sigma_{V_{LP,I}(t_0+kT_s)}^2 = \sigma_{V_{LP,Q}(t_0+kT_s)}^2 \approx \\ \frac{Z_{TIA}^2}{T_s} \left[\frac{R_{pd}P_x e}{4L_{Tx}L_{Rx}} |H_f(f_c)|^2 + \frac{3R_{pd}^2 P_x^2 \tau_c}{128L_{Rx}^2 L_{Tx}^2} |H_f(f_c)|^4 + S_{th} \right]. \quad (7.109)$$

For QPSK each symbol A_k represents two bits. From the equations it follows that the individual detection of the first bit of symbol A_k (which is done by thresholding $V_{LP,I}(t_0 + kT_s)$) is only affected by the first bits of the symbols A_{k-1} , A_k and A_{k+1} , and not by their second bits. Hence, the bit error probability can be calculated in the similar way as in the previous subsection, resulting in

$$P_e \approx \frac{1}{4}Q(\sqrt{\gamma_{QPSK}}) + \frac{1}{2}Q\left(\left(1 - \frac{T_1}{\pi T_s}\right)\sqrt{\gamma_{QPSK}}\right) \\ + \frac{1}{4}Q\left(\left(1 - \frac{T_1}{2\pi T_s}\right)\sqrt{\gamma_{QPSK}}\right), \quad (7.110)$$

in case of first order CD with $|T_1| < T_s$, and

$$P_e \approx \frac{1}{4}Q(\sqrt{\gamma_{QPSK}}) + \frac{1}{4}Q\left(\left(1 - 0.0124\frac{T_2}{T_s}\right)\sqrt{\gamma_{QPSK}}\right) \\ + \frac{1}{4}Q\left(\left(1 - 0.0682\frac{T_2}{T_s}\right)\sqrt{\gamma_{QPSK}}\right) \\ + \frac{1}{4}Q\left(\left(1 - 0.0558\frac{T_2}{T_s}\right)\sqrt{\gamma_{QPSK}}\right), \quad (7.111)$$

in case of second order CD with $|T_2| < 3T_s$, where

$$\gamma_{QPSK} \triangleq \left(\gamma_{sn}^{-1} + \gamma_{bn}^{-1} + \gamma_{tn}^{-1}\right)^{-1}, \quad (7.112)$$

with

$$\gamma_{\text{sn}} = \frac{R_{\text{pd}} P_x T_s}{32 L_{\text{Tx}} L_{\text{Rx}} e} |H_f(f_c)|^2, \quad (7.113)$$

$$\gamma_{\text{bn}} = \frac{T_s}{6\tau_c} |H_f(f_c)|^4, \quad (7.114)$$

$$\gamma_{\text{tn}} = \frac{R_{\text{pd}}^2 P_x^2 T_s}{128 L_{\text{Rx}}^2 L_{\text{Tx}}^2 S_{\text{th}}}. \quad (7.115)$$

For a PA the latter three equations should be replaced by (6.79) through (6.81).

Example 7.5

The calculations in Examples 7.3 and 7.4 are repeated with QPSK and $\tau_c = 100$ fs. The results are shown in Figure 7.7(a) and 7.7(b), respectively.

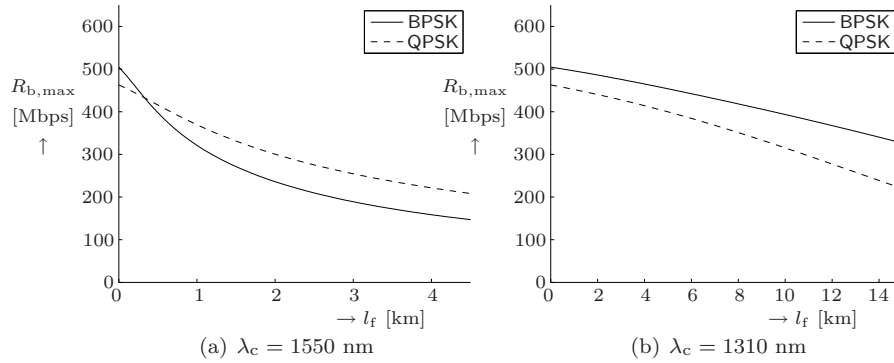


Figure 7.7: Maximum bit rate per channel R_b as a function of fiber length l_f in a 16-channel PA with BPSK or QPSK modulation, for center wavelengths $\lambda_c = 1550$ nm and $\lambda_c = 1310$ nm

For $\lambda_c = 1550$ nm, BPSK performs slightly better than QPSK for short fiber lengths, because the two-way balanced BPSK receiver has a lower insertion loss than the four-way balanced QPSK receiver (also see Example 6.5). QPSK performs better for long fiber lengths, however, because the symbol time T_s in case of QPSK is twice as large as the symbol time in case of BPSK modulation, for the same bit rate R_b . Hence, QPSK is less susceptible to CD.

The same story does not seem to hold for $\lambda = 1310$ nm: BPSK is always better in that situation. This is caused by the fact that the delay spread per unit length for $\lambda = 1310$ nm is smaller than for $\lambda = 1550$ nm, so that CD becomes significant at much longer fiber lengths, whereas the attenuation per unit length for $\lambda_c = 1310$ nm is larger than for $\lambda_c = 1550$ nm. Hence, the decrease in maximum bit rate with increasing fiber length in Figure 7.7(b) is mainly caused by attenuation rather than by CD.

This is confirmed by the results in Figure 7.8(a) and 7.8(b), where the computations have been repeated for an 8-channel PA.

In that case, there is less beat noise and less splitting loss, so that the bit rates that can be achieved are much larger. Hence, CD becomes significant at shorter fiber lengths, so that attenuation becomes less of an issue, and QPSK becomes better than BPSK. The difference is small for the considered fiber lengths, however. (For longer fiber lengths, the approximations for the bit error rates no longer hold.)

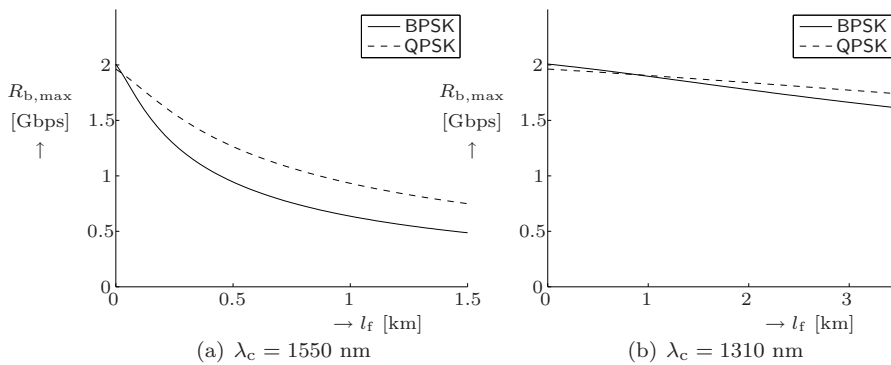


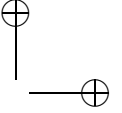
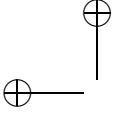
Figure 7.8: Maximum bit rate per channel R_b as a function of fiber length l_f in an 8-channel PA with BPSK or QPSK modulation, for center wavelengths $\lambda_c = 1550$ nm and $\lambda_c = 1310$ nm

The bit error rate analysis for M -ary PSK with $M \geq 8$ is a lot more complicated: it can be verified that the expression for the symbol error rate consists of $\frac{1}{2}M^2$ terms, because each symbol value has a different effect on neighboring symbols. Therefore, M -ary PSK with $M \geq 8$ is not further considered here.

7.4 Equalization techniques

In the previous section it has been shown that the performance of a CM system can be significantly affected by ISI when no special measures are taken to cope with the CD in the transmission fiber.

In this section some possible strategies for combating the ISI will be discussed briefly. These can be divided in electrical and optical equalization techniques.



7.4.1 Electrical equalization techniques

A first approach for improving the performance of a CM system suffering from CD is to consider the entire CM system in Figure 7.1—from the modulator input in the transmitter to the low-pass filter input in the receiver— as a black box. In the previous sections it has been shown that, for relatively narrowband modulating signals, this black box can be considered as a time-invariant linear low-pass filter with (normalized) impulse response (7.25) and transfer function (7.30). When BPSK or QPSK modulation is performed, the behavior of the noise is not affected by CD, and the portion that spectrally coincides with the modulating signals can be considered as white and Gaussian distributed.

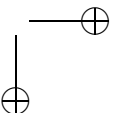
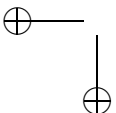
A straightforward approach is hence to consider the CM system as a band-limited additive white Gaussian noise (AWGN) channel, and then apply known transmission concepts like pulse-shaping, correlative coding, linear equalization, decision-feedback equalization (DFE) and/or maximum likelihood sequence estimation (MLSE); see for example [81] for an extensive discussion of such techniques. Linear equalization and DFE have actually been illustrated for point-to-point LED transmission over single-mode fiber [86, 87] and an OCDM system based on periodic spectral coding [88].

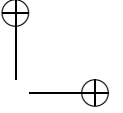
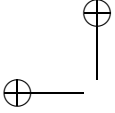
For an AWGN channel it follows from Shannon's capacity theorem [89] that the maximum transmission rate of binary digits that can be accommodated at an arbitrarily low error rate is limited by the bandwidth of the channel and the signal-to-noise ratio. The error rate can be made arbitrarily small by applying a suitable combination of the techniques mentioned above. When transmission is performed at a higher rate, the error rate cannot be made arbitrarily small, no matter what kind of equalization is performed.

Similarly, the black box model of a CM system with a given number of channels, center wavelength, coherence time and fiber length has a limited bandwidth due to CD, and a limited signal-to-noise ratio due to optical beat interference. Hence, there is a bound to the transmission rate with arbitrarily small bit error rate that can be achieved by applying any of the electrical equalization techniques mentioned above.

7.4.2 Optical equalization techniques

A more effective approach is to increase the bandwidth of the black box by reducing the CD in the fiber. This can be done by using dispersion-shifted fiber (DSF) or dispersion-flattened fiber (DFF) instead of standard SMF, or by cascading a standard SMF with dispersion-compensating fiber (DCF) [49]. The disadvantage of DSF and DFF is that they are significantly more expensive than standard SMF, and hence not desirable for installation in typical CM applications like LANs and access networks. The main disadvantage of DCF is that its length has to be adapted to the length of the SMF to which it is cascaded, which increases installation costs.





The best solution from a cost point of view is probably to integrate a dispersion-compensating device with the MZI in the optical receiver circuit. The main design criteria for such a device would be to have it match the fiber's dispersion characteristic over a large wavelength range (tens of nanometers) and to make it (easily) tunable with a tuning range that corresponds to the proper fiber length range. This is not considered in further detail here.

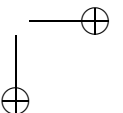
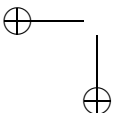
7.5 Conclusions

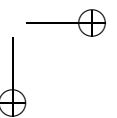
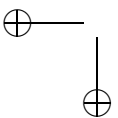
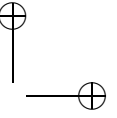
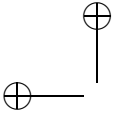
It has been shown both by analysis and simulation that the performance of CM systems can be degraded by attenuation and CD in the transmission fiber, depending on optical center wavelength, coherence time, fiber length and bandwidth of the modulating signal. In case of significant CD, the output signal of the receiver suffers from ISI, resulting in a significant reduction of the maximum bit rate that can be achieved when no further measures are taken.

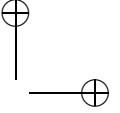
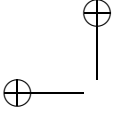
Furthermore it has been shown that—in cases where the performance of the system is determined by CD rather than by losses— QPSK modulation results in a better performance than BPSK modulation, since BPSK requires a higher symbol rate than QPSK for the same bit rate.

Moreover the performance can be improved by applying equalization techniques. This can be done either electrically or optically. The latter is the most effective because it results in a fundamental increase of the transmission bandwidth that the CM system accommodates.

Part of the results that have been presented in this chapter were published in [90].







Chapter 8

Radio-frequency signal distribution

8.1 Introduction

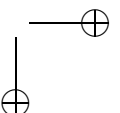
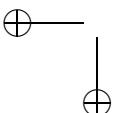
In the previous chapters CM has been considered as a means to multiplex digital signals through a common optical fiber cable. In this chapter it will be shown that CM can also be used to multiplex analog signals. More specifically, the aim is to investigate the applicability of CM as a means to distribute radio-frequency (RF) signals, or in other words, to use CM as an optical RF feeder technology.

The need for RF feeder technologies has been given impetus by the recent interest in cellular wireless communications systems. As an example, consider the indoor wireless access system in Figure 8.1.

The main issue in such a system is that the high transmission frequencies of modern wireless access systems (several GHz up to several tens of GHz) limit the transmission range of the mobile terminals (MTs) to relatively small cells. Therefore, many radio access points (RAPs) are required in order to provide coverage to the MTs such that they can connect to the central node (CN) from anywhere in the envisioned service area. Moreover, the deployment density might even be increased further in case a large number of MTs are to be supported in a relatively small service area.

A second issue is that wireless transmission requires quite some complicated functions like coders, modulators and frequency upconverters (mixers). If the corresponding hardware were installed in the RAPs, this would make a wireless access system very expensive, especially in case a lot of RAPs are required in order to provide coverage over a large area.

A less expensive alternative could be to concentrate functionalities like coding, modulation and mixing in the CN and hence convert the signals into air wave format prior to distributing them through the access network, so that the CN in fact acts as a remote base station.



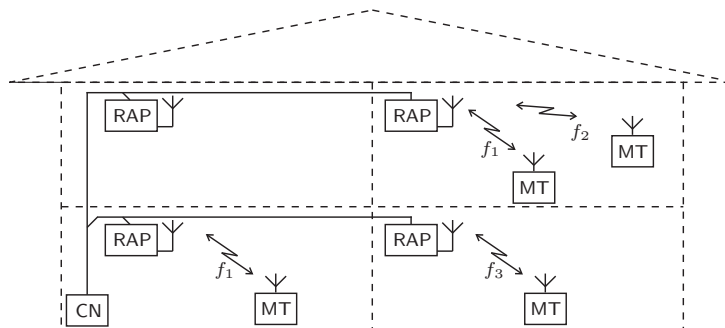
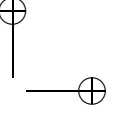
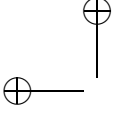


Figure 8.1: Example of a simple indoor wireless access system (CN=central node, RAP=radio access point, MT=mobile terminal)

Since copper cables do not provide enough bandwidth to distribute such signals over reasonable distances, optical fiber should be used as a transmission medium. In that case, the RAPs only need to contain an opto-electronic converter and a power amplifier. This concept is known as *Radio over Fiber (RoF) transmission* [91]. Besides the reduced RAP complexity, RoF shares common advantages with other optical fiber communication techniques, such as reliability, transparency and low attenuation and dispersion (see Section 1.1). Depending on the required number of RAPs, RoF could hence result in a less expensive, more reliable and more flexible access system with a larger network span than in the case where all the RAPs are full base stations, connected by copper transmission media.

When part of the network consists of a common transmission fiber, optical multiplexing is required in order to enable the CN to distribute signals to several RAPs at the same time and hence serve multiple MTs simultaneously. Because of its potentially simple implementation, CM could be an interesting candidate to distinguish between RAPs. Moreover, SCM (see Subsection 1.4.3) could be used on top of CM [92–94], for example to support multiple MTs through the same RAP, or to support multi-carrier modulation formats.

In the next section coherence multiplexing and demultiplexing of individual RF signals will be discussed, both for PM and IM. The impact of CD and noise on the performance will be analyzed. Section 8.3 will describe how the methods described in Chapter 6 (phase synchronization, self-heterodyning and phase diversity detection) can be used to stabilize the output of a CM receiver in case of RF modulation. In Section 8.4 it will be explained how multiple RF signals can be simultaneously transmitted through the same CM channel by means of SCM, and how this affects the noise performance and the applicability of the above-mentioned output stabilization methods. The chapter will end with conclusions.



8.2 Coherence (de)multiplexing of radio-frequency signals

We start with the simple case that each CM channel in a PA with N transmitters and balanced receivers conveys only one RF signal. The low-pass filters in the receivers (see Figure 4.12) are replaced by band-pass filters with impulse response $h_{\text{BP}}(t)$, and each receiver r is assumed to be matched to transmitter r on a coherence time scale (so $|T_{\text{Rx},r} - T_{\text{Tx},r}| \ll \tau_c \forall r$ and $|T_{\text{Rx},r} - T_{\text{Tx},i}| \gg \tau_c$ for $r \neq i$). Phase modulation and intensity modulation will be considered separately in the following two subsections. Then the impact of CD will be described and analyzed, followed by an analysis of the noise performance.

8.2.1 Phase modulation (PM)

When PM is applied to modulate the RF signals onto the CM channels, each modulating signal $\phi_{\text{mod},i}(t)$ can be written as

$$\phi_{\text{mod},i}(t) = \beta_i(t) \sin(2\pi f_i t + \psi_i(t)), \quad (8.1)$$

where $\beta_i(t)$, f_i and $\psi_i(t)$ are the amplitude, carrier frequency and phase of the RF signal, respectively. The behavior of $\beta_i(t)$ and $\psi_i(t)$ depends on the RF signal format, which is for example prescribed by a corresponding wireless transmission standard.

When CD is neglected (we will come back to this later), the expected value of the output signal $V_{\text{BP},r}(t)$ of the band-pass filter in receiver r follows from (6.3) as

$$\begin{aligned} \mathbb{E}[V_{\text{BP},r}(t)] &= \frac{Z_{\text{TIA}} R_{\text{pd}} P_x}{4L_{\text{Tx}} L_{\text{Rx}} L_{\text{nw}}} \int_{-\infty}^{\infty} h_{\text{BP}}(t - \rho) \\ &\quad \cdot \cos(\Delta\phi_r + \beta_r(\rho) \sin(2\pi f_r t + \psi_r(\rho))) \, d\rho. \end{aligned} \quad (8.2)$$

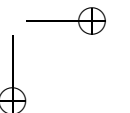
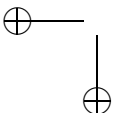
where $\Delta\phi_r \triangleq 2\pi f_c (T_{\text{Rx},r} - T_{\text{Tx},r})$. Using the trigonometric identity

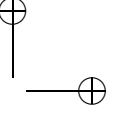
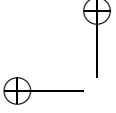
$$\cos(x + y) = \cos x \cos y - \sin x \sin y, \quad (8.3)$$

this can be written as an expression that contains terms of the form $\cos(\beta \sin \Phi)$ and $\sin(\beta \sin \Phi)$, where $\beta = \beta_r(t)$ and $\Phi = 2\pi f_r t + \psi_r(t)$. Using a Fourier series expansion these can be written as

$$\cos(\beta \sin \Phi) = \sum_n J_n(\beta) \cos(n \Phi), \quad (8.4)$$

$$\sin(\beta \sin \Phi) = \sum_n J_n(\beta) \sin(n \Phi), \quad (8.5)$$





where the Fourier coefficients $J_n(\cdot)$ are Bessel functions of the first kind and order n :

$$J_n(x) \triangleq \frac{1}{2\pi} \int_0^{2\pi} \cos(x \sin \theta - n \theta) d\theta. \quad (8.6)$$

Consequently, we can write

$$\begin{aligned} E[V_{\text{BP},r}(t)] &= \frac{Z_{\text{TIA}} R_{\text{pd}} P_x}{4L_{\text{Tx}} L_{\text{Rx}} L_{\text{nw}}} \int_{-\infty}^{\infty} h_{\text{BP}}(t - \rho) \\ &\cdot \left[\cos(\Delta\phi_r) \sum_n J_n(\beta_r(\rho)) \cos(2\pi n f_r \rho + n \psi_r(\rho)) \right. \\ &\quad \left. - \sin(\Delta\phi_r) \sum_n J_n(\beta_r(\rho)) \sin(2\pi n f_r \rho + n \psi_r(\rho)) \right] d\rho. \quad (8.7) \end{aligned}$$

From (8.6) one can verify that Bessel functions satisfy the following property

$$J_{-n}(x) = (-1)^n J_n(x), \quad n \in \mathbb{Z}, \quad (8.8)$$

so that we get

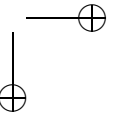
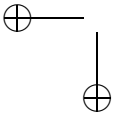
$$\begin{aligned} E[V_{\text{BP},r}(t)] &= \frac{Z_{\text{TIA}} R_{\text{pd}} P_x}{4L_{\text{Tx}} L_{\text{Rx}} L_{\text{nw}}} \int_{-\infty}^{\infty} h_{\text{BP}}(t - \rho) \\ &\cdot \left\{ \cos(\Delta\phi_r) \left[J_0(\beta_r(\rho)) + 2 \sum_{\substack{n=2 \\ n \text{ even}}}^{\infty} J_n(\beta_r(\rho)) \cos(2\pi n f_r \rho + n \psi_r(\rho)) \right] \right. \\ &\quad \left. - 2 \sin(\Delta\phi_r) \sum_{\substack{n=1 \\ n \text{ odd}}}^{\infty} J_n(\beta_r(\rho)) \sin(2\pi n f_r \rho + n \psi_r(\rho)) \right\} d\rho. \quad (8.9) \end{aligned}$$

Apparently, harmonic distortion occurs due to the intrinsic non-linearity of the demodulation principle. As a result, the output signal contains a baseband term and an infinite sum of RF terms with carrier frequencies that are integer multiples of f_r . The desired part is the RF term with carrier frequency f_r . Hence, the band-pass filter should be dimensioned such that this term is completely passed and the other terms are completely suppressed. The amplitude of the resulting signal can be optimized by setting $\Delta\phi_r = \frac{3\pi}{2}$ (how to do this will be discussed in Section 8.3), resulting in

$$E[V_{\text{BP},r}(t)] = \frac{Z_{\text{TIA}} R_{\text{pd}} P_x}{2L_{\text{Tx}} L_{\text{Rx}} L_{\text{nw}}} |H_{\text{BP}}(f_r)| J_1(\beta_r(t)) \sin(2\pi f_r t + \psi_r(t)), \quad (8.10)$$

where $H_{\text{BP}}(f)$ is the transfer function of the band-pass filter. An irrelevant phase shift has been omitted.

The relation between the amplitude of this signal and the amplitude $\beta_r(t)$ of the RF signal is non-linear. This follows from Figure 8.2, where the first order Bessel function of the first kind $J_1(\cdot)$ has been plotted.



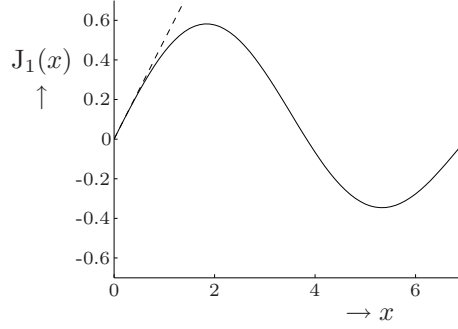


Figure 8.2: First order Bessel function of the first kind

Hence, when the RF feeder system is used in an application where the amplitude $\beta_r(t)$ of the RF signal is modulated by an analog signal (like for example in analog TV distribution) or by means of a multilevel digital modulation technique (like for example M -ary PAM or QAM), then $\beta_r(t)$ should be kept in such a range that $J_1(x)$ can be approximated by its first order Taylor expansion (dashed line):

$$J_1(x) \approx \frac{1}{2}x. \quad (8.11)$$

It can be shown that the relative error is smaller than 1% when $|x| < 0.2819$. Hence, when $|\beta_r(t)| < 0.2819$, the output signal of the band-pass filter can be approximated as

$$E[V_{\text{BP},r}(t)] \approx \frac{Z_{\text{TIA}}R_{\text{pd}}P_x}{4L_{\text{Tx}}L_{\text{Rx}}L_{\text{nw}}} |H_{\text{BP}}(f_r)| \beta_r(t) \sin(2\pi f_r t + \psi_r(t)). \quad (8.12)$$

On the other hand, when the RF feeder system is used in an application where $\beta_r(t)$ is a constant β (or eventually: when $\beta_r(t)$ only takes the values 0 and β), then the amplitude of the output signal can be maximized by choosing β such that $J_1(\beta)$ is maximized. Since the derivative of $J_1(\cdot)$ is given by

$$J_1'(x) = J_0(x) - \frac{J_1(x)}{x}, \quad (8.13)$$

we find

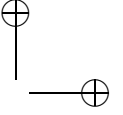
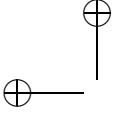
$$\beta J_0(\beta) = J_1(\beta). \quad (8.14)$$

Numerically solving for β then results in

$$\beta \approx 1.8412 \Rightarrow J_1(\beta) \approx 0.5819, \quad (8.15)$$

so that the output signal with maximum amplitude is given by

$$E[V_{\text{BP},r}(t)] \approx \frac{0.291Z_{\text{TIA}}R_{\text{pd}}P_x}{L_{\text{Tx}}L_{\text{Rx}}L_{\text{nw}}} |H_{\text{BP}}(f_r)| \sin(2\pi f_r t + \psi_r(t)). \quad (8.16)$$



8.2.2 Intensity modulation (IM)

Since, as a rule, broadband sources cannot be directly modulated by signals in the GHz range, IM by RF signals should be applied by means of external modulation, for example by means of an MZI or an electro-absorption modulator. In general, external intensity modulators have a non-linear relation between the modulating signal and the modulated intensity at the output. Hence, when external IM is applied in a CM system for distributing RF signals, the non-linearity already occurs in the modulation (whereas it occurs in the demodulation in case of PM).

In this subsection, it will be assumed that IM is performed by means of an MZ-based intensity modulator. In case of RF modulation it can be shown that the effective modulating signal of such a modulator is given by

$$m_{\text{mod},i}(t) = \frac{1}{2} \left[1 + \sin\left(\beta_i(t) \sin\left(2\pi f_i t + \psi_i(t)\right)\right) \right]. \quad (8.17)$$

Using (8.5) and (8.8) this can be written as

$$m_{\text{mod},i}(t) = \frac{1}{2} + \sum_{\substack{n=1 \\ n \text{ odd}}}^{\infty} J_n\left(\beta_i(t)\right) \sin\left(2\pi n f_i t + n \psi_i(t)\right). \quad (8.18)$$

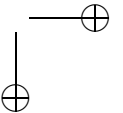
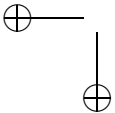
The resulting output signal of the band-pass filter in a matched receiver can be found by substituting this in (6.3), resulting in

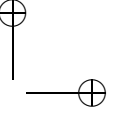
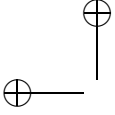
$$\begin{aligned} E[V_{\text{BP},r}(t)] &= \frac{Z_{\text{TIA}} R_{\text{pd}} P_x}{8L_{\text{Tx}} L_{\text{Rx}} L_{\text{nw}}} \cos(\Delta\phi_r) \int_{-\infty}^{\infty} h_{\text{BP}}(t - \rho) \\ &\quad \cdot \left[1 + 2 \sum_{\substack{n=1 \\ n \text{ odd}}}^{\infty} J_n\left(\beta_r(t)\right) \sin\left(2\pi n f_r t + n \psi_r(t)\right) \right] d\rho. \end{aligned} \quad (8.19)$$

Apparently, the output signal now contains a baseband term and RF terms with frequencies that are odd multiples of f_r . In contrary to the PM case, all terms have amplitudes that are proportional to $\cos(\Delta\phi_r)$, so $\Delta\phi_r = 0$ should be chosen to maximize the amplitude of the desired term. (This will be further discussed in Section 8.3.) Furthermore, the band-pass filter should be dimensioned such that only the desired RF signal (with carrier frequency f_r) is passed through, resulting in

$$E[V_{\text{BP},r}(t)] = \frac{Z_{\text{TIA}} R_{\text{pd}} P_x}{4L_{\text{Tx}} L_{\text{Rx}} L_{\text{nw}}} |H_{\text{BP}}(f_r)| J_1\left(\beta_r(t)\right) \sin\left(2\pi f_r t + \psi_r(t)\right). \quad (8.20)$$

This is the same as (8.10), apart from a factor $1/2$. Hence, $\beta_r(t)$ should be optimized in the same way as for PM, resulting in an output signal that is 6 dB weaker.





Another disadvantage of IM is that puts similar requirements on the CMRR of the balanced detector configuration as in the case of OOK modulation, as described in Subsection 4.8.3, because both the common terms and the differential terms contain both baseband and RF terms when IM is performed. Hence, when the balanced detector is not well-balanced, crosstalk between the CM channels will occur when two or more CM channels carry RF signals with the same carrier frequency. Note that this does not occur for PM, because the common terms in the photodiode currents are then baseband terms whereas the differential terms appear at RF.

8.2.3 Chromatic dispersion

As we have seen in the previous chapter, the influence of CD on the expected output signal of the receiver filter can be modeled by the insertion of a linear time-invariant low-pass filter with an impulse response $h_{CD}(t)$ that is given by (7.25) and transfer function $H_{CD}(f)$ that is given by (7.30). In case of RF signal distribution this can have two effects:

1. The RF carrier is reduced in amplitude when $|H_{CD}(f_r)|$ is significantly smaller than 1;
2. The envelope of the RF carrier is distorted due to amplitude distortion and/or group delay dispersion of $H_{CD}(f)$ in the frequency range of the RF signal.

When we consider PM, the expected output signal of the band-pass filter can be found using (7.17) and (8.10), resulting in

$$E[V_{BP,r}(t)] = \frac{Z_{TIA}R_{pd}P_x}{2L_{Tx}L_{Rx}L_{nw}} |H_f(f_c)|^2 |H_{BP}(f_r)| \cdot \int_{-\infty}^{\infty} h_{CD}(\rho) J_1(\beta_r(t - \rho)) \sin(2\pi f_r(t - \rho) + \psi_r(t - \rho)) d\rho. \quad (8.21)$$

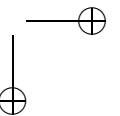
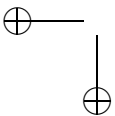
When the bandwidths of $\beta_r(t)$ and $\psi_r(t)$ are much smaller than the bandwidth of $h_{CD}(t)$, or in other words, when $\beta_r(t)$ and $\psi_r(t)$ change only negligibly on a time scale in the order of the duration of $h_{CD}(t)$, this can be written as

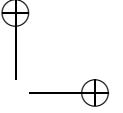
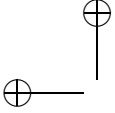
$$E[V_{BP,r}(t)] \approx \frac{Z_{TIA}R_{pd}P_x}{2L_{Tx}L_{Rx}L_{nw}} |H_f(f_c)|^2 |H_{BP}(f_r)| \cdot J_1(\beta_r(t)) \int_{-\infty}^{\infty} h_{CD}(\rho) \sin(2\pi f_r(t - \rho) + \psi_r(t)) d\rho. \quad (8.22)$$

Since $h_{CD}(t)$ is the inverse Fourier transform of $H_{CD}(f)$, this can be written as

$$E[V_{BP,r}(t)] \approx \frac{Z_{TIA}R_{pd}P_x}{2L_{Tx}L_{Rx}L_{nw}} |H_f(f_c)|^2 |H_{BP}(f_r)| \cdot |H_{CD}(f_r)| J_1(\beta_r(t)) \sin(2\pi f_r t + \psi_r(t)), \quad (8.23)$$

where an irrelevant constant phase shift has been omitted.





Apparently, the effect of CD on the RF signal at the output of the band-pass filter can then be modeled by a power penalty of $-20 \log |H_{\text{CD}}(f_r)|$ dB. Using (7.33) and (7.35) this becomes

$$-20 \log |H_{\text{CD}}(f_r)| \text{ dB} \approx 27.29 f_r^2 T_1^2 \text{ dB}, \quad (8.24)$$

when first order CD is dominant, and

$$-20 \log |H_{\text{CD}}(f_r)| \text{ dB} \approx 5 \log \left(1 + \frac{1}{4} f_r^2 T_2^2 \right) \text{ dB}, \quad (8.25)$$

when second order CD is dominant.

Example 8.1

As an example, consider the case where the proposed RF signal distribution concept is applied in an indoor distribution network for 11 Mbps wireless LAN, according to the IEEE 802.11b standard [95]. It operates in the 2.4 GHz Industrial, Scientific and Medical (ISM) band.

A reasonable network span for such an indoor network would be $l_f = 500$ m, and it is assumed that standard SMF is used. If optical sources with a center wavelength $\lambda_c = 1550$ nm and coherence time $\tau_c = 0.1$ ps were used, first order CD would be dominant. Using (7.23) and (2.56) one can then find

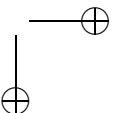
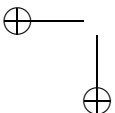
$$T_1 = -\frac{500 \cdot 160 \cdot 10^{-27}}{\sqrt{2} \cdot 0.1 \cdot 10^{-12}} \text{ s} \approx -0.57 \text{ ns}. \quad (8.26)$$

From (7.29) it then follows that this corresponds to a root-mean-square delay

$$\sigma_T = \frac{0.57 \cdot 10^{-9}}{\sqrt{2\pi}} \text{ s} \approx 90 \text{ ps}. \quad (8.27)$$

In the 11 Mbps mode, IEEE 802.11b uses complementary code keying (CCK) modulation as a direct sequence spread spectrum (DSSS) technique, with a chip rate of 11 Mcps. The coded chips are transmitted using QPSK modulation. The resulting effective channel bandwidth after spectral shaping is approximately 17 MHz. Hence, the envelope of the RF signals can be assumed constant on a time scale in the order of the duration of $h_{\text{CD}}(t)$, so that envelope distortion can indeed be neglected.

The RF carrier itself cannot be assumed constant on such a time scale, so its amplitude will reduce due to CD: using (8.24) a penalty at 2.4 GHz of approximately 50 dB can be calculated. Apparently, sources with $\lambda_c = 1550$ nm and $\tau_c = 0.1$ ps are not suitable for distributing 2.4 GHz signals over 500 m of non-equalized standard SMF. □



Example 8.2

If optical sources with center wavelength $\lambda_c = 1310$ nm were used instead, second order CD would be dominant. Using (7.24) and (2.58) one can then find

$$T_2 = \frac{500 \cdot 3.3 \cdot 10^{-39}}{(0.1 \cdot 10^{-12})^2} \text{ s} \approx 0.17 \text{ ns}. \quad (8.28)$$

From (7.29) it then follows that this corresponds to a root-mean-square delay

$$\sigma_T = \frac{0.17 \cdot 10^{-9}}{4\pi\sqrt{2}} \text{ s} \approx 9.3 \text{ ps}. \quad (8.29)$$

Hence, both the envelope and the RF carrier itself can be assumed constant on a time scale in the order of the duration of $h_{\text{CD}}(t)$, so both envelope distortion and RF carrier amplitude reduction can be neglected. This also follows from (8.25): the penalty at 2.4 GHz is approximately 0.1 dB, which is negligible. \square

8.2.4 Noise performance

The influence of noise can be analyzed by calculating the variance of the output signal of the band-pass filter $V_{\text{BP},r}(t)$. It will be assumed that CD can be neglected, and that each balanced receiver is phase-synchronized to the corresponding transmitter. PM is considered, because a PM receiver is more robust to detector imbalances and can be phase-synchronized more easily than an IM receiver. Using (5.14) and (8.1), one can find

$$\begin{aligned} \sigma_{V_{\text{BP},r}(t)}^2 &= R_{V_{\text{BP},r},V_{\text{BP},r}}(t,t) - E^2[V_{\text{BP},r}(t)] \\ &\approx \frac{Z_{\text{TIA}}^2 R_{\text{pd}} P_x e N}{2L_{\text{Tx}} L_{\text{Rx}} L_{\text{nw}}} \int_{-\infty}^{\infty} h_{\text{BP}}^2(\rho) \text{ d}\rho \\ &\quad + \frac{Z_{\text{TIA}}^2 R_{\text{pd}}^2 P_x^2 \tau_c}{32L_{\text{Tx}}^2 L_{\text{Rx}}^2 L_{\text{nw}}^2} \int_{-\infty}^{\infty} h_{\text{BP}}^2(\rho) \left[4N^2 + 2N \right. \\ &\quad \left. + \cos\left(2\Delta\phi_r + 2\beta_r(t-\rho) \sin\left(2\pi f_r(t-\rho) + \psi_r(t-\rho)\right)\right) \right] \text{ d}\rho \\ &\quad + Z_{\text{TIA}}^2 S_{\text{th}} \int_{-\infty}^{\infty} h_{\text{BP}}^2(\rho) \text{ d}\rho. \end{aligned} \quad (8.30)$$

In Subsection 8.2.1 we have seen that $\Delta\phi_r$ should be set to $\frac{3\pi}{2}$ in order to achieve a maximum output signal amplitude. Using (8.4) and (8.8) we can then write

$$\begin{aligned} \cos\left(2\Delta\phi_r + 2\beta_r(t-\rho) \sin\left(2\pi f_r(t-\rho) + \psi_r(t-\rho)\right)\right) &= -J_0\left(2\beta_r(t-\rho)\right) \\ &\quad - 2 \sum_{\substack{n=2 \\ n \text{ even}}}^{\infty} J_n\left(2\beta_r(t-\rho)\right) \cos\left(2\pi n f_r(t-\rho) + n \psi_r(t-\rho)\right). \end{aligned} \quad (8.31)$$

For convenience it is assumed that the modulation of the RF carrier does not affect the variance at the output of the band-pass filter, so we take $\beta_r(t) = \beta$ and $\psi_r(t) = \psi$. This results in

$$\begin{aligned} \sigma_{V_{BP,r}(t)}^2 &\approx \frac{Z_{TIA}^2 R_{pd} P_x e N}{2L_{Tx} L_{Rx} L_{nw}} \int_{-\infty}^{\infty} h_{BP}^2(\rho) d\rho \\ &\quad + \frac{Z_{TIA}^2 R_{pd}^2 P_x^2 \tau_c}{32L_{Tx}^2 L_{Rx}^2 L_{nw}^2} \int_{-\infty}^{\infty} h_{BP}^2(\rho) \left[4N^2 + 2N - J_0(2\beta) \right. \\ &\quad \quad \left. - 2 \sum_{\substack{n=2 \\ n \text{ even}}}^{\infty} J_n(2\beta) \cos(2\pi n f_r(t - \rho) + n\psi) \right] d\rho \\ &\quad + Z_{TIA}^2 S_{th} \int_{-\infty}^{\infty} h_{BP}^2(\rho) d\rho. \end{aligned} \quad (8.32)$$

By writing the impulse response $h_{BP}(t)$ as the inverse Fourier transform of the transfer function $H_{BP}(f)$ of the band-pass filter, this becomes

$$\begin{aligned} \sigma_{V_{BP,r}(t)}^2 &\approx \frac{Z_{TIA}^2 R_{pd} P_x e N}{2L_{Tx} L_{Rx} L_{nw}} \int_{-\infty}^{\infty} |H_{BP}(f)|^2 df \\ &\quad + \frac{Z_{TIA}^2 R_{pd}^2 P_x^2 \tau_c}{32L_{Tx}^2 L_{Rx}^2 L_{nw}^2} \left\{ [4N^2 + 2N - J_0(2\beta)] \int_{-\infty}^{\infty} |H_{BP}(f)|^2 df \right. \\ &\quad \quad - \sum_{\substack{n=2 \\ n \text{ even}}}^{\infty} J_n(2\beta) \left[\exp(j2\pi n f_r t + jn\psi) \int_{-\infty}^{\infty} H_{BP}(f) H_{BP}(n f_r - f) df \right. \\ &\quad \quad \quad \left. + \exp(-j2\pi n f_r t - jn\psi) \int_{-\infty}^{\infty} H_{BP}(f) H_{BP}(-n f_r - f) df \right] \left. \right\} \\ &\quad + Z_{TIA}^2 S_{th} \int_{-\infty}^{\infty} |H_{BP}(f)|^2 df. \end{aligned} \quad (8.33)$$

The time-varying terms can be removed by averaging over time, resulting in

$$\begin{aligned} \langle \sigma_{V_{BP,r}(t)}^2 \rangle &\approx 2Z_{TIA}^2 |H_{BP}(f_r)|^2 W_{BP} \left\{ \frac{R_{pd} P_x e N}{2L_{Tx} L_{Rx} L_{nw}} \right. \\ &\quad \left. + \frac{R_{pd}^2 P_x^2 [4N^2 + 2N - J_0(2\beta)] \tau_c}{32L_{Tx}^2 L_{Rx}^2 L_{nw}^2} + S_{th} \right\}, \end{aligned} \quad (8.34)$$

where $\langle \cdot \rangle$ denotes time-averaging, and W_{BP} is the equivalent noise bandwidth of the band-pass filter [53]:

$$W_{BP} \triangleq \frac{\int_0^{\infty} |H_{BP}(f)|^2 df}{|H_{BP}(f_r)|^2}. \quad (8.35)$$

The carrier-to-noise ratio (CNR) at the output of the band-pass filter now follows from (8.10) and (8.34) as

$$CNR_{BP} = \frac{\langle E^2[V_{BP,r}(t)] \rangle}{\langle \sigma_{V_{BP,r}(t)}^2 \rangle} = \left(CNR_{sn}^{-1} + CNR_{bn}^{-1} + CNR_{tn}^{-1} \right)^{-1} \quad (8.36)$$

where

$$CNR_{sn} = \frac{R_{pd} P_x \langle J_1^2(\beta_r(t)) \rangle}{8N L_{Tx} L_{Rx} L_{nw} e W_{BP}}, \quad (8.37)$$

$$CNR_{bn} = \frac{2 \langle J_1^2(\beta_r(t)) \rangle}{[4N^2 + 2N - J_0(2\beta)] \tau_c W_{BP}}, \quad (8.38)$$

$$CNR_{tn} = \frac{R_{pd}^2 P_x^2 \langle J_1^2(\beta_r(t)) \rangle}{16L_{Tx}^2 L_{Rx}^2 L_{nw}^2 S_{th} W_{BP}}, \quad (8.39)$$

are the carrier-to-shot noise ratio, carrier-to-beat noise ratio, and carrier-to-thermal noise ratio, respectively.

Example 8.3

Now consider an 11 Mbps WLAN distribution network like considered in Example 8.1 and 8.2, with N RAPs and hence N coherence modulators and demodulators, in a parallel array configuration. The optical sources have center wavelength $\lambda_c = 1310$ nm so that CD can be neglected. For the remaining parameters of the optical distribution network the same values as in Example 5.2 are assumed. The propagation loss at $\lambda_c = 1310$ nm is typically $\alpha = 0.35$ dB/km, which comes to a total loss of 0.175 dB (1.041) for 500 m of fiber. Hence, the total network loss comes to $L_{nw} \approx 1.047 \cdot 1.041 N^2 \approx 1.090 N^2$.

The band-pass filters are assumed to have an equivalent noise bandwidth that equals the effective channel bandwidth of the CCK-spread RF carriers, so $W_{BP} = 17$ MHz.

Although the spectral shaping will result in a fluctuation of the amplitude $\beta_i(t)$ of the RF carriers, it will be assumed that this does not significantly affect the performance, so we assume that $\beta_i(t) = \beta$. When β is then chosen such that the amplitude of the RF signal at the output of the band-pass filter is maximized (see Subsection 8.2.1), we have

$$\beta \approx 1.8412 \Rightarrow J_1(\beta) \approx 0.5819 \quad (8.40)$$

$$J_0(2\beta) \approx -0.3982. \quad (8.41)$$

When all N channels are active, the CNR at the output of the band-pass filter in each RAP then follows from (8.36). The resulting CNR has been plotted as a function of the number of channels N in Figure 8.3.

A criterion for the minimum CNR at the output of the band-pass filter can be formulated by considering the performance of the receiver in the MT.

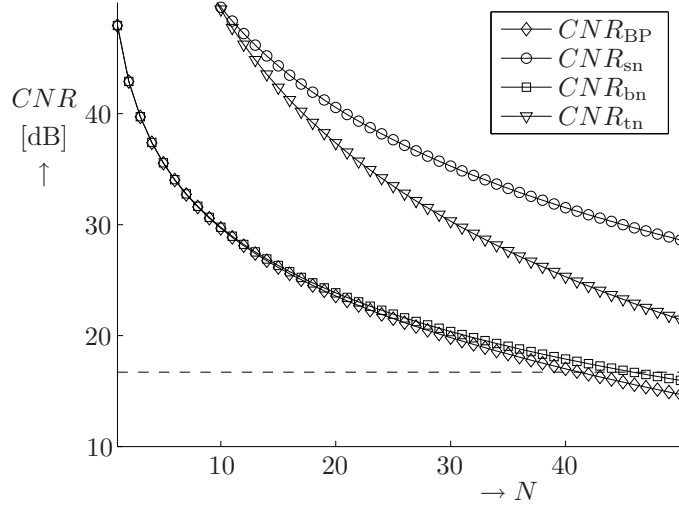


Figure 8.3: Carrier-to-noise ratios at the output of the band-pass filter as a function of number of RAPs N in a WLAN IEEE 802.11b distribution network based on CM

The detected signal in the MT consists of three parts:

- the desired signal, $S(t)$;
- the noise that is introduced by the optical distribution system, $N_{\text{opt}}(t)$;
- the noise that is introduced in the amplifier of the MT itself, $N_{\text{MT}}(t)$.

$S(t) + N_{\text{opt}}(t)$ can be considered as an attenuated version of the output signal of the band-pass filter $V_{\text{BP},r}(t)$, so the CNR at the output of the band-pass filter is equal to the ratio of the powers of $S(t)$ and $N_{\text{opt}}(t)$:

$$CNR_{\text{BP}} = \frac{P_S}{P_{N_{\text{opt}}}}. \quad (8.42)$$

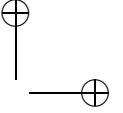
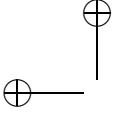
The CNR at the MT is equal to the ratio of the power of $S(t)$ and the total power in $N_{\text{opt}}(t)$ and $N_{\text{MT}}(t)$:

$$CNR_{\text{MT}} = \frac{P_S}{P_{N_{\text{opt}}} + P_{N_{\text{MT}}}}. \quad (8.43)$$

Without the optical distribution system, the CNR at the MT would have been

$$CNR'_{\text{MT}} = \frac{P_S}{P_{N_{\text{MT}}}}, \quad (8.44)$$

provided that the conditions for the wireless interface remain the same.



Suppose that we allow the optical distribution system to introduce a penalty of at most 1 dB to the link budget of the wireless interface. We can then write

$$CNR'_{MT} = 10^{0.1}CNR_{MT} . \tag{8.45}$$

Combining (8.42) through (8.45) it can be found that the required CNR at the output of the band-pass filter is related to the required CNR at the MT as

$$\begin{aligned} CNR_{BP} &= \left[CNR_{MT}^{-1} - (CNR'_{MT})^{-1} \right]^{-1} \\ &= \frac{CNR_{MT}}{1 - 10^{-0.1}} \approx 4.86 CNR_{MT} , \end{aligned} \tag{8.46}$$

so the CNR at the output of the band-pass filter should be approximately 6.9 dB higher than the CNR at the MT.

Since the CCK modulation does not provide any processing gain in the 11 Mbps mode (the chip rate is equal to the bit rate in that case), the CNR per bit after despreading is approximately equal to the CNR per chip of the received signal. Since QPSK modulation is used, the bit error rate follows from [81]

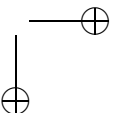
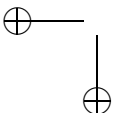
$$P_e \approx Q \left(\sqrt{CNR_{MT}} \right) . \tag{8.47}$$

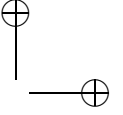
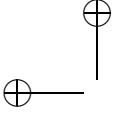
Hence, the CNR at the MT should be approximately 9.6 (9.8 dB) in order to have a bit error rate of 10^{-3} . This requires a CNR at the output of the band-pass filter of 9.8 dB + 6.9 dB = 16.7 dB. This value is represented by the dashed line in Figure 8.3.

Given the requirement it follows that at most 41 RAPs can be supported using this RF distribution concept, and that this number is mainly determined by the amount of beat noise that arises when 41 CM channels are active. □

In cases like this example, where the maximum number of RAPs is limited by beat noise, the number of RAPs can be further increased by simply increasing the number of CM transmitters and receivers, and letting them operate in burst-mode. Only a limited number of RAPs can be active at the same time, and CM channels that correspond to inactive RAPs are simply turned off. (Hence, the maximum number of MTs that can simultaneously be supported in such a system is smaller than the number of RAPs.) Increasing the number of RAPs will also increase the combining and splitting loss in the optical network, however, so that thermal noise might become a limiting factor. This can be compensated for by using tunable CM transmitters, so that the number of transmitters can be the same as the maximum number of active RAPs, which reduces the combining loss.

Another option to improve the carrier-to-beat noise ratio is to use the SIRL system as CM topology instead of the PA (see Chapter 5). This cannot be used in the return path, however.





8.3 Output stabilization

As already noted in Section 8.2, coherence demodulation of RF-modulated CM channels still requires special measures in order to account for small differences between the delays in a matched transmitter-receiver pair, and hence stabilize the receiver output signal. In this section, the three solutions that were discussed in Chapter 6 (phase synchronization, self-heterodyning and phase diversity) will be reconsidered in the context of RF feeding.

8.3.1 Phase synchronization

In Subsection 6.3.1 we have seen that in the case of digital modulation, the desired signal has an amplitude that is proportional to $\cos(\Delta\phi_r)$ (where $\Delta\phi_r \triangleq 2\pi f_c(T_{\text{Rx},r} - T_{\text{Tx},r})$), so that a feedback loop is required which controls the value of $\Delta\phi_r$ to 0 or a (small) integer multiple of 2π . This is done using a frequency dithering technique, in order to create a signal that is proportional to $\sin(\Delta\phi_r)$ so that the value of $\Delta\phi_r$ can be unambiguously controlled.

In case of RF modulation by means of PM, however, it follows from (8.9) that the amplitude of the output signal is proportional to $-\sin(\Delta\phi_r)$. Hence, the value of $\Delta\phi_r$ should be locked to $\frac{3\pi}{2}$ (plus an integer number of 2π , eventually), which could be done if a signal proportional to $\cos(\Delta\phi_r)$ were available. It also follows from (8.9), however, that the signal at the input of the band-pass filter also contains a baseband term with an amplitude that is proportional to $\cos(\Delta\phi_r)$. When the input signal of the band-pass filter is also fed to a low-pass filter with impulse response $h_{\text{LP}}(t)$ such that all the RF terms are suppressed, then the output signal of this filter is given by

$$\mathbb{E}[V_{\text{LP},r}(t)] = \frac{Z_{\text{TIA}}R_{\text{pd}}P_x}{4L_{\text{Tx}}L_{\text{Rx}}L_{\text{nw}}} \cos(\Delta\phi_r) \int_{-\infty}^{\infty} h_{\text{LP}}(t-\rho) J_0(\beta_r(\rho)) d\rho. \quad (8.48)$$

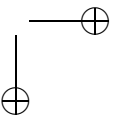
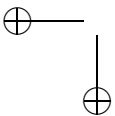
A suitable control signal results when the low-pass filter also suppresses variations in $\beta_r(t)$, if necessary. Note that frequency dithering is not required for synchronization in this case.

This cannot be applied in case of RF modulation by IM, since in that case, it follows from (8.19) that all the terms have amplitudes proportional to $\cos(\Delta\phi_r)$. As a result, one has to refer to frequency dithering in case of IM.

8.3.2 Self-heterodyning

Alternatively, self-heterodyning can be applied in either the transmitters or the receivers, as described in Subsection 6.3.2. In the particular case of RF distribution, this can be done by using a frequency shift f_s that is equal to the RF frequency f_r , and modulate the CM channels by the corresponding RF amplitude and phase, so $m_{\text{mod},r}(t) = \beta_r(t)$ (with $0 \leq \beta_r(t) \leq 1$) and $\phi_{\text{mod},r}(t) = \psi_r(t)$. From (6.11) it follows that the output signal is then given by

$$\mathbb{E}[V_{\text{out},r}(t)] \approx \frac{Z_{\text{TIA}}R_{\text{pd}}P_x}{4L_{\text{Tx}}L_{\text{Rx}}L_{\text{nw}}} \beta_r(t) \cos(2\pi f_r t + \Delta\phi_r + \psi_r(t)). \quad (8.49)$$



No harmonic distortion occurs so that an even stronger output signal can be obtained which is inherently stable.

For the downlink, the frequency shifter should be put in the transmitters, since these are all located in the central node so that an RF oscillator can be shared by the transmitters that transmit CM channels containing RF signals with the same carrier frequency.

The problem is that this concept cannot be applied in the uplink, since the input signals of the transmitters for the return path are already in modulated RF format.

8.3.3 Phase diversity detection

A third option for stabilizing the output signal of the receiver is to use a phase diversity receiver. IM and PM require different receiver structures.

IM Phase diversity detection

When the same structure as in Subsection 6.4.1 is used, a band-pass filter has to be added at the output. (Later it will become clear why this is required.) This is shown in Figure 8.4.

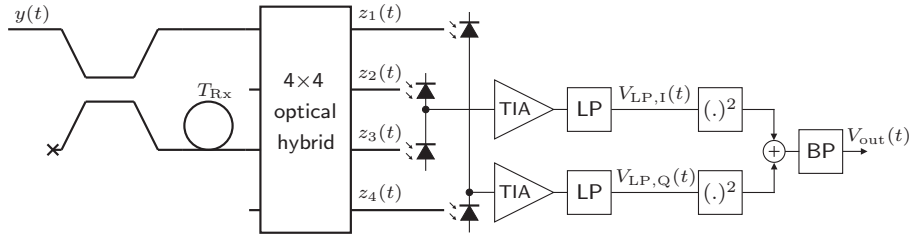


Figure 8.4: A four-way IM phase diversity receiver

In case of high carrier-to-noise ratios at the output of the low-pass filters, the expected output signal in case of a PA topology follows from (6.34) as:

$$\begin{aligned}
 E[V_{\text{out},r}(t)] &= \frac{Z_{\text{TIA}}^2 R_{\text{pd}}^2 P_x^2}{64 L_{\text{Tx}}^2 L_{\text{Rx}}^2 L_{\text{nw}}^2} \int_{-\infty}^{\infty} h_{\text{BP}}(t - \rho_1) \\
 &\cdot \left\{ \left[\int_{-\infty}^{\infty} h_{\text{LP}}(\rho_1 - \rho_2) m_{\text{mod},r}(\rho_2) \cos(\phi_{\text{mod},r}(\rho_2)) d\rho_2 \right]^2 \right. \\
 &\quad \left. + \left[\int_{-\infty}^{\infty} h_{\text{LP}}(\rho_1 - \rho_2) m_{\text{mod},r}(\rho_2) \sin(\phi_{\text{mod},r}(\rho_2)) d\rho_2 \right]^2 \right\} d\rho_1. \quad (8.50)
 \end{aligned}$$

In case of RF modulation by means of IM, the expected output signal follows from (8.18) and $\phi_{\text{mod},r}(t) = 0$, resulting in

$$\begin{aligned} \mathbb{E}[V_{\text{out},r}(t)] &= \frac{Z_{\text{TIA}}^2 R_{\text{pd}}^2 P_x^2}{64L_{\text{Tx}}^2 L_{\text{Rx}}^2 L_{\text{nw}}^2} \int_{-\infty}^{\infty} h_{\text{BP}}(t - \rho_1) \left\{ \int_{-\infty}^{\infty} h_{\text{LP}}(\rho_1 - \rho_2) \right. \\ &\quad \cdot \left. \left[\frac{1}{2} + \sum_{\substack{n=1 \\ n \text{ odd}}}^{\infty} J_n(\beta_r(\rho_2)) \sin(2\pi n f_r \rho_2 + n \psi_r(\rho_2)) \right] d\rho_2 \right\}^2 d\rho_1. \quad (8.51) \end{aligned}$$

After squaring it will appear that the output contains a DC term and RF terms with frequencies that are both odd and even multiples of f_r , and amplitudes that depend on the transfer functions of the filters. When the low-pass filters are assumed to have a narrow passband at DC and a flat passband in the frequency range of the first order RF carrier, and to suppress all other frequencies, then the expected output signal can be written as

$$\begin{aligned} \mathbb{E}[V_{\text{out},r}(t)] &= \frac{Z_{\text{TIA}}^2 R_{\text{pd}}^2 P_x^2}{64L_{\text{Tx}}^2 L_{\text{Rx}}^2 L_{\text{nw}}^2} \int_{-\infty}^{\infty} h_{\text{BP}}(t - \rho) \left[\frac{1}{2} H_{\text{LP}}(0) \right. \\ &\quad \left. + |H_{\text{LP}}(f_r)| J_1(\beta_r(\rho)) \sin(2\pi f_r \rho + \psi_r(\rho)) \right]^2 d\rho \\ &= \frac{Z_{\text{TIA}}^2 R_{\text{pd}}^2 P_x^2}{256L_{\text{Tx}}^2 L_{\text{Rx}}^2 L_{\text{nw}}^2} \int_{-\infty}^{\infty} h_{\text{BP}}(t - \rho) \left[H_{\text{LP}}^2(0) + 2|H_{\text{LP}}(f_r)|^2 J_1^2(\beta_r(\rho)) \right. \\ &\quad \left. + 4H_{\text{LP}}(0)|H_{\text{LP}}(f_r)| J_1(\beta_r(\rho)) \sin(2\pi f_r \rho + \psi_r(\rho)) \right. \\ &\quad \left. - 2|H_{\text{LP}}(f_r)|^2 J_1^2(\beta_r(\rho)) \cos(4\pi f_r \rho + 2\psi_r(\rho)) \right] d\rho, \quad (8.52) \end{aligned}$$

where an irrelevant phase shift has been omitted. The desired RF carrier can now be selected by means of the band-pass filter: it should have a passband around the desired frequency f_r and suppress all other frequencies, resulting in:

$$\begin{aligned} \mathbb{E}[V_{\text{out},r}(t)] &= \frac{Z_{\text{TIA}}^2 R_{\text{pd}}^2 P_x^2}{64L_{\text{Tx}}^2 L_{\text{Rx}}^2 L_{\text{nw}}^2} H_{\text{LP}}(0) |H_{\text{LP}}(f_r)| |H_{\text{BP}}(f_r)| \\ &\quad \cdot J_1(\beta_r(t)) \sin(2\pi f_r t + \psi_r(t)), \quad (8.53) \end{aligned}$$

where an irrelevant phase shift has been omitted.

This receiver structure is not suitable for demodulation in case RF modulation is performed by means of PM. This follows by substituting (8.1), (8.4) and (8.5) into (8.50), resulting in

$$\begin{aligned}
 E[V_{\text{out},r}(t)] &= \frac{Z_{\text{TIA}}^2 R_{\text{pd}}^2 P_x^2}{64 L_{\text{Tx}}^2 L_{\text{Rx}}^2 L_{\text{nw}}^2} \int_{-\infty}^{\infty} h_{\text{BP}}(t - \rho_1) \\
 &\cdot \left\{ \left[\int_{-\infty}^{\infty} h_{\text{LP}}(\rho_1 - \rho_2) \sum_{n \text{ even}} J_n(\beta_r(\rho_2)) \cos(2\pi n f_r \rho_2 + n \psi_r(\rho_2)) d\rho_2 \right]^2 \right. \\
 &\quad + \left[\int_{-\infty}^{\infty} h_{\text{LP}}(\rho_1 - \rho_2) \right. \\
 &\quad \cdot \left. \left. \sum_{n \text{ odd}} J_n(\beta_r(\rho_2)) \sin(2\pi n f_r \rho_2 + n \psi_r(\rho_2)) d\rho_2 \right]^2 \right\} d\rho_1. \quad (8.54)
 \end{aligned}$$

Obviously, the expected output signal will only consist of a baseband term and RF terms with frequencies that are *even* multiples of the desired frequency f_r (and amplitudes that depend on the transfer functions of the filters).

It can be concluded that this phase diversity receiver is only suitable for demodulating RF-modulated CM channels in case IM is performed.

PM Phase diversity detection

PM can be demodulated by means of an FM demodulation circuit, as illustrated in Figure 8.5.

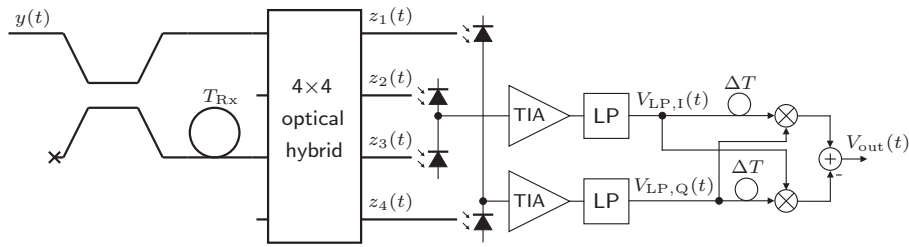


Figure 8.5: A four-way PM phase diversity receiver

The expected output signal of this receiver can be written as

$$\begin{aligned}
 E[V_{\text{out},r}(t)] &= E[V_{\text{LP},Q,r}(t)V_{\text{LP},I,r}(t - \Delta T) - V_{\text{LP},I,r}(t)V_{\text{LP},Q,r}(t - \Delta T)] \\
 &= R_{V_{\text{LP},I,r}V_{\text{LP},Q,r}}(t - \Delta T, t) - R_{V_{\text{LP},I,r}V_{\text{LP},Q,r}}(t, t - \Delta T). \quad (8.55)
 \end{aligned}$$

Using (5.2), (6.31), (6.32) and (B.12), and substituting $m_{\text{mod},r}(t) = 1$, we find

$$\begin{aligned}
\mathbb{E}[V_{\text{out},r}(t)] &= \mathbb{E}[V_{\text{LP},\text{Q},r}(t)]\mathbb{E}[V_{\text{LP},\text{I},r}(t - \Delta T)] \\
&\quad - \mathbb{E}[V_{\text{LP},\text{I},r}(t)]\mathbb{E}[V_{\text{LP},\text{Q},r}(t - \Delta T)] \\
&= \frac{Z_{\text{TIA}}^2 R_{\text{pd}}^2 P_x^2}{64L_{\text{Tx}}^2 L_{\text{Rx}}^2 L_{\text{nw}}^2} \left[\int_{-\infty}^{\infty} h_{\text{LP}}(t - \rho) \cos\left(\Delta\phi_r + \phi_{\text{mod},r}(\rho) + \frac{3\pi}{4}\right) d\rho \right. \\
&\quad \cdot \int_{-\infty}^{\infty} h_{\text{LP}}(t - \Delta T - \rho) \cos\left(\Delta\phi_r + \phi_{\text{mod},r}(\rho) - \frac{3\pi}{4}\right) d\rho \\
&\quad - \int_{-\infty}^{\infty} h_{\text{LP}}(t - \rho) \cos\left(\Delta\phi_r + \phi_{\text{mod},r}(\rho) - \frac{3\pi}{4}\right) d\rho \\
&\quad \left. \cdot \int_{-\infty}^{\infty} h_{\text{LP}}(t - \Delta T - \rho) \cos\left(\Delta\phi_r + \phi_{\text{mod},r}(\rho) + \frac{3\pi}{4}\right) d\rho \right] \\
&= \frac{Z_{\text{TIA}}^2 R_{\text{pd}}^2 P_x^2}{64L_{\text{Tx}}^2 L_{\text{Rx}}^2 L_{\text{nw}}^2} \int_{-\infty}^{\infty} \int_{-\infty}^{\infty} h_{\text{LP}}(t - \rho_1) h_{\text{LP}}(t - \rho_2) \\
&\quad \cdot \sin\left(\phi_{\text{mod},r}(\rho_1) - \phi_{\text{mod},r}(\rho_2 - \Delta T)\right) d\rho_1 d\rho_2. \quad (8.56)
\end{aligned}$$

When ΔT is much smaller than the inverse of the bandwidth of $\phi_{\text{mod},r}(t)$ (so when $f_r \Delta T \ll 1$), we can approximate

$$\begin{aligned}
&\sin\left(\phi_{\text{mod},r}(\rho_1) - \phi_{\text{mod},r}(\rho_2 - \Delta T)\right) \approx \\
&\sin\left(\phi_{\text{mod},r}(\rho_1) - \phi_{\text{mod},r}(\rho_2)\right) - \Delta T \frac{d}{d\rho_2} \sin\left(\phi_{\text{mod},r}(\rho_1) - \phi_{\text{mod},r}(\rho_2)\right) \\
&= \sin\left(\phi_{\text{mod},r}(\rho_1)\right) \cos\left(\phi_{\text{mod},r}(\rho_2)\right) - \cos\left(\phi_{\text{mod},r}(\rho_1)\right) \sin\left(\phi_{\text{mod},r}(\rho_2)\right) \\
&\quad + \Delta T \phi'_{\text{mod},r}(\rho_2) \left[\cos\left(\phi_{\text{mod},r}(\rho_1)\right) \cos\left(\phi_{\text{mod},r}(\rho_2)\right) \right. \\
&\quad \left. + \sin\left(\phi_{\text{mod},r}(\rho_1)\right) \sin\left(\phi_{\text{mod},r}(\rho_2)\right) \right], \quad (8.57)
\end{aligned}$$

resulting in

$$\begin{aligned}
\mathbb{E}[V_{\text{out},r}(t)] &\approx \frac{Z_{\text{TIA}}^2 R_{\text{pd}}^2 P_x^2 \Delta T}{64L_{\text{Tx}}^2 L_{\text{Rx}}^2 L_{\text{nw}}^2} \left[\int_{-\infty}^{\infty} h_{\text{LP}}(t - \rho) \cos\left(\phi_{\text{mod},r}(\rho)\right) d\rho \right. \\
&\quad \cdot \int_{-\infty}^{\infty} h_{\text{LP}}(t - \rho) \phi'_{\text{mod},r}(\rho) \cos\left(\phi_{\text{mod},r}(\rho)\right) d\rho \\
&\quad + \int_{-\infty}^{\infty} h_{\text{LP}}(t - \rho) \sin\left(\phi_{\text{mod},r}(\rho)\right) d\rho \\
&\quad \left. \cdot \int_{-\infty}^{\infty} h_{\text{LP}}(t - \rho) \phi'_{\text{mod},r}(\rho) \sin\left(\phi_{\text{mod},r}(\rho)\right) d\rho \right]. \quad (8.58)
\end{aligned}$$

According to Carson's rule [56], approximately 98 % of the power of the angle-modulated signals $\sin(\phi_{\text{mod},r}(t))$ and $\cos(\phi_{\text{mod},r}(t))$ is confined within the bandwidth $(\beta + 1)B$, where β is the modulation index and B is the bandwidth of the modulating signal $\phi_{\text{mod},r}(t)$, which is approximately f_r in this case. Hence, when the low-pass filters have a rectangular transfer function with this bandwidth, then the expected output signal can be approximated as

$$\mathbb{E}[V_{\text{out},r}(t)] \approx \frac{Z_{\text{TIA}}^2 R_{\text{pd}}^2 P_x^2 \Delta T}{64L_{\text{Tx}}^2 L_{\text{Rx}}^2 L_{\text{nw}}^2} H_{\text{LP}}^2(0) \phi'_{\text{mod},r}(t). \quad (8.59)$$

Substituting (8.1) this becomes

$$\begin{aligned} \mathbb{E}[V_{\text{out},r}(t)] &\approx \frac{Z_{\text{TIA}}^2 R_{\text{pd}}^2 P_x^2 \Delta T}{64L_{\text{Tx}}^2 L_{\text{Rx}}^2 L_{\text{nw}}^2} H_{\text{LP}}^2(0) \left\{ \beta'_r(t) \sin(2\pi f_r t + \psi_r(t)) \right. \\ &\quad \left. + [2\pi f_r + \psi'_r(t)] \beta_r(t) \cos(2\pi f_r t + \psi_r(t)) \right\} \\ &= \frac{Z_{\text{TIA}}^2 R_{\text{pd}}^2 P_x^2 \Delta T}{64L_{\text{Tx}}^2 L_{\text{Rx}}^2 L_{\text{nw}}^2} H_{\text{LP}}^2(0) \beta_r(t) \sqrt{\left[\frac{\beta'_r(t)}{\beta_r(t)} \right]^2 + [2\pi f_r + \psi'_r(t)]^2} \\ &\quad \cdot \cos \left(2\pi f_r t + \psi_r(t) - \arctan \left\{ \frac{\beta'_r(t)}{\beta_r(t) [2\pi f_r + \psi'_r(t)]} \right\} \right). \quad (8.60) \end{aligned}$$

When the variations in $\beta_r(t)$ and $\psi_r(t)$ are relatively slow with respect to the carrier oscillations, this can be approximated as

$$\mathbb{E}[V_{\text{out},r}(t)] \approx \frac{\pi Z_{\text{TIA}}^2 R_{\text{pd}}^2 P_x^2 f_r \Delta T}{32L_{\text{Tx}}^2 L_{\text{Rx}}^2 L_{\text{nw}}^2} H_{\text{LP}}^2(0) \beta_r(t) \cos(2\pi f_r t + \psi_r(t)). \quad (8.61)$$

The approximation in (8.58) only holds when $f_r \Delta T \ll 1$, so the resulting output signal will be relatively small with respect to the output signal of the IM phase diversity receiver, since it is proportional to $f_r \Delta T$.

Note, however, that there is a perfect linear relation between the expected output signal and $\beta_r(t)$. For the IM phase diversity receiver this relation can only be approximated as linear when $\beta_r(t)$ is small.

Moreover, the noise variance at the output of the PM phase diversity receiver is much smaller than the noise variance at the output of the IM phase diversity receiver, because the signals that are subtracted in the PM phase diversity receiver are correlated. This has not been studied in detail, however.

One should also note that the large bandwidth requirements on the low-pass filter also hold for the equivalent dispersion-induced transfer function $H_{\text{CD}}(f)$. That is, CD should be negligible for RF frequencies up to $(\beta + 1)B$; otherwise the output signal will still suffer from harmonic distortion.

Differential PM Phase diversity detection

Alternatively, ΔT can be chosen in the order of $1/f_r$. In that case, the output signal follows from (8.56) and (8.1) as

$$\begin{aligned}
\mathbb{E}[V_{\text{out},r}(t)] &= \frac{Z_{\text{TIA}}^2 R_{\text{pd}}^2 P_x^2}{64L_{\text{Tx}}^2 L_{\text{Rx}}^2 L_{\text{nw}}^2} \left[\int_{-\infty}^{\infty} h_{\text{LP}}(t-\rho) \sin(\phi_{\text{mod},r}(\rho)) \, \text{d}\rho \right. \\
&\quad \cdot \int_{-\infty}^{\infty} h_{\text{LP}}(t-\rho) \cos(\phi_{\text{mod},r}(\rho - \Delta T)) \, \text{d}\rho \\
&\quad - \int_{-\infty}^{\infty} h_{\text{LP}}(t-\rho) \cos(\phi_{\text{mod},r}(\rho)) \, \text{d}\rho \\
&\quad \left. \cdot \int_{-\infty}^{\infty} h_{\text{LP}}(t-\rho) \sin(\phi_{\text{mod},r}(\rho - \Delta T)) \, \text{d}\rho \right] \\
&= \frac{Z_{\text{TIA}}^2 R_{\text{pd}}^2 P_x^2}{64L_{\text{Tx}}^2 L_{\text{Rx}}^2 L_{\text{nw}}^2} \left[\sum_n \int_{-\infty}^{\infty} h_{\text{LP}}(t-\rho) J_n(\beta_r(\rho)) \sin(2\pi n f_r \rho + n \psi_r(\rho)) \, \text{d}\rho \right. \\
&\quad \cdot \sum_n \int_{-\infty}^{\infty} h_{\text{LP}}(t-\rho) J_n(\beta_r(\rho - \Delta T)) \\
&\quad \cdot \cos(2\pi n f_r(\rho - \Delta T) + n \psi_r(\rho - \Delta T)) \, \text{d}\rho \\
&\quad - \sum_n \int_{-\infty}^{\infty} h_{\text{LP}}(t-\rho) J_n(\beta_r(\rho)) \cos(2\pi n f_r \rho + n \psi_r(\rho)) \, \text{d}\rho \\
&\quad \cdot \sum_n \int_{-\infty}^{\infty} h_{\text{LP}}(t-\rho) J_n(\beta_r(\rho - \Delta T)) \\
&\quad \left. \cdot \sin(2\pi n f_r(\rho - \Delta T) + n \psi_r(\rho - \Delta T)) \, \text{d}\rho \right]. \quad (8.62)
\end{aligned}$$

Assuming that ΔT is much smaller than the RF signal bandwidth, we have

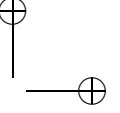
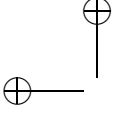
$$\beta_r(t - \Delta T) \approx \beta_r(t), \quad (8.63)$$

$$\psi_r(t - \Delta T) \approx \psi_r(t), \quad (8.64)$$

so when the low-pass filters are assumed to have a transfer function which is flat around DC and frequency f_r , the expected output signal becomes

$$\begin{aligned}
\mathbb{E}[V_{\text{out},r}(t)] &\approx \frac{Z_{\text{TIA}}^2 R_{\text{pd}}^2 P_x^2}{32L_{\text{Tx}}^2 L_{\text{Rx}}^2 L_{\text{nw}}^2} H_{\text{LP}}(0) |H_{\text{LP}}(f_r)| J_0(\beta_r(t)) J_1(\beta_r(t)) \\
&\quad \cdot \left[\sin(2\pi f_r t + \psi_r(t)) - \sin(2\pi f_r(t - \Delta T) + \psi_r(t)) \right] \\
&= \frac{Z_{\text{TIA}}^2 R_{\text{pd}}^2 P_x^2}{16L_{\text{Tx}}^2 L_{\text{Rx}}^2 L_{\text{nw}}^2} H_{\text{LP}}(0) |H_{\text{LP}}(f_r)| J_0(\beta_r(t)) J_1(\beta_r(t)) \\
&\quad \cdot \cos(2\pi f_r t - \pi f_r \Delta T + \psi_r(t)) \sin(\pi f_r \Delta T), \quad (8.65)
\end{aligned}$$

where an irrelevant phase shift has been omitted.



Hence, the amplitude of the output signal is maximized by choosing ΔT as

$$\Delta T = \frac{1}{2f_r}, \quad (8.66)$$

resulting in

$$\begin{aligned} \mathbb{E}[V_{\text{out},r}(t)] \approx & \frac{Z_{\text{TIA}}^2 R_{\text{pd}}^2 P_x^2}{16L_{\text{Tx}}^2 L_{\text{Rx}}^2 L_{\text{nw}}^2} H_{\text{LP}}(0) |H_{\text{LP}}(f_r)| J_0(\beta_r(t)) J_1(\beta_r(t)) \\ & \cdot \sin(2\pi f_r t + \psi_r(t)). \end{aligned} \quad (8.67)$$

The amplitude of this signal is maximized by choosing β such that

$$J'_0(\beta)J_1(\beta) + J_0(\beta)J'_1(\beta) = 0. \quad (8.68)$$

Using

$$J'_0(x) = -J_1(x), \quad (8.69)$$

$$J'_1(x) = J_0(x) - \frac{J_1(x)}{x}, \quad (8.70)$$

this becomes

$$\beta J_1^2(\beta) + J_0(\beta)J_1(\beta) = \beta J_0^2(\beta). \quad (8.71)$$

Numerically solving for β gives

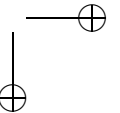
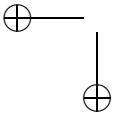
$$\beta \approx 1.0820 \Rightarrow J_0(\beta)J_1(\beta) \approx 0.3390, \quad (8.72)$$

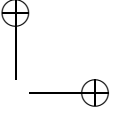
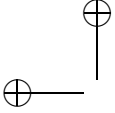
which results in

$$\begin{aligned} \mathbb{E}[V_{\text{out},r}(t)] \approx & \frac{0.0212 Z_{\text{TIA}}^2 R_{\text{pd}}^2 P_x^2}{L_{\text{Tx}}^2 L_{\text{Rx}}^2 L_{\text{nw}}^2} H_{\text{LP}}(0) |H_{\text{LP}}(f_r)| \sin(2\pi f_r t + \psi_r(t)). \end{aligned} \quad (8.73)$$

The advantages of this differential PM phase diversity receiver with respect to the previously described PM phase diversity receiver are that it has a stronger output signal and smaller filter bandwidth. A proper noise analysis would have to be carried out in order to find out whether this results in a better noise performance, however.

The main disadvantages are its non-linearity and the fact that ΔT needs to be optimized for a specific RF carrier frequency. The latter is not a problem when the envisioned carrier frequencies have relatively small mutual differences.





8.4 Subcarrier multiplexing over coherence multiplexing

In the previous sections it had been assumed that each CM channel carried only one RF signal. The way in which different carrier frequencies are assigned to the CM channels depends on the *frequency planning* of the corresponding cellular wireless network [96]. That is, RF signals emitted by RAPs in neighboring cells should not have the same carrier frequency (in order to avoid co-channel interference), and a particular carrier frequency can be reused if the corresponding cells are geographically sufficiently spaced apart. This is not considered in further detail in this thesis, however.

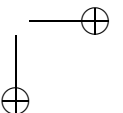
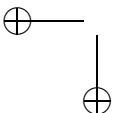
Multiple RF signals can be frequency-multiplexed in each CM channel by performing *subcarrier multiplexing* (SCM, also see Subsection 1.4.3) on top of CM [92–94]. This means that several RF signals with different carrier frequencies are coherence-modulated onto (an) optical carrier(s) that are characterized by a certain relative delay T_{Tx} , and then multiplexed in the optical domain by combining optical signals with different relative delays. Demultiplexing is carried out by first performing coherence demodulation and then applying band-pass filtering in order to select the desired subcarrier.

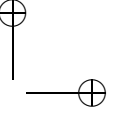
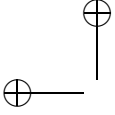
There can be several reasons for using SCM on top of CM:

- Since assigning individual frequencies to individual RAPs provides another way to distinguish between RAPs, the number of CM channels can be reduced by multiplexing several RF signals per CM channel. This can reduce the number of required optical transmitters for the uplink and/or the number of receivers for the downlink, resulting in cost reduction and performance improvement through reduced splitting losses and eventual beat noise reduction;
- Multiple MTs can be supported through the same RAP if they transmit at different RF carrier frequencies. CM then provides the means to distinguish between the RAPs, whereas SCM provides the means to distinguish between the MTs that communicate through the same RAP. (This is also illustrated in Figure 8.1);
- Multi-carrier modulation formats like orthogonal frequency division multiplexing (OFDM, amongst others used in WLAN according to the IEEE 802.11g standard [97]) require simultaneous transmission of different RF carriers through the same CM channel.

SCM can be performed on top of CM in two ways:

1. by transmitting different subcarriers by separate coherence modulators that have the same path imbalance T_{Tx} (single-channel SCM);
2. by first multiplexing the subcarriers in the electrical domain and then modulating the composite signal onto an optical carrier by means of one coherence modulator (multi-channel SCM).





These two alternatives will be discussed in the following two subsections. It will be assumed that PM is performed for modulating the RF signals onto the CM channels, that CM is performed by means of a PA, that coherence demodulation is performed by balanced detection and that CD can be neglected. The noise performance will be analyzed and the impact on the applicability of the output stabilization methods that were described in the previous section will be discussed

8.4.1 Single-channel subcarrier multiplexing

Multiplexing and demultiplexing

Suppose K RF signals are transmitted through the same CM channel by means of single-channel SCM. When there are N CM channels, this requires NK coherence modulators, each transmitting one RF signal. The coherence modulators are assumed to be configured in a PA topology, together producing a composite optical signal

$$y(t) = \frac{1}{2\sqrt{L_{Tx}L_{nw}}} \sum_{i=1}^N \sum_{k=1}^K \left[x_{i,k}(t) - x_{i,k}(t - T_{Tx,i,k}) \exp(j\phi_{\text{mod},i,k}(t)) \right], \quad (8.74)$$

where $x_{i,k}(t)$, $\phi_{\text{mod},i,k}(t)$ and $T_{Tx,i,k}$ are the optical input signal, modulating signal and MZI-imbalance of the coherence modulator that corresponds to the k -th SCM channel in the i -th CM channel. The delays $T_{Tx,i,k}$ are chosen as

$$T_{Tx,i,k} \approx iT_{Tx,1}, \quad (8.75)$$

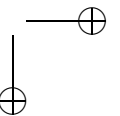
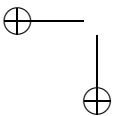
where the approximation is on a coherence time scale ($|T_{Tx,i,k} - iT_{Tx,1}| \ll \tau_c$). Hence, the coherence modulators are divided in N groups of K transmitters having approximately the same MZI-imbalance, resulting in N CM channels.

The modulating signals $\phi_{\text{mod},i,k}(t)$ are given by

$$\phi_{\text{mod},i,k}(t) = \beta_{i,k}(t) \sin(2\pi f_k t + \psi_{i,k}(t)), \quad (8.76)$$

where $\beta_{i,k}(t)$, f_k and $\psi_{i,k}(t)$ are the amplitude, carrier frequency and phase of the k -th SCM channel in the i -th CM channel, respectively. Hence, each CM channel carries K SCM channels that are assumed to be centered around a set of (different) carrier frequencies $\{f_k\}$. This set of frequencies is assumed to be the same for each CM channel. (Because of the transparency of CM it can be shown, however, that similar results would be obtained if different CM channels had different carrier frequency sets.)

Note that the SIRL and DS system topologies cannot be used for multiplexing the SCM channels, because having multiples branches with approximately the same path-delay in a SIRL system or serially cascading coherence modulators with approximately the same MZI-imbalance in a DS system would both result in intensity modulation of the received signal $y(t)$.



The autocorrelation function of (8.74) is given by

$$R_{y^*y}(t_1, t_2) \triangleq \mathbb{E}[y^*(t_1)y(t_2)] \approx \frac{1}{4L_{\text{Tx}}L_{\text{nw}}} \sum_{i=1}^N \sum_{k=1}^K \left[2R_{x^*x}(t_2 - t_1) - R_{x^*x}(t_2 - t_1 - T_{\text{Tx},i,k}) \exp(j\phi_{\text{mod},i,k}(t_1)) - R_{x^*x}(t_2 - t_1 + T_{\text{Tx},i,k}) \exp(-j\phi_{\text{mod},i,k}(t_1)) \right]. \quad (8.77)$$

Suppose $y(t)$ is received by N balanced CM receivers, where each receiver r has MZI-imbalance $T_{\text{Rx},r}$ and K parallel band-pass filters at the output of the TIA with impulse responses $h_{\text{BP},k}(t)$. Assuming that all MZI-imbalance $T_{\text{Tx},i,k}$ and $T_{\text{Rx},i}$ are much larger than the coherence time τ_c , the expected output signal of the j -th band-pass filter of receiver r follows from (4.45) and (8.77) as

$$\begin{aligned} \mathbb{E}[V_{\text{BP},r,j}(t)] &\approx -\frac{Z_{\text{TIA}}R_{\text{pd}}}{2L_{\text{Rx}}} \int_{-\infty}^{\infty} h_{\text{BP},j}(t - \rho) \text{Re}\{R_{y^*y}(\rho - T_{\text{Rx},r}, \rho)\} d\rho \\ &\approx \frac{Z_{\text{TIA}}R_{\text{pd}}P_x}{4L_{\text{Tx}}L_{\text{Rx}}L_{\text{nw}}} \sum_{i=1}^N \sum_{k=1}^K \exp\left(-\frac{\pi}{2} \left(\frac{T_{\text{Rx},r} - T_{\text{Tx},i,k}}{\tau_c}\right)^2\right) \\ &\quad \cdot \int_{-\infty}^{\infty} h_{\text{BP},j}(t - \rho) \cos\left(2\pi f_c(T_{\text{Rx},r} - T_{\text{Tx},i}) + \phi_{\text{mod},i,k}(\rho)\right) d\rho. \end{aligned} \quad (8.78)$$

When the receivers have MZI-imbalance

$$T_{\text{Rx},i} \approx T_{\text{Tx},i,k}, \quad (8.79)$$

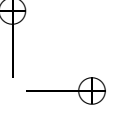
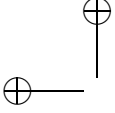
then this reduces to

$$\begin{aligned} \mathbb{E}[V_{\text{BP},r,j}(t)] &\approx \frac{Z_{\text{TIA}}R_{\text{pd}}P_x}{4L_{\text{Tx}}L_{\text{Rx}}L_{\text{nw}}} \sum_{k=1}^K \int_{-\infty}^{\infty} h_{\text{BP},j}(t - \rho) \\ &\quad \cdot \cos\left(2\pi f_c(T_{\text{Rx},r} - T_{\text{Tx},r,k}) + \phi_{\text{mod},r,k}(\rho)\right) d\rho. \end{aligned} \quad (8.80)$$

Substituting (8.76) and proceeding in a similar way as in Subsection 8.2.1, this can be rewritten as

$$\begin{aligned} \mathbb{E}[V_{\text{BP},r,j}(t)] &= \frac{Z_{\text{TIA}}R_{\text{pd}}P_x}{4L_{\text{Tx}}L_{\text{Rx}}L_{\text{nw}}} \sum_{k=1}^K \int_{-\infty}^{\infty} h_{\text{BP},j}(t - \rho) \\ &\quad \cdot \left\{ \cos(\Delta\phi_{r,k}) \left[J_0(\beta_{r,k}(\rho)) + 2 \sum_{\substack{n=2 \\ n \text{ even}}}^{\infty} J_n(\beta_{r,k}(\rho)) \cos(2\pi n f_k \rho + n \psi_{r,k}(\rho)) \right] \right. \\ &\quad \left. - 2 \sin(\Delta\phi_{r,k}) \sum_{\substack{n=1 \\ n \text{ odd}}}^{\infty} J_n(\beta_{r,k}(\rho)) \sin(2\pi n f_k \rho + n \psi_{r,k}(\rho)) \right\} d\rho, \end{aligned} \quad (8.81)$$

where $\Delta\phi_{r,k} \triangleq 2\pi f_c(T_{\text{Rx},r} - T_{\text{Tx},r,k})$.



Apparently, harmonic distortion occurs in the demodulation of the individual SCM channels. (As the SCM channels are modulated onto separate optical signals, there is no non-linear interaction between the SCM channels during coherence demodulation and hence no intermodulation distortion.)

The amplitudes of the desired RF signal terms are maximized by setting

$$\Delta\phi_{r,k} = \frac{3\pi}{2}, \quad (8.82)$$

(note that this requires the MZI-imbalances $T_{\text{Tx},i,k}$ in the coherence modulators for the same CM channel i to be exactly the same; we will come back to this later), resulting in

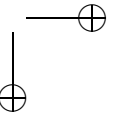
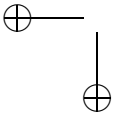
$$\begin{aligned} \mathbb{E}[V_{\text{BP},r,j}(t)] &= \frac{Z_{\text{TIA}}R_{\text{pd}}P_x}{4L_{\text{Tx}}L_{\text{Rx}}L_{\text{nw}}} \sum_{k=1}^K \int_{-\infty}^{\infty} h_{\text{BP},j}(t-\rho) \\ &\quad \cdot \sum_{\substack{n=1 \\ n \text{ odd}}}^{\infty} J_n(\beta_{r,k}(\rho)) \sin(2\pi n f_k \rho + n \psi_{r,k}(\rho)) d\rho. \end{aligned} \quad (8.83)$$

As the result, a band-pass filter can select a particular SCM channel and suppress all other channels provided that odd multiples of the carrier frequencies of the other channels are well outside the passband of the filter. In case of minimum channel spacing this implies that the carrier frequencies of the SCM channels should be chosen such that the maximum carrier frequency is less than three times larger than the minimum carrier frequency.

When the band-pass filters are dimensioned such that the j -th filter completely passes the RF signal with carrier frequency f_j and completely suppresses signals with other frequencies, then its expected output signal can be written as

$$\begin{aligned} \mathbb{E}[V_{\text{BP},r,j}(t)] &= \\ &= \frac{Z_{\text{TIA}}R_{\text{pd}}P_x}{2L_{\text{Tx}}L_{\text{Rx}}L_{\text{nw}}} |H_{\text{BP},j}(f_j)| J_1(\beta_{r,j}(t)) \sin(2\pi f_j t + \psi_{r,j}(t)), \end{aligned} \quad (8.84)$$

where an irrelevant phase shift has been omitted. Note that this expression is similar to (8.10). Therefore, $\beta_{i,k}(t)$ should be optimized in the same way as $\beta_i(t)$ in the case without SCM, resulting in a similar output signal. The main difference is that the network losses L_{nw} will now be K times larger because an NK -port combiner is needed instead of an N -port combiner, so that the output signal will be K times weaker. When the SCM channels in one CM channel are demultiplexed by K separate CM receivers with one band-pass filter each (instead of one CM receiver with K band-pass filters), then the output signal will be another K times weaker.



Noise performance

The variance of the noise at the output of a band-pass filter can be found from (5.8):

$$\begin{aligned}
\sigma_{V_{\text{BP},r,j}(t)}^2 &= R_{V_{\text{BP},r,j}V_{\text{BP},r,j}}(t,t) - \text{E}^2[V_{\text{BP},r,j}(t)] \\
&\approx \frac{Z_{\text{TIA}}^2 R_{\text{pd}} e}{2L_{\text{Rx}}} \int_{-\infty}^{\infty} h_{\text{BP},j}^2(t-\rho) \text{E}[P_y(\rho) + P_y(\rho - T_{\text{Rx},r})] d\rho \\
&\quad + \frac{Z_{\text{TIA}}^2 R_{\text{pd}}^2}{8L_{\text{Rx}}^2} \int_{-\infty}^{\infty} \int_{-\infty}^{\infty} h_{\text{BP},j}(t-\rho_1) h_{\text{BP},j}(t-\rho_2) \\
&\quad \cdot \text{Re} \left\{ R_{y^*y}(\rho_1, \rho_2) R_{y^*y}(\rho_2 - T_{\text{Rx},r}, \rho_1 - T_{\text{Rx},r}) \right. \\
&\quad \quad \left. + R_{y^*y}(\rho_1 - T_{\text{Rx},r}, \rho_2) R_{y^*y}(\rho_2 - T_{\text{Rx},r}, \rho_1) \right\} d\rho_1 d\rho_2 \\
&\quad + Z_{\text{TIA}}^2 S_{\text{th}} \int_{-\infty}^{\infty} h_{\text{BP},j}^2(t-\rho) d\rho. \tag{8.85}
\end{aligned}$$

Using (8.75), (8.77), and (8.79) one can find

$$\text{E}[P_y(\rho)] \approx \text{E}[P_y(\rho - T_{\text{Rx},r})] \approx \frac{N K P_x}{2L_{\text{Tx}} L_{\text{nw}}}, \tag{8.86}$$

$$\begin{aligned}
R_{y^*y}(\rho_1, \rho_2) R_{y^*y}(\rho_2 - T_{\text{Rx},r}, \rho_1 - T_{\text{Rx},r}) &\approx \\
\frac{1}{16L_{\text{Tx}}^2 L_{\text{nw}}^2} &\left\{ 4N^2 K^2 |R_{x^*x}(\rho_2 - \rho_1)|^2 \right. \\
&+ \sum_{i=1}^N \sum_{k_1=1}^K \sum_{k_2=1}^K \left[|R_{x^*x}(\rho_2 - \rho_1 - T_{\text{Tx},i,k_1})|^2 \right. \\
&\quad \cdot \exp\left(j 2\pi f_c (T_{\text{Tx},i,k_1} - T_{\text{Tx},i,k_2}) \right. \\
&\quad \quad \left. \left. + j \phi_{\text{mod},i,k_1}(\rho_1) - j \phi_{\text{mod},i,k_2}(\rho_1) \right) \right. \\
&\quad \left. + |R_{x^*x}(\rho_2 - \rho_1 + T_{\text{Tx},i,k_1})|^2 \right. \\
&\quad \cdot \exp\left(j 2\pi f_c (T_{\text{Tx},i,k_2} - T_{\text{Tx},i,k_1}) \right. \\
&\quad \quad \left. \left. + j \phi_{\text{mod},i,k_2}(\rho_1) - j \phi_{\text{mod},i,k_1}(\rho_1) \right) \right] \left. \right\}, \tag{8.87}
\end{aligned}$$

$$\begin{aligned}
R_{y^*y}(\rho_1 - T_{\text{Rx},r}, \rho_2) R_{y^*y}(\rho_2 - T_{\text{Rx},r}, \rho_1) &\approx \\
\frac{1}{16L_{\text{Tx}}^2 L_{\text{nw}}^2} &\sum_{k_1=1}^K \sum_{k_2=1}^K |R_{x^*x}(\rho_2 - \rho_1)|^2 \\
&\quad \cdot \exp\left(j 2\pi f_c (2T_{\text{Rx},r} - T_{\text{Tx},r,k_1} - T_{\text{Tx},r,k_2}) \right. \\
&\quad \quad \left. + j \phi_{\text{mod},r,k_1}(\rho_1) + j \phi_{\text{mod},r,k_2}(\rho_1) \right). \tag{8.88}
\end{aligned}$$

Substituting these in (8.85) and using the approximation in (4.51) results in

$$\begin{aligned}
\sigma_{V_{\text{BP},r,j}(t)}^2 &\approx \frac{Z_{\text{TIA}}^2 R_{\text{pd}} P_x e N K}{2L_{\text{Tx}} L_{\text{Rx}} L_{\text{nw}}} \int_{-\infty}^{\infty} h_{\text{BP},j}^2(t-\rho) \, d\rho \\
&+ \frac{Z_{\text{TIA}}^2 R_{\text{pd}}^2 P_x^2 \tau_c}{32L_{\text{Tx}}^2 L_{\text{Rx}}^2 L_{\text{nw}}^2} \int_{-\infty}^{\infty} h_{\text{BP},j}^2(t-\rho) \left[4N^2 K^2 \right. \\
&+ 2 \sum_{i=1}^N \sum_{k_1=1}^K \sum_{k_2=1}^K \cos\left(2\pi f_c (T_{\text{Tx},i,k_1} - T_{\text{Tx},i,k_2}) + \phi_{\text{mod},i,k_1}(\rho) - \phi_{\text{mod},i,k_2}(\rho)\right) \\
&+ \sum_{k_1=1}^K \sum_{k_2=1}^K \cos\left(2\pi f_c (2T_{\text{Rx},r} - T_{\text{Tx},r,k_1} - T_{\text{Tx},r,k_2}) \right. \\
&\quad \left. \left. + \phi_{\text{mod},r,k_1}(\rho) + \phi_{\text{mod},r,k_2}(\rho)\right) \right] \, d\rho \\
&+ Z_{\text{TIA}}^2 S_{\text{th}} \int_{-\infty}^{\infty} h_{\text{BP},j}^2(t-\rho) \, d\rho. \tag{8.89}
\end{aligned}$$

Substituting (8.76) and (8.82), assuming that the modulation of the RF carrier does not affect the variance (so we take $\beta_{i,k}(t) = \beta_{i,k}$ and $\psi_{i,k}(t) = \psi_{i,k}$), and then using (8.4) and (8.5) one can find

$$\begin{aligned}
&\cos\left(2\pi f_c (T_{\text{Tx},i,k_1} - T_{\text{Tx},i,k_2}) + \phi_{\text{mod},i,k_1}(\rho) - \phi_{\text{mod},i,k_2}(\rho)\right) = \\
&\cos\left(\phi_{\text{mod},i,k_1}(\rho)\right) \cos\left(\phi_{\text{mod},i,k_2}(\rho)\right) + \sin\left(\phi_{\text{mod},i,k_1}(\rho)\right) \sin\left(\phi_{\text{mod},i,k_2}(\rho)\right) \\
&= \cos\left(\beta_{i,k_1} \sin\left(2\pi f_{k_1} \rho + \psi_{i,k_1}\right)\right) \cos\left(\beta_{i,k_2} \sin\left(2\pi f_{k_2} \rho + \psi_{i,k_2}\right)\right) \\
&\quad + \sin\left(\beta_{i,k_1} \sin\left(2\pi f_{k_1} \rho + \psi_{i,k_1}\right)\right) \sin\left(\beta_{i,k_2} \sin\left(2\pi f_{k_2} \rho + \psi_{i,k_2}\right)\right) \\
&= \sum_{n_1} \sum_{n_2} J_{n_1}(\beta_{i,k_1}) J_{n_2}(\beta_{i,k_2}) \\
&\quad \cdot \cos\left(2\pi(n_1 f_{k_1} - n_2 f_{k_2})\rho + n_1 \psi_{i,k_1} - n_2 \psi_{i,k_2}\right), \tag{8.90}
\end{aligned}$$

$$\begin{aligned}
&\cos\left(2\pi f_c (2T_{\text{Rx},r} - T_{\text{Tx},r,k_1} - T_{\text{Tx},r,k_2}) + \phi_{\text{mod},r,k_1}(\rho) + \phi_{\text{mod},r,k_2}(\rho)\right) = \\
&-\cos\left(\phi_{\text{mod},r,k_1}(\rho)\right) \cos\left(\phi_{\text{mod},r,k_2}(\rho)\right) + \sin\left(\phi_{\text{mod},r,k_1}(\rho)\right) \sin\left(\phi_{\text{mod},r,k_2}(\rho)\right) \\
&= -\cos\left(\beta_{r,k_1} \sin\left(2\pi f_{k_1} \rho + \psi_{r,k_1}\right)\right) \cos\left(\beta_{r,k_2} \sin\left(2\pi f_{k_2} \rho + \psi_{r,k_2}\right)\right) \\
&\quad + \sin\left(\beta_{r,k_1} \sin\left(2\pi f_{k_1} \rho + \psi_{r,k_1}\right)\right) \sin\left(\beta_{r,k_2} \sin\left(2\pi f_{k_2} \rho + \psi_{r,k_2}\right)\right) \\
&= \sum_{n_1} \sum_{n_2} J_{n_1}(\beta_{r,k_1}) J_{n_2}(\beta_{r,k_2}) \\
&\quad \cdot \cos\left(2\pi(n_1 f_{k_1} + n_2 f_{k_2})\rho + n_1 \psi_{r,k_1} + n_2 \psi_{r,k_2}\right). \tag{8.91}
\end{aligned}$$

Substituting these in (8.89), writing the impulse response $h_{\text{BP},j}(t)$ as the inverse Fourier transform of the transfer function $H_{\text{BP},j}(f)$ of the band-pass filter, and applying phase-averaging over the $\psi_{i,k}$ s and time-averaging, we can write

$$\begin{aligned} \langle \sigma_{V_{\text{BP},r,j}(t)}^2 \rangle &\approx 2Z_{\text{TIA}}^2 |H_{\text{BP},j}(f_j)|^2 W_{\text{BP}} \left\{ \frac{R_{\text{pd}} P_x e N K}{2L_{\text{Tx}} L_{\text{Rx}} L_{\text{nw}}} \right. \\ &\quad + \frac{R_{\text{pd}}^2 P_x^2 \tau_c}{32L_{\text{Tx}}^2 L_{\text{Rx}}^2 L_{\text{nw}}^2} \left[4N^2 K^2 + 2 \sum_{i=1}^N \sum_{k=1}^K \sum_n J_n^2(\beta_{i,k}) \right. \\ &\quad \left. \left. - \sum_{k=1}^K \sum_n J_n(\beta_{r,k}) J_{-n}(\beta_{r,k}) \right] + S_{\text{th}} \right\}. \end{aligned} \quad (8.92)$$

Using

$$\sum_n J_n^2(x) = 1, \quad (8.93)$$

$$\sum_n J_n(x) J_{-n}(x) = J_0(2x), \quad (8.94)$$

and assuming that all $\beta_{r,k}$ s are the same, this becomes

$$\begin{aligned} \langle \sigma_{V_{\text{BP},r,j}(t)}^2 \rangle &\approx 2Z_{\text{TIA}}^2 |H_{\text{BP},j}(f_j)|^2 W_{\text{BP}} \left\{ \frac{R_{\text{pd}} P_x e N K}{2L_{\text{Tx}} L_{\text{Rx}} L_{\text{nw}}} \right. \\ &\quad \left. + \frac{R_{\text{pd}}^2 P_x^2 \tau_c}{32L_{\text{Tx}}^2 L_{\text{Rx}}^2 L_{\text{nw}}^2} [4N^2 K^2 + 2N K - K J_0(2\beta)] + S_{\text{th}} \right\}. \end{aligned} \quad (8.95)$$

The CNR at the output of the band-pass filter now follows from (8.84) and (8.95) as

$$CNR_{\text{BP}} = \frac{\langle E^2[V_{\text{BP},r,j}(t)] \rangle}{\langle \sigma_{V_{\text{BP},r,j}(t)}^2 \rangle} = \left(CNR_{\text{sn}}^{-1} + CNR_{\text{bn}}^{-1} + CNR_{\text{tn}}^{-1} \right)^{-1} \quad (8.96)$$

where

$$CNR_{\text{sn}} = \frac{R_{\text{pd}} P_x \langle J_1^2(\beta_{r,j}(t)) \rangle}{8N K L_{\text{Tx}} L_{\text{Rx}} L_{\text{nw}} e W_{\text{BP}}}, \quad (8.97)$$

$$CNR_{\text{bn}} = \frac{2 \langle J_1^2(\beta_{r,j}(t)) \rangle}{[4N^2 K^2 + 2N K - K J_0(2\beta)] \tau_c W_{\text{BP}}}, \quad (8.98)$$

$$CNR_{\text{tn}} = \frac{R_{\text{pd}}^2 P_x^2 \langle J_1^2(\beta_{r,j}(t)) \rangle}{16L_{\text{Tx}}^2 L_{\text{Rx}}^2 L_{\text{nw}}^2 S_{\text{th}} W_{\text{BP}}}. \quad (8.99)$$

(Note that these correspond to (8.36) through (8.39) when $K = 1$.)

Example 8.4

Suppose that single-channel SCM is used on top of CM in the downlink of the WLAN distribution network that was considered in Example 8.3, in order to distinguish between RAPs that share a CM channel. Since three non-overlapping channels are defined for IEEE 802.11b [95], we assume that three SCM channels are multiplexed per CM channel, so $K = 3$. The CM network now contains $3N$ coherence modulators and $3N$ coherence demodulators, so the total network loss now becomes $L_{\text{nw}} \approx 1.090 \cdot 9N^2 \approx 9.810N^2$. The other network parameters are assumed to be the same as in the previous example. The resulting CNR follows from (8.96) through (8.99) and has been plotted as a function of the number of CM channels N in Figure 8.6.

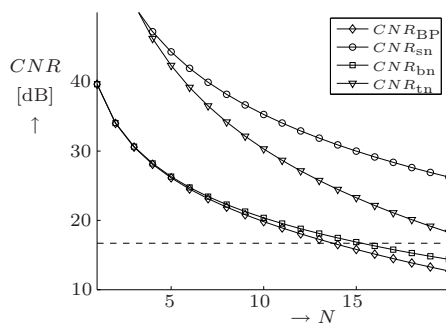
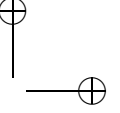
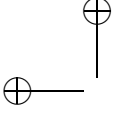


Figure 8.6: Carrier-to-noise ratios at the output of the band-pass filter as a function of number of CM channels N in a WLAN IEEE 802.11b distribution network based on CM and single-channel SCM, with 3 SCM channels per CM channel

Maintaining the 16.7 dB criterion, it follows that at most 13 CM channels, and hence $3 \cdot 13 = 39$ RAPs can be supported, which is nearly the same as the 41 RAPs in the previous example, without SCM. This should not be surprising, because coherence modulators with identical MZI-imbalances cause approximately the same amount of beat noise as an identical number of coherence modulators with different MZI-imbalances. The main difference is that the amount of loss has increased, but it follows from Figure 8.6 that this still does not prevent beat noise from being the dominant noise source.

Hence, when the same concept is used in the uplink, where the receivers for the different SCM channels in one CM channel can be combined into one CM receiver, this will result in improved carrier-to-shot noise and carrier-to-thermal noise ratios, but this will not significantly improve the overall CNR because the carrier-to-beat noise ratio is still much lower. □

**Output stabilization**

From (8.81) it followed that the amplitudes of the SCM channels at the output of the band-pass filters could be maximized by setting

$$\Delta\phi_{r,k} = 2\pi f_c(T_{\text{Rx},r} - T_{\text{Tx},r,k}) = \frac{3\pi}{2}, \forall k. \quad (8.100)$$

When the SCM channels are detected by one CM receiver, this implies that the delays $T_{\text{Tx},r,k}$ of all the transmitters corresponding to the r -th CM channels have to have exactly the same delay. In case of significant fabrication inaccuracies (like in Example 6.1), temperature sensitivity or component aging, this can only be realized in case some kind of “master” transmitter provides synchronization signals in the return path, like described in [98]. This will not be considered in further detail here.

In case the SCM channels are separately detected by different CM receivers, the transmitters corresponding to the same CM channel no longer need to have exactly the same delay, but each receiver still needs to have a fixed phase relation to the corresponding transmitter:

$$\Delta\phi_{r,k} = 2\pi f_c(T_{\text{Rx},r,k} - T_{\text{Tx},r,k}) = \frac{3\pi}{2}, \forall k, \quad (8.101)$$

where $T_{\text{Rx},r,k}$ is the MZI-imbalance of the CM receiver corresponding to the k -th SCM channel in the r -th CM channel. This phase synchronization cannot be obtained in the same way as described in Subsection 8.3.1, however. The output of the low-pass filter of a particular CM receiver for SCM channel j in CM channel r would in that case follow from (8.81) as

$$\begin{aligned} \mathbb{E}[V_{\text{LP},r,j}(t)] &= \frac{Z_{\text{TIA}}R_{\text{pd}}P_x}{4L_{\text{Tx}}L_{\text{Rx}}L_{\text{nw}}} \sum_{k=1}^K \cos\left(2\pi f_c(T_{\text{Rx},r,j} - T_{\text{Tx},r,k})\right) \\ &\quad \cdot \int_{-\infty}^{\infty} h_{\text{LP}}(t - \rho) J_0(\beta_{r,k}(\rho)) d\rho, \quad (8.102) \end{aligned}$$

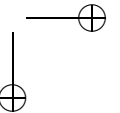
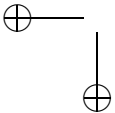
so it contains terms from all transmitters corresponding to the r -th CM channel. Since it is not possible to distinguish between these terms, the signal does not provide a means to phase-synchronize the CM receiver specifically to the corresponding CM transmitter.

This can be solved by replacing the low-pass filter by the circuit in Figure 8.7(a). The band-pass filter in the upper branch of the circuit has center frequency f_j , so its output signal $V_{\text{BP}}(t)$ actually corresponds to the desired RF signal. When the carrier frequencies f_k are chosen within one octave of bandwidth, it follows from (8.81) that the expected value of $V_{\text{BP}}(t)$ is proportional to

$$-\sin(\Delta\phi_{r,j})J_1(\beta_{r,j}(t)) \sin(2\pi f_j t + \psi_{r,j}(t)), \quad (8.103)$$

where $\Delta\phi_{r,j} \triangleq 2\pi f_c(T_{\text{Rx},r,j} - T_{\text{Tx},r,j})$. After squaring and band-pass filtering around center frequency $2f_j$, an RF signal results which is proportional to

$$-\sin^2(\Delta\phi_{r,j})J_1^2(\beta_{r,j}(t)) \cos(4\pi f_j t + 2\psi_{r,j}(t)). \quad (8.104)$$



The band-pass filter in the vertical branch also has center frequency $2f_j$. From (8.81) it follows that the output signal of this band-pass filter is proportional to

$$\cos(\Delta\phi_{r,j})J_2(\beta_{r,j}(t))\cos(4\pi f_j t + 2\psi_{r,j}(t)). \quad (8.105)$$

Hence, multiplication and low-pass filtering result in a baseband signal which is proportional to

$$-\sin^2(\Delta\phi_{r,j})\cos(\Delta\phi_{r,j})\langle J_1^2(\beta_{r,j}(t))J_2(\beta_{r,j}(t)) \rangle. \quad (8.106)$$

This has been plotted in Figure 8.7(b), where the circle denotes the desired value of $\Delta\phi_{r,j}$. Apparently, the value of $T_{R\text{x},r,j}$ should be increased when the output signal of the circuit is positive, and decreased when it is negative, so it indeed results in an unambiguous control signal.

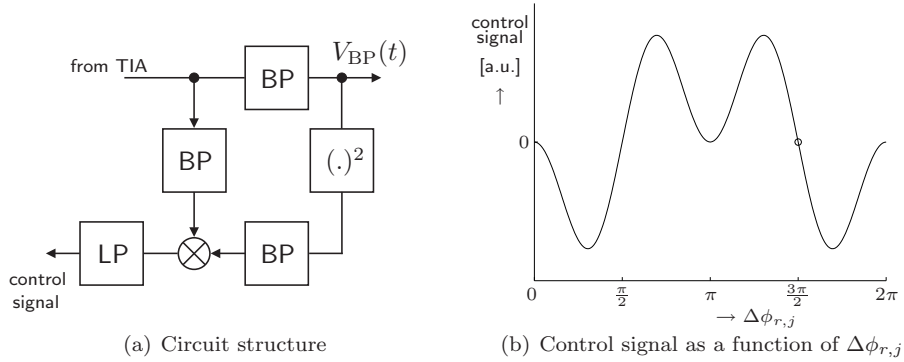


Figure 8.7: Phase-synchronization circuit for single-channel SCM over CM with separate CM receivers for different SCM channels

Alternatively, the self-heterodyning method described in Subsection 8.3.2 can be used, provided that the frequency shifters are put in the transmitters, since each transmitter should have a different frequency shift. When self-heterodyning is applied, the PA topology can eventually be replaced by a SIRL or DS topology, where each branch or cascaded coherence modulator contains a different frequency shifter.

It can be verified (this will not be discussed in detail) that the phase diversity receivers that were considered in Subsection 8.3.3 are not suitable for demodulating CM channels in which multiple SCM channels are multiplexed through single-channel SCM, because the output signals of the low-pass filters, $V_{LP,I,r}(t)$ and $V_{LP,Q,r}(t)$, would then contain multiple terms with different phase offsets, so that $V_{LP,I,r}(t)$ and $V_{LP,Q,r}(t)$ would no longer have a quadrature relation.

8.4.2 Multi-channel subcarrier multiplexing

Multiplexing and demultiplexing

Suppose K RF signals are transmitted through the same CM channel i by means of multi-channel SCM. The SCM channels, denoted by (8.76), are then first multiplexed in the electrical domain, resulting in a composite signal

$$\phi_{\text{mod},i}(t) = \sum_{k=1}^K \phi_{\text{mod},i,k}(t) = \sum_{k=1}^K \beta_{i,k}(t) \sin(2\pi f_k t + \psi_{i,k}(t)). \quad (8.107)$$

The composite signals can then be coherence-multiplexed by means of any of the multiplexing topologies that have been described in Chapter 5. When a PA is used, for example, this requires N coherence modulators, where N is the number of CM channels. When there are N balanced CM receivers which are matched to the corresponding transmitters (so $|T_{\text{Rx},r} - T_{\text{Tx},r}| \ll \tau_c \forall r$ and $|T_{\text{Rx},r} - T_{\text{Tx},i}| \gg \tau_c$ for $r \neq i$), with K band-pass filters for selecting the SCM channels, then the expected value of the output signal $V_{\text{BP},r,j}(t)$ of the band-pass filter j in CM receiver r follows directly from (6.3) and (8.107) as

$$\begin{aligned} \mathbb{E}[V_{\text{BP},r,j}(t)] &= \frac{Z_{\text{TIA}} R_{\text{pd}} P_x}{4L_{\text{Tx}} L_{\text{Rx}} L_{\text{nw}}} \int_{-\infty}^{\infty} h_{\text{BP},j}(t - \rho) \\ &\quad \cdot \cos\left(\Delta\phi_r + \sum_{k=1}^K \beta_{r,k}(\rho) \sin(2\pi f_k \rho + \psi_{r,k}(\rho))\right) d\rho. \end{aligned} \quad (8.108)$$

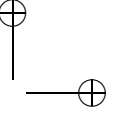
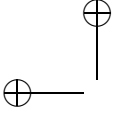
Using (8.3) again this can be written as an expression that contains terms of the form $\cos\left(\sum_{k=1}^K \beta_k \sin \Phi_k\right)$ and $\sin\left(\sum_{k=1}^K \beta_k \sin \Phi_k\right)$, where $\beta_k = \beta_{r,k}(t)$ and $\Phi_k = 2\pi f_k t + \psi_{r,k}(t)$. Using (8.4) and (8.5) one can find

$$\begin{aligned} \exp\left(j \sum_{k=1}^K \beta_k \sin \Phi_k\right) &= \prod_{k=1}^K \exp(j \beta_k \sin \Phi_k) \\ &= \prod_{k=1}^K \left[\cos(\beta_k \sin \Phi_k) + j \sin(\beta_k \sin \Phi_k) \right] = \prod_{k=1}^K \sum_n J_n(\beta_k) \exp(j n \Phi_k) \\ &= \sum_{n_1} \sum_{n_2} \cdots \sum_{n_K} \left[\prod_{k=1}^K J_{n_k}(\beta_k) \right] \exp\left(j \sum_{k=1}^K n_k \Phi_k\right), \end{aligned} \quad (8.109)$$

so that we can write

$$\cos\left(\sum_{k=1}^K \beta_k \sin \Phi_k\right) = \sum_{n_1} \sum_{n_2} \cdots \sum_{n_K} \left[\prod_{k=1}^K J_{n_k}(\beta_k) \right] \cos\left(\sum_{k=1}^K n_k \Phi_k\right), \quad (8.110)$$

$$\sin\left(\sum_{k=1}^K \beta_k \sin \Phi_k\right) = \sum_{n_1} \sum_{n_2} \cdots \sum_{n_K} \left[\prod_{k=1}^K J_{n_k}(\beta_k) \right] \sin\left(\sum_{k=1}^K n_k \Phi_k\right). \quad (8.111)$$



Therefore, (8.108) can be written as

$$\begin{aligned} \mathbb{E}[V_{\text{BP},r,j}(t)] &= \frac{Z_{\text{TIA}}R_{\text{pd}}P_x}{4L_{\text{Tx}}L_{\text{Rx}}L_{\text{nw}}} \int_{-\infty}^{\infty} h_{\text{BP},j}(t-\rho) \\ &\cdot \sum_{n_1} \sum_{n_2} \cdots \sum_{n_K} \left[\prod_{k=1}^K J_{n_k}(\beta_{r,k}(\rho)) \right] \\ &\cdot \left\{ \cos(\Delta\phi_r) \cos\left(\sum_{k=1}^K n_k [2\pi f_k \rho + \psi_{r,k}(\rho)]\right) \right. \\ &\quad \left. - \sin(\Delta\phi_r) \sin\left(\sum_{k=1}^K n_k [2\pi f_k \rho + \psi_{r,k}(\rho)]\right) \right\} d\rho. \quad (8.112) \end{aligned}$$

Apparently, intermodulation distortion (IMD) between the SCM channels occurs due to the intrinsic non-linearity of the demodulation principle. As a result, the output signal contains one baseband term (that is the term for which $n_1 = n_2 = \dots = n_K = 0$) and an infinite sum of RF terms with carrier frequencies that are linear combinations of the carrier frequencies f_k of the SCM channels. The desired RF signal terms are the ones with carrier frequency f_j and phase $\psi_{r,j}(t)$. Hence, the band-pass filter should be dimensioned such that these terms are completely passed and the other terms are suppressed as much as possible. This does not cancel all the undesired IMD products, however, because some of them will be in the same frequency range as the desired RF signal terms. We will come back to this later.

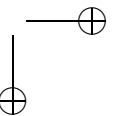
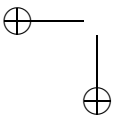
Obviously, the desired RF signal terms are the ones that have

$$n_k = \begin{cases} \pm 1 & , k = j, \\ 0 & , k \neq j. \end{cases} \quad (8.113)$$

From (8.8) it then follows that the amplitude of their sum can be maximized by setting $\Delta\phi_r = \frac{3\pi}{2}$ (we will come back to this later), resulting in a desired RF signal

$$\begin{aligned} \mathbb{E}[V_{\text{BP},r,j}(t)]_{\text{desired}} &= \frac{Z_{\text{TIA}}R_{\text{pd}}P_x}{2L_{\text{Tx}}L_{\text{Rx}}L_{\text{nw}}} |H_{\text{BP},j}(f_j)| \left[\prod_{\substack{k=1 \\ k \neq j}}^K J_0(\beta_{r,k}(t)) \right] \\ &\cdot J_1(\beta_{r,j}(t)) \sin(2\pi f_j t + \psi_{r,j}(t)), \quad (8.114) \end{aligned}$$

where an irrelevant phase shift has been omitted.



Intermodulation distortion (IMD)

Apart from the desired RF signal terms, the expected output signal also contains IMD products. Substituting $\Delta\phi_r = \frac{3\pi}{2}$ in (8.112) we find

$$\begin{aligned} E[V_{\text{BP},r,j}(t)] &= \frac{Z_{\text{TIA}} R_{\text{pd}} P_x}{4L_{\text{Tx}} L_{\text{Rx}} L_{\text{nw}}} \int_{-\infty}^{\infty} h_{\text{BP},j}(t - \rho) \\ &\quad \cdot \sum_{n_1} \sum_{n_2} \cdots \sum_{n_K} \left[\prod_{k=1}^K J_{n_k}(\beta_{r,k}(\rho)) \right] \\ &\quad \cdot \sin \left(\sum_{k=1}^K n_k [2\pi f_k \rho + \psi_{r,k}(\rho)] \right) d\rho. \end{aligned} \quad (8.115)$$

Hence, the amplitudes of the IMD products are products of Bessel functions of the first kind. Four of these are plotted in Figure 8.8

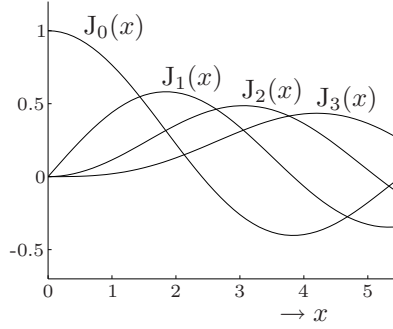
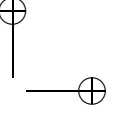
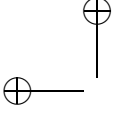


Figure 8.8: Bessel function of the first kind and order zero, one, two and three

According to (8.114) the amplitude of the desired term is proportional to

$$\left[\prod_{\substack{k=1 \\ k \neq j}}^K J_0(\beta_{r,k}(t)) \right] J_1(\beta_{r,j}(t)). \quad (8.116)$$

When the amplitudes $\beta_{r,k}(t)$ are modulated, it follows from Figure 8.8 that the maximum value of $\beta_{r,k}(t)$ should be well below one in order to suppress variations due to interfering SCM channels (the zero-order Bessel functions). On the other hand, this maximum value should not be too small because the amplitude of the desired term increases with increasing $\beta_{r,j}(t)$ (due to the first order Bessel function), so there is a trade-off when choosing the maximum value of $\beta_{r,k}(t)$. The optimum value of this maximum lies somewhere between zero and one, and decreases with increasing number of SCM channels K . There is a similar trade-off when the amplitudes $\beta_{r,k}(t)$ are a constant β ; the amplitude of the desired term is then maximized by choosing β somewhere between zero and one.



From Figure 8.8 it follows that for such values of $\beta_{r,k}(t)$, the value of $J_n(\beta_{r,k}(t))$ rapidly decreases with increasing n . Therefore, the IMD is dominated by the terms in (8.115) with the smallest values of n_k . Some possible combinations will be considered:

- The product of Bessel functions is maximum when $n_k = 0 \forall k$, but then the sine function is zero. Hence, this combination does not result in a contribution (provided that $\Delta\phi_r = \frac{3\pi}{2}$);

- When

$$n_k = \begin{cases} \pm 1 & , k = k_1, \\ 0 & , k \neq k_1, \end{cases} \quad (8.117)$$

this results in two identical terms of the form

$$\frac{Z_{\text{TIA}} R_{\text{pd}} P_x}{4L_{\text{TX}} L_{\text{RX}} L_{\text{nw}}} \int_{-\infty}^{\infty} h_{\text{BP},j}(t - \rho) \left[\prod_{\substack{k=1 \\ k \neq k_1}}^K J_0(\beta_{r,k}(\rho)) \right] J_1(\beta_{r,k_1}(\rho)) \cdot \sin(2\pi f_{k_1} \rho + \psi_{r,k_1}(\rho)) \, d\rho. \quad (8.118)$$

This actually corresponds to one individual RF carrier. It is suppressed by the band-pass filter when $k_1 \neq j$, whereas (8.114) results when $k = j$.

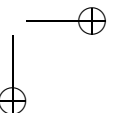
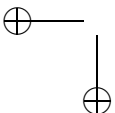
- When

$$n_k = \begin{cases} \pm 1 & , k = k_1, \\ \pm 1 & , k = k_2, \\ 0 & , k \neq k_1 \text{ and } k \neq k_2, \end{cases} \quad (8.119)$$

with $k_1 \neq k_2$, this results in four terms of the form

$$\frac{Z_{\text{TIA}} R_{\text{pd}} P_x}{4L_{\text{TX}} L_{\text{RX}} L_{\text{nw}}} \int_{-\infty}^{\infty} h_{\text{BP},j}(t - \rho) \left[\prod_{\substack{k=1 \\ k \notin \{k_1, k_2\}}}^K J_0(\beta_{r,k}(\rho)) \right] \cdot J_1(\beta_{r,k_1}(\rho)) J_1(\beta_{r,k_2}(\rho)) \cdot \sin\left(\pm [2\pi f_{k_1} \rho + \psi_{r,k_1}(\rho)] \pm [2\pi f_{k_2} \rho + \psi_{r,k_2}(\rho)]\right) \, d\rho. \quad (8.120)$$

This is called *second order IMD*. It appears at frequencies which are sums and differences of the RF carrier frequencies f_k . In general, second order IMD in SCM systems can be prevented by choosing these frequencies within one octave of bandwidth, so that the second order IMD terms do not appear in the passband of the band-pass filter [99]. In the case of multi-channel SCM over CM, however, it can be easily verified that the second order IMD terms cancel each other automatically (provided that $\Delta\phi_r = \frac{3\pi}{2}$).



- When

$$n_k = \begin{cases} \pm 2 & , k = k_1, \\ 0 & , k \neq k_1, \end{cases} \quad (8.121)$$

this results in two terms of the form

$$\begin{aligned} \frac{Z_{\text{TIA}} R_{\text{pd}} P_x}{4L_{\text{TX}} L_{\text{RX}} L_{\text{nw}}} \int_{-\infty}^{\infty} h_{\text{BP},j}(t - \rho) \left[\prod_{\substack{k=1 \\ k \neq k_1}}^K J_0(\beta_{r,k}(\rho)) \right] J_2(\beta_{r,k_1}(\rho)) \\ \cdot \sin\left(\pm \left[2\pi f_{k_1} \rho + \psi_{r,k_1}(\rho) \right]\right) d\rho. \end{aligned} \quad (8.122)$$

These are also second order IMD products, which again cancel each other.

- When

$$n_k = \begin{cases} \pm 1 & , k = k_1, \\ \pm 1 & , k = k_2, \\ \pm 1 & , k = k_3, \\ 0 & , k \neq k_1 \text{ and } k \neq k_2 \text{ and } k \neq k_3, \end{cases} \quad (8.123)$$

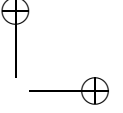
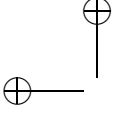
with $k_1 \neq k_2$, $k_1 \neq k_3$ and $k_2 \neq k_3$, this results in eight terms, grouped in pairs of two identical terms of the form

$$\begin{aligned} \frac{Z_{\text{TIA}} R_{\text{pd}} P_x}{4L_{\text{TX}} L_{\text{RX}} L_{\text{nw}}} \int_{-\infty}^{\infty} h_{\text{BP},j}(t - \rho) \left[\prod_{\substack{k=1 \\ k \notin \{k_1, k_2, k_3\}}}^K J_0(\beta_{r,k}(\rho)) \right] \\ \cdot J_1(\beta_{r,k_1}(\rho)) J_1(\beta_{r,k_2}(\rho)) J_1(\beta_{r,k_3}(\rho)) \\ \cdot \sin\left(2\pi f_{k_1} \rho + \psi_{r,k_1}(\rho) \pm \left[2\pi f_{k_2} \rho + \psi_{r,k_2}(\rho) \right] \right. \\ \left. \pm \left[2\pi f_{k_3} \rho + \psi_{r,k_3}(\rho) \right] \right) d\rho. \end{aligned} \quad (8.124)$$

This is called *third order IMD*. Third order IMD products appear around frequencies $f_{k_1} \pm f_{k_2} \pm f_{k_3}$, and hence coincide with the passband of the band-pass filter when $f_{k_1} \pm f_{k_2} \pm f_{k_3} \approx f_j$. It can be verified that this will certainly occur when there are three or more SCM channels with equal differences between the carrier frequencies.

- When

$$n_k = \begin{cases} \pm 2 & , k = k_1, \\ \pm 1 & , k = k_2, \\ 0 & , k \neq k_1 \text{ and } k \neq k_2, \end{cases} \quad (8.125)$$



with $k_1 \neq k_2$, this results in four terms of the form

$$\begin{aligned} & \frac{Z_{\text{TIA}} R_{\text{pd}} P_x}{4L_{\text{TX}} L_{\text{RX}} L_{\text{nw}}} \int_{-\infty}^{\infty} h_{\text{BP},j}(t - \rho) \left[\prod_{\substack{k=1 \\ k \neq \{k_1, k_2\}}}^K J_0(\beta_{r,k}(\rho)) \right] \\ & \quad \cdot J_2(\beta_{r,k_1}(\rho)) J_1(\beta_{r,k_2}(\rho)) \\ & \quad \cdot \sin\left(4\pi f_{k_1} \rho + 2\psi_{r,k_1}(\rho) \pm \left[2\pi f_{k_2} \rho + \psi_{r,k_2}(\rho)\right]\right) d\rho. \end{aligned} \quad (8.126)$$

These are also third order IMD products. Their center frequencies coincide with the passband of the band-pass filter when $2f_{k_1} \pm f_{k_2} \approx f_j$.

- When

$$n_k = \begin{cases} \pm 3 & , k = k_1, \\ 0 & , k \neq k_1, \end{cases} \quad (8.127)$$

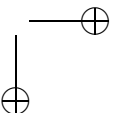
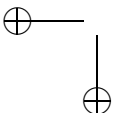
this results in two terms of the form

$$\begin{aligned} & \frac{Z_{\text{TIA}} R_{\text{pd}} P_x}{4L_{\text{TX}} L_{\text{RX}} L_{\text{nw}}} \int_{-\infty}^{\infty} h_{\text{BP},j}(t - \rho) \left[\prod_{\substack{k=1 \\ k \neq k_1}}^K J_0(\beta_{r,k}(\rho)) \right] J_3(\beta_{r,k_1}(\rho)) \\ & \quad \cdot \sin\left(6\pi f_{k_1} \rho + 3\psi_{r,k_1}(\rho)\right) d\rho. \end{aligned} \quad (8.128)$$

These are also third order IMD products. Their center frequencies coincide with the passband of the band-pass filter when $3f_{k_1} \approx f_j$. This will not occur when the carrier frequencies are chosen within a sufficiently small bandwidth.

- It can be verified that all other combinations of the n_k s lead to (higher order) IMD products with smaller amplitudes. These are therefore neglected.

Apparently, IMD in a phase-synchronized CM receiver for multi-channel SCM over CM is dominated by third order IMD. The number of third order IMD products that appear in the passband of the band-pass filter depends on the choice of the carrier frequencies f_k , and their amplitude depends on the modulation format of the SCM channels and the transfer function of the band-pass filter. When both the power spectral density of the modulated SCM channels and the transfer function of the band-pass filter are approximated as rectangular functions with identical bandwidth W_{BP} and center frequency f_j , then it can be shown that approximately $\frac{2}{3}$ of the power of a third order IMD product is passed through by the band-pass filter [100].



Hence, when it is assumed that the $\beta_{r,k}$ s are a constant β , and that only negligible power of third order IMD products leaks into adjacent channels, then the carrier-to-intermodulation ratio (CIR) follows from (8.114), (8.124), (8.126) and (8.128) as

$$\begin{aligned} CIR_{\text{IMD}} &\triangleq \frac{\langle E^2[V_{\text{BP},r,j}(t)]_{\text{desired}} \rangle}{\langle E^2[V_{\text{BP},r,j}(t)]_{\text{IMD}} \rangle} \\ &= \frac{3J_0^{2K-2}(\beta)J_1^2(\beta)}{K_{111}J_0^{2K-6}(\beta)J_1^6(\beta) + K_{21}J_0^{2K-6}(\beta)J_1^2(\beta)J_2^2(\beta) + K_3J_0^{2K-6}(\beta)J_3^2(\beta)} \\ &= \frac{3J_0^4(\beta)J_1^2(\beta)}{K_{111}J_1^6(\beta) + K_{21}J_1^2(\beta)J_2^2(\beta) + K_3J_3^2(\beta)}, \end{aligned} \quad (8.129)$$

where K_{111} , K_{21} and K_3 are the number of terms of the form (8.124), (8.126) and (8.128), respectively, that appear at center frequency f_j .

Example 8.5

Again consider the network of Example 8.4, but now with multi-channel SCM instead of single-channel SCM. The European center frequencies for the three non-overlapping channels in IEEE 802.11b are given by

$$f_1 = 2412 \text{ MHz}, \quad (8.130)$$

$$f_2 = 2442 \text{ MHz}, \quad (8.131)$$

$$f_3 = 2472 \text{ MHz}. \quad (8.132)$$

Hence, one can verify that the following combinations of carrier frequencies each lead to two third order IMD products that appear at a carrier frequency:

- $2f_2 - f_3 = f_1$;
- $f_1 - f_2 + f_3 = f_2$;
- $2f_2 - f_1 = f_3$.

As a result, channel 1 and 3 have $K_{111} = K_3 = 0$ and $K_{12} = 2$, and channel 2 has $K_{12} = K_3 = 0$ and $K_{111} = 2$. Hence, we find

$$CIR_{\text{IMD}} = \frac{3J_0^4(\beta)}{2J_2^2(\beta)}, \quad (8.133)$$

for channel 1 and 3 and

$$CIR_{\text{IMD}} = \frac{3J_0^4(\beta)}{2J_1^4(\beta)}, \quad (8.134)$$

for channel 2. These are plotted as a function of β in Figure 8.9.

Obviously, the CIR decreases with increasing β , and the CIR for the middle channel is always worse than the CIR of the other two channels. □

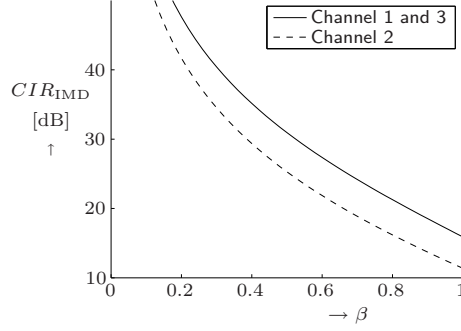


Figure 8.9: Carrier-to-intermodulation ratios

Noise performance

The variance of the noise of the band-pass filter follows from (5.14) and (8.107) as

$$\begin{aligned}
\sigma_{V_{BP,r,j}(t)}^2 &= R_{V_{BP,r,j}V_{BP,r,j}}(t, t) - \mathbb{E}^2[V_{BP,r,j}(t)] \\
&\approx \frac{Z_{TIA}^2 R_{pd} P_x e N}{2L_{Tx} L_{Rx} L_{nw}} \int_{-\infty}^{\infty} h_{BP}^2(t - \rho) d\rho \\
&\quad + \frac{Z_{TIA}^2 R_{pd}^2 P_x^2 \tau_c}{32L_{Tx}^2 L_{Rx}^2 L_{nw}^2} \int_{-\infty}^{\infty} h_{BP}^2(t - \rho) \left[4N^2 + 2N \right. \\
&\quad \quad \left. + \cos \left(2\Delta\phi_r + 2 \sum_{k=1}^K \beta_{r,k}(\rho) \sin(2\pi f_k \rho + \psi_{r,k}(\rho)) \right) \right] d\rho \\
&\quad + Z_{TIA}^2 S_{th} \int_{-\infty}^{\infty} h_{BP}^2(t - \rho) d\rho. \tag{8.135}
\end{aligned}$$

In Subsection 8.4.2 we have seen that $\Delta\phi_r$ should be set to $\frac{3\pi}{2}$ in order to achieve a maximum output signal amplitude. Assuming that the modulation of the RF carrier does not affect the variance (so we take $\beta_{r,k}(t) = \beta_{r,k}$ and $\psi_{r,k}(t) = \psi_{r,k}$), and using (8.110) we can then write

$$\begin{aligned}
&\cos \left(2\Delta\phi_r + 2 \sum_{k=1}^K \beta_{r,k}(\rho) \sin(2\pi f_k \rho + \psi_{r,k}(\rho)) \right) = \\
&\quad - \sum_{n_1} \sum_{n_2} \cdots \sum_{n_K} \left[\prod_{k=1}^K J_{n_k}(2\beta_{r,k}) \right] \cos \left(\sum_{k=1}^K n_k [2\pi f_k \rho + \psi_{r,k}] \right). \tag{8.136}
\end{aligned}$$

Substituting these in (8.135), writing the impulse response $h_{\text{BP},j}(t)$ as the inverse Fourier transform of the transfer function $H_{\text{BP},j}(f)$ of the band-pass filter, and applying phase-averaging over the $\psi_{r,k}$ s and time-averaging, only the terms with $n_1 = n_2 = \dots = n_K = 0$ remain, resulting in

$$\begin{aligned} \langle \sigma_{V_{\text{BP},r,j}(t)}^2 \rangle &\approx 2Z_{\text{TIA}}^2 |H_{\text{BP},j}(f_j)|^2 \left\{ \frac{R_{\text{pd}} P_x e N}{2L_{\text{Tx}} L_{\text{Rx}} L_{\text{nw}}} \right. \\ &\quad \left. + \frac{R_{\text{pd}}^2 P_x^2 \tau_c}{32L_{\text{Tx}}^2 L_{\text{Rx}}^2 L_{\text{nw}}^2} \left[4N^2 + 2N - \prod_{k=1}^K J_0(2\beta_{r,k}) \right] + S_{\text{th}} \right\}. \end{aligned} \quad (8.137)$$

Assuming that all $\beta_{r,k}$ s are the same, this reduces to

$$\begin{aligned} \langle \sigma_{V_{\text{BP},r,j}(t)}^2 \rangle &\approx 2Z_{\text{TIA}}^2 |H_{\text{BP},j}(f_j)|^2 \left\{ \frac{R_{\text{pd}} P_x e N}{2L_{\text{Tx}} L_{\text{Rx}} L_{\text{nw}}} \right. \\ &\quad \left. + \frac{R_{\text{pd}}^2 P_x^2 \tau_c}{32L_{\text{Tx}}^2 L_{\text{Rx}}^2 L_{\text{nw}}^2} \left[4N^2 + 2N - J_0^K(2\beta) \right] + S_{\text{th}} \right\}. \end{aligned} \quad (8.138)$$

The carrier-to-noise and intermodulation ratio (CNIR) at the output of the band-pass filter now follows from (8.114), (8.129) and (8.138) as

$$\begin{aligned} \text{CNIR}_{\text{BP}} &\triangleq \frac{\langle \text{E}^2[V_{\text{BP},r,j}(t)]_{\text{desired}} \rangle}{\langle \sigma_{V_{\text{BP},r,j}(t)}^2 \rangle + \langle \text{E}^2[V_{\text{BP},r,j}(t)]_{\text{IMD}} \rangle} \\ &= \left(\text{CNR}_{\text{sn}}^{-1} + \text{CNR}_{\text{bn}}^{-1} + \text{CNR}_{\text{tn}}^{-1} + \text{CIR}_{\text{IMD}}^{-1} \right)^{-1}, \end{aligned} \quad (8.139)$$

where

$$\text{CNR}_{\text{sn}} = \frac{R_{\text{pd}} P_x \langle J_1^2(\beta_{r,j}(t)) \rangle}{8N L_{\text{Tx}} L_{\text{Rx}} L_{\text{nw}} e W_{\text{BP}}} \prod_{\substack{k=1 \\ k \neq j}}^K \langle J_0^2(\beta_{r,k}(t)) \rangle, \quad (8.140)$$

$$\text{CNR}_{\text{bn}} = \frac{2 \langle J_1^2(\beta_{r,j}(t)) \rangle}{[4N^2 + 2N - J_0^K(2\beta)] \tau_c W_{\text{BP}}} \prod_{\substack{k=1 \\ k \neq j}}^K \langle J_0^2(\beta_{r,k}(t)) \rangle, \quad (8.141)$$

$$\text{CNR}_{\text{tn}} = \frac{R_{\text{pd}}^2 P_x^2 \langle J_1^2(\beta_{r,j}(t)) \rangle}{16L_{\text{Tx}}^2 L_{\text{Rx}}^2 L_{\text{nw}}^2 S_{\text{th}} W_{\text{BP}}} \prod_{\substack{k=1 \\ k \neq j}}^K \langle J_0^2(\beta_{r,k}(t)) \rangle, \quad (8.142)$$

and CIR_{IMD} is given by (8.129).

Note that on one hand Figure 8.9 suggests that β should be chosen as small as possible in order to get a high CIR, whereas on the other hand Figure 8.8 suggests that β should be given an optimum value somewhere between zero and one in order to maximize the amplitude of the desired signal and hence maximize the CNRs. As a result, there is a trade-off in choosing β . Optimization cannot be performed analytically so it should be done numerically.

Example 8.6

Again consider the network of Example 8.5. Suppose that the multi-channel SCM is used to distinguish between single-channel RAPs, like in Example 8.4, so there are N coherence modulators and NK coherence demodulators. Hence, the network losses are $L_{\text{nw}} \approx 1.090 \cdot 3N^2 \approx 3.271N^2$. The other parameters are assumed to be the same as in the previous examples. The resulting CNIR for channel 2 follows from (8.134) and (8.139) through (8.142) and is numerically optimized with respect to β . The resulting maximum CNIR values are plotted as a function of the number of CM channels N in Figure 8.10(a). The corresponding optimum values of β are shown in Figure 8.10(b).

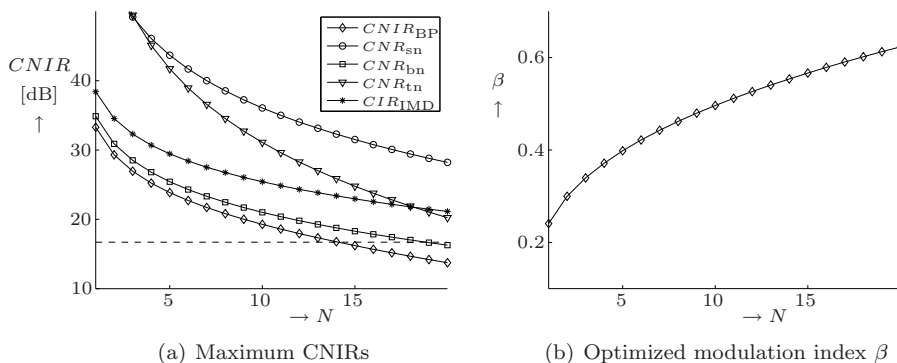
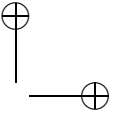
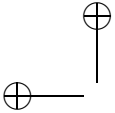


Figure 8.10: Carrier-to-noise and intermodulation ratios (CNIRs) at the output of the band-pass filter as a function of number of CM channels N in a WLAN IEEE 802.11b distribution network based on CM and multi-channel SCM, with 3 SCM channels per CM channel and optimized modulation index β

Maintaining the 16.7 dB criterion, it follows that at most 13 CM channels, and hence 39 RAPs can be supported, which is the same as with single-channel SCM in Example 8.4. Apparently, the reduction in beat noise is more or less compensated for by the fact that the modulation index β had to be decreased due to IMD.



Alternatively, one could use CM to distinguish between the RAPs and use multi-channel SCM to distinguish between MTs that are served by the same RAP. This can be done in both the uplink and downlink direction. Since only N coherence demodulators would be required in that case, the network losses would decrease by 4.7 dB with respect to the case described above. This is not expected to increase the maximum number of CM channels, however, since the CNIR is mainly determined by beat noise and IMD, which do not depend on the losses. □

Output stabilization

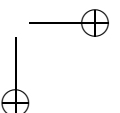
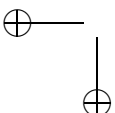
In case of multi-channel SCM, the SCM channels are modulated onto a CM channel by one single coherence modulator. Hence, the coherence demodulators only have to match their MZI-imbalance T_{RX} to this single coherence modulator in order to demultiplex any of the SCM channels in the corresponding CM channel. This can be done in exactly the same way as described in Subsection 8.3.1, without the kind of problems that occur for single-channel SCM.

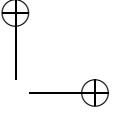
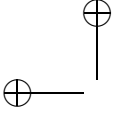
The self-heterodyning method that was described in Subsection 8.3.2 cannot be used in case of multi-channel SCM, because the different SCM channels require different frequency shifts. This cannot be realized when the different SCM channels are first multiplexed in the electrical domain and then modulated onto a CM channel by means of one coherence modulator.

In contrast to single-channel SCM, multi-channel SCM does enable coherence demodulation by means of any of the phase diversity receivers that were considered in Subsection 8.3.3. The output signals of the low-pass filters, $V_{LP,I,r}(t)$ and $V_{LP,Q,r}(t)$, do contain multiple terms like for single-channel SCM, but in case of multi-channel SCM these terms all have the same phase offset, so that $V_{LP,I,r}(t)$ and $V_{LP,Q,r}(t)$ do have a quadrature relation.

For the IM and differential PM phase diversity receiver the proper SCM channels can be selected by dimensioning the filters like described in 8.3.3, according to the carrier frequency of the desired SCM channel. In case multiple SCM channels are to be demultiplexed by the same phase diversity receiver, the low-pass filters should comprise multiple passbands, and the SCM channels are demultiplexed by means of parallel band-pass filters at the output of the phase diversity receiver. In case of a differential PM phase diversity receiver, the carrier frequency should be closely spaced so that the value of ΔT approximately matches to all the SCM channels. IMD will occur in both cases.

For the PM phase diversity receiver the low-pass filter should be dimensioned according to the highest carrier frequency, and the SCM channels can be demultiplexed by means of parallel band-pass filters at the output of the receiver. The advantage of the PM phase diversity receiver is that its output signal has a linear relation with the composite modulating signal (provided that CD can be neglected for all frequencies in the passband of the low-pass filter), so that IMD does not occur.





8.5 Conclusions

It has been shown that RF signals can be distributed by means of CM, for example to distinguish between RAPs in a wireless distribution system. The RF signals can be modulated onto the CM channels by means of either PM or IM. Harmonic distortion will occur in both cases; for PM this is caused by the non-linearity in the demodulation whereas for IM it is caused by the non-linearity in the modulation. PM turned out to result in a stronger output signal, and moreover it can more easily cope with detector imbalances.

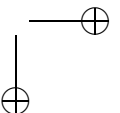
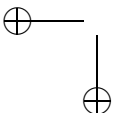
The impact of CD has been described and analyzed, showing that CD effectively results in an attenuation of the RF signal at the output of the CM receiver. In a CM distribution system for IEEE 802.11b wireless LAN with a network span of 500 m and optical sources with 1550 nm center wavelength and 0.1 ps coherence time, a dramatic dispersion penalty of approximately 50 dB would result, whereas center wavelengths of 1310 nm would result in a negligible dispersion penalty of approximately 0.1 dB.

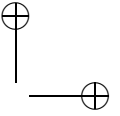
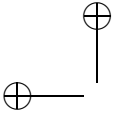
Noise performance analysis has shown that approximately 41 RAPs can be simultaneously supported by CM, when the distribution system is allowed to introduce a penalty of 1 dB to the link budget of the wireless interface.

It has been shown that the output signal of a CM receiver can be stabilized by phase synchronization, self-heterodyning or phase diversity detection. Phase synchronization requires frequency dithering in case of IM, but this can be omitted in case of PM. Self-heterodyning can be performed by applying a frequency shift that corresponds to the carrier frequency of the transmitted RF signal, which has the additional advantage that demodulation can be performed without harmonic distortion so that a stronger output signal can be obtained. Analog phase diversity receivers have been proposed based on IM, PM and differential PM.

Multiple RF channels can be multiplexed into one CM channel by using SCM on top of CM. It has been shown that this can be performed either by transmitting multiple optical carriers in the same CM channel, each containing one SCM channel (single-channel SCM) or by first multiplexing the SCM channels in the electrical domain and modulating the composite signal onto one CM channel (multi-channel SCM).

Single-channel SCM has the advantage that it can be used when the different SCM channels are generated in different transmission nodes. Each coherence modulator still introduces a comparable amount of beat noise and shot noise, so that the noise performance is comparable to the case where each RF signal is transmitted in a separate CM channel. When the SCM channels are to be demultiplexed by one single CM receiver, the MZI-imbalances of the corresponding CM transmitters have to be carefully matched, which requires mutual coordination between the transmitters. A dedicated phase synchronization circuit has been proposed for matching the delays of a transmitter-receiver pair in the case where each SCM channel is demultiplexed by a separate CM receiver.





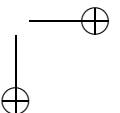
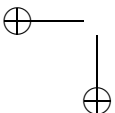
Self-heterodyning can be performed, provided that frequency shifting is applied in the transmitters. Phase diversity detection cannot be performed, because the different channels have different phase offsets, so that the output signals of the low-pass filters in a phase diversity receiver would not have a quadrature relation.

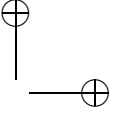
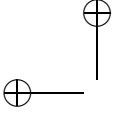
Multi-channel SCM has the advantage that less coherence modulators are required, which reduces the costs and the network losses. It can only be used when all the SCM channels in one CM channel are generated in the same node, however. The main disadvantage is that IMD occurs due to the non-linearity of coherence modulation and demodulation. Although the amount of beat noise is reduced due to the reduced number of coherence modulators, IMD requires the modulation index to be reduced to such a value that the resulting noise performance is comparable to the single-channel SCM case. Phase synchronization can be performed in the same way as in the case where each CM channel carries only one RF signal. Self-heterodyning cannot be performed, because different SCM channels require different frequency shifts. Modifications have been proposed in order to enable the proposed phase diversity receivers to demultiplex the SCM channels in case of multi-channel SCM. The PM phase diversity receiver then has the specific advantage that the output signal has a linear relation with the individual SCM channels, so that IMD does not occur.

An interesting property of CM is that it is transparent, in the sense that the channels can operate independently. Hence, CM can be applied in a system where both digital and analog signals are distributed, supporting fixed terminals at high speeds and mobile terminals at relatively low speeds.

IEEE 802.11b was considered as an example of a wireless transmission standard that can be supported by optical RF distribution. Alternatively, a higher data rate system like IEEE 802.11g [97] could be considered as well, but this has the problem that 52 OFDM carriers are used per MT, which requires a large number of SCM channels per CM channel. This will either introduce large network losses and beat noise power (single-channel SCM) or considerable IMD (multi-channel SCM). The latter could be reduced by using predistortion techniques prior to optical modulation, or by performing coherence demodulation by means of the proposed PM phase diversity receiver. As described, the linearity of this receiver can only be guaranteed when CD is negligible for all RF frequencies in the passband of the low-pass filter. This can eventually be achieved by using optical dispersion compensation techniques.

Part of the results that have been presented in this chapter were published in [94].





Chapter 9

Conclusions and directions for further research

This chapter will summarize the conclusions that can be drawn from the research that has been described in this thesis. Moreover some directions for further research will be suggested.

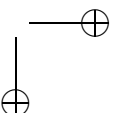
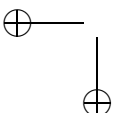
9.1 Conclusions

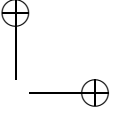
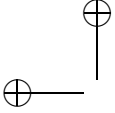
The previous chapters have described the operation principles of coherence multiplexing (CM). Moreover, several new concepts have been proposed, evaluated by means of theoretical analyses and illustrated by means of waveform simulations. The latter are performed using a custom-designed tool based on Simulink[™]. The main conclusions will be recapitulated here in short; for more detailed conclusions the reader is referred to the corresponding chapters.

CM can be used to multiplex several information channels over a common optical fiber cable. The information channels are modulated onto broadband optical carriers using coherence modulation. This implies that different channels are characterized by the relative delay between two versions of a broadband optical signal, which are generated by means of a broadband optical source and an interferometer with a large path-imbalance, which acts as an optical encoding device. The actual modulation can be performed by applying phase modulation (PM) to one of the versions, or intensity modulation (IM) to both.

Optical decoding can be performed by means of another interferometer with a path-imbalance that corresponds to the relative delay in the channel that is to be demultiplexed. In case of PM, detection can be performed either by means of single-ended or balanced detection; IM requires balanced detection.

The optical encoders and/or decoders can be made tunable by means of optical switches and multiple delay lines; two alternative configurations have been proposed. Half-duplex transmission can be realized by alternately using an interferometer as an encoding and decoding device, by means of a switch.





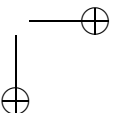
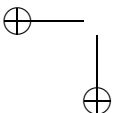
The performance of CM transmission is mainly hampered by optical beat interference noise, thermal receiver noise and chromatic fiber dispersion. This limits the bandwidth of the information signals, the number of channels that can be multiplexed and the distance between transmitters and receivers. Digital transmission by means of binary phase shift keying (BPSK) and on-off keying (OOK) has been illustrated. BPSK has been shown to result in a better performance than OOK, especially when balanced detection is performed.

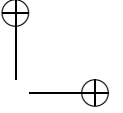
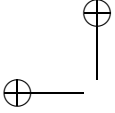
Three different topologies for multiplexing the coherence-modulated signals have been considered, each having specific advantages or disadvantages with respect to complexity, flexibility and performance. All topologies have in common that their performance degrades with increasing number of channels, due to increasing splitting losses and increasing number of beat noise products. The single intrinsic reference ladder (SIRL) system has been proposed and shown to result in a superior noise performance with respect to previously proposed coherence multiplexing topologies.

Under certain conditions the output signal of a CM receiver can become unstable due to temperature drift, fabrication tolerances or component aging, resulting in an unwanted offset in the phase difference between the interfering light waves in the receiver. In previously described systems this had been solved by means of either a phase synchronization scheme with a feedback loop or self-heterodyne detection using an optical frequency shifter. A new coherence demodulation concept using balanced optical phase diversity has been proposed and analyzed, showing that it can be used for passively stabilizing the output signal of a CM receiver. Several modulation formats like OOK, binary DPSK, DQPSK and M -ary DPSK were considered and analyzed, showing that phase diversity introduces some performance degradation, due to both the increased optical insertion losses and the fundamental performance difference between synchronized and non-synchronized detection.

The performance of any CM system degrades with increasing distance between transmitters and receivers, due to attenuation and chromatic dispersion (CD) in the transmission fiber. Both phenomena heavily depend on the center wavelength of the optical sources. For standard single-mode fiber, for example, the attenuation is minimum at 1550 nm, whereas the CD is minimum at 1310 nm. The impact of attenuation and CD on digital transmission has been studied in detail, showing that, in case of significant CD, QPSK modulation results in a better performance than BPSK modulation. The performance can be further improved by using electrical or optical equalization techniques. Optical equalization is more effective because it results in a fundamental increase of the transmission bandwidth that the CM system accommodates.

The bit rates, number of channels and link lengths that can be achieved are mutually dependent and depend on multiplexing topology, modulation format, detection technique and several system parameters. Moreover the actual performance limitation (beat noise, thermal noise and/or CD) also depends on these specifications. For example, when BPSK modulation and phase-synchronized detection are used in a parallel array (PA) topology, and the system parame-





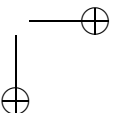
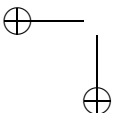
ters are chosen according to the numerical examples that are presented in this thesis, then the following specifications can be achieved with bit error rates below 10^{-9} :

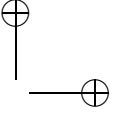
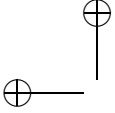
- In an access network with a maximum span length of 10 km and bit rate of 100 Mbps per channel, the maximum number of channels that can be supported is in the order of 10 for 1550 nm sources and in the order of 30 for 1310 nm sources, mainly limited by CD and beat noise;
- In a LAN with a maximum span length of 400 m and bit rates of 1 Gbps per channel, the maximum number of channels that can be supported is in the order of 8 for 1550 nm sources and in the order of 11 for 1310 nm sources, mainly limited by beat noise;
- In an optical interconnect with 850 nm sources and CMOS photoreceivers with a bit rate of 3 Gbps per channel, photodetector responsivity of 0.41 A/W and equivalent input noise current of 10 pA/ $\sqrt{\text{Hz}}$ (according to Radovanović' design [3]) and short fiber lengths so that CD and attenuation can be neglected, approximately 5 channels can be supported, resulting in a total interconnect transmission rate of 15 Gbps. This is mainly limited by thermal noise.

Apart from digital transmission, CM can also be used to distribute radio-frequency (RF) signals, for example to distinguish between radio access points (RAPs) in a wireless access system. The frequency-fiber length product is then limited by CD. Multiple RF signals can be multiplexed through one CM channel by means of subcarrier multiplexing (SCM), either by using multiple coherence modulators (single-channel SCM) or by multiplexing the SCM channels in the electrical domain prior to coherence modulation (multi-channel SCM). A particular problem in RF distribution is the inherent non-linearity in coherence modulation and/or demodulation, which results in harmonic distortion and — in case of multi-channel SCM— intermodulation distortion (IMD). This can be reduced by means of predistortion techniques. The noise performance in case of RF modulation has been analyzed and illustrated for the distribution of wireless LAN signals based on the IEEE 802.11b standard, showing that approximately 40 RAPs could be supported. Several ways of stabilizing the output signal of a CM receiver in case of RF transmission have been proposed.

Considering the numerical results that have been given above, it can be concluded that CM indeed has potential for utilization in short range communication applications like subscriber networks, LANs and interconnects. CM has the following advantages with respect to more mature multiplexing techniques like WDM, TDM, SCM and OCDM (see Section 1.4):

- It can be implemented using relatively simple components like broadband sources and (integrated) Mach-Zehnder interferometers;
- The multiplexing and demultiplexing operation is rather robust: no active stabilization is required for avoiding crosstalk between channels;





- The transmitters do not require mutual synchronization;
- A channel can be set up in a relatively short time because a receiver only needs to synchronize to the received signal on symbol timing level, and not on code chip or even carrier phase level;
- The multiplexing principle is relatively flexible because the network does not need to be reconfigured when a channel is added;
- It is transparent in the sense that channels operate independently and the modulation technique imposes only minor conditions on the format of the signal that is to be transmitted.

These properties enable simultaneous distribution of a wide range of services like analog radio and TV, telephony, high-speed fixed Internet access and wireless access based on Radio over Fiber transmission.

The results in the numerical examples have to be handled with care, however. They are based on assumptions with respect to subsystems and components that have not been considered in great detail, since this requires knowledge in different research areas. This definitely calls for further research including experimental verification; directions for this will be given in the next section.

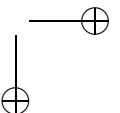
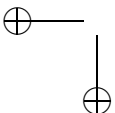
Although the resulting technology could lead to relatively inexpensive implementation of optical transmitters and receivers, the actual technology development is rather costly, because it requires research in several areas, including (expensive) integrated circuit design. Moreover, CM suffers from a lack of appeal due to its conceptual complexity. This hampers the acquisition of funds for doing research on CM implementation, although it is an excellent topic for doing multidisciplinary academic research, which might result in huge cost savings in case of massive deployment of CM-based networks. An economic feasibility study can only be done after further technological research, however.

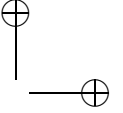
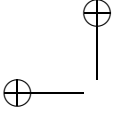
9.2 Directions for further research

In this section some directions for further research will be suggested. These include an extension of the system level research that has been described in this thesis, possible improvements for the simulation tool that has been described in Chapter 3, and research in related areas, namely optical source design, integrated optics technology, optical receiver design and network-related topics. Moreover some directions for applying CM-like techniques in wireless transmission will be given.

9.2.1 System level research

First some suggestions will be given for filling up some “gaps” in the system level research that has been described in this thesis.





Apart from the digital modulation schemes that were considered in this thesis (OOK, PSK and DPSK), alternative formats like quadrature amplitude modulation (QAM), frequency shift-keying (FSK) and (differential) polarization shift-keying (POLSK/DPOLSK) could be studied. QAM requires a combination of PM and IM and can be demodulated by means of a four-way phase-synchronized receiver, similar to the M -ary PSK receiver that was proposed in Subsection 6.4.3 (see Figure 6.8). FSK involves applying external FSK modulation in one of the interferometer arms of the coherence modulator, and can be demodulated by means of a phase diversity receiver with an FSK demodulation circuit, similar to the PM phase diversity receiver that was proposed in Subsection 8.3.3 (see Figure 8.5). (D)POLSK can be performed by modulating the state of polarization (SOP) of the light waves (or difference in SOP between the light waves), and can be demodulated by means of polarization beam splitters. The implementation aspects of the corresponding transmitters and receivers should be studied and their performances should be evaluated and compared.

In Chapter 7, the impact of CD on digital transmission has only been derived for BPSK and QPSK, and should be extended to OOK, M -ary PSK and DPSK, and eventually to QAM, FSK and (D)POLSK. Moreover, it should be studied how these modulation formats can be combined with optical pulse-shaping, electrical equalization (see Subsection 7.4.1) and/or optical equalization (see Subsection 7.4.2) and how well they would perform in that case.

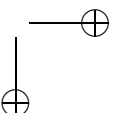
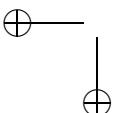
In Subsection 8.3.3, different phase diversity receivers were proposed for demodulating RF-modulated CM channels, but their performances have not been compared yet. This would require further analysis, incorporating the effect of noise and CD.

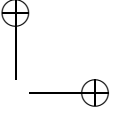
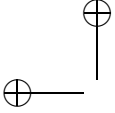
In cases where thermal noise dominates, and it turns out to be difficult to increase the optical source power or improve the optical receivers, optical amplification can become an option, for example by means of an Erbium-doped fiber amplifier (EDFA) or semiconductor optical amplifier (SOA). Note, however, that this would decrease the signal-to-beat noise ratio due to the amplified spontaneous emission noise [92,93], and eventually due to the fact that the amplification window of the amplifier might not completely cover the spectrum of the optical source signal, resulting in an increased coherence time [48].

Of course, the so-far obtained theoretical results have to be experimentally verified. This will probably lead to refinement of the models and eventually give rise to a study of so-far neglected phenomena.

9.2.2 Simulation

The simulation tool that has been described in Chapter 3 only partly fulfills the goals that were formulated in Section 3.1. That is, the tool is merely used for getting a thorough understanding of the operation principle of the considered systems, for example by verifying whether the actual signal waveforms comply with the expectations that arise from the theory.





The tool did not turn out to be suitable for verifying the actual bit error rate performance results that have been derived, mainly because of the excessive simulation time that would be required. This is related to three specific aspects of the simulation tool and the systems that are simulated:

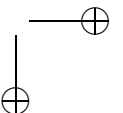
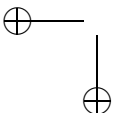
- First of all, the considered bit error rates are so low, that many bits would have to be simulated in order to get enough bit errors for obtaining a sufficiently accurate estimation of the bit error probability. To estimate bit error rates in the order of 10^{-9} would require 10^{11} simulation trials to achieve an accuracy of $\pm 20\%$ with 95% confidence [101];
- Furthermore, the bit time in a CM system should be much larger than the coherence time in order to get a large processing gain and hence achieve such low bit error rates. Since the sample time should be in the order of half the coherence time, this implies that the simulation of one bit already takes many samples. The total number of samples in a simulation run is even further increased by the fact that multiple transmitters have to be simulated, and moreover each sample is subjected to quite some signal processing steps, especially in the SMF model;
- Finally, although Simulink[™] is a relatively user-friendly and flexible simulation tool, it results in relatively slow simulations, since the actual calculations are performed by Matlab[™], which compiles the simulation code during the simulation run.

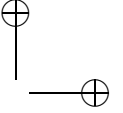
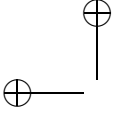
This last problem can be solved by carefully optimizing the signal processing algorithms that have been described in Chapter 3 for simulation on a computer, and programming these in a lower-level programming language like C++ [102].

The actual number of samples that have to be processed might be reduced by applying so-called importance sampling techniques [101]. This involves biasing the random number generators in such a way that the actual number of errors that occur is increased, which —after a suitable correction— results in accurate estimations of low bit error rates using relative few calculations. Further research is required for evaluating the feasibility of reducing the simulation time in that way.

Another shortcoming of the current simulation tool is that the simulation models are not more sophisticated than the models that have been used in the theoretical analyses. Hence, the tool can only be used to verify the accuracy of the approximations in the theoretical analyses, and not whether the models on which the analyses are based are sufficiently realistic. The validation of the models requires experimental verification.

Finally, an improved version of the simulation should contain more features for displaying and analyzing results, for example for plotting eye diagrams or estimating bit error rates as a function of certain system parameters.





9.2.3 Broadband optical sources

A technological topic that has not been considered in much detail is broadband optical sources. The parameter values that were assumed in the numerical examples were conservatively chosen after surveying several data sheets of commercially available SLED sources. These are still rather expensive, however, since they are mainly in used in quite specialized applications like optical component characterization, optical sensing, medical imaging and navigation. This might change once SLEDs are massively produced for consumer applications.

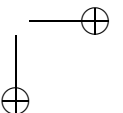
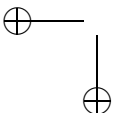
Instead of using commercially available (pigtailed) sources, the production and installation costs might be reduced by designing dedicated sources for application in CM systems, eventually integrated together with the optical encoding circuit on a single transmitter chip.

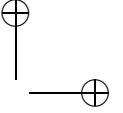
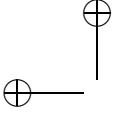
From the research that has been presented in this thesis it can be concluded that several criteria have to be taken into account when such sources are to be purchased or designed.

First of all it is critical that the source is able to couple enough optical power into the encoding circuit, which puts requirements on the total amount of emitted power and the coupling efficiency. This required power depends on the optical losses in the optical circuits in transmitters and receivers, in the transmission fiber (and hence on the network span) and in the optical splitters and combiners in the network (and hence on the number of transmitters and receivers). It also depends on the sensitivity of the optical receivers, which depends on the modulation format and detection technique, the responsivity of the photodiodes and the amount of thermal noise in the electronic receiver circuit. On the other hand, the emitted power should not be too large since this will increase the costs of the driving and cooling circuit and it might introduce non-linearities in the transmission fiber. (Further study would be required to find out at what source power and span length fiber non-linearity starts to play a role, and what typical implications it has in a CM system.)

The choice for the center wavelength depends on several aspects. First of all different wavelength regions require different active materials, which determine the material costs and how easily the source can be fabricated and eventually integrated with the optical encoding circuit. Furthermore the wavelength region also determines which material should be used for the photodetector, resulting in a similar design issue in the receiver. And finally, the attenuation and CD in the transmission fiber strongly depend on the optical center wavelength. Its impact on the choice for the center wavelength depends on the envisioned network span and whether or not optical amplification and/or dispersion compensation will be performed.

On one hand we have seen that the bandwidth of the emitted signal should be as large as possible, in order to have a low coherence time, and hence a high signal-to-beat noise ratio. Moreover this enables encoding and decoding to be performed by means of MZIs with relatively small path delay differences, with sufficient suppression of undesired channels. On the other hand, the bandwidth should not be too large because this will lead to intersymbol interference (ISI)





due to CD. The choice of the coherence time hence depends on the network span and whether or not dispersion compensation will be performed.

The actual shape of the spectrum is also critical. It should not contain significant peaks or ripple, because this will introduce side lobes in the coherence function, resulting in crosstalk between the channels. Moreover, the center of the envelope of the coherence function should be as flat as possible, so that a small mismatch between the delays in transmitter and receiver will not result in a significant amplitude reduction of the (stabilized) receiver output signal. (The Gaussian approximation for the spectrum that has been assumed in this thesis is quite ideal in that sense: neither the spectrum nor the coherence function contains side lobes, so that both crosstalk and ISI are minimized. Moreover the center of the envelope of the coherence function is flat.)

Depending on the availability and costs of external modulators, direct modulation of the source might be desirable. This will be increasingly difficult for increasing modulation bandwidths.

Finally, reliability of the optical sources is an essential criterion. When installed at for example the customers' premises, relatively short source lifetimes will result in unacceptably high maintenance costs.

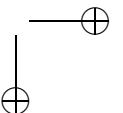
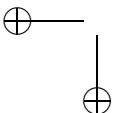
9.2.4 Integrated optics technology

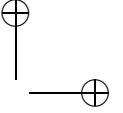
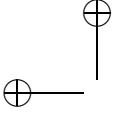
Although preliminary experiments can be done by means of fiber testbeds, the optical encoders and decoders for more advanced experiments or even commercial products should definitely be fabricated in integrated optics technology. This is the only way to realize the MZIs with small path delay differences sufficiently accurately, while guaranteeing that coherent light waves always have the same SOP, so that maximum interference occurs (see Section 2.4). Moreover optical integration removes the need of optical component alignment, eventually enables integration with sources, detectors and electronics, and will hence result in the lowest costs in case of mass production.

Application in CM systems puts very specific requirements on these optical circuits, so that existing component designs can probably not be used. This has not been considered in further detail in this thesis, so that further research is definitely required to investigate the feasibility of such circuits, and moreover enable proper experimental verification of the system level research that has been presented in this thesis. Some important design criteria will be recapitulated here.

A first criterion is that the waveguides in the optical circuits should be strictly single-mode, because different modes in a multimode waveguide would have different propagation constants and would hence result in different interference effects. This would significantly degrade the amplitude of the receiver output signal.

Furthermore, the desired functionality of the circuits should not only apply to a single operating wavelength, but rather to a relatively wide wavelength range, in the order of several tens of nanometers. This will be particularly





challenging for the phase diversity receiver circuits that were considered in Chapter 6, since these contain a multimode interference (MMI) coupler.

The functionality of the circuit would preferably also be polarization independent. In case this cannot be achieved, the optical source signal should be polarized before it is coupled into the encoding circuit, and polarization diversity should be applied in the receiver (see Subsection 6.6.1).

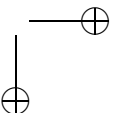
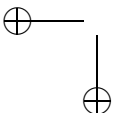
The fabrication technique that is used should be sufficiently accurate. A particularly critical design parameter is the coupling coefficient of the last coupler in the receiver, just in front of the photodiodes, especially when IM is performed. When this coupler is not uniform, balancing is not performed properly so that crosstalk between the CM channels will occur (it can be shown that this becomes significant with tolerances in the coupling coefficient beyond 0.1 %), unless some kind of (adaptive) compensation is applied in the electronic part of the receiver (see Subsection 4.8.3). Moreover, the group delay imbalance of the MZIs should be fabricated sufficiently accurately, so that the receiver does not require active coherence matching (see Example 6.1).

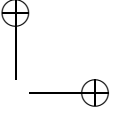
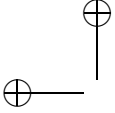
The losses of the optical circuits should be kept within reasonable bounds, so that optical amplification in the network can be omitted. The amount of loss that can be tolerated depends on the actual performance limitation of the system as a whole: as long as beat noise dominates over thermal noise, losses of several dB per optical encoder or decoder chip might be allowed, whereas losses below 1 dB per chip should be aimed at when thermal noise dominates.

A technology should be chosen that enables PM or IM, or at least enables easy integration with separate modulators, unless direct modulation of the source power is performed.

An interesting challenge would be to integrate a dispersion-compensating device with the decoding circuit, which can be adaptively tuned, so that it can match any length of the transmission fiber in a certain predefined range.

Especially Goedgebuer et al. have published many papers about the design and fabrication of integrated components for coherence modulation and demodulation, based on Lithium Niobate (LiNbO_3) [34–43] and GaAlAs-GaAs [44,45]. Chu and Dickey claimed that fabrication of LiNbO_3 -chips was in progress at the time of publication of their theoretical paper [29], but—to our knowledge—have never published experimental results based on these. Kani et al. report experiments for which “coherence encoders and decoders were fabricated using planar lightwave circuit (PLC) technology” [48], but they do provide any further information about the actual design and fabrication. All the other experiments on CM reported so far were either based on bulk optic components or fiber testbeds using fiber stretchers and polarization controllers. The aforementioned integrated circuit technologies are relatively expensive, whereas achieving low costs was the main reason for using CM in the first place. Therefore, it should be investigated whether components can be designed and fabricated that satisfy the aforementioned criteria, using relatively inexpensive materials and fabrication techniques, for example based on silicon oxynitride (SiON) technology [69].





9.2.5 Optical receiver design

CM also puts specific requirements on the design of the electronic part of the receiver circuit.

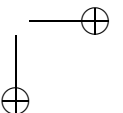
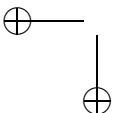
Obviously, the bandwidth specifications of the photodiodes, transimpedance amplifiers (TIAs) and processing electronics should comply with the bandwidth of the signal that is to be detected. In case this cannot be achieved, an electrical equalization circuit should be integrated into the receiver. The latter is also required when the received signal suffers from ISI, due to dispersion in the transmission fiber or limited bandwidth of the modulator in the transmitter.

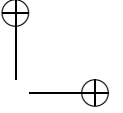
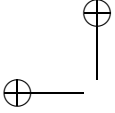
Since the optical power from the transmitters is preferably passively distributed over the receivers, the receivers should have a high sensitivity. This requires proper coupling between the optical and electronic part of the receiver (preferably through integration), a high responsivity for the photodiodes and a low equivalent input noise current for the TIAs. Precise requirements depend on the modulation format, detection technique, bit rate, optical source power, number of transmitters and receivers and optical losses, and follow from the equations that were presented in this thesis.

Even when the transmitted optical power, number of transmitters and receivers and optical losses are known, the actual amount of received power in a PA topology still depends on the number of transmitters that are active. Hence, the optical receiver should have a relatively large dynamic range.

Especially in case of IM, the balanced receiver should have a relatively high common-mode rejection ratio (CMRR). That is, its output signal should mainly depend on the difference in power between the optical input signals, and only negligibly on common power. Otherwise, crosstalk between the channels will occur (also see Subsections 4.8.3 and 5.5.5). Basically this means that the responsivities of the photodiodes should be sufficiently similar and the photodiode currents should be properly subtracted. Since the common power increases with increasing number of active channels, the required CMRR increases with increasing number of transmitters: the CMRR should be around 20 dB for a 1 channel system and should increase by 6 dB every time the number of channels doubles. In case the last optical coupler in front of the photodiodes is not properly uniform, or the photodiode responsivities are not sufficiently similar, some kind of (adaptive) electronic compensation will be required, which becomes increasingly difficult with increasing signal bandwidth.

For lowering the costs of the total receiver circuit, the photodiodes could be integrated with the electronic circuit. This requires them to be fabricated in the same technology as the electronic circuit (for example CMOS [3]), which restricts the operating wavelength: for Si photodiodes the sensitivity range is about 400–850 nm. This wavelength range is not suitable for relatively long range transmission because of the relatively high attenuation and CD. Therefore, this can probably only be applied effectively in optical interconnects.





9.2.6 Transmission and networking standards

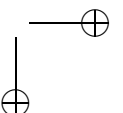
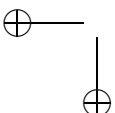
When coherence-multiplexed networks are realized for application, CM will either have to be combined with existing transmission and/or networking standards like Ethernet [7], or new standards might have to be defined. Several transmission and networking issues then deserve further attention.

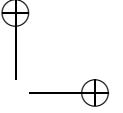
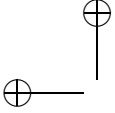
Because of eventual reflections in the transmission path, simultaneous bidirectional (full-duplex) CM transmission in the same CM channel might not be a wise thing to do. One MZI can be alternately used as an encoding and decoding device (see Section 4.5) when half-duplex transmission is performed using a PA topology. Moreover, instead of simply assigning a separate CM channel to each user, several users could perform multiple access on one CM channel, for example by means of Ethernet. However, in both cases the question is how to perform collision detection, because carrier sense during transmission is not possible in case the MZIs are alternately used as encoding and decoding devices or when two or more transmitters transmit in the same CM channel in the same direction.

Depending on the network parameters, the bit error rate and hence packet error rate in a PA might become unacceptably high in case too many transmitters become active at the same time, as discussed in Subsection 5.2.5. Although some possible traffic control protocols have been proposed for solving this problem [66], their compatibility with existing standards should be further investigated.

CM has been illustrated as an RF distribution technique for IEEE 802.11b, but newer standards like IEEE 802.11g and 802.11n could be investigated as well. Apart from assuring the transparency of the distribution network, it should be investigated whether the increased delay between the remote base station and the mobile terminals will have any implications at the protocol level.

Another networking topic that has recently received considerable attention in optical communications is security. CM transmission is relatively secure in the sense that—in case PM is applied—the modulating signal is not directly visible in the total power of the transmitted signal. However, it has been demonstrated that an eavesdropper can easily tap the modulation signal by means of narrowband wavelength filtering [103]. Various security enhancement schemes have been proposed based on phase scrambling using recirculating delay loops [104], spectral coding [12, 13], combining CM with CDMA [105], dispersion coding [106] and scrambling of the modulating signal [107, 108]. All these schemes introduce a significant increase in complexity with respect to the basic CM concept (especially when keying synchronization between transmitter and receiver is required), so it is questionable whether security enhancement in the optical domain is a better idea than (relatively inexpensive) cryptography in the digital domain.





Obviously, when a coherence-multiplexed network is designed, the networks with which it is interfacing should be taken into account. This involves the maximum amount of traffic that can be handled, but also choosing a transmission format that can be efficiently converted to the transmission format in the interfacing network, such that the amount of processing in the intermediate node is minimized.

9.2.7 Application as wireless transmission technique

Although this thesis has only considered the concept of CM as a means to perform multiple access on a common optical fiber cable, it can also be applied for performing multiple access on a wireless channel. This has been analyzed and experimentally demonstrated in [109]. In radio transmission the concept has two specific advantages:

- Expensive spectrally pure oscillators and band-pass filters can be omitted because pure noise or a pseudo-noise sequence is used as the information bearer;
- Although a large processing gain is achieved, carrier synchronization can be performed in a relatively short time, since—in contrast to other ultra-wideband (UWB) transmission techniques—an unmodulated reference signal is transmitted along with the modulated signal. This might considerably reduce the power consumption of burst mode receivers.

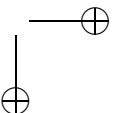
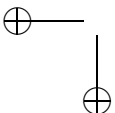
Therefore, the transmission concept is particularly suitable for wireless ad hoc communications, where idle communication nodes continuously or at least regularly have to sense the communication medium for eventual transmissions, whereas minimum energy consumption is critical in order to maximize battery lifetime.

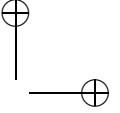
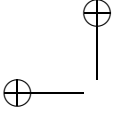
An alternative scheme in which the reference signal is frequency-shifted instead of delayed with respect to the modulated signal has been proposed, analyzed and experimentally demonstrated [110].

In both schemes the performance is degraded by frequency-selective fading, where the actual degradation depends on the relation between the multipath delays, the coherence time and the channel selection parameters (time delay or frequency shift, respectively) [111].

The advantage of the frequency-offset system with respect to the time-offset system is that multipath fading cannot result in crosstalk between the channels. On the other hand, the frequency shifter in the receiver has to be phase-synchronized to the frequency shift in the received signal, which is not possible in case of severe multipath fading.

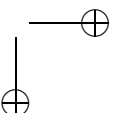
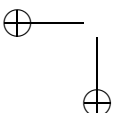
More research is required in order to optimize the design of the corresponding transmitters and receivers, realize them as integrated microwave circuits and compare these with existing UWB equipment.

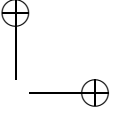
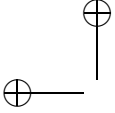




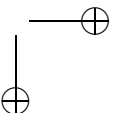
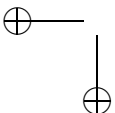
References

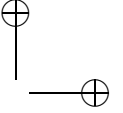
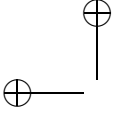
- [1] The International Telecommunication Union, *Characteristics of a single-mode optical fibre and cable*, ITU-T Recommendation G.652, 2003.
- [2] I. Radovanović, *Optical local area networks: New solutions for fiber-to-the-desk applications*, PhD dissertation, University of Twente, Enschede, The Netherlands, December 2003.
- [3] S. Radovanović, *High-speed photodiodes in standard CMOS technology*, PhD dissertation, University of Twente, Enschede, The Netherlands, December 2004.
- [4] The International Telecommunication Union, *Spectral grids for WDM applications: DWDM frequency grid*, ITU-T Recommendation G.694.1, 2002.
- [5] The International Telecommunication Union, *Spectral grids for WDM applications: CWDM frequency grid*, ITU-T Recommendation G.694.2, 2003.
- [6] The International Telecommunication Union, *Broadband optical access systems based on passive optical networks (PON)*, ITU-T Recommendation G.983.1, 1998.
- [7] The Institute of Electrical and Electronics Engineers, *IEEE standard for information technology—Telecommunications and information exchange between systems—Local and metropolitan area networks—Specific requirements—Part 3: Carrier sense multiple access with collision detection (CSMA/CD) access method and physical layer specifications*, IEEE Standard 802.3, 2002.
- [8] D. D. Sampson, G. J. Pendock, and R. A. Griffin, “Photonic code-division multiple-access communications,” *Fiber Integr. Opt.*, vol. 16, no. 2, pp. 129–157, 1997.
- [9] L. Tancevski and I. Andanovic, “Wavelength hopping/time spreading code division multiple access systems,” *Electron. Lett.*, vol. 30, no. 17, pp. 1388–1390, August 1994.



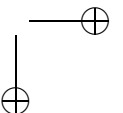
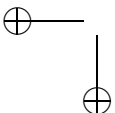


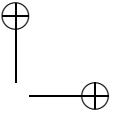
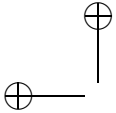
- [10] S. Yegnanarayanan, A. S. Bhushan, and B. Jalali, "Fast wavelength-hopping time-spreading Encoding/Decoding for optical CDMA," *IEEE Photonics Technol. Lett.*, vol. 12, no. 5, pp. 573–575, May 2000.
- [11] W. C. Kwong, G.-C. Yang, and C.-Y. Chang, "Wavelength-hopping time-spreading optical CDMA with bipolar codes," *J. Lightwave Technol.*, vol. 23, no. 1, pp. 260–267, January 2005.
- [12] R. A. Griffin, D. D. Sampson, and D. A. Jackson, "Modification of optical coherence using spectral phase coding for use in photonic code-division multiple-access systems," *Electron. Lett.*, vol. 29, no. 25, pp. 2214–2216, December 1993.
- [13] R. A. Griffin, D. D. Sampson, and D. A. Jackson, "Coherence coding for photonic code-division multiple-access networks," *J. Lightwave Technol.*, vol. 13, no. 9, pp. 1826–1837, September 1995.
- [14] D. Zaccarin and M. Kavehrad, "An optical CDMA system based on spectral encoding of LED," *IEEE Photonics Technol. Lett.*, vol. 4, no. 4, pp. 479–482, April 1993.
- [15] M. Kavehrad and D. Zaccarin, "Optical code-division-multiplexed systems based on spectral encoding of noncoherent sources," *J. Lightwave Technol.*, vol. 13, no. 3, pp. 534–545, March 1995.
- [16] L. Nguyen, T. Dennis, B. Aazhang, and J. F. Young, "Experimental demonstration of bipolar codes for optical spectral amplitude CDMA communication," *J. Lightwave Technol.*, vol. 15, no. 9, pp. 1647–1653, September 1997.
- [17] T. Pfeiffer, B. Deppisch, M. Kaiser, and R. Heidemann, "High speed optical network for asynchronous multiuser access applying periodic spectral coding of broadband sources," *Electron. Lett.*, vol. 33, no. 33, pp. 2141–2142, December 1997.
- [18] E. D. J. Smith, R. J. Blaikie, and D. P. Taylor, "Performance enhancement of spectral-amplitude-coding optical CDMA using pulse-position modulation," *IEEE Trans. Commun.*, vol. 46, no. 9, pp. 1176–1185, September 1998.
- [19] C. F. Lam, D. T. K. Tong, M. C. Wu, and E. Yablonovitch, "Experimental demonstration of bipolar optical CDMA system using a balanced transmitter and complementary spectral encoding," *IEEE Photonics Technol. Lett.*, vol. 10, no. 10, pp. 1504–1506, October 1998.
- [20] X. Zhou, H. Shalaby, C. Lu, and T. Cheng, "Code for spectral amplitude coding optical CDMA systems," *Electron. Lett.*, vol. 36, no. 8, pp. 728–729, April 2000.



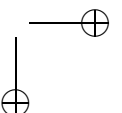
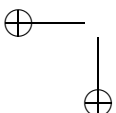


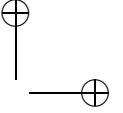
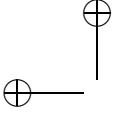
- [21] J. A. Salehi, "Code division multiple-access techniques in optical fiber networks—Part I: Fundamental principles," *IEEE Trans. Commun.*, vol. 37, no. 8, pp. 824–833, August 1989.
- [22] N. Karafolas and D. Uttamchandani, "Optical fiber code division multiple access networks: A review," *Optical Fiber Technology*, vol. 2, no. 2, pp. 149–168, 1996.
- [23] K. Kitayama, H. Sotobayashi, and N. Wada, "Optical code division multiplexing (OCDM) and its applications to photonic networks," *IEICE Trans. Fundam. Electron. Commun. Comput. Sci.*, vol. E82-A, no. 12, pp. 2616–2626, December 1999.
- [24] T. Pfeiffer, "OCDM(A) networks—will they become competitive?" *Proc. 28th European Conf. Opt. Commun.*, Copenhagen, Denmark, September 2002, paper 11.5.1.
- [25] A. S. Stok and E. H. Sargent, "The role of optical CDMA in access networks," *IEEE Commun. Mag.*, vol. 50, no. 9, pp. 83–87, Sept. 2002.
- [26] C. Delisle and P. Cielo, "Application de la modulation spectrale à la transmission de l'information (Application of spectral modulation to information transmission)," *Can. J. Phys.*, vol. 53, pp. 1047–1053, 1975.
- [27] P. Cielo and C. Delisle, "Multiplexage en communication optique par interférométrie à grande différence de marche en lumière blanche (Multiplexing in optical communications by interferometry with a large path-length difference in white light)," *Can. J. Phys.*, vol. 54, pp. 2322–2331, 1976.
- [28] J.-P. Goedgebuer and A. Hamel, "Coherence multiplexing using a parallel array of electrooptic modulators and multimode semiconductor lasers," *IEEE J. Quantum Elect.*, vol. 23, no. 12, pp. 2224–2237, December 1987.
- [29] K. W. Chu and F. M. Dickey, "Optical coherence multiplexing for inter-processor communications," *Opt. Eng.*, vol. 30, no. 3, pp. 337–344, March 1991.
- [30] J.-P. Goedgebuer, J. Salcedo, and J. C. Vienot, "Multiplex communication via electro-optic phase-modulation of white light," *Opt. Acta*, vol. 29, no. 4, pp. 471–477, 1982.
- [31] J.-P. Goedgebuer, R. Ferrière, and H. Porte, "Nouvelle technique de modulation électro-optique adaptée aux sources à spectre large (A novel electro-optic modulation technique suitable for modulating broad-band sources)," *J. Optics*, vol. 15, no. 6, pp. 403–407, 1984.
- [32] H. Porte, J.-P. Goedgebuer, and A. Hamel, "Two TV channel multimode fibre link using a single mode laser diode (820 nm) and path-difference



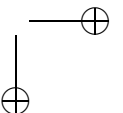
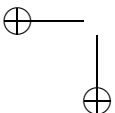


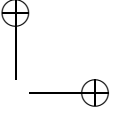
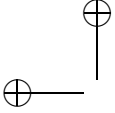
- multiplexing," *Electron. Lett.*, vol. 22, no. 22, pp. 1189–1191, October 1986.
- [33] J.-P. Goedgebuer, H. Porte, and A. Hamel, "Electrooptic modulation of multilongitudinal mode laser diodes: Demonstration at 850 nm with simultaneous data transmission by coherence multiplexing," *IEEE J. Quantum Electron.*, vol. 23, no. 7, pp. 1135–1144, July 1987.
- [34] H. Porte, R. Ferrière, and J.-P. Goedgebuer, "Integrated waveguide modulator using a LiNbO₃ TE-TM converter for electrooptic coherence modulation of light," *J. Lightwave Technol.*, vol. 6, no. 6, pp. 892–897, June 1988.
- [35] H. Porte, J.-P. Goedgebuer, R. Ferrière, and N. Fort, "Integrated TE-TM mode converter on Y-cut Z-propagating LiNbO₃ with an electrooptic phase matching for coherence multiplexing," *IEEE J. Quantum Electron.*, vol. 25, no. 8, pp. 1760–1762, August 1989.
- [36] H. Porte, J.-P. Goedgebuer, and R. Ferrière, "An LiNbO₃ integrated coherence modulator," *J. Lightwave Technol.*, vol. 10, no. 6, pp. 760–766, June 1992.
- [37] C. Gutiérrez-Martínez, H. Porte, and J.-P. Goedgebuer, "Microwave integrated optics Ti : LiNbO₃ coherence modulator for high-speed optical communications," *Microw. Opt. Technol. Lett.*, vol. 10, no. 1, pp. 66–70, September 1997.
- [38] C. Gutiérrez-Martínez, H. Porte, J.-P. Goedgebuer, B. Sánchez-Rinza, and J. Hauden, "A microwave coherence-multiplexed optical transmission system on Ti : LiNbO₃ integrated optics technology," *Microw. Opt. Technol. Lett.*, vol. 14, no. 1, pp. 64–69, January 1997.
- [39] P. Mollier, H. Porte, and J.-P. Goedgebuer, "Proton exchanged imbalanced Ti : LiNbO₃ Mach-Zehnder modulator," *Appl. Phys. Lett.*, vol. 60, pp. 274–276, 1992.
- [40] J. Hauden, H. Porte, and J.-P. Goedgebuer, "Quasi-polarization-independent Mach-Zehnder coherence modulator/demodulator integrated in Z-propagating lithium-niobate," *IEEE J. Quantum Electron.*, vol. 30, no. 10, pp. 2325–2331, October 1994.
- [41] J. Hauden, H. Porte, and J.-P. Goedgebuer, "Demonstration of a single source bidirectional fibre link using polarisation insensitive LiNbO₃ integrated coherence modulators," *Electron. Lett.*, vol. 32, no. 8, pp. 751–752, April 1996.
- [42] H. Porte, J.-P. Goedgebuer, W. Elflein, A. Terras, F. Ledeventec, and N. Butterlin, "Linear phase tracking in a coherence modulation electrical sensor system using integrated LiNbO₃ modulator/demodulator," *IEEE J. Sel. Top. Quantum Electron.*, vol. 2, no. 2, pp. 319–325, June 1996.



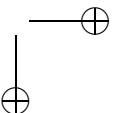
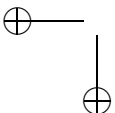


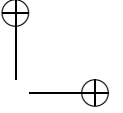
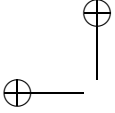
- [43] J. Hauden, H. Porte, J.-P. Goedgebuer, J. Abiven, C. Gibassier, and C. Gutiérrez-Martínez, "Polarization independent bidirectional fiber link using coherence Multi/Demultiplexing LiNbO₃ integrated electrooptical circuits," *J. Lightwave Technol.*, vol. 14, no. 7, pp. 1630–1638, July 1996.
- [44] S. Khalfallah, P. Dubreuil, L. Escotte, R. Legros, C. Fontaine, A. Muñoz-Yagüe, B. Beche, and H. Porte, "A GaAlAs-GaAs integrated coherence modulator," *J. Lightwave Technol.*, vol. 17, no. 1, pp. 103–107, January 1999.
- [45] S. Khalfallah, P. Dubreuil, R. Legros, C. Fontaine, A. Muñoz-Yagüe, B. Beche, H. Porte, R. Warno, and M. Karpierz, "Highly unbalanced GaAlAs-GaAs integrated Mach-Zehnder interferometer for coherence modulation at 1.3 μm ," *Opt. Commun.*, vol. 167, pp. 67–76, August 1999.
- [46] J. L. Brooks, R. H. Wentworth, R. C. Youngquist, M. Tur, B. Y. Kim, and H. J. Shaw, "Coherence multiplexing of fiber-optic interferometric sensors," *J. Lightwave Technol.*, vol. 3, no. 5, pp. 1062–1072, October 1985.
- [47] R. H. Wentworth, "Theoretical noise performance of coherence-multiplexed interferometric sensors," *J. Lightwave Technol.*, vol. 7, no. 6, pp. 941–956, June 1989.
- [48] J. Kani, K. Iwatsuki, N. Takachio, and N. Fujii, "A simple broad-band coherence multiplexed optical access network and its scalability," *J. Lightwave Technol.*, vol. 19, no. 4, pp. 456–464, April 2001.
- [49] W. van Etten and J. van der Plaats, *Fundamentals of optical fiber communications*, New York: Prentice Hall, 1991.
- [50] M. Born and E. Wolf, *Principles of optics*, 6th ed., Oxford: Pergamon Press, 1980.
- [51] J. W. Goodman, *Statistical optics*, New York: John Wiley & Sons, 1985.
- [52] R. Priest, "Analysis of fiber interferometer utilizing 3×3 fiber coupler," *IEEE J. Quantum Elect.*, vol. 18, no. 10, pp. 1601–1603, October 1982.
- [53] W. van Etten, *Introduction to random signals and noise*, Chisester, West Sussex: John Wiley & Sons, 2005.
- [54] The MathWorks, Inc., *Simulink—dynamic system simulation for Matlab*, 1996.
- [55] The MathWorks, Inc., *Matlab—The language of technical computing*, 1996.



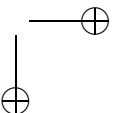
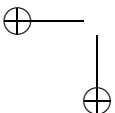


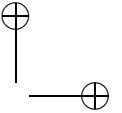
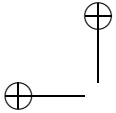
- [56] S. S. Haykin, *An Introduction to analog and digital communications*, New York: John Wiley & Sons, 1989.
- [57] R. A. Roberts and C. T. Mullis, *Digital signal processing*, Reading, Massachusetts: Addison-Wesley, 1987.
- [58] J.-P. Goedgebuer, R. Ferrière, and A. Hamel, "Polarization-independent transmission on a single-mode fiber using coherence modulation of light," *IEEE J. Quantum Electron.*, vol. 27, no. 8, pp. 1963–1967, August 1991.
- [59] G. J. Pendock, M. J. L. Cahill, and D. D. Sampson, "Multi-gigabit per second demonstration of photonic code-division multiplexing," *Electron. Lett.*, vol. 31, pp. 819–820, 1995.
- [60] G. J. Pendock and D. D. Sampson, "Increasing the transmission capacity of coherence multiplexed communication systems by using differential detection," *IEEE Photonics Technol. Lett.*, vol. 7, pp. 1504–1506, 1995.
- [61] G. J. Pendock and D. D. Sampson, "Capacity of coherence-multiplexed CDMA networks," *Opt. Commun.*, vol. 143, pp. 109–117, 1997.
- [62] G. J. Pendock and D. D. Sampson, "Noise in coherence-multiplexed optical fiber systems," *Appl. Optics*, vol. 36, pp. 9536–9540, 1997.
- [63] M. J. L. Cahill, G. J. Pendock, and D. D. Sampson, "Hybrid coherence multiplexing/coarse wavelength-division multiplexing passive optical network for customer access," *IEEE Photonics Technol. Lett.*, vol. 9, no. 7, pp. 1032–1034, July 1997.
- [64] A. W. Davis, M. J. Pettitt, J. P. King, and S. Wright, "Phase diversity techniques for coherent optical receivers," *J. Lightwave Technol.*, vol. 5, no. 4, pp. 561–572, April 1987.
- [65] D. A. Blair and G. D. Cormack, "Optimal source linewidth in a coherence multiplexed optical fiber communications system," *J. Lightwave Technol.*, vol. 10, no. 6, pp. 804–810, June 1992.
- [66] R. J. Blokpoel, A. Meijerink, and W. van Etten, "Traffic control in coherence-multiplexed networks," *Proc. of the 12th SCVT in the Benelux*, Enschede, The Netherlands, November 2005, to be published.
- [67] K. Bløtekjær, R. H. Wentworth, and H. J. Shaw, "Choosing relative optical path delays in series-topology interferometric sensor arrays," *J. Lightwave Technol.*, vol. 5, no. 2, pp. 229–235, February 1987.
- [68] A. Meijerink, R. O. Taniman, G. H. L. M. Heideman, and W. van Etten, "Comparison of three coherence multiplex system topologies," *Proc. of the 7th IEEE/LEOS Symp. in the Benelux*, Enschede, The Netherlands, November 2003, pp. 141–144.



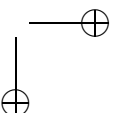
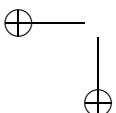


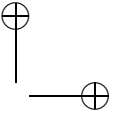
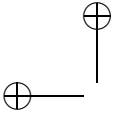
- [69] K. Wörhoff, P. V. Lambeck, and A. Driessen, "Design, tolerance analysis, and fabrication of silicon oxynitride based planar optical waveguides for communication devices," *J. Lightwave Technol.*, vol. 17, no. 8, pp. 1401–1407, August 1999.
- [70] R. A. Griffin, D. D. Sampson, and D. A. Jackson, "Demonstration of data-transmission using coherent correlation to reconstruct a coded pulse sequence," *IEEE Photonics Technol. Lett.*, vol. 4, no. 5, pp. 513–515, May 1992.
- [71] D. W. Smith, P. Healey, G. P. Fry, and K. Clayton, "A frequency chirped heterodyne spread spectrum optical fibre multiple access technique," *Proc. 14th European Conf. Opt. Commun.*, Brighton, East Sussex, September 1988, pp. 82–85.
- [72] K. Iiyama, M. Harano, K. Hayashi, Y. Ida, T. Kadoshima, and Y. Kurawasa, "Detection scheme of coherence multiplexed sensor signals by using optical loop incorporating frequency shifter," *Electron. Lett.*, vol. 28, no. 2, pp. 169–171, January 1992.
- [73] X. Q. Zhou, K. Iiyama, and K. Hayashi, "Detection scheme of coherence-multiplexed sensor signals using an optical loop with a frequency shifter: Sensitivity enhancement," *IEEE Photonics Technol. Lett.*, vol. 6, no. 6, pp. 767–769, June 1994.
- [74] X. Q. Zhou, K. Iiyama, and K. Hayashi, "Effect of laser phase-induced intensity noise on multiplexed fiber-optic sensor system using optical loop with frequency shifter," *IEICE Trans. Electron.*, vol. E79-C, no. 3, pp. 437–443, March 1996.
- [75] K. Iiyama and K. Hayashi, "Frequency domain detection of coherence multiplexed sensor signals by using an optical loop with a frequency shifter," *J. Lightwave Technol.*, vol. 15, no. 11, pp. 2069–2075, November 1997.
- [76] P. Healey, "Dimensioning an optical-fiber spread-spectrum multiple-access communication system," *Opt. Lett.*, vol. 12, no. 6, pp. 425–427, June 1987.
- [77] W. van Etten and A. Meijerink, "Optical stabilization of coherence multiplex output signal by means of a phase diversity network," *Proc. of the 6th IEEE/LEOS Symp. in the Benelux*, Brussels, Belgium, December 2001, pp. 149–152.
- [78] A. Meijerink, G. H. L. M. Heideman, and W. van Etten, "Performance evaluation of an OOK coherence multiplex receiver based on 4×4 phase diversity detection," *Proc. of the XXVIIth URSI G.A.*, Maastricht, The Netherlands, August 2002, paper D7.O.6.



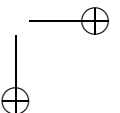
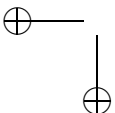


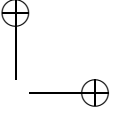
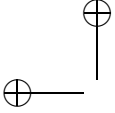
- [79] J. M. Heaton and M. J. Jenkins, "General matrix theory of self-imaging in multimode interference (MMI) couplers," *IEEE Photonics Technol. Lett.*, vol. 11, no. 2, pp. 212–214, February 1999.
- [80] A. Meijerink, G. H. L. M. Heideman, and W. van Etten, "*M*-ary (D)PSK modulation in coherence multiplex systems," *Proc. of the 7th IEEE/LEOS Symp. in the Benelux*, Amsterdam, The Netherlands, December 2002, pp. 207–210.
- [81] J. G. Proakis, *Digital communications*, 4th ed., Singapore: McGraw-Hill, 2001.
- [82] A. Meijerink, G. H. L. M. Heideman, and W. van Etten, "BER analysis of a DPSK phase diversity receiver for coherence multiplexing," *Proc. of the 23rd Symp. on Inform. Theory in the Benelux*, Louvain-la-Neuve, Belgium, May 2002, pp. 269–276.
- [83] J. Siuzdak, *Optical couplers for coherent phase diversity systems*, EUT Report 88-E-190, Eindhoven University of Technology, Eindhoven, The Netherlands, March 1988.
- [84] A. Meijerink, G. H. L. M. Heideman, and W. van Etten, "Balanced optical phase diversity receivers for coherence multiplexing," *J. Lightwave Technol.*, vol. 22, no. 11, pp. 2393–2408, November 2004.
- [85] J. L. Gimlett and N. K. Cheung, "Dispersion penalty analysis for LED/Single-mode fiber transmission systems," *J. Lightwave Technol.*, vol. 4, no. 9, pp. 1381–1392, September 1986.
- [86] T. Pfeiffer, M. Witte, and B. Deppisch, "High-speed transmission of broad-band thermal light pulses over dispersive fibers," *IEEE Photonics Technol. Lett.*, vol. 11, no. 3, pp. 385–387, March 1999.
- [87] M. Witte, F. Buchali, and T. Pfeiffer, "Reducing the optical power penalty for electronically dispersion compensated LED pulse transmission by using multi-bit shift decision feedback," *Electron. Lett.*, vol. 36, no. 5, pp. 450–451, March 2000.
- [88] T. Pfeiffer, J. Kissing, J. P. Elbers, B. Deppisch, M. Witte, H. Schmuck, and E. Voges, "Coarse WDM/CDM/TDM concept for optical packet transmission in metropolitan and access networks supporting 400 channels at 2.5 Gb/S peak rate," *J. Lightwave Technol.*, vol. 18, no. 12, pp. 1928–1938, December 2000.
- [89] C. E. Shannon and W. Weaver, *The mathematical theory of communication*, 4th paperback ed., Urbana, Illinois: Illini Books, 1969.
- [90] A. Meijerink, N. Niëns, G. H. L. M. Heideman, and W. van Etten, "Chromatic fiber dispersion in single-mode coherence multiplex systems," *Proc.*



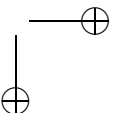
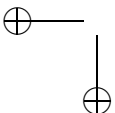


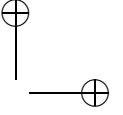
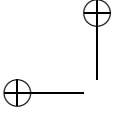
- of the 10th SCVT in the Benelux, Eindhoven, The Netherlands, November 2003, paper 9.
- [91] H. Al-Raweshidy and S. Komaki, *Radio over fiber technologies for mobile communications networks*, Norwood, Massachusetts: Artech House, 2002.
- [92] H. Uehara and I. Sasase, "Coherence multiplexed subcarrier multiplexing (CM/SCM) lightwave system for microcellular mobile communications," *IEICE Trans. Commun.*, vol. E79-B, no. 5, pp. 708–715, May 1996.
- [93] H. Uehara, I. Sasase, and M. Yokoyama, "Fiber optic subcarrier transmission systems using coherence multiplexing techniques for broad-band distribution networks," *IEICE Trans. Commun.*, vol. E80-B, no. 7, pp. 1027–1034, July 1997.
- [94] R. O. Taniman, A. Meijerink, W. van Etten, and J. C. Haartsen, "Indoor RF signal distribution using a coherence multiplexed/subcarrier multiplexed optical transmission system," *Proc. of the 10th SCVT in the Benelux*, Eindhoven, The Netherlands, November 2003, paper 17.
- [95] The Institute of Electrical and Electronics Engineers, *Supplement to IEEE standards for information technology—Telecommunications and information exchange between systems—Local and metropolitan area networks—Specific requirements—Part 11: Wireless LAN medium access control (MAC) and physical layer (PHY) specifications: Higher speed physical layer extension in the 2.4 GHz band*, IEEE standard 802.11b, 1999.
- [96] T. S. Rappaport, *Wireless communications—Principles and practice*, Upper Saddle River, New Jersey: Prentice Hall, 1996.
- [97] The Institute of Electrical and Electronics Engineers, *Supplement to IEEE standards for information technology—Telecommunications and information exchange between systems—Local and metropolitan area networks—Specific requirements—Part 11: Wireless LAN medium access control (MAC) and physical layer (PHY) specifications: Further higher data rate extension in the 2.4 GHz band*, IEEE standard 802.11g, 2003.
- [98] R. A. Griffin, D. D. Sampson, and D. A. Jackson, "Optical-phase coding for code-division multiple access networks," *IEEE Photonics Technol. Lett.*, vol. 4, no. 12, pp. 1401–1404, December 1992.
- [99] R. Gross and R. Olhansky, "Third-order intermodulation distortion in coherent subcarrier-multiplexed systems," *IEEE Photonics Technol. Lett.*, vol. 1, no. 4, pp. 91–93, April 1989.
- [100] Y.-H. Lee, J. Wu, and H.-W. Tsao, "The impact of laser phase noise on the coherent subcarrier multiplexing system," *J. Lightwave Technol.*, vol. 9, no. 3, pp. 347–355, March 1991.





- [101] R. Srinivasan, *Importance sampling—applications in communications and detection*, Berlin: Springer-Verlag, 2002.
- [102] L. Ammeraal, *C++ for Programmers*, 2nd ed., Chisester, West Sussex: John Wiley & Sons, 1995.
- [103] B. Wacogne and D. A. Jackson, “Security vulnerability in coherence modulation communication systems,” *IEEE Photonics Technol. Lett.*, vol. 8, no. 3, pp. 947–949, March 1996.
- [104] W. Wells, R. Stone, and E. Miles, “Secure communications by optical homodyne,” *IEEE J. Sel. Area Commun.*, vol. 11, no. 5, pp. 770–777, June 1993.
- [105] N. Karafolas, G. C. Gupta, and D. Uttamchandani, “Combining code division multiplexing and coherence multiplexing for private communications in optical fiber multiple access networks,” *Opt. Commun.*, vol. 123, pp. 11–18, 1996.
- [106] Y. T. Mazurenko, R. Giust, and J. P. Goedgebuer, “Spectral coding for secure optical communications using refractive index dispersion,” *Opt. Commun.*, vol. 133, pp. 87–92, 1997.
- [107] B. Wacogne and D. A. Jackson, “Enhanced security in a coherence modulation system using optical path difference corruption,” *IEEE Photonics Technol. Lett.*, vol. 8, no. 7, pp. 947–949, July 1996.
- [108] B. Wacogne, W. Elfein, C. Pieralli, P. Mollier, H. Porte, and D. A. Jackson, “Secrecy improvement in confidential coherence modulation by means of a new keying structure,” *Opt. Commun.*, vol. 154, pp. 350–358, 1998.
- [109] J. C. Haartsen, A. Meijerink, A. Bekkaoui, A. Taban, and J. L. Tauritz, “Novel wireless modulation technique based on noise,” *Proc. of the 11th SCVT in the Benelux*, Ghent, Belgium, November 2004, paper 8.
- [110] J. C. Haartsen, A. Meijerink, X. Shang, J. W. Balkema, and J. L. Tauritz, “New wireless modulation scheme based on frequency-offset technique,” *Proc. of the 12th SCVT in the Benelux*, Enschede, The Netherlands, November 2005, to be published.
- [111] J. Wang and J. C. Haartsen, “Performance of transmit-reference radio systems in frequency-selective channels,” *Proc. of the 12th SCVT in the Benelux*, Enschede, The Netherlands, November 2005, to be published.
- [112] C. W. Helstrom, *Statistical theory of signal detection*, Oxford: Pergamon Press, 1975.





Appendix A

Doubly-stochastic Poisson processes

A.1 Definition

Consider a doubly-stochastic inhomogeneous Poisson process [53]

$$X(t) = \sum_i \delta(t - t_i). \quad (\text{A.1})$$

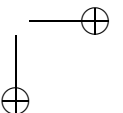
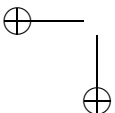
The random events times $\{t_i\}$ of this process are related to the *rate* $\Lambda(t)$ of the process. For doubly-stochastic inhomogeneous Poisson processes, this rate is a random process with expected value $E[\Lambda(t)]$ and autocorrelation function $R_{\Lambda\Lambda}(t_1, t_2)$. For a given realization $\lambda(t)$ of $\Lambda(t)$, the number of events (impulses) K in a time interval $[t_1, t_2]$ is governed by a Poisson distribution:

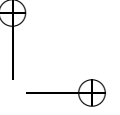
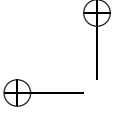
$$P[K = k | \Lambda(t) = \lambda(t)] = \frac{1}{k!} \left(\int_{t_1}^{t_2} \lambda(t) dt \right)^k \exp \left(- \int_{t_1}^{t_2} \lambda(t) dt \right). \quad (\text{A.2})$$

The process $X(t)$ is filtered by a linear time-invariant filter with an impulse response $h(t)$, resulting in a process

$$Y(t) = \int_{-\infty}^{\infty} h(t - \rho) X(\rho) d\rho = \sum_i h(t - t_i), \quad (\text{A.3})$$

In the following sections the expected value and autocorrelation function of $Y(t)$ will be derived. Although the derivation procedure is quite similar to the one that is used in [53], the results will be more general because the rate $\Lambda(t)$ is assumed to be non-stationary here, whereas in [53], $\Lambda(t)$ is assumed to be a wide-sense stationary process. Moreover, the cross-correlation between two Poisson processes will be derived.





A.2 Expected value

In order to calculate the expected value of $Y(t)$, the time axis is subdivided in small intervals of length Δt , which are chosen to be so small that the number of events K_n in a time interval $[n \cdot \Delta t, (n+1) \cdot \Delta t]$ is either 0 or 1, with conditional probabilities that can be approximated by

$$P[K_n = k | \Lambda(t) = \lambda(t)] \approx \begin{cases} 1 - \lambda(n \cdot \Delta t) \cdot \Delta t & , k = 0 \\ \lambda(n \cdot \Delta t) \cdot \Delta t & , k = 1 \end{cases} . \quad (\text{A.4})$$

The division in discrete-time intervals allows us to approximate $Y(t)$ by

$$\hat{Y}(t) = \sum_n h(t - n \cdot \Delta t) K_n . \quad (\text{A.5})$$

Using (A.4), the expected value of $\hat{Y}(t)$ under the condition $\Lambda(t) = \lambda(t)$ can be written as

$$E[\hat{Y}(t) | \Lambda(t) = \lambda(t)] = \sum_n h(t - n \cdot \Delta t) E[K_n | \Lambda(t) = \lambda(t)] \quad (\text{A.6})$$

$$= \sum_n h(t - n \cdot \Delta t) \lambda(n \cdot \Delta t) \cdot \Delta t . \quad (\text{A.7})$$

Since the condition $\Lambda(t) = \lambda(t)$ actually reduces to the condition $\Lambda(n \cdot \Delta t) = \lambda(n \cdot \Delta t) \forall n \in \mathbb{Z}$, we can find the expected value of $\hat{Y}(t)$ by multiplying the conditional expected value in (A.6) with the joint probability density function of all the values of $\Lambda(t)$ at the discrete-time instants $n \cdot \Delta t$ and integrating over all the $\lambda(n \cdot \Delta t)$'s. This results in

$$E[\hat{Y}(t)] = \sum_n h(t - n \cdot \Delta t) E[\Lambda(n \cdot \Delta t)] \cdot \Delta t . \quad (\text{A.8})$$

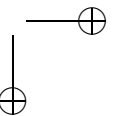
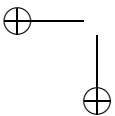
When Δt is made infinitesimally small, the summation turns into an integral and $\hat{Y}(t)$ becomes exactly equal to $Y(t)$, resulting in

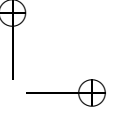
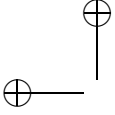
$$E[Y(t)] = \int_{-\infty}^{\infty} h(t - \rho) E[\Lambda(\rho)] d\rho . \quad (\text{A.9})$$

A.3 Autocorrelation function

Using the same approximation $\hat{Y}(t)$ as in the previous section, we can calculate the autocorrelation function

$$R_{\hat{Y}\hat{Y}}(t_1, t_2) \triangleq E[\hat{Y}(t_1)\hat{Y}(t_2)] . \quad (\text{A.10})$$





This is done by first calculating the conditional expected value. Using (A.5) and interchanging the order of summation and expectation, we get:

$$\begin{aligned} \mathbb{E} \left[\hat{Y}(t_1) \hat{Y}(t_2) | \Lambda(t) = \lambda(t) \right] = \\ \sum_{n_1} \sum_{n_2} h(t_1 - n_1 \Delta t) h(t_2 - n_2 \Delta t) \mathbb{E} [K_{n_1} K_{n_2} | \Lambda(t) = \lambda(t)]. \end{aligned} \quad (\text{A.11})$$

The number of events in disjunct intervals are independent. (This is a basic property of Poisson processes.) Hence, for $n_1 = n_2$ we get

$$\mathbb{E} [K_{n_1} K_{n_2} | \Lambda(t) = \lambda(t)] = \mathbb{E} [K_{n_1}^2 | \Lambda(t) = \lambda(t)] = \lambda(n_1 \Delta t) \cdot \Delta t, \quad (\text{A.12})$$

whereas for $n_1 \neq n_2$ we get

$$\begin{aligned} \mathbb{E} [K_{n_1} K_{n_2} | \Lambda(t) = \lambda(t)] &= \mathbb{E} [K_{n_1} | \Lambda(t) = \lambda(t)] \mathbb{E} [K_{n_2} | \Lambda(t) = \lambda(t)] \\ &= \lambda(n_1 \Delta t) \lambda(n_2 \Delta t) \cdot (\Delta t)^2. \end{aligned} \quad (\text{A.13})$$

As a result, the double summation in (A.11) can be written as

$$\begin{aligned} \mathbb{E} \left[\hat{Y}(t_1) \hat{Y}(t_2) | \Lambda(t) = \lambda(t) \right] &= \sum_n h(t_1 - n \cdot \Delta t) h(t_2 - n \cdot \Delta t) \lambda(n \cdot \Delta t) \cdot \Delta t \\ &+ \sum_{n_1} \sum_{n_2 \neq n_1} h(t_1 - n_1 \Delta t) h(t_2 - n_2 \Delta t) \lambda(n_1 \Delta t) \lambda(n_2 \Delta t) \cdot (\Delta t)^2. \end{aligned} \quad (\text{A.14})$$

The condition $\Lambda(t) = \lambda(t)$ can be removed by multiplying with the joint probability density function and integrating, like in the previous section, resulting in

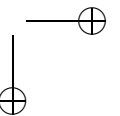
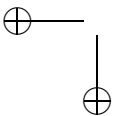
$$\begin{aligned} R_{\hat{Y}\hat{Y}}(t_1, t_2) &= \sum_n h(t_1 - n \cdot \Delta t) h(t_2 - n \cdot \Delta t) \mathbb{E} [\Lambda(n \cdot \Delta t)] \cdot \Delta t \\ &+ \sum_{n_1} \sum_{n_2 \neq n_1} h(t_1 - n_1 \Delta t) h(t_2 - n_2 \Delta t) R_{\Lambda\Lambda}(n_1 \Delta t, n_2 \Delta t) \cdot (\Delta t)^2. \end{aligned} \quad (\text{A.15})$$

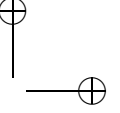
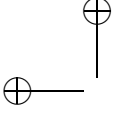
Finally, the autocorrelation function of $Y(t)$ can be found by making Δt infinitesimally small, resulting in

$$\begin{aligned} R_{YY}(t_1, t_2) &= \int_{-\infty}^{\infty} h(t_1 - \rho) h(t_2 - \rho) \mathbb{E} [\Lambda(\rho)] \, d\rho \\ &+ \int_{-\infty}^{\infty} \int_{-\infty}^{\infty} h(t_1 - \rho_1) h(t_2 - \rho_2) R_{\Lambda\Lambda}(\rho_1, \rho_2) \, d\rho_1 \, d\rho_2. \end{aligned} \quad (\text{A.16})$$

A.4 Cross-correlation function

Now consider the (more general) case where we have two Poisson impulse processes $X_1(t)$ and $X_2(t)$ with random rates $\Lambda_1(t)$ and $\Lambda_2(t)$, respectively, which have cross-correlation function $R_{\Lambda_1\Lambda_2}(t_1, t_2)$.





Although $\Lambda_1(t)$ and $\Lambda_2(t)$ are correlated, the random mechanisms that convert $\Lambda_1(t)$ and $\Lambda_2(t)$ in $X_1(t)$ and $X_2(t)$, respectively, are independent. (Note that this is a realistic assumption for the power-current conversion mechanism in two separate photodiodes, for example.) Hence, for *given realizations* $\lambda_1(t)$ and $\lambda_2(t)$, the two processes are independent.

$X_1(t)$ and $X_2(t)$ are filtered by linear time-invariant filters with impulse responses $h_1(t)$ and $h_2(t)$, resulting in filtered processes $Y_1(t)$ and $Y_2(t)$, respectively. Their expected values and autocorrelation functions follow from the preceding two sections.

The cross-correlation function $R_{Y_1 Y_2}(t_1, t_2) \triangleq E[Y_1(t_1)Y_2(t_2)]$ can be found using similar approximations $\hat{Y}_1(t)$ and $\hat{Y}_2(t)$ as in the previous two sections. For given realizations $\lambda_1(t)$ and $\lambda_2(t)$ the number of events K_{1,n_1} and K_{2,n_2} in the processes $X_1(t)$ and $X_2(t)$, respectively, in time intervals $[n_1\Delta t, (n_1+1)\cdot\Delta t]$ and $[n_2\Delta t, (n_2+1)\cdot\Delta t]$, are independent (even when $n_1 = n_2$), so we can write

$$\begin{aligned} P[K_{1,n_1} = k_1, K_{2,n_2} = k_2 | \Lambda_1(t) = \lambda_1(t), \Lambda_2(t) = \lambda_2(t)] = \\ P[K_{1,n_1} = k_1 | \Lambda_1(t) = \lambda_1(t)] P[K_{2,n_2} = k_2 | \Lambda_2(t) = \lambda_2(t)], \quad (\text{A.17}) \end{aligned}$$

where the individual probabilities are similar to (A.4). Hence, the conditional cross-correlation function can be written as

$$\begin{aligned} E[\hat{Y}_1(t_1)\hat{Y}_2(t_2) | \Lambda_1(t) = \lambda_1(t), \Lambda_2(t) = \lambda_2(t)] &= \sum_{n_1} \sum_{n_2} h_1(t_1 - n_1\Delta t) \\ &\quad \cdot h_2(t_2 - n_2\Delta t) E[K_{1,n_1} | \Lambda_1(t) = \lambda_1(t)] E[K_{2,n_2} | \Lambda_2(t) = \lambda_2(t)] \\ &= \sum_{n_1} \sum_{n_2} h_1(t_1 - n_1\Delta t) h_2(t_2 - n_2\Delta t) \lambda_1(n_1\Delta t) \lambda_2(n_2\Delta t) \cdot (\Delta t)^2. \quad (\text{A.18}) \end{aligned}$$

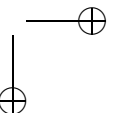
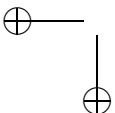
The conditions $\Lambda_1(t) = \lambda_1(t)$ and $\Lambda_2(t) = \lambda_2(t)$ can be removed by multiplying with the joint probability density function and integrating, like in the previous two sections. This results in:

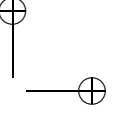
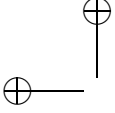
$$\begin{aligned} R_{\hat{Y}_1 \hat{Y}_2}(t_1, t_2) = \\ \sum_{n_1} \sum_{n_2} h_1(t_1 - n_1\Delta t) h_2(t_2 - n_2\Delta t) R_{\Lambda_1 \Lambda_2}(n_1\Delta t, n_2\Delta t) \cdot (\Delta t)^2. \quad (\text{A.19}) \end{aligned}$$

The cross-correlation function of $Y_1(t)$ and $Y_2(t)$ follows by making Δt infinitesimally small:

$$\begin{aligned} R_{Y_1 Y_2}(t_1, t_2) = \\ \int_{-\infty}^{\infty} \int_{-\infty}^{\infty} h_1(t_1 - \rho_1) h_2(t_2 - \rho_2) R_{\Lambda_1 \Lambda_2}(\rho_1, \rho_2) d\rho_1 d\rho_2. \quad (\text{A.20}) \end{aligned}$$

Using (A.9) it can be proven that the autocorrelation functions in this equation can be replaced by the corresponding covariance functions. This shows that the correlation between $\Lambda_1(t)$ and $\Lambda_2(t)$ induces correlation between $Y_1(t)$ and $Y_2(t)$, which reflects the actual doubly-stochastic behavior of the processes.





Appendix B

Bit error rate analysis of phase diversity receivers

In this appendix, analytical expressions are derived for the bit error probabilities of the phase diversity receivers that are described in Section 6.4. First a general analysis is performed on the output samples of the low-pass filters in the four-way receivers. The results are used in the succeeding sections, where the bit error rates of four-way receivers for OOK, QPSK, M -ary PSK, binary DPSK, DQPSK and M -ary DPSK are derived, respectively. Finally, the bit error rate of a three-way OOK phase diversity receiver is derived.

B.1 Noise in four-way phase diversity receivers

The output samples of the low-pass filters can be written as a vector

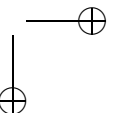
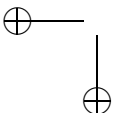
$$\mathbf{V}_{\text{LP},r,k} \triangleq \begin{bmatrix} V_{\text{LP},\text{I},r}(k T_s) \\ V_{\text{LP},\text{Q},r}(k T_s) \end{bmatrix}. \quad (\text{B.1})$$

The expected value of $\mathbf{V}_{\text{LP},r,k}$ follows by substituting (5.2) in (6.31) and (6.32), respectively. In case of digital modulation and matched filtering this becomes

$$\mathbb{E}[\mathbf{V}_{\text{LP},r,k}] = \frac{Z_{\text{TIA}} R_{\text{pd}} P_x}{8 L_{\text{Tx}} L_{\text{Rx}} L_{\text{nw}}} m_{r,k} \begin{bmatrix} \cos\left(\Delta\phi_r + \phi_{r,k} - \frac{3\pi}{4}\right) \\ \cos\left(\Delta\phi_r + \phi_{r,k} + \frac{3\pi}{4}\right) \end{bmatrix}. \quad (\text{B.2})$$

The covariance matrix of $\mathbf{V}_{\text{LP},r,k}$ follows from

$$\begin{aligned} \mathbf{C}_{\mathbf{V}_{\text{LP},r,k} \mathbf{V}_{\text{LP},r,k}} &\triangleq \mathbb{E}[\mathbf{V}_{\text{LP},r,k} \mathbf{V}_{\text{LP},r,k}^{\text{T}}] - \mathbb{E}[\mathbf{V}_{\text{LP},r,k}] \mathbb{E}[\mathbf{V}_{\text{LP},r,k}^{\text{T}}] \\ &= \begin{bmatrix} \sigma_{V_{\text{LP},\text{I},r}(k T_s)}^2 & C_{V_{\text{LP},\text{I},r}(k T_s) V_{\text{LP},\text{Q},r}(k T_s)} \\ C_{V_{\text{LP},\text{I},r}(k T_s) V_{\text{LP},\text{Q},r}(k T_s)} & \sigma_{V_{\text{LP},\text{Q},r}(k T_s)}^2 \end{bmatrix}. \end{aligned} \quad (\text{B.3})$$



The variances of the output samples $\sigma_{V_{LP,I,r}(kT_s)}^2$ and $\sigma_{V_{LP,Q,r}(kT_s)}^2$ and the covariance of the output samples $C_{V_{LP,I,r}(kT_s)V_{LP,Q,r}(kT_s)}$ can be found by calculating the autocorrelation and cross-correlation functions of the output signals. The latter can be found in a similar way as in Section 4.6 and are given by

$$\begin{aligned}
R_{V_{LP,I,r}V_{LP,I,r}}(t_1, t_2) &= \\
& Z_{TIA} R_{pd} e \int_{-\infty}^{\infty} h_{LP}(t_1 - \rho) h_{LP}(t_2 - \rho) E[P_{z_2}(\rho) + P_{z_3}(\rho)] d\rho \\
& + Z_{TIA}^2 R_{pd}^2 \int_{-\infty}^{\infty} \int_{-\infty}^{\infty} h_{LP}(t_1 - \rho_1) h_{LP}(t_2 - \rho_2) \left[R_{P_{z_2}P_{z_2}}(\rho_1, \rho_2) \right. \\
& \quad \left. - R_{P_{z_2}P_{z_3}}(\rho_1, \rho_2) - R_{P_{z_3}P_{z_2}}(\rho_1, \rho_2) + R_{P_{z_3}P_{z_3}}(\rho_1, \rho_2) \right] d\rho_1 d\rho_2 \\
& + Z_{TIA}^2 S_{th} \int_{-\infty}^{\infty} h_{LP}(t_1 - \rho) h_{LP}(t_2 - \rho) d\rho, \tag{B.4}
\end{aligned}$$

$$\begin{aligned}
R_{V_{LP,Q,r}V_{LP,Q,r}}(t_1, t_2) &= \\
& Z_{TIA} R_{pd} e \int_{-\infty}^{\infty} h_{LP}(t_1 - \rho) h_{LP}(t_2 - \rho) E[P_{z_1}(\rho) + P_{z_4}(\rho)] d\rho \\
& + Z_{TIA}^2 R_{pd}^2 \int_{-\infty}^{\infty} \int_{-\infty}^{\infty} h_{LP}(t_1 - \rho_1) h_{LP}(t_2 - \rho_2) \left[R_{P_{z_1}P_{z_1}}(\rho_1, \rho_2) \right. \\
& \quad \left. - R_{P_{z_1}P_{z_4}}(\rho_1, \rho_2) - R_{P_{z_4}P_{z_1}}(\rho_1, \rho_2) + R_{P_{z_4}P_{z_4}}(\rho_1, \rho_2) \right] d\rho_1 d\rho_2 \\
& + Z_{TIA}^2 S_{th} \int_{-\infty}^{\infty} h_{LP}(t_1 - \rho) h_{LP}(t_2 - \rho) d\rho, \tag{B.5}
\end{aligned}$$

$$\begin{aligned}
R_{V_{LP,I,r}V_{LP,Q,r}}(t_1, t_2) &= \\
& Z_{TIA}^2 R_{pd}^2 \int_{-\infty}^{\infty} \int_{-\infty}^{\infty} h_{LP}(t_1 - \rho_1) h_{LP}(t_2 - \rho_2) \left[R_{P_{z_2}P_{z_1}}(\rho_1, \rho_2) \right. \\
& \quad \left. - R_{P_{z_2}P_{z_4}}(\rho_1, \rho_2) - R_{P_{z_3}P_{z_1}}(\rho_1, \rho_2) + R_{P_{z_3}P_{z_4}}(\rho_1, \rho_2) \right] d\rho_1 d\rho_2. \tag{B.6}
\end{aligned}$$

Substituting (2.36), (2.41) and (6.17) through (6.30) these become

$$\begin{aligned}
R_{V_{LP,I,r}V_{LP,I,r}}(t_1, t_2) &= E[V_{LP,I,r}(t_1)] E[V_{LP,I,r}(t_2)] \\
& + \frac{Z_{TIA} R_{pd} e}{4L_{Rx}} \int_{-\infty}^{\infty} h_{LP}(t_1 - \rho) h_{LP}(t_2 - \rho) E[P_y(\rho) + P_y(\rho - T_{Rx,r})] d\rho \\
& + \frac{Z_{TIA}^2 R_{pd}^2}{32L_{Rx}^2} \int_{-\infty}^{\infty} \int_{-\infty}^{\infty} h_{LP}(t_1 - \rho_1) h_{LP}(t_2 - \rho_2) \\
& \quad \cdot \text{Re} \left\{ R_{y^*y}(\rho_1, \rho_2) R_{y^*y}(\rho_2 - T_{Rx,r}, \rho_1 - T_{Rx,r}) \right. \\
& \quad \left. + j R_{y^*y}(\rho_1 - T_{Rx,r}, \rho_2) R_{y^*y}(\rho_2 - T_{Rx,r}, \rho_1) \right\} d\rho_1 d\rho_2 \\
& + Z_{TIA}^2 S_{th} \int_{-\infty}^{\infty} h_{LP}(t_1 - \rho) h_{LP}(t_2 - \rho) d\rho, \tag{B.7}
\end{aligned}$$

$$\begin{aligned}
R_{V_{LP,Q,r}V_{LP,Q,r}}(t_1, t_2) &= \mathbb{E}[V_{LP,Q,r}(t_1)]\mathbb{E}[V_{LP,Q,r}(t_2)] \\
&+ \frac{Z_{TIA}R_{pd}e}{4L_{Rx}} \int_{-\infty}^{\infty} h_{LP}(t_1 - \rho)h_{LP}(t_2 - \rho)\mathbb{E}[P_y(\rho) + P_y(\rho - T_{Rx,r})] d\rho \\
&+ \frac{Z_{TIA}^2R_{pd}^2}{32L_{Rx}^2} \int_{-\infty}^{\infty} \int_{-\infty}^{\infty} h_{LP}(t_1 - \rho_1)h_{LP}(t_2 - \rho_2) \\
&\quad \cdot \operatorname{Re}\left\{R_{y^*y}(\rho_1, \rho_2)R_{y^*y}(\rho_2 - T_{Rx,r}, \rho_1 - T_{Rx,r})\right. \\
&\quad \quad \left. - j R_{y^*y}(\rho_1 - T_{Rx,r}, \rho_2)R_{y^*y}(\rho_2 - T_{Rx,r}, \rho_1)\right\} d\rho_1 d\rho_2 \\
&+ Z_{TIA}^2S_{th} \int_{-\infty}^{\infty} h_{LP}(t_1 - \rho)h_{LP}(t_2 - \rho) d\rho, \tag{B.8}
\end{aligned}$$

$$\begin{aligned}
R_{V_{LP,I,r}V_{LP,Q,r}}(t_1, t_2) &= \mathbb{E}[V_{LP,I,r}(t_1)]\mathbb{E}[V_{LP,Q,r}(t_2)] \\
&+ \frac{Z_{TIA}^2R_{pd}^2}{32L_{Rx}^2} \int_{-\infty}^{\infty} \int_{-\infty}^{\infty} h_{LP}(t_1 - \rho_1)h_{LP}(t_2 - \rho_2) \\
&\quad \cdot \operatorname{Re}\left\{R_{y^*y}(\rho_1 - T_{Rx,r}, \rho_2)R_{y^*y}(\rho_2 - T_{Rx,r}, \rho_1)\right\} d\rho_1 d\rho_2. \tag{B.9}
\end{aligned}$$

In case of a PA, one should substitute (5.9), (5.10) and (5.13) and use approximation (4.51), resulting in

$$\begin{aligned}
R_{V_{LP,I,r}V_{LP,I,r}}(t_1, t_2) &= \mathbb{E}[V_{LP,I,r}(t_1)]\mathbb{E}[V_{LP,I,r}(t_2)] \\
&+ \frac{Z_{TIA}^2R_{pd}P_xe}{4L_{Tx}L_{Rx}L_{nw}} \int_{-\infty}^{\infty} h_{LP}(t_1 - \rho)h_{LP}(t_2 - \rho) \sum_{i=1}^N m_{\text{mod},i}(\rho) d\rho \\
&+ \frac{Z_{TIA}^2R_{pd}^2P_x^2\tau_c}{128L_{Tx}^2L_{Rx}^2L_{nw}^2} \int_{-\infty}^{\infty} h_{LP}(t_1 - \rho)h_{LP}(t_2 - \rho) \\
&\quad \cdot \left[4 \sum_{i_1=1}^N \sum_{i_2=1}^N m_{\text{mod},i_1}(\rho)m_{\text{mod},i_2}(\rho) + 2 \sum_{i=1}^N m_{\text{mod},i}^2(\rho) \right. \\
&\quad \quad \left. + m_{\text{mod},r}^2(\rho) \cos\left(2\Delta\phi_r + 2\phi_{\text{mod},r}(\rho) + \frac{\pi}{2}\right) \right] d\rho \\
&+ Z_{TIA}^2S_{th} \int_{-\infty}^{\infty} h_{LP}(t_1 - \rho)h_{LP}(t_2 - \rho) d\rho, \tag{B.10}
\end{aligned}$$

$$\begin{aligned}
R_{V_{LP,Q,r}V_{LP,Q,r}}(t_1, t_2) &= E[V_{LP,Q,r}(t_1)]E[V_{LP,Q,r}(t_2)] \\
&+ \frac{Z_{TIA}^2 R_{pd} P_x e}{4L_{Tx}L_{Rx}L_{nw}} \int_{-\infty}^{\infty} h_{LP}(t_1 - \rho)h_{LP}(t_2 - \rho) \sum_{i=1}^N m_{\text{mod},i}(\rho) d\rho \\
&+ \frac{Z_{TIA}^2 R_{pd}^2 P_x^2 \tau_c}{128L_{Tx}^2 L_{Rx}^2 L_{nw}^2} \int_{-\infty}^{\infty} h_{LP}(t_1 - \rho)h_{LP}(t_2 - \rho) \\
&\quad \cdot \left[4 \sum_{i_1=1}^N \sum_{i_2=1}^N m_{\text{mod},i_1}(\rho)m_{\text{mod},i_2}(\rho) + 2 \sum_{i=1}^N m_{\text{mod},i}^2(\rho) \right. \\
&\quad \quad \left. + m_{\text{mod},r}^2(\rho) \cos\left(2\Delta\phi_r + 2\phi_{\text{mod},r}(\rho) - \frac{\pi}{2}\right) \right] d\rho \\
&+ Z_{TIA}^2 S_{\text{th}} \int_{-\infty}^{\infty} h_{LP}(t_1 - \rho)h_{LP}(t_2 - \rho) d\rho, \tag{B.11}
\end{aligned}$$

$$\begin{aligned}
R_{V_{LP,I,r}V_{LP,Q,r}}(t_1, t_2) &= E[V_{LP,I,r}(t_1)]E[V_{LP,Q,r}(t_2)] \\
&+ \frac{Z_{TIA}^2 R_{pd}^2 P_x^2 \tau_c}{128L_{Tx}^2 L_{Rx}^2 L_{nw}^2} \int_{-\infty}^{\infty} h_{LP}(t_1 - \rho)h_{LP}(t_2 - \rho) \\
&\quad \cdot m_{\text{mod},r}^2(\rho) \cos\left(2\Delta\phi_r + 2\phi_{\text{mod},r}(\rho)\right) d\rho. \tag{B.12}
\end{aligned}$$

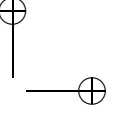
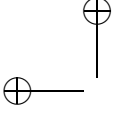
In case of digital modulation and matched filtering the following variances and covariances can be found for the output samples

$$\begin{aligned}
\sigma_{V_{LP,I,r}}^2(kT_s) &= R_{V_{LP,I,r}V_{LP,I,r}}(kT_s, kT_s) - E[V_{LP,I,r}(kT_s)]E[V_{LP,I,r}(kT_s)] \\
&= \frac{Z_{TIA}^2 R_{pd} P_x e}{4L_{Tx}L_{Rx}L_{nw}T_s} \sum_{i=1}^N m_{i,k} + \frac{Z_{TIA}^2 R_{pd}^2 P_x^2 \tau_c}{128L_{Tx}^2 L_{Rx}^2 L_{nw}^2 T_s} \left[4 \sum_{i_1=1}^N \sum_{i_2=1}^N m_{i_1,k}m_{i_2,k} \right. \\
&\quad \left. + 2 \sum_{i=1}^N m_{i,k}^2 + m_{r,k}^2 \cos\left(2\Delta\phi_r + 2\phi_{r,k} + \frac{\pi}{2}\right) \right] + \frac{Z_{TIA}^2 S_{\text{th}}}{T_s}, \tag{B.13}
\end{aligned}$$

$$\begin{aligned}
\sigma_{V_{LP,Q,r}}^2(kT_s) &= R_{V_{LP,Q,r}V_{LP,Q,r}}(kT_s, kT_s) - E[V_{LP,Q,r}(kT_s)]E[V_{LP,Q,r}(kT_s)] \\
&= \frac{Z_{TIA}^2 R_{pd} P_x e}{4L_{Tx}L_{Rx}L_{nw}T_s} \sum_{i=1}^N m_{i,k} + \frac{Z_{TIA}^2 R_{pd}^2 P_x^2 \tau_c}{128L_{Tx}^2 L_{Rx}^2 L_{nw}^2 T_s} \left[4 \sum_{i_1=1}^N \sum_{i_2=1}^N m_{i_1,k}m_{i_2,k} \right. \\
&\quad \left. + 2 \sum_{i=1}^N m_{i,k}^2 + m_{r,k}^2 \cos\left(2\Delta\phi_r + 2\phi_{r,k} - \frac{\pi}{2}\right) \right] + \frac{Z_{TIA}^2 S_{\text{th}}}{T_s}, \tag{B.14}
\end{aligned}$$

$$\begin{aligned}
C_{V_{LP,I,r}V_{LP,Q,r}}(kT_s) &= R_{V_{LP,I,r}V_{LP,Q,r}}(kT_s, kT_s) \\
&\quad - E[V_{LP,I,r}(kT_s)]E[V_{LP,Q,r}(kT_s)] \\
&= \frac{Z_{TIA}^2 R_{pd}^2 P_x^2 \tau_c}{128L_{Tx}^2 L_{Rx}^2 L_{nw}^2 T_s} m_{r,k}^2 \cos\left(2\Delta\phi_r + 2\phi_{r,k}\right). \tag{B.15}
\end{aligned}$$

The output samples of the low-pass filters can be assumed to be jointly Gaussian distributed, for similar reasons as described in Section 4.7.



In order to be able to derive the conditional probability density function of the output signal of a four-way phase diversity receiver, it is useful to decorrelate the output samples of the low-pass filters, which means that we write them as linear combinations of two independent Gaussian variables $V'_{LP,I,r}(kT_s)$ and $V'_{LP,Q,r}(kT_s)$. If we write the latter two as a vector $\mathbf{V}'_{LP,r,k}$, then we can write

$$\mathbf{V}_{LP,r,k} = \mathbf{A}_{r,k} \mathbf{V}'_{LP,r,k} \quad (\text{B.16})$$

where

$$\mathbf{A}_{r,k} \triangleq [\mathbf{v}_1 \quad \mathbf{v}_2] \quad (\text{B.17})$$

is a unitary matrix with columns \mathbf{v}_1 and \mathbf{v}_2 that correspond to the eigenvectors of the covariance matrix $\mathbf{C}_{\mathbf{V}_{LP,r,k} \mathbf{V}_{LP,r,k}}$. The variances of $V'_{LP,I,r}(kT_s)$ and $V'_{LP,Q,r}(kT_s)$ are equal to the eigenvalues of $\mathbf{C}_{\mathbf{V}_{LP,r,k} \mathbf{V}_{LP,r,k}}$, which are given by

$$\begin{aligned} \lambda_{1,2} = & \frac{Z_{\text{TIA}}^2 R_{\text{pd}} P_x e}{4L_{\text{Tx}} L_{\text{Rx}} L_{\text{nw}} T_s} \sum_{i=1}^N m_{i,k} \\ & + \frac{Z_{\text{TIA}}^2 R_{\text{pd}}^2 P_x^2 \tau_c}{128L_{\text{Tx}}^2 L_{\text{Rx}}^2 L_{\text{nw}}^2 T_s} \left[4 \sum_{i_1=1}^N \sum_{i_2=1}^N m_{i_1,k} m_{i_2,k} + 2 \sum_{i=1}^N m_{i,k}^2 \pm m_{r,k}^2 \right] \\ & + \frac{Z_{\text{TIA}}^2 S_{\text{th}}}{T_s}. \end{aligned} \quad (\text{B.18})$$

The corresponding (normalized) eigenvectors are given by

$$\mathbf{v}_1 = \begin{bmatrix} \cos(\Delta\phi_r + \phi_{r,k} - \frac{3\pi}{4}) \\ \cos(\Delta\phi_r + \phi_{r,k} + \frac{3\pi}{4}) \end{bmatrix}, \quad (\text{B.19})$$

$$\mathbf{v}_2 = \begin{bmatrix} \cos(\Delta\phi_r + \phi_{r,k} - \frac{\pi}{4}) \\ \cos(\Delta\phi_r + \phi_{r,k} - \frac{3\pi}{4}) \end{bmatrix}. \quad (\text{B.20})$$

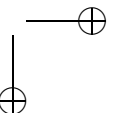
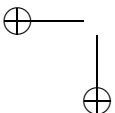
Hence, the expected value of $\mathbf{V}'_{LP,r,k}$ follows from (B.2) as

$$\begin{aligned} \mathbf{E}[\mathbf{V}'_{LP,r,k}] &= \mathbf{E}[\mathbf{A}_{r,k}^{-1} \mathbf{V}_r(l \cdot T_s)] = \mathbf{A}_{r,k}^T \mathbf{E}[\mathbf{V}_r(l \cdot T_s)] \\ &= \frac{Z_{\text{TIA}} R_{\text{pd}} P_x}{8L_{\text{Tx}} L_{\text{Rx}} L_{\text{nw}}} m_{r,k} \begin{bmatrix} 1 \\ 0 \end{bmatrix}. \end{aligned} \quad (\text{B.21})$$

B.2 Four-way phase diversity detection of OOK

For the four-way OOK receiver the output samples $V_{\text{out},r}(kT_s)$ can be written as

$$\begin{aligned} V_{\text{out},r}(kT_s) &= V_{LP,I,r}^2(kT_s) + V_{LP,Q,r}^2(kT_s) = \mathbf{V}_{LP,r,k}^T \mathbf{V}_{LP,r,k} \\ &= \left(\mathbf{V}'_{LP,r,k} \right)^T \mathbf{A}_{r,k}^T \mathbf{A}_{r,k} \mathbf{V}'_{LP,r,k}. \end{aligned} \quad (\text{B.22})$$



Since $\mathbf{A}_{r,k}$ is a unitary matrix, $\mathbf{A}_{r,k}^T \mathbf{A}_{r,k}$ equals the unit matrix. As a result, we can write

$$\begin{aligned} V_{\text{out},r}(k T_s) &= \left(\mathbf{V}'_{\text{LP},r,k} \right)^T \mathbf{V}'_{\text{LP},r,k} \\ &= \left(V'_{\text{LP},\text{I},r}(k T_s) \right)^2 + \left(V'_{\text{LP},\text{Q},r}(k T_s) \right)^2. \end{aligned} \quad (\text{B.23})$$

Since we have OOK modulation (see Subsection 4.7.2) the conditional expected values of $V'_{\text{LP},\text{I},r}(k T_s)$ and $V'_{\text{LP},\text{Q},r}(k T_s)$ are given by

$$\begin{aligned} \text{E} \left[V'_{\text{LP},\text{I},r}(k T_s) \mid A_{r,k} = 0 \right] &= \text{E} \left[V'_{\text{LP},\text{Q},r}(k T_s) \mid A_{r,k} = 0 \right] \\ &= \text{E} \left[V'_{\text{LP},\text{Q},r}(k T_s) \mid A_{r,k} = 1 \right] = 0, \end{aligned} \quad (\text{B.24})$$

$$\text{E} \left[V'_{\text{LP},\text{I},r}(k T_s) \mid A_{r,k} = 1 \right] = \frac{Z_{\text{TIA}} R_{\text{pd}} P_x}{8 L_{\text{Tx}} L_{\text{Rx}} L_{\text{nw}}}. \quad (\text{B.25})$$

When the conditional variances of $V'_{\text{LP},\text{I},r}(k T_s)$ and $V'_{\text{LP},\text{Q},r}(k T_s)$ for $N_1 = n$ and a binary zero are denoted by $\sigma_{\text{I},0}^2$ and $\sigma_{\text{Q},0}^2$, respectively, and the conditional variances of $V'_{\text{LP},\text{I},r}(k T_s)$ and $V'_{\text{LP},\text{Q},r}(k T_s)$ for $N_1 = n$ and a binary one are denoted by $\sigma_{\text{I},1}^2$ and $\sigma_{\text{Q},1}^2$, respectively, we can write

$$\sigma_{\text{I},0}^2 = \sigma_{\text{Q},0}^2 = \frac{Z_{\text{TIA}}^2}{T_s} \left[\frac{n R_{\text{pd}} P_x e}{4 L_{\text{Tx}} L_{\text{Rx}} L_{\text{nw}}} + \frac{(4n^2 + 2n) R_{\text{pd}}^2 P_x^2 \tau_c}{128 L_{\text{Tx}}^2 L_{\text{Rx}}^2 L_{\text{nw}}^2} + S_{\text{th}} \right], \quad (\text{B.26})$$

$$\sigma_{\text{I},1}^2 = \frac{Z_{\text{TIA}}^2}{T_s} \left[\frac{(n+1) R_{\text{pd}} P_x e}{4 L_{\text{Tx}} L_{\text{Rx}} L_{\text{nw}}} + \frac{(4n^2 + 10n + 7) R_{\text{pd}}^2 P_x^2 \tau_c}{128 L_{\text{Tx}}^2 L_{\text{Rx}}^2 L_{\text{nw}}^2} + S_{\text{th}} \right], \quad (\text{B.27})$$

$$\sigma_{\text{Q},1}^2 = \frac{Z_{\text{TIA}}^2}{T_s} \left[\frac{(n+1) R_{\text{pd}} P_x e}{4 L_{\text{Tx}} L_{\text{Rx}} L_{\text{nw}}} + \frac{(4n^2 + 10n + 5) R_{\text{pd}}^2 P_x^2 \tau_c}{128 L_{\text{Tx}}^2 L_{\text{Rx}}^2 L_{\text{nw}}^2} + S_{\text{th}} \right]. \quad (\text{B.28})$$

Now the conditional probability functions $f_0(v)$ and $f_1(v)$ (for a binary zero and binary one, respectively) of the output samples $V_{\text{out},r}(k T_s)$ can be calculated. Following the theory in Subsection 5.2.5 the average probability of error is then given by

$$P_e = \left(\frac{1}{2} \right)^N \sum_{n=0}^{N-1} \binom{N-1}{n} \left[\int_{V_{\text{Th}}}^{\infty} f_0(v) dv + \int_{-\infty}^{V_{\text{Th}}} f_1(v) dv \right]. \quad (\text{B.29})$$

This is illustrated in Figure B.1, where the output sample $V_{\text{out},r}(k T_s)$ is constructed from $V_{\text{LP},\text{I},r}(k T_s)$ and $V_{\text{LP},\text{Q},r}(k T_s)$ as the square of the distance to the origin. As a result, the decision regions for a binary zero and a binary one are separated by a circle, of which the square of the radius equals the decision threshold V_{Th} . This is the dashed circle in Figure B.1. The dashed lines represent the projection axes from which the values of $V'_{\text{LP},\text{I},r}(k T_s)$ and $V'_{\text{LP},\text{Q},r}(k T_s)$ can be found. The angle between the $V'_{\text{LP},\text{I},r}(k T_s)$ -axis and the $V_{\text{LP},\text{Q},r}(k T_s)$ -axis is equal to $\Delta\phi_r - \frac{3\pi}{4}$.

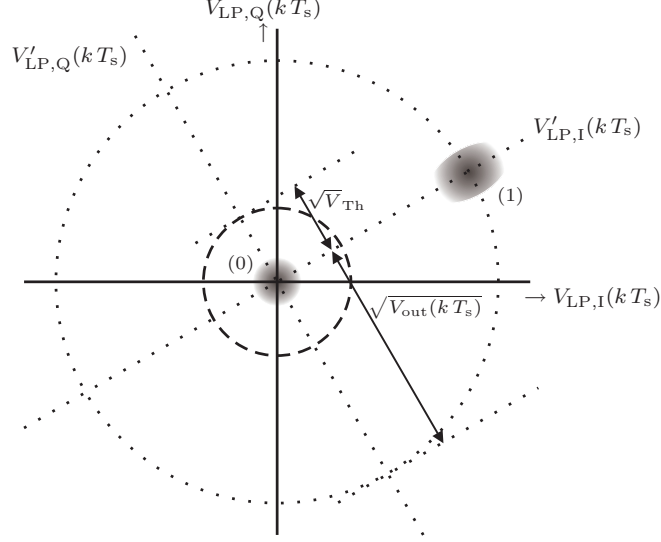


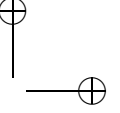
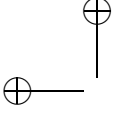
Figure B.1: Graphical construction of the output sample $V_{\text{out}}(k T_s)$ of a four-way OOK phase diversity receiver from the output samples of the low-pass filters $V_{\text{LP,I}}(k T_s)$ and $V_{\text{LP,Q}}(k T_s)$

When a binary zero is transmitted (so $A_{r,k} = 0$), both $V'_{\text{LP,I},r}(k T_s)$ and $V'_{\text{LP,Q},r}(k T_s)$ have zero mean and identical variances. (This is represented by the circular probability density cloud in the center of Figure B.1.) From (B.23) it then follows that the output sample $V_{\text{out},r}(k T_s)$ is central χ^2 -distributed with two degrees of freedom:

$$f_0(v) = \begin{cases} \frac{1}{2\sigma_{\text{I},0}^2} \exp\left(-\frac{v}{2\sigma_{\text{I},0}^2}\right) & , v \geq 0, \\ 0 & , v < 0. \end{cases} \quad (\text{B.30})$$

When a binary one is transmitted (so $A_{r,k} = 1$), $V'_{\text{LP,I},r}(k T_s)$ has a non-zero mean and the variances of $V'_{\text{LP,I},r}(k T_s)$ and $V'_{\text{LP,Q},r}(k T_s)$ are not the same anymore. (This is represented by the elliptical probability density cloud in Figure B.1.) Hence, it is not possible to find an exact analytical expression for the probability density function of $V_{\text{out},r}(k T_s)$. An approximation can be made for high SNRs, however: from the figure it follows that the probability that $V_{\text{out},r}(k T_s) < V_{\text{Th}}$ can be approximated by the probability that $V'_{\text{LP,I},r}(k T_s) < \sqrt{V_{\text{Th}}}$. In other words: when a binary one is transmitted, we can approximate

$$V_{\text{out},r}(k T_s) \approx \left(V'_{\text{LP,I},r}(k T_s)\right)^2, \quad (\text{B.31})$$



so that the conditional probability density function of $V_{\text{out},r}(kT_s)$ can be approximated as a non-central χ^2 -distribution with one degree of freedom:

$$f_1(v) \approx \begin{cases} \frac{1}{\sigma_{I,1}^2 \sqrt{2\pi v}} \exp\left(-\frac{v + \text{E}^2[V'_{\text{LP},I,r}(kT_s) | A_{r,k} = 1]}{2\sigma_{I,1}^2}\right) \\ \quad \cdot \cosh\left(\frac{\sqrt{v} \text{E}[V'_{\text{LP},I,r}(kT_s) | A_{r,k} = 1]}{\sigma_{I,1}^2}\right), & v \geq 0, \\ 0, & v < 0. \end{cases} \quad (\text{B.32})$$

When binary zeros and ones occur with equal probability, the optimum decision threshold corresponds to the point of intersection of (B.30) and (B.32), which can be approximated by

$$V_{\text{Th}} \approx \frac{1}{4} \text{E}^2[V'_{\text{LP},I,r}(kT_s) | A_{r,k} = 1] = \frac{Z_{\text{TIA}}^2 R_{\text{pd}}^2 P_x^2}{256 L_{\text{Tx}}^2 L_{\text{Rx}}^2 L_{\text{nw}}^2}. \quad (\text{B.33})$$

The average bit error probability now follows by carrying out the integration in (B.29), which results in (6.67).

B.3 Four-way phase-synchronized detection of QPSK

In a four-way phase-synchronized QPSK receiver (see Section 6.4.3) the expected values of the output samples of the low-pass filters are given by (6.56) and (6.57). When the conditional variances and covariance of $V_{\text{LP},I,r}(kT_s)$ and $V_{\text{LP},I,r}(kT_s)$ for a given value $a \in \{0, 1, 2, 3\}$ of the information symbol $A_{r,k}$ are denoted by $\sigma_{I,a}^2$, $\sigma_{Q,a}^2$ and $C_{\text{IQ},a}$, respectively, they can be found by substituting $m_{r,k} = 1$, (6.54) and $\Delta\phi_r = \frac{3\pi}{4}$ in (B.13) through (B.15), resulting in

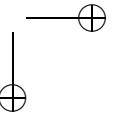
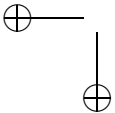
$$\sigma_{I,a}^2 = \sigma_{Q,a}^2 = \frac{Z_{\text{TIA}}^2}{T_s} \left[\frac{N R_{\text{pd}} P_x e}{4 L_{\text{Tx}} L_{\text{Rx}} L_{\text{nw}}} + \frac{(4N^2 + 2N) R_{\text{pd}}^2 P_x^2 \tau_c}{128 L_{\text{Tx}}^2 L_{\text{Rx}}^2 L_{\text{nw}}^2} + S_{\text{th}} \right], \quad (\text{B.34})$$

$$C_{\text{IQ},a} = \frac{Z_{\text{TIA}}^2 R_{\text{pd}}^2 P_x^2 \tau_c}{128 L_{\text{Tx}}^2 L_{\text{Rx}}^2 L_{\text{nw}}^2 T_s} (-1)^a. \quad (\text{B.35})$$

This is illustrated in Figure B.2, which shows the probability density clouds for the four different transmitted symbols. Note that these are not circular due to the correlation between the output samples. This implies that the bit errors in one symbol are correlated. (The probability that the second bit in one symbol is detected incorrectly given the fact that the first bit is detected incorrectly is larger than the average bit error rate.) From the symmetry of Figure B.2 it follows that the average bit error rate can be calculated as

$$P_e = \text{P}[V_{\text{LP},Q,r}(kT_s) < 0 | A_{r,k} = 0], \quad (\text{B.36})$$

which directly results in (6.78), because $V_{\text{LP},I,r}(kT_s)$ and $V_{\text{LP},Q,r}(kT_s)$ are Gaussian distributed for a given value of $A_{r,k}$.



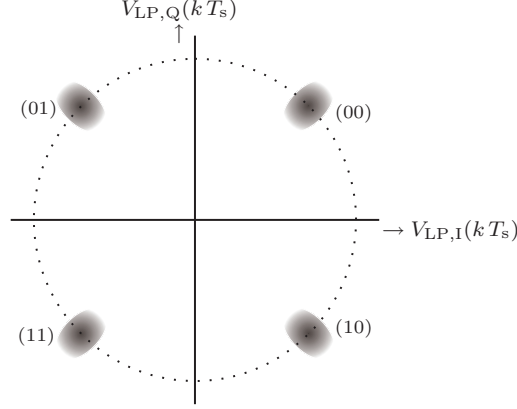


Figure B.2: Output samples of the low-pass filters $V_{LP,I,r}(kT_s)$ and $V_{LP,Q,r}(kT_s)$ in a four-way QPSK phase-synchronized receiver

B.4 Four-way phase-synchronized detection of M -ary PSK

In a four-way phase-synchronized M -ary PSK receiver with $M \geq 8$ (see Section 6.4.3) the expected values of the output samples of the low-pass filters are given by (6.56) and (6.57). The conditional variances and covariance $\sigma_{I,a}^2$, $\sigma_{Q,a}^2$ and $C_{IQ,a}$ can be found by substituting $m_{r,k} = 1$, (6.55) and $\Delta\phi_r = \frac{3\pi}{4}$ in (B.13) through (B.15), resulting in

$$\sigma_{I,a}^2 = \frac{Z_{TIA}^2}{T_s} \left\{ \frac{N R_{pd} P_x e}{4L_{Tx} L_{Rx} L_{nw}} + \left[\frac{4N^2 + 2N + \cos\left(\frac{a\pi}{M}\right)}{128L_{Tx}^2 L_{Rx}^2 L_{nw}^2} \right] R_{pd}^2 P_x^2 \tau_c + S_{th} \right\}, \quad (\text{B.37})$$

$$\sigma_{I,a}^2 = \frac{Z_{TIA}^2}{T_s} \left\{ \frac{N R_{pd} P_x e}{4L_{Tx} L_{Rx} L_{nw}} + \left[\frac{4N^2 + 2N - \cos\left(\frac{a\pi}{M}\right)}{128L_{Tx}^2 L_{Rx}^2 L_{nw}^2} \right] R_{pd}^2 P_x^2 \tau_c + S_{th} \right\}, \quad (\text{B.38})$$

$$C_{IQ,a} = \frac{Z_{TIA}^2 R_{pd}^2 P_x^2 \tau_c}{128L_{Tx}^2 L_{Rx}^2 L_{nw}^2 T_s} \sin\left(\frac{a\pi}{M}\right), \quad (\text{B.39})$$

where $a \in \{0, 1, \dots, M-1\}$. This is illustrated for 8-PSK in Figure B.3, which shows the probability clouds for the eight different transmitted symbols.

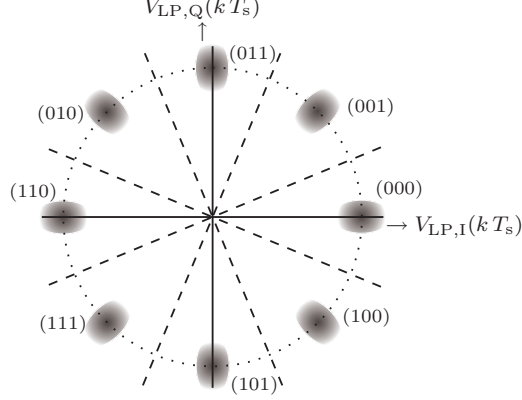


Figure B.3: Output samples of the low-pass filters $V_{\text{LP},I,r}(kT_s)$ and $V_{\text{LP},Q,r}(kT_s)$ in a four-way 8-PSK phase-synchronized receiver

From the symmetry of Figure B.3 it follows that the average symbol error rate can be calculated as the conditional probability of symbol error when $A_{r,k} = 0$ is transmitted. In that case, it follows from (B.39) that $V_{\text{LP},I,r}(kT_s)$ and $V_{\text{LP},Q,r}(kT_s)$ are uncorrelated and hence—since they are jointly Gaussian distributed—independent. Since $V_{\text{LP},Q,r}(kT_s)$ has zero mean the conditional joint probability function can be written as

$$f_{\text{IQ},0}(v_I, v_Q) = \frac{1}{2\pi\sigma_{\text{I},0}\sigma_{\text{Q},0}} \exp\left(-\frac{(v_I - \mu_{\text{I},0})^2}{2\sigma_{\text{I},0}^2} - \frac{v_Q^2}{2\sigma_{\text{Q},0}^2}\right), \quad (\text{B.40})$$

where

$$\mu_{\text{I},0} \triangleq \text{E}[V_{\text{LP},I,r}(kT_s) | A_{r,k} = 0] = \frac{Z_{\text{TIA}} R_{\text{pd}} P_x}{8L_{\text{Tx}} L_{\text{Rx}} L_{\text{nw}}}, \quad (\text{B.41})$$

$$\begin{aligned} \sigma_{\text{I},0}^2 &\triangleq \sigma_{V_{\text{LP},I,r}(kT_s) | A_{r,k}=0}^2 \\ &= \frac{Z_{\text{TIA}}^2}{T_s} \left[\frac{N R_{\text{pd}} P_x e}{4L_{\text{Tx}} L_{\text{Rx}} L_{\text{nw}}} + \frac{(4N^2 + 2N + 1) R_{\text{pd}}^2 P_x^2 \tau_c}{128L_{\text{Tx}}^2 L_{\text{Rx}}^2 L_{\text{nw}}^2} + S_{\text{th}} \right], \end{aligned} \quad (\text{B.42})$$

$$\begin{aligned} \sigma_{\text{Q},0}^2 &\triangleq \sigma_{V_{\text{LP},Q,r}(kT_s) | A_{r,k}=0}^2 \\ &= \frac{Z_{\text{TIA}}^2}{T_s} \left[\frac{N R_{\text{pd}} P_x e}{4L_{\text{Tx}} L_{\text{Rx}} L_{\text{nw}}} + \frac{(4N^2 + 2N - 1) R_{\text{pd}}^2 P_x^2 \tau_c}{128L_{\text{Tx}}^2 L_{\text{Rx}}^2 L_{\text{nw}}^2} + S_{\text{th}} \right]. \end{aligned} \quad (\text{B.43})$$

The conditional probability function of the estimated phase Φ_0 can be obtained by making the following variable transformation in (B.40):

$$R = \sqrt{V_{\text{LP},I,r}^2(kT_s) + V_{\text{LP},Q,r}^2(kT_s)}, \quad (\text{B.44})$$

$$\Phi = \arctan \left[\frac{V_{\text{LP},Q,r}(kT_s)}{V_{\text{LP},I,r}(kT_s)} \right]. \quad (\text{B.45})$$

This results in a conditional joint probability density function

$$f_{R\Phi,0}(r, \phi) = \begin{cases} \frac{r}{2\pi\sigma_{I,0}\sigma_{Q,0}} \exp\left\{ -\frac{\sigma_{Q,0}^2 + (\sigma_{I,0}^2 - \sigma_{Q,0}^2) \sin^2 \phi}{2\sigma_{I,0}^2\sigma_{Q,0}^2} \right. \\ \quad \cdot \left(r - \frac{\mu_{I,0} \sigma_{Q,0}^2 \cos \phi}{\sigma_{Q,0}^2 + (\sigma_{I,0}^2 - \sigma_{Q,0}^2) \sin^2 \phi} \right)^2 \\ \quad \left. - \frac{\frac{1}{2}\mu_{I,0}^2 \sin^2 \phi}{\sigma_{Q,0}^2 + (\sigma_{I,0}^2 - \sigma_{Q,0}^2) \sin^2 \phi} \right\}, & r \geq 0, \\ 0 & , r < 0. \end{cases} \quad (\text{B.46})$$

Since $(\sigma_{I,0}^2 - \sigma_{Q,0}^2) \ll \sigma_{Q,0}^2$, this can be approximated as

$$f_{R\Phi,0}(r, \phi) \approx \begin{cases} \frac{r}{2\pi\sigma_{I,0}\sigma_{Q,0}} \exp\left(-\frac{(r - \mu_{I,0} \cos \phi)^2}{2\sigma_{I,0}^2} - \frac{\mu_{I,0}^2 \sin^2 \phi}{2\sigma_{Q,0}^2} \right), & r \geq 0, \\ 0 & , r < 0. \end{cases} \quad (\text{B.47})$$

The conditional probability density function of Φ can be found by integrating this over the range of r . For high SNRs (so when $\mu_{I,0} \gg \sigma_{I,0}$) and $\phi \leq \pi/M$ this can be approximated as

$$\begin{aligned} f_{\Phi,0}(\phi) &= \int_0^\infty f_{R\Phi,0}(r, \phi) \, dr \\ &\approx \frac{1}{2\pi\sigma_{I,0}\sigma_{Q,0}} \int_{-\infty}^\infty \mu_{I,0} \cos \phi \exp\left(-\frac{(r - \mu_{I,0} \cos \phi)^2}{2\sigma_{I,0}^2} - \frac{\mu_{I,0}^2 \sin^2 \phi}{2\sigma_{Q,0}^2} \right) \, dr \\ &\approx \frac{\mu_{I,0}}{\sigma_{Q,0}\sqrt{2\pi}} \cos \phi \exp\left(-\frac{\mu_{I,0}^2 \sin^2 \phi}{2\sigma_{Q,0}^2} \right). \end{aligned} \quad (\text{B.48})$$

The probability of a symbol error now follows from

$$\begin{aligned} P_{\text{es}} &= 1 - \int_{-\pi/M}^{\pi/M} f_{\Phi,0}(\phi) \, d\phi \\ &\approx 1 - \frac{\mu_{I,0}}{\sigma_{Q,0}\sqrt{2\pi}} \int_{-\pi/M}^{\pi/M} \cos \phi \exp\left(-\frac{\mu_{I,0}^2 \sin^2 \phi}{2\sigma_{Q,0}^2} \right) \, d\phi. \end{aligned} \quad (\text{B.49})$$

Substituting $x = \sin \phi$ we find

$$\begin{aligned} P_{\text{es}} &\approx 1 - \frac{\mu_{I,0}}{\sigma_{Q,0}\sqrt{2\pi}} \int_{-\sin(\pi/M)}^{\sin(\pi/M)} \exp\left(-\frac{\mu_{I,0}^2 x^2}{2\sigma_{Q,0}^2} \right) \, dx \\ &= 2 \, \text{Q}\left(\sqrt{2\gamma_{\text{MPSK}}} \sin\left(\frac{\pi}{M} \right) \right), \end{aligned} \quad (\text{B.50})$$

where

$$\gamma_{\text{MPSK}} = \frac{\mu_{I,0}^2}{2\sigma_{Q,0}^2} = \left(\gamma_{\text{sn}}^{-1} + \gamma_{\text{bn}}^{-1} + \gamma_{\text{tn}}^{-1} \right)^{-1}, \quad (\text{B.51})$$

and

$$\gamma_{\text{sn}} = \frac{R_{\text{pd}} P_x T_s}{32N L_{\text{Tx}} L_{\text{Rx}} L_{\text{nw}} e}, \quad (\text{B.52})$$

$$\gamma_{\text{bn}} = \frac{T_s}{(4N^2 + 2N - 1)\tau_c}, \quad (\text{B.53})$$

$$\gamma_{\text{tn}} = \frac{R_{\text{pd}}^2 P_x^2 T_s}{128L_{\text{Tx}}^2 L_{\text{Rx}}^2 L_{\text{nw}}^2 S_{\text{th}}}. \quad (\text{B.54})$$

When Gray coding is used for assigning m bits to one symbol, adjacent symbols differ by only one bit (see Figure 6.9). Hence, when an error occurs in an m -bit symbol, then there is a high probability that it results in only one bit error. Therefore, the probability of a bit error can be approximated as

$$P_e \approx \frac{1}{m} P_{e_s}, \quad (\text{B.55})$$

which results in (6.83).

B.5 Four-way phase diversity detection of binary DPSK

For the four-way binary DPSK phase diversity receiver the output samples $\{V_{\text{out},r}(kT_s)\}$ can be written as

$$\begin{aligned} V_{\text{out},r}(kT_s) &= V_{\text{LP},I,r}(kT_s)V_{\text{LP},I,r}((k-1)T_s) \\ &\quad + V_{\text{LP},Q,r}(kT_s)V_{\text{LP},Q,r}((k-1)T_s) \\ &= \mathbf{V}_{\text{LP},r,k}^T \mathbf{V}_{\text{LP},r,k-1} = \left(\mathbf{V}'_{\text{LP},r,k} \right)^T \mathbf{A}_{r,k}^T \mathbf{A}_{r,k-1} \mathbf{V}'_{\text{LP},r,k-1}. \end{aligned} \quad (\text{B.56})$$

From (6.61), (B.17), (B.19) and (B.20) it follows that in case of binary DPSK modulation we have

$$\mathbf{A}_{r,k}^T \mathbf{A}_{r,k-1} = \begin{bmatrix} (-1)^{A_{r,k}} & 0 \\ 0 & (-1)^{A_{r,k}} \end{bmatrix}, \quad (\text{B.57})$$

so that (B.56) reduces to

$$\begin{aligned} V_{\text{out},r}(kT_s) &= (-1)^{A_{r,k}} \left(\mathbf{V}'_{\text{LP},r,k} \right)^T \mathbf{V}'_{\text{LP},r,k-1} \\ &= (-1)^{A_{r,k}} \left[V'_{\text{LP},I,r}(kT_s)V'_{\text{LP},I,r}((k-1)T_s) \right. \\ &\quad \left. + V'_{\text{LP},Q,r}(kT_s)V'_{\text{LP},Q,r}((k-1)T_s) \right], \end{aligned} \quad (\text{B.58})$$

where $V'_{LP,I,r}(kT_s)$, $V'_{LP,I,r}((k-1)T_s)$, $V'_{LP,Q,r}(kT_s)$ and $V'_{LP,Q,r}((k-1)T_s)$ are independent Gaussian random variables with expected values and variances

$$\mathbb{E} [V'_{LP,I,r}(kT_s)] = \mathbb{E} [V'_{LP,I,r}((k-1)T_s)] = \frac{Z_{TIA} R_{pd} P_x}{8L_{Tx} L_{Rx} L_{nw}}, \quad (\text{B.59})$$

$$\mathbb{E} [V'_{LP,Q,r}(kT_s)] = \mathbb{E} [V'_{LP,Q,r}((k-1)T_s)] = 0, \quad (\text{B.60})$$

$$\begin{aligned} \sigma_{V'_{LP,I,r}(kT_s)}^2 &= \sigma_{V'_{LP,I,r}((k-1)T_s)}^2 \\ &= \frac{Z_{TIA}^2}{T_s} \left[\frac{N R_{pd} P_x e}{4L_{Tx} L_{Rx} L_{nw}} + \frac{(4N^2 + 2N + 1) R_{pd}^2 P_x^2 \tau_c}{128L_{Tx}^2 L_{Rx}^2 L_{nw}^2} + S_{th} \right], \end{aligned} \quad (\text{B.61})$$

$$\begin{aligned} \sigma_{V'_{LP,Q,r}(kT_s)}^2 &= \sigma_{V'_{LP,Q,r}((k-1)T_s)}^2 \\ &= \frac{Z_{TIA}^2}{T_s} \left[\frac{N R_{pd} P_x e}{4L_{Tx} L_{Rx} L_{nw}} + \frac{(4N^2 + 2N - 1) R_{pd}^2 P_x^2 \tau_c}{128L_{Tx}^2 L_{Rx}^2 L_{nw}^2} + S_{th} \right]. \end{aligned} \quad (\text{B.62})$$

From the symmetry of (B.58) it follows that the probability of a bit error is given by

$$\begin{aligned} P_e &= \mathbb{P} [V_{out,r}(kT_s) < 0 \mid A_{r,k} = 0] \\ &= \mathbb{P} [V'_{LP,I,r}(kT_s)V'_{LP,I,r}((k-1)T_s) \\ &\quad + V'_{LP,Q,r}(kT_s)V'_{LP,Q,r}((k-1)T_s) < 0]. \end{aligned} \quad (\text{B.63})$$

By defining

$$\begin{aligned} \alpha &\triangleq \left[V'_{LP,I,r}(kT_s) + V'_{LP,I,r}((k-1)T_s) \right]^2 \\ &\quad + \left[V'_{LP,Q,r}(kT_s) + V'_{LP,Q,r}((k-1)T_s) \right]^2, \end{aligned} \quad (\text{B.64})$$

$$\begin{aligned} \beta &\triangleq \left[V'_{LP,I,r}(kT_s) - V'_{LP,I,r}((k-1)T_s) \right]^2 \\ &\quad + \left[V'_{LP,Q,r}(kT_s) - V'_{LP,Q,r}((k-1)T_s) \right]^2, \end{aligned} \quad (\text{B.65})$$

we can write

$$\begin{aligned} \alpha - \beta &= 4 \left[V'_{LP,I,r}(kT_s)V'_{LP,I,r}((k-1)T_s) \right. \\ &\quad \left. + V'_{LP,Q,r}(kT_s)V'_{LP,Q,r}((k-1)T_s) \right], \end{aligned} \quad (\text{B.66})$$

so that (B.63) can be written as

$$P_e = \mathbb{P} [\beta > \alpha]. \quad (\text{B.67})$$

Since α and β can be proven to be independent, this can be written as

$$P_e = \int_0^\infty f_\alpha(a) \int_a^\infty f_\beta(b) db da. \quad (\text{B.68})$$

Since $V'_{\text{LP,I},r}(kT_s)$, $V'_{\text{LP,I},r}((k-1)T_s)$, $V'_{\text{LP,Q},r}(kT_s)$ and $V'_{\text{LP,Q},r}((k-1)T_s)$ are Gaussian with nearly identical variances, α is approximately non-central χ^2 -distributed with two degrees of freedom and β is approximately central χ^2 -distributed with two degrees of freedom:

$$f_\alpha(a) \approx \begin{cases} \frac{1}{2\sigma^2} \exp\left(-\frac{a+\mu^2}{2\sigma^2}\right) I_0\left(\frac{\sqrt{a}\mu}{\sigma^2}\right) & , a \geq 0, \\ 0 & , a < 0, \end{cases} \quad (\text{B.69})$$

$$f_\beta(b) \approx \begin{cases} \frac{1}{2\sigma^2} \exp\left(-\frac{b}{2\sigma^2}\right) & , b \geq 0, \\ 0 & , b < 0, \end{cases} \quad (\text{B.70})$$

where

$$\mu \triangleq 2E[V'_{\text{LP,I},r}(kT_s)], \quad (\text{B.71})$$

$$\sigma^2 \triangleq 2\sigma_{V'_{\text{LP,I},r}(kT_s)}^2, \quad (\text{B.72})$$

and $I_n(\cdot)$ is the modified Bessel function of the first kind and order n :

$$I_n(x) \triangleq \frac{1}{2\pi} \int_0^{2\pi} \exp(x \cos \theta) \cos(n\theta) d\theta, \quad n \in \mathbb{Z}. \quad (\text{B.73})$$

As a result, we can write

$$\begin{aligned} P_e &\approx \int_0^\infty \frac{1}{2\sigma^2} \exp\left(-\frac{a+\mu^2}{2\sigma^2}\right) I_0\left(\frac{\sqrt{a}\mu}{\sigma^2}\right) \int_a^\infty \frac{1}{2\sigma^2} \exp\left(-\frac{a}{2\sigma^2}\right) db da \\ &= \int_0^\infty \frac{1}{2\sigma^2} \exp\left(-\frac{2a+\mu^2}{2\sigma^2}\right) I_0\left(\frac{\sqrt{a}\mu}{\sigma^2}\right) da \\ &= \frac{1}{2} \exp\left(-\frac{\mu^2}{4\sigma^2}\right) \int_0^\infty \frac{1}{2\left(\frac{1}{2}\sigma^2\right)} \exp\left(-\frac{a+\left(\frac{1}{2}\mu\right)^2}{2\left(\frac{1}{2}\sigma^2\right)}\right) I_0\left(\frac{\sqrt{a}\frac{1}{2}\mu}{\frac{1}{2}\sigma^2}\right) da. \end{aligned} \quad (\text{B.74})$$

The expression inside the integral is recognized as a χ^2 -distribution, so that the integral evaluates to one and the bit error probability in (6.89) results.

B.6 Four-way phase diversity detection of DQPSK

The output samples $\{V_{\text{DI},r}(kT_s)\}$ of the four-way DQPSK phase diversity receiver are given by the expression for $V_{\text{out},r}(kT_s)$ in (B.56), whereas the output

samples $\{V_{\text{DQ},r}(k T_s)\}$ follow from

$$\begin{aligned}
V_{\text{DQ},r}(k T_s) &= V_{\text{LP},\text{Q},r}(k T_s)V_{\text{LP},\text{I},r}((k-1)T_s) \\
&\quad + V_{\text{LP},\text{Q},r}(k T_s)V_{\text{LP},\text{I},r}((k-1)T_s) \\
&= \mathbf{V}_{\text{LP},r,k}^{\text{T}} \begin{bmatrix} 0 & -1 \\ 1 & 0 \end{bmatrix} \mathbf{V}_{\text{LP},r,k-1} \\
&= \left(\mathbf{V}'_{\text{LP},r,k}\right)^{\text{T}} \mathbf{A}_{r,k}^{\text{T}} \begin{bmatrix} 0 & -1 \\ 1 & 0 \end{bmatrix} \mathbf{A}_{r,k-1} \mathbf{V}'_{\text{LP},r,k-1}. \quad (\text{B.75})
\end{aligned}$$

From (6.63), (B.17), (B.19) and (B.20) it follows that in case of DQPSK modulation we have

$$\mathbf{A}_{r,k}^{\text{T}} \mathbf{A}_{r,k-1} = \begin{bmatrix} \cos\left((2A_{r,k} + 1)\frac{\pi}{4}\right) & \sin\left((2A_{r,k} + 1)\frac{\pi}{4}\right) \\ -\sin\left((2A_{r,k} + 1)\frac{\pi}{4}\right) & \cos\left((2A_{r,k} + 1)\frac{\pi}{4}\right) \end{bmatrix}, \quad (\text{B.76})$$

$$\begin{aligned}
\mathbf{A}_{r,k}^{\text{T}} \begin{bmatrix} 0 & -1 \\ 1 & 0 \end{bmatrix} \mathbf{A}_{r,k-1} &= \\
&\begin{bmatrix} \sin\left((2A_{r,k} + 1)\frac{\pi}{4}\right) & -\cos\left((2A_{r,k} + 1)\frac{\pi}{4}\right) \\ \cos\left((2A_{r,k} + 1)\frac{\pi}{4}\right) & \sin\left((2A_{r,k} + 1)\frac{\pi}{4}\right) \end{bmatrix}. \quad (\text{B.77})
\end{aligned}$$

Now we can write for the output samples

$$\begin{aligned}
V_{\text{DI},r}(k T_s) &= \cos\left((2A_{r,k} + 1)\frac{\pi}{4}\right) \left[V'_{\text{LP},\text{I},r}(k T_s)V'_{\text{LP},\text{I},r}((k-1)T_s) \right. \\
&\quad \left. + V'_{\text{LP},\text{Q},r}(k T_s)V'_{\text{LP},\text{Q},r}((k-1)T_s) \right] \\
&\quad + \sin\left((2A_{r,k} + 1)\frac{\pi}{4}\right) \left[V'_{\text{LP},\text{I},r}(k T_s)V'_{\text{LP},\text{Q},r}((k-1)T_s) \right. \\
&\quad \left. - V'_{\text{LP},\text{Q},r}(k T_s)V'_{\text{LP},\text{I},r}((k-1)T_s) \right], \quad (\text{B.78})
\end{aligned}$$

$$\begin{aligned}
V_{\text{DQ},r}(k T_s) &= \sin\left((2A_{r,k} + 1)\frac{\pi}{4}\right) \left[V'_{\text{LP},\text{I},r}(k T_s)V'_{\text{LP},\text{I},r}((k-1)T_s) \right. \\
&\quad \left. + V'_{\text{LP},\text{Q},r}(k T_s)V'_{\text{LP},\text{Q},r}((k-1)T_s) \right] \\
&\quad - \cos\left((2A_{r,k} + 1)\frac{\pi}{4}\right) \left[V'_{\text{LP},\text{I},r}(k T_s)V'_{\text{LP},\text{Q},r}((k-1)T_s) \right. \\
&\quad \left. - V'_{\text{LP},\text{Q},r}(k T_s)V'_{\text{LP},\text{I},r}((k-1)T_s) \right]. \quad (\text{B.79})
\end{aligned}$$

where $V'_{\text{LP,I},r}(kT_s)$, $V'_{\text{LP,I},r}((k-1)T_s)$, $V'_{\text{LP,Q},r}(kT_s)$ and $V'_{\text{LP,Q},r}((k-1)T_s)$ are independent Gaussian random variables with expected values and variances that are given in (B.59) through (B.62). From the symmetry of (B.78) and (B.79) it follows that the probability of a bit error is given by

$$\begin{aligned} P_e &= \text{P} \left[V_{\text{DI},r}(kT_s) < 0 \mid A_{r,k} = 0 \right] \\ &= \text{P} \left[V'_{\text{LP,I},r}(kT_s)V'_{\text{LP,I},r}((k-1)T_s) \right. \\ &\quad + V'_{\text{LP,Q},r}(kT_s)V'_{\text{LP,Q},r}((k-1)T_s) \\ &\quad + V'_{\text{LP,I},r}(kT_s)V'_{\text{LP,Q},r}((k-1)T_s) \\ &\quad \left. - V'_{\text{LP,Q},r}(kT_s)V'_{\text{LP,I},r}((k-1)T_s) < 0 \right]. \end{aligned} \quad (\text{B.80})$$

By defining

$$\begin{aligned} \alpha &\triangleq \left[V'_{\text{LP,I},r}(kT_s) + V'_{\text{LP,Q},r}(kT_s) + \sqrt{2}V'_{\text{LP,Q},r}((k-1)T_s) \right]^2 \\ &\quad + \left[V'_{\text{LP,I},r}(kT_s) + \sqrt{2}V'_{\text{LP,I},r}((k-1)T_s) - V'_{\text{LP,Q},r}(kT_s) \right]^2, \end{aligned} \quad (\text{B.81})$$

$$\begin{aligned} \beta &\triangleq \left[V'_{\text{LP,I},r}(kT_s) + V'_{\text{LP,Q},r}(kT_s) - \sqrt{2}V'_{\text{LP,Q},r}((k-1)T_s) \right]^2 \\ &\quad + \left[V'_{\text{LP,I},r}(kT_s) - \sqrt{2}V'_{\text{LP,I},r}((k-1)T_s) - V'_{\text{LP,Q},r}(kT_s) \right]^2, \end{aligned} \quad (\text{B.82})$$

we can write

$$\begin{aligned} \alpha - \beta &= 4\sqrt{2} \left[V'_{\text{LP,I},r}(kT_s)V'_{\text{LP,I},r}((k-1)T_s) \right. \\ &\quad + V'_{\text{LP,Q},r}(kT_s)V'_{\text{LP,Q},r}((k-1)T_s) \\ &\quad + V'_{\text{LP,I},r}(kT_s)V'_{\text{LP,Q},r}((k-1)T_s) \\ &\quad \left. - V'_{\text{LP,Q},r}(kT_s)V'_{\text{LP,I},r}((k-1)T_s) \right], \end{aligned} \quad (\text{B.83})$$

so that (B.80) can be written as

$$P_e = \text{P}[\beta > \alpha]. \quad (\text{B.84})$$

When the variances of the output samples of the low-pass filters are approximated by

$$\begin{aligned} \sigma_{V'_{\text{LP,I},r}(kT_s)}^2 &= \sigma_{V'_{\text{LP,I},r}((k-1)T_s)}^2 \approx \sigma_{V'_{\text{LP,Q},r}(kT_s)}^2 = \sigma_{V'_{\text{LP,Q},r}((k-1)T_s)}^2 \\ &\approx \frac{Z_{\text{TIA}}^2}{T_s} \left[\frac{N R_{\text{pd}} P_x e}{4L_{\text{Tx}} L_{\text{Rx}} L_{\text{nw}}} + \frac{(4N^2 + 2N) R_{\text{pd}}^2 P_x^2 \tau_c}{128L_{\text{Tx}}^2 L_{\text{Rx}}^2 L_{\text{nw}}^2} + S_{\text{th}} \right], \end{aligned} \quad (\text{B.85})$$

then we find that α and β are independent and non-central χ^2 -distributed with two degrees of freedom:

$$f_\alpha(a) \approx \begin{cases} \frac{1}{2\sigma^2} \exp\left(-\frac{a + \mu_\alpha^2}{2\sigma^2}\right) I_0\left(\frac{\sqrt{a}\mu_\alpha}{\sigma^2}\right) & , a \geq 0, \\ 0 & , a < 0, \end{cases} \quad (\text{B.86})$$

$$f_\beta(b) \approx \begin{cases} \frac{1}{2\sigma^2} \exp\left(-\frac{b + \mu_\beta^2}{2\sigma^2}\right) I_0\left(\frac{\sqrt{b}\mu_\beta}{\sigma^2}\right) & , b \geq 0, \\ 0 & , b < 0, \end{cases} \quad (\text{B.87})$$

where

$$\begin{aligned} \mu_\alpha &\triangleq \sqrt{\text{E}^2[V'_{\text{LP},\text{I},r}(kT_s)] + \text{E}^2[V'_{\text{LP},\text{I},r}(kT_s) + \sqrt{2}V'_{\text{LP},\text{I},r}((k-1)T_s)]} \\ &= \sqrt{4 + 2\sqrt{2}\text{E}[V'_{\text{LP},\text{I},r}(kT_s)]}, \end{aligned} \quad (\text{B.88})$$

$$\begin{aligned} \mu_\beta &\triangleq \sqrt{\text{E}^2[V'_{\text{LP},\text{I},r}(kT_s)] + \text{E}^2[V'_{\text{LP},\text{I},r}(kT_s) - \sqrt{2}V'_{\text{LP},\text{I},r}((k-1)T_s)]}, \\ &= \sqrt{4 - 2\sqrt{2}\text{E}[V'_{\text{LP},\text{I},r}(kT_s)]} \end{aligned} \quad (\text{B.89})$$

$$\begin{aligned} \sigma^2 &\triangleq \sigma_{V'_{\text{LP},\text{I},r}(kT_s)}^2 + \sigma_{V'_{\text{LP},\text{Q},r}(kT_s)}^2 + 2\sigma_{V'_{\text{LP},\text{Q},r}((k-1)T_s)}^2 \\ &\approx \frac{4Z_{\text{TIA}}^2}{T_s} \left[\frac{N R_{\text{pd}} P_x e}{4L_{\text{Tx}} L_{\text{Rx}} L_{\text{nw}}} + \frac{(4N^2 + 2N) R_{\text{pd}}^2 P_x^2 \tau_c}{128L_{\text{Tx}}^2 L_{\text{Rx}}^2 L_{\text{nw}}^2} + S_{\text{th}} \right]. \end{aligned} \quad (\text{B.90})$$

Hence, we find for the bit error probability

$$\begin{aligned} P_e &= \int_0^\infty f_\alpha(a) \int_a^\infty f_\beta(b) db da \\ &= \int_0^\infty \int_a^\infty \frac{1}{4\sigma^4} \exp\left(-\frac{a+b+\mu_\alpha^2+\mu_\beta^2}{2\sigma^2}\right) I_0\left(\frac{\sqrt{a}\mu_\alpha}{\sigma^2}\right) I_0\left(\frac{\sqrt{b}\mu_\beta}{\sigma^2}\right) db da \\ &= \int_0^\infty \int_x^\infty xy \exp\left(-\frac{1}{2}(x^2+y^2+4\gamma_{\text{DQPSK}})\right) I_0\left(x\sqrt{2+\sqrt{2}\sqrt{\gamma_{\text{DQPSK}}}}\right) \\ &\quad \cdot I_0\left(y\sqrt{2-\sqrt{2}\sqrt{\gamma_{\text{DQPSK}}}}\right) dy dx \\ &= \int_0^\infty x \exp\left(-\frac{1}{2}(x^2+B^2)\right) I_0(Bx) \\ &\quad \cdot \int_x^\infty y \exp\left(-\frac{1}{2}(y^2+A^2)\right) I_0(Ay) dy dx, \end{aligned} \quad (\text{B.91})$$

where

$$A \triangleq \sqrt{2 - \sqrt{2}} \sqrt{\frac{\gamma_{\text{DQPSK}}}{2}}, \quad (\text{B.92})$$

$$B \triangleq \sqrt{2 + \sqrt{2}} \sqrt{\frac{\gamma_{\text{DQPSK}}}{2}}, \quad (\text{B.93})$$

$$\gamma_{\text{DQPSK}} \triangleq \frac{\mu_\alpha^2 + \mu_\beta^2}{4\sigma^2} = \frac{\text{E}^2[V'_{\text{LP},\text{I},r}(kT_s)]}{2\sigma_{V'_{\text{LP},\text{I},r}(kT_s)}^2}. \quad (\text{B.94})$$

According to [112] this can be rewritten as

$$P_e = Q_1(A, B) - \frac{1}{2} \exp\left(-\frac{1}{2}(A^2 + B^2)\right) I_0(AB), \quad (\text{B.95})$$

where $Q_1(\cdot, \cdot)$ is Marcum's Q-function:

$$Q_1(A, B) \triangleq \int_B^\infty x \exp\left(-\frac{1}{2}(x^2 + A^2)\right) I_0(Ax) dx. \quad (\text{B.96})$$

Since Marcum's Q-function can also be written as

$$Q_1(A, B) = \exp\left(-\frac{1}{2}(A^2 + B^2)\right) \sum_{n=0}^{\infty} \left(\frac{A}{B}\right)^n I_n(AB), \quad (\text{B.97})$$

the bit error probability can be reduced to (6.95).

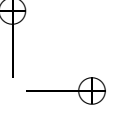
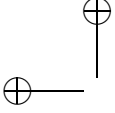
B.7 Three-way phase diversity detection of OOK

Like in the case of the four-way receiver, the output samples of the low-pass filters can be written as a vector

$$\mathbf{V}_{\text{LP},r,k} \triangleq \begin{bmatrix} V_{\text{LP},a,r}(kT_s) \\ V_{\text{LP},b,r}(kT_s) \\ V_{\text{LP},c,r}(kT_s) \end{bmatrix}. \quad (\text{B.98})$$

The expected value of $\mathbf{V}_{\text{LP},r,k}$ follows by substituting (5.2) in (6.50) through (6.52). In case of OOK modulation and matched filtering this becomes

$$\text{E}[\mathbf{V}_{\text{LP},r,k}] = \frac{Z_{\text{TIA}} R_{\text{pd}} P_x T_s}{4\sqrt{3} L_{\text{Tx}} L_{\text{Rx}} L_{\text{nw}}} m_{r,k} \begin{bmatrix} \cos\left(\Delta\phi_r + \frac{2\pi}{3}\right) \\ \cos(\Delta\phi_r) \\ \cos\left(\Delta\phi_r - \frac{2\pi}{3}\right) \end{bmatrix}. \quad (\text{B.99})$$

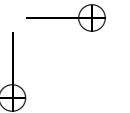
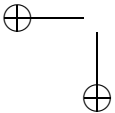


The elements of the covariance matrix of $\mathbf{V}_{LP,r,k}$ depend on the implementation form of the three-way receiver, as amplification can be performed either prior to or after balancing. These situations can be analyzed simultaneously, however, by denoting the equivalent input noise current of an eventual TIA before balancing by $S_{th,pre}$ and an eventual TIA after balancing by $S_{th,post}$. (So $S_{th,pre} = 0$ if amplification is performed after balancing and $S_{th,post} = 0$ if amplification is performed prior to balancing.) This results in the following elements of the covariance matrix:

$$\begin{aligned}
 R_{V_{LP,a,r}V_{LP,a,r}}(t_1, t_2) = & \\
 & Z_{TIA} R_{pd} e \int_{-\infty}^{\infty} h_{LP}(t_1 - \rho) h_{LP}(t_2 - \rho) E[P_{z_1}(\rho) + P_{z_2}(\rho)] d\rho \\
 & + Z_{TIA}^2 R_{pd}^2 \int_{-\infty}^{\infty} \int_{-\infty}^{\infty} h_{LP}(t_1 - \rho_1) h_{LP}(t_2 - \rho_2) \left[R_{P_{z_1}P_{z_1}}(\rho_1, \rho_2) \right. \\
 & \quad \left. - R_{P_{z_1}P_{z_2}}(\rho_1, \rho_2) - R_{P_{z_2}P_{z_1}}(\rho_1, \rho_2) + R_{P_{z_2}P_{z_2}}(\rho_1, \rho_2) \right] d\rho_1 d\rho_2 \\
 & + Z_{TIA}^2 (2S_{th,pre} + S_{th,post}) \int_{-\infty}^{\infty} h_{LP}(t_1 - \rho) h_{LP}(t_2 - \rho) d\rho, \quad (B.100)
 \end{aligned}$$

$$\begin{aligned}
 R_{V_{LP,b,r}V_{LP,b,r}}(t_1, t_2) = & \\
 & Z_{TIA} R_{pd} e \int_{-\infty}^{\infty} h_{LP}(t_1 - \rho) h_{LP}(t_2 - \rho) E[P_{z_2}(\rho) + P_{z_3}(\rho)] d\rho \\
 & + Z_{TIA}^2 R_{pd}^2 \int_{-\infty}^{\infty} \int_{-\infty}^{\infty} h_{LP}(t_1 - \rho_1) h_{LP}(t_2 - \rho_2) \left[R_{P_{z_2}P_{z_2}}(\rho_1, \rho_2) \right. \\
 & \quad \left. - R_{P_{z_2}P_{z_3}}(\rho_1, \rho_2) - R_{P_{z_3}P_{z_2}}(\rho_1, \rho_2) + R_{P_{z_3}P_{z_3}}(\rho_1, \rho_2) \right] d\rho_1 d\rho_2 \\
 & + Z_{TIA}^2 (2S_{th,pre} + S_{th,post}) \int_{-\infty}^{\infty} h_{LP}(t_1 - \rho) h_{LP}(t_2 - \rho) d\rho, \quad (B.101)
 \end{aligned}$$

$$\begin{aligned}
 R_{V_{LP,c,r}V_{LP,c,r}}(t_1, t_2) = & \\
 & Z_{TIA} R_{pd} e \int_{-\infty}^{\infty} h_{LP}(t_1 - \rho) h_{LP}(t_2 - \rho) E[P_{z_1}(\rho) + P_{z_3}(\rho)] d\rho \\
 & + Z_{TIA}^2 R_{pd}^2 \int_{-\infty}^{\infty} \int_{-\infty}^{\infty} h_{LP}(t_1 - \rho_1) h_{LP}(t_2 - \rho_2) \left[R_{P_{z_1}P_{z_1}}(\rho_1, \rho_2) \right. \\
 & \quad \left. - R_{P_{z_1}P_{z_3}}(\rho_1, \rho_2) - R_{P_{z_3}P_{z_1}}(\rho_1, \rho_2) + R_{P_{z_3}P_{z_3}}(\rho_1, \rho_2) \right] d\rho_1 d\rho_2 \\
 & + Z_{TIA}^2 (2S_{th,pre} + S_{th,post}) \int_{-\infty}^{\infty} h_{LP}(t_1 - \rho) h_{LP}(t_2 - \rho) d\rho, \quad (B.102)
 \end{aligned}$$



$$\begin{aligned}
R_{V_{LP,a,r}V_{LP,b,r}}(t_1, t_2) &= \\
& Z_{TIA}^2 R_{pd}^2 \int_{-\infty}^{\infty} \int_{-\infty}^{\infty} h_{LP}(t_1 - \rho_1) h_{LP}(t_2 - \rho_2) \left[R_{P_{z_1}P_{z_2}}(\rho_1, \rho_2) \right. \\
& \quad \left. - R_{P_{z_1}P_{z_3}}(\rho_1, \rho_2) - R_{P_{z_2}P_{z_2}}(\rho_1, \rho_2) + R_{P_{z_2}P_{z_3}}(\rho_1, \rho_2) \right] d\rho_1 d\rho_2 \\
& - Z_{TIA}^2 S_{th,pre} \int_{-\infty}^{\infty} h_{LP}(t_1 - \rho) h_{LP}(t_2 - \rho) d\rho \quad (B.103)
\end{aligned}$$

$$\begin{aligned}
R_{V_{LP,a,r}V_{LP,c,r}}(t_1, t_2) &= \\
& Z_{TIA}^2 R_{pd}^2 \int_{-\infty}^{\infty} \int_{-\infty}^{\infty} h_{LP}(t_1 - \rho_1) h_{LP}(t_2 - \rho_2) \left[R_{P_{z_1}P_{z_3}}(\rho_1, \rho_2) \right. \\
& \quad \left. - R_{P_{z_1}P_{z_1}}(\rho_1, \rho_2) - R_{P_{z_2}P_{z_3}}(\rho_1, \rho_2) + R_{P_{z_2}P_{z_1}}(\rho_1, \rho_2) \right] d\rho_1 d\rho_2 \\
& - Z_{TIA}^2 S_{th,pre} \int_{-\infty}^{\infty} h_{LP}(t_1 - \rho) h_{LP}(t_2 - \rho) d\rho \quad (B.104)
\end{aligned}$$

$$\begin{aligned}
R_{V_{LP,a,r}V_{LP,b,r}}(t_1, t_2) &= \\
& Z_{TIA}^2 R_{pd}^2 \int_{-\infty}^{\infty} \int_{-\infty}^{\infty} h_{LP}(t_1 - \rho_1) h_{LP}(t_2 - \rho_2) \left[R_{P_{z_2}P_{z_3}}(\rho_1, \rho_2) \right. \\
& \quad \left. - R_{P_{z_2}P_{z_1}}(\rho_1, \rho_2) - R_{P_{z_3}P_{z_3}}(\rho_1, \rho_2) + R_{P_{z_3}P_{z_1}}(\rho_1, \rho_2) \right] d\rho_1 d\rho_2 \\
& - Z_{TIA}^2 S_{th,pre} \int_{-\infty}^{\infty} h_{LP}(t_1 - \rho) h_{LP}(t_2 - \rho) d\rho. \quad (B.105)
\end{aligned}$$

For a PA with OOK modulation and matched filtering a similar procedure can be used as in Section B.1, resulting in

$$\begin{aligned}
\sigma_{V_{LP,a,r}}^2(k T_s) &= R_{V_{LP,a,r}}(k T_s, k T_s) - E[V_{LP,a,r}(k T_s)]E[V_{LP,a,r}(k T_s)] \\
& \approx \frac{Z_{TIA}^2 R_{pd} P_x e}{3L_{Tx} L_{Rx} L_{nw} T_s} \sum_{i=1}^N m_{i,k} + \frac{Z_{TIA}^2 R_{pd}^2 P_x^2 \tau_c}{96L_{Tx}^2 L_{Rx}^2 L_{nw}^2 T_s} \left[4 \sum_{i_1=1}^N \sum_{i_2=1}^N m_{i_1,k} m_{i_2,k} \right. \\
& \quad \left. + 2 \sum_{i=1}^N m_{i,k}^2 + m_{r,k}^2 \cos\left(2\Delta\phi_r + 2\phi_{r,k} - \frac{2\pi}{3}\right) \right] \\
& + \frac{Z_{TIA}^2}{T_s} (2S_{th,pre} + S_{th,post}), \quad (B.106)
\end{aligned}$$

$$\begin{aligned}
\sigma_{V_{LP,b,r}}^2(k T_s) &= R_{V_{LP,b,r}}(k T_s, k T_s) - E[V_{LP,b,r}(k T_s)]E[V_{LP,b,r}(k T_s)] \\
& \approx \frac{Z_{TIA}^2 R_{pd} P_x e}{3L_{Tx} L_{Rx} L_{nw} T_s} \sum_{i=1}^N m_{i,k} + \frac{Z_{TIA}^2 R_{pd}^2 P_x^2 \tau_c}{96L_{Tx}^2 L_{Rx}^2 L_{nw}^2 T_s} \left[4 \sum_{i_1=1}^N \sum_{i_2=1}^N m_{i_1,k} m_{i_2,k} \right. \\
& \quad \left. + 2 \sum_{i=1}^N m_{i,k}^2 + m_{r,k}^2 \cos\left(2\Delta\phi_r + 2\phi_{r,k}\right) \right] \\
& + \frac{Z_{TIA}^2}{T_s} (2S_{th,pre} + S_{th,post}), \quad (B.107)
\end{aligned}$$

$$\begin{aligned}
\sigma_{V_{LP,c,r}(kT_s)}^2 &= R_{V_{LP,c,r}V_{LP,c,r}}(kT_s, kT_s) - \mathbb{E}[V_{LP,c,r}(kT_s)]\mathbb{E}[V_{LP,c,r}(kT_s)] \\
&\approx \frac{Z_{TIA}^2 R_{pd} P_x e}{3L_{Tx}L_{Rx}L_{nw}T_s} \sum_{i=1}^N m_{i,k} + \frac{Z_{TIA}^2 R_{pd}^2 P_x^2 \tau_c}{96L_{Tx}^2 L_{Rx}^2 L_{nw}^2 T_s} \left[4 \sum_{i_1=1}^N \sum_{i_2=1}^N m_{i_1,k} m_{i_2,k} \right. \\
&\quad \left. + 2 \sum_{i=1}^N m_{i,k}^2 + m_{r,k}^2 \cos\left(2\Delta\phi_r + 2\phi_{r,k} + \frac{2\pi}{3}\right) \right] \\
&\quad + \frac{Z_{TIA}^2}{T_s} \left(2S_{th,pre} + S_{th,post} \right), \tag{B.108}
\end{aligned}$$

$$\begin{aligned}
C_{V_{LP,a,r}(kT_s)V_{LP,b,r}(kT_s)} &= R_{V_{LP,a,r}V_{LP,b,r}}(kT_s, kT_s) \\
&\quad - \mathbb{E}[V_{LP,a,r}(kT_s)]\mathbb{E}[V_{LP,b,r}(kT_s)] \\
&\approx \frac{Z_{TIA}^2 R_{pd}^2 P_x^2 \tau_c}{96L_{Tx}^2 L_{Rx}^2 L_{nw}^2 T_s} m_{r,k}^2 \cos\left(2\Delta\phi_r + 2\phi_{r,k} + \frac{2\pi}{3}\right) - \frac{Z_{TIA}^2 S_{th,pre}}{T_s}, \tag{B.109}
\end{aligned}$$

$$\begin{aligned}
C_{V_{LP,a,r}(kT_s)V_{LP,c,r}(kT_s)} &= R_{V_{LP,a,r}V_{LP,c,r}}(kT_s, kT_s) \\
&\quad - \mathbb{E}[V_{LP,a,r}(kT_s)]\mathbb{E}[V_{LP,c,r}(kT_s)] \\
&\approx \frac{Z_{TIA}^2 R_{pd}^2 P_x^2 \tau_c}{96L_{Tx}^2 L_{Rx}^2 L_{nw}^2 T_s} m_{r,k}^2 \cos\left(2\Delta\phi_r + 2\phi_{r,k}\right) - \frac{Z_{TIA}^2 S_{th,pre}}{T_s}, \tag{B.110}
\end{aligned}$$

$$\begin{aligned}
C_{V_{LP,b,r}(kT_s)V_{LP,c,r}(kT_s)} &= R_{V_{LP,b,r}V_{LP,c,r}}(kT_s, kT_s) \\
&\quad - \mathbb{E}[V_{LP,b,r}(kT_s)]\mathbb{E}[V_{LP,c,r}(kT_s)] \\
&\approx \frac{Z_{TIA}^2 R_{pd}^2 P_x^2 \tau_c}{96L_{Tx}^2 L_{Rx}^2 L_{nw}^2 T_s} m_{r,k}^2 \cos\left(2\Delta\phi_r + 2\phi_{r,k} - \frac{2\pi}{3}\right) - \frac{Z_{TIA}^2 S_{th,pre}}{T_s}. \tag{B.111}
\end{aligned}$$

where it has been assumed that $N > 1$.

Like in Section B.1, we can write

$$\mathbf{V}_{LP,r,k} = \mathbf{A}_{r,k} \mathbf{V}'_{LP,r,k} \tag{B.112}$$

where $\mathbf{V}'_{LP,r,k}$ is a vector of three independent Gaussian random variables

$$\mathbf{V}'_{LP,r,k} \triangleq \begin{bmatrix} V'_{LP,I,r}(kT_s) \\ V'_{LP,Q,r}(kT_s) \\ V'_{LP,X,r}(kT_s) \end{bmatrix}. \tag{B.113}$$

and

$$\mathbf{A}_{r,k} \triangleq [\mathbf{v}_1 \quad \mathbf{v}_2 \quad \mathbf{v}_3] \tag{B.114}$$

is a unitary matrix with columns that correspond to the eigenvectors of the covariance matrix $\mathbf{C}_{V_{LP,r,k}V_{LP,r,k}}$.

The variances of $V'_{LP,I,r}(kT_s)$, $V'_{LP,Q,r}(kT_s)$ and $V'_{LP,X,r}(kT_s)$ are equal to the eigenvalues of $\mathbf{C}_{\mathbf{V}_{LP,r,k}} \mathbf{V}_{LP,r,k}$, which are given by

$$\begin{aligned} \lambda_{1,2} = & \frac{Z_{\text{TIA}}^2 R_{\text{pd}} P_x e}{2L_{\text{Tx}} L_{\text{Rx}} L_{\text{nw}} T_s} \sum_{i=1}^N m_{i,k} \\ & + \frac{Z_{\text{TIA}}^2 R_{\text{pd}}^2 P_x^2 \tau_c}{64L_{\text{Tx}}^2 L_{\text{Rx}}^2 L_{\text{nw}}^2 T_s} \left[4 \sum_{i_1=1}^N \sum_{i_2=1}^N m_{i_1,k} m_{i_2,k} + 2 \sum_{i=1}^N m_{i,k}^2 \pm m_{r,k}^2 \right] \\ & + \frac{Z_{\text{TIA}}^2}{T_s} (3S_{\text{th,pre}} + S_{\text{th,post}}), \end{aligned} \quad (\text{B.115})$$

$$\lambda_3 = \frac{Z_{\text{TIA}}^2 S_{\text{th,post}}}{T_s}. \quad (\text{B.116})$$

The corresponding (normalized) eigenvectors are given by

$$\mathbf{v}_1 = \sqrt{\frac{2}{3}} \begin{bmatrix} \cos(\Delta\phi_r + \frac{2\pi}{3}) \\ \cos(\Delta\phi_r) \\ \cos(\Delta\phi_r - \frac{3\pi}{4}) \end{bmatrix}, \quad (\text{B.117})$$

$$\mathbf{v}_2 = \sqrt{\frac{2}{3}} \begin{bmatrix} \cos(\Delta\phi_r + \frac{\pi}{6}) \\ \cos(\Delta\phi_r - \frac{\pi}{2}) \\ \cos(\Delta\phi_r + \frac{5\pi}{6}) \end{bmatrix}, \quad (\text{B.118})$$

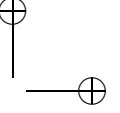
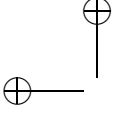
$$\mathbf{v}_3 = \frac{1}{\sqrt{3}} \begin{bmatrix} 1 \\ 1 \\ 1 \end{bmatrix}, \quad (\text{B.119})$$

Hence, the expected value of $\mathbf{V}'_{LP,r,k}$ follows from (B.99) as

$$\begin{aligned} \mathbb{E}[\mathbf{V}'_{LP,r,k}] &= \mathbb{E}[\mathbf{A}_{r,k}^{-1} \mathbf{V}_r(l \cdot T_s)] = \mathbf{A}_{r,k}^T \mathbb{E}[\mathbf{V}_r(l \cdot T_s)] \\ &= \frac{Z_{\text{TIA}} R_{\text{pd}} P_x}{4\sqrt{2}L_{\text{Tx}} L_{\text{Rx}} L_{\text{nw}}} m_{r,k} \begin{bmatrix} 1 \\ 0 \\ 0 \end{bmatrix}. \end{aligned} \quad (\text{B.120})$$

For the three-way OOK receiver the output samples $V_{\text{out},r}(kT_s)$ can now be written as

$$\begin{aligned} V_{\text{out},r}(kT_s) &= V_{LP,a,r}^2(kT_s) + V_{LP,b,r}^2(kT_s) + V_{LP,c,r}^2(kT_s) \\ &= \mathbf{V}_{LP,r,k}^T \mathbf{V}_{LP,r,k} = \left(\mathbf{V}'_{LP,r,k} \right)^T \mathbf{A}_{r,k}^T \mathbf{A}_{r,k} \mathbf{V}'_{LP,r,k}. \end{aligned} \quad (\text{B.121})$$



Since $\mathbf{A}_{r,k}$ is a unitary matrix, $\mathbf{A}_{r,k}^T \mathbf{A}_{r,k}$ equals the unit matrix. As a result, we can write

$$\begin{aligned} V_{\text{out},r}(kT_s) &= \left(\mathbf{V}'_{\text{LP},r,k} \right)^T \mathbf{V}'_{\text{LP},r,k} \\ &= \left(V'_{\text{LP},\text{I},r}(kT_s) \right)^2 + \left(V'_{\text{LP},\text{Q},r}(kT_s) \right)^2 + \left(V'_{\text{LP},\text{X},r}(kT_s) \right)^2 \end{aligned} \quad (\text{B.122})$$

Since we have OOK modulation (see Subsection 4.7.2) the conditional expected values of $V'_{\text{LP},\text{I},r}(kT_s)$, $V'_{\text{LP},\text{Q},r}(kT_s)$ and $V'_{\text{LP},\text{X},r}(kT_s)$ are given by

$$\begin{aligned} \text{E} \left[V'_{\text{LP},\text{I},r}(kT_s) \mid A_{r,k} = 0 \right] &= \text{E} \left[V'_{\text{LP},\text{Q},r}(kT_s) \mid A_{r,k} = 0 \right] \\ &= \text{E} \left[V'_{\text{LP},\text{X},r}(kT_s) \mid A_{r,k} = 0 \right] = \text{E} \left[V'_{\text{LP},\text{Q},r}(kT_s) \mid A_{r,k} = 1 \right] \\ &= \text{E} \left[V'_{\text{LP},\text{X},r}(kT_s) \mid A_{r,k} = 1 \right] = 0, \end{aligned} \quad (\text{B.123})$$

$$\text{E} \left[V'_{\text{LP},\text{I},r}(kT_s) \mid A_{r,k} = 1 \right] = \frac{Z_{\text{TIA}} R_{\text{pd}} P_x}{4\sqrt{2} L_{\text{Tx}} L_{\text{Rx}} L_{\text{nw}}}, \quad (\text{B.124})$$

When the conditional variances of $V'_{\text{LP},\text{I},r}(kT_s)$, $V'_{\text{LP},\text{Q},r}(kT_s)$ and $V'_{\text{LP},\text{X},r}(kT_s)$ for $N_1 = n$ and a binary zero are denoted by $\sigma_{\text{I},0}^2$, $\sigma_{\text{Q},0}^2$ and $\sigma_{\text{X},0}^2$, respectively, and the conditional variances of $V'_{\text{LP},\text{I},r}(kT_s)$, $V'_{\text{LP},\text{Q},r}(kT_s)$ and $V'_{\text{LP},\text{X},r}(kT_s)$ for $N_1 = n$ and a binary one are denoted by $\sigma_{\text{I},1}^2$, $\sigma_{\text{Q},1}^2$ and $\sigma_{\text{X},1}^2$, respectively, we can write

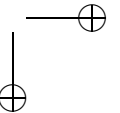
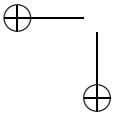
$$\begin{aligned} \sigma_{\text{I},0}^2 = \sigma_{\text{Q},0}^2 &= \frac{Z_{\text{TIA}}^2}{T_s} \left[\frac{n R_{\text{pd}} P_x e}{2L_{\text{Tx}} L_{\text{Rx}} L_{\text{nw}}} + \frac{(4n^2 + 2n) R_{\text{pd}}^2 P_x^2 \tau_c}{64L_{\text{Tx}}^2 L_{\text{Rx}}^2 L_{\text{nw}}^2} \right. \\ &\quad \left. + 3S_{\text{th,pre}} + S_{\text{th,post}} \right], \end{aligned} \quad (\text{B.125})$$

$$\begin{aligned} \sigma_{\text{I},1}^2 &= \frac{Z_{\text{TIA}}^2}{T_s} \left[\frac{(n+1) R_{\text{pd}} P_x e}{2L_{\text{Tx}} L_{\text{Rx}} L_{\text{nw}}} + \frac{(4n^2 + 10n + 7) R_{\text{pd}}^2 P_x^2 \tau_c}{64L_{\text{Tx}}^2 L_{\text{Rx}}^2 L_{\text{nw}}^2} \right. \\ &\quad \left. + 3S_{\text{th,pre}} + S_{\text{th,post}} \right], \end{aligned} \quad (\text{B.126})$$

$$\begin{aligned} \sigma_{\text{Q},1}^2 &= \frac{Z_{\text{TIA}}^2}{T_s} \left[\frac{(n+1) R_{\text{pd}} P_x e}{2L_{\text{Tx}} L_{\text{Rx}} L_{\text{nw}}} + \frac{(4n^2 + 10n + 5) R_{\text{pd}}^2 P_x^2 \tau_c}{64L_{\text{Tx}}^2 L_{\text{Rx}}^2 L_{\text{nw}}^2} \right. \\ &\quad \left. + 3S_{\text{th,pre}} + S_{\text{th,post}} \right], \end{aligned} \quad (\text{B.127})$$

$$\sigma_{\text{X},0}^2 = \sigma_{\text{X},1}^2 = \frac{Z_{\text{TIA}}^2 S_{\text{th,post}}}{T_s}. \quad (\text{B.128})$$

Now the conditional probability functions of the output samples $V_{\text{out},r}(kT_s)$ can be calculated.



When amplification is performed prior to balancing, we have $S_{\text{th,post}} = 0$ and $S_{\text{th,pre}} = S_{\text{th}}$, and hence, both the expected value and variance of $V'_{\text{LP},X,r}(k T_s)$ are zero, so we simply have $V'_{\text{LP},X,r}(k T_s) = 0$. As a result, (B.122) reduces to (B.23), so the derivation of the probability of error for the three-way OOK receiver is similar to the derivation in Section B.2. Hence, one can find the probability of error that is given in (6.71).

When amplification is performed after balancing, however, we have $S_{\text{th,pre}} = 0$ and $S_{\text{th,post}} = S_{\text{th}}$. When a binary zero is transmitted the expected values of $V'_{\text{LP},I,r}(k T_s)$, $V'_{\text{LP},Q,r}(k T_s)$ and $V'_{\text{LP},X,r}(k T_s)$ are zero, whereas the variances of $V'_{\text{LP},I,r}(k T_s)$ and $V'_{\text{LP},Q,r}(k T_s)$ are the same but different from the variance of $V'_{\text{LP},X,r}(k T_s)$. Hence, the conditional probability density function of the output sample for a binary zero can be found by convolving a central χ^2 -distribution with two degrees of freedom

$$f_{I^2+Q^2,0}(v) = \begin{cases} \frac{1}{2\sigma_{I,0}^2} \exp\left(-\frac{v}{2\sigma_{I,0}^2}\right) & , v \geq 0, \\ 0 & , v < 0, \end{cases} \quad (\text{B.129})$$

and a central χ^2 -distribution with one degree of freedom

$$f_{X^2,0}(v) = \begin{cases} \frac{1}{\sigma_{X,0}\sqrt{2\pi}v} \exp\left(-\frac{v}{2\sigma_{X,0}^2}\right) & , v \geq 0, \\ 0 & , v < 0, \end{cases} \quad (\text{B.130})$$

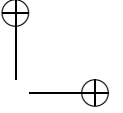
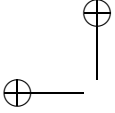
resulting in

$$\begin{aligned} f_0(v) &= \int_{-\infty}^{\infty} f_{I^2+Q^2,0}(v-x)f_{X^2,0}(x) dx \\ &= \begin{cases} \frac{\exp\left(-\frac{v}{2\sigma_{I,0}^2}\right)}{2\sigma_{I,0}^2\sigma_{X,0}\sqrt{2\pi}} \int_0^v \frac{1}{\sqrt{x}} \exp\left(\frac{x}{2\sigma_{I,0}^2} - \frac{x}{2\sigma_{X,0}^2}\right) dx & , v \geq 0, \\ 0 & , v < 0. \end{cases} \end{aligned} \quad (\text{B.131})$$

Substituting $x = y^2$ this can easily be shown to result in

$$f_0(v) = \begin{cases} \frac{\exp\left(-\frac{v}{2\sigma_{I,0}^2}\right)}{\sigma_{I,0}\sqrt{\sigma_{X,0}^2 - \sigma_{I,0}^2}} \left[\frac{1}{2} - Q\left(\sqrt{\frac{v}{\sigma_{X,0}^2} - \frac{v}{\sigma_{I,0}^2}}\right) \right] & , v \geq 0, \\ 0 & , v < 0. \end{cases} \quad (\text{B.132})$$

When a binary one is transmitted, a similar approximation can be made as in the case of the four-way receiver; see (B.32). Performing a similar analysis as for the four-way receiver then results in the probability of error that is given by (6.74).



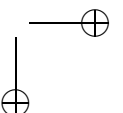
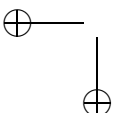
Acknowledgments

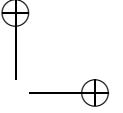
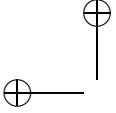
The research work that is described in this thesis was carried out in the Telecommunication Engineering (TE) group at the University of Twente. This would not have been possible without the generous financial support of Philips Research. Moreover, the thesis would not have been completed in its current form without the help of several colleagues, friends and relatives that I would like to acknowledge here.

First of all I would like to express my gratitude to my promoter, professor Wim van Etten. He offered me the opportunity to do this PhD project, and gave me the freedom to carry out my research work largely according to my own wish and insight. We spent many hours on fruitful discussions during which he provided me with comments after carefully reading draft versions of my publications and thesis. I benefited much from his sharing of interesting experiences, and I am most grateful for his patience and confidence during the times when things did not run as smoothly as both of us would have liked them to. My assistant promoter Geert Heideman is acknowledged for his guidance during the first two years of my PhD research, and for taking the time to read my thesis, even after his retirement.

I would also like to thank the remaining members of my PhD committee, professors Ton Mouthaan, Jaap Haartsen, Alfred Driessen, Kees van Bochove, Alle-Jan van der Veen and Geert Morthier for taking the time to read my thesis and come to Enschede to be part of the opposition during the ceremony.

The other colleagues of the TE group and related groups should be acknowledged here as well. Bo Tian, Igor Radovanović, Hamid Malkaoui, David Marpaung and Rajeev Roy have made working in room 9164 of the EL/tn building a real pleasure. Thank you all for that. Chris Roelofzzen, thank you very much for sharing your experience in integrated optics technology with me, and for your assistance in the laboratory work, which was crucial in order to find out that I should really focus on theoretical work within the framework of this particular project... Rajan Srinivasan, thank you for your help with L^AT_EX and the English language, and for our interesting discussions on “what doing science is all about”. Douwe Geuzebroek and Roland Meijerink, thank you both for your useful advices on the thesis printing and on organizational matters around my PhD defense. Annemiek Janssen, thank you for taking most of the administrative burden out of my hands.



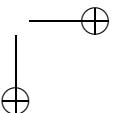
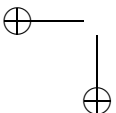


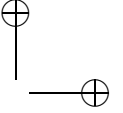
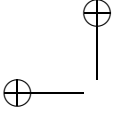
Several students contributed to this project by doing their research assignments on related topics. Martijn Souman, Niek Niëns, Robert Taniman, Qi Cui, Leimeng Zhuang and Robbin Blokpoel, thank you for your contributions, for being a sounding board to discuss my research ideas with, and for enabling me to work on my teaching skills. It was a real pleasure to work with you.

One of the most important things I have learned during my PhD period is that being both happy and successful in a job in engineering science not only requires talent, effort, persistence and determination, but also an ability to cope with disappointments and to shift your mind to other things at proper times. For that I would not only like to thank Paul Vogel and Lena Hummel for their professional advice, but also my friends Tom and Emilijah Tornij, Niels and Laura de Ruiter, Peter Visser, René and Joke Kromhof, Bernd Holstein, Hans Roelofs, Paul Wijnstra, Edwin Mulkens, Jeroen Thijs, Ralph Maassen, Niels de Pril and —last but not least— all my team mates and staff at football club “v.v. Drienerlo” in Enschede.

Most of all I must thank my parents Ferdinand and Jannie, and my brothers Wilco and Roland for their support and unconditional care, especially during times when I needed it the most.

Arjan Meijerink
Enschede, The Netherlands
November 16, 2005





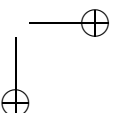
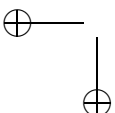
Biography

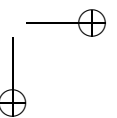
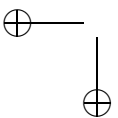
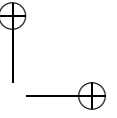
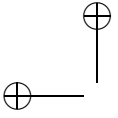
Arjan Meijerink was born in Almelo, The Netherlands, in 1976. He attended secondary school and high school in Almelo, and obtained his “Atheneum” diploma from “C.S.G. Het Noordik” in 1995.

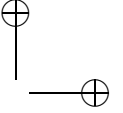
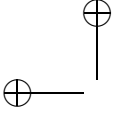
Subsequently he started studying electrical engineering at the University of Twente in Enschede, The Netherlands. After finishing the compulsory part of the curriculum, he attended several elective courses on telecommunications, telematics and signal processing. In 2000 he did an internship at Ericsson Business Mobile Networks in Enschede, developing error concealment techniques for Bluetooth[™] voice links, resulting in a patent. He received the MSc degree (with honors) in 2001, for his thesis on performance analysis of a time-slotted generalized coherence multiplexing system.

From 2001 to 2005 he was employed as a research assistant in the Telecommunication Engineering group at the University of Twente. He was engaged in research on optical communication systems based on coherence multiplexing, resulting in this thesis. During his PhD research he authored and co-authored several papers for international journals, conferences and symposia. He was presented the Best Young Researcher Presentation award at the 22nd Symposium on Information and Communication Theory in the Benelux in May 2001, the second prize in the IEEE Region 8 Student Paper Contest in July 2001 and the second prize in the KIVI Telecommunication Award contest in April 2004.

Arjan Meijerink is currently employed as a postdoctoral researcher in the Telecommunication Engineering group at the University of Twente. His work involves designing the front-end of a satellite receiver system based on optical beam forming.



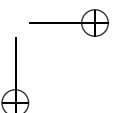
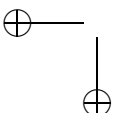


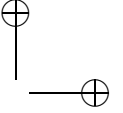
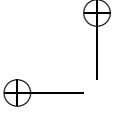


List of publications

Publications related to this thesis

1. W. van Etten and A. Meijerink, "Optical stabilization of coherence multiplex output signal by means of a phase diversity network," *Proc. of the 6th IEEE/LEOS Symp. in the Benelux*, Brussels, Belgium, December 2001, pp. 149–152.
2. A. Meijerink, G. H. L. M. Heideman, and W. van Etten, "BER analysis of a DPSK phase diversity receiver for coherence multiplexing," *Proc. of the 23rd Symp. on Inform. Theory in the Benelux*, Louvain-la-Neuve, Belgium, May 2002, pp. 269–276.
3. A. Meijerink, G. H. L. M. Heideman, and W. van Etten, "Performance evaluation of an OOK coherence multiplex receiver based on 4×4 phase diversity detection," *Proc. of the XXVIIIth URSI G.A.*, Maastricht, The Netherlands, August 2002, paper D7.O.6.
4. A. Meijerink, G. H. L. M. Heideman, and W. van Etten, "Performance evaluation of an OOK coherence multiplex receiver based on 4×4 phase diversity detection," *Tijdschrift van het NERG*, vol. 67, no. 3, 2002, pp. 113–116.
5. A. Meijerink, G. H. L. M. Heideman, and W. van Etten, " M -ary (D)PSK modulation in coherence multiplex systems," *Proc. of the 7th IEEE/LEOS Symp. in the Benelux*, Amsterdam, The Netherlands, December 2002, pp. 207–210.
6. A. Meijerink, N. Niëns, G. H. L. M. Heideman, and W. van Etten, "Chromatic fiber dispersion in single-mode coherence multiplex systems," *Proc. of the 10th SCVT in the Benelux*, Eindhoven, The Netherlands, November 2003, paper 9.
7. R. O. Taniman, A. Meijerink, W. van Etten, and J. C. Haartsen, "Indoor RF signal distribution using a coherence multiplexed/subcarrier multiplexed optical transmission system," *Proc. of the 10th SCVT in the Benelux*, Eindhoven, The Netherlands, November 2003, paper 17.

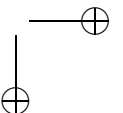
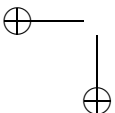




8. A. Meijerink, R. O. Taniman, G. H. L. M. Heideman, and W. van Etten, "Comparison of three coherence multiplex system topologies," *Proc. of the 7th IEEE/LEOS Symp. in the Benelux*, Enschede, The Netherlands, November 2003, pp. 141–144.
9. A. Meijerink, G. H. L. M. Heideman, and W. van Etten, "Balanced optical phase diversity receivers for coherence multiplexing," *J. Lightwave Technol.*, vol. 22, no. 11, pp. 2393–2408, November 2004.
10. R. J. Blokpoel, A. Meijerink, and W. van Etten, "Traffic control in coherence-multiplexed networks," *Proc. of the 12th SCVT in the Benelux*, Enschede, The Netherlands, November 2005, to be published.

Other publications

1. A. Meijerink, G. H. L. M. Heideman, W. van Etten, "A generalization of a coherence multiplexing system," *Proc. of the 7th SCVT in the Benelux*, Leuven, Belgium, October 2000, pp. 5–12.
2. A. Meijerink, G. H. L. M. Heideman, W. van Etten, "Generalization and performance improvement of a coherence multiplexing system," *Proc. of the 22nd Symp. on Inform. Theory in the Benelux*, Enschede, The Netherlands, May 2001, pp. 59–66.
3. A. Meijerink, "Performance improvement of a generalized coherence multiplexing system," *Proc. of the IEEE Region 8 Eurocon'2001 Int. Conf. on Trends in Commun.*, Bratislava, Slovakia, July 2001, pp. XXXII–XXXV.
4. I. Radovanović, G. H. L. M. Heideman, H. Siasi, A. Meijerink, W. van Etten, "Addressable spectrally encoded optical CDMA system for application in access and local area networks," *Proc. of the XXVIIIth URSI G.A.*, Maastricht, The Netherlands, August 2002, paper D7.O.4.
5. J. C. Haartsen, A. Meijerink, A. Bekkaoui, A. Taban, and J. L. Tauritz, "Novel wireless modulation technique based on noise," *Proc. of the 11th SCVT in the Benelux*, Ghent, Belgium, November 2004, paper 8.
6. J. C. Haartsen, A. Meijerink, X. Shang, J. W. Balkema, and J. L. Tauritz, "New wireless modulation scheme based on frequency-offset technique," *Proc. of the 12th SCVT in the Benelux*, Enschede, The Netherlands, November 2005, to be published.





Optical communication has made an enormous advance in the last two decades. The core network of modern public telecommunication systems mainly consists of optical fiber transmission systems, supporting high-speed transmission over large distances. Fortunately, the huge costs of such systems are shared by a vast number of users.

Increasing bandwidth demands of end users have led to a call for optical transmission in short-range systems, such as subscriber networks, local area networks, and interconnects. Costs are a critical issue in such systems since every single user has to settle for his individual part of the infrastructure.

Coherence multiplexing is an interesting technique from a cost point of view. It enables multiple users to share a common optical fiber using broadband optical sources and relatively simple planar optical circuits.

This thesis addresses the applicability of coherence multiplexing in typical short-range applications, including RF feeding. The basic principles are explained, and several multiplexing and demultiplexing techniques are proposed and analyzed. Principal issues dealt with are number of channels that can be multiplexed, maximum bit rates that can be supported, and maximum link lengths that can be realized. Although the research is focussed on system-level aspects, specific directions for further research in related areas are given.

